PREDICTION OF TWO DIMENSIONAL SEPARATED FLOWS ABOUT A CIRCULAR CYLINDER IN THE PRESENCE OF BOUNDARIES

by

WISNU WARDHANA

A Thesis submitted for the degree of
Doctor of Philosophy

Department of Marine Technology

The University of Newcastle Upon Tyne
March 1995

ABSTRACT

The behaviour of the hydrodynamic loading experienced by a circular cylinder in the presence of boundaries has been the subject of investigation by various investigators in recent years. Amongst other things it is relevant to the design of offshore structures and subsea pipelines. It is important to be able to assess the behaviour of such components of an offshore structure because it has to be designed to withstand loading due to flow interactions which are complicated in nature and not yet fully understood.

To gain a clearer insight into the effects of anodes on the overall loading of an offshore structure, for example, the local flow around a cylindrical member in the presence of boundaries must be understood. In the present study, a numerical model based on the Discrete Vortex Method has been developed as a means of analysis of such flows since, in comparison to experimental methods, it is a less expensive and less time consuming approach in gaining that knowledge. The algorithm is developed in such a way as to enable application to a range of cylinder / cylinder, cylinder / anode, and cylinder / wall configurations subject to a variety of steady and time dependent flows.

The technique has been applied in a number of case studies which include the investigation of the flow interactions occuring when two cylinders are in close proximity and also when a cylinder is close to a plane boundary. The engineering applications are the interference of structurel members, the loading on structural elements due to the presence of anodes, and the loading on free spanning subsea pipelines.

The in-line and transvese force coefficients arising from the case studies and also the flow patterns obtained are presented in order to provide a more detail description of the flow phenomena and interactions involved. The comparison of the results with both experimental and numerical evidence is also presented and the range within which the algorithm produces good results is identified.

This work is dedicated to my mother Ny. Soepartiningsih,
who passed away during this study, and to my father
R. Soedjalmo Anggodiredjo, for all their sacrifices.

ACKNOWLEDGMENTS

The author would like to express his deepest gratitude to his supervisor, Martin J. Downie PhD. for his patience, continual assistance and encouragement during the whole period of this study. His personality, his expertise and experience in fluid dynamics and his many efforts in helping the author in some difficult situations will be remembered by the author as a priceless contribution.

The author also wishes to thank to R.L. Townsin PhD. for his advice and supervision in the early years of this study.

This stage would have never been reached without the provision and guidance in understanding the Discrete Vortex Method algorithm devised by Brian A. Murray PhD. from which this present work originated. All his efforts and friendship are deeply appreciated.

Special thanks is also given to Paul J. Binks for his help in typing, to Christos Atalianis for his contribution in producing pictures, and to Paulus Indiyono, C. Matsuhira, Siddhi Saputro, and Tjipto Leksono, for their help in the final preparation of this thesis.

This study would never have been realized without any support from Ir. Naufal Bahreisy, the Director of the PPIL-PIDT, BPP Teknologi Jakarta and without the financial support of Ir. Auzai and Ir. Suleman Wiriadidjaja, the directors of PT. PAL Surabaya Indonesia, to whom the author would also like to thank.

Last but not least, a special word of thanks is also given to the author's wife Meitha Soetardjo, his daughter Diar M. Wardhana and his son Ede M. Wardhana, for their moral support, patience and understanding during these six years of study and separate lives.

Contents

Chapter I

INTRODUCTION

The hydrodynamics of the circular cylinder has been the subject of many theoretical and experimental studies, particularly since the development of the offshore industry in *1940*'s. The circular cylinder is the most common shape used in the design of the offshore structures due to its simple geometry, ease to manufacture and also its good hydrodynamic behaviour. Furthermore, data related to cylinder hydrodynamics and structural characteristics are widely available, which is convenient in the design process.

Offshore platforms have to be designed so as to withstand the environmental forces, such as those due to waves, currents and wind, either singly or in combination. The fluid loading on the cylindrical members of such structures makes a most significant contribution to the overall structural loading.

When a cylinderical member of one of these structures is located in isolation or far from the others, its hydrodynamic characteristics will be similar to those of a cylindrical member in a fluid with a free surface but otherwise unbounded. However, its characteristics can be significantly different when another member is positioned near to it or when it is placed close to an impermiable boundary such as the sea bed. Sometimes in such structures two members can be very close together such as in the case of a cylindrical member and a sacrificial anode. The change in hydrodynamic characteristics can be seen in the change of the wake created around or behind the cylinder in terms of the flow pattern, the local velocity or the local pressure.

Some hydrodynamic phenomena related to the flow around one or more cylindrical bodies, are still not fully understood due to their complexity. Examples are separation, boundary layer interactions, turbulence interaction, vortex shedding, and recirculating flows. On the other hand the investigation of vortex shedding is important in aerodynamic drag, structural vibration and turbulent mixing and so many experiments have been conducted to get a greater understading of these flow phenomena. The earliest recorded observation of the phenomena of vortex shedding can be found in the surface pattern of a fluid streaming past an obstacle, drawn by Leonardo da Vinci in about sixteenth century. In recent years,

investigators such as **Sarpkaya** [**84**] and **Sarpkaya** and **Isaacson** [**87**] have made exhaustive studies of the flow around cylinders in uni-directional and oscillatory flows. Such experiments have been performed in wind tunnels and towing tanks for the uni-directional flows, and in oscillating water column U-Tubes and wave flumes for the oscillatory flows.

It has been shown that the interaction of fluid and structure can produce a vortex-induced oscillation of the structure if its natural frequency is near the Strouhal frequency at which vortices are shed from it. This can results in a large extra load on the structure and can produce a severe fatigue damage that is not only costly but potentially can lead to loss of life.

The nature of the fluid / structure interaction can be influenced by the presence of a boundary such as that of another cylinder or the sea bed, in a manner that depends on the distance of the gap between the two, expressed in terms of the gap diameter ratio, and on the cylinder configuration, such as whether they are a side by side, tandem or staggered arrangement. The flow phenomena around two cylinders in interaction is obviously more complex than that around an isolated one, especially at the stage when the boundary layer around the two cylinders interact with each other.

Zdravkovich [**116**] shows that when two cylinders are arranged in a side-by-side configuration, the drag of each cylinder can increase significantly for a gap less than four times the cylinder diameter. A significant change in the vortex ahedding from the cylinders can be detected when the gap reduces to less than two cylinder diameters, the wake shed by the two cylinders is attached alternately to one or other of the cylinders. In this case, the frequency of oscillation has dual values which could be double or half that of an isolated cylinder and this, in turn, can lead to a greater potential damage of a structure having such a configuration. This phenomenon can be attributed to the boundary layer interaction in the gap region as the gap gets closer. Similar effects can also occur in other configurations, even though they are generally less pronounced compared to the case of the side-by-side arrangement.

When a structure is arranged in such a way that it is similar to a cylinder placed between two walls, the effect of blockage can increase the drag by up to *200*% higher than that of an isolated cylinder if the gap is less than two and half cylinder diameters (**Stansby** and **Slaouti** [**102**]). This is mainly due to an effect in which the fluid flowing between the walls is now 'blocked' by the presence of the

cylinder which leads to an increase in the drag caused by the increase in the local velocity around the gap region and also the reflected wake around it (**Lewis [60]**). The wall-cylinder boundary layer interaction can make the flow phenomena even more complicated and usually results in a more 'noisy' vortex shedding process.

A practical example of an undesirable effect due to flow about a cylinder in close proximity to a plane boundary is the cylinder/sea bed interaction as occurring for under water pipelines used by the offshore industry. Due to the development of an 'asymetric' wake, a lift force directed away from the sea bed occurs and this can cause sea bed instabilities and can be a damaging factor for the pipe line. In designing a structure to be capable of withstanding environmental loads of this nature, it is necessary to be able to assess its unsteady behaviour in relation to fluid/structure interaction, and be able to predict the hydrodynamic loads involved.

In this modern era, in which computing costs are decreasing year by year, numerical approaches are increasingly used in simulating the type of complex flow described above. In developing any numerical method it is necessary to validate the method by detailed comparison with experimental result and other theoretical studies where they are available. To this end a wide ranging literature survey has been undertaken. Searches have been carried out on topics relating to the underlying physical processes associated with the phenomena modelled in the present study, experimental work undertaken by other authors in the same area, and relevant theoretical and numerical work in the literature. The topics dealt with in the present study cover a range subjects which are described in separate chapters. Each chapter references works relevant to the physical phenomena and the theoretical and numerical studies reported in the literature that are relevant to the subject under discussion. In this manner the results of the case studies can be assessed in the context of the works of other investigators and the model, to a greater or lesser degree, validated.

Generally, time dependent flow problems are solved numerically using either the Navier Stokes equations or the more simple potential flow theory. The finite difference solution of the Navier-Stokes equations is a grid dependent solution and in general is practical only for low Reynolds number regimes. This is because in order to obtain good definition of the flow, larger and larger numbers of grid points are required in the region close to the body since the vorticity is increasingly confined narrower and narrower regions as the Reynolds number is increased. At high Reynolds number regimes, the convection terms are much larger than the

diffusive one and this results in a tendency for the finite difference scheme to become ill-conditioned.

Solution of time dependent separated flows has been achieved using a potential flow approach known as the discrete vortex method which involves the continuous representation of vorticity in the flow by discrete point vortices. The foundations of the study of vortex dynamics were laid down by **Helmholtz** in *1858* and **Lord Kelvin** in *1869*. The concept of vortex dynamics is based on the idea that the physical representation of the mechanics of the flow as vortex motion determines all the physical characteristics of the flow. The model represents the fluid as an irrotational incompressible flow, in which the vorticity takes the form of embedded singularties and in which the evolution of the distribution of vorticity can be determined in accordance with the Helmholtz and Kelvin theorems. From the vortex motion the velocity and pressure fields can be calculated. There are advantages in describing fluid flows in terms of their vortex dynamics. The study of vortex field structures in real flows leads to a deeper comprehension of the nature of the physical phenomena involved (see **Moore** [**68**]). The method is in some ways more convenient and relatively easier to use than its alternatives as it is based on a Lagrangian representation of the flow than can be simply translated into an algorithm which, although computationally intensive, can be effectively implemented on modern computers.

Another advantage of the basic discrete vortex method is that it is grid independent. In fact, most contemporary methods introduce a grid over the computational domain as it increases the computational efficiency and allows the introduction of many more discrete vortices. However, in such cases the grid can be chosen to give high resolution in those areas in which it is required and the calculations confined to active grid nodes.

The present study is concerned with modelling interaction flows between cylinders in close proximity to one another, and between cylinders and plane surfaces. The approach is a numerical one using the discrete vortex based method mentioned above. Highly sophisticated models of this type have been developed for the flow about single cylinders, but their very sophistication can make them difficult to adapt for more complex flows. In this case a simple basic model has been adopted and the study has concentrated on developing techniques for dealing with cylinder / cylinder and cylinder / wall interactions. The model has been used to simulate the flows described in detail in the later sections. The numerical strategies will be presented in chapter *IV* after the next two chapters which introduce the fluid

phenomena and the basic theory involved. A number of case studies have been undertaken for various types of cylinder configuration and also for the case of flow about a cylinder in close proximity to one or two plane surfaces. The computed results have been compared with experiment and the numerical results of other investigators where possible. An account of these studies and the results obtained is presented in the following chapters. In the final chapter the model is assessed in the context of the case study results and suggestions are made for further work and other implementations that may be undertaken in the future.

Chapter II

THE FLOW PHENOMENA

2.1 The Flow Around A Cylinder

2.1.1 Uni-Directional Flow

Experimental results show that there are several flow phenomena that can be observed when a body is placed in a flowing stream. One of the important aspects of the flow is the behaviour of the fluid as it passes over the body surface in the regions defined as the boundary layers. Two boundary layers are developed, each starting at the forward stagnation point and extending backwards until it reaches the backward stagnation point. The stagnation points represent two points of zero flux on the upstream and downstream faces of the body.

When the Reynolds number is around *three*, the boundary layers experience an adverse pressure gradient on the rear face of the body which forces them to separate from its surface before reaching the downstream stagnation point. The location at the surface where the boundary layers start to separate is called the separation point and the angle between the downstream stagnation point and these separation points is termed the separation angle.

An increase of the Reynolds number beyond *three* causes the boundary layers to extend out from the surface to develop the shear layers. These layers represent regions where the fluid velocity just outside and inside the layers are different in magnitude. Eventually they roll-up to form regular, symmetric vortices immediately behind, and attached to the body. These vortices continue to grow until the Reynolds number reaches around 40, at which point the separation angle has reduced to about $130°$.

At this point asymmetry begins to appear and when the Reynolds number reaches around 80 or 90, one of the vortices breaks away from the body and is convected downstream. During the formation of a new vortex in its place, the second vortex breaks away also and a regular pattern of skew-symmetric vortices begins.

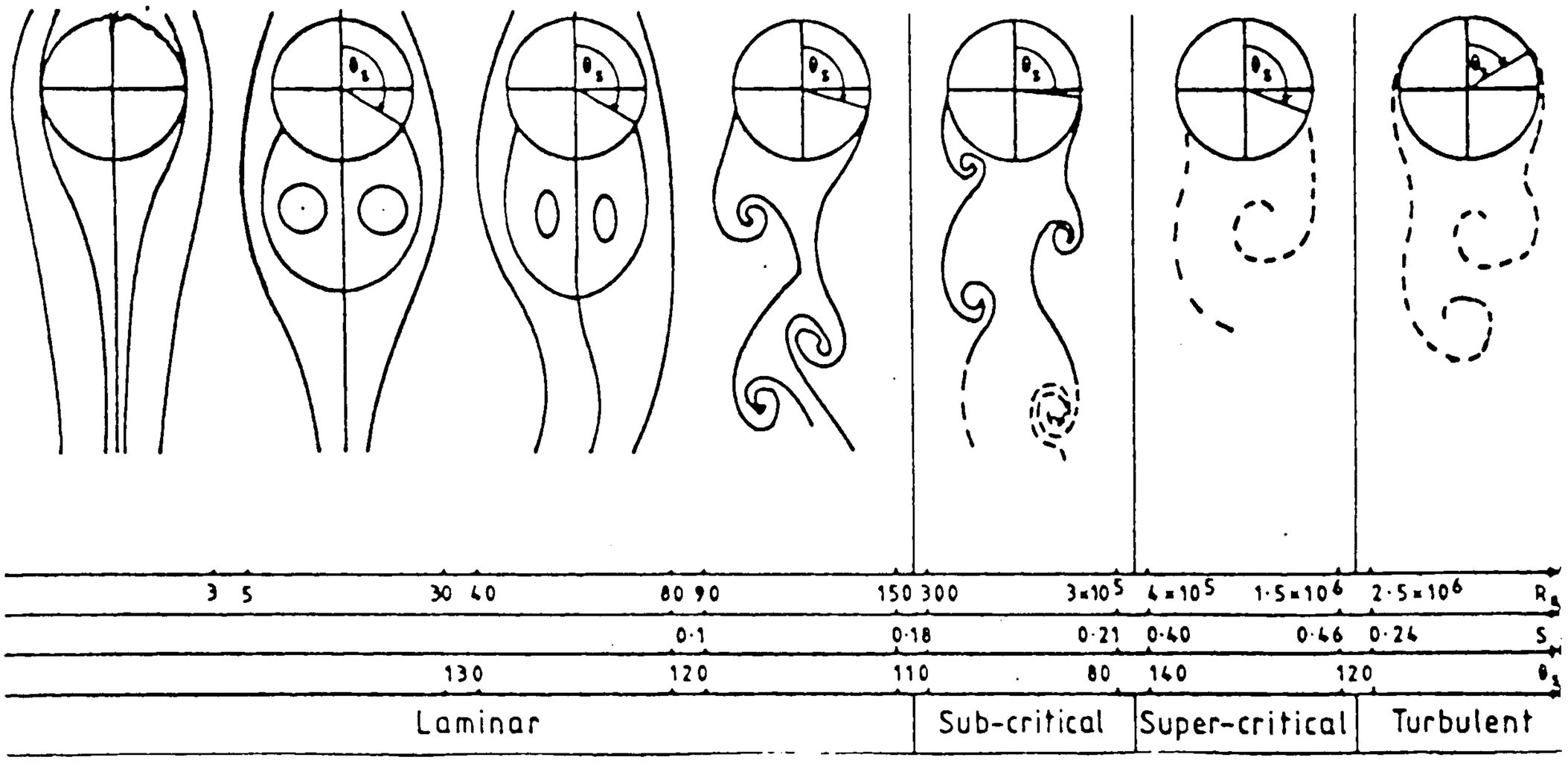

Figure 2.1.- *Flow Regime of a Cylinder in Uni-Directional Flow.*

Downie[26] produced the flow regime diagram in figure (**2.1**), which shows that at the Reynolds number between *100* and *300* the vortex street remains laminar for up to about *100* diameters downstream of the body, with the Strouhal number ($\frac{nf}{D}$) between *0.1* and *0.18* and the separation angle decreasing to around *110°*, as shown in figure (**2.2**). For Reynolds numbers closer to *300*, turbulence starts to develop and this behaviour continues to spread along the street towards the body as the Reynolds number reaches above *300*. Street vortices, as close as *50* diameters to the body, begin to lose their skew-symmetric structure and the turbulence effects begin to move closer to the body along the shear layer.

At about the end of this sub-critical region ($R_e = 300 \sim 3 \times 10^5$) the flow around the stagnation point is now becoming turbulent. At this stage the Strouhal number increases to around *0.2* and the separation angle decreases to as low as *80°*. At Reynolds number of about 4×10^5, the separation angle suddenly increases to

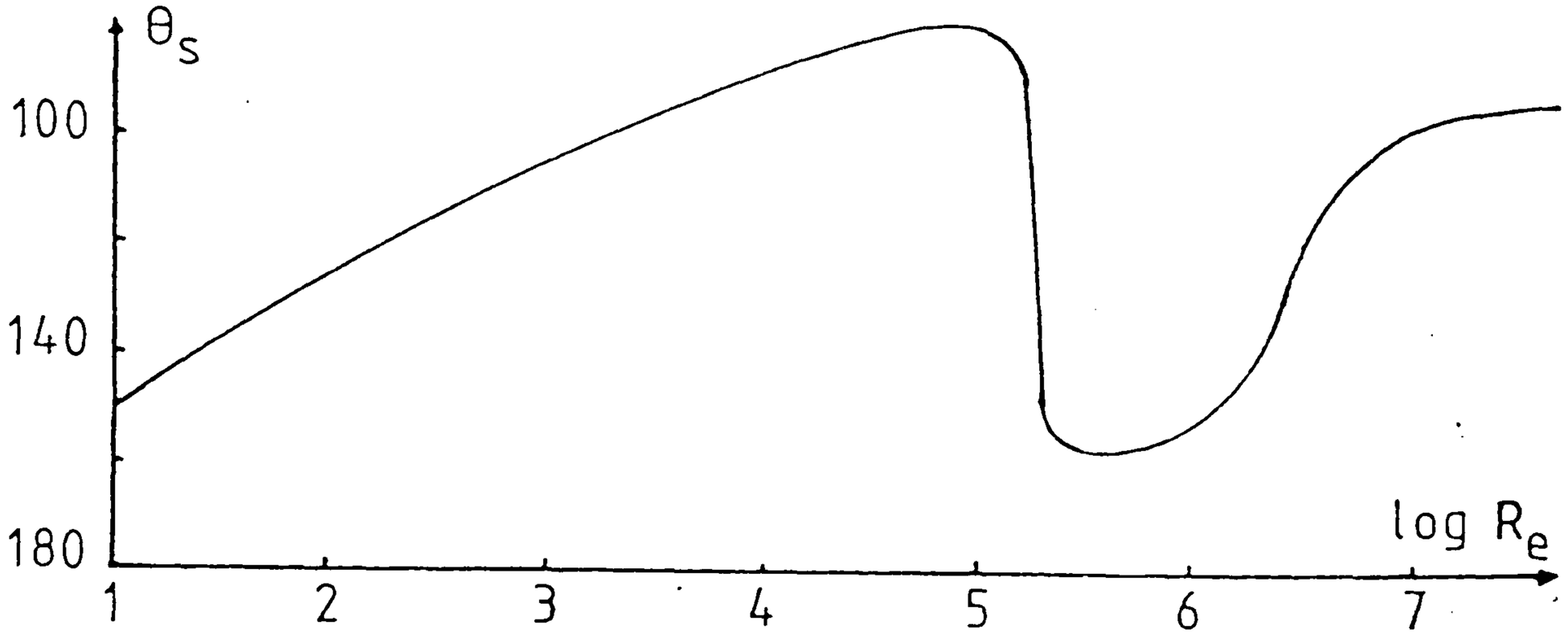

Figure 2.2.- *Separation Angle Vs. Reynolds Number.*

140° as the boundary layer itself becomes turbulent because turbulent boundary layers are more resistant to an adverse pressure gradient than the laminar boundary layers, and so separation occurs further downstream just after transition than it did just before transition.

The flow condition at Reynolds number above this and up to 15×10^5 is characterised by increasing turbulence in the boundary layer and a decrease in the separation angle. The Strouhal number reach a value as high as *0.46*. At Reynolds number above 25×10^5, the boundary layer becomes fully turbulent and the separation angle decreases to about 110°.

The forces experienced by the body are directly related to the cycle of the vortex shedding. The pressure distribution around the body changes continously as vortices are shed and travel downstream and this leads to periodic changes in the force experienced. The component of force in line with the direction of the ambient flow is termed the *drag force*, while the other orthogonal component to this force is called the *lift force*.

The influence of the above flow phenomena on the separation angle and the Strouhal number as described above, and on the force coefficients is illustrated in

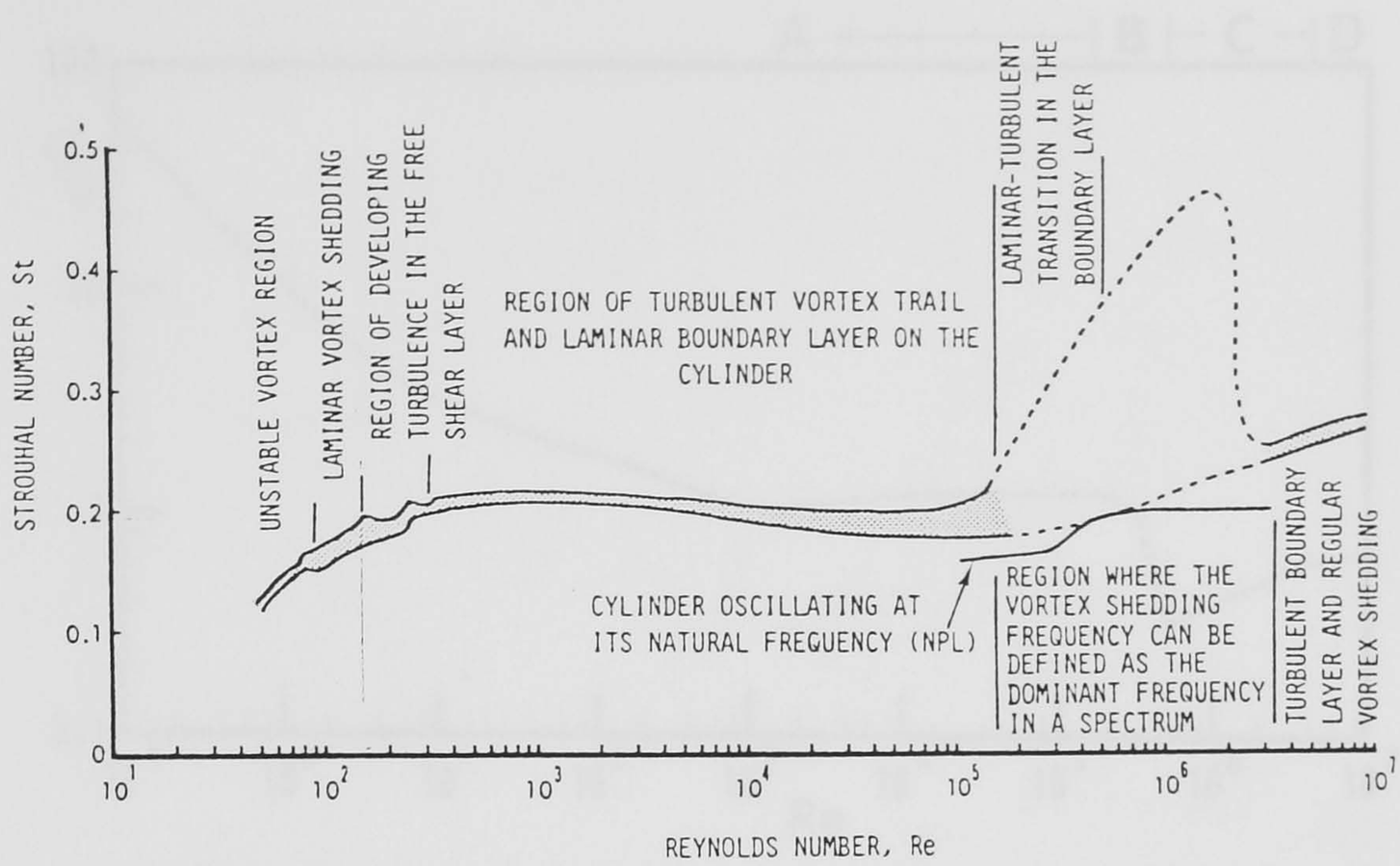

Figure 2.3.- *Strouhal number Vs. Reynolds Number.*

figures (**2.2**), (**2.3**), and (**2.4**), respectively. The drag force consistently decreases as the Reynolds number increases from laminar to sub-critical flow regimes. It reaches a relatively constant value of around *1.2* at the Reynolds number between 1×10^3 - 2×10^5. As mentioned earlier, a drop in the drag coefficient due to the turbulent effects in the boundary layer occurs between Reynolds number 3×10^5 - 5×10^5. The drag coefficient drops from *1.2* to as low as *0.3* and flows in this regime are said to have undergone the '*drag crisis*'.

This can be attributed to a narrowing of the wake as the separation points move downstream immediately following transition of the boundary layers to turbulence. The energy in the wake in this region is banded and vortices are difficult to discern. Beyond this Reynolds number, the drag starts to rise again until it reaches a value of about *0.6* at a Reynolds number of 3×10^5, at which point it appears to level off again. The process become narrow banded again and vortices can be clearly distinguished. The flow, however, is now fully turbulent.

The other force coefficient, the lift coefficient has also been investigated by many authors, see **Sarpkaya** [88]. The variation of the lift coefficient with the

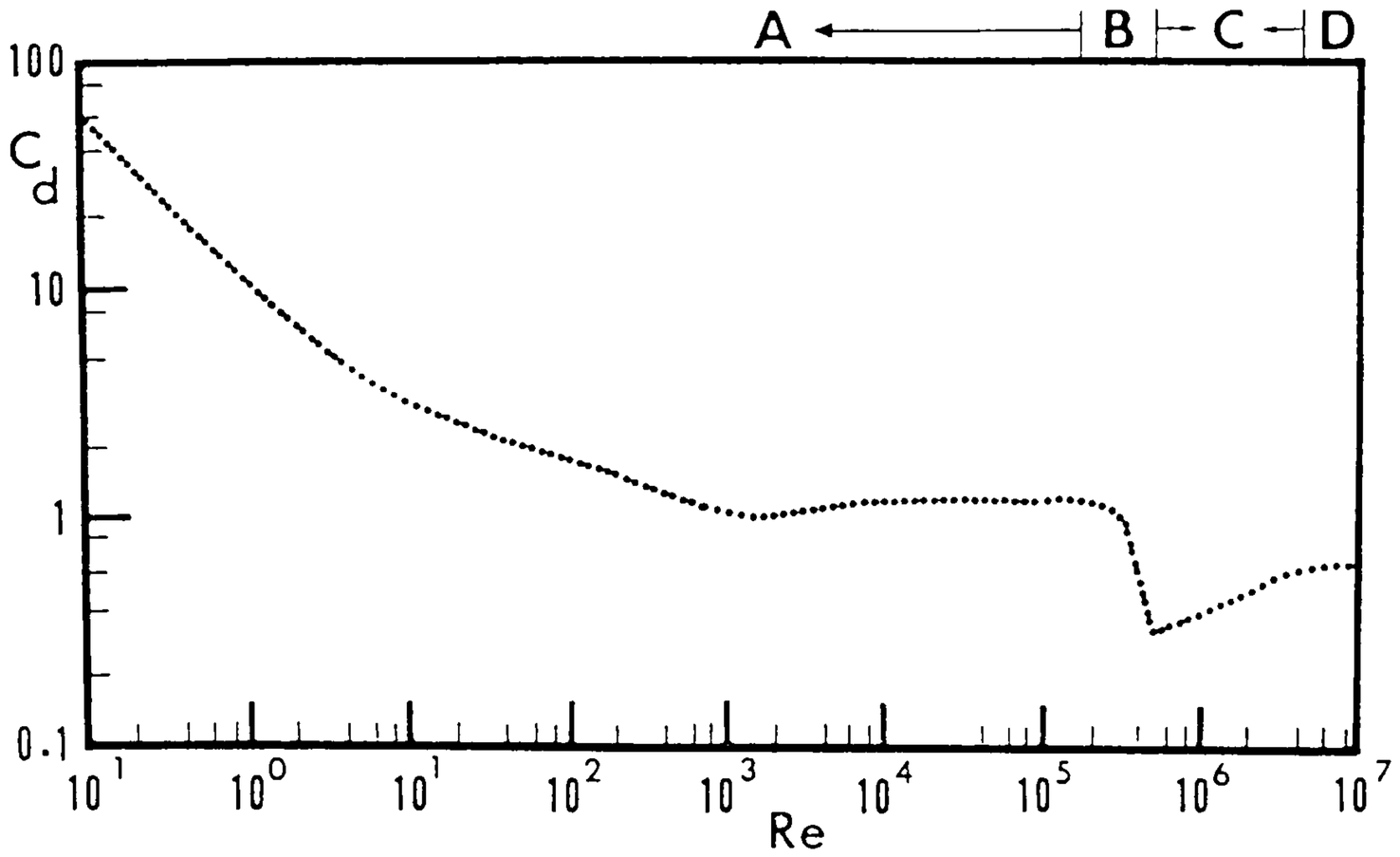

Figure 2.4.- *Drag Coefficient Vs. Reynolds Number.*

Reynolds number, as illustrated in figure (**2.5**), is expressed in terms of the peak, the mean or the root mean square values, since the lift coefficient is a fluctuating quantity.

In the laminar regime of Reynolds number under *150*, the mean value of the maximum lift coefficient of about *0.8* is to be expected. At higher Reynolds number, there is a spread in reported values of the lift coefficient (ever allowing for different approaches to presentation) which is probably connected with differences in experimental conditions and techniques adopted by different investigators. The force coefficients are difficult to quantify in the drag crisis. As the Reynolds number increases beyond this region into the super-critical and turbulent regimes, the fluctuating lift is more readily determined and may be seen to have a lower value than for the lower Reynolds number range.

The magnitude of the periodic component of the drag force is small compared with that of the steady drag and the fluctuating lift forces. The drag coefficient fluctuates with an amplitude in the order of 0.05 to 0.1 with a frequency of twice that of the lift fluctuations and the alternate vortex shedding.

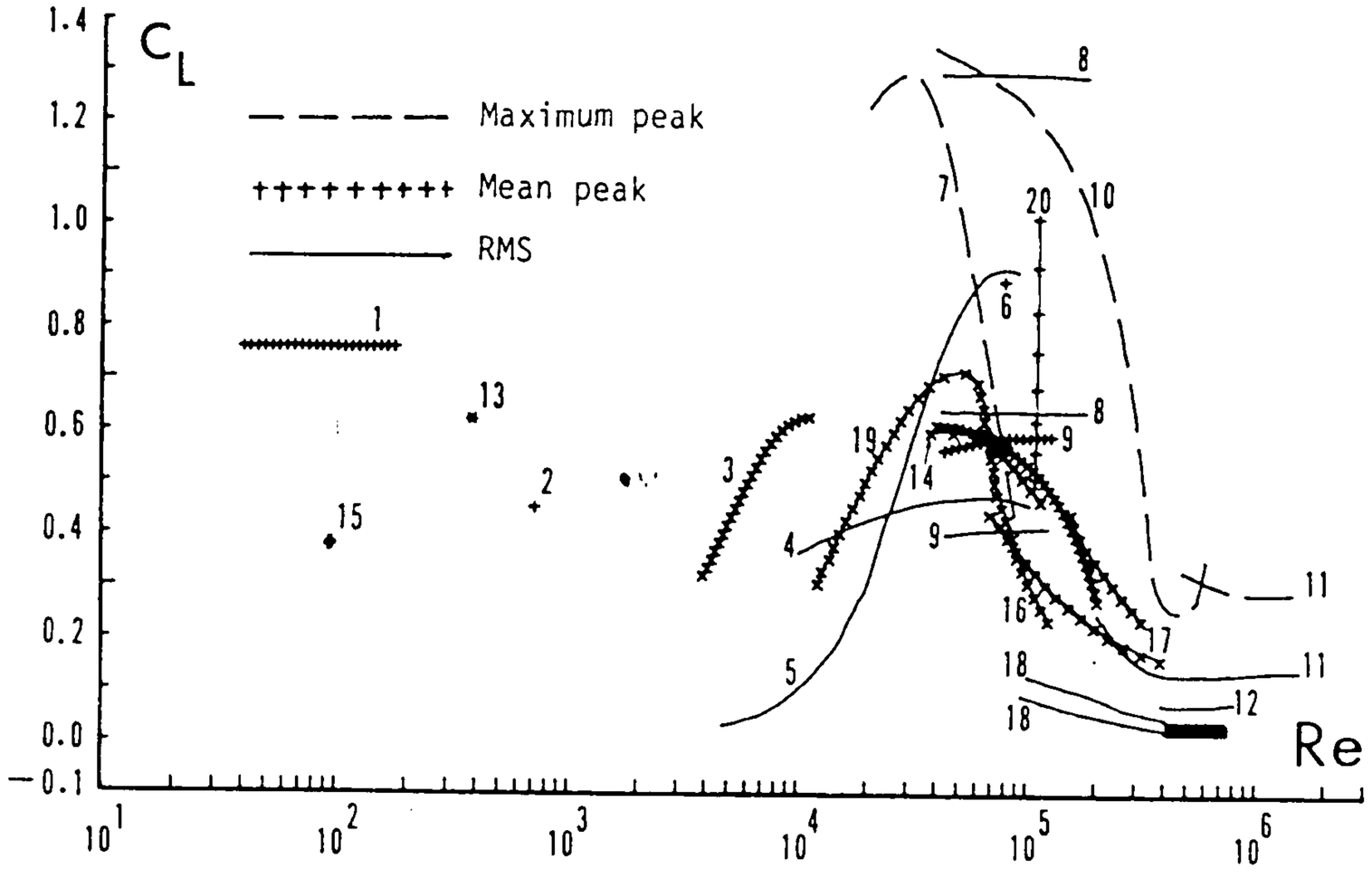

Figure 2.5.- *Lift Coefficient Vs. Reynolds Number.*

2.1.2 Oscillatory Flows

In oscillatory flows the fluid particles move repeatedly back and forth with each cycle occurring over a certain period of time. In other words, the flows do not only accelerate from and decelerate to zero but change direction as well during each cycle. If a cylinder is placed in such a flow, the vortices created over the first half cycle together with those created when the flow changes direction effect the fluid loading on the cylinder significantly differently to those generated by a cylinder placed in a uni-directional flow as described above. The separation points consequently undergo large excurtions. The boundary layer might also change from laminar to a partially or fully turbulent state, and the Reynolds number might also range from subcritical to pos-supercritical over a given cycle. The interaction of the vortices shed from cycle to cycle also plays a significant role in the development of the flow pattern and the fluid loading, which in turn may also differ from cycle to cycle.

The Keulegan-Carpenter number, $Kc = \frac{u_\infty T}{D}$, is normally used to classify oscillatory flow regimes. The symbols u_∞, T, and D here are the free stream velocity, the period of the flow and the cylinder diameter respectively. This number shows the relative magnitude of the fluid particle orbits to the characteristic length of the body over a cycle of the motion. **Bearman** [8] and **Obasaju et.al** [71] divided the flow into the six following regimes: $Kc < 4$, $4 < Kc < 8$, $8 < Kc < 15$, $15 < Kc < 22$, $22 < Kc < 30$, and $Kc > 30$. The first four regimes are called the *symmetric*, the *asymmetric*, the *transverse*, and the *diagonal* regimes respectively. The fifth regime is called the *thirdvortex* regime while the last regime is named the $quasi-steady$ regime. Each regime is identified with a distinct vortex shedding mechanism.

For small values of the Keulegan-Carpenter number less than 4, in the symmetric regime, pairs of vortices experience flow reversal before they are shed. The flow therefore remains symmetrical and the generated vortices remain close to the body. No transverse forces are experienced by the cylinder.

As the Keulegan-Carpenter number increases beyond 8 to enter the asymmmetric regime, the convection and diffusion of vorticity starts to create a distinctive pattern of vortex shedding. Vortex pairs are formed with different strengths before the reverse flow sweeps them back to interact with the pair subsequently forming on the opposite side. This causes the flow to be asymmetric and as a consequence, the transverse force becomes noticeable.

Two opposing vortices formed during the first half cycle of the flow, which is similar to that of uni-directional flow, can appear in the transverse regime, which occurs at a Keulegan-Carpenter number of about 15. One of these vortices develops larger than the other and is swept back during the next half cycle of the flow to combine with the newly formed vortices of opposite sign. The two pairs of vortices also behave similarly in the following half cycle of the flow. In this regime the transverse force becomes significant.

Bearman[9] shows that in the diagonal regime, at a Keulegan-Carpenter number of 15 to 22, there are two diametrically opposite streets of vorticity making an angle 45 degrees to the axis of the flow. In this regime there are two modes of shedding, which should be separated when evaluating force coefficients.

The evolution of this pattern also occurs for the Keulegan-Carpenter number number approaching that of 22 to 30, and is the third vortex regime. In this

regime a Karman vortex street begins to form over each half cycle in which three vortex pairs are shed and begin to form steady structures.

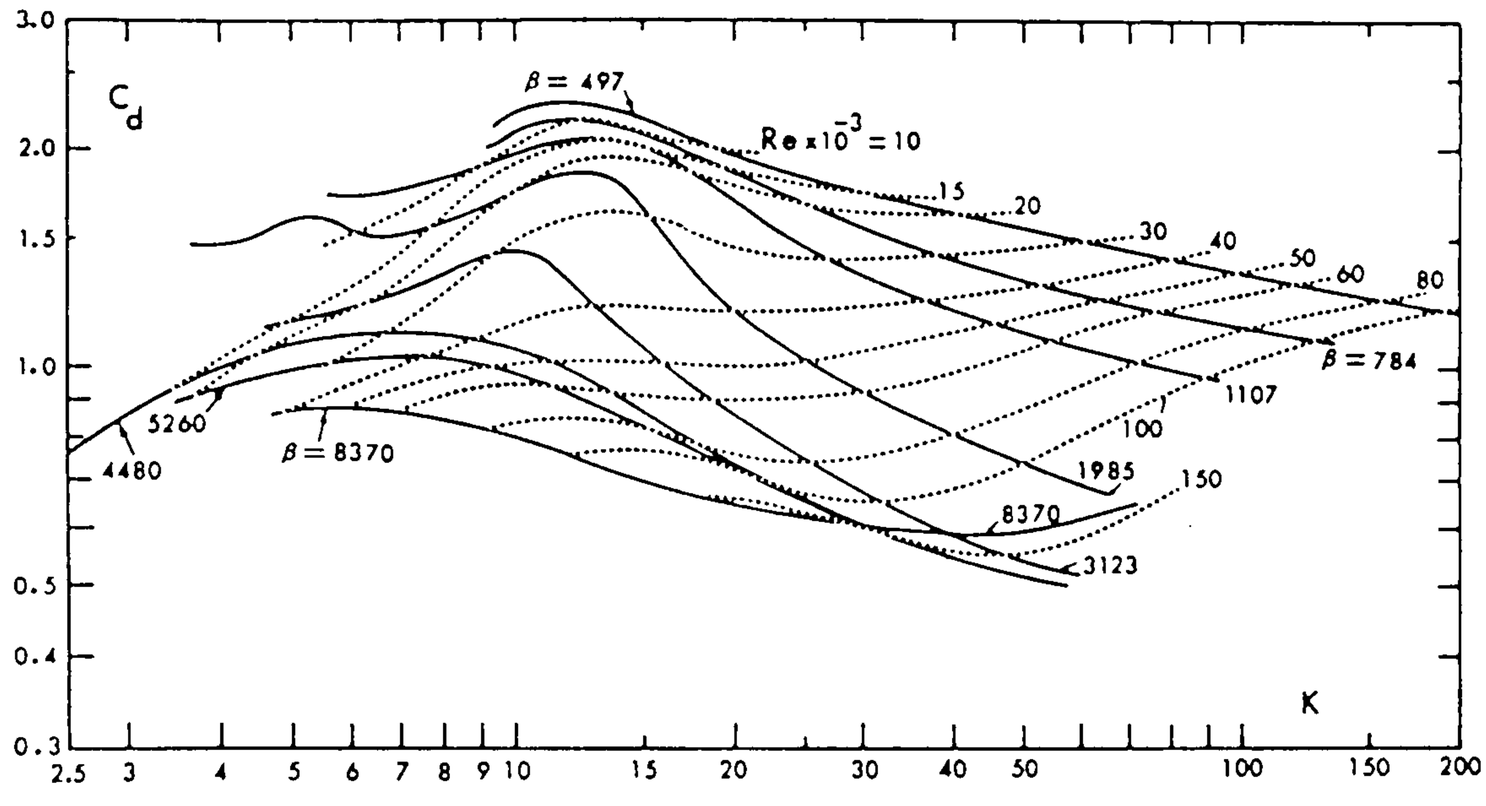

Figure 2.6.- *Drag Coefficient Vs. the Keulegan-Carpenter number.*

In the Keulegan-Carpenter number range of *22* to *30*, which is called the quasi-steady regime, an additional vortex is shed after each increment of *8* to the Keulegan-Carpenter number. This eventually gives streets similar to those of the steady flows. There is no further changes of the characteristics of force coefficients.

The in-line force experienced by a cylinder in an oscillatory flow can be estimated using the *Morison equation* (**Morison** and **O'Brien** [69]). This equation defines the in-line forces in terms of drag and inertia components which are proportional to the flow velocity and the flow acceleration as follows.

$$F = \rho\, a\, |u|\, u\, Cd + \rho\, \pi\, a^2\, \frac{du}{dt}\, Cm \qquad (2.1)$$

Where ρ is the density of the fluid, a is cylinder radius. The undisturbed *velocity*, u, and *acceleration*, $\frac{du}{dt}$, of the flow must be determined by some suitable

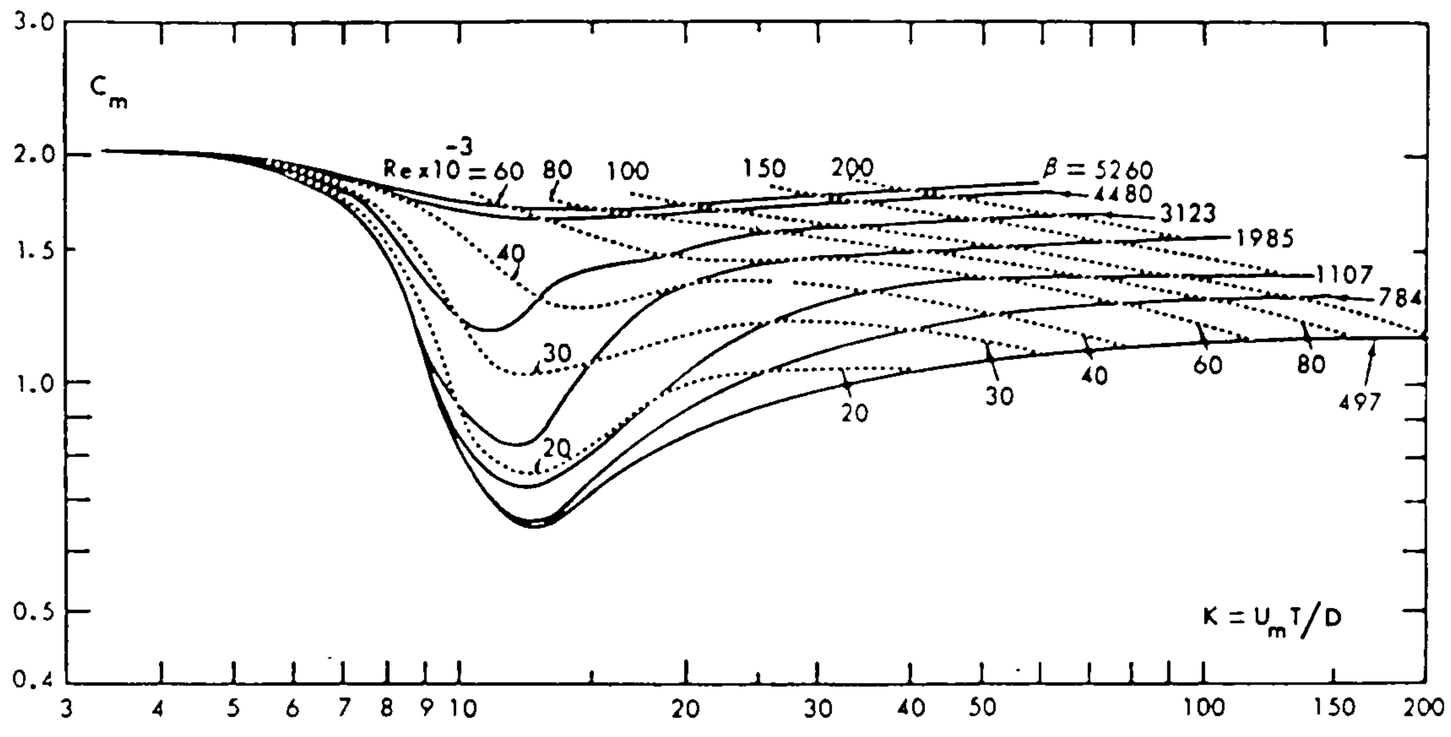

Figure 2.7.- *Inertia Coefficient Vs. the Keulegan-Carpenter number.*

method. For example, first order potential theory is often used in the case of cylinders in waves. The drag coefficient, Cd, and the inertia coefficient, Cm, must have appropriate values assigned to them. In their original work, Morison and O'Brien determined them by fitting the equation to experimental results obtained with a cylinder in waves. Subsequently considerable work has been done in this area to establish suitable coefficients to be used with the Morison equation for determining the fluid loading on offshore structures.

Sarpkaya [83] have carried out exhaustive experiments using a U-Tube. The time averaged coefficients evaluated by Sarpkaya are given by

$$Cd = \frac{3\pi}{4T}\int_0^T \frac{F(t)}{\frac{1}{2}\rho u^2 D}\ cos(\frac{2\pi t}{T})\ dt \qquad (2.2)$$

$$Cm = \frac{-u}{\pi^2 a}\int_0^T \frac{F(t)}{\frac{1}{2}\rho u^2 D}\ sin(\frac{2\pi t}{T})\ dt \qquad (2.3)$$

where T is the flow period, D is the cylinder diameter. and $F(t)$ is the time dependent in-line force per unit length measured by experiment. The force coefficients are determined by the flow regime existing, and so are functions of the Reynolds number, Keulegan-Carpenter number and cylinder roughness.

As explained by **Sarpkaya** and **Isaacson** [**87**], the behaviour of this flow can also be described with reference to the frequency parameter $\beta = \frac{Re}{Kc}$, where Re and Kc are the Reynolds number and the Keulegan-Carpenter number respectively. When the force coefficients are plotted for constant β, it can be seen that at a Keulegan-Carpenter number of around *15* the drag and inertia coefficients reach their maximum and minimum values respectively and this becomes increasingly pronounced for lower Reynolds number or β parameter. The values of Cd and Cm over the whole range of the Keulegan-Carpenter number and also at various values of the frequency parameter β are displayed in figures (**2.6**) and (**2.7**) respectively. It can be seen that Cd and Cm do not vary appreciably when the Reynolds number is less than 2×10^4. The plot of Cd and Cm as functions of Reynolds number for constant value of the Keulegan-Carpenter number are also shown in figure (**2.8**) and (**2.9**) respectively. These figures show that for most values of the Keulegan-Carpenter number, Cd decreases with increasing value of the Reynolds number. It tends to an asymptotic value at post-supercritical Reynolds number. The inertia coefficient increases with increasing the Reynolds number and tends to an asymptotic value of about *1.85*.

As described earlier, various flow regimes are associated with distinct vortex shedding mechanisms, most of which lead to distributions of vorticity that are asymmetric about the axis through the cylinder parallel to the direction of the flow. For this reason, the cylinder also experiences time dependent forces in a direction orthogonal to the flow. The Morison equation is only concerned with the force in-line with the flow. The force coefficient representing the transverse force, is referred to as the lift coefficient. In the case of oscillatory flows it is normalised with respect to the velocity amplitude. Figure (**2.9**), (**2.10**) and (**2.11**) show that this coefficient is a larger proportion of the total force at lower Keulegan-Carpenter number. It exhibits a similar behaviour to the drag and inertia coefficients whose maximum values occur at a Keulegan-Carpenter number of around *15*.

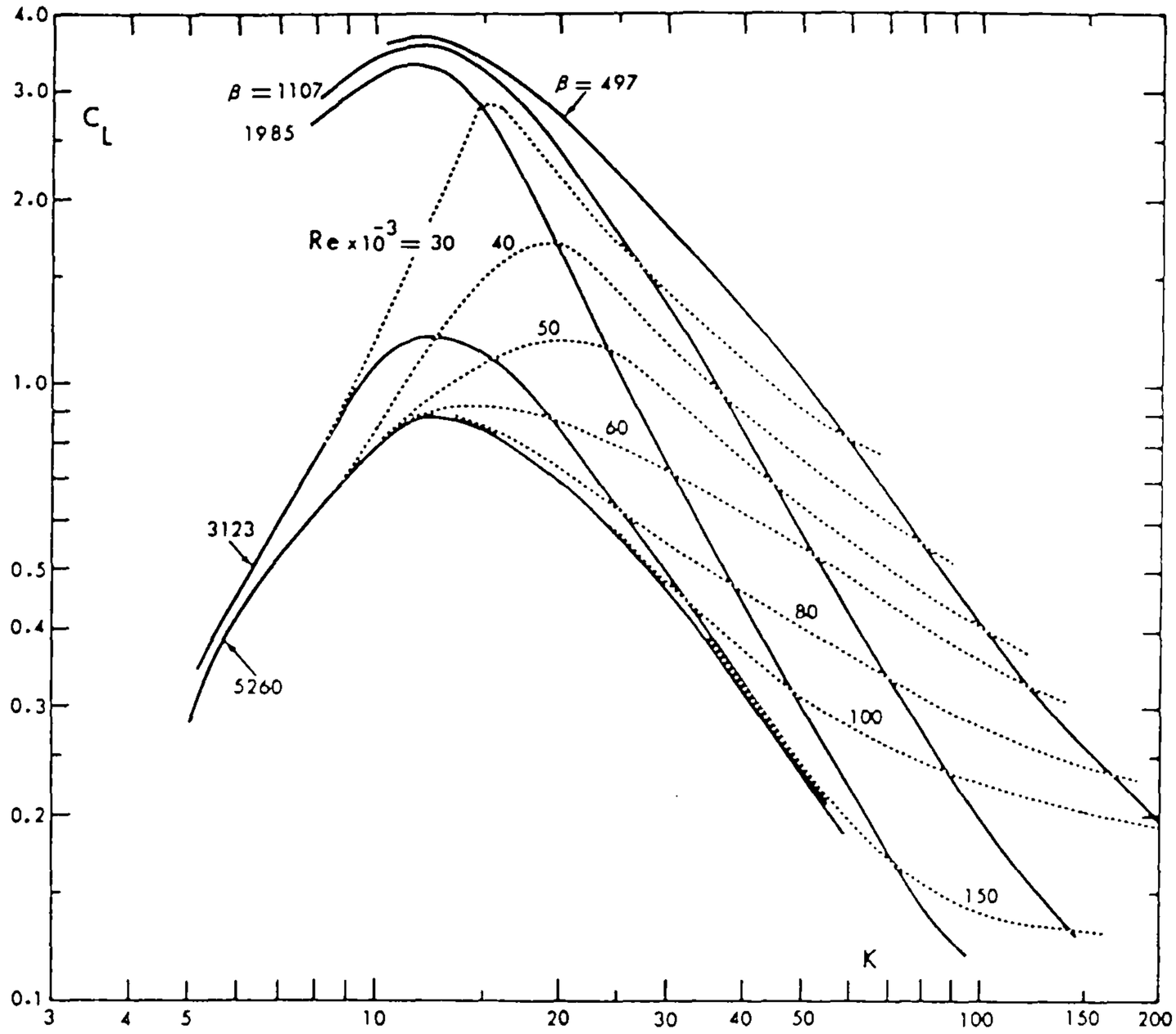

Figure 2.8.- *Lift Coefficient Vs. the Keulegan-Carpenter number.*

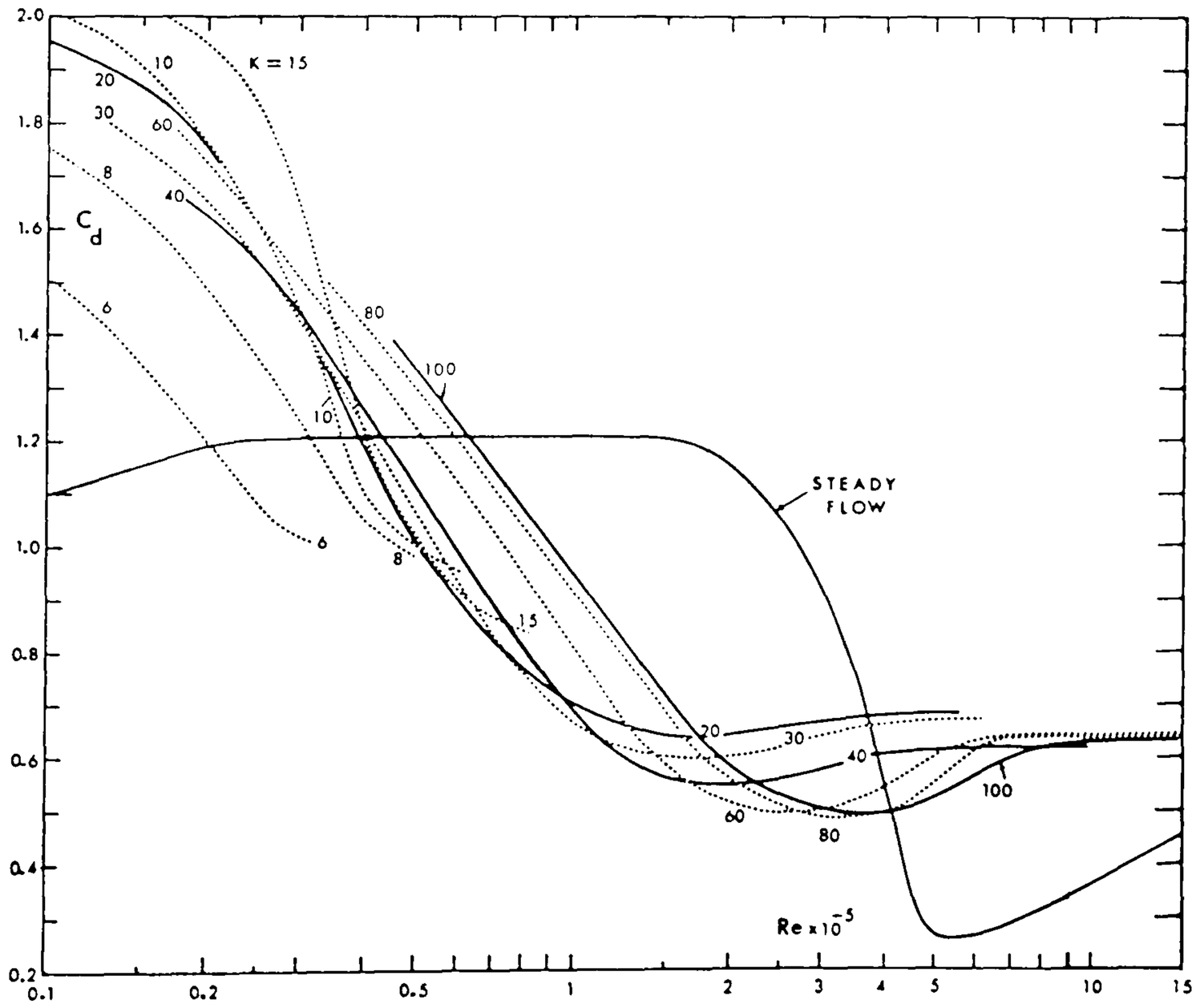

Figure 2.9.- *Drag Coefficient Vs. the Reynolds number.*

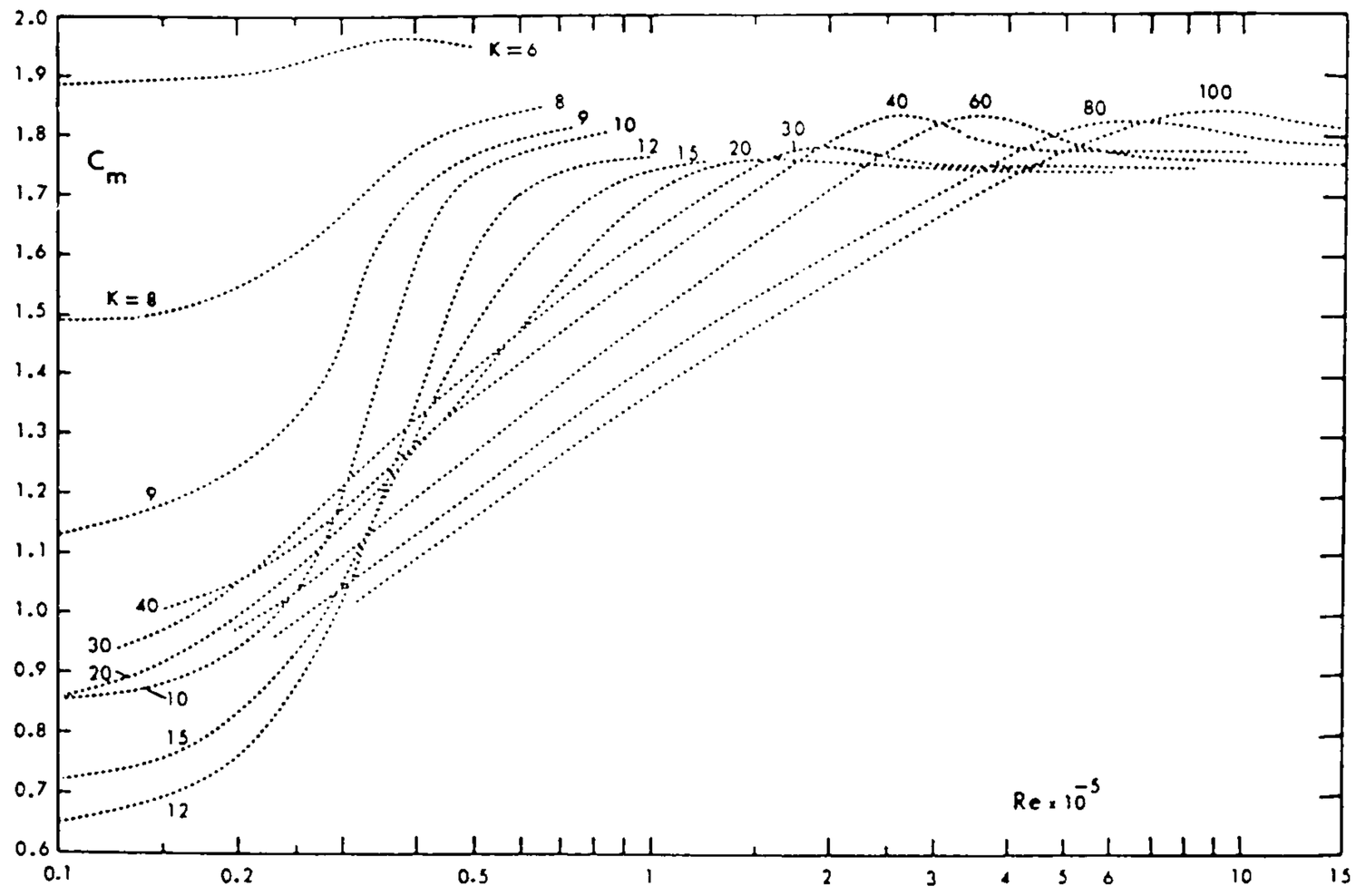

Figure 2.10.- *Inertia Coefficient Vs. the Reynolds number.*

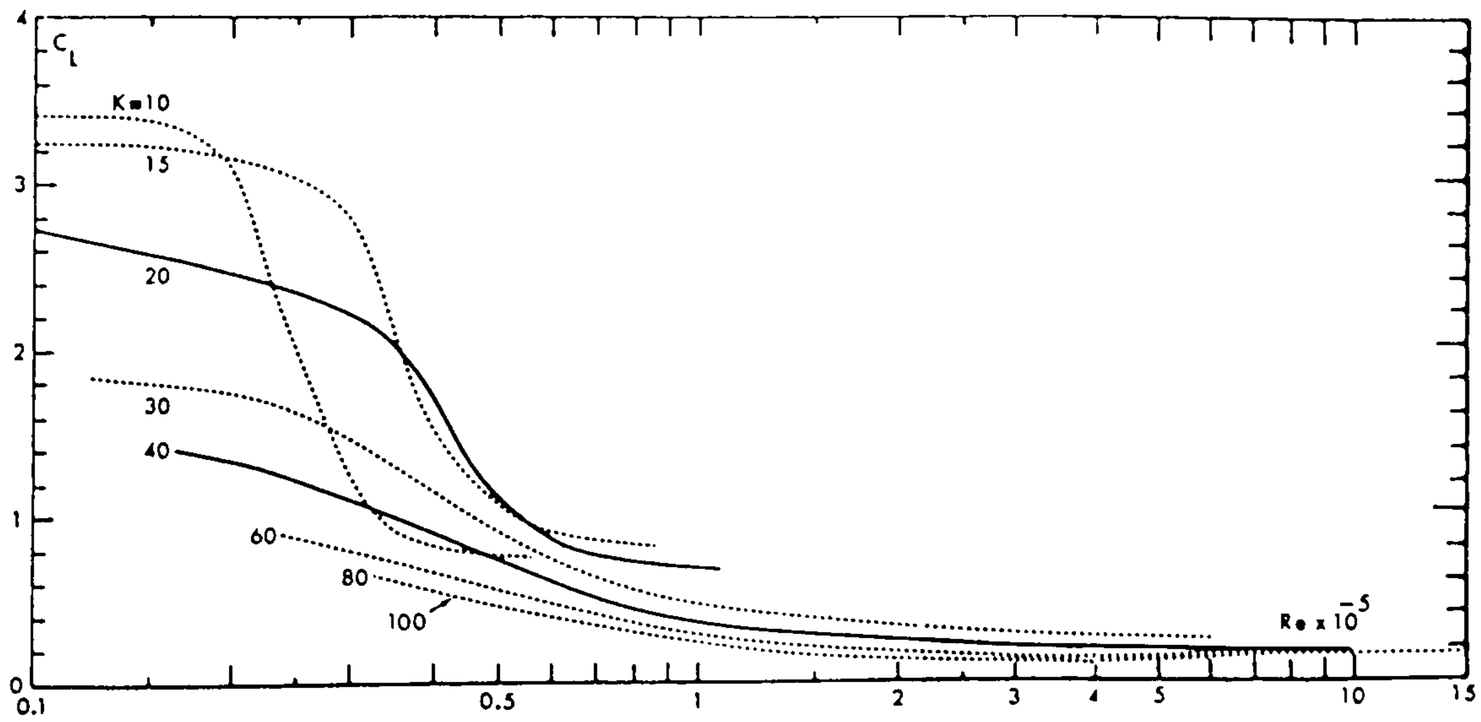

Figure 2.11.- *Lift Coefficient Vs. the Reynolds number.*

2.2 The Flow Around Two Cylinders

The flows about adjacent bodies may interact in such a way as cause the force on individual members to decrease or increase over the single member value. An example, of such an interaction is the flow about the structural members and conductor pipes of an offshore platform (see **Mair** and **Maull** [62]). The interaction is due to the structural geometry affecting the flow behaviour. The upstream or downstream velocity relative to a given structural member can be altered significantly by the presence of adjacent members. Several studies have been carried out for the flow around group of cylinders.

The interference between two cylinders will occur either when they are sufficiently close to each other or when the rear cylinder is adjacent to or within the wake of the upstream cylinder. Based on the arrangement of the cylinders, according to **Zdravkovich** [116]. there are four regimes. which can be plotted as shown in figure (2.12).

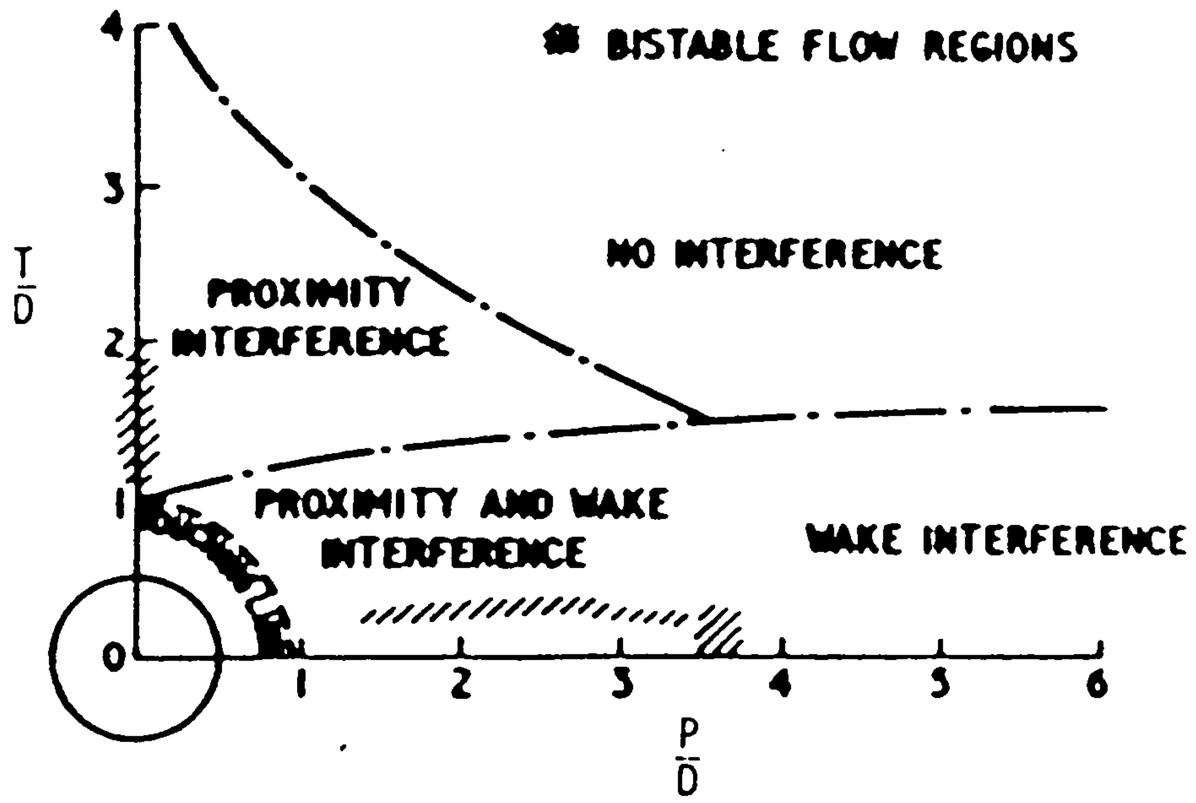

Figure 2.12.- *Interference Regimes for the Flow of Two Cylinders.*

The processes associated with the regimes are as follows:

- *Proximity interference*: the flow field or motion of either cylinder affects the other and this mainly occurs in side-by-side and slightly staggered arrangements.

- *Wake interference*: the flow or motion of the upstream cylinder affects the cylinder in the wake and this happens in both tandem and staggered arrangements when the distance is greater than four diameters.

- *Proximity and wake interference*: the wake behind the upstream cylinder is influenced by the downstream cylinder and this can occur at small spacings in both tandem and staggered arrangements with distances smaller than four diameters.

- *No interference* region.

The boundaries of the different regimes are dictated by parameters such as the free stream velocity, level of turbulence and surface roughness and will be described in more detail in the following sections.

2.2.1 The Side-By-Side Arrangement

The problem of predicting the flow around cylindrical offshore structures in close proximity has been approached in a number of ways. One is the investigation of the flow about a pair of circular cylinders separated in a plane normal to the free stream. This arrangement is different from the the flow described previously as it exhibits a discontinuity in the flow and measured forces at certain spacings, **Sarpkaya** and **Isaacson** [**87**] and **Zdravkovich**[**116**].

Biermann and **Herrnstein** [**13**] carried out measurements of the drag force when two circular cylinders are arranged side by side in a wind tunnel. They displayed the measured forces in terms of the *interference drag* coefficients, which is defined as the difference of the drag coefficient of a single cylinder in this present arrangement with that in isolation, as shown in figure (**2.13**).They noticed that at all spacings greater than *5* diameters, the interference drag is zero, or in other words, no mutual interference between the two cylinders is detected in this range. The interference drag increases as the spacing decreases, but only down to $2\frac{1}{4}$ diameters. At less than this critical spacing there is an indication of a discontinuity in the measured forces and two different bistable nature flow patterns.

A similar behaviour was also found by **Lanweber** [**57**] who undertook a photographic study of the wake behind two cylinders towed in water. He chose the spacings of 1, $1\frac{1}{4}$, $1\frac{1}{2}$, 2, $2\frac{1}{2}$, 3 and 4 diameters and found a single vortex street for the first two spacings, 'confused' four rows of vortices for the third and two

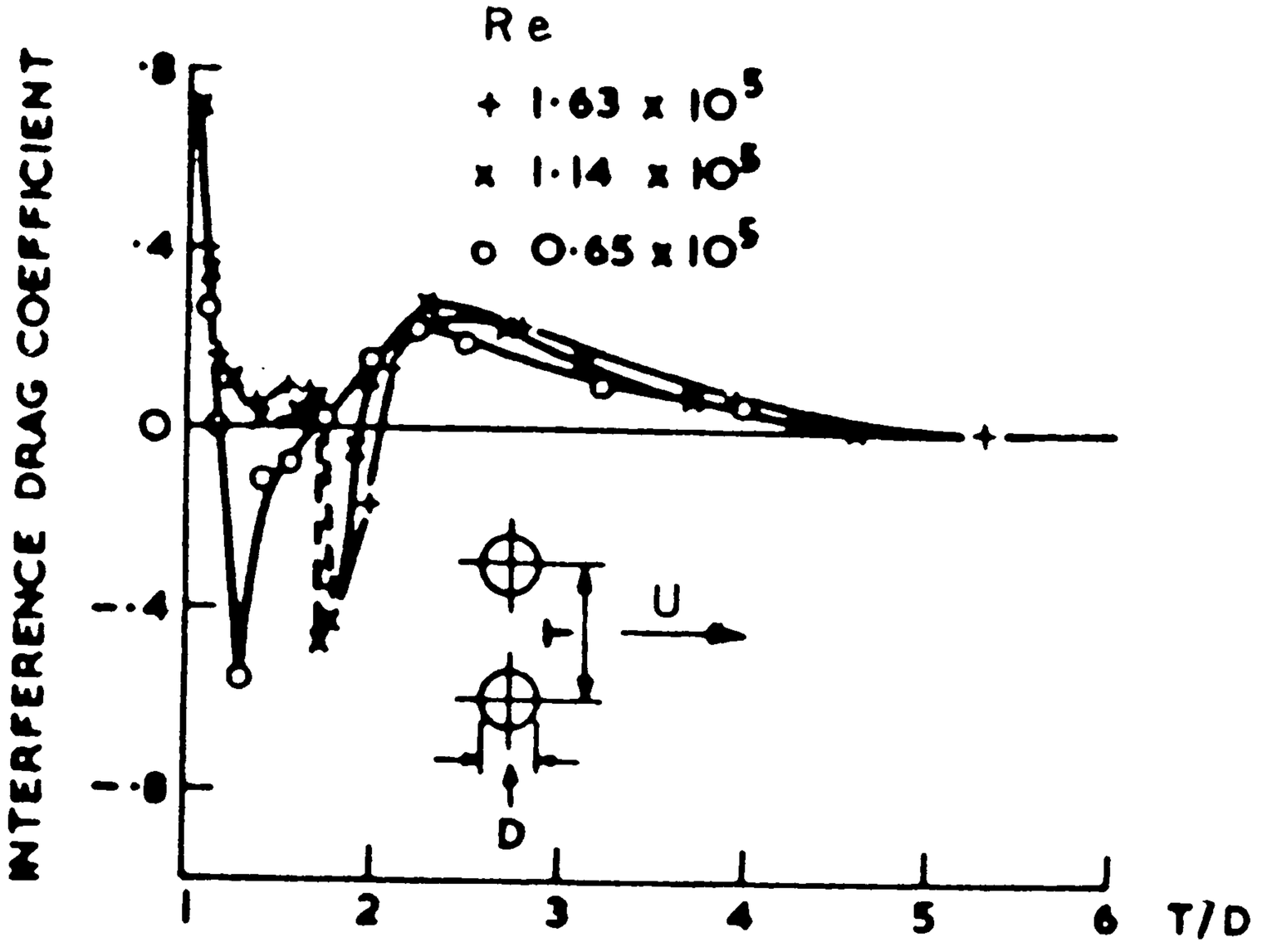

Figure 2.13.- *Interference Drag Coefficients for side-by-side arrangement.*

vortex streets for the rest. **Ishigai et.al.** [48] took the photograph of the formation region around the cylinder at various gap distances as shown in figure (**2.14**) below. He referred to the 'confused' row of vortices resulting from the close proximity of the cylinders as the *Coanda effect* which can lead to a different size of the formation region and shedding frequency from one cylinder to the other. In this case, the wakes from each cylinder combine into a single wake in the downstream region, and form a conventional Karman vortex street.

In an experiment carried out by **Hori** [47] at Reynolds number 8×10^4, a discontinuous change of the base pressure coefficient at spacings of *1.2* and *2.0* diameter, was also identified.

Another observation of a similar variation in the base pressure was reported by **Bearman** and **Wadcock** [11] who measured it on both cylinders. Their results for the Strouhal number, base pressure coefficient and also lift and drag coefficients

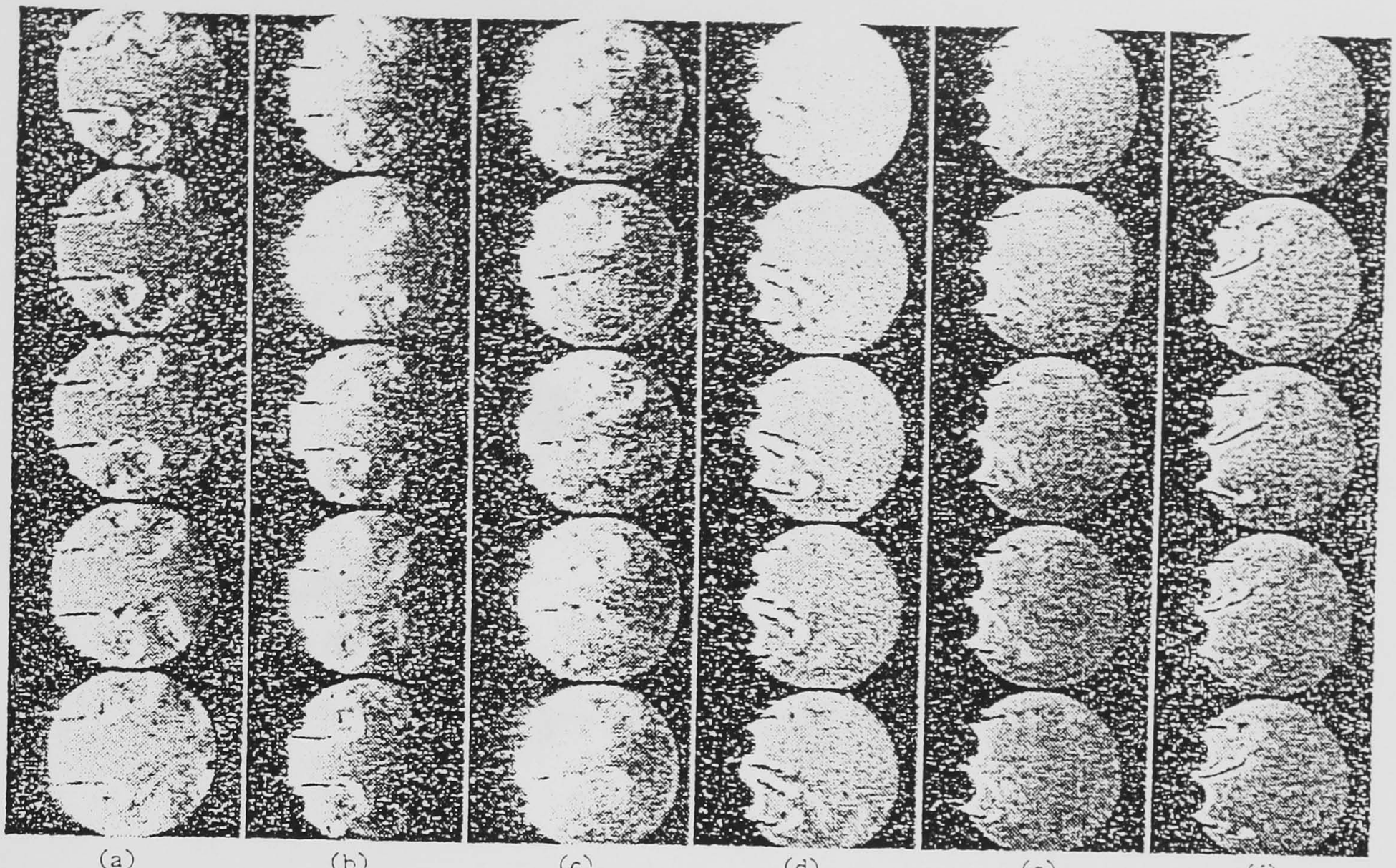

(a) $H/D = 3$, $R_e = 4\,000$ — (b) $H/D = 2.5$, $R_e = 8\,450$ — (c) $H/D = 2$, $R_e = 3\,800$ — (d) $H/D = 1.5$, $R_e = 4\,000$ — (e) $H/D = 1.25$, $R_e = 3\,600$ — (f) $H/D = 1.25$, $R_e = 3\,600$

Figure (2.14).- *Pictures of formation region for side-by-side arrangement.*

are displayed in figures (**2.15**), (**2.16**), and (**2.17**).

The vortex shedding frequency was also investigated by **Ishigai et.al.** [**48**]. They showed that when the gap is greater than twice the diameter there is no change of Strouhal number compare to that of a single cylinder. For less than this value, two different values of the Strouhal number exist. The higher is for the cylinder towards which the flow between the cylinders is deflected, while the lower is for the other cylinder. This is due, as explained above, to the bi-stable nature of the flow whose direction is not stable and changes at random time-intervals one direction to another. **Spivak** [**96**] also observed this phenomenon and his graph of the dual value of the Strouhal number at different spacing is reproduced in figure (**2.15**) below.

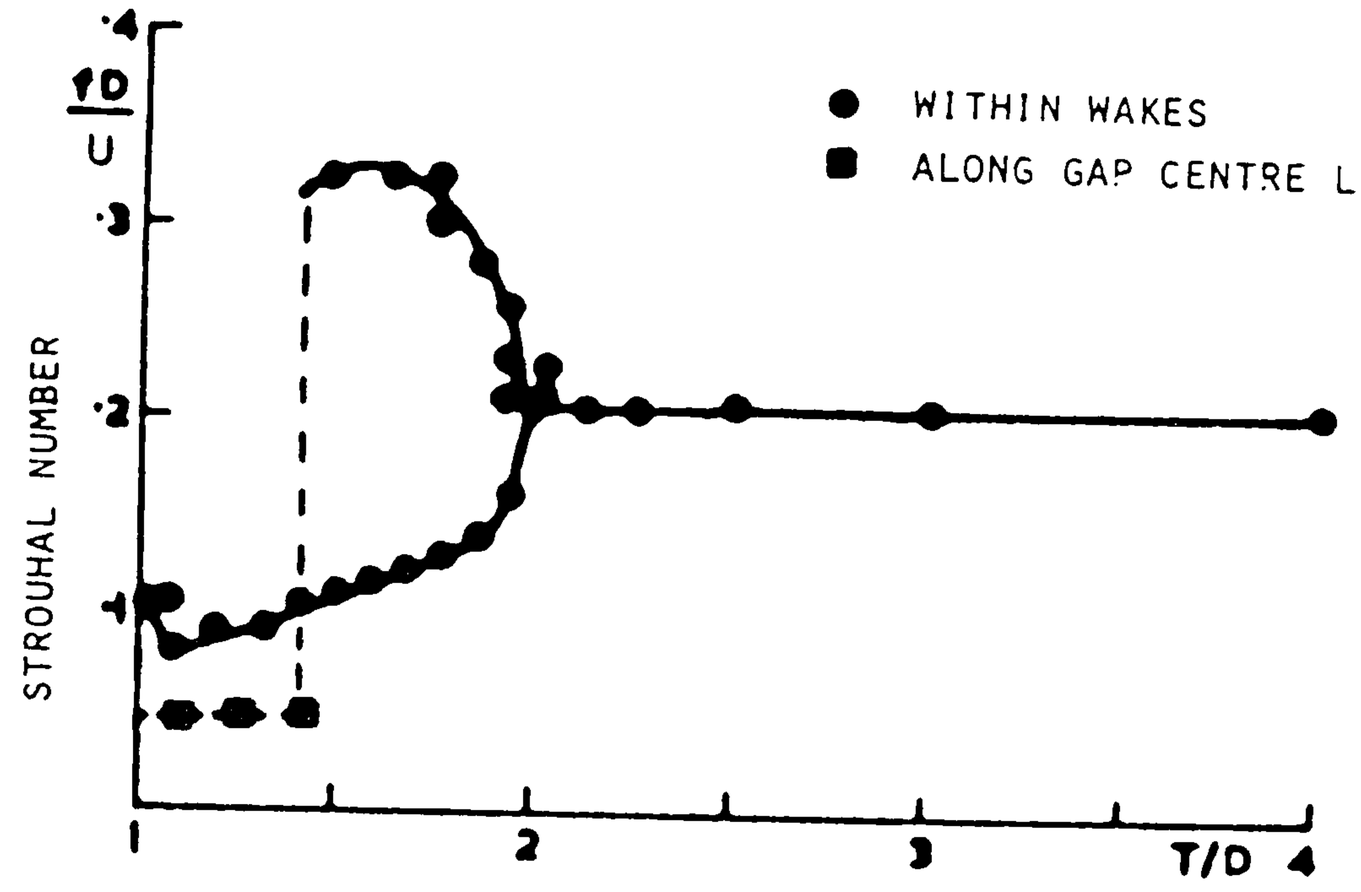

Figure (2.15).- *Strouhal number for side-by-side arrangement.*

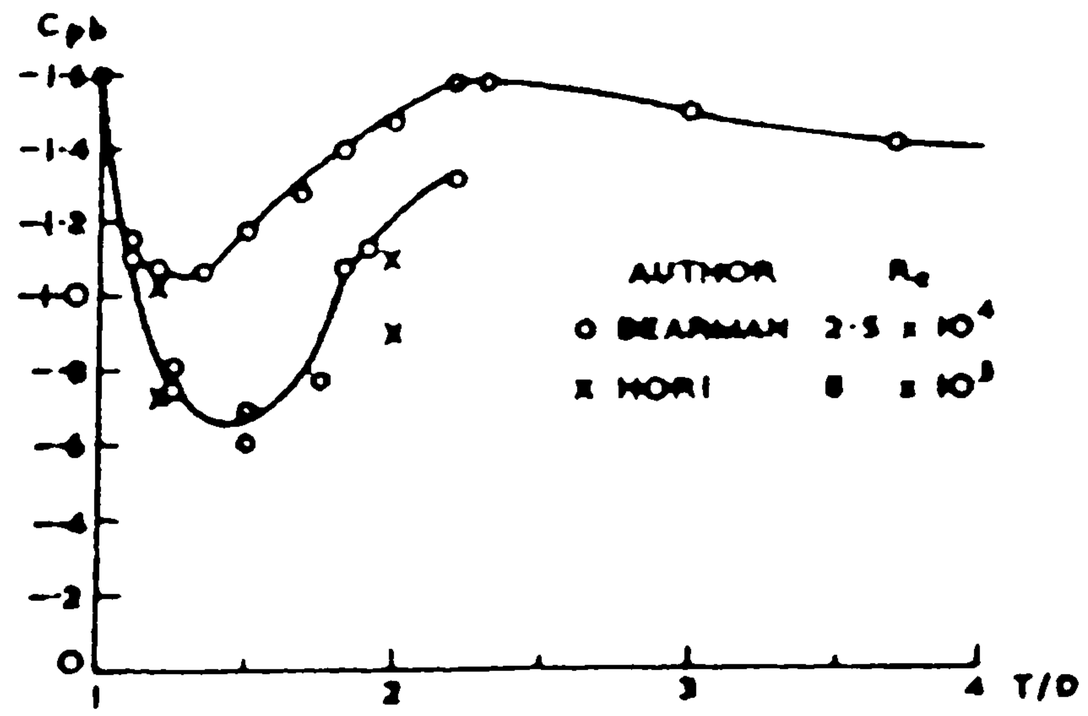

Figure (2.16).- *Base pressure for side-by-side arrangement.*

The interference drag, the flow visualisation, the frequency of vortex shedding, and the base pressure have been plotted, and in figure (2.18) **Zdravkovich [116]** defined four flow regimes for two equivalent cylinders set up normal to the flow.

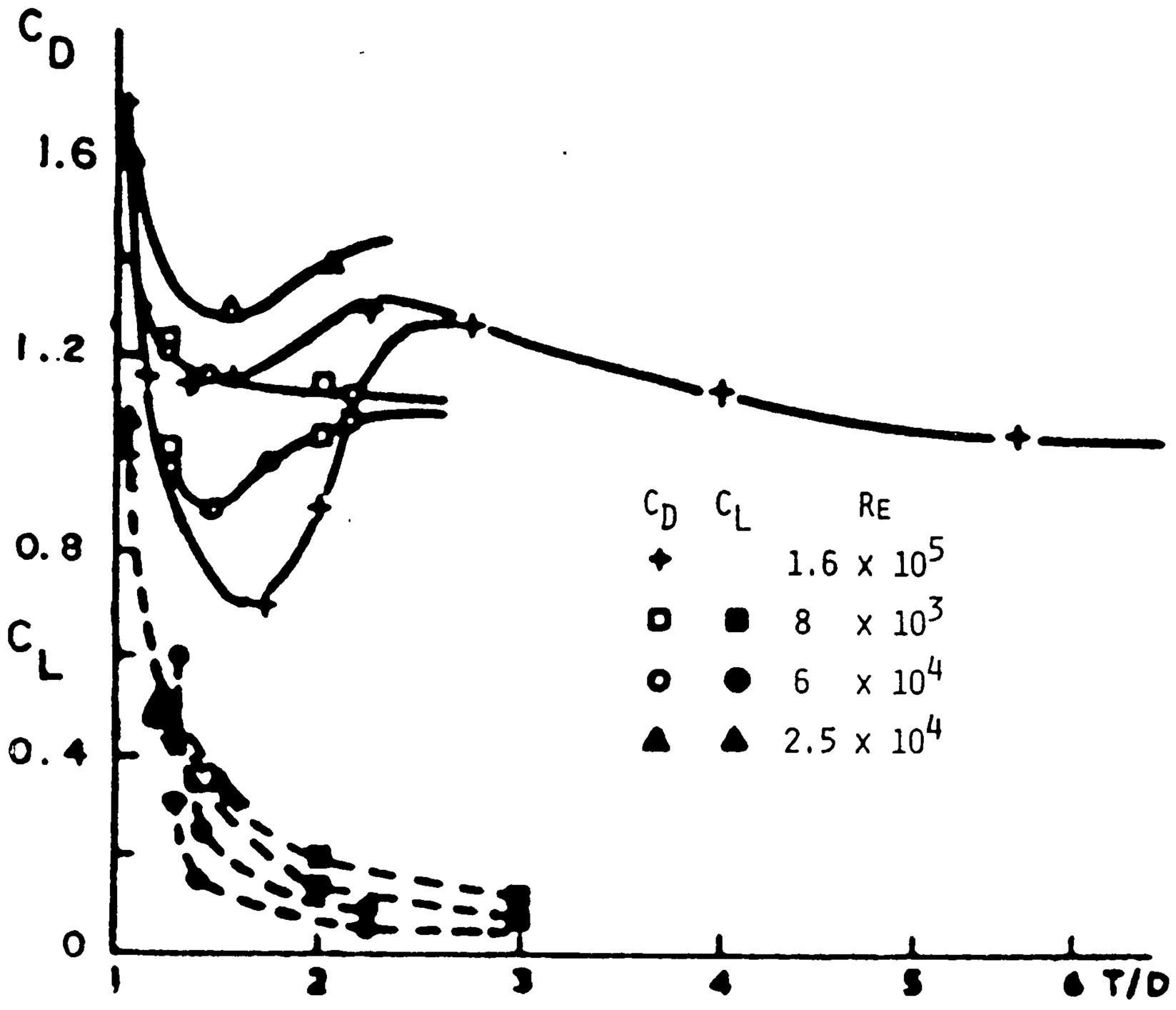

Figure 2.17.- *Drag and Lift Coefficients for Side-by-Side Arrangement.*

When the gap-diameter ratio $\frac{G}{D}$ is greater than *3*, and the flow resembles the flow around an isolated cylinder, it is classified as the *no – interference* regime. This means that the mean value of the lift coefficient is zero and the drag coefficient oscillates at twice the frequency of that of the lift coefficient, about its mean value of *1.2*. The Stouhal number is expected to be *0.2*.

The *coupled vortex street* regime is identified with the situation where the two cylinders are with a gap-diameter $\frac{G}{D}$ range of *2* to *4*. At this stage the interference drag and lift coefficients are gradually increased while the Stouhal number is still the same. Two vortex streets of equal frequency are detected and are coupled out-of-phase with one another. This means that vortices formed and shed from the gap side of the cylinders are in phase as are those from the other sides. This results in a Karman vortex streets behind each cylinder. Some interaction between

the cylinders and the wake is detected.

As the gap decreases to between *1.2* to *2* diameters. in the *bistable* regime. a strong interaction occurs and the flow in the gap is bistable and intermittantly biased to one side or the other. This gives rise two values of the Strouhal number and discontinuity of the drag and lift coefficients.

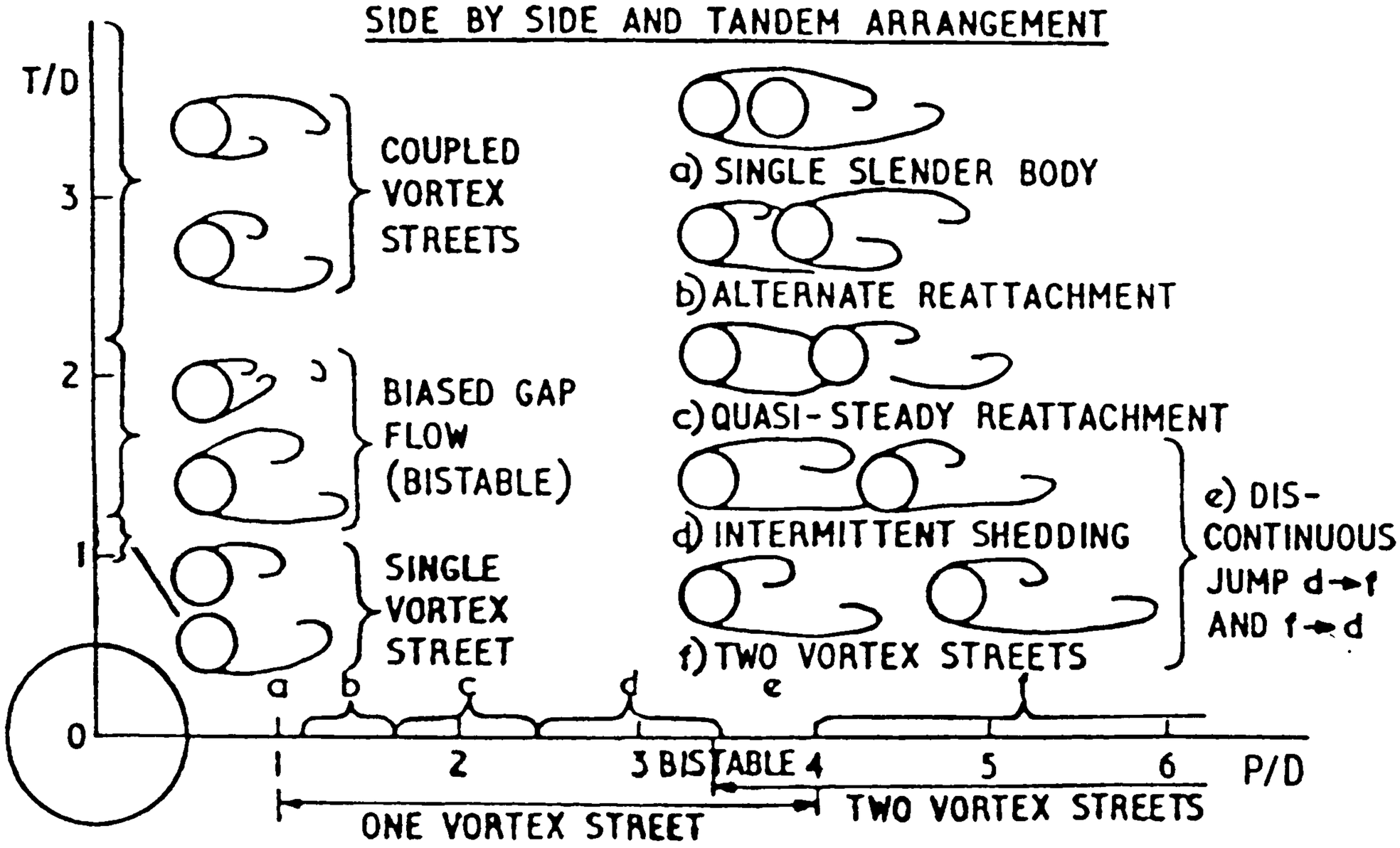

Figure (2.18).- *The Flow Regime for side-by-side and Tandem Arrangements*

The *single vortex street* regime defines the phenomenon when the gap-diameter ratio is less than *1.2*. As implied by the name. the vortices shed from the two cylinders combine to form a single vortex street downstream as if the two cylinders were one body. Both drag and lift coefficients rise sharply and the Strouhal number. as shown in figure (**2.15**). has only one value as the two cylinders are strongly coupled by the flow field.

2.2.2 The Staggered Arrangement

In engineering applications, such as fixed offshore structures, when the direction of the oncoming flow constantly changes, the fluid-structure interaction problem for much of the time will be much closer to this type of arrangement. From his experiments with two equal cylinders with three spacings of *1.2*, *2.0*, and *3.0*, **Hori** [47] was able to plot the resultant interference force coefficients as displayed in figure (**2.19**). The force coefficient were obtained by vectorially subtracting the drag coefficient for the single cylinder from the given force coefficients. The interference effects are proportional to the vectors shown in the figure.

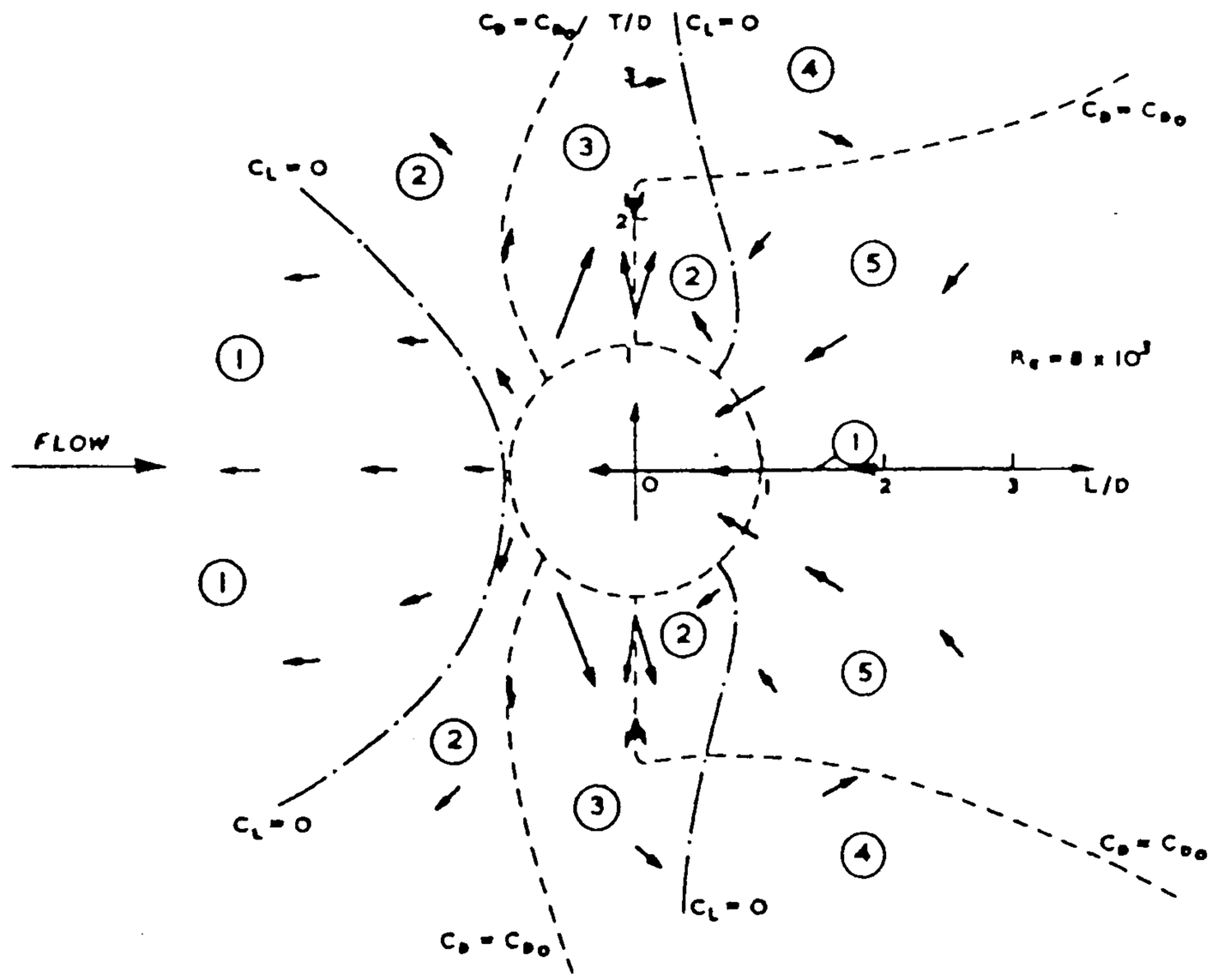

Figure 2.19.- *Interference Force Coefficients for All Arrangements.*

If the direction of the vector is to the left, it indicates that the drag at that position is less than that of the single cylinder and vise versa. The upward direction in the upper half or downward direction in the lower half of the figure indicates

repulsive lift force experienced the two cylinder if another cylinder is situated in that position.

By comparing the interference force coefficients to those of the single cylinder. **Hori** [**47**], classified the regions around a cylinder bounded by lines of zero lift or zero interference drag coefficients. As mentioned by **Zdravkovich** [**119**], the upstream cylinder can then be situated in three regions, which are also displayed in figure (**2.19**), as the region in which there is:

1. A negligible lift force and reduced drag force.

2. A small repulsive force and reduced drag force.

3. A repulsive lift force and increased drag force.

In addition to the above, the downstream cylinder can be situated in the following regions in which there is

4. A negligible lift force and increased drag force in which beyond this region there is no interference.

5. A negative lift force and decreased drag force.

It is shown in this figure that the upstream and downstream cylinders in any staggered arrangement usually belong to different regions. The cylinders in tandem arrangements for spacings less than the critical, and side-by-side arrangement beyond the bistable range, are both in the same region. When the cylinders are in the side-by-side arrangement within the bistable range, one belongs to region *3* and the other to region *2*, or vice versa.

Kiya et.al. [**57**] divided the arrangement of two cylinders into *5* regions, as shown in figure (**2.20**), based on the Strouhal numbers which are drawn using linear interpolation over the measured values. They carried out their experiment at a Reynolds number of 1.58×10^4.

The regions, were based on the value of the Strouhal numbers compared with those of a single cylinder and the characteristics of the wake pattern. The regions classified in this way are as follows;

1. The region where the Strouhal number is higher than that for a single cylinder.

2. The region where its value is less than for a single cylinder.

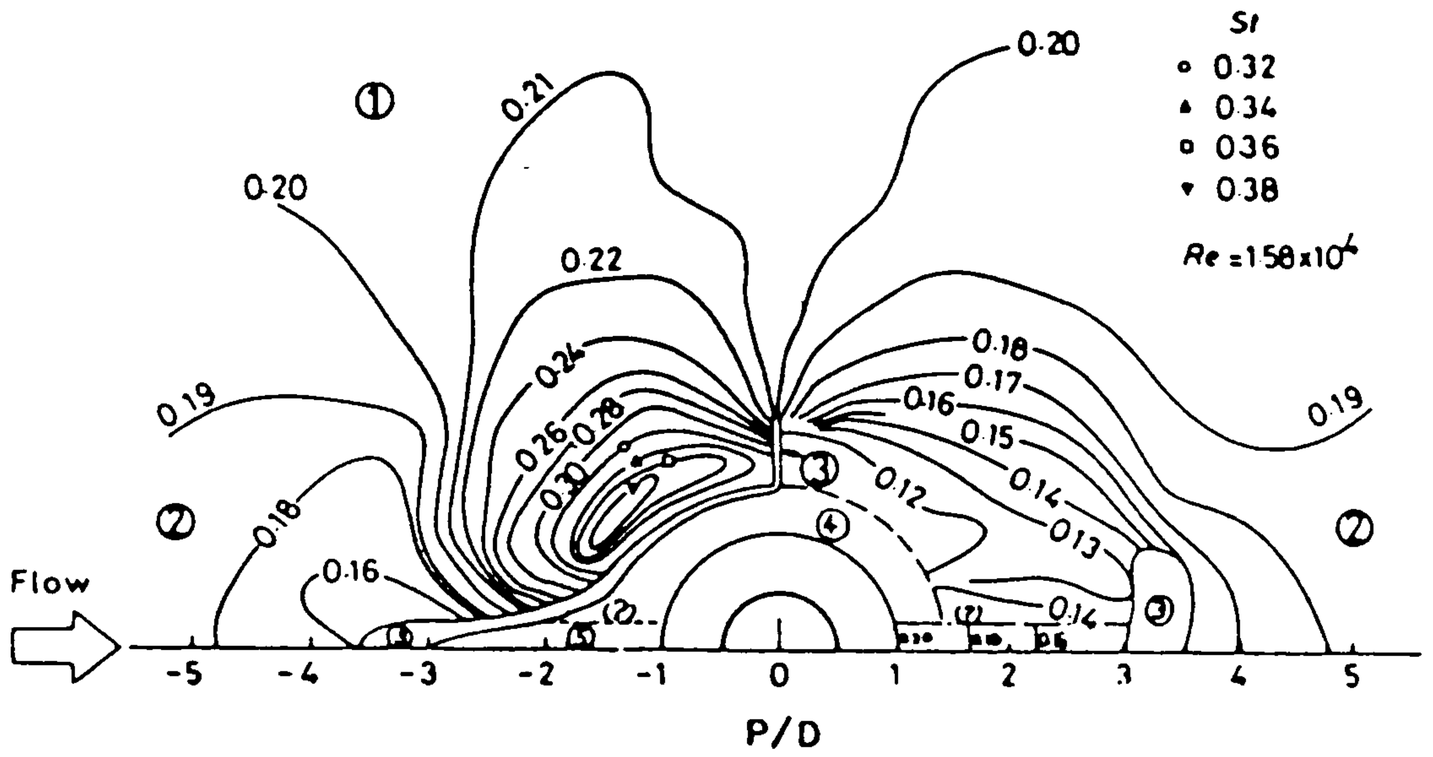

Figure 2.20.- *Strouhal number for Two Cylinder in Staggered Arrangement.*

3. The region where its bistable vortex shedding appears.

4. The region where the vortex shedding behaves as for single cylinder.

5. A region with weak vortex shedding.

Zdravkovich and **Pridden** [117] also produced results for steady lift and drag coefficients for the downstream cylinders at a Reynolds number of 6×10^4, as shown in figures (**2.21**) and (**2.22**) respectively. The upstream flow has a significant effect on the variations in the dynamic effect on the downstream cylinder. This is because of the total pressure defect in the wake and also of the high turbulence level of the upstream flow. The minimum drag curve is plotted in a chain-dot line.

The lift coefficients give a positive repulsive force in the vicinity of side-by-side arrangements while the other staggered arrangements give a negative force directed toward the wake centre. The negative lift force gradually decreases its value towards a minimum one. There are two separate curves representing the maximum lift coefficient; one inside the wake for distances less than *3* diameters and the other near the wake boundary for distance greater than *2.7* diameters.

Ishigai et.al. [48] took photographs of the formation region near the cylinder and the results are displayed in figure (**2.23**) above. He also studied the effect of

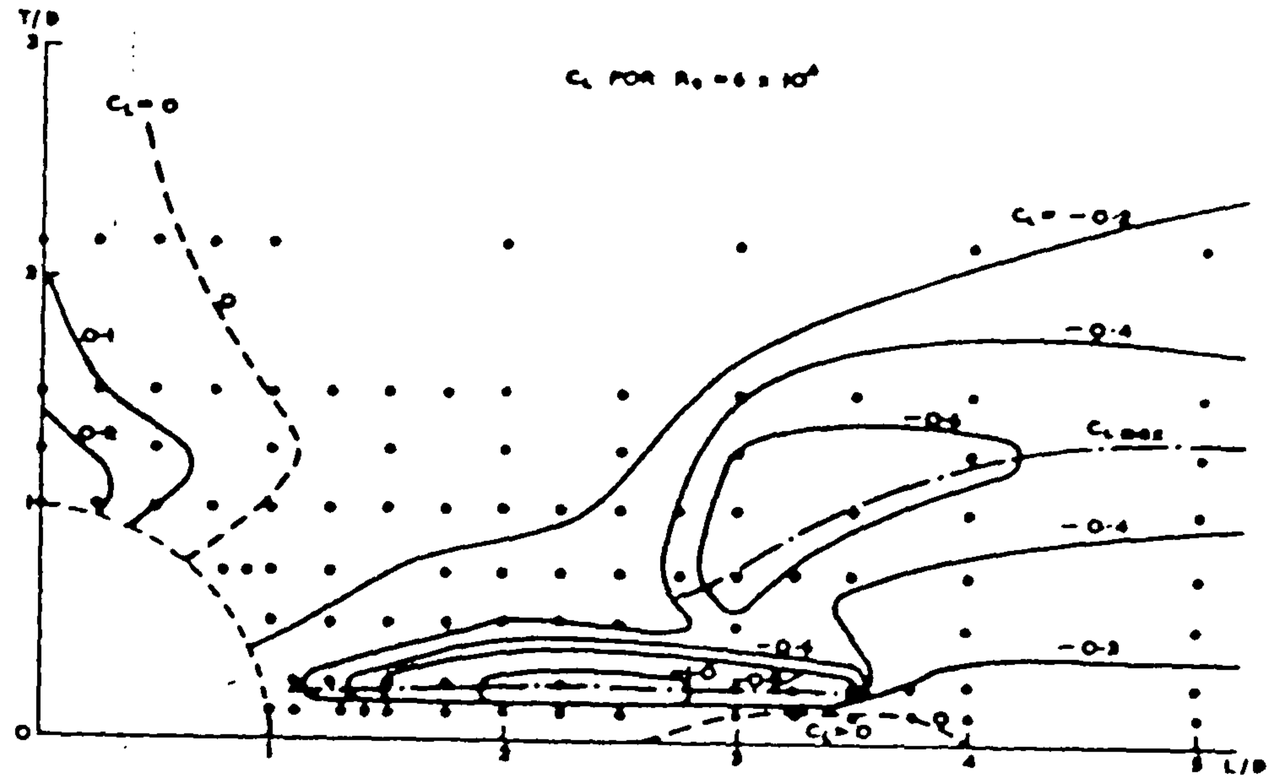

Figure 2.21.- *Lift Coefficients for a downstream cylinder.*

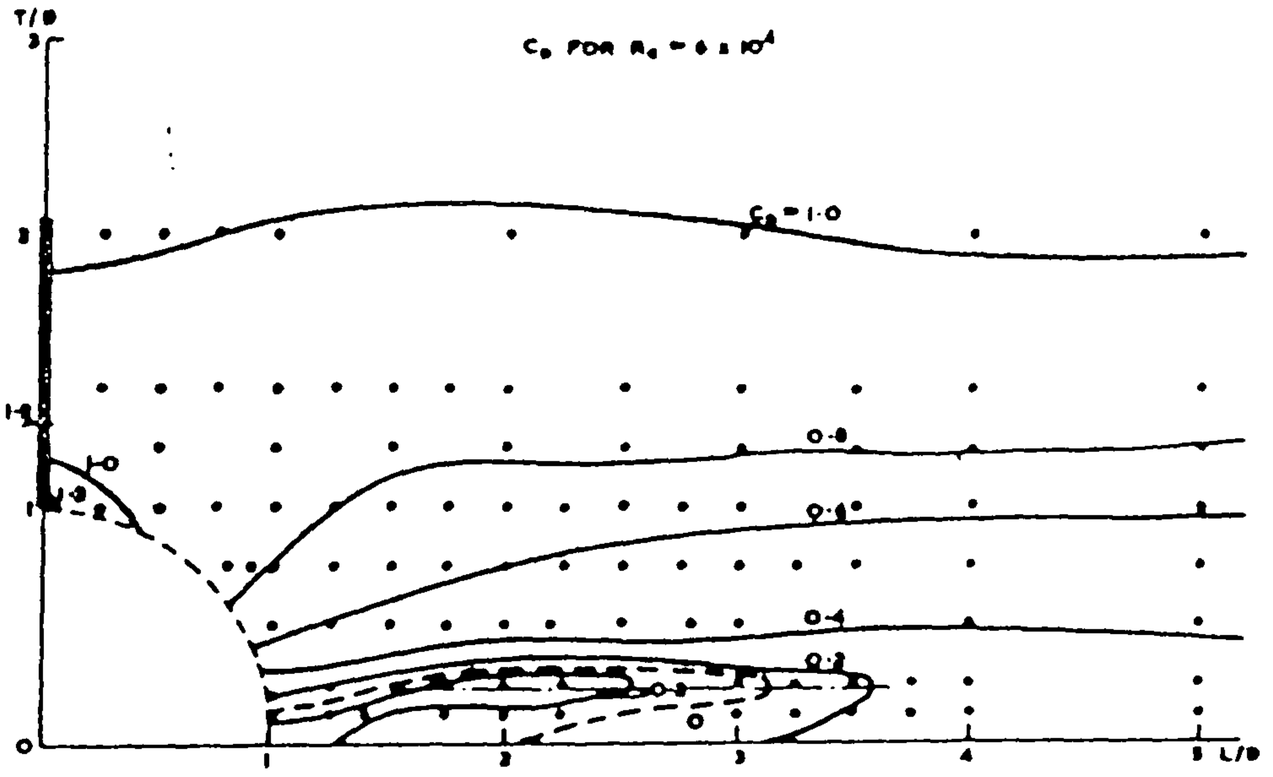

Figure 2.22.- *Drag Coefficients for a Downstream Cylinder.*

different arrangements on the flow pattern and force coefficients. **Bokaian** and **Geoola [14][15]** also carried out similar measurements for the drag and the lift force coefficients and presented the results in graphs with variation of their relative position.

Kiya et.al.[57] summarized the general features of the flow around the two cylinders in a various arrangement as follows:

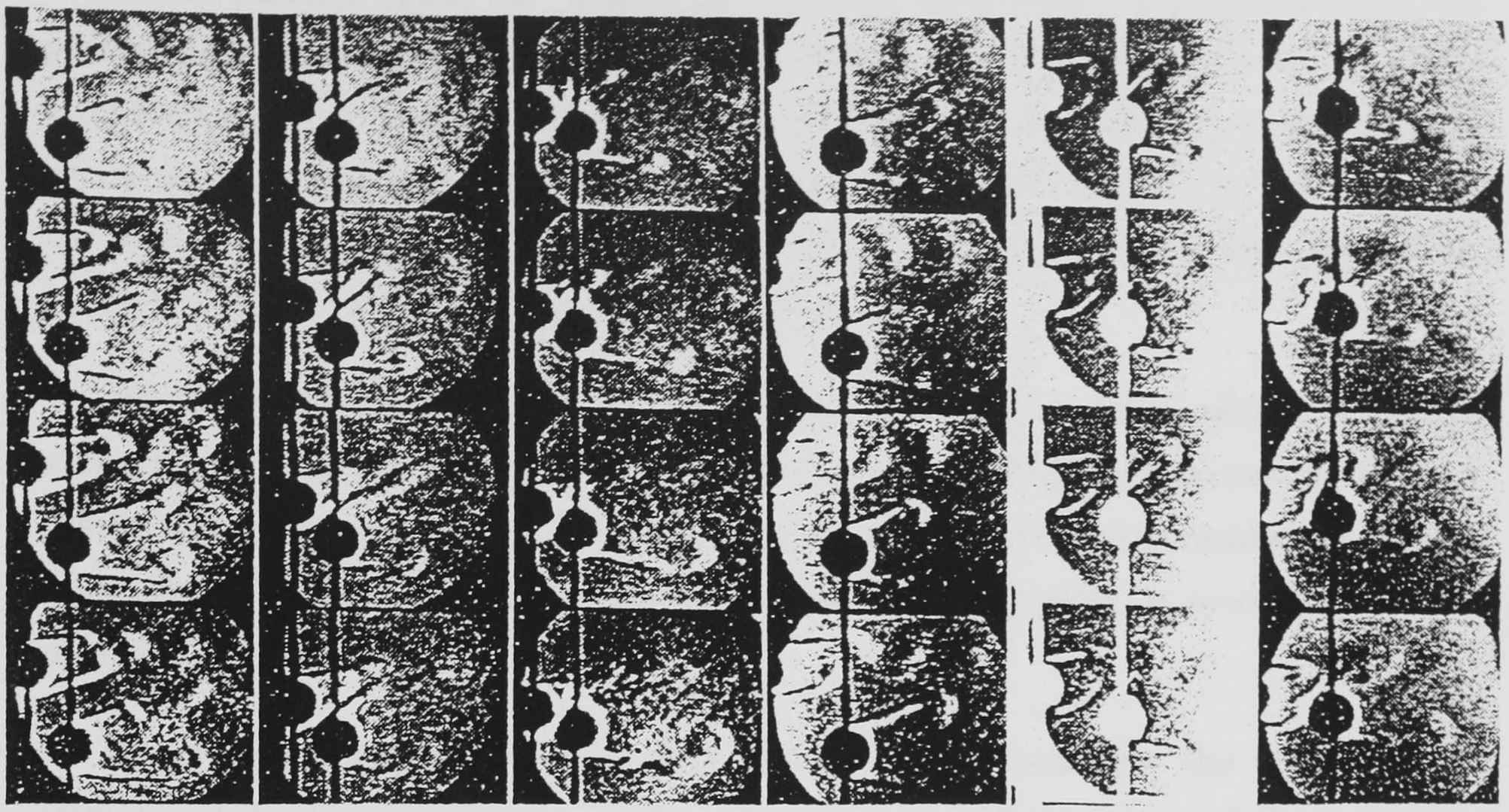

(a) $L/D=1$, $H/D=2$, $R_e=2\,580$
(b) $L/D=1$, $H/D=1$, $R_e=2\,140$
(c) $L/D=1$, $H/D=0.5$, $R_e=2\,560$
(d) $L/D=2$, $H/D=2$, $R_e=3\,900$
(e) $L/D=2$, $H/D=1$, $R_e=3\,500$
(f) $L/D=2$, $H/D=0.5$, $R_e=1\,690$

Figure 2.23.- *Vortex formation region for staggered arrangement.*

- With respect to vortex shedding, the cylinders behave as a single body when the distance between their centres is less than *1.4* diameters.
- For the upstream cylinder, there exists a region in which the Strouhal number is higher than that of the single cylinder.
- In general, the Strouhal number of the downstream cylinder is lower than for the single cylinder except when the spacing is less than *1.4* diameter in a tandem arrangement.
- The gap flow between the cylinders is biased to the upstream cylinder and this causes the wake behind the upstream cylinder to be much narrower than that of the downstream cylinder. This also shows that narrower wakes correspond to higher Strouhal numbers.

2.2.3 The Tandem Arrangement

Zdravkovich [**115**] and **Zdravkovich** and **Stanhope** [**118**] conducted experiments in a wind tunnel in which the vortex street was made visible by the introduction of a "smoke" filament into the free stream from injector tubes located upstream of the cylinder, near the end of the contraction. He noticed that the wake at some spacings and velocity range significantly differed from that of an isolated cylinder as a result of the interaction.

The comparison of the single cylinder at Reynolds numbers of *83*, *92*, *121*, and *156* to a tandem spacing of *12* diameter shows that the vortices decay and diffuse downstream very fast and this intensified as the Reynolds number increases. The transition to turbulence, which starts from the beginning, is seen at Reynolds numbers *121* and *156*.

As the spacing between cylinders reduces to *8* diameters, the transition to turbulence is delayed although at Reynolds number *156* the wake is fully turbulent right behind the tandem cylinders.

Other experiments at spacing of *3* diameter show that a fully developed vortex street appear at Reynolds numbers *121* and *156*. At a Reynolds number of *83* sinous oscillations are seen in the wake of tandem cylinders, starting some distance downstream.

More regular and laminar vortex streets are generated as the spacing reduces to two diameters for all investigated Reynolds numbers.

Zdravkovich concluded that there is a suppression of transition to turbulence in the wakes of the tandem cylinders when the spacing is less than four diameters. He demonstrate this by decreasing the spacing between cylinders from *12* to one diameter. At bigger spacing he found no regular shedding of vortices and a turbulent wake appeared at a lower Reynold Number. At the spacing of four diameters a Karman vortex street was generated behind the tandem cylinders later than is the case for a single cylinder. At spacings less than four diameters transition to turbulence in the tandem cylinders wake was delayed as the spacing was decreased.

Biermann and **Herrnstein** [**13**] investigated the effect of spacing on the cylinder drag as shown in figure (**2.24**). They plotted the results in terms of an interference drag defined as the difference between the drag of one cylinder, or two cylinders in tandem, and the drag or sum of drags on the single cylinder.

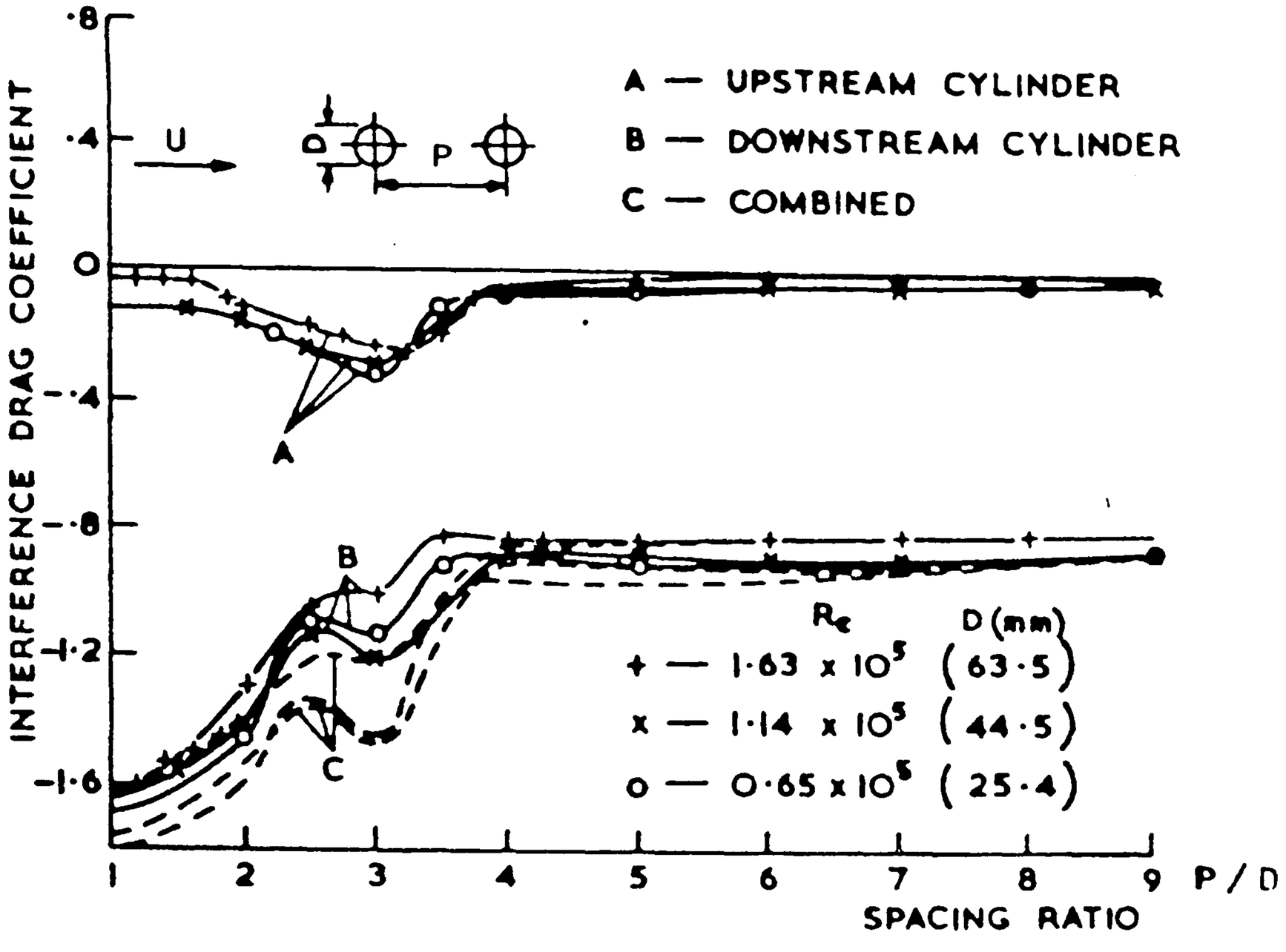

Figure (2.24).- *Drag Coefficient Vs. Gap.*

Curve A represents the interference drag coefficient of the front cylinder in the presence of the rear one. The interference drag coefficient is effectively zero for all spacings except in the range between two and four. The curve B represents the interference drag coefficient of the rear cylinder in the presence of the front one. The interference drag is negative for all spacings, and for spacing less than two is less than minus that of the cylinder in isolation. This is termed the 'shielding effect' in which the rear cylinder experiences a forward thrust. Curve C represents the total interference drag coefficient, which appears to be negative for all spacings. Thus the overall drag of the cylinders in tandem is less than the drag of the single one taken twice, as mentioned by **Zdravkovich [115][116]**.

Ishigai et.al. [48] conducted some experiments at higher Reynolds numbers by varying the gap distance from *1.1* to *5* diameters and visualising the formation region around the two cylinders as shown in figure (**2.25**). In an arrangement with a small gap, the formation region of the upstream cylinder elongates down stream beyond the downstream cylinder. For a sufficiently large gap, the downstream cylinder is beyond the formation region of the upstream cylinder and each cylinder forms Karman vortex streets.

Hori [47] measured the pressure distribution around two cylinders for three spacing configurations; i.e. *1.2*, *2.0*, and *3.0* diameters apart and he found that the side of the downstream cylinder facing the gap had a very low negative pressure whose value was almost the same as the base pressure of the upstream cylinder. This is an indication that the flow in the gap is almost stagnant. Confirmation by **Ishigai et.al.**[48] suggested a similar evidence for this. He also noticed that the negative gap pressure in front of the downstream cylinder exceeded that on the base side behind and this shows that the downstream cylinder experienced a negative drag-thrust force.

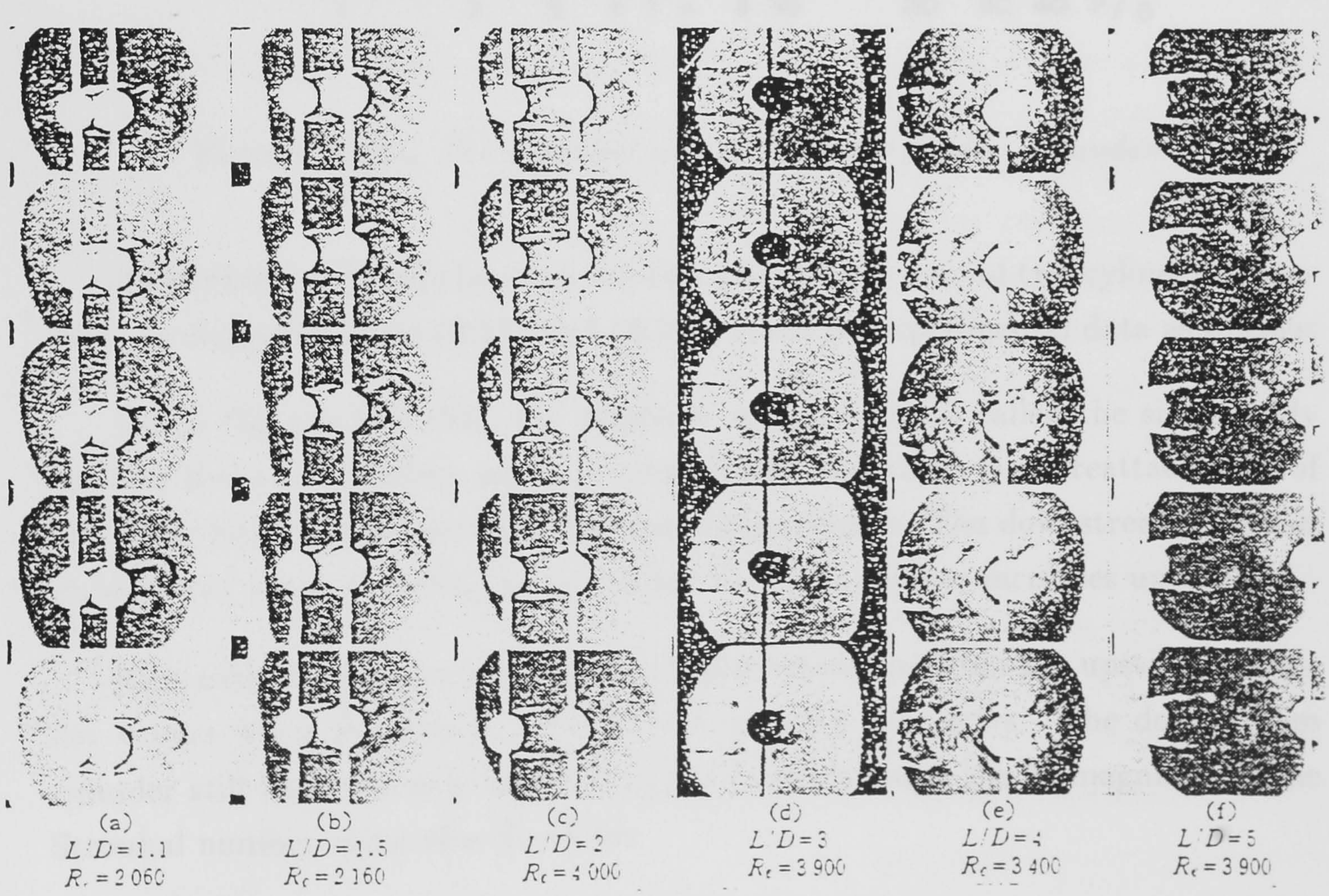

Figure 2.25.- *Vortex Formation Region for In-Line Arrangement.*

The characteristics of the velocity fluctuations, measured in the Strouhal number, depend strongly on the location in the wake. **Ishigai et.al**[48] showed that there exists a critical gap of about *3.8* cylinders, below which the regular frequency fluctuation is observed only behind the downstream cylinder. At greater gaps the vortex shedding frequency of both cylinders are equal as both cylinders form a Karman vortex street. They also showed that the velocity fluctutation and hence the Stouhal number is strongly influenced by the pressure coefficient.

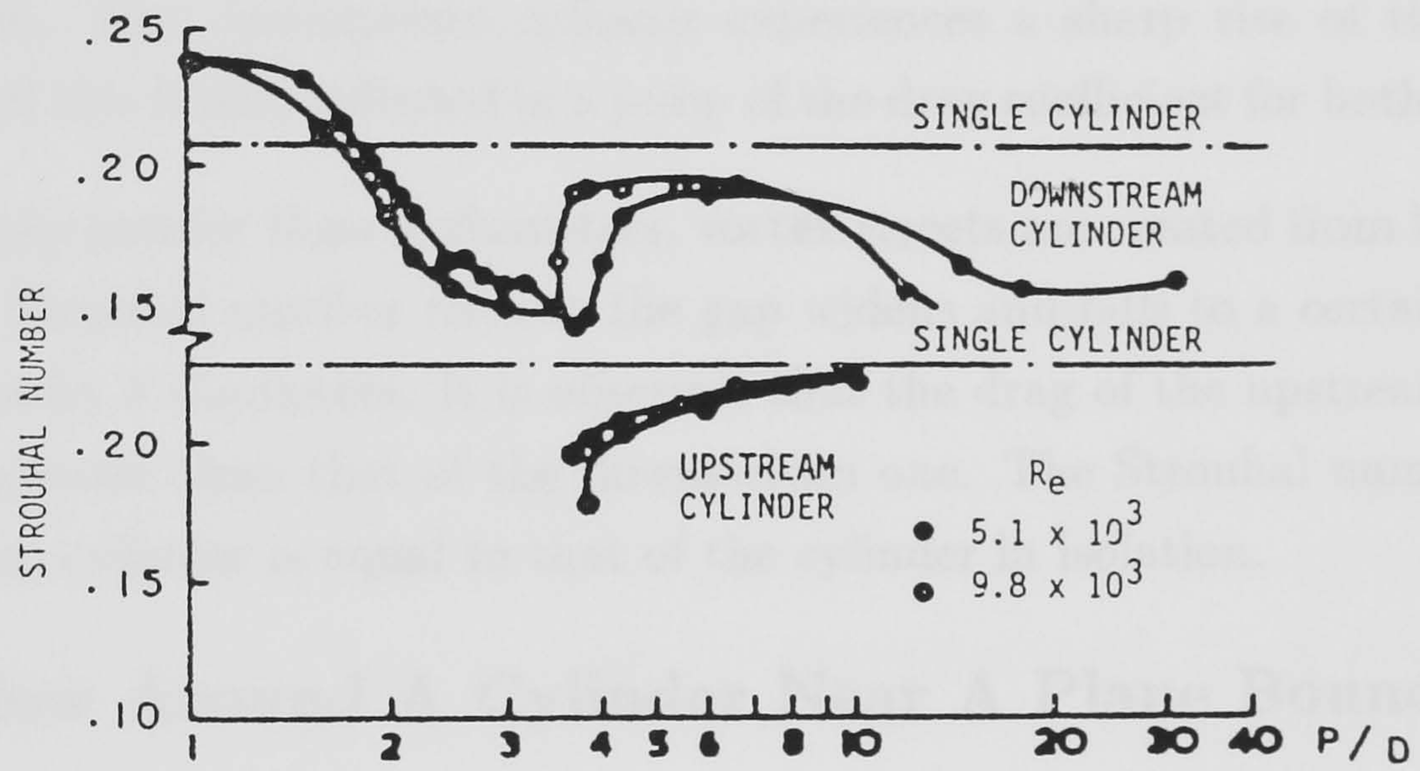

Figure 2.26.- *The Strouhal number behind cylinder in tandem.*

Zdravkovich [118] classified the flow phenomena around two cylinder in tandem, as shown in figure (**2.17**) and (**2.26**), based on experimental data as follows;

When the gap less than *0.1* diameter apart, which is called the single body regime, the two cylinders act as a single body and there is no reattachment of the shear layers separated from the upstream cylinder. The downstream cylinder experiences a negative drag force and the Strouhal number increases up to *0.24*.

Alternate reattachment of the shear layer separating from the upstream cylinder occurs when the gap is between *0.1* and *0.6* diameters. The downstream cylinder still experiences a negative thrust force although less in magnitude. The Strouhal number value also decreases.

A quasi-steady reattachment on the front side of the downstream cylinder is noticable when the gap ranges from *0.6* to *2.4* diameters. Both the drag and the

Strouhal number decrease as the gap decreases.

At a gap of *1.4* to *2.5* diameters, an intermittent shedding appears in which one of the reattached layers is disturbed but there is still no regular vortex shedding from the upstream cylinder. The drag and the Strouhal number of the upstream cylinder continue to decrease, while the downstream cylinder starts to experience a positive drag force.

The near wake region becomes unstable as the gap reaches *2.5* to *3* diameters. In this regime, vortex shedding behind the upstream cylinder persists for sometime and then is intermittently suppressed and replaced by the previous reattachment flow regime. The downstream cylinder experiences a sharp rise of the Stouhal number and this is also reflected in a jump of the drag coefficient for both cylinders.

For a gap greater than *3* diameters, vortex streets are created from both cylinders. The Strouhal number rises as the gap widens and falls to a certain value as the gap reachs *8* diameters. It is observed that the drag of the upstream cylinder is always greater than that of the downstream one. The Strouhal number of the downstream cylinder is equal to that of the cylinder in isolation.

2.3 The Flow Around A Cylinder Near A Plane Boundary

In oil exploration activities, the design and installation of pipelines in water offshore, is one of the major problems to be tackled. There are various difficulties that have to be overcome in the design of unburied pipelines laid on or near the ocean bottom. Contributory factors include wave-current combinations, scour, vibratory motion, roughness and its growth with marine fauna and flora, sediment motion, wind and free surface effect, nonlinear waves and wave trains. Any one of these factors at sea bed level can cause some level of damage to the pipes lying on it.

Various studies involving cylinders in close proximity to an impermiable surface have been conducted using computers and laboratory. For example, **Sarpkaya** [**83**] has carried out U-Tube experiments, **Bearman** and **Zdravkovich** [**12**] have performed wind tunnel experiments and **Angrilli** [**2**], **Fredsoe et.al** [**34**], **Grass** [**41**] and **Summer et.al** [**105**] have conducted experiments in open water channels. Investigations have been carried out in both uni-directional and oscillatory flows.

2.3.1 Uni-Directional Flow

Bearman and **Zdravkovich** [**12**] conducted experiments in a wind tunnel with a Reynolds number of 4.5×10^4 for the flow around a circular cylinder placed at various heights above a plane boundary. They revealed that regular vortex shedding persisted at the same Strouhal number for all gaps down to $\frac{G}{D} = 0.3$. where G is the gap and D is diameter of the cylinder. For all values $\frac{G}{D} < 0.3$ strong regular vortex shedding began to be suppressed, and when the cylinder touched the wall there was no regular shedding of vortices.

This is in line with the results presented by **Grass et.al.** [**42**] who carried out their experiment in an open flow channel and at a subcritical Reynolds number about 10^3.

As the cylinder was moved away from the wall plate the pressure distribution around the cylinder became more symmetric about the front stagnation point and by $\frac{G}{D} = 0.4$ it was perfectly symmetric. At small gaps the separation point on the side nearest the wall moved down stream of the narrowest point of the gap. The flow around a cylinder close to a wall can be considered to be analogous to the flow around two cylinders in a side by side arrangement. For $\frac{G}{D}$ above 0.5 the two flows are similar. However, the flow about two cylinders becomes bistable for $\frac{G}{D} < 0.5$ whereas a cylinder near a wall shows no such instability.

The flow pattern at various gaps of 0, 0.2, 0.3, 0.4, 0.8, 1.0, 1.2 and 2.0 diameters are reproduced from **Bearman** and **Zdravkovich** [**12**] and also from **Grass et.al.** [**42**] and displayed in figures (**2.27**) and (**2.28**).

Roshko et.al [**77**] measured lift and drag coefficients on a circular cylinder near a wall at $\frac{G}{D}$ from 0 to 6. The experiment was carried out at a Reynolds number of 2×10^4. They found that at large $\frac{G}{D}$ the drag coefficient was about 1.2 and that is slightly increase as $\frac{G}{D}$ reduced to 0.6. However, further reduction of $\frac{G}{D}$ will decrease the the drag coefficient until the cylinder touches the wall. They suggested that this reduction is mainly caused by the interference of the wall with the vortex shedding and the immersion of the cylinder in the lower energy wall-boundary layer flow.

Other data on the predicted increase in shedding frequency and Strouhal number unfortunately appears to be contradictory. **Goktun** [**36**] reported an increase in Strouhal number to a maximum of the order of 5 per cent which occured at a bed gap of about 0.5 diameter. **Bearman** and **Zdravkovich** [**12**] found that the

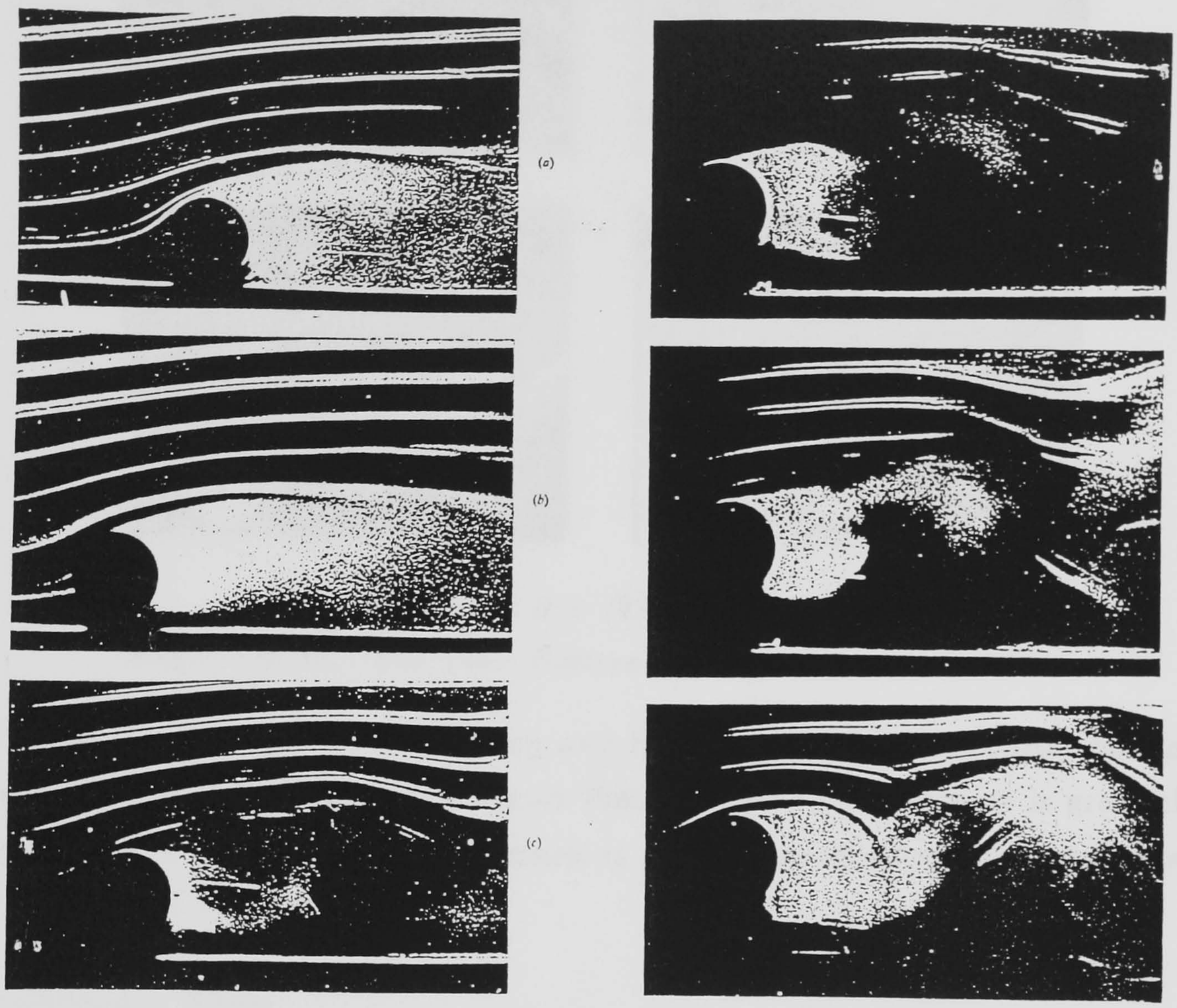

(a) G/D = 0 ; (b) G/D = 0.2; (c) G/D = 0.4
(d) G/D = 0.8; (b) G/D = 1.2; (c) G/D = 2.0

Figure 2.27.- *The Flow Pattern of a cylinder near a wall*

vortex shedding frequency, as computed by digital spectral analysis, was relatively constant with respect to gap variations. However, their data appears to reveal an upward trend in the recorded values of Strouhal number of approximately 5 per cent at a gap of *0.75* diameters. **Angrilli et.al.** [2] argued that this effect is caused by a reduction of the scale of the vortex formation region due to the proximity of the wall, and that when the shear layers are brought closer together, their interaction is facilitated and the shedding period is shortened. He then plotted the

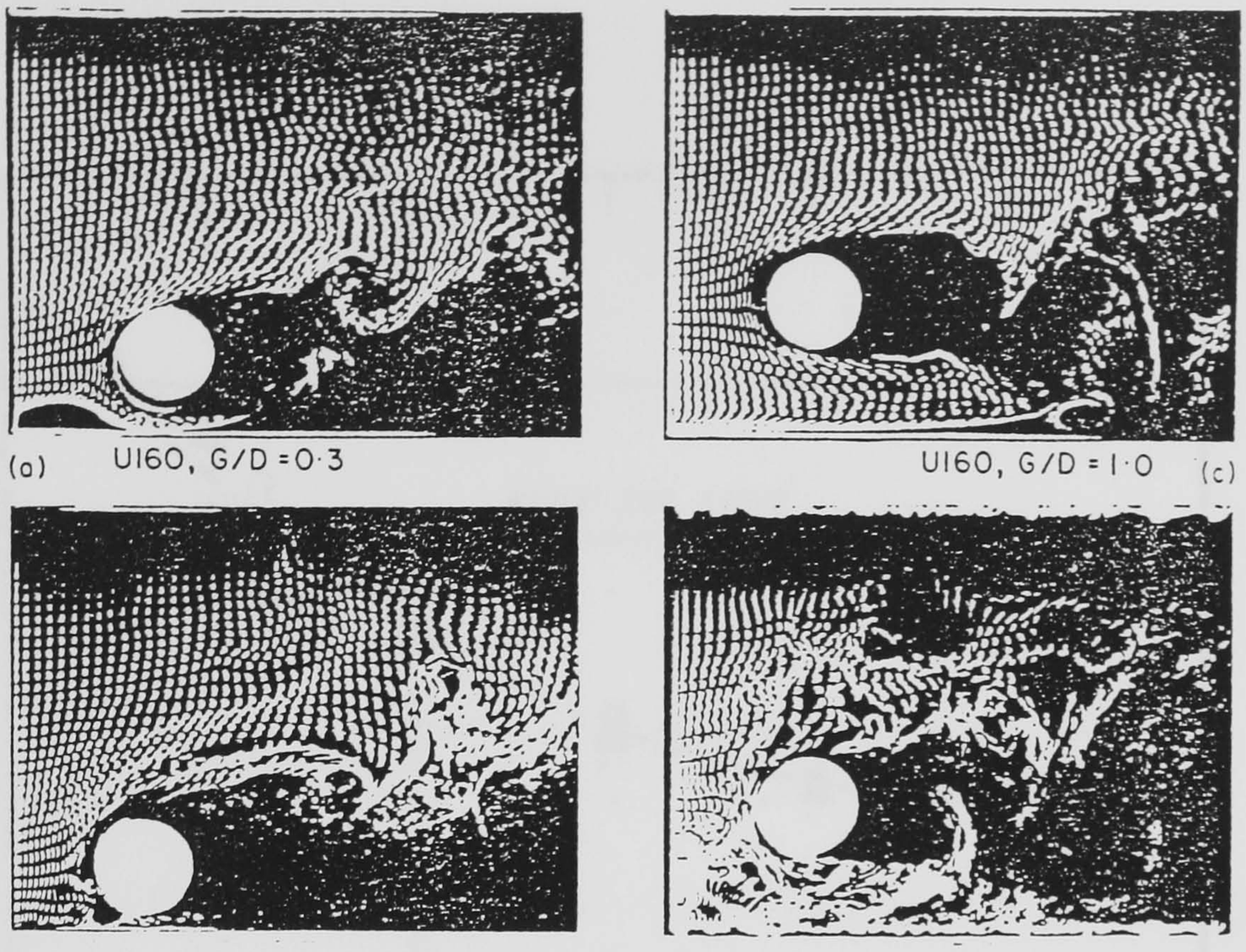

(a) G/D = 0.3; (b) G/D = 1.0

Figure 2.28.- *The Flow Pattern of a cylinder near a wall*

variation of vortex shedding frequency as a function of wall distance from the test cylinder, see figure (**2.29**) which shows that the shedding frequency is gradually increased as the gap is reduced. As much as *10* per cent increase is expected when the gap is very small.

2.3.2 Oscillatory Flow

Yamamoto et.al. [113], carried out experiments in the range of Reynolds numbers from *2000* to *30000*. In this unseparated range, the wake dependent drag force is negligible and the in-line as well as the transverse forces are mainly due to the wave acceleration. Under such conditions, the use of potential theory to calculate the force coefficients is adequate. The results of his study show that a net force exists away from the wall when the cylinder touches the wall while a net force exists toward the wall when a small gap exists between the cylinder and the wall.

Sarpkaya [83] measured the in-line and transverse forces on cylinders near a wall in a fluid oscillating sinusoidally in the range of subcritical Reynolds numbers. He conducted the experiment in a U-shaped, vertical water tunnel in which the fluid in the tunnel is oscillated pneumatically and the cylinder model is placed at

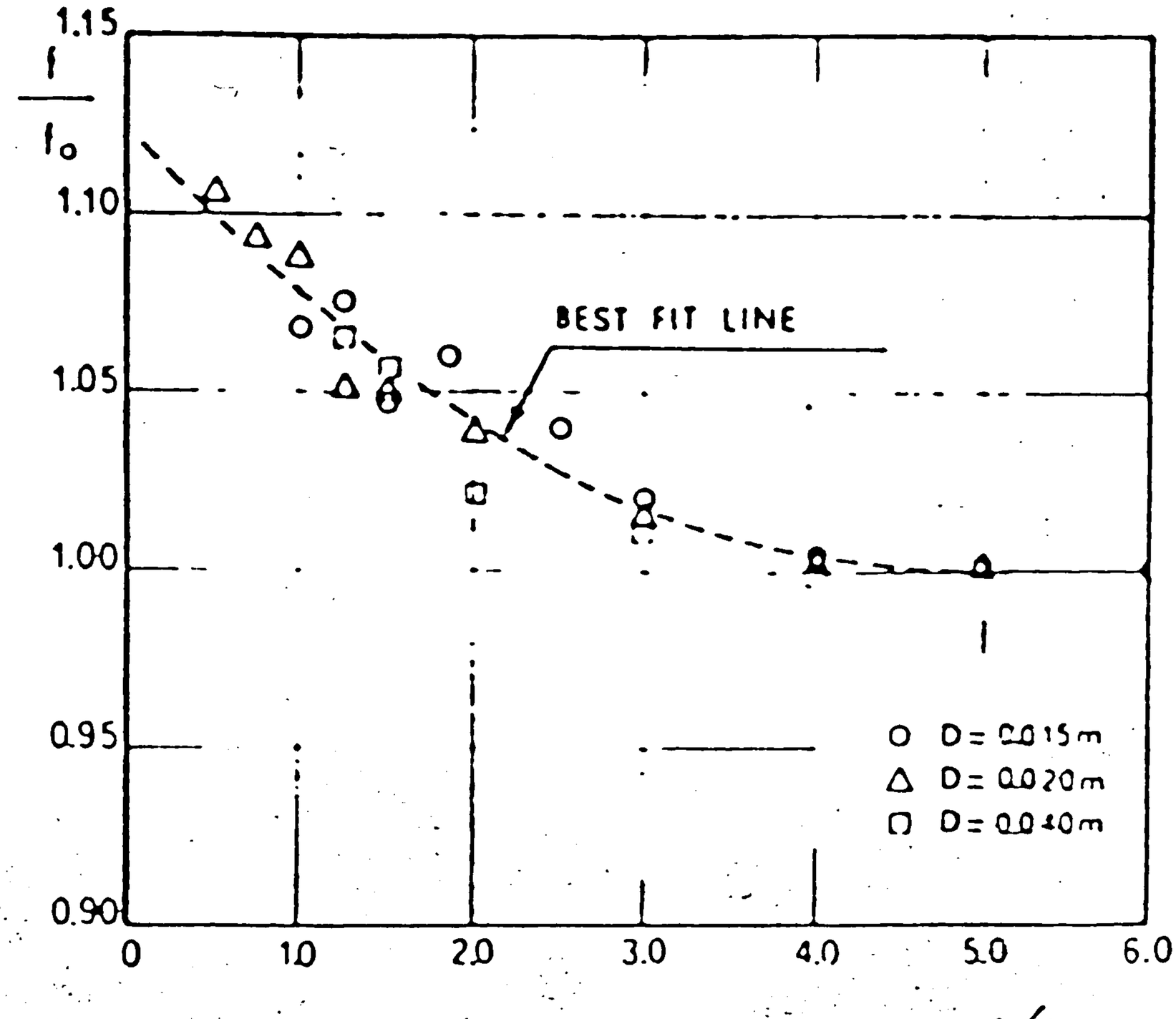

Figure 2.29.- *Vortex shedding frequency Vs. Wall Distance*

a variable distance from the tunnel wall.

The asymmetric flow created when a cylinder is placed near the plane wall generates lift and drag forces which can be of considerable magnitude for small gaps. In unseparated flow, the lift force acts in a downward direction, which is generally different from that due to separation and vortex shedding, in which, when the cylinder touches the boundary, a net force exists away from the wall. An alternating lift force can be produced, if there is a small gap between the cylinder and the wall, due to asymmetry in the flow along with and vortex shedding about the cylinder.

Sarpkaya [82] and **Sarpkaya** and **Isaacson** [87] also showed that the force coefficients depend not only on the Reynolds number and the relative gap between

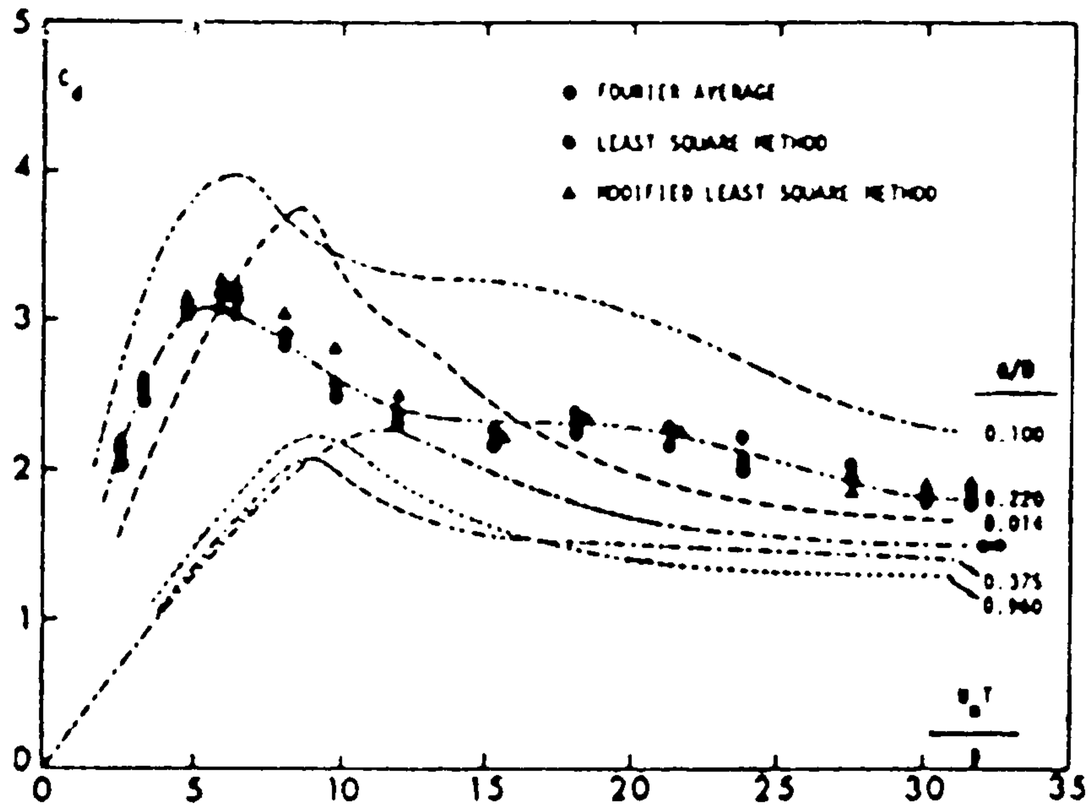

Figure 2.30.- *Drag Coefficient Vs. Keulegan-Carpenter Numbers for Various Values of Gap Ratios*

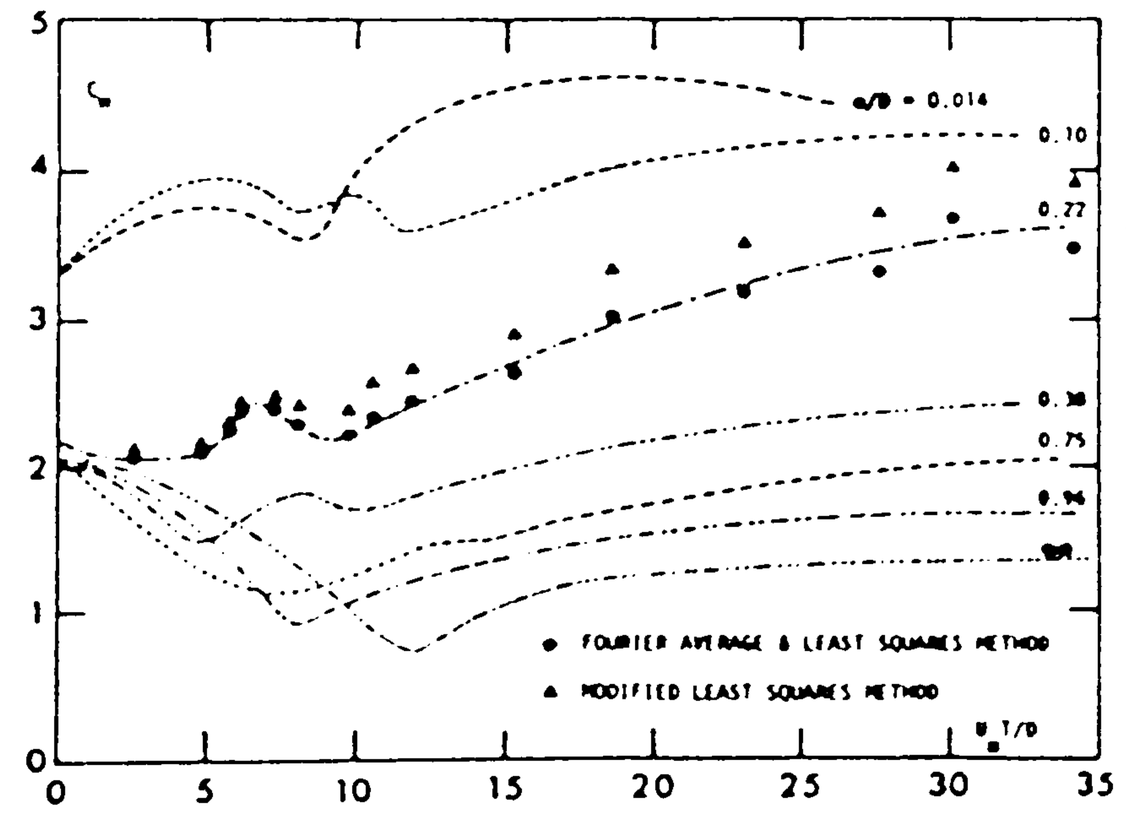

Figure 2.31.- *Inertia Coefficient Vs. Keulegan Carpenter Numbers for Various Values of Gap Ratios*

the cylinder and the plane boundary but also on the Keulegan-Carpenter number and the time dependent laminar or turbulent boundary layer characteristics.

Sarpkaya [82]'s results for the force coefficients as a function of the wall proximity at various values of Keulegan-Carpenter numbers are displayed in figures

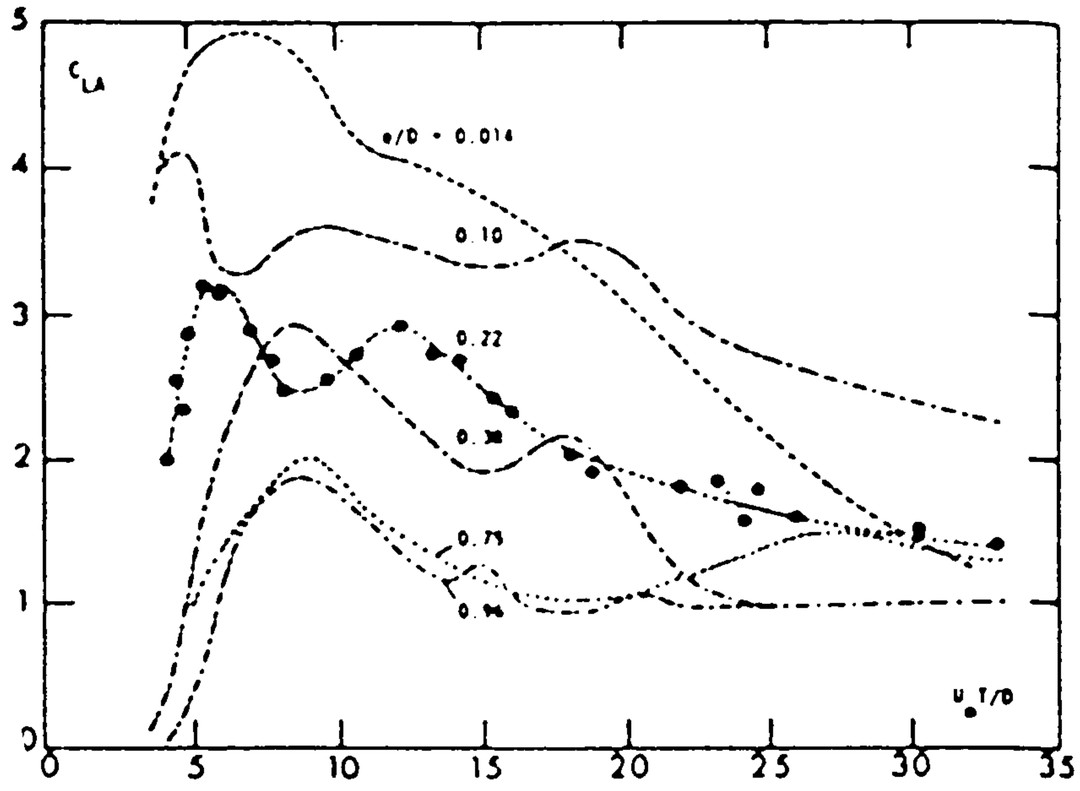

Figure 2.32.- *Lift Coefficient Vs. Keulegan Carpenter Numbers for Various Values of Gap Ratios*

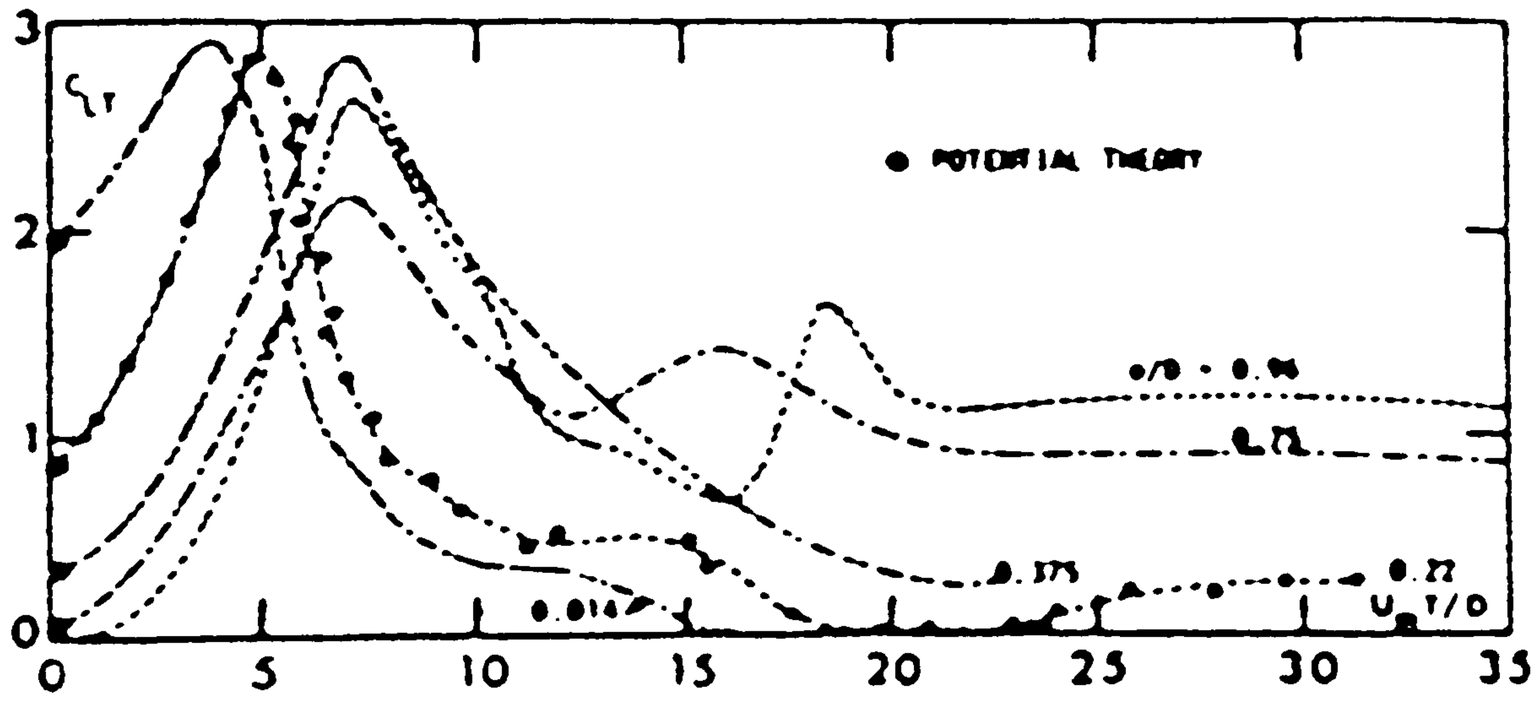

Figure 2.33.- *Lift Coefficient for Force toward the Wall Vs. Keulegan Carpenter Numbers for Various Values of Gap Ratios*

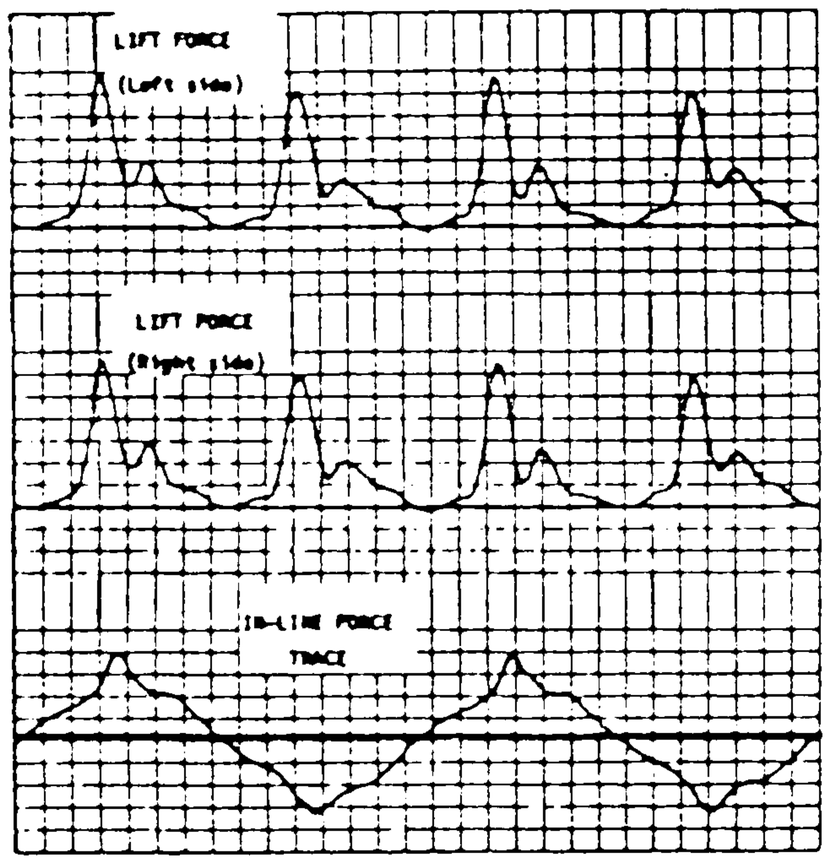

Figure 2.34.- *Representative Lift and in-Line Force tracesfor* $G/D = 0.125$ **(2.30), (2.31), (2.32), (2.33),** and **(2.34).**

These figures show that large lift force both away from and toward the wall could occur in a given cycle of oscillation. The practical significance of this is that these oscillations could cause scour and fatigue. The coupled motion between the in-line and transverse oscillations may lead to disastrous consequences.

Chapter III

THEORETICAL BACKGROUND

3.1 Introduction

The behaviour of an incompressible fluid is governed by the Navier-Stokes equations which are derived on the basis of conservation of momentum in the fluid during its motion and may be written as follows (**Milne – Thompson [67]**):

$$\frac{Du}{Dt} = \frac{\partial u}{\partial t} + u.\nabla u = \nu\nabla^2 u - \frac{1}{\rho}\nabla p + F \qquad \textbf{(3.1)}$$

The derivative term $\frac{D}{Dt}$ incorporates both the local rate of change of velocity, $\frac{du}{dt}$, of a fluid element at a certain position and the convective rate of change $u.\nabla u$ due to the transport of the element to a different position. The total derivative $\frac{D}{Dt} = \frac{\partial}{\partial t} + u.\nabla$ is known as a Lagrangian type of derivative.

The equation relates the rate of change of momentum of a fluid element to the forces due to viscosity $\mu\nabla^2 u$, to the negative pressure gradient $-\nabla p$ and also to the body forces acting on the fluid element F. The kinematic viscosity ν is defined as the dynamic viscosity μ divided by the fluid density ρ.

A motion which involves no change in fluid volume is termed isochoric. If the mass, m and the density, ρ of an isochoric fluid are related by $dm = \rho dv$, the conservation of the volume of a fluid during its motion is,

$$\frac{\partial}{\partial t}\int_V \rho dV = \int_S \rho u.ndS = -\int_V \nabla.(\rho u)dV \qquad \textbf{(3.2)}$$

by Gauss's theorem. A fixed surface S can be defined as a closed curve bounding a fluid body of volume V. Thus,

$$\int_V \left(\frac{\partial \rho}{\partial t} + \nabla(\rho u)\right) dV = 0$$

Since the surface S can be replaced by any arbitrary closed surface drawn within it, then

$$\frac{\partial \rho}{\partial t} + \nabla(\rho u) = 0.$$

If the Lagrangian derivative is applied then,

$$\frac{D\rho}{Dt} + \nabla(\rho u) = 0 \tag{3.3}$$

From this it becomes clear that an isochoric fluid, with constant density, may have constant mass if and only if it satisfies the continuity equation:

$$\nabla . u = 0 \tag{3.4}$$

The circulation around a closed curve C drawn in the fluid is,

$$\Gamma(C) = \oint_C u.dl = \int_S (\nabla \times u).ndS \tag{3.5}$$

using Stokes's theorem. Since the term $\nabla \times u$ is the vorticity ω, then

$$\Gamma(C) = \int_S \omega.ndS \tag{3.6}$$

A flow is said to be irrotational if the value of vorticity $\omega = \nabla \times u = 0$ and for such a flow there exists a well defined scalar function ϕ called the velocity potential, such that

$$u = \nabla\phi \tag{3.7}$$

and therefore the equation of continuity (**3.4**) for a fluid in irrotational motion becomes,

$$\nabla^2\phi = 0 \tag{3.8}$$

which is known as the Laplace equation.

Thus a fluid can not move according to an arbitrarily assigned law of distribution of velocity but must satisfy the equation of continuity. Furthermore, irrotational motions of a liquid are subject to the condition that the velocity potential ϕ shall satisfy Laplace's equation. Functions satisfying this equation are termed harmonic functions. Taking the curl of the Navier-Stokes equation, leads to

$$\frac{D\omega}{Dt} = \frac{\partial\omega}{\partial t} + u.\nabla\omega = \omega.\nabla u + \nu\nabla^2\omega \tag{3.9}$$

This equation is known as the vorticity transport equation and it plays a central role in the Discrete Vortex Method as described in the following chapter.

In comparison to the Navier-Stokes equation (**3.1**), the vorticity transport equation (**3.9**) is more convenient to use since it involves the vorticity ω in the formulation. In the two dimensional case, the first term on the right hand side of equation (**3.9**) is equal to zero, since this term contributes to the vortex stetching in the third axis. In this case, it is seen that the net viscous force on an element of incompressible fluid is determined by the gradient of vorticity. When the fluid viscosity ν is small, the net viscous force is significant only at places where the vorticity gradients are large and if for some reason the vorticity is zero over a region of flow, viscous stresses make no contribution to the net force on elements of fluid and may be ignored for most purposes.

The second term of the left hand side of equation (**3.9**) is the familiar rate of change due to convection of fluid in which the vorticity is non-uniform past a given point. The last term represents the rate of change of vorticity in exactly the way that $\nabla^2\omega$ represents the contribution to the acceleration from the diffusion of velocity (or momentum). In an inviscid fluid, in which the viscousity $\nu = 0$, the Navier-Stokes equation (**3.1**) reduces to the Euler equation;

$$\frac{Du}{Dt} = \frac{\partial u}{\partial t} + u.\nabla u = -\nabla\left(\frac{p}{\rho} - \Omega\right) \qquad \textbf{(3.10)}$$

where Ω is the conservative force. Further simplification of this equation will result in the unsteady Bernoulli equation as follows:

$$\frac{\partial \phi}{\partial t} + \frac{p}{\rho} + \Omega + \frac{1}{2}|\nabla\phi|^2 = f(t) \qquad \textbf{(3.11)}$$

where f is some function of t. For steady flow, the first term on the left hand side of the equation will be zero and $f(t)$ will be constant along a streamline.

In two dimensional, time dependent and incompressible, but not necessarily irrotational flow, the stream function can be found by applying Green's theorem to equation (**3.4**),

$$\oint_\Lambda u_2 dx_1 - u_1 dx_2 = -\int_S \nabla.u dx_1 dx_2 = 0$$

the scalar function,

$$\psi(\tilde{x}, t) = \int^{\tilde{x}} u_2 dx_1 - u_1 dx_2$$

is therefore independent of the path and

$$\frac{\partial \psi}{\partial x_1} = u_2 \quad and \quad \frac{\partial \psi}{\partial x_2} = -u_1 \qquad \textbf{(3.12)}$$

This function, which shows the flow rate across any line connecting the two points, is called the stream function and can be shown to be related to the vorticity through Poisson equation

$$\nabla^2 \psi = -\omega \tag{3.13}$$

From equation (**3.7**) and (**3.11**) it becomes obvious that:

$$\frac{\partial \phi}{\partial x} = -\frac{\partial \psi}{\partial y} \quad and \quad \frac{\partial \phi}{\partial y} = \frac{\partial \psi}{\partial x} \tag{3.14}$$

the complex potential and stream function therefore satisfy the Cauchy-Riemann equation and are differentiable. This shows that equi-potential lines always intersect the streamlines at a right angle.

Due to this property, the complex potential $w(z)$ in complex plane can be written as,

$$w(z) = \phi(z) + i\psi(z) \tag{3.15}$$

where $z = x + iy$ is an arbitrary complex point. From equation (**3.7**), (**3.12**) and (**3.14**) it is clear that,

$$\frac{dw(z)}{dz} = \bar{u}(z) \tag{3.16}$$

where $\bar{u}(z)$ represents the complex conjugate of complex velocity u at certain point z in the fluid domain.

The complex potential is a convenient variable to work with in describing fluid motion as it is made up of the stream function and the velocity potential from which the fluid kinematics and pressures can be easily obtained.

3.2 Free Stream Potential

For a fluid flowing with uniform velocity u_∞ along the positive x axis, the complex potential w_∞ can be easily obtained as

$$w_\infty(z) = u_\infty z \tag{3.17}$$

where u_∞ is the far field fluid velocity and z is an arbitrary point in the complex plane. If the vector of the velocity makes an angle to a fixed reference, it can be easily modified as follows,

$$w_\infty(z) = u_\infty z e^{-i\alpha} \tag{3.18}$$

where α is the counter clockwise rotation of the angle of the velocity vector with respect to the positive x axis.

3.3 Vortex Potential

The discrete vortex method which will be described in the following chapter allows the modelling of flow structures arising out of flow separation by arrays of discrete vortices embeded in an otherwise irrotational flow

The complex potential of a discrete vortex, with circulation Γ (positive for a clockwise direction) in an unbounded fluid is given by **Sarpkaya** [**78**] as,

$$w(z) = \frac{i\Gamma}{2\pi} \ln(z - z_p) \tag{3.19}$$

The velocity potential and stream function can be easily derived from this equation by using equation (**3.14**) as follows,

$$\phi = \frac{\Gamma}{2\pi}\theta \quad and \quad \psi = -\frac{\Gamma}{2\pi} \ln(r) \tag{3.20}$$

where θ is an angle measured from the positive x axis and r is the distance from the vortex core to any point in fluid domain.

It can be seen that the equi-potential lines are lines with different angles emanating from the vortex core whereas the streamlines are a family of concentric circles with their radii rapidly increasing away from their centre.

3.4 Source Potential

Solid boundaries can also be modelled by using arrays of singularities. In later chapters, arrays of sources will be used to model plane boundaries.

The complex potential of a source with strength σ in unbounded fluid is given as

$$w(z) = \frac{\sigma}{2\pi} \ln(z - z_p) \tag{3.21}$$

where z_p is the location of the source. The velocity potential and stream function will then be

$$\phi = \frac{\sigma}{2\pi} \ln(r) \quad and \quad \psi = \frac{\sigma}{2\pi}\theta \tag{3.22}$$

where θ is an angle measured from the positive x axis and r is the distance from the source to any point in the fluid domain.

It can be seen that the equi-potential lines and the stream lines are an orthogonal set to those obtained for the irrotational vortex.

3.5 Wave Potential

The velocity potential for a regular long crested wave travelling with respect to a Cartesian coordinate system with $X-$axis measured in the direction of wave propagation and with the y axis measured upward from the still water level can be simply derived. It is assumed that the waves are progressive in the positive X direction and that they propagate over a smooth horizontal bed in water of constant undisturbed depth, d.

The fluid is taken to be incompressible and inviscid and the flow to be irrotational. The velocity potential of wave therefore satisfies the Laplace equation,

$$\frac{\partial^2 \phi_w}{\partial x^2} + \frac{\partial^2 \phi_w}{\partial y^2} = 0 \qquad \textbf{(3.23)}$$

and will be subject to boundary conditions defined by the physical properties of the waves and their environment.

On the free surface the velocity normal to the surface of a typical fluid particle is equivalent to that of the wave itself in that direction. Therefore,

$$\frac{\partial \phi_w}{\partial y} + u.\nabla \phi_w = \frac{\partial \eta}{\partial t} + u.\nabla \eta$$

gives,

$$\frac{\partial \eta}{\partial t} + \frac{\partial \phi_w}{\partial x}\frac{\partial \eta}{\partial x} - \frac{\partial \phi_w}{\partial y} = 0 \quad at \quad y = \eta \qquad \textbf{(3.24.a.)}$$

where $\eta(x,t)$ is the free surface elevation measured from the still water level. This is often referred to as the Kinematic Boundary Condition.

Also on the free surface, the Dynamic Boundary Condition states that the pressure on the surface expressed in terms of the Bernoulli equation, is constant. Thus,

$$\frac{\partial \phi_w}{\partial t} + \frac{1}{2}|\nabla \phi_w|^2 + g\eta = f(t) \quad at \quad y = \eta(x,t) \qquad \textbf{(3.24.b.)}$$

where g is the acceleration due to gravity.

The boundary condition to be applied to the sea bed is the condition which states it is impermeable i.e. no fluid particle can penetrate it. Thus

$$\frac{\partial \phi_w}{\partial y} = 0 \quad y \quad = -d \qquad \textbf{(3.25)}$$

The second terms in equations (**3.24.a.**) and (**3.24.b.**) are non-linear and in small amplitude wave theory, which neglects terms of order higher than 1. these terms will be dropped from the equations. The two free surface boundary conditions can be combined to give

$$\frac{\partial^2 \phi_w}{\partial t^2} + g\frac{\partial \phi_w}{\partial y} = 0 \quad at \quad y = 0 \tag{3.26}$$

The solution for the velocity potential $\phi_w(x, y, t)$ can be obtained by the method of separation of variables in which ϕ_w is written in the form,

$$\phi_w(x, y, t) = f(y)\phi_w(x - ct)$$

which is possible due to the periodic nature of the wave and where wave celerity c is defined to be the wave length divided by the wave period. By this approach and through the satisfaction of the boundary condition the velocity potential can be shown to take the form,

$$\phi_w(x, y, t) = \frac{gH\cosh(k(y + d))}{2kc\cosh(kd)}\sin(k(x - ct) \tag{3.27}$$

where H is the wave height and $k = \frac{2\pi}{\lambda}$ is the wave number, with λ being the wave length. The boundary condition (5) may now be used to obtain an expression for celerity c in terms of k, which is called the linear dispersion equation,

$$c^2 = \left(\frac{g}{k}\right)\tanh(kd) \tag{3.28}$$

which describes how the wave celerity increases with the wave length. If a wave is defined in terms of its wave height and period, the particle kinematics and pressure at any point beneath the waves can be calculated by using equations (**3.11**) and (**3.23**) above.

The horizontal and vertical fluid particle velocities can be calculated by differentiating the velocity potential ϕ_w with respect to the X and Y -axis. Then particle orbit can then be found for shallow, intermediate and deep water depths as shown by **Sarpkaya** and **Isaacson** [**87**]. In modelling flows around cylinder by laboratory experiment, planar oscillatory flows are used in preference to real wave flows since they are more easily controlled. Most numerical models are of *two* dimensional horizontal planes through the cylinder, where the particle orbits are also planar oscillatory. The use of planar oscillatory flow to numerically model wave flow phenomena is, therefore, a well established and accepted practice.

Chapter IV

THE DISCRETE VORTEX MODEL;
The Flow Around A Cylinder In An Infinite Fluid

4.1 General Description

When a body is moving in a fluid at any velocity, vorticity is generated in the boundary layers forming on the surface of the body. This formation is due to the fact that the velocity of the water relative to the velocity of the body is zero on the body surface and becomes equal to the free stream velocity at some small distance from the surface. This distance is called the boundary layer thickness δ. In an attached flow problem, where no separated flow exists, the velocity gradient in the boundary layer causes the fluid particles to move in a circular manner about a certain axis.

In an inviscid potential flow, where the Reynolds number is infinite, the boundary layer vorticity is compressed into an infinitely thin vorticity sheet across which the velocity parallel to the surface changes discontinuously from zero in contact with the wall to the potential flow value just outside the vorticity sheet. For this type of flow, at high Reynolds number , the effect of viscous diffusion becomes less influential, as is evident from the vorticity transport equation (**3.9**) in which the viscous terms become less significant. The flow can then be modelled with the vorticity transport equation (**3.9**) simplified as follows;

$$\frac{\partial \omega}{\partial t} + (\nabla \phi) \cdot (\nabla \omega) = 0 \qquad (\mathbf{4.1})$$

The vorticity which is restricted to small sub-domains within the fluid, is convected with the free stream and can be modelled by arrays of discrete vortices. Outside these sub-domains the flow can be considered to be inviscid and irrotational.

In a real flow, where viscosity is present, its influence is to diffuse the vorticity normal to the body surface, resulting in the viscous boundary layer. The vorticity is the product of the dynamic behaviour of the outer flow, and the rate of vorticity production adjacent to the surface is directly related to the pressure gradient, see **Lewis** and **Porthouse** [**61**].

The influence of the diffusion becomes increasingly significant for Reynold numbers in the intermediate regime, typically between 10^2 and 10^5, and this must be taken into account when modelling the vorticity transport equation.

It is shown from some experiments that the strengths of vortices decreased as they travel downstream from a body. This is due to the exchange and cancellation of oppositely signed circulation within the wake. The latter mainly occurs in the flow field just beyond the rear stagnation points, when oppositely signed circulation separates from the separation points, interacts and then cancels between the two shear layers. However, according to **Fage** and **Johansen** [**33**] this type of circulation reduction only contributes about one tenth of the total.

There are two main approaches to modeling the diffusion part of the vorticity transport equation

$$\frac{\partial \omega}{\partial t} = \nu \nabla^2 \omega \qquad (\mathbf{4.2})$$

namely, the Finite Difference and Random Walk schemes.

Xin and **Wong** [**111**] modelled the diffusion part using a second order *Lax − Wendroff* difference scheme and this is combined with the two level expression for the vorticity of convection part. **Chorin** [**18**][**19**] modelled the vortex decay explicitly by the introduction of viscous diffusion using the method of 'operator splitting' as also mentioned by **Sarpkaya** [**85**] . This can be illustrated by expressing the vorticity transport equation (**3.9**) in the form;

$$\frac{\partial \omega}{\partial t} = (T_D - T_C)\,\omega \ . \qquad (\mathbf{4.3})$$

where $T_D = \nu \nabla^2$ and $T_C = u \cdot \nabla$ are the diffusion and convection operators respectively, which are modelled through the use of separate process.

In the construction of a Finite Difference scheme to model the diffusion part, **Graham** [**40**] and **Graham** and **Cozens** [**41**] developed a scheme on a cartesian coordinate grid, through a conformal mapping, as the use of a radially expanding polar grid leads to very complicated difference formulae. The Euler and Central Difference models, are chosen for their simplicity and ease of use to solve the numerical expression and are two-level in time and three-level in space. Another approach came from **Stansby** and **Dixon** [**100**][**101**] who solved the Poisson equation through the value of vorticity at four grid nodes by a similar finite difference formulation. The velocity at those surrounding nodes can be calculated afterward and can be used with a bilinear interpolation to calculate the vortex velocities.

As reported by **Sarpkaya** [**84**][**85**], stable and realistic results are obtained on implementing a Finite Difference scheme to model the diffusion, especially, at low Reynolds number. However, constructing a Finite Difference scheme can be quite complicated when dealing with an arbitrary shaped body or with a multi-body case, as boundary conditions must be satisfied on the body surface. This complication is mainly due to the complex derivation for the conformal mapping required to transform an arbitrary shape and/or multi-bodies to a cylindrical body.

The present study uses a much simpler approach in modelling the diffusion, namely the Random Walk, which was pioneered by **Chorin** [**18**][**19**], and **Lewis** and **Porthouse** [**61**]. The basis of this method is the use of a stochastic approach in modelling the diffusion equation using an equation for the vorticity decay of a line vortex, as described in more detail in a later section.

The remainder of this chapter will illustrate and describe a method and an algorithm which involves the use of a polar grid whose nodes are used to represent all the vortices distributed over the grid. The principal steps of the algorithm are listed in the flow chart shown in figure (**4.1**). The number of surface elements is equal to the number of grid nodes in one ring. A surface node is located at the centre of each surface element and this shows that the vortex distribution around the cylinder surface is now concentrated at each body node. The calculation of the surface velocity is done at the surface nodes through the use of the Martensen equation by imposing the Dirichlet boundary condition of zero tangential velocity on the surface.

At the beginning of each time-step a pre-defined number of vortices are introduced around the surface of the cylinder, located at the nodes of the first ring of the grid out of the cylinder.

The nodal distribution is then used in a Biot-Savart velocity calculation, thus decreasing the degree to which vortex to vortex dependencies are involved. The velocity of grid nodes is then interpolated using a bi-linear interpolation to get the velocity of the vortices, which is used to convect the vortices from their current positions. The strengths of the vortices are then once again re-distributed using the same bi-linear interpolation involving the surrounding grid nodes. The grid nodes strengths are also employed in the calculation of surface velocity and force coefficients for the next time step.

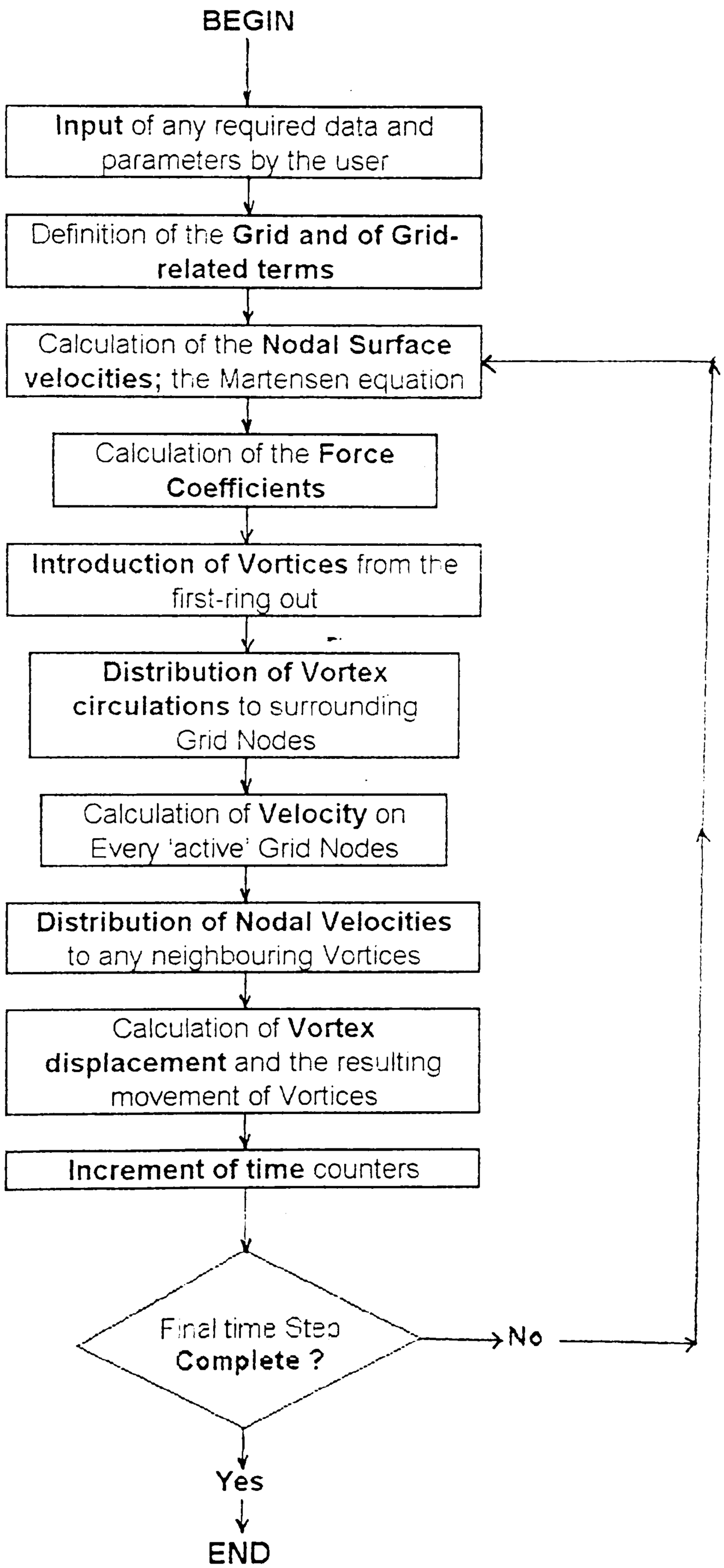

Figure 4.1.- *Flow Chart for the Discrete Vortex Algorithm*

In the cylinder surface and grid node velocity calculation, the key element behind the scheme is the formulation of the complex potential function, from which the velocities may be calculated. This complex potential is composed of a sum of the individual components which have already been described in previous chapter.

The components define uniform flow around a circular cylinder and the surface vorticity distribution around the cylinder in the presence of a number of discrete vortices. Using these components, the complex potential function may be written as follows:

$$w(z) = u_\infty e^{-i\alpha_\infty} z + \frac{i}{2\pi}\sum_{e=1}^{N_e} \gamma_e dS_e \ln(z - z_e) + \frac{i}{2\pi}\sum_{\nu=1}^{N_\nu} \Gamma_\nu \ln(z - z_\nu) \qquad \textbf{(4.4)}$$

where, u_∞ is the free stream velocity, α_∞ is the tangent angle of the free stream velocity measured in counter clockwise direction from the positive $X-$axis, N_e is the number of cylinder elements, N_ν is the total number of the shed vortices, z_e is the cylinder node position, z_ν is the vortices position, γ_e is the strength of the cylinder vortex, Γ_ν is the strength of the shed vortices, dS_e is the length of the body element, and i is the complex number $\sqrt{-1}$.

4.2 The Surface Singularity Method

Based on zero velocity on the cylinder surface, known as the Dirichlet boundary condition, the influence of the surface vorticity and uniform free stream $\vec{u}_\infty$ on a point on a two dimensional cylinder surface S_m with local tangent vector $\vec{d}S_m$ was derived by **Martensen** [**64**] and can be written as follows,

$$-\frac{1}{2}\gamma_m + \oint k_{mn}\gamma_n dS_n + \vec{u}_\infty \cdot \vec{d}S_m = 0 \qquad \textbf{(4.5)}$$

where the integral is taken around the closed body surface. γ_n is the vorticity strength and k_{mn} is the kernal of the integral as described later. The first term is the velocity discontinuity experienced if we move from the centre of the vorticity sheet onto the body surface beneath, as explained in *Appendix A*. The use of equation (**3.5**) is more flexible than the image method, in the sense that the equation can be used to calculate the surface velocity on bodies of arbitrary shape and number.

In the case of a single or two cylinder problem, see **Stansby** [**97**][**98**], the disadvantage of this method is that it takes a higher CPU time in evaluating the

surface velocity since the integration must be done numerically on the discretized body surface.

The flow characteristics around the body after shedding vortices can then be evaluated using the following modified Martensen equation

$$-\frac{1}{2}\gamma_m + \oint k_{mn}\gamma_n dS_n + \vec{u}_\infty \cdot \vec{d}S_m + \sum_{\nu=1}^{N_\nu} l_{m\nu}\Gamma_\nu = 0 \qquad (4.6)$$

The first three terms are identical to those which form the Martensen equation (**4.5**), whereas the last term represents the contribution to the Dirichlet boundary condition of zero parallel velocity at surface element m due to the N_ν discrete vortices Γ_ν which form the vortex cloud. It is seen that $l_{m\nu}$ is thus in form identical to the general Martensen kernel integral k_{mn}. The application of this equation in the discrete vortex method still holds the principle of potential flow and thus it can be implemented in a quasi-steady sense (see **Basu** and **Hancock** [**5**]).

Consider now a two dimensional arbitrary shaped body in an infinite fluid with uniform velocity $\vec{u}_\infty$ as shown in figure (**4.2**) below. The surface of the body is modelled by a discrete element with a uniform distribution of vortices of strength γ_n. S_n is the element where the vortex is uniformly distributed.

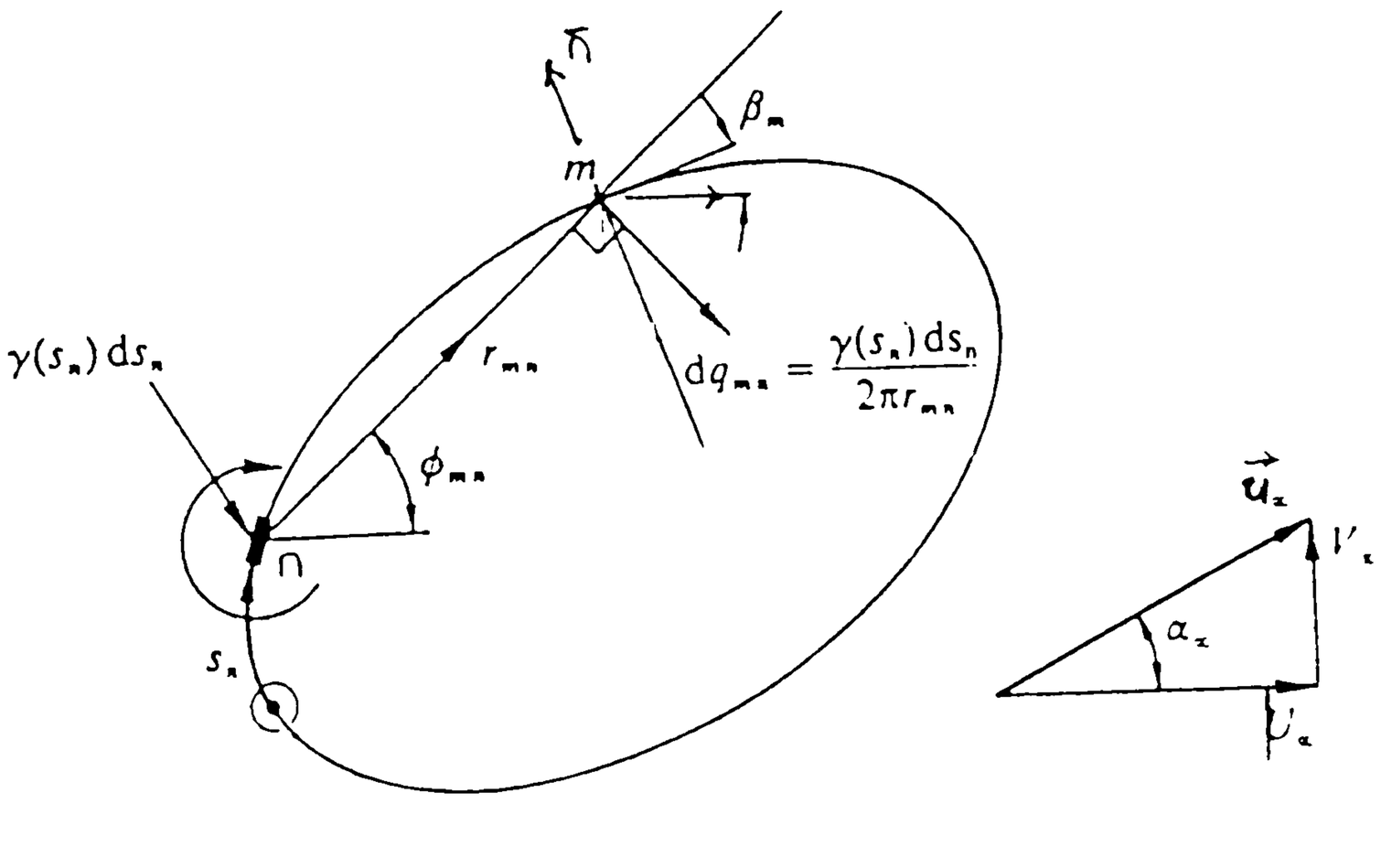

Figure 4.2.- *Schematic of the vortex influence.*

The complex potential of the uniform free stream can be written as

$$w_\infty = u_\infty e^{-i\alpha_\infty} z \tag{4.7}$$

and the complex direction of an element is $e^{i\beta_m}$, where α_∞ is the direction angle of the free stream velocity and β_m is the tangent angle of the element S_m measured in a counter clockwise sense from the positive X-axis.

The tangential component of the freestream velocity at element S_m will be

$$\vec{u}_{\infty t} = \vec{u}_\infty \cdot \vec{d}S_m$$

$$\vec{u}_{\infty t} = \Re\left(\frac{dw_\infty}{dz} e^{i\beta_m}\right) \tag{4.8}$$

which is the real part of the RHS of this equation.

The complex velocity at point z due to a vortex (and source) can be written from derivation of equation (**3.19**) and (**3.21**) as follows,

$$u_z - iv_z = \frac{\partial w(z)}{\partial z} = \frac{\sigma_n + i\Gamma_n}{2\pi} \frac{1}{z - z_n} \tag{4.9}$$

where, σ_n is the source strength, Γ_n is the vortex strength, z_n is the vortex location, and z is the point where the calculation is taken.

The induced tangential velocity at element S_m due to a vortex (and source) at element S_n is then

$$\vec{u}_{t_m} = \Re\left(\frac{dw(z)}{dz} e^{i\beta_m}\right) \tag{4.10}$$

where dS_n is the element length in which the vortex is assumed uniformly distributed. Bearing in mind that $\Gamma_n = \gamma_n dS_n$, this equation can be written as,

$$\vec{u}_{t_m} = \frac{dS_n}{2\pi} \Re\left(\frac{\sigma_n + i\gamma_n}{z_m - z_n} e^{i\beta_m}\right) \tag{4.11}$$

If the perturbation flow is modelled by vortex only, the equation (**4.11**) will reduce to,

$$\vec{u}_{t_m} = \begin{cases} \frac{dS_n}{2\pi} \Re\left(\frac{i\gamma_n e^{i\beta_m}}{z_m - z_n}\right) & for\ m \neq n \\ \frac{-\gamma_m}{2} & for\ m = n \end{cases} \tag{4.12}$$

in which the later shows the self induced velocity at an element m.

After shedding vortices to form the wake around the cylinder, the influence of these vortices upon the cylinder could be represented through a coupling coefficient $l_{m\nu}$ as follows,

$$l_{m\nu} = \sum_{\nu} \frac{\Gamma_\nu}{2\pi} \Re \left(\frac{i e^{i\beta_m}}{z_m - z_\nu} \right) \tag{4.13}$$

Hence the discrete form of equation (3.6) will be,

$$-\frac{\gamma_m}{2} + \sum_{n=1, n\neq m}^{N_e} \frac{\Delta S_n}{2\pi} \Re \left(\frac{i\gamma_n e^{i\beta_m}}{z_m - z_n} \right) + \Re \left(u_\infty e^{-i(\alpha_\infty - \beta_m)} \right) + \sum_{\nu=1}^{N_\nu} \frac{\Gamma_v}{2\pi} \Re \left(\frac{i e^{i\beta_m}}{z_m - z_\nu} \right) = 0 \tag{4.14}$$

The only unknown variable in this equation is γ_n. Since the others depends only on the cylinder geometry and the free stream velocity.

If we define K_{mn} as the influence *matrix* which shows the induced velocity at element S_m due to a vortex at element S_n with strength equal to unity and also bearing in mind that the first term in equation (**4.14**) is absorbed into this coupling influence matrix, we have,

$$k_{mn} = \begin{cases} \frac{dS_n}{2\pi} \Re \left(\frac{i e^{i\beta_m}}{z_m - z_n} \right) & for\ m \neq n \\ \frac{-1}{2} & for\ m = n \end{cases} \tag{**4.15**}$$

and the matrix will be,

$$[K_{mn}]\,[\gamma_n] = [RHS]$$

where

$$[RHS] = -\Re \left(u_\infty e^{-i(\alpha_\infty - \beta_m)} \right) - \sum_{\nu=1}^{N_\nu} \frac{\Gamma_v}{2\pi} \Re \left(\frac{i e^{i\beta_m}}{z_m - z_\nu} \right)$$

Hence,

$$[\gamma_n] = [K_{mn}]^{-1}\,[RHS] \tag{4.16}$$

The equation (**4.16**) above shows that the solution of the flow problem is now reduced to the solution of a set of simultanous equations with unknown vortex strength γ_n.

In the present study the wave flows presented in the previous chapter are simplified to planar oscillatory flow so that the unsteady free stream velocity u_∞ is modelled in a simple form as

$$u_\infty(t) = u_o \; cos\left(\frac{2\pi t}{T}\right) \tag{4.17}$$

where T is the period of the oscillatory flow and t is the time history of the flow and u_o is the amplitude of the free stream velocity.

The inclusion of this unsteady free stream flow in the method can be accomplished by modifying the right hand side of the Martensen equation (**3.6**) in which the free stream part has to be calculated at each time step. This certainly will increase the degree of the non-linearity of the problem as the RHS is now dependent not only on the shed vortices but also on the free stream part. It may be noted the matrix $[K_{mn}]$ is never singular and hence the solution can be carried out easily using normal matrix inversion procedure.

4.3 Segmentation of the Domain

It can be seen from equation (3.4) that after shedding vortices, $N_v + 1$ terms must be evaluated when performing the velocity calculation for any point or vortex in the flow. In a cloud vortex method, where a direct vortex to vortex calculation is used, it would require ${N_\nu}^2$ operations which is computationally expensive as the number of vortices increases. The number of calculation can be dramatically reduced by covering the computational domain with grid, distributing the vortices on its nodes, and calculating only nodal interactions. The number of operations is now of order $(N_{jk})^2$, where N_{jk} is the number of active grid nodes. Over long time periods, N_{jk} is much smaller than N_ν.

Another saving in the CPU time is also found during the surface vorticity calculation in which for the vortex to vortex method, the influence of each vortex on a point element of the cylinder surface involves N_ν calculations. This will result in $N_e N_\nu$ calculations for all the surface elements, N_e. Using grid nodes will result in only $N_e N_{j,k}$ calculations which is less.

Since the singularity model is used, another obvious advantage in using grids is to avoid 'singular problems' during the evaluation of the surface velocity since the nodes of the grid are always a fixed and pre-determined distance apart.

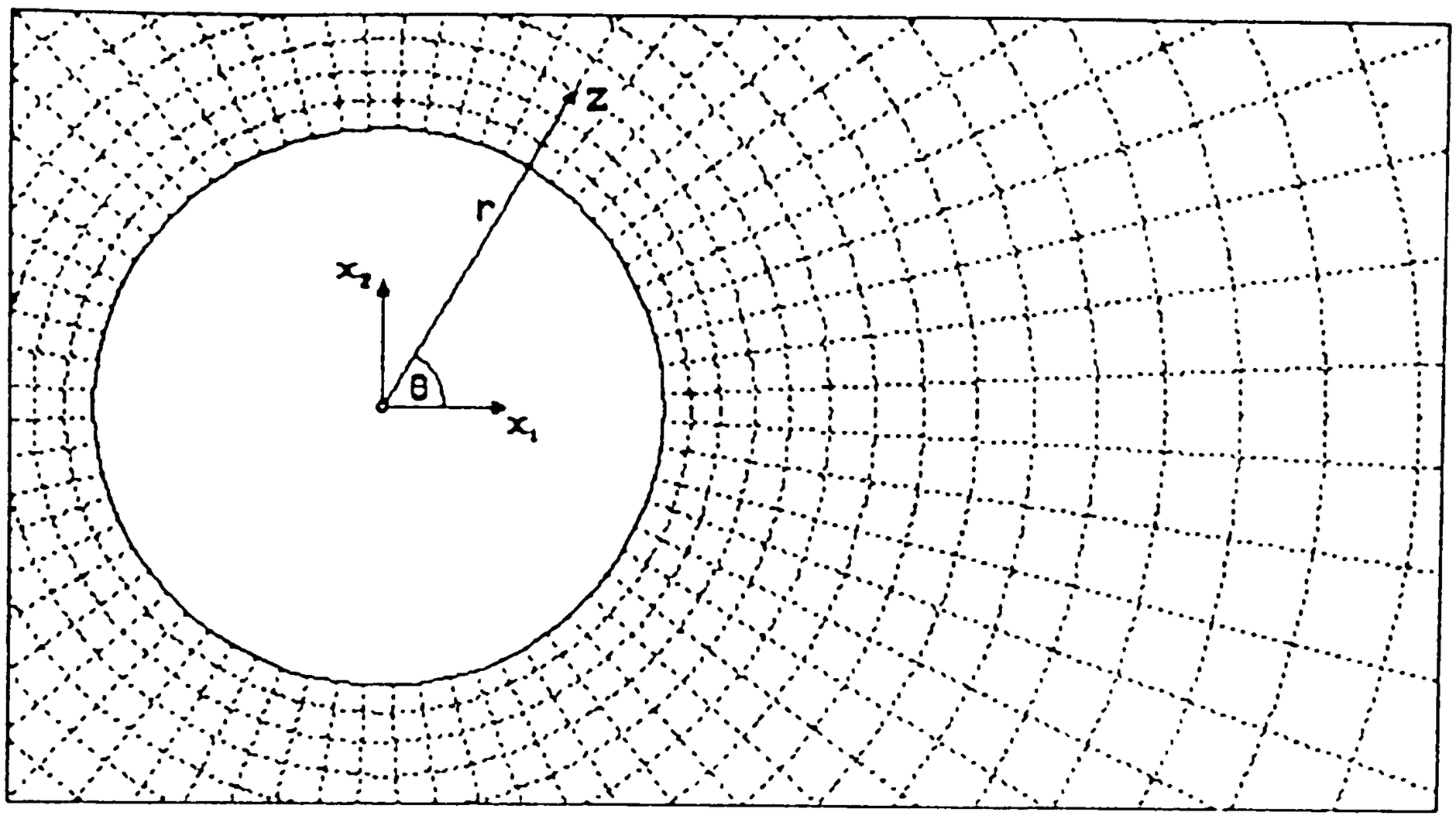

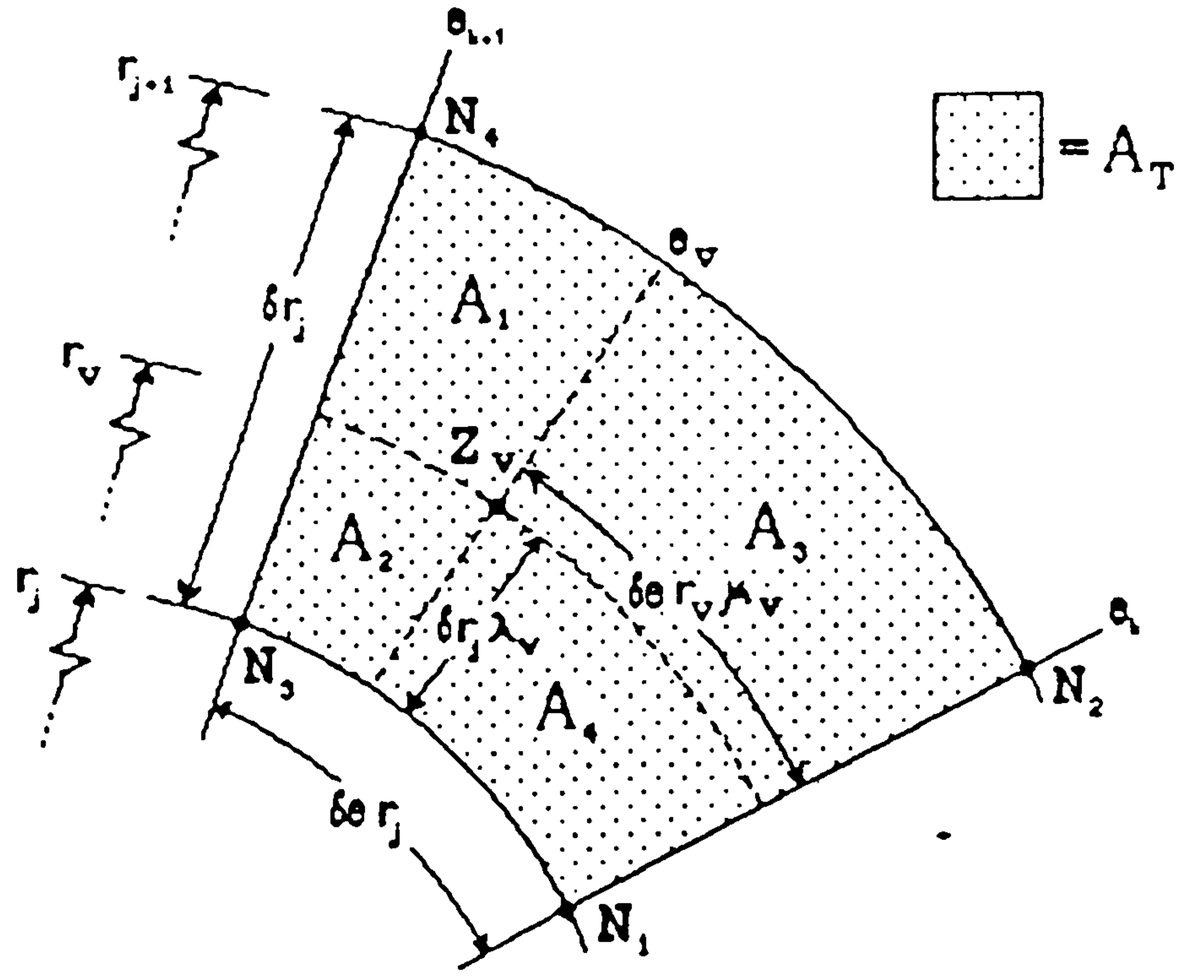

Figure 4.3.- *The Structure of a Grid Surrounding a Circular Cylinder*

A polar grid with N_ϵ elements surrounding a circular cylinder is used to represent the fluid domain. This grid has 'square' elements which increase in area in the radial direction as illustrated in the figures (**4.3**) below:

The span angle is;

$$\delta\theta = \frac{2\pi}{N_e} \tag{4.18}$$

where N_e is the number of segments surrounding the cylinder. To achieve the square elements, the distance,

$$\delta r_j = \delta\theta r_j \qquad j = 1, 2, \cdots \tag{4.19}$$

is required in the radial direction. Hence;

$$r_{j+1} = r_j + \delta r_j \qquad j = 1, 2 \;\; r_1 = a \tag{4.20}$$

where r_j is the radius of the grid ring j.

The element angle is offset by half a segment and is defined as follows,

$$\theta_k = \left(k - \frac{1}{2}\right)\delta\theta \qquad k = 1, 2, \cdots N_{seg}$$

The node grid points can be evaluated from these definitions above as follows

$$z_{j,k} = r_j \; e^{i\theta_k} \tag{4.21}$$

where $j = 1, 2, \cdots$ and $k = 1, 2, \cdots N_e$.

4.4 Introduction of Vortices into the Flow

Following the potential flow analysis at each time step, the surface vorticity $\Gamma_n = \gamma_n \; \Delta S_n$ created at every boundary element is released from the surface and shed into the fluid as a new discrete vortex (see **Katz** [**53**]). In relation to this, the modelling of boundary layers in the discrete vortex model can be done in two ways.

1. Random walk method, in which the newly created vorticity initially lying on the surface can be diffused by random walk, **Chorin** [**18**][**19**].

2. Offset method, in which each discrete vortex of strength $\Gamma = \gamma_n \Delta S_n$ may be offset by a fixed distance ε from the body surface.

Kamemoto and **Bearman** [**51**] studying flow about a flat plate concluded that the non-dimensional number $\frac{a}{u_\infty dt}$ is an important parameter in the selection of a suitable position for the nascent vortices and the size of the time interval

between the introduction of each new vortex. They studied the relation between the value of this non-dimensional number and the resulting flow characteristics around a flat plate and found that the optimal value of this parameter is about *0.19 - 0.38*. In this range, the flow pattern and the force coefficients are expected to resemble the real phenomena.

The value recommended by **Porthouse** [**74**] is Reynolds number dependent and is $\sqrt{\frac{4\nu\Delta t}{3}}$. This parameter is intended to model the diffusion of a vortex sheet which will be very small at high Reynolds number. However, this can lead to an erroneous solution to Martensen's equation, especially at a strongly curved region of the body surface.

The offset value proposed by **Downie** [**26**] is based on the optimal value for a given surface distribution of vortices and is approximately equal to the local element length adopted in this study. It was found after many trials of the optimal position giving the smoothest induced body surface velocity.

In the modelling of the flow, **Chorin** [**19**] recommended that the strength of vortices should be doubled due to the fact that on a random basis half of the vortices will penetrate the cylinder and be removed from the flow although the vorticity should be conserved during diffusion and convection processes for each time step. He also suggested that if the strengths of the vortices are kept at their original value, any vortices that penetrate the cylinder should be reflected back to the fluid domain at their image position.

The method used by **Downie** [**26**] and **Murray** [**70**] of releasing a ring of vortices from the first ring out of the cylinder is also adopted in this study. At low Reynolds number, the radius of this ring can be adjusted to be a function which is inversely proportional to the square root of the Reynolds number, i.e. $\frac{k}{Re^{\frac{1}{2}}}$, to model the effect of the laminar boundary layer around the cylinder, **Hoerner** [**45**][**46**]. The constant k can be chosen to give the best representation of the flow pattern and the force coefficients as will be described later.

4.5 Distribution of Circulation to the Grid

As proposed for the first time by **Christiansen** [**21**] this step is meant to reduce the CPU time of evaluating the velocity at any point in the fluid domain similar to the previous discussion. This step involves the distribution of the vortex strength Γ_ν onto its four surrounding nodes using a bi-linear interpolation scheme based on the relative distance of each vortex from its surrounding node. It is possible

to do this because Γ_ν is not in reality a discrete vortex but only a simplified representation of the local distributed vorticity.

The surrounding nodes are identified as $N_1 = z_{j,k}$ $N_2 = z_{j+1,k}$ $N_3 = z_{j,k+1}$ and $N_4 = z_{j+1,k+1}$ as shown in figure (**4.3**). The parameters

$$\lambda_v = \frac{(r_v - r_j)}{\delta r_j}$$

$$\mu_v = \frac{(\theta_v - \theta_k)}{\delta\theta} \tag{4.23}$$

represent the ratio of the vortex radial and angular position (relative to node $z_{j,k}$) to the respective sides of the grid element.

The area of the grid element inner radius r_j, is given by

$$A_r(j) = \frac{1}{2}(2 + \delta\theta)\delta r_j^2 \tag{4.24}$$

The areas of the element's sub regions are given by,

$$A_1(v) = \frac{1}{2}(1 - \lambda_v)(1 - \mu_v)(2 + (1 + \lambda_v)\delta\theta)\delta r_j^2$$

$$A_2(v) = \frac{1}{2}\lambda_v(1 - \mu_v)(2 + \lambda_v\delta\theta)\delta r_j^2$$

$$A_3(v) = \frac{1}{2}(1 - \lambda_v)\mu_v(2 + (1 + \lambda_v)\delta\theta)\delta r_j^2$$

$$A_4(v) = \frac{1}{2}\lambda_v\mu_v(2 + \lambda_v\delta\theta)\delta r_j^2 \tag{4.25}$$

These equations act as the weighting functions for distributing the vortex strengths and are a measure of the relative closeness of a vortex to each of its surrounding nodes.

The proportion of the total circulation assigned to each node is given as follows:

$$P_1(v) = \frac{(1 - \lambda_v)(1 - \mu_v)(2 + (1 + \lambda_v)\delta\theta)}{(2 + \delta\theta)}$$

$$P_2(v) = \frac{\lambda_v(1 - \mu_v)(2 + \lambda_v\delta\theta)}{(2 + \delta\theta)}$$

$$P_3(v) = \frac{(1-\lambda_v)\mu_v(2+(1+\lambda_v)\delta\theta)}{(2+\delta\theta)}$$

$$P_4(v) = \frac{\lambda_v\mu_v(2+\lambda_v\delta\theta)}{(2+\delta\theta)} \qquad (4.26)$$

Using the weighting function the node circulation is given by,

$$\Gamma_{j,k} = \sum_v P_\mu(\nu)\Gamma_v \qquad (4.27)$$

where the vortices of the strength Γ_ν are contained in an element with a base node $z_{j,k}$. $\mu = 1-4$ shows the node number.

4.6 Calculation of Velocities

After introducing the surface vorticity on the first ring out from the cylinder and distributing the strengths of all shed vortices onto grid nodes, the vortex velocity can be calculated through the active grid nodes N_μ $(\mu = 1-4)$ velocities, surrounding a vortex using the Biot-Savart Law as follows,

$$u_p(N_\mu) = u_\infty e^{i\alpha_\infty} - \frac{i}{2\pi}\sum_{j,k}\frac{\Gamma_{j,k}}{N_\mu - z_{j,k}} \qquad (4.30)$$

This velocity is then redistributed to the vortex velocity through the bi-linear interpolation of the polar grid as follows

$$u_\nu = u_p(z_v) = P_1(v)u_p(N_1) + P_2(\nu)u_p(N_2) + P_3(\nu)u_p(N_3) + P_4(\nu)u_p(N_4) \qquad (4.31)$$

where the area ratios are those defined by equation (**4.26**) and the node points are those surrounding the vortex, as depicted in figure (**4.3**).

4.7 Random Walk Method

Since it was proposed by **Chorin** [**18**][**19**], the random walk method has been widely used to model the viscous diffusion of high Reynolds number flow using the discrete vortex method. The basis of this scheme is to give a random displacement to each vortex to produce a scatter equivalent to the diffusion of vorticity in the continuum.

In two dimensions the solution of the diffusion equation (**4.2**) is the vorticity decay of a line vortex as follows

$$\omega(r,t) = \frac{\Gamma}{4\pi\nu t}\exp\left(-\frac{r^2}{4\nu t}\right) \tag{4.32}$$

which is a function of radius r and time t. Hence, the vorticity decays as the distance from its centre increases and it also decays as the time increases. In this equation Γ is assumed to consist of a large number of small vortivity elements all initially located at the origin, but free to diffuse outwards independently of one another over a period of time. By regarding this equation as a vorticity density probability distribution curve to be matched by the random displacements to which we will subject the small elements during the numerical diffusion simulation process, **Lewis** [**60**] and **Lewis** and **Porthouse** [**61**].

Due to the r^2 factor, it can be seen that the vorticity decay equation is an even function relative to its centre. If equation (**4.32**) is integrated in terms of the area of a circle whose centre is at the vorticity centre, it will result in

$$P(r,t) = 1 - \exp\left(-\frac{r^2}{4\nu t}\right) \tag{4.33}$$

in which P states the probability that a given element will lie somewhere within a circle radius r and this equation also represents the Gaussian normal distribution of zero mean and standard deviation $\sqrt{4\nu t}$. It follows from this that given two random numbers P_1 and P_2, within the interval $(0,1)$, the values,

$$r = \sqrt{4\nu\Delta \ln\frac{1}{1-P_1}}$$

and

$$\theta = 2\pi P_2 \tag{4.34}$$

will give representative displacements

$$\delta z_\nu^{rw} = r\ e^{i\theta} \tag{4.35}$$

, for a group of vortices in radial and angular direction under this distribution of probability.

4.8 Vortex Displacement

The vortex displacement over the time step can be calculated after all the vortex velocities are known. This displacement is used to find the new positions of the vortices of the next time step. A simple first order Euler scheme is used to obtain solutions of the form;

$$z_\nu^{(t+\delta t)} = z_\nu^{(t)} + \delta z_\nu^{rw} + \delta t u_\nu^{(t)} \tag{4.36}$$

where δt is the size of the time step used. The second term on the right hand side is due to the Random Walk diffusion process as explained in the previous section.

This step completes the calculation of the kinematics of the flow over a single time-step. It remains to calculate the forces and then to return to the step described in section (**4.2**) to start the next time step.

4.9 Force and Pressure Calculation

The force on the cylinder can be calculated through the use of Blasius' theorem as generalized by **Milne – Thompson** [**66**]

$$C_d - iC_l = i\frac{\rho}{2}\oint_c \left(\frac{\partial w}{\partial t}\right)^2 dz + i\rho\frac{\partial}{\partial t}\oint_c \bar{w}d\bar{z} \tag{4.37}$$

Introduction of the complex potential (**Sarpkaya** [**78**][**79**] and **Clement** [**22**], and **Kiya** and **Ari** [**55**][**56**]) leads to an expression allowing the calculation of the forces from a knowledge of the strengths and posisitons of the discrete vortices.

Various authors, such as **Graham** [**37**], **Downie et.al.** [**28**] and **Murray** [**70**] have adopted this approach which uses the following expression

$$C_d + iC_l = \rho\left(2\pi a^2\frac{\partial u_\infty}{\partial t} - i\sum_{\nu=1}^{N_v}(u_v - u_{-v})\Gamma_v + i\sum_{v=1}^{N_v}(z_{-v}+a)\frac{\partial \Gamma_v}{\partial t}\right) \tag{4.38}$$

where z_{-v}, signify the vortex image position and velocity.

It is implicit from this equation that those authors were using the image method in their analysis of the flow around one body.

Another approach to force calculation is exemplified by **Lewis** [**60**], **Stansby** and **Smith** [**103**], and **Porthouse** [**74**] who used boundary elements as the basis

of their Discrete Vortex calculations. As described in the previous chapter, the use of images is avoided and surface vorticity is used instead. These force calculations are consistent with the discrete vortex scheme, in which the solution of the Navier-Stokes equations is seperated into the convection, diffusion and force sequence of calculations, although in the real fluid motion these processes occur simultaneously and continuously and not in a sequence demanded by computational practicality.

The force calculation can thus be carried out after the convection and diffusion processes by solving the following equation

$$\frac{\partial u}{\partial t} = -\frac{1}{\rho}\nabla p \qquad \textbf{(4.39)}$$

and hence,

$$p = p_s - \int_{S_1}^{S} \rho \frac{\partial \gamma(S)}{\partial t} dS$$

which is derived from the Navier-Stokes equation on the basis that at any point S_n on the cylinder surface, the velocity parallel to the surface is given by $\vec{u}_t = \gamma_n$. From that equation, a numerical expression for the change in surface pressure over the surface element n during the discrete time step Δt, can be obtained as

$$\Delta p_n = -\rho \frac{\gamma_n \Delta S_n}{\Delta t} = -\rho \frac{\Gamma_n}{\Delta t}$$

The difference of pressure Δp_n is measured from the stagnation pressure $p_s = \frac{1}{2}\rho u_\infty^2$ at the stagnation point S_s. Hence the pressure at element m will be

$$p_n = p_s - \frac{\rho}{\Delta t} \sum_{n=1}^{m} \Gamma_n \qquad \textbf{(4.40.a)}$$

The other force that contributes to the drag and lift forces is the one due to the skin friction (viscous drag) on the surface of the cylinder. This force comes from the shearing stress at the surface,

$$\tau_n = \mu \left(\frac{\partial u_s}{\partial n}\right)_w$$

where μ is the dynamic viscousity and $\frac{\partial u_s}{\partial n}$ is the gradient in the normal direction of the tangential velocity on the surface, which is equal to the local circulation ω_n on a surface node. Hence,

$$\tau_n = \mu\ \omega_n = \mu\ \frac{\gamma_n dS_n}{dA_n}$$

where dA_n is the local element area which is approximately equal to the local element length times the standard deviation $(4\nu\Delta t)^{1/2}$ of the Random Walk diffusion movement on the surface. Thus,

$$\tau_n = \nu\ \rho\ \frac{\Gamma_n}{a\delta\theta\ (\nu\Delta t)^{1/2}} \qquad \textbf{(4.40.b)}$$

where a is the radius of the cylinder and $\delta\theta$ is the segment angle of the local element.

The form drag, lift and skin friction coefficients, corresponding to the force components directed respectively along the horizontal and vertical reference, can be calculated from an integration of the average pressure distribution $\bar{p}_n = \frac{1}{2}\ (p_n + p_{n+1})$ and $\bar{\tau}_n = \frac{1}{2}\ (\tau_n + \tau_{n+1})$ as follows,

$$C_d = \frac{D}{\frac{1}{2}\rho u_\infty^2 d} = \frac{2}{\rho u_\infty^2 d} \sum_{n=1}^{m} (\bar{p}_n \sin\beta_n \Delta S_n + \bar{\tau}_n \cos\beta_n \Delta S_n)$$

$$C_l = \frac{L}{\frac{1}{2}\rho u_\infty^2 d} = -\frac{2}{\rho u_\infty^2 d} \sum_{n=1}^{m} (\bar{p}_n \cos\beta_n \Delta S_n - \bar{\tau}_n \sin\beta_n \Delta S_n) \qquad \textbf{(4.41)}$$

where, d is the diameter of the cylinder and β_n is the tangent angle of the element.

Since these equations only use the surface vorticity strength, they can be easily adopted for the case of multi-body problems, U-tube simulations and also for the body moving under a free surface. A similar approach was taken by **Smith** and **Stansby** [**93**][**94**] in their force calculation but they used polar coordinates in their derivation. **Quartepelle** and **Napolitano** [**76**] obtained a general formula for the force acting on rigid bodies in incompressible flow, which requires a knowledge of the entire vorticity field and is derived directly from Navier-Stokes equation.

As explained in the previous chapter, for the case of oscillatory flows, some further modifications have to be carried out in calculating the force coefficients,i.e. the lift and drag coefficients. This is because in this kind of flow, the in-line force coefficient can be described by the Morison equation which consists of two components with an associated drag coefficient C_d and inertia coefficient C_m. These

coefficients can be calculated using the Fourier method, as explained in more detail in **Sarpkaya** [**81**][**82**].

$$C_d(p) = \frac{3\pi}{4T} \sum_{t_n=(p-1)T}^{pT} Cd(t_n)\ cos(\frac{2\pi t_n}{T})\ dt \tag{3.41}$$

$$C_m(p) = \frac{-u}{\pi^2 a} \sum_{t_n=(p-1)T}^{pT} Cd(t_n)\ sin(\frac{2\pi t_n}{T})\ dt \tag{3.42}$$

where $t_n = n\ \Delta t$ and $p = 1, 2, ...$ are the relevant period number. The transverse force coefficient can still be calculated as before since the Morison equation only deals with the in-line force coefficients. As explained earlier, the drag force is assiciated with flow separation and vortex shedding and is proportional to the velocity, and the inertia force is associated with the acceleration of the fluid particles.

4.10 Method Enhancements

4.10.1 Influence of the ring vortices and time step

A. Steady free stream flow

As described previously, the vortices are introduced on the first ring out whose distance from the cylinder's surface is proportional to the boundary layer thickness. As shown by **Schlichting** [**90**] the boundary layer thickness can be expressed as $k_{fs}\ Re^{-1/2}$, where k_{fs} is a constant of proportionality. This approach is carried out to simulate the complicated nature of the boundary layer using the simplest model possible without really implementing a detailed model of it, **Stansby** [**98**] and **Lewis** [**60**].

It is recognised that this approach cannot capture the fine detail of the boundary layer. However, as the results will demonstrate, a surprisingly good description of the gross characteristics of the flow and of the forces experienced by the cylinder can be obtained by this method. It has the advantage that the model can then be further extended to other applications whilst still requiring only modest computer resources.

Numerically the diameter of the first-ring-out has a significant influence on the behaviour of the model as the newly created vortices located on this ring are closest to the cylinder surface. **Lewis** [**60**] shows that when a vortex is located at a distance away from the surface of less than one surface element length, a large

induced velocity to the surface element exists. This length is therefore used as the minimum displacement of the ring vortices so as to ensure a relatively smooth distribution of the induced velocity in steady free stream flow.

Another factor that contributes to the behaviour of the model is the size of the time step which is influencial on the force coefficient as is implied in equation (**4.40.a**) above. Using a small time step generally produces a smooth and better flow pattern but it requires a relatively long computation time. A large time step, on the other hand, can save the computation time but leads to a relatively coarse flow pattern. If it is too large the vortices can not follow the streamlines in the region of high curvature which sometimes causes an instability problem and unrealistic flow patterns.

The choice of parameters, **Kamemoto** and **Bearman** [**52**] investigated the influence of the position of the nascent vortex in their model of the flow around a flat plate. They concluded that the nondimensional number k_{fs} defined as $\frac{\Delta a}{u_\infty \Delta t}$ is thought to be an important parameter in determining suitable positions for the nascent vortices and a reasonable size for the time interval Δt. They also found that if the distance from the plate Δa is sufficiently small compared with the width of the plate, similar values of this number will result in similar flow characteristics.

Downie [**26**] used the same analogy in releasing a ring of vortices from a cylinder, a method also adopted in this study, by varying the diameter of the ring vortices and the time step. The resulting induced velocity around the cylinder surface, the flow patterns and also the behaviour of the force coefficients was then examined. The best value of the parameters in the widest possible range of the Reynolds number was then chosen to be used in the model.

A similar study was carried out with the present model. The influence of the variation of the ring diameter on the drag and lift coefficients is displayed in figures (**3.4**) and (**3.4**). These calculations were carried out using three different values of Reynolds numbers of 10^5, 10^4, and 10^2 with distances of the ring vortices from the cylinder surface of $0.04D$, $0.05D$ and $0.06D$ and for the time step calculations of 0.1, 0.15, and 0.2. In term of the non dimensional parameter above, these preliminary calculations were carried out within the range 0.2 to 0.6.

The general trend of the results indicate that the smaller the Reynolds number, while the other variables are kept constant, the higher is the drag coefficient which is in line with the trend of the experimental results. This is due to the fact that at

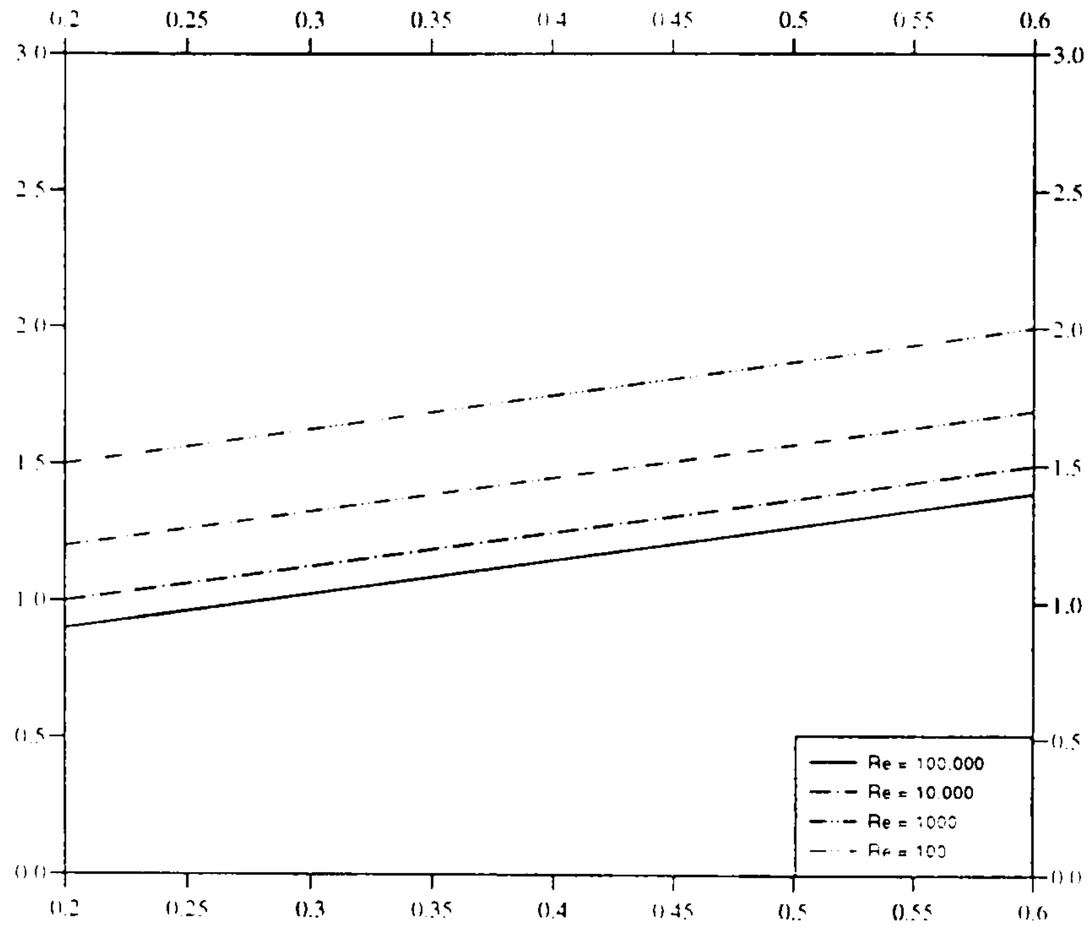

Figure 4.4.-*Cd Vs.* $\frac{\Delta a}{u_\infty \Delta t}$

this range, the laminar boundary layer becomes thicker as the Reynolds number decreases as the diffusion part becomes more significant.

The variation of the diameter of the ring vortices, which give a very crude measure of boundary layer effects, shows that the closer the ring is to the cylinder surface, the less is the value of the drag coefficient. This is also in line with the trend of the boundary layer thickness becomes thinner as the Reynolds number increases and produces a smaller value of the drag coefficient.

The effect of the size of the time step is as significant as the parameter above. It not only effects the smoothness of the flow pattern produced, in which for small time step the computing time will increase considerably, but it also gives a quite significant change to the value of the force coefficients as would be expected from equation (4.40).

From figures (**4.4**) it can be concluded that when the $\frac{\Delta a}{u_\infty \Delta t}$ around *1.35*, that is a ring of vortices with distance from the cylinder surface equal to the element length, the best results for the free stream steady flow with $u_\infty = 1$ and the size of the time step is *0.15*, are obtained. The behaviour of the model by choosing these values of parameter will be discussed in detail in the next sections.

B. Oscillatory Flow

As mentioned by **Schlichting** [90], the thickness of the boundary layer on the cylinder surface in an oscillatory flow is equal to $k_{osc}\ \beta^{\frac{-1}{2}}$. where k_{osc} is the constant of proportionality. β is equal to $\frac{Re}{Kc}$. Re is the Reynolds number and $Kc = \frac{u_\infty T}{D}$ is the the Keulegan- Carpenter number. The Keulegan-Carpenter number is a parameter which shows the scale of the motion of the water particles relative to the cylinder diameter. As in the analysis described previously. it is necessary to investigate the behaviour of the present model upon the variation of the diameter of the first ring relative to the cylinder diameter and also of the time step.

The main difference between oscillatory flows and steady flows is that when the flow reverses after the end of the half cycle. vortices shed previously will be pushed back toward the cylinder and this influences the behaviour of vorticity created on the cylinder surface in succeding time steps. This means that the history of the flow will be more significant in this particular case and this also affects the behaviour of the boundary layer and its transition to turbulence.

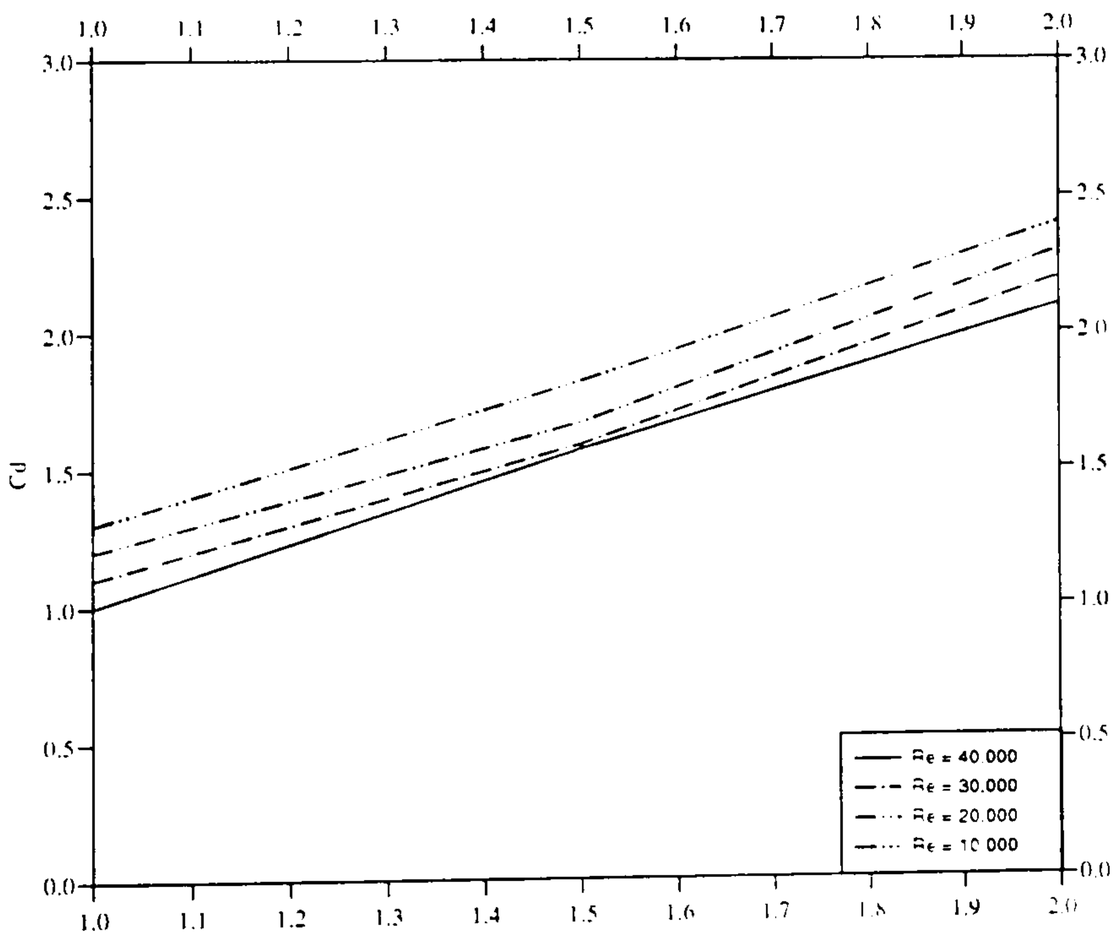

Figure 4.5a.-*Cd Vs.* k_{osc}

Numerically. as the strength of vortices are distributed and summed up on the grid nodes. the returning vortices will cause the strength of the active grid nodes

close to the cylinder to differ significantly from those of the steady case. The simple simulation of the boundary layer by releasing the ring vortices from the first ring out with a constant diameter of $0.55D$ can no longer be maintained and another condition involving the effect of the oscillatory flow characteristics. expressed in terms of the Keulegan-Carpenter number Kc. and the Reynolds number Re is required. This means that as the factor Δa. the distance of the first ring out to the cylinder surface, in $\frac{\Delta a}{u_\infty \Delta t}$ is now a function of Kc and Re, these parameters need to be reassessed to get the best possible performance of the model in oscillatory flows.

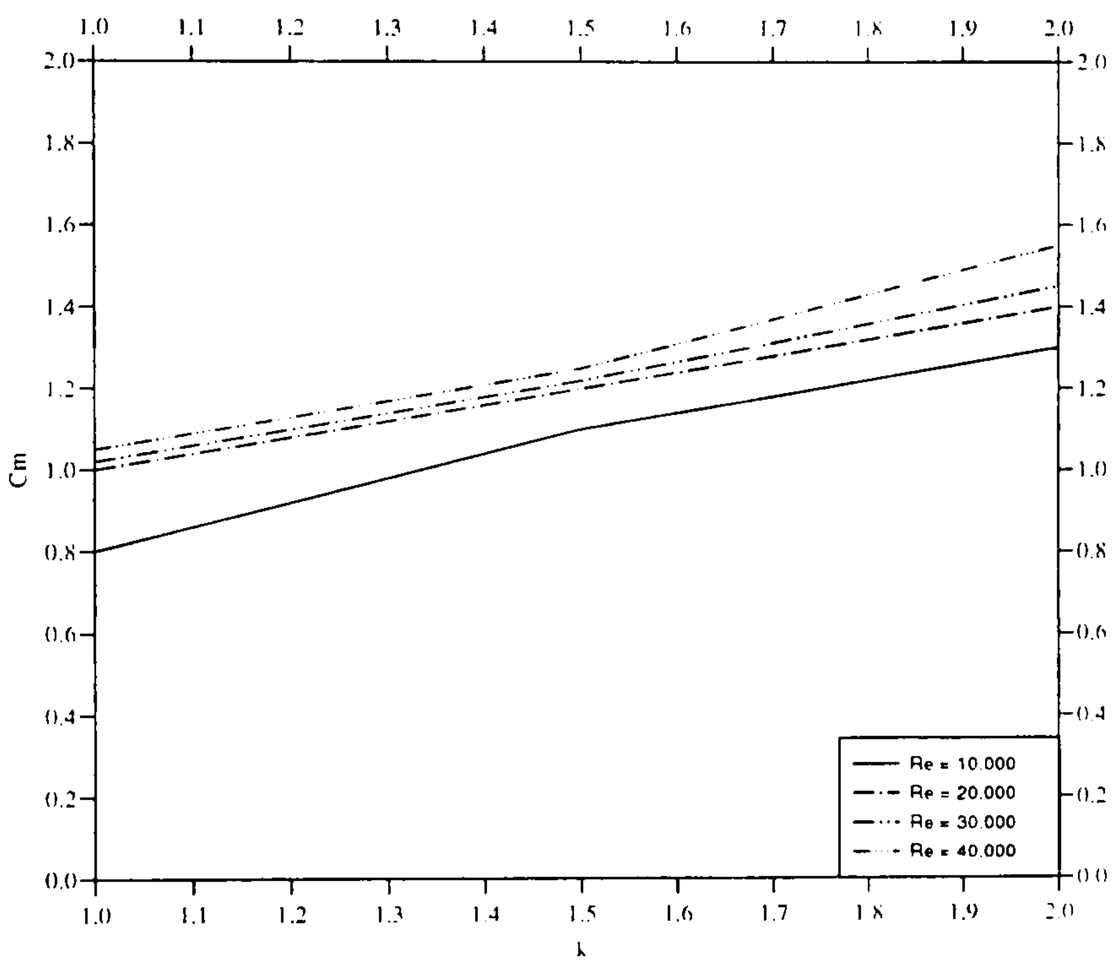

Figure 4.5b.-*Cm Vs.* k_{osc}

A large number of preliminary calculation were carried out using Reynolds numbers of 2.10^3, 10^4, 3.10^4, 4.10^4 with ring radii of $0.51D$ to $0.56D$ using the time steps of 0.05, 0.1, and 0.15. These Reynolds number values were chosen as the drag and inertia coefficient do not vary a lot for quite a wide range of Keulegan-Carpenter numbers. especially greater than 10. as shown in figures (**2.6**) and (**2.7**) in the previous chapter. The grid system with 64 number of elements is still maintained for the oscillatory flows and the value of the drag and inertia coefficients due to the variation of the constant of proportionality k_{osf} are shown in figures (**4.5a**). (**4.5b**) respectively. It is seen from these figures that using k_{osc} of 1.55. the model gives quite good results over the chosen range of Reynolds

number. The figures will be discussed later in detail in the section entitled Result and Discussion.

4.10.2 The Kelvin Theorem

It is a consequence of the Kelvin circulation theorem that the net circulation around the profile interior induced by a surface vorticity element $\gamma_n \Delta S_n$ plus any other singularity point in the fluid domain is zero. The part of fluid in the cylinder interior can thus be considered as 'quiescant fluid' which does not move relative to a frame of reference fixed to the cylinder.

When two or more cylinder elements are close to each other or when a vortex is close to the cylinder surface, the condition of zero net circulation can not be maintained due to a so called 'velocity leakage', caused by the dominant influence of the nearby vortex.

This condition could occur for the interaction of the trailing edge elements of an aerofoil in the closest elements in the case of a multi-cylinder problem or when a vortex is very close to the cylinder surface in the discrete vortex method.

There are two methods to eliminate this leakage i.e. by the use of sub-elements (**Lewis [60]**, **Williamson [110]**) and back diagonal correction (**Jacob** and **Riegel [49]**).

The principal strategy of sub-element correction is by re-discretizing an element S_n into N_i sub-elements and the influence due to that element to a point S_m is calculated as the average value of all sub-element contributions. Thus,

$$k_{mn} = \frac{1}{\delta S_n} \int_0^{\delta S_n} \bar{k}_{mn} dS_n$$

or in numerical form

$$\bar{k}_{mn} = \frac{dS_n}{2\pi N_i} \sum_{i=1}^{N_i} \Re \left(\frac{i e^{i\beta_m}}{z_m - c_i} \right) \qquad \textbf{(4.43)}$$

This correction can be implemented when the distance between two vortices is less than twice the element length.

The use of back diagonal correction is done by directly enforcing the Kelvin's zero net circulation in the influence matrix $[K_{mn}]$.

$$k_{in} = -\frac{1}{\delta S_i} \sum_{n=1, n\neq i}^{N_e} k_{mn} \delta S_n \qquad \textbf{(4.44)}$$

This means that the influence of the closest element is now replaced by the average influence of the rest of the elements. This correction can be implemented when the distance between two element is less than twice the element length.

4.10.3 Correction for Vorticity conservation

During convection and diffusion process, some vortices could penetrate the boundaries such as the cylinder surface. This condition will cause, consequently, a loss of vorticity in the fluid domain, which is not consistent with the Kelvin theorem as stated above.

This can be corrected by modifying the Martensen equation (**4.14**) since the surface vorticity and previously shed vortices should satisfy the following conditions assuming that there was zero net vorticity in the flow regime at $time = t$,

$$\sum_{n=1}^{N} \gamma_n \Delta S_n + \sum_{\nu=1}^{N_\nu} \Gamma_\nu = 0$$

which must hold throughout the whole time history.

Due to the loss of vorticity, an additional statement of vorticity conservation is required which can now be expressed in the following form

$$\sum_{n=1}^{N} \gamma_n \Delta S_n + \sum_{\nu=1}^{N_\nu} \Gamma_\nu - \Gamma_{loss} = 0$$

where Γ_{loss} is the cumulative strength of all vortices which are removed for various reasons as mentioned above, as the calculation proceeds. Initially Γ_{loss} must be set to zero and later increased by a certain amount for any discrete vortex removed from the field. Incorporating this equation into the discrete Martensen equation produces the following modification,

$$\sum_{n=1}^{N} (k_{mn} + \Delta S_n)\gamma_n = -u_\infty \cos(\alpha_\infty - \beta_m) - \frac{1}{2\pi} \sum_{\nu=1}^{N_\nu} \Gamma_\nu (l_{m,\nu} + 1) + \Gamma_{loss} \quad \textbf{(4.45)}$$

which now maintains the vorticity conservation throughout the whole time history.

4.10.4 Right Hand Side Correction

Further improvements in CPU time performance can be achieved by applying the active grid node vortex strength $\Gamma_{j,k}$ instead of the shed vortex strength Γ_ν.

in the calculation of the coupling coefficient l_{mn} in equation (**4.13**) above. This is due to the fact that the number of the active grid nodes is much less than the number of the shed vortices in the fluid regime. Hence,

$$RHS_\nu = \frac{1}{2\pi}\sum_{\nu=1}^{N_\nu} l_{m\nu}\Gamma_\nu \approx \frac{1}{2\pi}\sum_{j,k} l_{m,(j,k)}\Gamma_{j,k}$$

It is proposed that for this case, any influence from grid nodes at distances less than four times the body element ds, the sub element correction method as described in the previous paragraph is implemented, while for the grid nodes less than twice the cylinder element ds, a correction similar to the back diagonal correction is used as follows

$$RHS_p = -\frac{1}{\Delta S_p}\sum_{\nu} RHS_\nu \Delta S_\nu \qquad (\mathbf{4.46})$$

where RHS_ν is as shown in equation (**4.16**).

4.10.5 Curvature Effect on the Self-Induced Velocity

In the equation (**4.5**), the first term $-\frac{1}{2}\gamma_m$, which indicates the velocity discontinuity experienced in moving from the centre of the vorticity sheet onto the body surface beneath, allows for no self induced velocity of the element S_m and this is only valid if the element is straight.

The effect of the element curvature, which modifies this term, and is used in this study, was reported by **Lewis** [**58**] and has the form

$$K_{mm} = -\frac{1}{2} - \frac{\Delta\beta_m}{4\pi} \qquad (\mathbf{4.47})$$

where $\Delta\beta_m$ is the change of profile slope from one end of the element to the other. He claimed that by using this curvature correction, a given degree of accuracy can be achieve with fewer elements than when the correction is not applied.

4.10.6 Enforcement of Asymmetric Flow

In the symmetric flows, such as the flow around a circular cylinder, the vorticity distribution over the upper and lower half of the cylinder are symmetrical until the accumulation of the numerical rounding error is enough to produce asymmetric effects.

To trigger this effect,some authors such as **Sarpkaya** [**85**], **Stansby** [**97**][**98**], **Graham** [**41**] etc, implemented forced asymmetry by shifting the upper or lower

half of the shed vortices by a certain small distance at the early stages of the calculation.

In this manner, asymmetric flows and their associated lift force are achieved much earlier in the time history. In other words, the time delay associated with the accumulation of the rounding errors is now replaced by a deliberate forced asymmetry of the location of the very first vortices. It is also claimed by those authors that its implementation is not significant to the subsequent value of the force coefficients although it facilitates the early development of realistic flow patterns.

4.11 Results and Comparisons

4.11.1 Uni-Directional Flows

The surface velocity of the element of the first quadrant element is compared with the exact solution, image method and the present surface singularity method at $\hat{t} = 0$ as shown in the table (**4.1**) below. The exact solution for the surface velocity due to a uniform stream u_∞ parallel to the $X-$ axis, **Batchelor** [**7**] is

$$u_{\infty t} = 2u_\infty \sin\theta \tag{4.48}$$

where θ is an angle measured in counter clockwise direction from the positive axis. In the Discrete vortex method, at time $t = 0$, no vortices have been shed and hence the surface vorticity can then be compared with equation (**4.48**). It is seen that for this unseparated flow condition, the velocity at the stagnation points with $\theta = 0$ and 180 degrees, is equal to zero, while at $\theta = 90$ or 270 degrees the velocity reaches its maximum value of 2.

In the image method, **Murray** [**70**] used 64 vortices which were shed from the first ring out at each non-dimensional time step of 0.15. The close results of surface vorticity distribution from both exact and the surface singularity method is obtained within 1% difference as displayed in table (**4.1**).

Pivotal point	I V_∞ exact	II Image method	III Surface Singularity Method
1	0.098135	0.098135	0.0980
2	0.293461	0.293460	0.2935
3	0.485961	0.485960	0.4859
4	0.673779	0.673779	0.6738
5	0.855110	0.855110	0.8551
6	1.028205	1.028205	1.0281
7	1.1913986	1.191398	1.1912
8	1.3431179	1.343117	1.3431
9	1.4819023	1.481902	1.4818
10	1.6064151	1.606415	1.6063
11	1.7154572	1.715457	1.7153
12	1.8079786	1.807978	1.8078
13	1.8830881	1.883088	1.8830
14	1.9400625	1.940062	1.9401
15	1.978353	1.978353	1.9784
16	1.997591	1.997590	1.9974

Table (4.1).- *Velocity on the surface of cylinder* $u_\infty = 1\ m\,sec$

The grid system used in this particular case is of *64* cylinder surface elements with length around *0.49D*. The vortices are introduced from the first ring out with distance equal to the element length. This condition is chosen based on the mesh analysis described previously in section (**4.10.1**). As shown in figure (**4.4**), with this configuration and non-dimensional time step $\frac{u_\infty \Delta t}{2a}$ equals *0.15*, this model can cover a quite wide range of Reynolds numbers as shown later. For similar case, **Stansby** [**101**] and **Lewis** [**60**] used parameters of a similar order with time step $\frac{u_\infty \Delta t}{2a} = 0.12$ at Reynolds number 2.10^4 and he moved back vortices which are drifted nearer than *0.05D* to the surface. They could produce quite good results in term of the force coefficients and the Strouhal number when the number of element equaled *32*.

The use of the algorithm based on the structure, application and theory as

described previously can now be illustrated with Reynolds number of 10^5 . In this section the result produced from modelling some typical flows are presented with both flow visualisations and graphs showing the accompanying force coefficients.

For easy comparation with the results presented by other authors, a non-dimensional time of $\hat{t} = \frac{u_\infty t}{2a}$ is used throughout this study.

For $\hat{t} = 1$ and $\hat{t} = 5$ the initial development of the flow field is as shown in figure (4.6). in which the vortices are shed from separation points with a separation angle of around 100°. This is similar to the experimental results with Reynolds number about 10^5. It is seen from these figures that at $\hat{t} = 5$ the shed vortices are beginning to roll-up behind the cylinder.

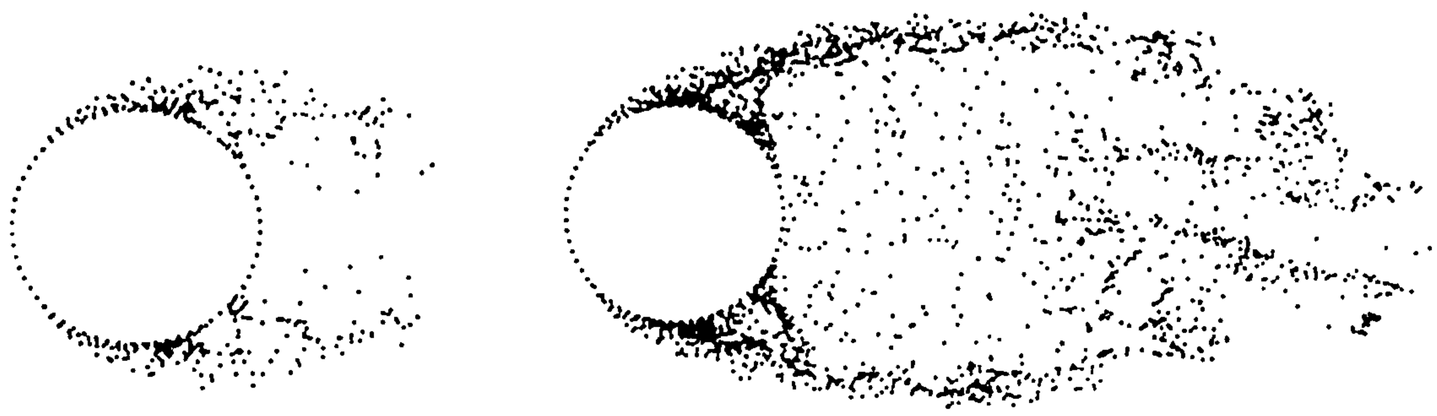

Figure 4.6.- *Flow pattern at* $\hat{t} = 1$ *and* $\hat{t} = 5$: *Surface Singularity Method*

Comparison with the results of the image method by Murray [69] show the accuracy of this method at the same non-dimensional time as shown in figure [4.7] below.

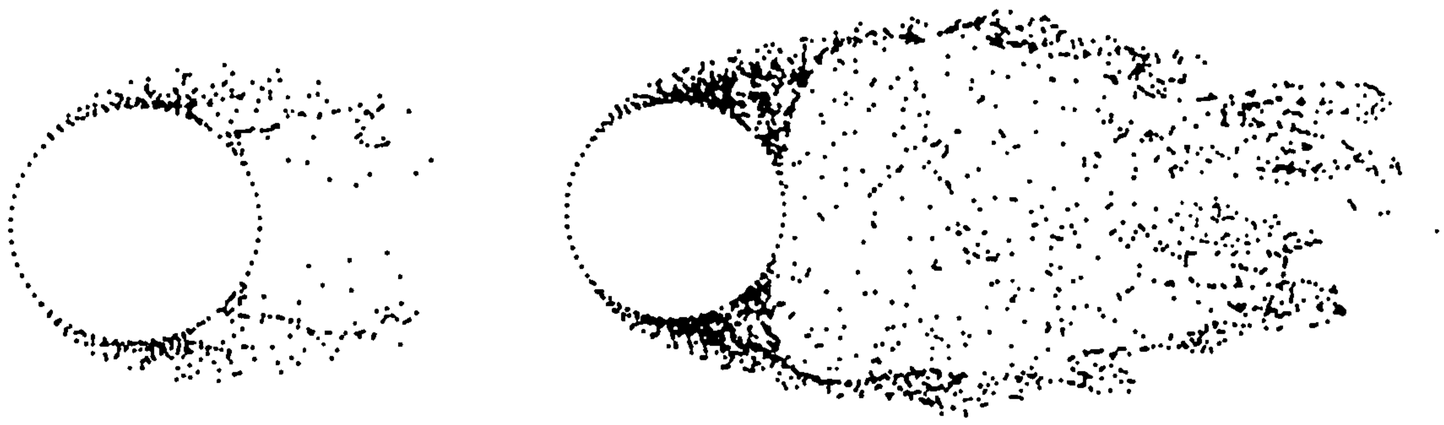

Figure 4.7.- *Flow pattern at* $\hat{t} = 1$ *and* $\hat{t} = 5$: *Image Method.*

At $\hat{t} = 5$. in which the flow is more developed the wake behind the body has extended to between one and two cylinder diameters downstream with asymmetric

form. This asymmetry will only appear in the numerical model when the accumulative rounding errors have become significant, which does not model impulsively started flows realistically. **Sarpkaya** and **Shoaff** [**89**] therefore introduced an artificial perturbation of the vortices, a technique also adopted in this study. This forced asymmetry enforcement is introduced at $\hat{t} = 1$.

A regular vortex shedding process similar to a Karman vortex street, emerges as the flow develops further in time, as shown in figure (**3.7a**). The force coefficients associated with the flow pattern described above are displayed against time in figure (**3.7b**). As described in the previous sections, the force coefficients are found by integrating the pressure distribution around the cylinder surface. It can be seen that the mean value of the drag coefficient is about *1.14* and the Strouhal number is *0.2*, both of which are in good agreement with the experimental data for high Reynolds number at about 10^5. The frequency of oscillation of the lift coefficients can also be seen to be half of that of the drag coefficient. This effect, as explained in detail by **Sarpkaya** and **Isaacson** [**87**], and is related to the way in which the alternate vortex shedding influences the pressure distribution around the cylinder. The formation of the vortices which causes a pressure differential over the cylinder is subsequently modified as the vortices are shed and convected downstream. These fluctuations are reflected in the behaviour of the drag force for the shedding of each vortex while the lift force is controlled by the effect of a pair of vortices being shed from opposing sides of the cylinder. A complete cycle of the lift force corresponds to the growth and shedding of a vortex from one side of the cylinder.

The percentage CPU time used in calculating each of the steps in the discrete vortex scheme is displayed in table (**4.2**) below. The figures are based on the total time for the method to compute *600* time steps. At this time step, the flow is fully developed the number of active nodes is more than *560* and the number of vortices could reach more than *16100*, so that the data can be considered representative.

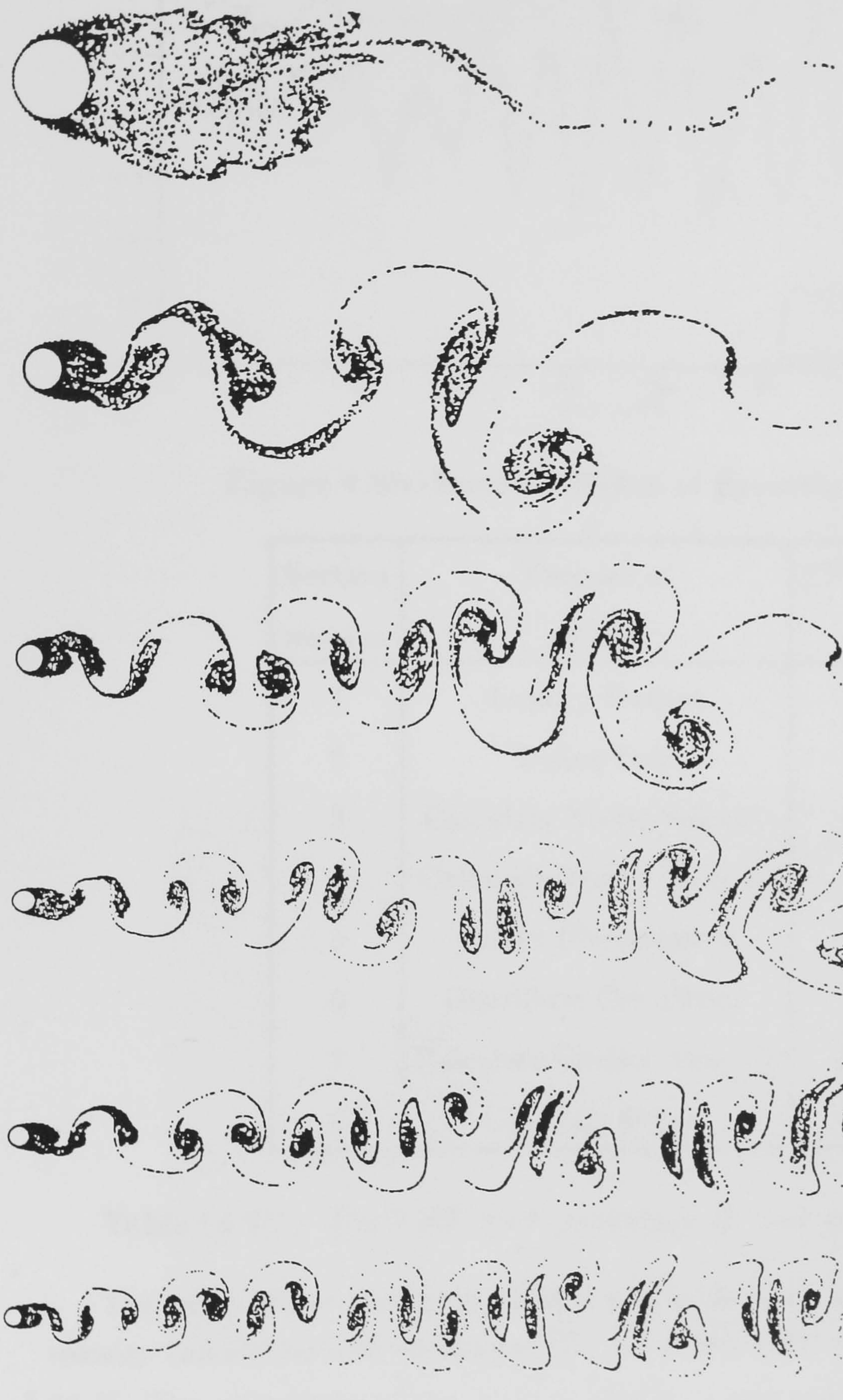

Figure 4.8a.-Flow Pattern at $\hat{t} = 10, 20, 30, 40, 50, 60$ at Reynolds number 10^5

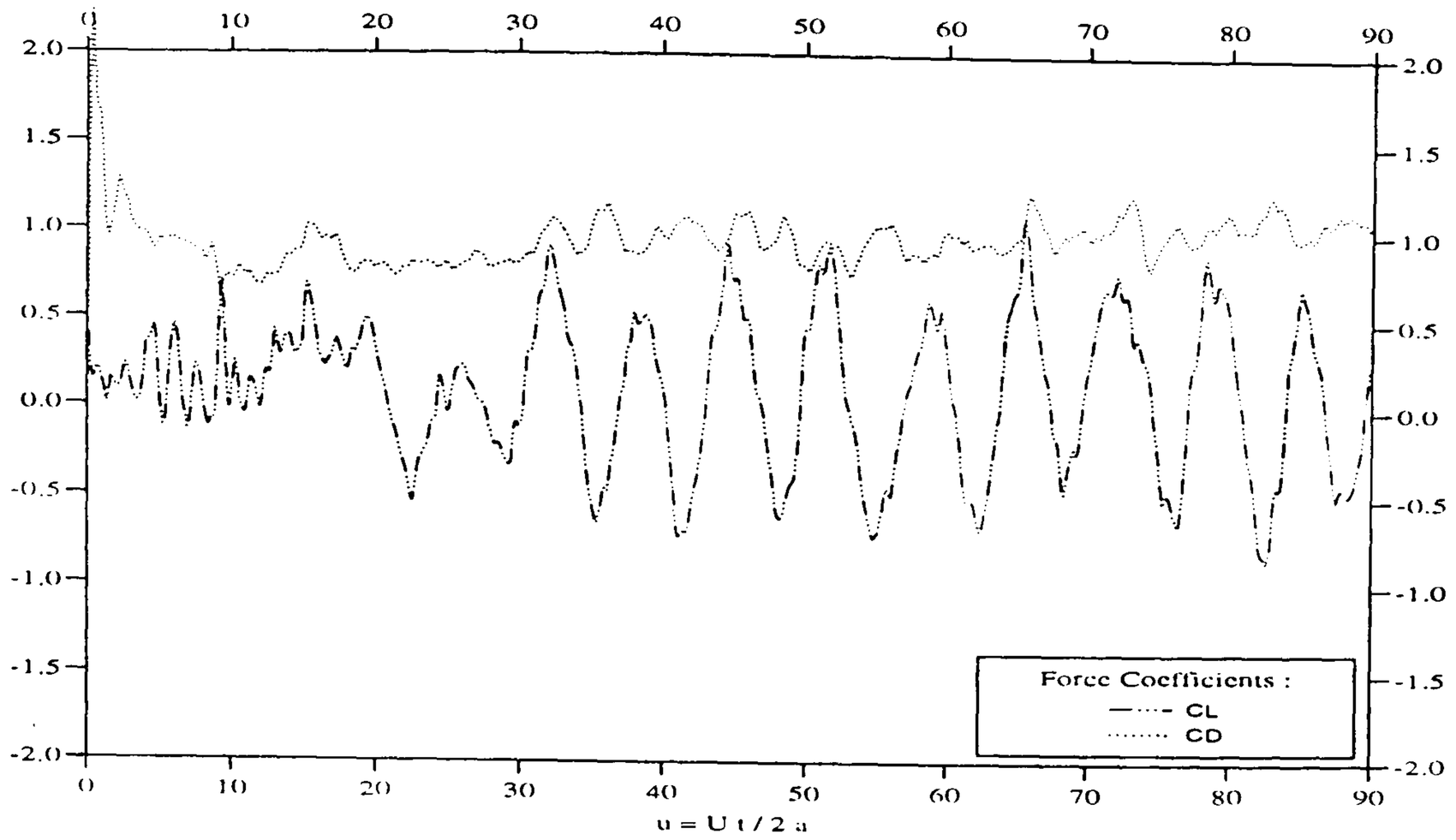

Figure 4.8b.-Force Coefficient at Reynolds number 10^5

Section number	Purpose of section	CPU Time
1	Input / Output	1.59
2	Define Grid	0.00
3	Calculate Nodal Velocity	61.99
4	Calculate Vortex Velocity	1.50
5	Vortex Displacement	4.6
6	Distribute Circulation	1.4
7	Calculate Surface Velocity	23.41
8	Calculate Forces	0.04

Table (4.2). – *The CPU time precentage of each section of the algorithm.*

The table shows that even though grid node-to-node interaction is used, the velocity calculation still dominates the use of the CPU time which is as much as *62 %*. The calculation of the surface velocity is also computationally intensive as it takes a considerable time in calculating the right hand side of equation **(4.15)** above.

For smaller values of Reynolds Numbers, in which the effect of viscosity is more important, the diffusion process will be more significant in the above scheme.

although it will still take the same CPU time. The main advantage of choosing the parameters of the grid and time with the non-dimensional number $\frac{\Delta a}{u_\infty \Delta t}$ as mentioned above will become clear at this stage. The behaviour of the model shows there is no need to vary the distance of the first ring out from the cylinder surface over a wide range of Reynolds number. The characteristics of the flow and force coefficients will be solely dictated by the random walk diffusion, as shown later. Using the Random Walk method with $Re = 140$, the early flow development shows the separation angle increased to around 110 degrees which is expected in this regime. It is shown that using the Random Walk Scheme, the physical phenomena are not so clearly defined in comparation with the experimental work by **Van Dyke [30]** shown in figure (**4.9**). This is due to the fact that at low Reynolds number, the value of random walk movement $r = \sqrt{4\nu\Delta \ln(\frac{1}{1-p})}$ is relatively high for the same value of random number p and free stream velocity u_∞ as the value of viscosity ν is now higher. The resolution of the pictures compared to those of Finite Difference Hybrid Method by **Murray [70]** reinforces the argument that the Random Walk approach is less appropriate for application to lower Reynolds number flows as shown in figure (**B.2**) in Appendix B.

Figure 4.9.- *Flow Visualisation by Van Dyke at Re = 140*

A Strouhal number of between 0.13 and 0.17 is expected for these flows and, whereas that obtained via the Finite Difference scheme of **Murray [70]** is around

0.14, this Random Walk scheme leads to a comparable value for the Strouhal number of around *0.15*.

The display of the flow visualizations produced from the present method at Reynolds number from *50* are presented in *Appendix B* from figures (**B.1**). The comparation with the results of the Finite Difference scheme of **Murray** [**69**] still shows the weak definition of the Random Walk method. although a Strouhal number of *0.15* is obtained by both schemes. Furthermore. it is shown that the average drag force obtained by the Random Walk is in good agreement with the expected value of *1.6*.

Further comparation of this scheme to that of the Finite Difference Hybrid Method at the higher Reynolds number at 2.5 10^5 are displayed in figures (**B.9**). The Reynolds number of 2.5 10^5 is of particular interest as the 'drag crisis' has an effect for the Reynolds number beyond this and it is not meaningful to carry out computations beyond this point.

As the value of the Reynolds number increases beyond a few hundred, in the physical flow, turbulence becomes increasingly apparent in the wake. At a value of around 10^5, it works its way back to the boundary layers which themselves undergo transition to turbulence. The relatively crude model of the boundary layer adopted in this study is not capable of representing the process of transition followed by a fully turbulence flow. There is no turbulence model in the discrete vortex model adopted and it is interesting to note that even so it can predict reasonably well the forces on the cylinder and the gross characteristics of the wake over Reynolds numbers ranging from *100* up to 10^5. Obviously the fine detail of the boundary layers and the wake will not be well modelled by this approach. The force coefficients at high Reynolds number, as indicated in the figures in *Appendix A*. are in general quite close to those predicted by both the Finite Difference and the Random Walk schemes. It is consistent with the argument described earlier that at this high Reynold number, the flow patterns are dominated by and resemble pure convective flow.

The global trend of this scheme over the specified Reynolds number range has been plotted in figure (**4.10a.**). It can be seen that over a range of Reynolds numbers between *50* to $2.5.10^5$ it produces a quite good prediction of the drag and lift coefficients. A slightly lower value than expected. by about *4%*. was obtained at intermediate to high Reynold numbers while at Reynolds number higher than the 'drag crisis', this scheme fails to give acceptable results. The lift

coefficients show maximum values of aroung *0.6* at low Reynolds numbers but slightly higher in the order around *9%* at higher Reynolds numbers. The Strouhal numbers are reasonably well predicted from a Reynolds number *250* onwards where it approximately equals *0.2* which is slightly lower than the experimental result of **Schlichting** [89] of around *0.21*.

At Reynolds numbers higher than 10^4 the Strouhal numbers are overestimated in comparation to the experimental data by *5%* as shown in figure (**4.10b**) above. The frequency of oscillation of the drag coefficients compare to that of the lift are generally seen to be around twice that of the lift coefficients.

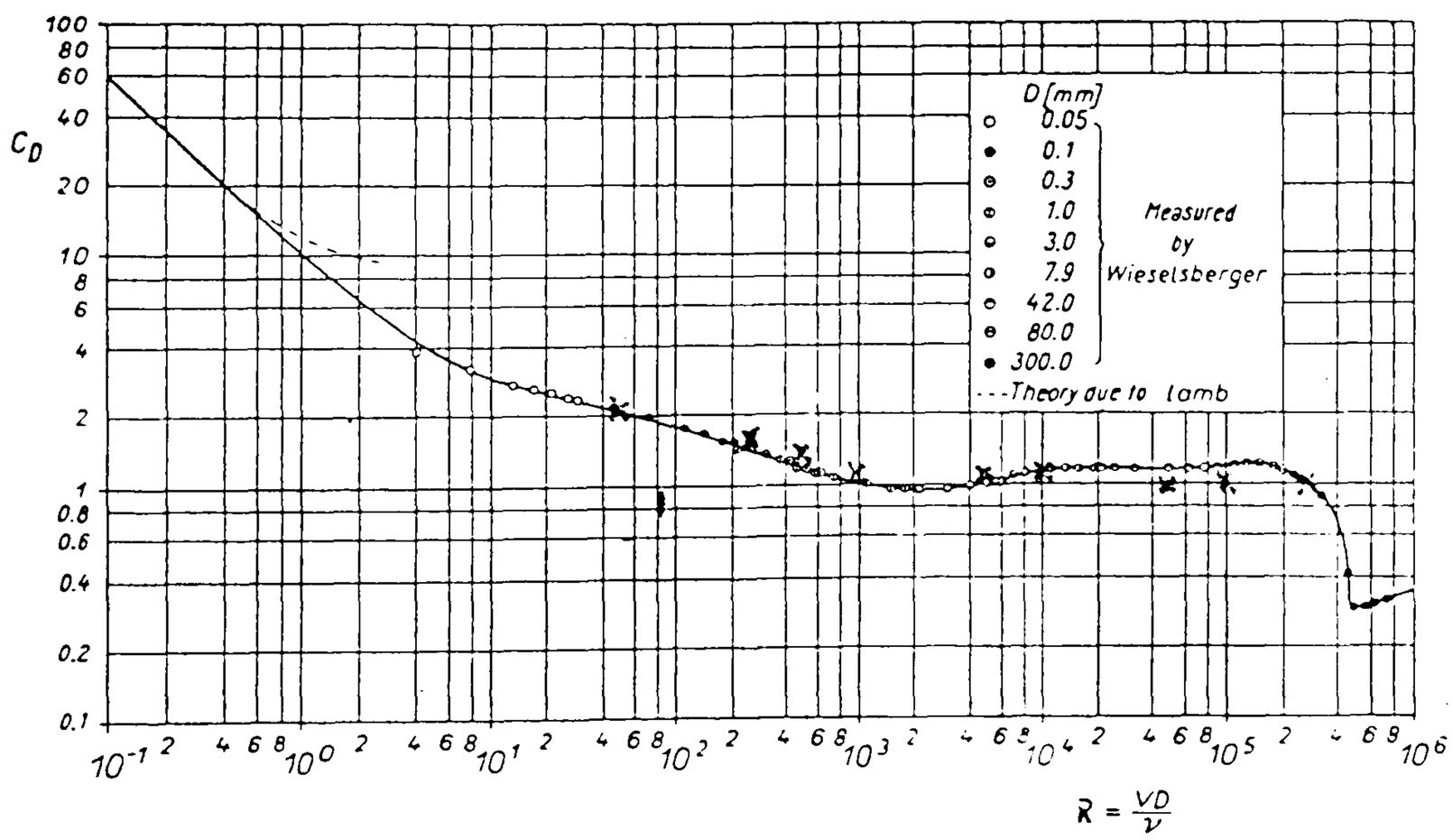

Figure 4.10.a.-*Cd Vs. Re*

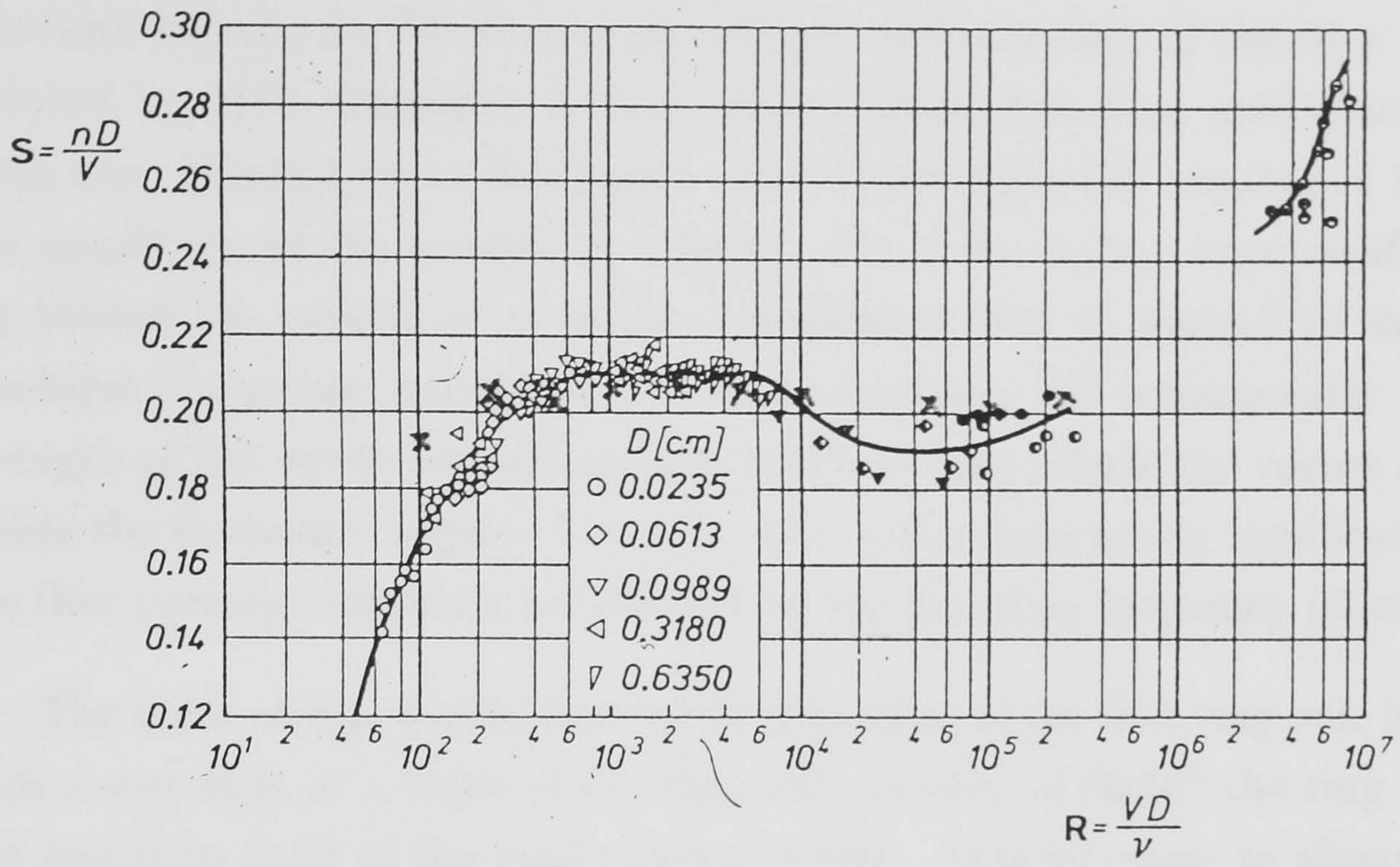

Figure 4.10.b.-*Strouhal Number Vs. Re*

4.11.2 Oscillatory Flow

As described in the previous section, the time dependent nature of the flow is modelled by converting the constant free stream velocity into a sinusoidal time dependent one as shown in equation (**4.17**). This alteration not only influences directly the third term of the Martensen equation (**4.14**) during the surface vorticity calculation but also the first term on the right hand side of equation (**4.30**) during the calculation of the active grid node velocities. The influence of the time dependent free stream on the force coefficient can be seen in the change of the value of the surface vorticity distribution as shown in equation (**4.40**) and (**4.41**).

The diameter of the first ring out from where the vortices are introduced, is proportional to the inverse square root value of the β number, as described in section (**4.10.2**). Consequently, the factor $\frac{\Delta a}{u_\infty \Delta t}$ has also to be readjusted as the Δa is now dependent also on the β value. Figures (**4.5a**) and (**4.5b**), show the behaviour of the model upon variation of the above factors. It is shown that with *64* cylinder elements , $\frac{u_\infty \Delta t}{2a}$ equals *0.1*. and a maximum free stream velocity of *1* , a constant of proportionality k_{osc} of *1.55* gives the best results in producing the closest value to the in-line force coefficients taken from the experimental results.

These values imply that the oscillatory flows needs a finer scale for the parameters, compared with that of the steady free stream flow. Flow definition in the vicinity of the cylinder becomes critical because vortices that are brought back close to the cylinder during the reverse flow interact with the newly created vortices and have to be distributed on the grid nodes as well. If the time step is not reduced by *34%*, compared to that of the steady flow case, preliminary calculations have shown that at the higher value of the Reynolds number of 8.10^4 using the amplitude of the oscillatory velocity of *1.0* the in-line force coefficients can lag behind the experimental result of **Sarpkaya** [**82**] by around *15* degrees at a Keulegan-Carpenter number of *15*. This reduction will consequently reduce the strength of the newly created vortices which in turn affects the vortex interaction inside the formation region. The near field vortex interaction significantly affects the flow pattern behaviour as reflected by the shedding frequency phase angle.

The value of k_{osc} which determines the radius of the first ring out, is chosen in such a way that at a value of the Reynolds number of 80.10^4 the ring distance is not less than *0.50* of the local element length. This increases to about twice the element length at lower Reynolds numbers. The magnitude of the diameter of the first ring out is chosen to give the best fit to root-mean-square of the in-line force coefficients taken from the experimental results of **Sarpkaya** and **Isaacson** [**87**] as described previously.

The model has been used to produce results for a cylinder placed in oscillatory flows at several values of the Keulegan-Carpenter number over a range of $5 - 30$. This range covers a substantial part of that in which the sea loading of offshore structures occurs. The flows were assessed starting at a Renolds number of 3.10^4 with a Keulegan-Carpenter number at *10*.

The flow development at $Kc = 10$ for several time steps are displayed in figure (**4.11**). These figures show how a high period flow develops in time and the force coefficients related to this flow are shown in figure (**4.12**). In this graph the components of the total in-line force coefficients, i.e. the drag and inertia components calculated using equation (**4.41**) and (**4.42**) over each flow period are included.

At this value of Re and Kc, the model produced higher values of the drag and inertia coefficients by about *9%* and *2%* compared to the experimental results of **Sarpkaya** [**82**], although it gives a close value of the root mean square of the in-line force coefficient. The plot of the predicted in-line force coefficient and of

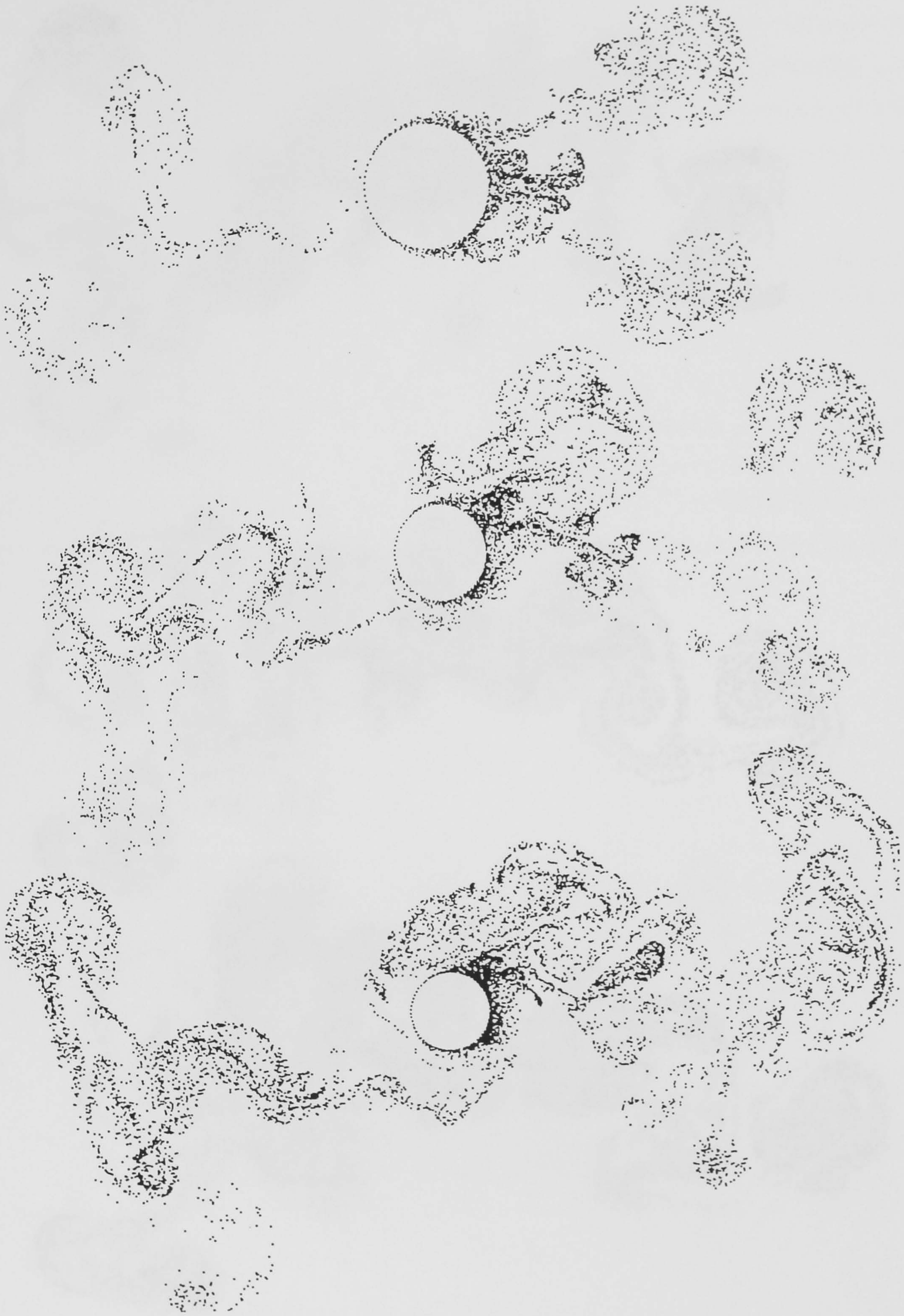

Figure 4.11.a.-Flow Pattern at t= 10, 20, 30, Kc = 10 and Re = 30000

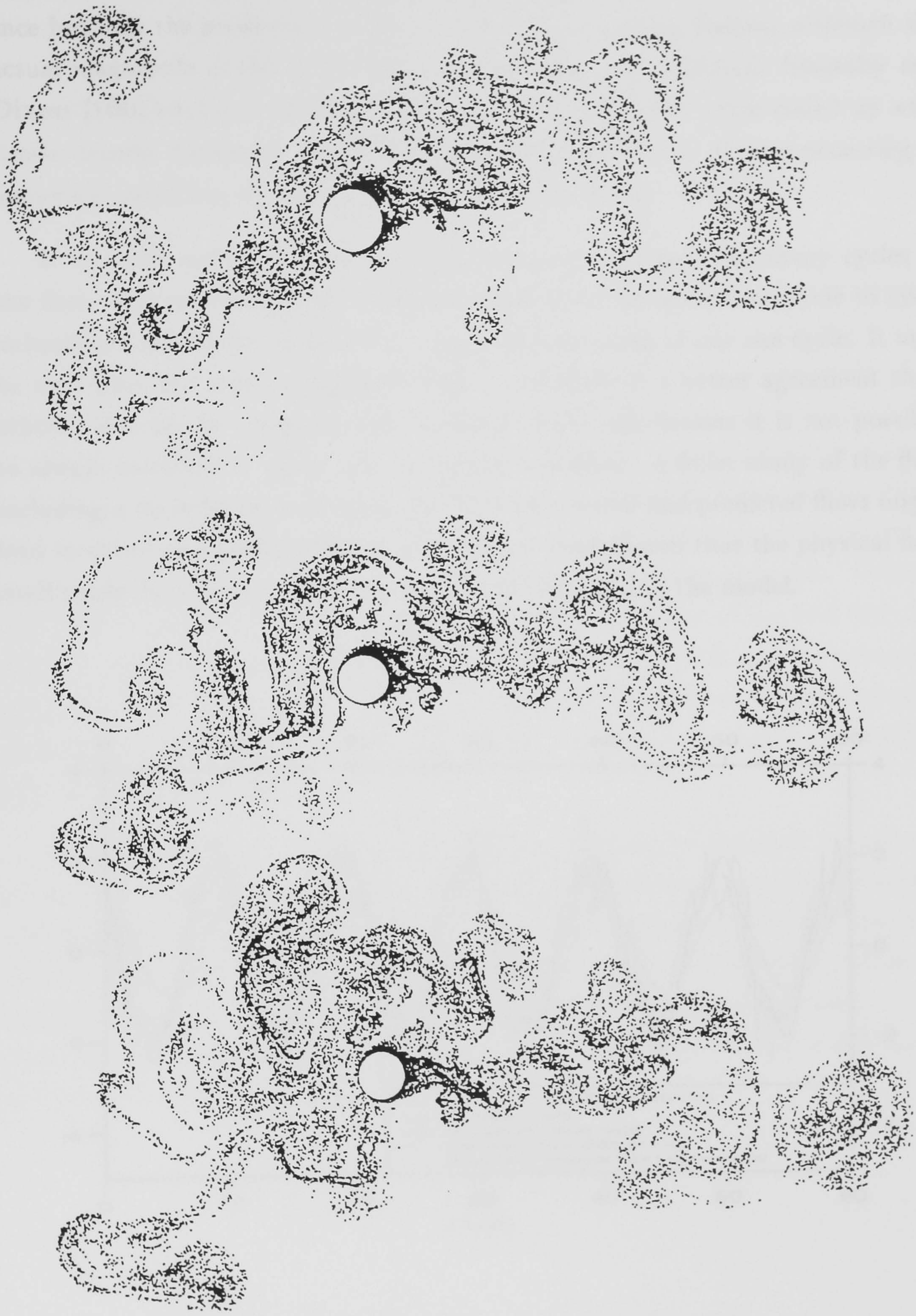

Figure 4.11.b.-Flow Pattern at t= 40, 50, 60, Kc = 10 and Re = 30000

the experimental results, taken by substituting Sarpkaya's drag and inertia coefficients into the Morison equation (**2.1**), suggests that there is a phase difference between the predicted and the actual vortex shedding process, although the actual magnitude of the in-line force is reasonably well predicted. **Stansby** and **Dixon** [100][101] and **Murray** [70] also produced models which ended up with similar trends. **Graham** [40] mentioned a similar possibility of error occurring in numerical modelling of a cylinder in an oscillatory flows.

It is worth noting that Sarpkaya's results are averaged over many cycles of the flow. The predicted force coefficients show some variation from cycle to cycle indicating a sensitivity to the vortex interaction occuring at any one cycle. It may be seen from the results that over some cycles there is a better agreement than others. Due to the computational intensity of the calculations it is not possible to always calculate as many cycle as might be wished. A fuller study of the flow including a cycle by cycle analysis of both experimental and predicted flows might lead to closer agreement although it should be remembered that the physical flow itself might have some attributes that are not included in the model.

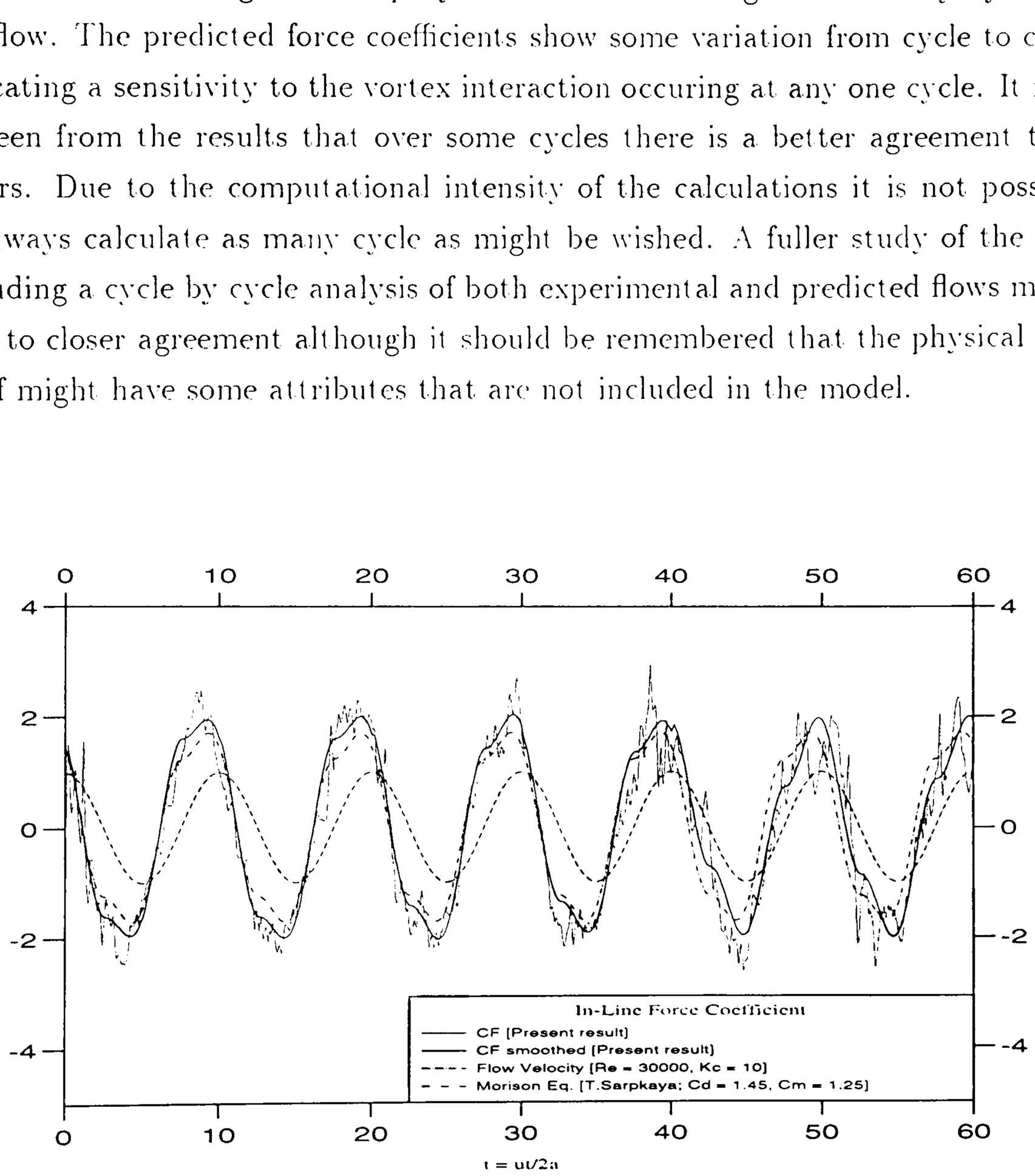

Figure 4.12.- *Force Coefficients at $K_c = 10$ and $Re = 30000$*

At the lower value of the Keulegan-Carpenter number of 5, in which the flow pattern and the in-line force coefficient are displayed in figures (**4.13**), the effect

of the phase different is more pronounced. In this relatively high frequency flow. the amplitude of the in-line force coefficient before smoothing seems to be close enough to the experimental result. However, due to the different phase angle, which becomes quite a large proportion of the period of the oscillation. this not only affects the shift of the smoothed in-line force coefficient but also reduces its amplitude significantly. This is also reflected in the value of the drag and inertia coefficients which are comparatively far higher and far lower than the experimental results, respectively.

Better agreement of the results is obtained at the Keulegan-Carpenter number *15*, as shown in figure (**4.14**) where the value of the drag and inertia coefficients are of the same trend and only differ slightly from those of the experiments. The graph of the in-line force coefficients shows quite close agreement in magnitude and the phase of the vortex shedding is also improving. This condition is maintained until the Keulegan-Carpenter number reachs *30*, as shown in figure (**4.17**), where the results from the present model start to deteriorate, especially with regard to the amplitude of the in-line force, at Reynolds numers higher than this. Numerically, this is because at very high Reynolds number the offset of the first ring-out, which is dependent on the factor $(\frac{Kc}{Re})^{\frac{1}{2}}$, becomes very small and its proximity to the cylinder surface and is a source of errors as the induced velocity becomes unrealistically high. This is a reflection of the inability of the model to represent fully developed turbulent flows.

A further measure of the realism of the model can be obtained by plotting the results on the experimental curves for the force coefficients given by **Sarpkaya** and **Isaacson** [**87**] as shown in figure (**4.18**). The difference between the predicted and the experimental phase angle at low Keulegan-Carpenter is striking when the results are presented in this way. However, the trends are similar over quite a wide range of Keulegan-Carptenter number and there is a good agreement at the middle to high and of the range investigated.

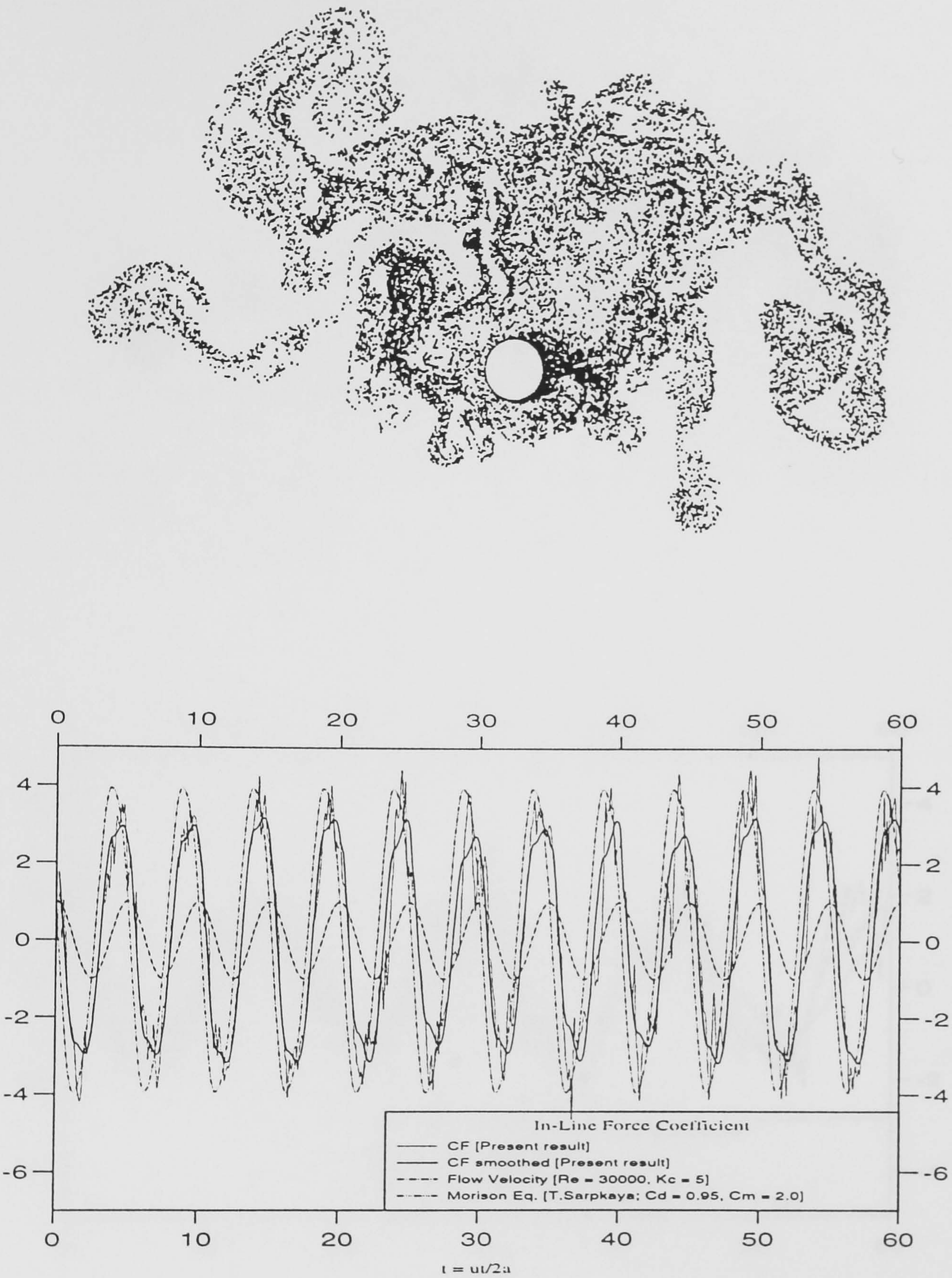

Figure 4.13.-*Flow Pattern at t= 60, and Force Coefficients for Kc = 5 and Re = 30000*

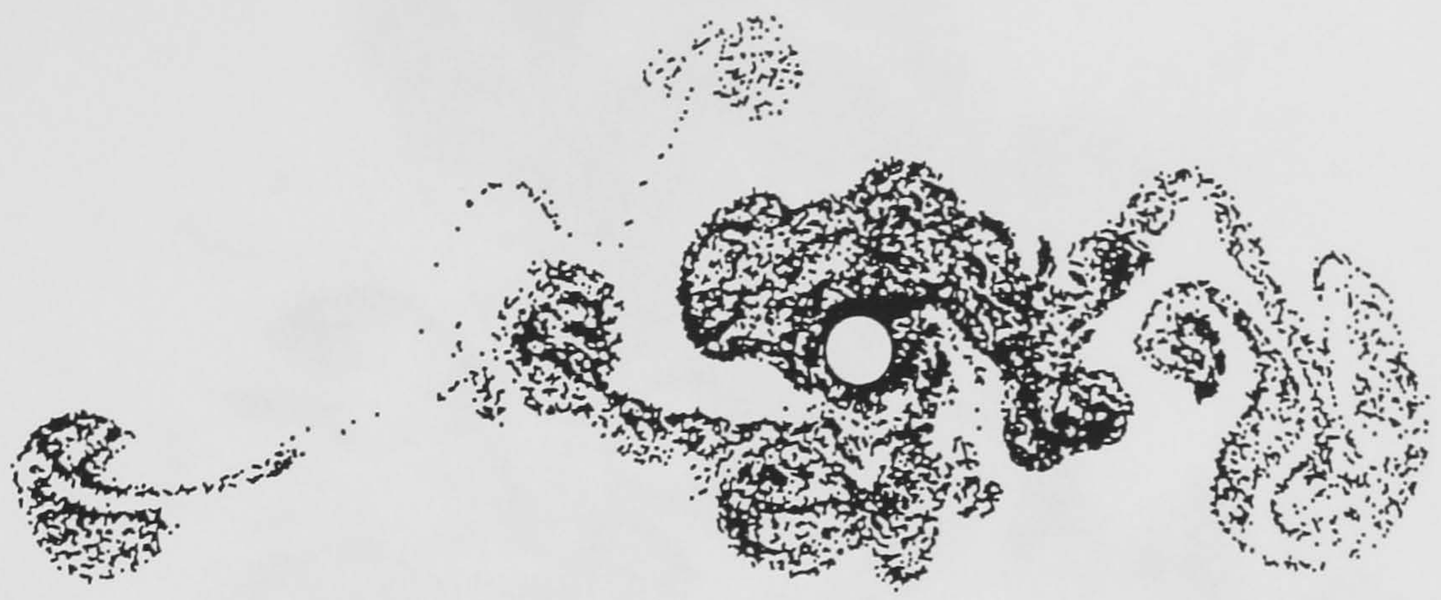

Figure 4.14.-*Flow Pattern at t= 60, and Force Coefficients for Kc = 15 and Re = 30000*

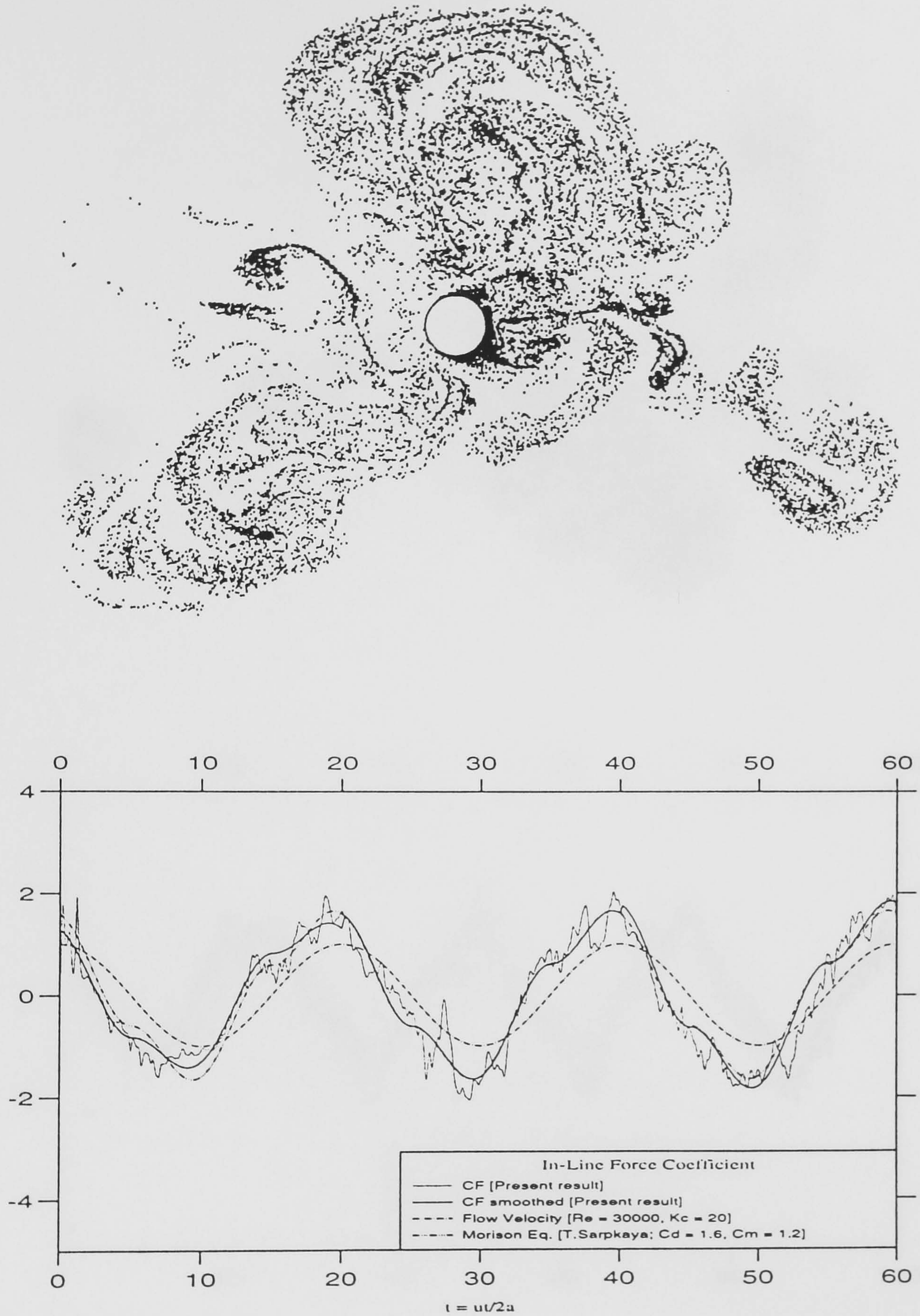

Figure 4.15.-*Flow Pattern at t= 60, and Force Coefficients for Kc = 20 and Re = 30000*

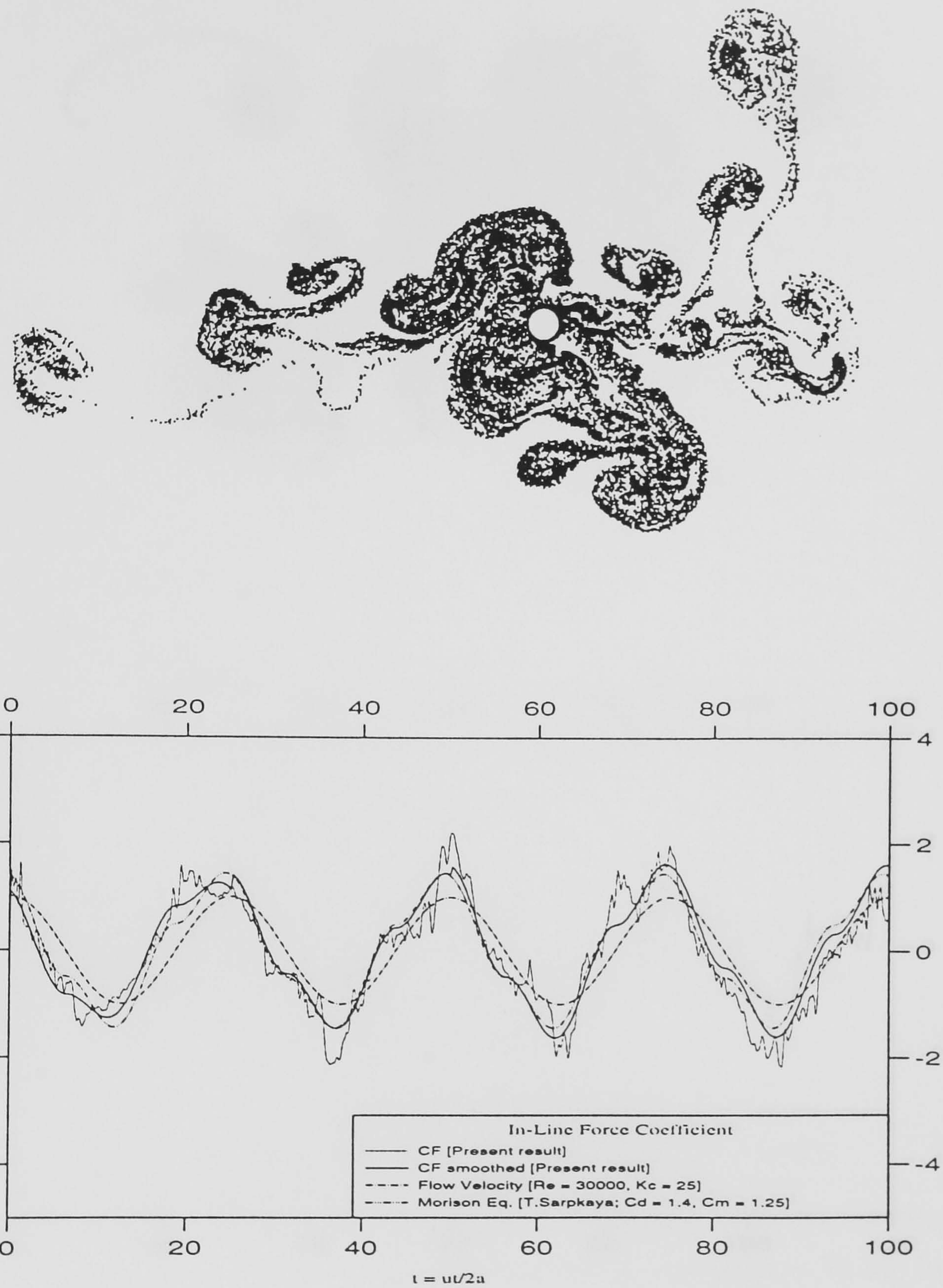

Figure 4.16.-*Flow Pattern at t= 60, and Force Coefficients for Kc = 25 and Re = 30000*

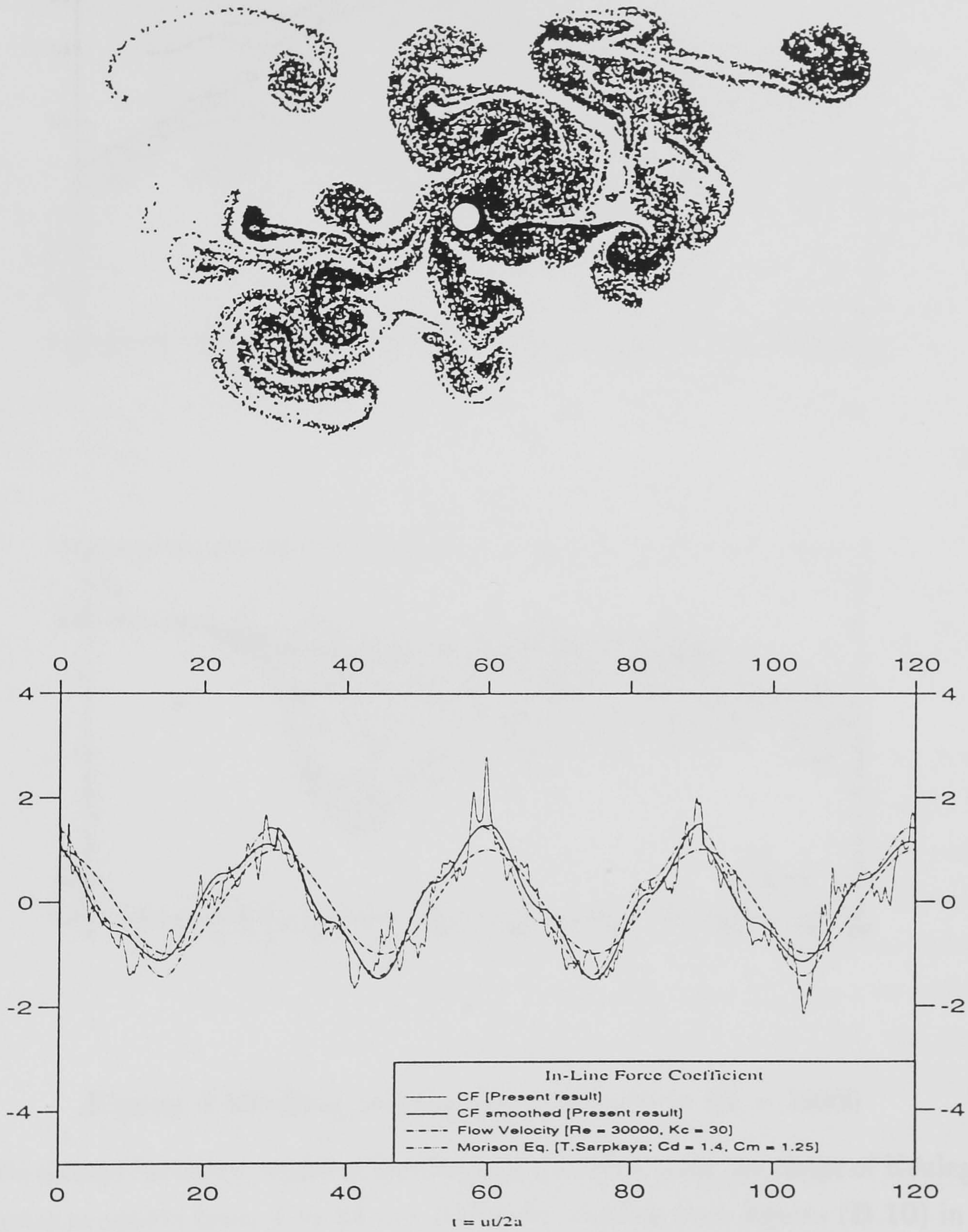

Figure 4.17.-*Flow Pattern at t= 60, and Force Coefficients for Kc = 30 and Re = 30000*

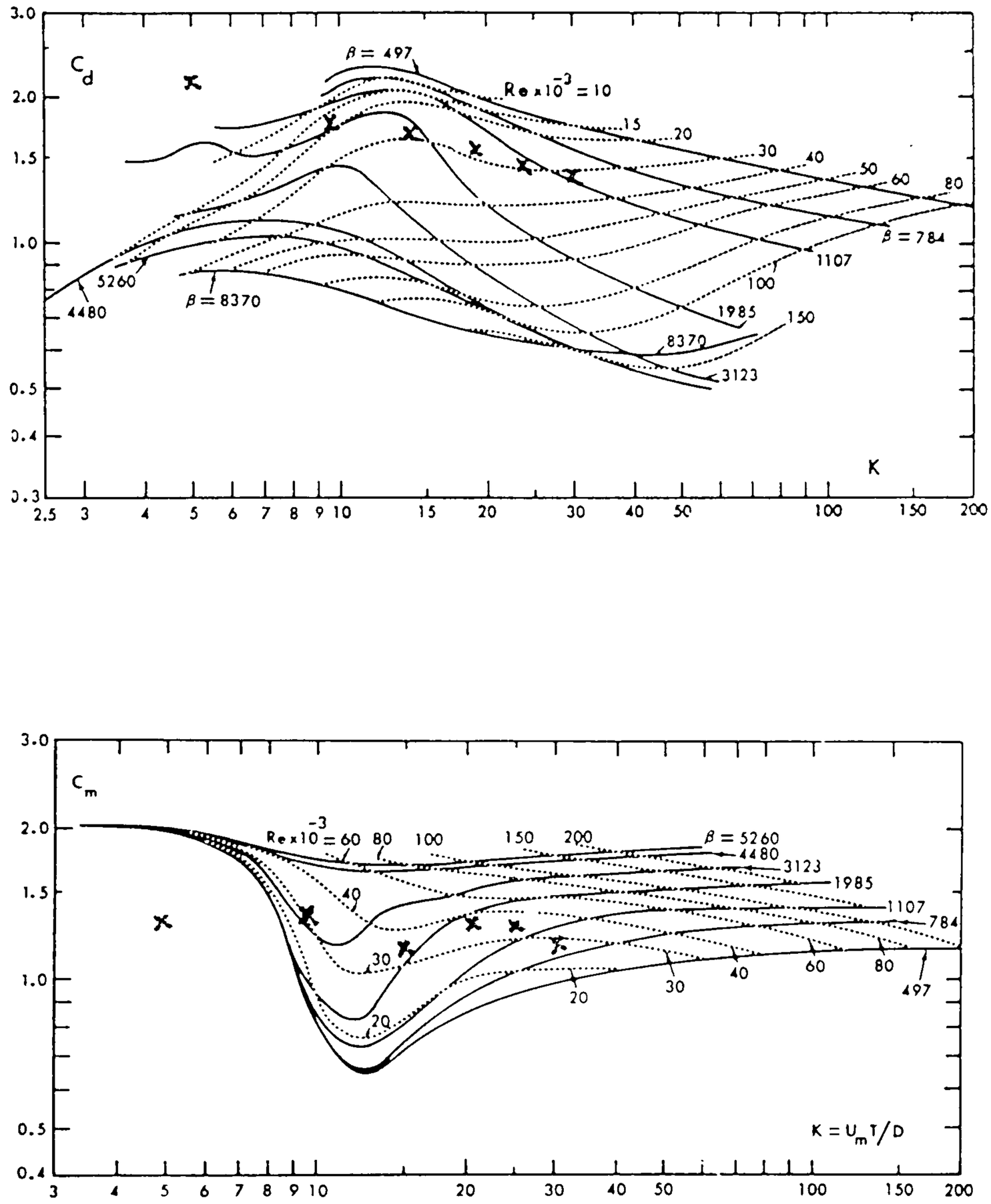

Figure 4.18.-Drag and Inertia coefficients at Re = 30000

The results for other values of the Reynolds number with the range of Keulegan-Carpenter numbers from *5* to *25* are displayed starting from figures (**B.10**) in the *Appendix B*. At a Keulegan-Carpenter number of *5*, it is seen that there is disagreement between the experimental and predicted values of the drag and inertia coefficients at lower Reynolds numbers of around *10000*. The predicted drag coefficients are higher by about *25%* while the inertia coefficients are lower than about *15%* on average. However, as in the previous case, the magnitude of the in-line force coefficient is quite well predicted. At intermediate Keulegan-Carpenter num-

bers, much better results are achieved both in the value of the drag and inertia coefficients although differences are still appear. Figures (**B.11**) to (**B.13**) show the plots of the flow pattern and the force coefficients for various Keulegan-Carpenter numbers at Reynolds number of *10000*. The results show a similar trend in which the drag coefficients are now becoming lower, and the inertia coefficients are higher than expected over almost the whole range of the Keulegan-Carpenter numbers, event hough the root-mean-square of the in-line force coefficient indicates quite good results, as displayed in figure (**4.19**).

Much closer agreement is obtained at a Reynolds number of *20000* in terms of the drag coefficients, even though the inertia coefficients still show slightly higher values than the experimental ones. Figure (**B.14**) shows that both coefficients follow the same trend as the experimental results, even though at a lower Keulegan-Carpenter number around *5*, there is a significant discrepancy. At higher values of Keulegan-Carpenter number the predicted values of the drag coefficients are about *15%* lower and the inertia coefficients are slightly higher at moderate Keulegan-Carpenter numbers with *8%* and about *12%* at high Keulegan-Carpenter numbers compared to the experimental values. Again the results for the in-line coefficient show good agreement in magnitude although although the phase differences compared to those of the experimental results taken from Sarpkaya's are slightly widened.

The results for the higher Reynolds numbers of *40000* show similar trends in which the drag coefficient tends to be higher while the inertia coefficient falls below the experimental values, as displayed from figures (**B.20**). Overall it can be seen that the phase difference is getting wider as the Reynolds number increases. This is presumably related to the nature of the boundary layer around the cylinder surface in which at high Reynolds number and low at Keulegan-Carpenter number, the level of turbulence is increased. According to **Sarpkaya** [**81**][**82**] the planar oscillatory flow becomes turbulent at $Kc = 2.8$ for $\beta = 196$. When the Kc is slightly larger than this value, the flow becomes turbulent only in part of the oscillation cycle or in the wake, and the boundary layer separation is predominantly laminar.

Numerically, these inaccuracies can be attributed to the crudeness of the model itself especially in the region of the boundary layer, in which the grid size around the cylinder and the time step were both relatively large. In a much finer model **C.Y.Zhou** [**120**] used the discrete vortex model to investigate the flow around a body in the combination motion of waves and current, using 128×80 meshes

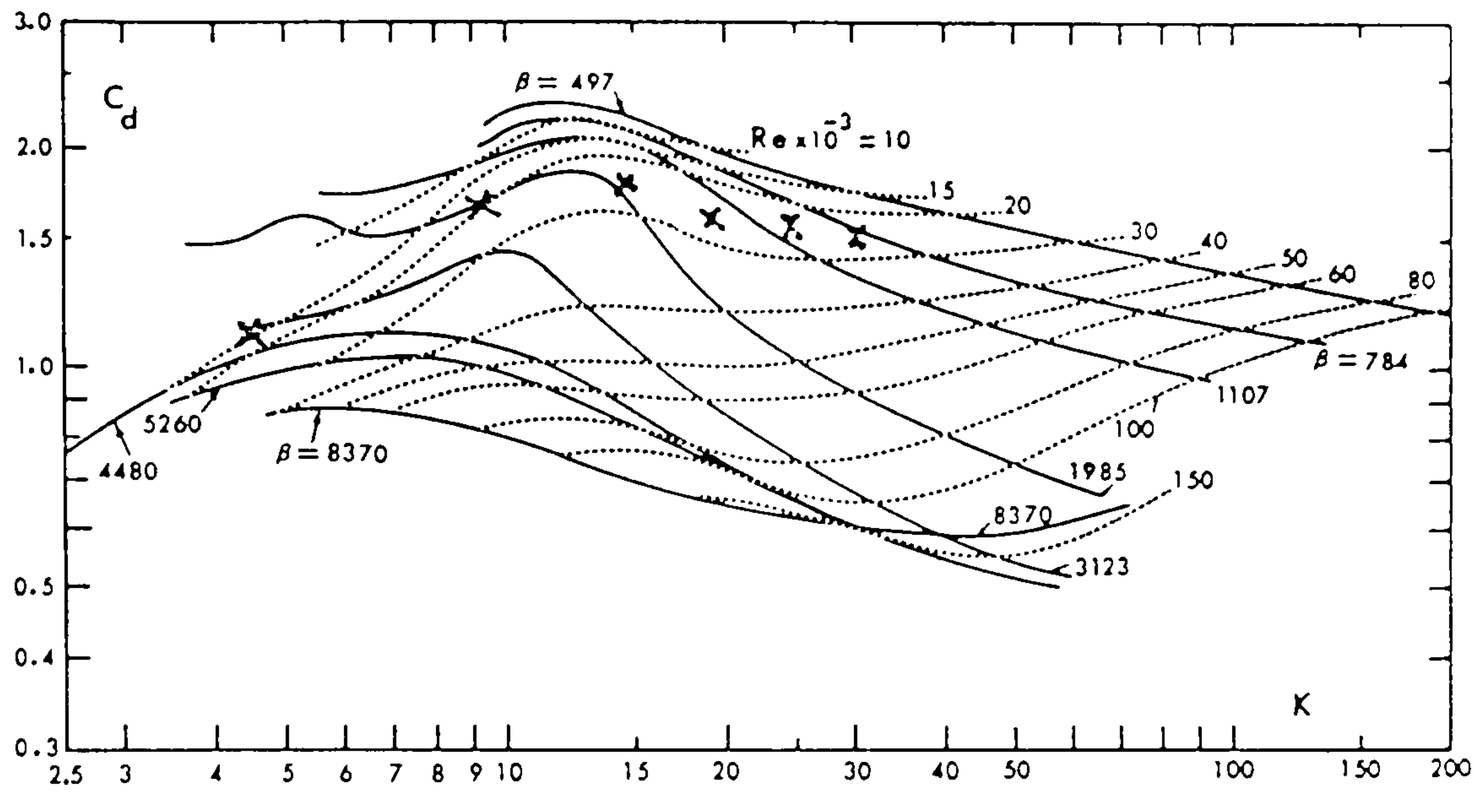

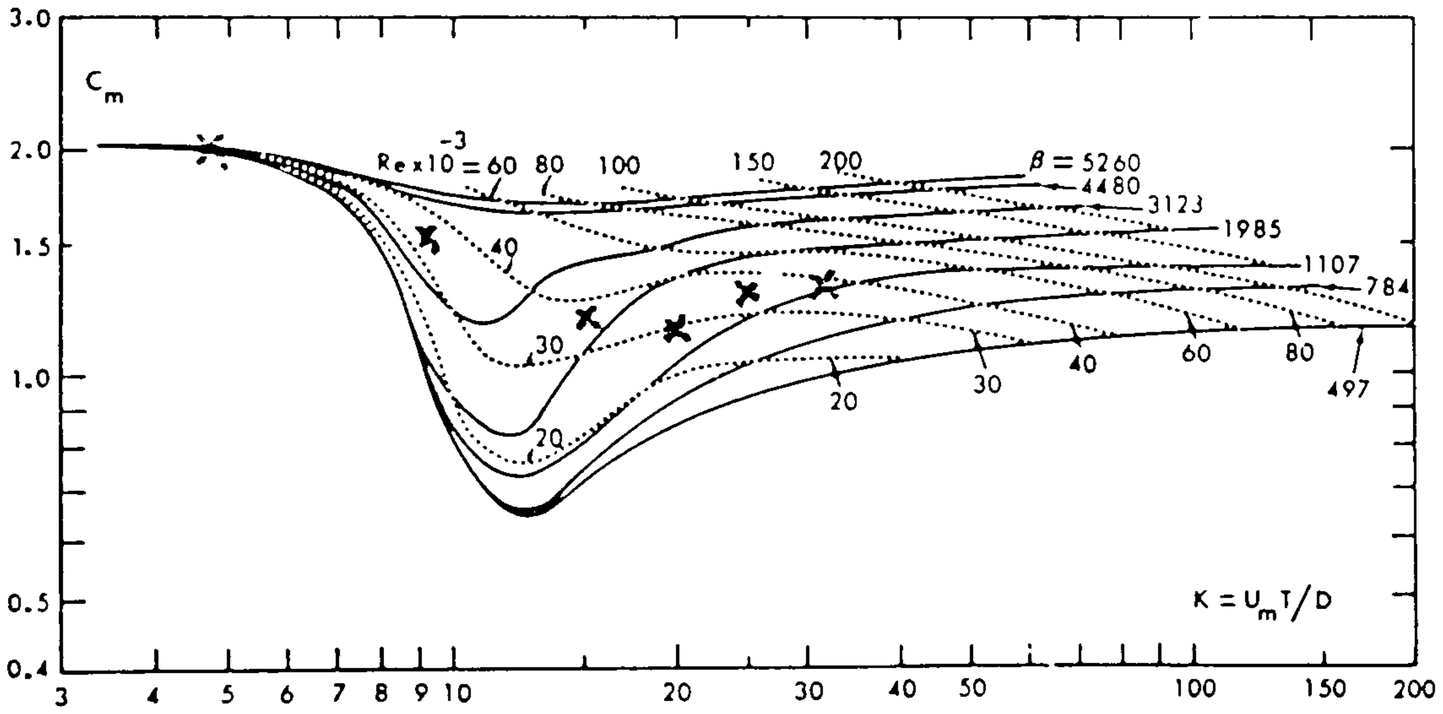

Figure 4.19.-Drag and Inertia coefficients at Re = 10000

and with a non dimensional time step $\frac{U_m \Delta t}{2a}$ varied from *0.001* to *0.0001* which is very much finer than the present model. With these parameters, she could produce good results both in the drag and inertia coefficients at values of *3* lower than *200* with less than *5%* dicrepancies.

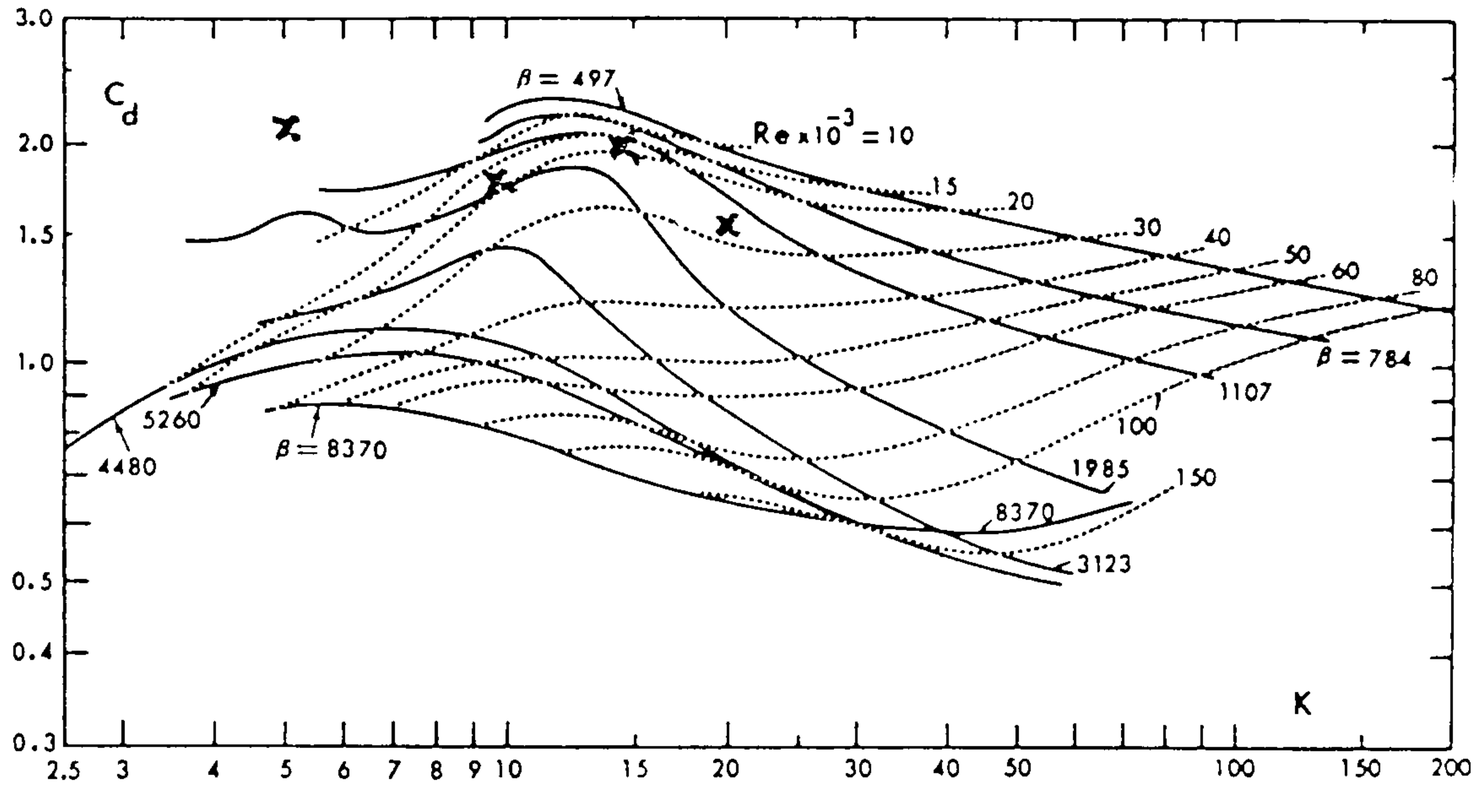

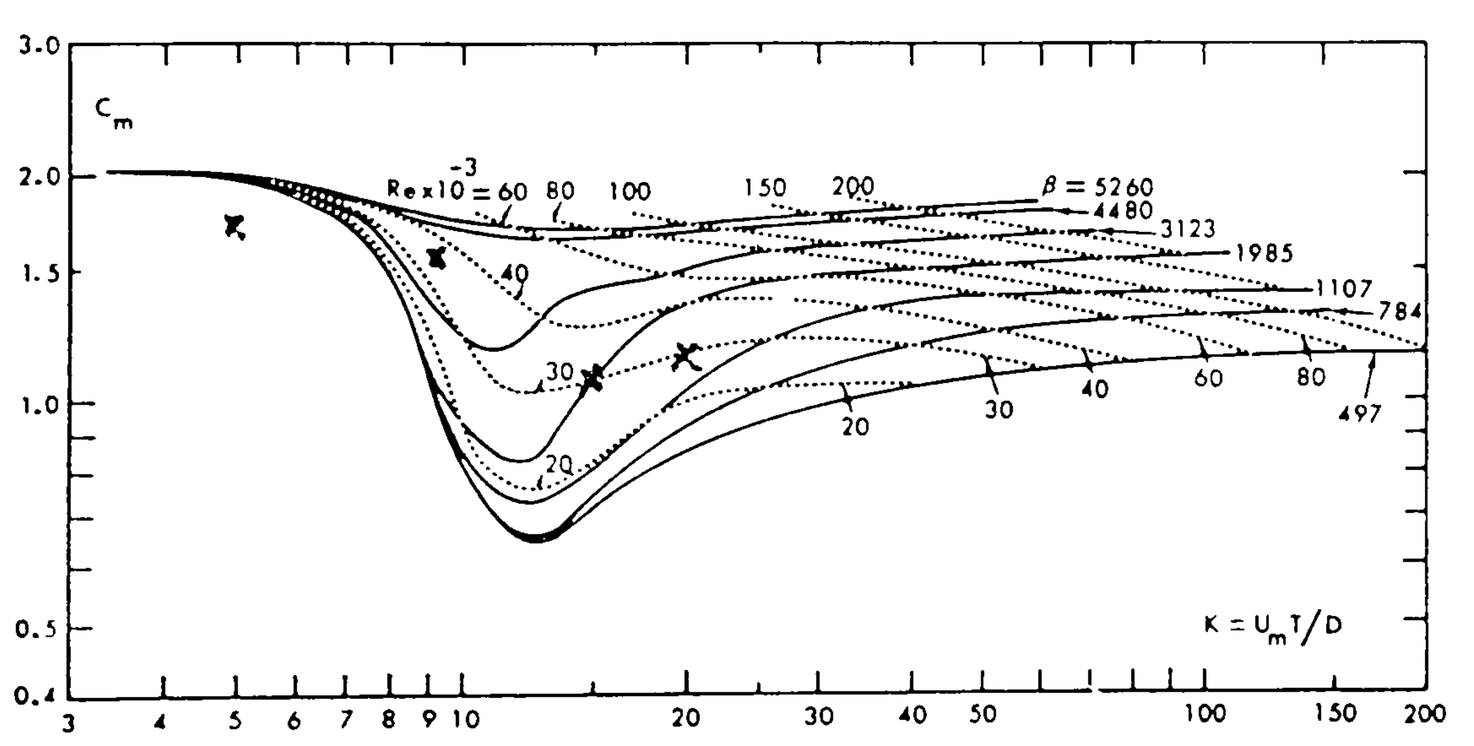

Figure 4.20.-Drag and Inertia coefficients at Re = 20000

4.12 Conclusion

In this chapter the basic discrete vortex model used for the study has been presented. The chief characteristics of the model itself and the numerical technique employed are their simplicity. Vortex model interactions are calculated using the

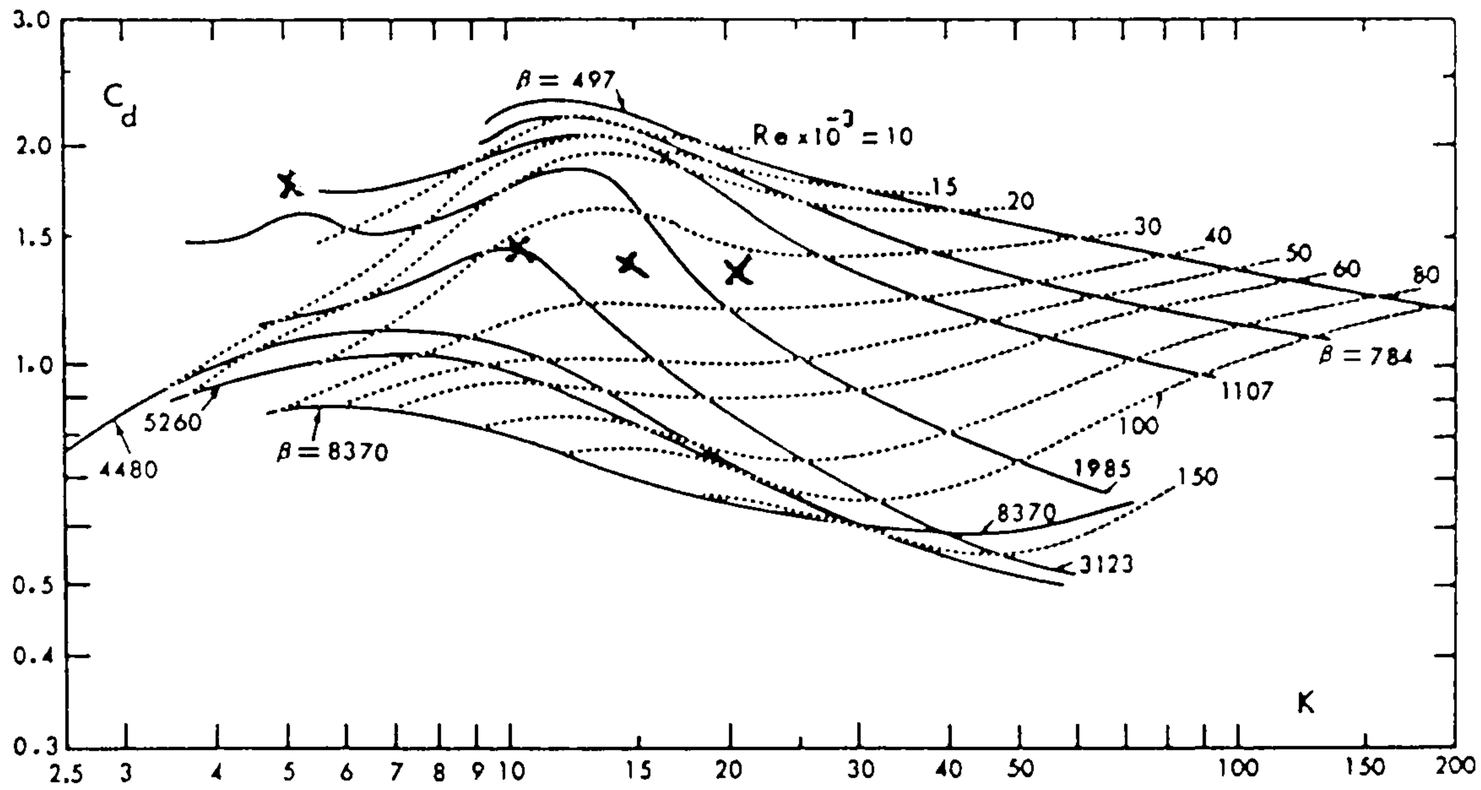

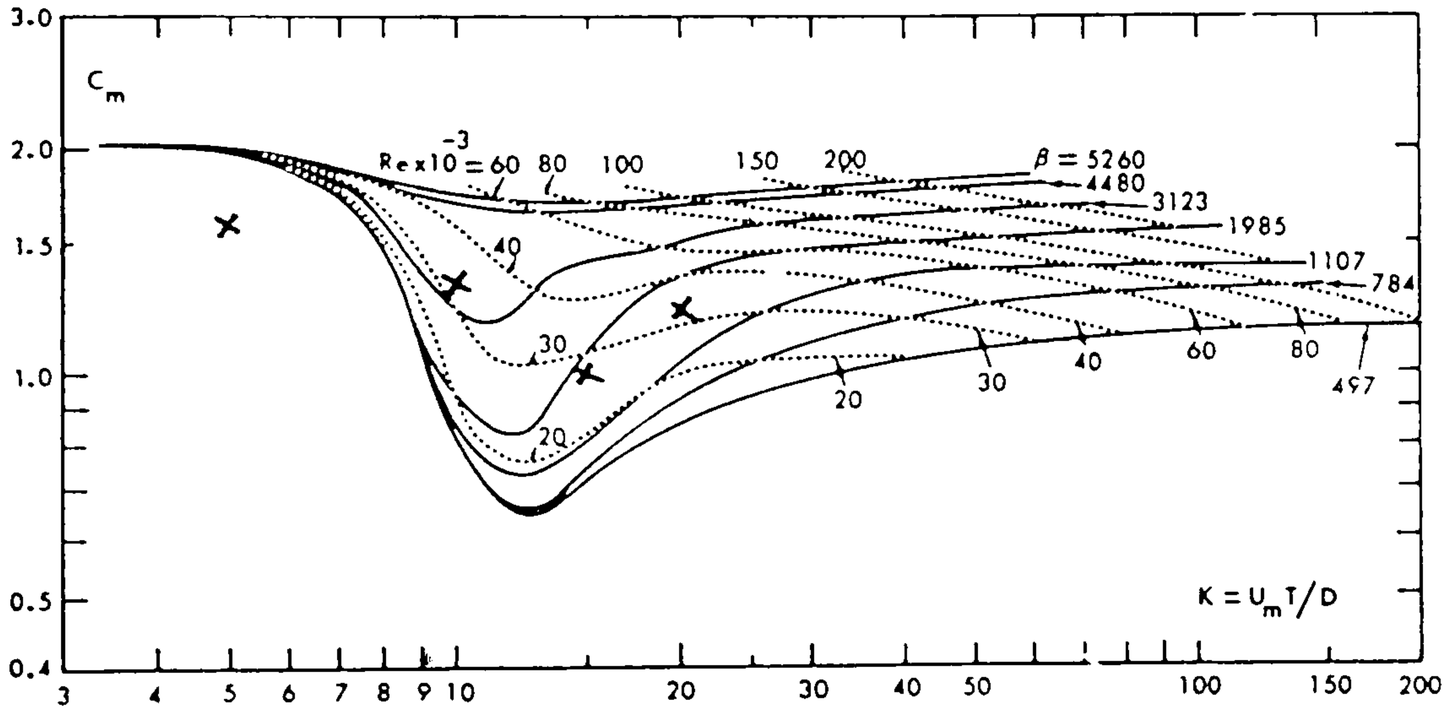

Figure 4.21.-Drag and Inertia coefficients at Re = 40000

Biot – Savart law and viscous diffusion is modelled using the *Random Walk*. The model is potentially more computationally expensive than more sophisticated approaches, but this is offset by the use of course grids and large time-steps.

Notwithstanding, the model shows good behaviour compared to experimental

results for the case of a steady uniform flow around a cylinder in an infinite fluid for Reynold numbers varying from *100* up to *drag crisis*. However, the resolution of the flow pattern is not as good as a finite difference model at low Reynolds numbers below *500*. The Random Walk model does not model viscous effects well for Reynolds number less than *500*. Notwithstanding, lift and drag coefficients compare favourably with experimental values for that range of Reynolds number considered.

In sinusoidal oscillatory flow, good results are only achieved in a certain range of β value as the boundary layer thickness is model as being proportional to its inverse. Best results are obtained when the 'layer' is larger than about *0.5* of the local element length or less than about twice the element length, or β value is over the range of *1000* to *4000*, measured from the cylinder surface. Within those constraints, the discrepancy between the predicted results and the experimental values of the force coefficients are around $10 - 15\%$. This difference is mainly due to the phase different between the predicted results and the experimental values. The magnitude of the in-line force is generally well predicted.

Better results could be achieved by refining the model further. However, it is capable of predicting the gross characteristics of the steady and unsteady flows considered. It is also easier to extend the model to more sophisticated applications, such as multi-bodies and bounded flows, than more refined models, particularly within the constraints imposed by modest computing resources. For these reasons, the present model has been adopted as the basis for the remainder of the study which invloves the computation of flows about two cylinders and cylinder in bounded flows.

Chapter V

THE FLOW AROUND TWO CYLINDERS IN AN INFINITE FLUID

5.1 General Description

During the last decade, various authors have attempted to model the flow around multiple cylinders. **Stansby et.al.** [**102**] provided a numerical model using a vortex in cell and random walk technique to simulate the convection and diffusion process of the flow around two cylinders. The calculation was done by solving the Poisson's equation which relates vorticity ω to the stream function ψ through

$$\nabla^2\psi = -\omega$$

Three types of overlapping meshes were adopted so that a very fine mesh was used to give definition in the boundary layers, an intermediate mesh size was used for computing vortex roll up in the near wake region and a coarse mesh was used to transport vortex structures downstream. Each cylinder had its own polar mesh. The Poisson's equations for rectangular and polar meshes were solved in finite difference form using the central difference approximation. Orthogonal velocities at mesh points were found from the stream function value at grid nodes as described in chapter *IV* and the velocity at a point inside a cell was obtained by bilinear interpolation.

A Similar approach was taken by **Hansen et.al.** [**43**] who used a curvilinear grid which was generated from a solution of the Laplace equation for uniform flow around the cylinders.

In another paper, **Stansby** [**98**] also proposed a discrete vortex method incorporated with an image doublet to satisfy boundary condition due to the presence of other bodies.

The problem of modelling the flow characteristics of a single cylinder in a uniform or oscillatory flow has been described in the previous chapter. It is shown that the Discrete Vortex model based on the Martensen equation could give a reasonably good prediction for a single cylinder compared with the other methods

i.e. **Downie**[**26**] , **Sarpkaya**[**79**][**80**][**81**], **Stansby**[**97**][**98**], and **Murray**[**70**]. As implied in section (**4.2**) due to the characteristic nature of the Martensen equation (**4.14**), it is possible that this model may be further extended for the case of flows around multi cylinders.

Similar to the case of the single cylinder problem, some attempts to model the flow around two cylinders were also based on modelling unseparated flow by using potential flow theory. As shown in **Dalton** and **Helfinstine**[**24**] and **Yamamoto**[**112**], this flow regime could be modelled by putting an infinite distribution of image doublets of converging strength.

Efthymiou and **Narayanan**[**32**] also used this principle to model the current induced forces on submarine pipelines as will be described in the next chapter. The strength and position of the doublets may be obtained through the use of the circle theorem, **Sarpkaya**[**78**][**82**].

In this approach the complex potential can be constructed to be a function of the free stream velocity and the strength, position and number of doublets inside the cylinders. **Stansby**[**97**][**98**] also used this approach to study the flow around two cylinders by incorporating the discrete vortex method. In his study, cylinder centres were always greater than three radii apart and generating four images from each isolated cylinder doublet ensured that velocities normal to the cylinder surface were everywhere less than $10^{-6}u_{\infty}$. After shedding vortices, the boundary condition of zero normal velocity was maintained by adding two image vortices in each cylinder for every vortex. The image pairs, explained in more detail in **Stansby**[**97**], were of opposite sign and of the same strength. With this configuration, one cylinder boundary condition was satified exactly. It was ensured that the normal velocity around the other was less than $10^{-4}u_{\infty}$ if a vortex of strength $10a\ u_{\infty}$ was moved within $0.1a$ of the cylinder surface (a is the cylinder radius).

In the present study, the method decribed in Chapter *IV* has been adopted with some modifications. The vorticity transport equation (**3.9**) is satisfied separately through the convection and diffusion parts as shown in equations (**4.1**) and (**4.2**) and its solution is carried out in a similar manner to the one described previously.

As there is more than one cylinder in the flow domain, the complex potential $w(z)$ of equation (**4.4**) has to be modified as follows.

$$w(z) = u_\infty e^{-i\alpha_\infty} z + \frac{i}{2\pi} \sum_{b=1}^{N_b} \sum_{e=1}^{N_e^b} \gamma_e^b dS_e^b \ln(z - z_e^b) + \frac{i}{2\pi} \sum_{b=1}^{N_b} \sum_{\nu=1}^{N_\nu^b} \Gamma_\nu^b \ln(z - z_\nu^b) \quad \textbf{(5.1)}$$

where N_b is the number of cylinder, γ_e^b is strength of vortices at element ϵ of body b, dS_e^b is the length of element e of body b, z_e^b is the position of element ϵ of body b, Γ_ν^b is the strength of a vortex ν shed by cylinder b, z_ν^b is the position of a vortex ν shed by cylinder b. The other variables are described as those in equation (**4.4**).

The polar grid system, as shown in figure (**4.3**) is still used for each individual cylinder to give good definition of the flow close to the cylinder surface. The grid nodes on the cylinder surface located at the centre of the surface elements provide the control points at which the Martensen equation (**4.14**) is solved to give zero tangential velocity and so satisfy the Dirichlet boundary condition. It is the nature of the Martensen equation that the approach can be easily extended to cater for a multi cylinder case by simply extending the components of the matrix influence equation (**4.16**) to involve the mutual influence of the other cylinders.

As described previously, an overlapping grid system is used to represent a distribution of a much higher number of discrete vortices than there were nodes. This proved to give a considerable reduction in terms of the CPU time especially during the calculation of the vortex velocity. A further reduction in the CPU time was also gained during calculation of the cylinder surface velocity using the Martensen equation as the individual polar grid nodes were used, instead of the point vortices, in the RHS of equation (**5.5**) to be presented later. It has been shown that this method is not only time efficient, but also gives a better distribution of surface vorticity as the scattered vortices around the body are now concentrated on grid points located a uniform distance from the body. The reason for this is that the vortices closest to the body are the most influential during the calculation of the surface vorticity strengths.

The introduction of vortices with circulations satisfying the boundary condition of zero tangential velocity is carried out in the same manner as before by releasing a ring of vortices on the second ring from the cylinder surface. **Lewis[60]** released the vortices directly by implementing the random walk principle

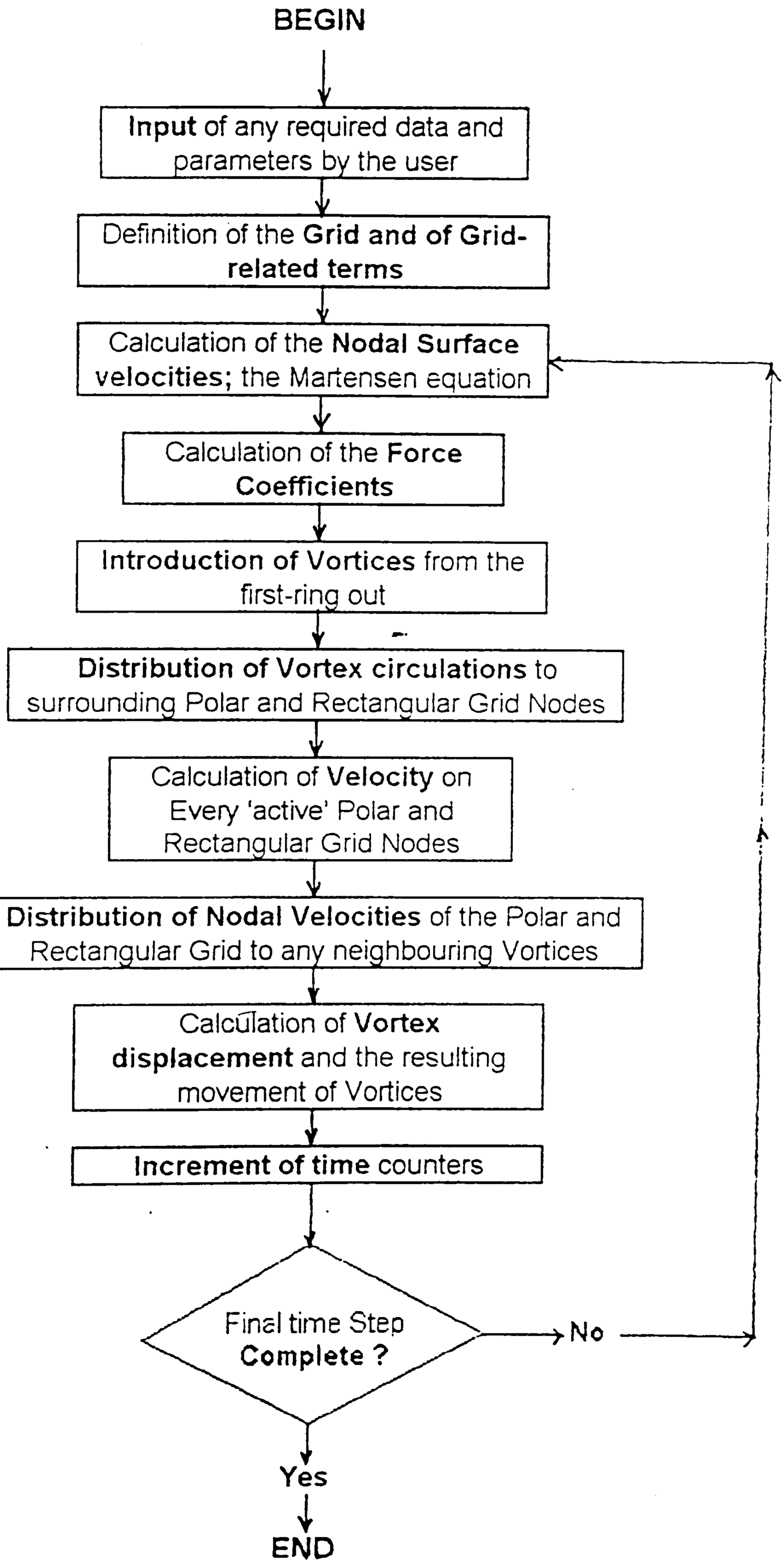

Figure 5.1.- *Flow Chart for the Discrete Vortex Algorithm*

while **Porthouse[73]** introduce vortices a certain distance from the body surface specified as a function of the Reynolds number and the time step.

In the present study the identification of vortices shed from any given cylinder is maintained over the whole process. The implementation of the Biot-Savart velocity calculation over the polar grid nodes is done only among those vortices shed from the same body. The contribution of the vortices shed from the other bodies is carried out through the overlapping rectangular grid nodes. This requires that each vortex has an individual polar based node and a global rectangular based node with which its relative position is identified at every time step with regard to both systems. This means that the area of proportions and the vortex strength distribution have to be calculated in either its own polar or rectangular grid system at every time step using a method similar to that described in the previous chapter.

The structure of the Discrete vortex algorithm as displayed in figure (**5.1**) therefore differs only slightly from that described in Chapter *IV*, especially with regard to the calculation of the vortex velocity and the distribution of the vortex circulation to surrounding polar and rectangular grid nodes.

5.2 Surface Velocity Calculation

The solution procedure in the multi-cylinder problem is exactly the same as that for the single cylinder problem except that now the induced velocity at an element S_n must include the influence of all cylinders in the fluid domain. Mathematically, this can be expressed in the following Martensen equation (**4.6**).

$$-\frac{1}{2}\gamma_m + \oint_{c_{N_b}} k_{mn}\gamma_n dS_n + \vec{u}_\infty \cdot \vec{d}S_m + \sum_{b=1}^{N_b}\sum_{\nu=1}^{N_\nu} l_{m\nu}\Gamma_\nu^b = 0 \qquad (\mathbf{5.2})$$

where : N_b is the number of the cylinder, Γ_ν^b is the strength of a vortex ν shed from cylinder b, while the other variables are the same as equation (**4.6**) above. In this equation, the second term has to be integrated around each cylinder in the domain. As described in *Appendix A*, the complex integration along a contour at infinity and along those two cylinders will reduce to that part of the contour enclosing the two cylinders only, as the limit of the value of the coupling coefficients k_{mn} will tend to zero as the distance from the cylinders approaches infinity. The integration along two parallel lines joining the contour at infinity and the cylinders

will be equal to zero as the contribution made by the first will cancel with that of the second.

Following the procedure described in chapter *IV*, sec (**4.14**), equation (**4.2**) can now be written in a discrete form as,

$$-\frac{\gamma_m^p}{2}+\sum_{q=1}^{N_b}\sum_{n=1}^{N_e^q}\frac{\Delta S_n^q}{2\pi}\Re\left(\frac{i\gamma_n^q e^{i\beta_m^p}}{z_m^p-z_n^q}\right)+\Re\left(u_\infty e^{-i(\alpha_\infty-\beta_m^p)}\right)+$$

$$\sum_{q=1}^{N_b}\sum_{\nu=1}^{N_\nu}\frac{\Gamma_\nu^q}{2\pi}\Re\left(\frac{ie^{i\beta_m^p}}{z_m^p-z_\nu^q}\right)=0 \qquad (\mathbf{5.3})$$

Equation (**5.3**) above satisfies the Dirichlet boundary condition at element m of cylinder p. The left hand side includes the contributions from all elements $(n=1,2,\cdots N_e)$ on each cylinder $(q=1,2,\cdots N_b)$. The number of elements N_e can be chosen independently for each cylinder according to the individual geometrical requirements. It can be seen from the last term of equation (**5.3**) that the vortices shed from one cylinder may be conveniently stored in an array separately from those shed from the other.

By absorbing the first term into the second term of coupling coefficient k_{mn}^{pq}, as shown by **Wilkinson[109]** in equation (**4.15**), the flow past N_b bodies may be represented by the following equation,

$$\sum_{q=1}^{N_b}\sum_{n=1}^{N_e^q}K_{mn}^{pq}+\Re\left(u_\infty e^{-i(\alpha_\infty-\beta_m^p)}\right)+\sum_{q=1}^{N_b}\sum_{\nu=1}^{N_\nu}\frac{\Gamma_\nu^q}{2\pi}\Re\left(\frac{ie^{i\beta_m^p}}{z_m^p-z_\nu^q}\right)=0 \qquad (\mathbf{5.4})$$

In matrix form the two cylinder problem can be written as,

$$\begin{pmatrix} k_{mn}^{11} & k_{mn}^{12} \\ \\ k_{mn}^{21} & k_{mn}^{22} \end{pmatrix}=\begin{pmatrix} RHS^1 \\ \\ RHS^2 \end{pmatrix} \qquad (\mathbf{5.5})$$

where k_{mn}^{11} means the coupling coefficient of cylinder *1* at element m due to a vortex at element n, k_{mn}^{12} means the coupling cefficient at element m of cylinder *1* due to a vortex at element n of cylinder *2*, k_{mn}^{21} means the coupling cefficient

at element m of cylinder *2* due to a vortex at element n of cylinder *1*, and the k_{mn}^{22} means the coupling cefficient of cylinder *2* at element m due to a vortex at element n. The RHS means the right hand side of equation (**5.4**) for the first and second cylinder respectively.

5.3 Segmentation of the Domain

Equation (**5.4**) above illustrates that after shedding vortices, $(\sum_{q=1}^{N_b} N_v^q)^2 + (0)$ operations must be carried out when performing the velocity calculation for all vortices in the flow. In the conventional discrete vortex method, where a direct vortex to vortex calculation is used, this is increasingly computationally expensive as the number of vortices N_v and of cylinders N_b increases.

By segmenting the domain into grids, the number of operation is reduced to $(\sum_{q=1}^{N_b} N_{j,k}^q + 1)^2$ where $N_{j,k}$ is the number of active grids. This increase in efficiency is due to the fact that grid node to grid node interaction, which obviously involves considerably less calculation, is now used instead of direct vortex to vortex interaction.

A similar saving in the CPU time can also be obtained during the surface vorticity calculation in which for the vortex to vortex method, the influence of each vortex on a point element of the cylinder surface involves $N_v + 1$ calculations. This will result in $\sum_{q=1}^{N_b} \sum_{e=1}^{N_e^q} N_v^q + 1$ calculations for all of the surface elements. Using grid nodes instead results in a calculation which takes less CPU time.

In this section, a simple overlapping grid system based on the methods described in the previous section is introduced to represent the fluid domain in the case of multi-cylinder problems. Each cylinder has its own polar grid system and forms a local domain. The centre of one of the cylinders is chosen as the global reference of the domain in which the coordinate of the rectangular grid nodes are measured and stored.

The positions of the grid points $z_{j,k}$ belonging to cylinder q relative to the centre of cylinder p, can then be described as

$$z_{j,k}^q = r_j^q e^{i\theta_k^q} + d_{pq} \tag{5.6}$$

where the RHS shows the complex position of a grid node at local domain q with reference to the local domain p. r_j^q is the grid radius j at each local domain q. d_{pq} is the complex distance of cylinder centres q (q = 1- N_b) to the reference cylinder

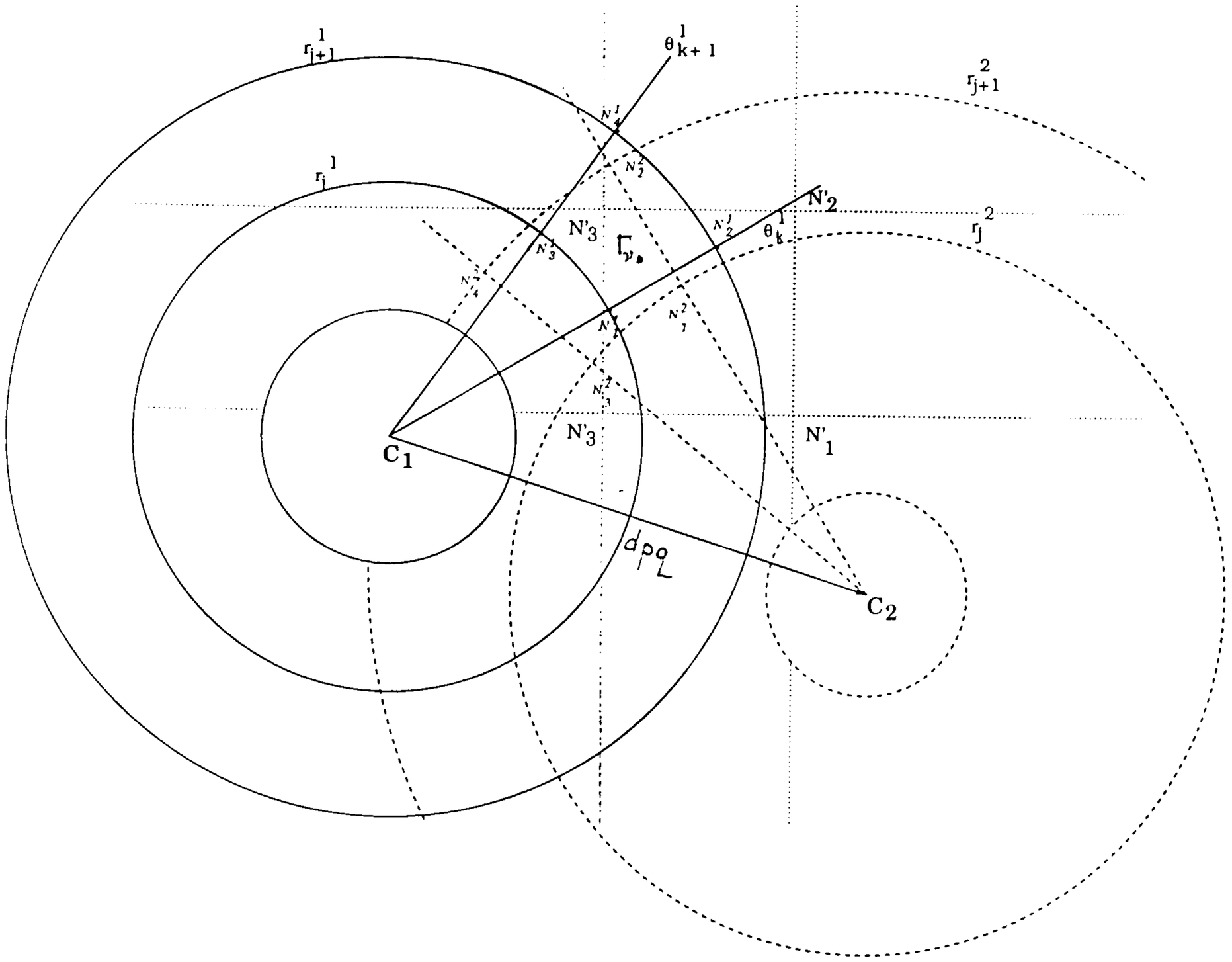

Figure 5.2.- *The Overlaping Grid System*

p (p = 1 - N_b). j (j = 1, 2,...) shows the radial number of ring and k (k = 1 - N_ϵ) shows the angular number of grid segments.

As previously mentioned, the size of grid segment in the polar grid system is expanding linearly from the surface of the cylinder as described by equation (**4.21**). In the two cylinder problem, there will be two overlapping polar grid systems expanding linearly from each cylinder surface. The polar grid is composed of square elements as shown in figure (**4.3**) above. In this figure, the node N_1 will be the base node for any vortex falling into the associated segment that has been shed from the cylinder belonging to this polar grid.

A rectangular grid system which overlaps the two polar grid systems is also incorporated in to the system. This rectangular grid has a uniform square element

throghout the whole domain. The structure of the grid system in the two cylinder problem is displayed in figure (**5.2**) below. Any vortex that falls into a position where two grid elements of the polar and rectangular system overlap each other. is located with reference to two base nodes for its relative position. These base nodes belong to the polar segment, as explained above, and the rectangular segment as shown in the figure (**5.2**) below.

The node points of the rectangular coordinate system are measured from the centre of the referenced cylinder. The coordinates of each node were defined starting from the top-left corner to right-bottom corner to form a rectangular domain. The size of the rectangular grid is constrained in such a way that all vortices are kept inside it during the whole calculation period. This can be achieved by estimating the possible maximum horizontal and vertical distance travelled by a vortex during the calculation. The distance is approximately equal to $u_\infty \times t$, where u_∞ is the free stream speed and t is the total time used, plus $k \times diameter$, in which the value of k is found from experiments.

5.4 Distribution Of Circulation To The Grid

In the case of multi-cylinder problems, a vortex of strength Γ_ν is not only distributed onto its four surrounding nodes in the polar grid, using the common bi-linear interpolation, but also onto nodes of the overlapping rectangular grid system. This means that each vortex has two base nodes i.e. the polar grid where it is shed from and the rectangular grid.

As shown in figure (**5.3**) above, the distribution of a vortex circulation onto the four polar grid nodes is carried out in exactly the same way as decribed in section (**4.5**). Its distribution onto the rectangular grid, is carried out in a similar manner but using much simpler expressions for the area of the rectangular segment.

As illustrated in figure (**5.2**), any vortex with strength Γ_v at a rectangular grid element $z(j', k')$ with size ds' can be distributed into the four rectangular grid nodes using the following bi-linear interpolation

$$\Gamma_{j',k'} = \sum_{\nu} Q_\mu(\nu)\, \Gamma_\nu \qquad \mu = 1 - 4$$

where,

$$Q_\mu(\nu) = \frac{A'_\mu}{A'} \tag{5.7}$$

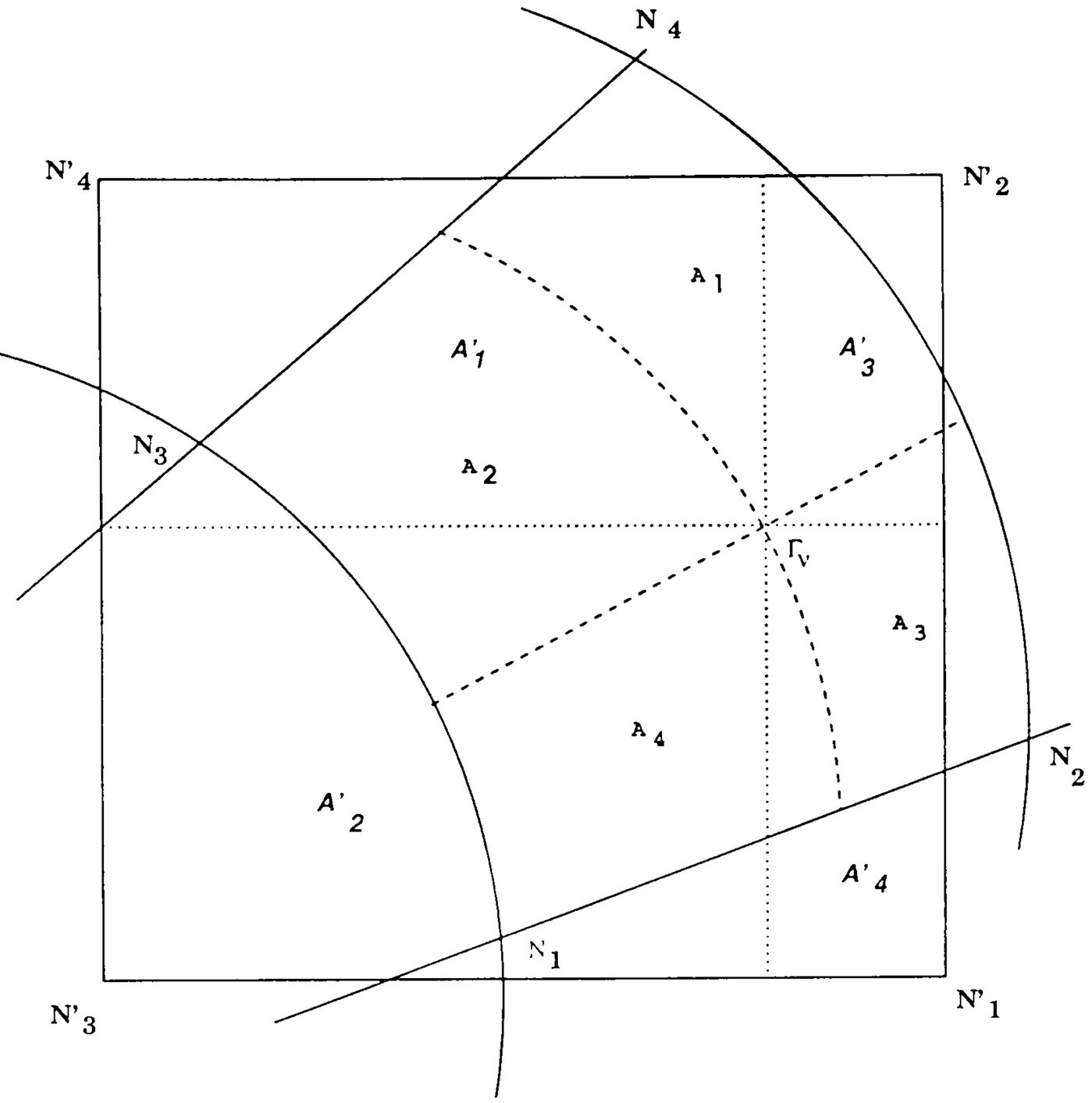

Figure 5.3.- *An Overlapping Grid Element*

where, A'_{μ} is the area of the rectangle diagonally opposite to cell corner μ and $A' = ds'^2$ is the grid element area.

As briefly mentioned above, the rectangular grid is used in the calculation of a vortex velocity due to the contribution from all other vortices shed from cylinders other than the one from which it originated. This implies that in the same segment, only vortices shed from the originating cylinder will have their strengths are summed on the surrounding grid nodes stored in the same array. Contribution from vortices shed from other cylinders will be summed in different arrays. This can also mean that the same rectangular grid nodes could be active with reference to one cylinder but be inactive with reference to the other cylinders.

Implementation of the distribution procedures over the polar rectangular grid systems as shown in equation (**5.7**) lead to

$$\Gamma_{j,k} = \sum_{\nu} P_{\mu}(\nu)\, \Gamma_{\nu}$$

$$\Gamma_{j',k'} = \sum_{\nu} Q_{\mu}(\nu)\, \Gamma_{\nu} \tag{5.8}$$

in which $P_{\mu}(\nu)$ and $Q_{\mu}(\nu)$ are as described in equation (**4.26**) and (**5.7**) respectively, with $\mu = 1$ - 4.

5.5 Calculation Of Velocities

For the multicylinder case, since each cylinder has its own polar grid which overlap with each other and the rectangular grid, the calculation of the velocities of a vortex shed from one cylinder due to the other vortices shed from the same cylinder is carried out with reference to their own individual polar grid. In addition there is a contribution from those shed from the other cylinder and this is computed with reference to the rectangular grid system. With reference to the figure (**5.2**), the velocity of a vortex z_{ν} shed from a cylinder p is then calculated using the following steps:

1. Calculate the velocity $u_{pp}(N_{\nu})$ at the nodes surrounding a vortex z_{ν}, shed by the cylinder p and located at a polar grid segment with base node N_1, due to the other active nodes of the polar grid system of the same cylinder p.

$$u_{pp}(N_{\mu}) = u_{\infty} e^{i\alpha_{\infty}} - \frac{i}{2\pi} \sum_{b=1}^{N_b} \sum_{z^p_{j,k} \neq z^p(N_{\mu})} \frac{\Gamma^{(p)}_{j,k}}{z^p(N_{\mu}) - z^p_{j,k}} \tag{5.9}$$

   where $\mu = 1$ - 4.

2. Using the rectangular grid system, calculate the velocity $u_{pq}(N'_{\mu})$, at the nodes surrounding a vortex at z_{ν} with base nodeN'_1, due to the other active nodes of the other cylinder q.

$$u_{pq}(N_{\mu}) = -\frac{i}{2\pi} \sum_{b=1}^{N_b} \sum_{z^q_{j',k'} \neq z^p(N'_{\mu})} \frac{\Gamma^{(q)}_{j',k'}}{z^p(N'_{\mu}) - z^q_{j',k'}} \tag{5.10}$$

   where $p \neq q$

3. Use both bi-linear interpolations to find the vortex velocity due to both polar and rectangular active grid nodes making use of the area of proportion $P_{\mu}(\nu)$ and $Q_{\mu}(\nu)$ as shown in equation (**4.26**) and (**5.7**) above.

$$u_{pp}(z_{\nu}) = P_1(\nu)u_{pp}(N_1) + P_2(\nu)u_{pp}(N_2) + P_3(\nu)u_{pp}(N_3) + P_4(\nu)u_{pp}(N_4)$$

$$u_{pq}(z_\nu) = Q_1(\nu)u_{pq}(N_1') + Q_2(\nu)u_{pq}(N_2') + Q_3(\nu)u_{pq}(N_3') + Q_4(\nu)u_{pq}(N_4') \tag{5.11}$$

4. Calculate the total velocity.

$$u(z_\nu) = u_{pp}(z_\nu) + u_{pq}(z_\nu) \tag{5.12}$$

As implied in the above procedures, there is no direct interaction between the nodes of the polar grids associated with each cylinder. Instead, the cylinder to cylinder node interactions are computed using the overlapping rectangular grid nodes. This strategy is chosen in an attempt to achieve a more uniform distribution of vorticity in the area in which the wakes of the cylinders interact.

5.6 Time Integration

As before a first order accurate Euler scheme is used in to find the new locations of the vortices, that is,

$$z_\nu^{(t+\Delta t)} = z_{\nu(t)} + \delta z_\nu^{rw} + \delta t u_\nu^{(t)}(z_\nu) \tag{5.13}$$

where δt is the size of the time step used . The second term of the RHS part is the displacement due to the random walk diffusion process.

As mentioned in the previous chapter, the random walk method is used in this study to simulate the diffusion process which becomes more important at a relatively low Reynolds number. Since the diffusion of the fluid is independent of the method of generating vorticity, the procedure adopted in section (**4.7**) is still valid to be implemented in multi-cylinder case. Each vortex shed by each body is given a Gaussian -type random motion as expressed in equation (**4.34**) and (**4.35**) above.

Since an overlapped grid system is used in the scheme, the new position of each vortex is then referenced to both polar and rectangular grid systems. In other words, each vortex has two base nodes from which its relative position at every time step is measured and renewed.

5.7 Force and pressure calculation.

The basic procedure previously used for calculating forces. based on the integration of the elemental pressure around a cylinder, can be extended to the case of the flow around two cylinders. At the beginning and at the end of each cycle of calculation, the surface vorticity over each cylinder has to be calculated using the Martensen equation (**5.3**) so as to satisfy the Dirichlet boundary condition. This necessary because the state of the flow around the cylinder changes at every time step as a result of the convection and diffusion process in the flow development.

The surface vorticity distribution can then be used to get to determine the pressure distribution around each cylinder through the use of equation (**4.40**) above, bearing in mind that the strength of the surface vorticity is equal to the tangential velocity at the cylinder surface. As described previously in section (**4.39**), a smoothing process using a spline method is incorporated in the algorithm to obtain a smooth and continuously varying pressure distribution.

The pressure around the cylinder can then be integrated numerically to get the value of the force coefficients.

5.8 Method Of Enhancements

5.8.1 Correction for close proximity

Methods for finding the influence coefficient of the elements in close proximity were described in section (**4.10**). Similar techniques can be adopted when two or more cylinders are close together.

In these circumstances the influence coefficient can be written,

$$K_{in}^{pq} = -\frac{1}{\delta S_i^p} \sum_{m=1, m\neq i}^{M_p} K_{mn}^{pq} \delta S_m^p \qquad \textbf{(5.14)}$$

The i^{th} element of cylinder p is the one in close proximity to element n of cylinder q.

5.8.2 Correction for the Approaching Wake

It is a numerical difficulty that when one cylinder is placed downstream from the other, shedding from the downstream cylinder becomes unstable as vorticity

from the upstream cylinder approaches. This is due to the fact that any asymmetrical properties produced by the upstream cylinder will cause an asymmetrical reattachment and pressure distribution on the downstream cylinder. The excessive influence from the upstream cylinder will create an error that accumulates as the flow develops further and this will cause a continuous growing asymmetric instability of one sign of the scheme.

As explained in the previous section, the polar grid nodes are used in the RHS of equation (**5.4**) to represent the contribution of the shed vortices in the calculation of the surface vorticity distribution. To remove the excessive influence of the shed vortices, those that get closer than $0.05D$ to the cylinder surface are deleted from the process even though their base node might still lie outside the cylinder. The total loss of the circulation due to this process must be compensated for in the RHS of equation (**5.5**) during the calculation of the surface vorticity. The total loss of circulation shed by one cylinder is stored in one array while that shed from the other cylinder is stored in another array. With this approach, the Kelvin theorem of total zero vorticity in the whole fluid domain can be maintained throughout the calculation period.

Another occurence that is possible during the surface vorticity calculation is that an active polar grid node could lie inside a cylinder even though the vortex it represents lies outside it. The contribution of this active node in the surface vorticity calculation is simply ignored as the strength of the active nodes inside a cylinder will be summed up in the RHS of equation (**5.5**).This means that all polar grid nodes inside the cylinder are considered as inactive nodes at all times.

Other authors, such as **Stansby** [**100**] and **Murray** [**70**], just removed and ignored around 10% vortices that penetrate the cylinder at every time step. They argued that the total circulation removed from the flow is relatively small as the positive and negative deleted vortices are cancelled out.

In the case of two cylinders in tandem with $\frac{G}{D}$ greater than the critical distance, the above argument can not be maintained as the difference of the amount of opposite sign of the deleted vortices could be significant. In the present approach, even though balancing the total circulation for each cylinder system separately is not justified by the Kelvin theorem, which states that total circulation in the whole field is zero, it can maintain reasonably good results for the drag and the lift coefficients over a range of $\frac{G}{D}$

5.8.3 Vorticity Reduction Scheme

As described in chapter *IV* the solution of the diffusive part of equation (**4.2**) can be considered Gaussian in nature with standard deviation given by $\sqrt{4\nu t}$.

The velocity field of a single diffusing vortex can therefore be written as

$$u_r = \frac{\Gamma(0)}{2\pi r}\,(1 - e^{\frac{-r^2}{4\nu t}}) \qquad \textbf{(5.15)}$$

which can be interprested as the velocity field of a vortex whose strength decays with time because of the diffusion process. In real flow the changing distribution of vorticity in the wake is not only due to viscous diffusion but also due to turbulent dissipation, cancelation of vorticity and three-dimensional deformation in the flow. In order to model those effects in their discrete vortex analyses, **Naylor** [**71**] and **Basuki** [**6**] used an empirical reduction scheme for the individual vortex strengths similar to the above equation and given by

$$\Gamma(t) = \Gamma(0)\; e^{-kt} \qquad \textbf{(5.16)}$$

with k is chosen around *22*.

Another authors such as **Hansen et.al.**[**43**] implemented a simpler model in which he reduced the strength of each individual vortex by a factor C at each calculation time and in which the constant was empirically determined.

In the present study, for the case of two cylinders in proximity, a vortex strength reduction method was incorporated in the algorithm, in addition to the *RandomWalk* scheme, to make allowance for the other real phenomena mentioned above. This approach was adopted because the random displacement given to each discrete vortex, for this special case, creates an accumulative asymmetry between the wake produced by both cylinders in the early development of the flow which results in an unrealistic flow pattern and force coefficients as time progresses.

The method used is similar to those of **Hansen et.al.**[**44**] and **Naylor** [**71**] and the reduction is accomplished through,

$$\Gamma^n(t) = C_\Gamma{}^n \Gamma(0) \qquad \textbf{(5.17)}$$

where C_Γ is a constant less than *1* and n is the number of iterations. With the time step $\Delta t = 0.15$, the effect of variation of C_Γ on the vortex strength $\Gamma(t)$ is displayed in figure (**5.4**).

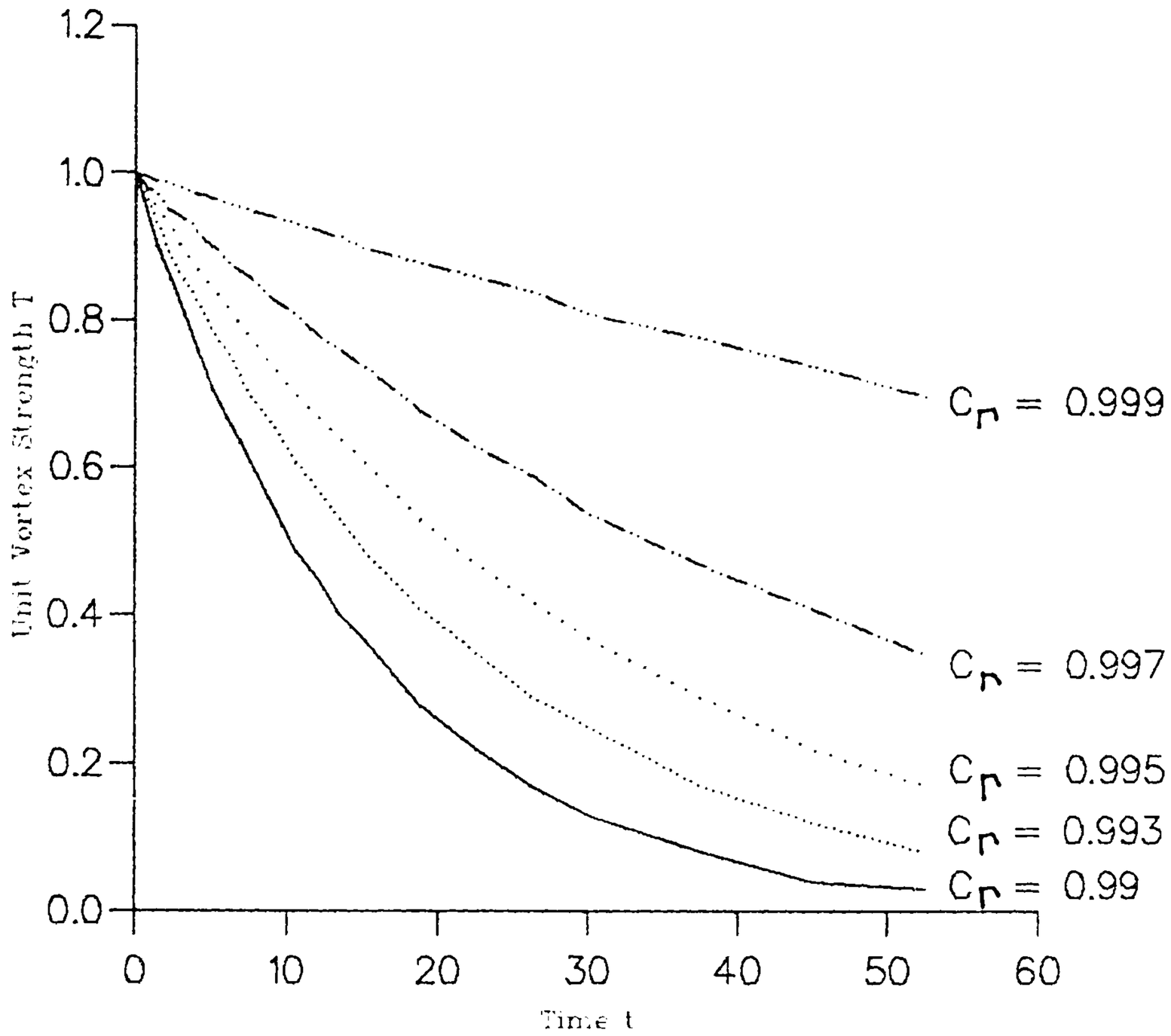

Figure 5.4.- $\Gamma(\hat{t})$ Vs. $\hat{t}$

As will be seen later, the implementation of the vortex reduction scheme produces some improvements in maintaining the symmetrical properties of the wake shed from both cylinders. Numerically, this is achieved because of the significant reduction in the interaction of the two vortex streets shed by both cylinders when they are close together.

5.8.4 Other Corrections

All the other corrections mentioned in section (**4.10**), such as: the RHS correction, the correction for the curvature of the elements, and the Asymmetric enforcement when the arrangement of the cylinders produces a symmetrical flow pattern such as for two cylinders in tandem, are also implemented in the present case study.

5.9 Results And Discussions

5.9.1 Two Cylinders in Side-by-Side Arrangements

The results produced by the algorithm described above and implemented, for the side-by-side case, will now be presented in this section. Using *64* surface elements for each cylinder, the time step of $\Delta t = 0.15$, the size of the rectangular grid of $\frac{dS_r}{D} = 0.2$ and with gap ratio (the ratio of the gap G to diameter of the cylinder D) $\frac{G}{D} = 2.0$, the present model was first tested for convective flow only, with no diffusion process included. The resulting flow and the force coefficients may be expected to resemble those at very high Reynolds numbers. The object of running the scheme for this condition was to seek to achieve the symmetrical properties of the flow as have been observed in experiments. At a non dimensional time $\hat{t} = \frac{u_\infty t}{2a}$ equal *1* and *5* the scheme produced flow patterns as shown in figures (5.5) below.

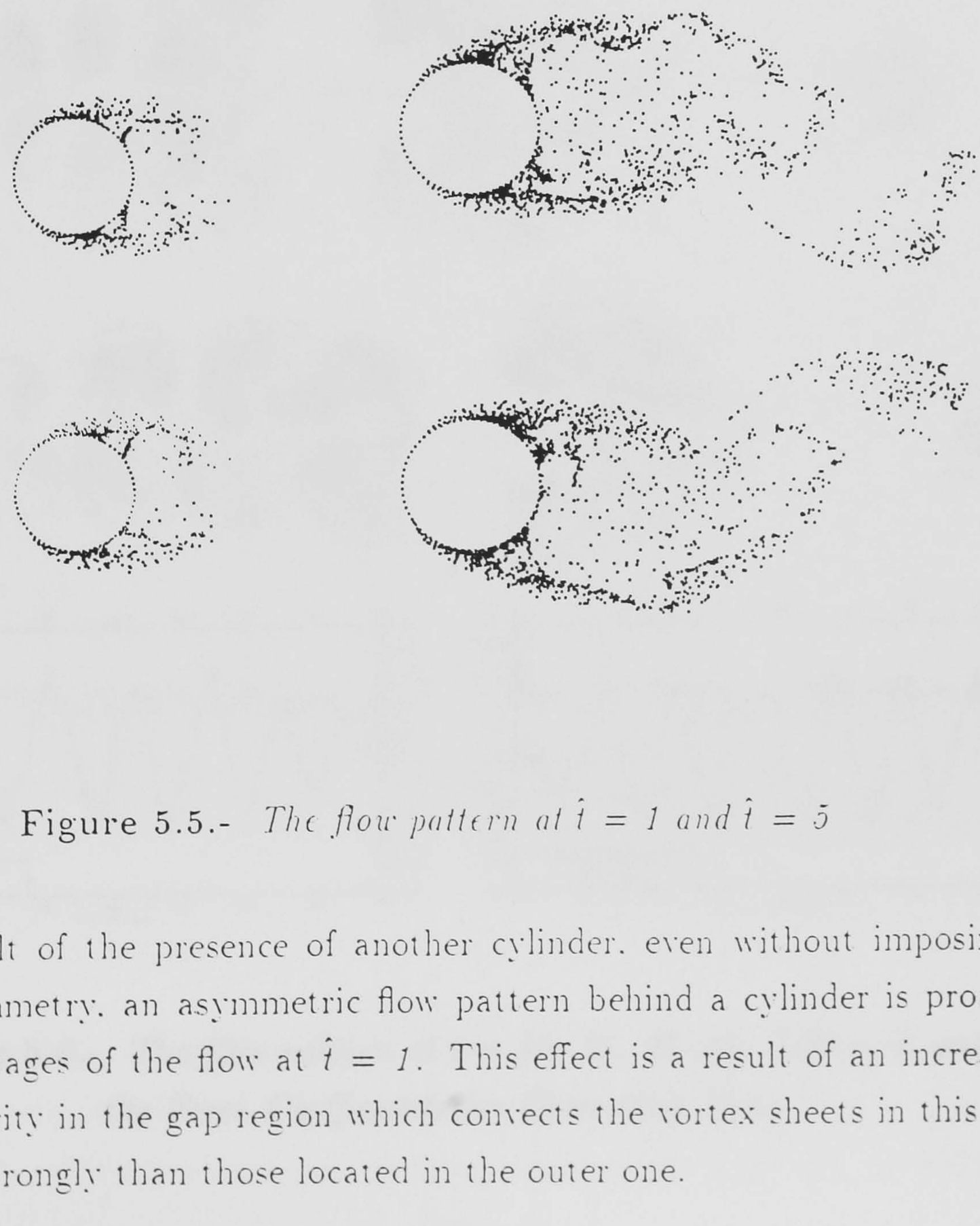

Figure 5.5.- *The flow pattern at $\hat{t} = 1$ and $\hat{t} = 5$*

As a result of the presence of another cylinder, even without imposing an enforced asymmetry, an asymmetric flow pattern behind a cylinder is produced in the early stages of the flow at $\hat{t} = 1$. This effect is a result of an increase in the local velocity in the gap region which convects the vortex sheets in this inner region more strongly than those located in the outer one.

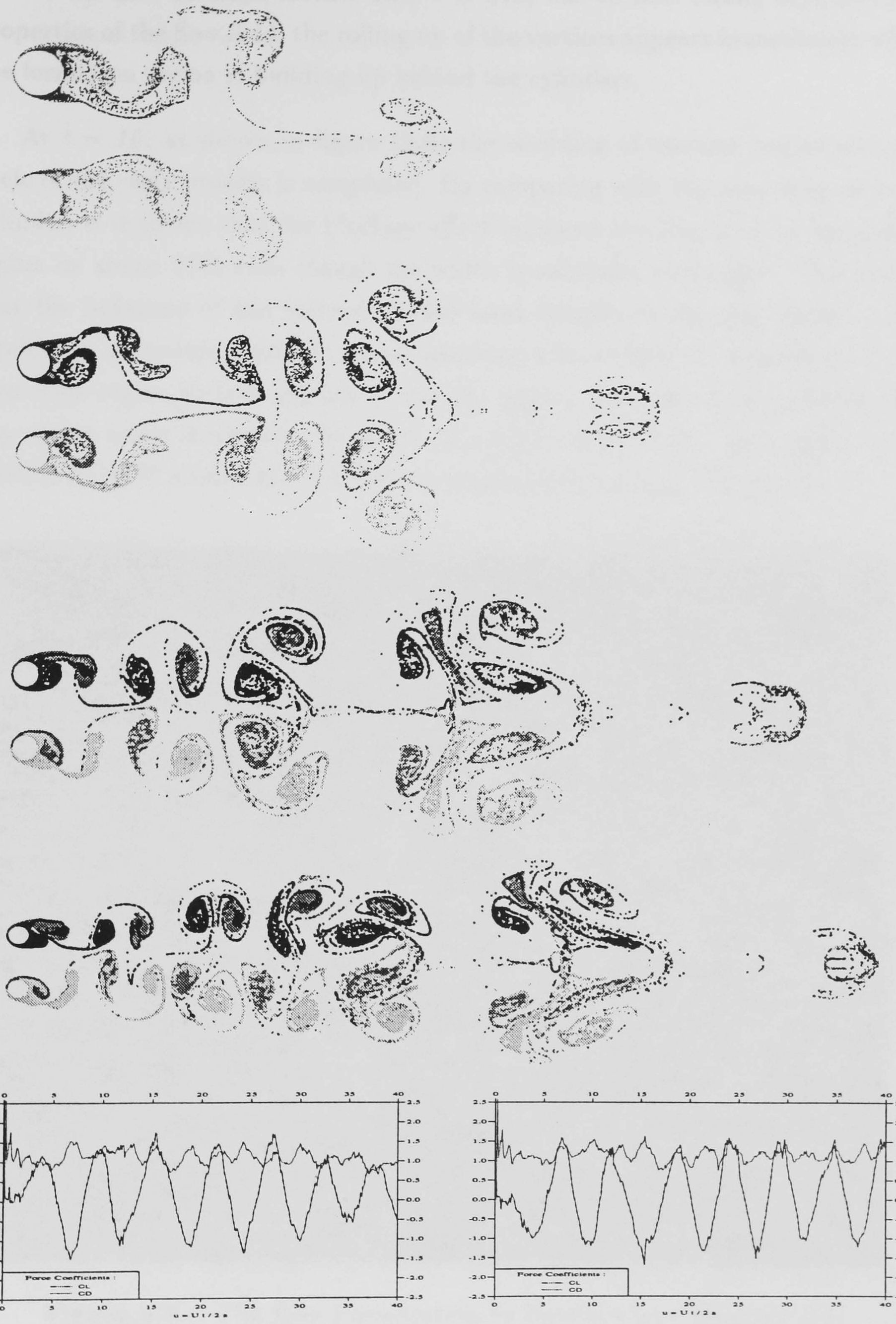

Figure 5.6.- *The flow pattern at t = 10, 20, 30, 40; G/D = 2, and the Force Coefficients for Convective Flow*

As the flow develops further until $\hat{t} = 5.0$, due to that strong asymmetrical properties of the flow field, the rolling up of the vortices appears immediately while the formation region is building up behind the cylinders.

At $\hat{t} = 10$, as shown in figure (**5.6**) the shedding of vortices begins and one cycle of the early process is completed. By comparing with the case of an isolated cylinder, it is shown that the blockage effect increases the length of the formation region by about *10*% even though the width is relatively unchanged. This means that the influence of the increase in the local velocity in the gap region is still significant up to this point. It is also seen that a lower level of irregularity of the formation region surface appears in the gap region. The separation points in the gap region move downwards to about *95*°, while those in the outer region move forward to *115*° measured from the rear stagnation points of the cylinders.

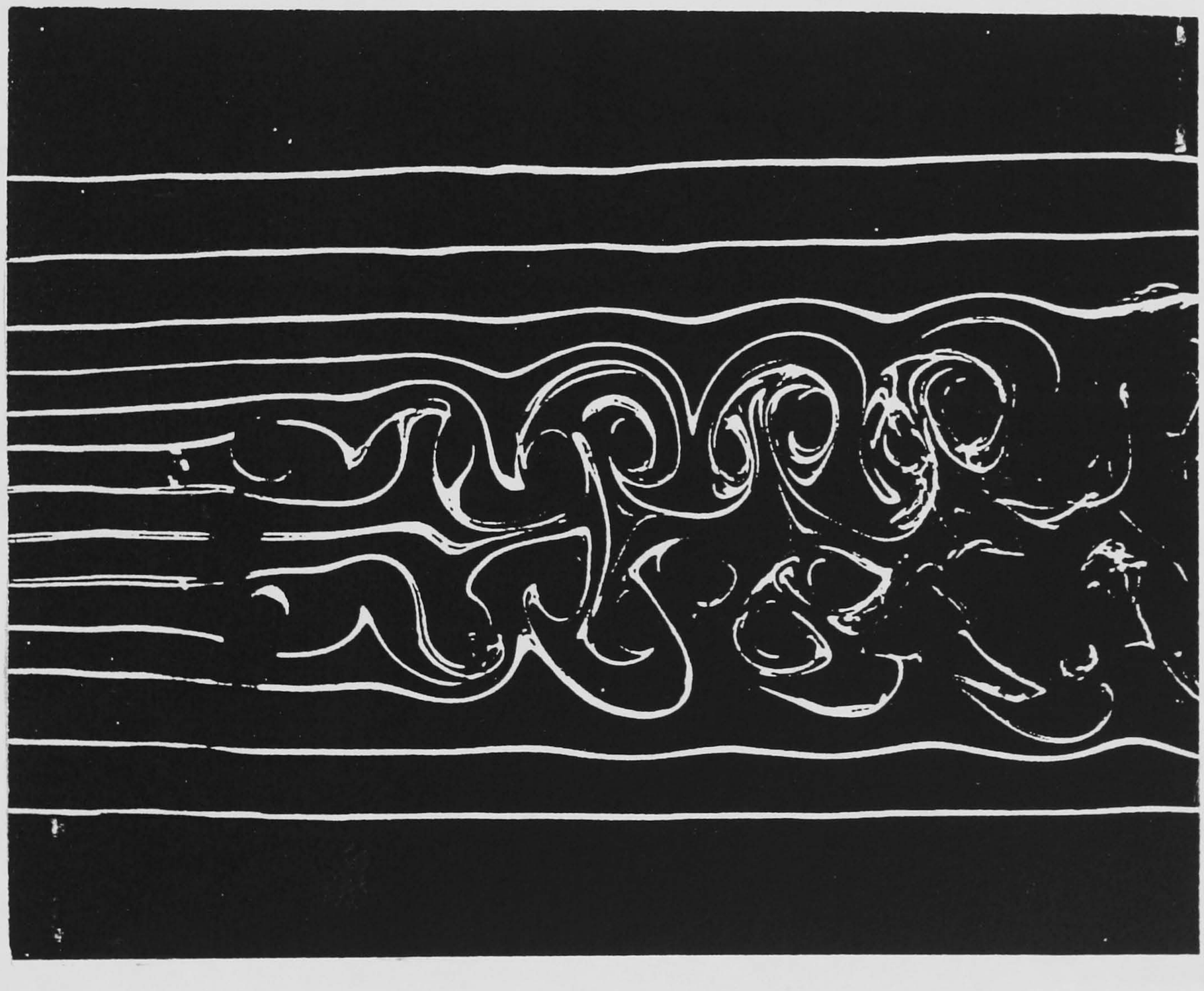

Figure.5.7.- *The flow Visualization by Bearman and Wadcock [11]*

A symmetric out-of-phase shedding pattern with no mixing between the two inner shear layers before roll-up is shown at $\hat{t} = 20$. The symmetry is maintained until $\hat{t} = 30$, where the wake interaction takes place at about *5D* behind the

cylinders. It is seen that the first two pairs of vortices shed by both cylinders in the early stages of the flow become close and combine together and then separete from the vortex pairs shed subsequently. This effect could be due to the initial conditions in which the strengths of the newly created vortices are relatively high, and this causes a strong interaction when they begin to coalesce as a group. Since there is no diffusion incorporated in the scheme, it could occur over quite a long period of calculation and result in a form of separate irregular vortex street. The comparison of the flow pattern simulated numerically with the experimental flow visualizations produced by **Bearman** and **Wadcock** [**11**] at $Re = 25000$ and shown in figure (**5.7**) shows good agreement between the two and suggests that the grid sizes and configuration used in the model are appropriate.

The polar and rectangular grid sizes play an important role in the algorithm since the flow definition depends on the value chosen. This is reflected in the calculation of vortex velocity in which the grid node-to-node interaction is used instead of the vortex-to-vortex interaction. It is shown that for this two cylinder problem, the rectangular grid size ds_r to cylinder diameter D ratio $\frac{ds_r}{D} = 0.2$ gives good results. The choice of the size, however, has a significant influence on the CPU time consumed during the calculation process for the vortex velocities.

The expected repulsive force between the cylinders can be seen from the force traces displayed in figure (**5.6**). It can be seen that the mean value of the transverse force coefficient for cylinder *1* has a positive value of about 0.2 while approximately equal and opposite force is experienced by cylinder 2. The drag coefficient has a tendency to increase from that of the isolated cylinder by about 10% and with the gap ratio 2 the average mean drag coefficient is about 1.15. The increase from the value of the isolated cylinder is close to the values deducted from the experiments of **Bearman** and **Wadcock** [**11**] at Reynolds number of 25000. The value of Strouhal Number settles to a value of around 0.2, similar to the isolated cylinder.

Section number	Purpose of section	CPU Time
1	Input / Output	0.03
2	Define Grid	0.00
3	Calculate Nodal Velocity	87.0
4	Calculate Vortex Velocity	0.33
5	Vortex Displacement	3.07
6	Distribute Circulation	0.37
7	Calculate Surface Velocity	8.61
8	Calculate Forces	0.01

Table 5.1. – *The CPU time precentage of each section of the algorithm.*

The percentage CPU time used in calculating each intermediate stage of the computation is displayed in table (**5.1**) below. The figures are based on a period of *400* time steps with around *570* active nodes for each cylinder polar grid and around *11000* vortices shed by each cylinder. In other words, there are around *1140* active nodes and *22000* vortices in the flow.

The results show that calculation of the node velocities still dominates the CPU time with a figure of *87*%. This result is even higher than before as the node velocity here includes those at both the active polar and rectangular grids. The calculation of the surface velocity is still the next most significant contribution as it is made up of the time consuming operation of the influence matrix and also the calculation of the right hand side term due to the presence of the other cylinder.

With respect to the interference drag coefficient, the computed result is in reasonable agreement with the experiment by **Biermann** and **Herrnstein jr.** [**13**] with the high Reynolds number of around 10^5 as shown in figure (**5.16**) below. The flow pattern characteristics for the other gaps of *0.8*, *3*, *4*, are displayed in figures (**5.8**), (**5.9**), and (**5.10**). The global results of the influence of the gap variations to the drag coefficient and the Strouhal number have been plotted and compared with the experimental results shown in figures (**5.16**) and (**5.17**).

These figures show the general trend in which the interaction between the two cylinders is weakened as the gap becomes wider. This means that each individual cylinder is behaving increasingly like an isolated cylinder. The drag coefficient also

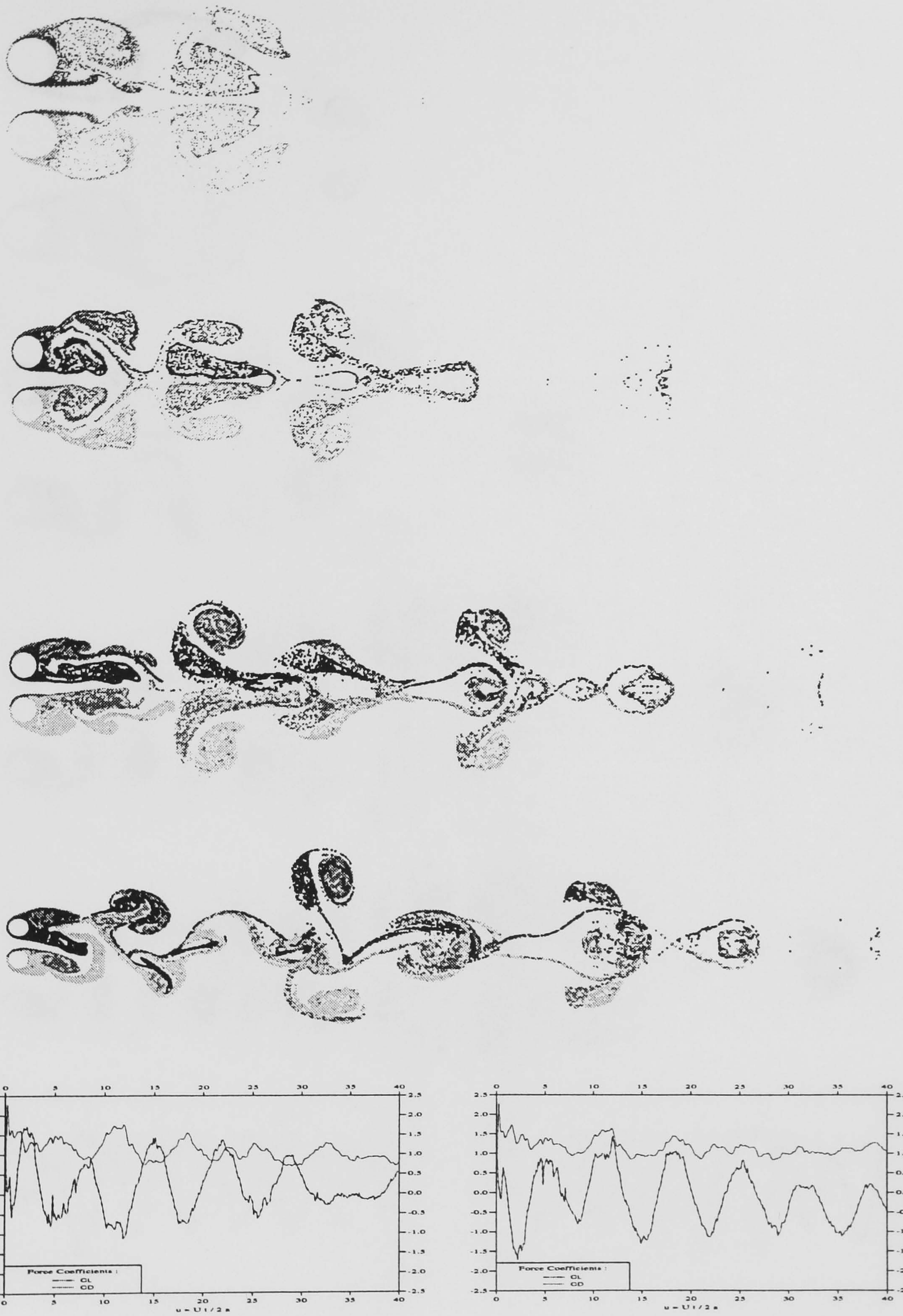

Figure 5.8.-*Flow Pattern at t = 10, 20, 30, 40; G/D = 0.8, and the Force Coefficients for Convective Flow*

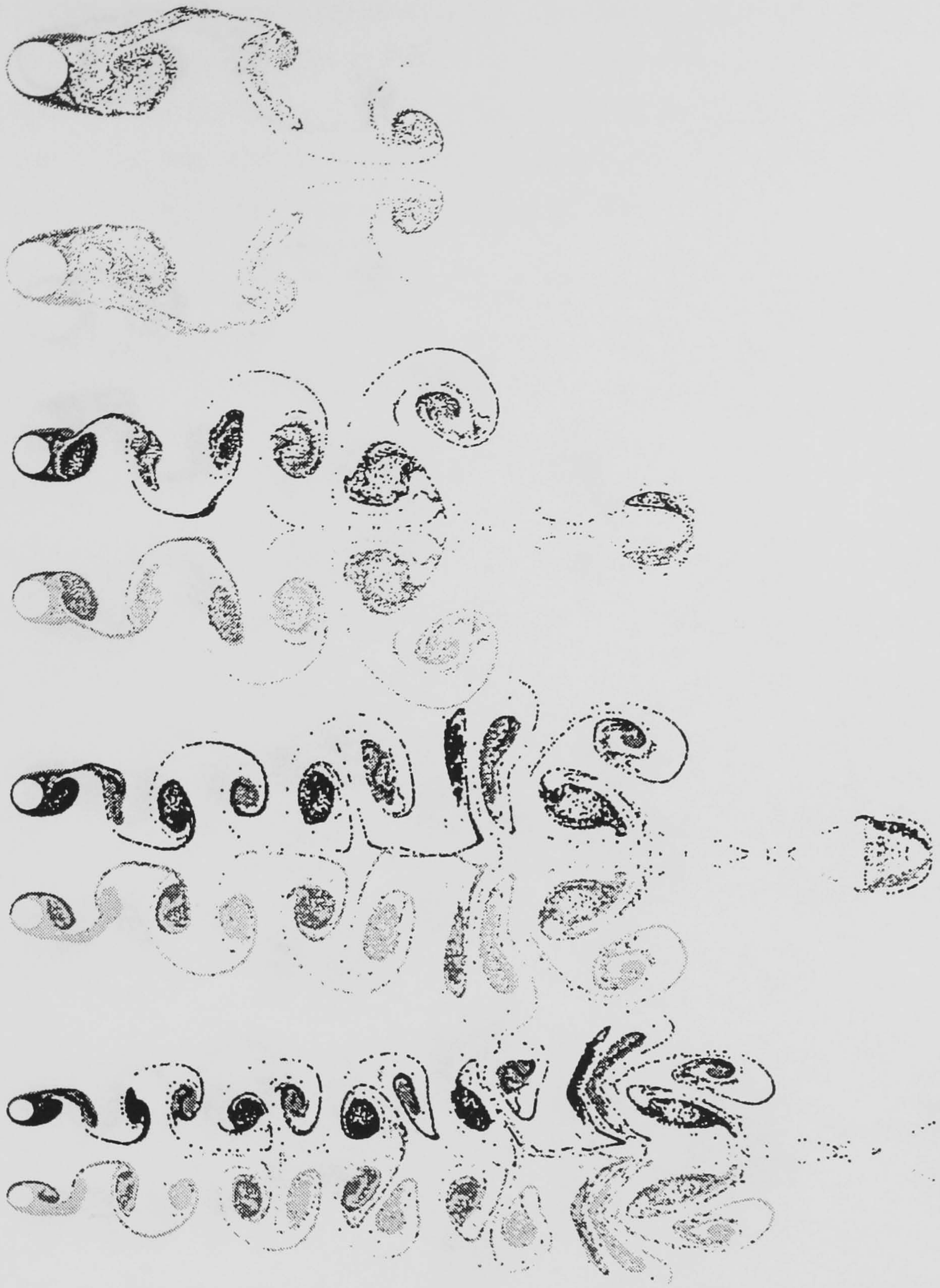

Figure 5.9.-*Flow Pattern at t = 10, 20, 30, 40; G/D = 3, and the Force Coefficients for Convective Flow*

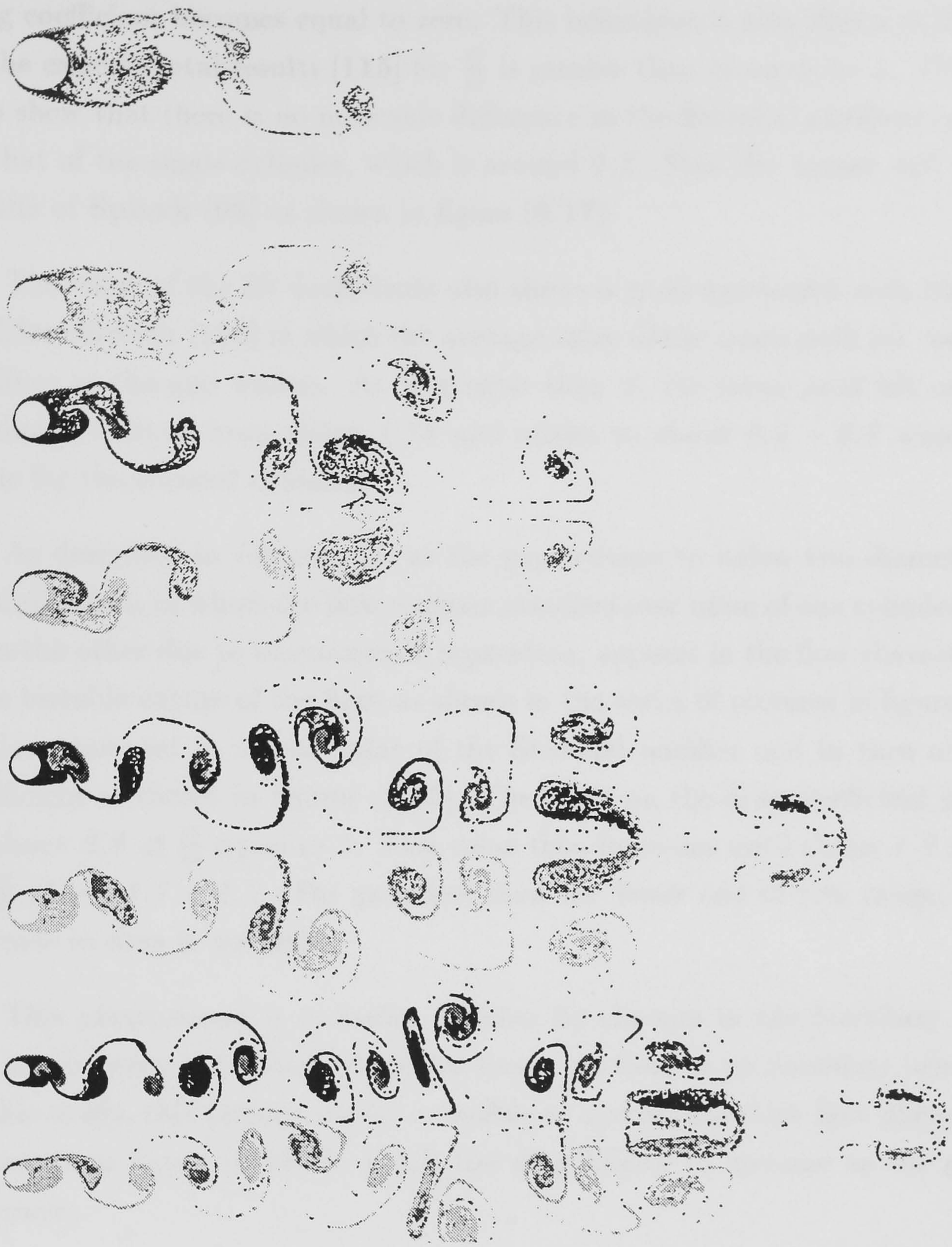

Figure 5.10.-*Flow Pattern at t = 10, 20, 30, 40; G/D = 4, and the Force Coefficients for Convective Flow*

approaches the value of around *1.14* or, in the other words, the interference drag coefficient becomes equal to zero. This behaviour is also shown in the figure of the experimental results [**115**] for $\frac{G}{D}$ is greater than or equal to *4*. The figures also show that there is no noticable difference in the Strouhal numbers compared to that of the single cylinder, which is around *0.2*. This also agrees well with the results of **Spivak** [**96**] as shown in figure (**5.17**).

The value of the lift coefficients also shows a good agreement with the results of **Zdravkovich** [**116**] in which the average value of the mean peak lift coefficients declines as the gap widens. At $\frac{G}{D}$ greater than *2*, the mean peak lift coefficient gradually reduces from about *1.25* and settles to about $0.6 - 0.8$ which is the value for the isolated cylinder.

As described in *Chapter II*, as the gap reduces to below two diameters, the Coanda effect, in which the flow remains attached over more of one cylinder surface than the other due to unsymmetric separation, appears in the flow characteristics. This bistable nature of the flow, as shown in the series of pictures in figure (**2.14**), is also expressed in a dual value of the Strouhal number and in turn of the lift coefficient as shown in figures (**5.17**). The effect on the drag coefficient is a drop to about *0.8* at $\frac{G}{D}$ equal to *2*. This value then increases until about *1.2* at range of $\frac{G}{D}$ about $1.3 - 1.7$. For gaps less than the lower end of this range, a sharp increase in drag is noticed.

This phenomenon is probably dictated by changes in the boundary layer as the gap between the cylinder becomes small. As there is no boundary layer model in this study, this present model is unable to accomodate this flow phenomenon, as shown in figure (**5.16**) in which the drag begins to increase as the gap gets narrower.

It is a limitation of the present scheme for this type of flow configuration that if the diffusion part is simulated using the Random Walk approach, a stable 'mirror-image' property of the flow behind both cylinders can not be maintained unless a vortex reduction scheme is incorporated, as shown in the flow pattern example in figure (**5.11**). This is due to the fact that the Random Walk method is based on the principle of the vorticity diffusion over a certain small area in the fluid by shifting the vortices randomly and not by reducing the strength of every single vortex. The result is that the random walk imposed on a vortex shed by one cylinder, will not always have a stable interaction with the group of vortices shed by both cylinders as the interaction in the group is too strong. This difference is

then accumulated and can create asymmetric wakes behind the two cylinders in the early stages of the flow, which then results in an unrealistic flow pattern after the flow developes further.

The results shown in this study therefore have been obtained by implementing a vortex reduction scheme, similar to those of **Naylor** [71] and **Basuki** [6], in which the strength of the vortices is reduced in such manner that the effect on the force coefficient and the flow pattern is as close as possible to that of the experimental results.

Figure 5.11.- *The example of the instability in the wake interaction at* $G/D = 2$

At a Reynolds number of *25000*, when compared with the results of **Bearman** and **Wadcock** [11] displayed in figure (**5.7**), the present scheme produces quite a good prediction of the force coefficients and the flow pattern at gap ratio $\frac{G}{D} = 2$ as shown in figure (**5.12**). At this Reynolds number value, the reduction factor for the vortex strength C_Γ, is chosen to be *0.993* in which the vortex strength will have been reduced by *50%* at $t = 10$.

Out-of-phase symmetric vortex streets are created behind the cylinders which interact only slightly in the region around half way between the two centres at distance greater than *5D* behind the cylinders. It is seen that by implementing the vortex reduction scheme, a high degree of symmetry for the vortex shedding from the two cylinders can be achieved.

The effect is reflected in the graphs of the lift coefficient for the cylinders, which oscillate out-of-phase relative to each other. The repulsive force, created due to the asymmetrical properties of the flow around each cylinder, also occurs and is shown by the finite mean values for the lift coefficients whose magnitude

are of around *0.2* and which are positive for the upper cylinder and negative for the

lower cylinder. The drag coefficient is around *1.2* for both cylinders which is close to the experimental results of **Bearman** and **Wadcock** [**11**], although the Strouhal number is around *0.15* which is *10%* lower than their result.

The results for a smaller gap ratio of $\frac{G}{D} = 1$ are presented in figure (**5.13**). As reported in Bearman and Wadcock's paper, at this gap ratio the flow is confused with no apparent dominant vortex structure. A filament passing between the cylinders is seen to be biased towards one of them. The flow would remain biased toward this cylinder for some time before swapping to the other. The drag coefficient is around *1.25*, the mean lift coefficient is slightly higher at *0.25* and the Strouhal number drops to about *0.12*.

As mentioned previously as the gap ratio $\frac{G}{D}$ increases the mutual interaction of the cylinders and their wakes decreases, as presented in the flow patterns and the force coefficients for $\frac{G}{D} = 3$ displayed in figure (**5.14**). The flow patterns look more regular with only little disturbance to their asymmetry. The drag coefficient reaches a value of *1.15* with a mean value of the lift coefficient of around *0.1* which is close to the expected values.

The force coefficients and the flow patterns behind an isolated cylinder are approached when the gap ratio $\frac{G}{D}$ approaches *4* as displayed in figure (**5.15**), even though some disturbances occurred when the vortices shed by both cylinders approached one another. The value of the force coefficients are close to those of the isolated cylinder at a value of the Reynolds number equal to around *25000*.

Results for the flow at the higher Reynolds number of *100000* and at $\frac{G}{D} = 2$, which can be compared with the convective flow described before, are presented and displayed in figure (**C.2**) in *Appendix C*. As described above, the constant reduction of the vortex strength C_Γ is chosen to be *0.993* and vortex strengths will have about half value after around *300* iterations.

The flow patterns created behind the cylinders are seen to be more regular compared to the same configuration in the convective flow shown in figure (**5.6**) before. This is due to the implementation of the vortex reduction scheme simulating turbulent dissipation and reducing the level of irregularity occuring in the group of vortices with high strengths created in the early stages of the calculation.

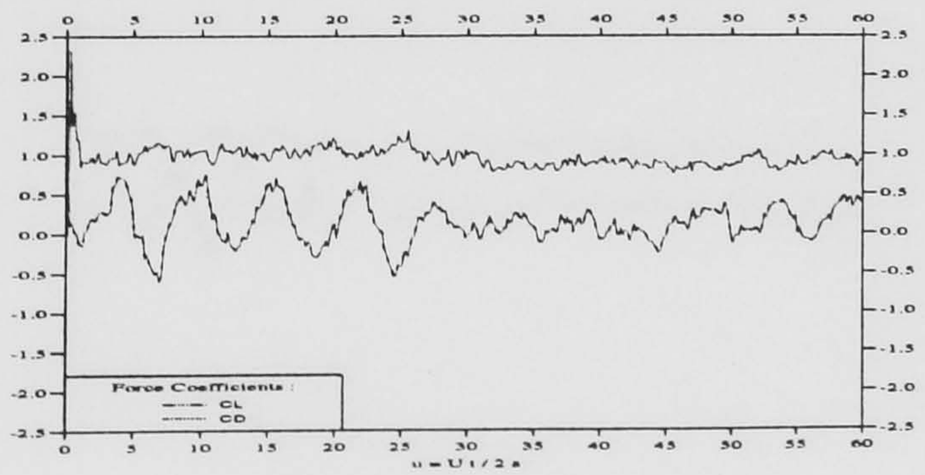

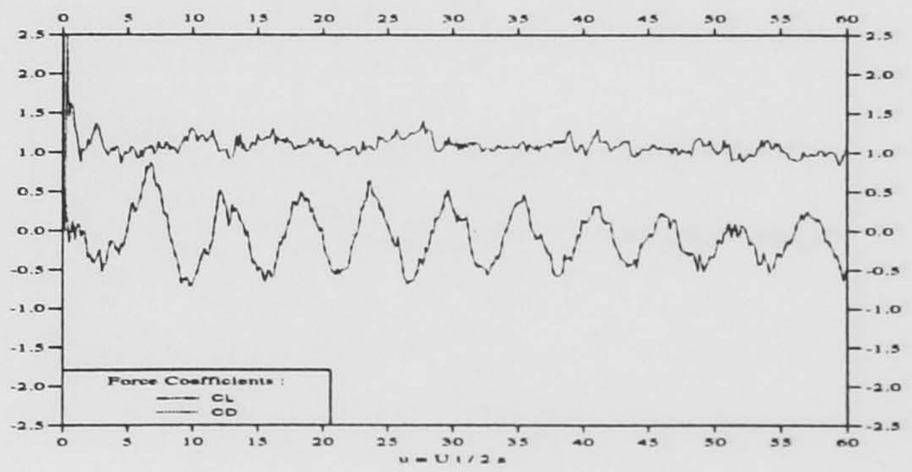

Figure 5.12.-*Flow Pattern at t = 10, 20, 30, 40; G/D = 2, and the Force Coefficients for Re = 25000*

Figure 5.13.-*Flow Pattern at t = 10, 20, 30, 40; G/D = 1, and the Force Coefficients for Re = 25000*

Figure 5.14.-*Flow Pattern at t = 10, 20, 30, 40; G/D = 3, and the Force Coefficients for Re = 25000*

Figure 5.15.-*Flow Pattern at t = 10, 20, 30, 40; G/D = 4, and the Force Coefficients for Re = 25000*

For the gap ratio of *two*, the mean value of the drag coefficient is around *1.17* which is slightly increased compared with that of the convective flow, while the mean values of the lift coefficients of the upper and lower cylinders are *0.2* and -0.2 respectively, which is close to the result of **Bearman** and **Wadcock** [11].

The results for other values of gap ratios are also presented in *Appendix C*. The values of the drag and lift coefficients and the Strouhal numbers are plotted in the graph of the experimental results as displayed in figure (5.16), and (5.17).

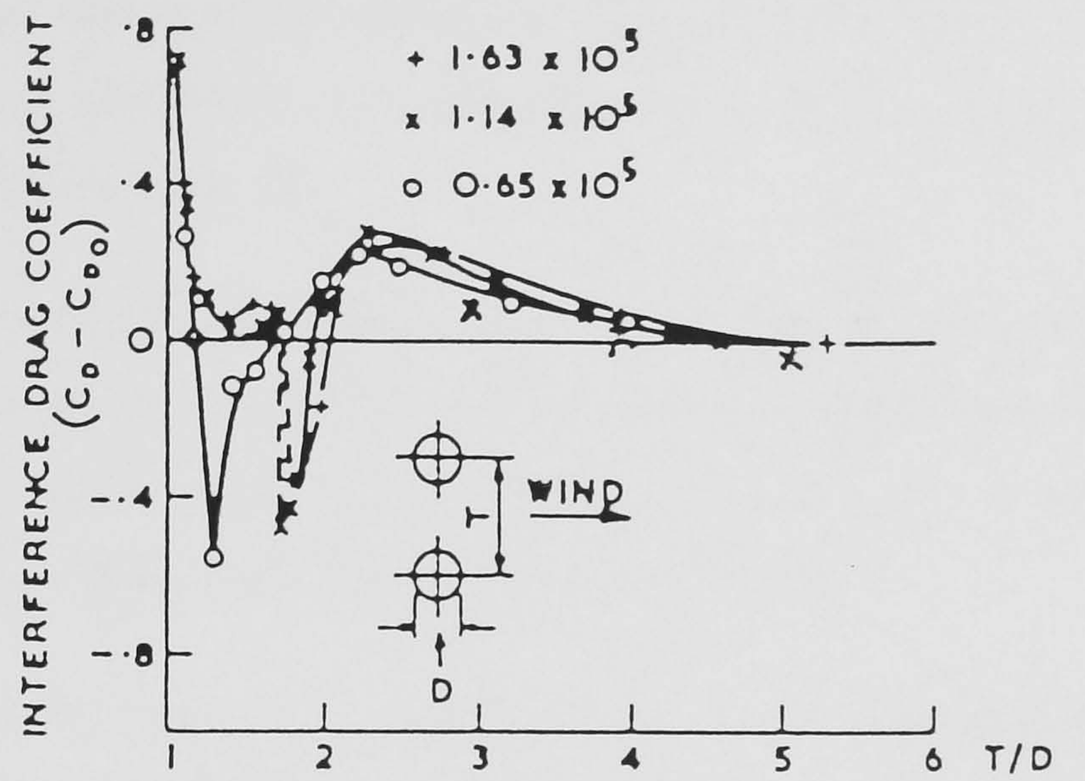

Figure 5.16.-*Drag and Lift Coefficients Vs. Gap Ratio G/D*

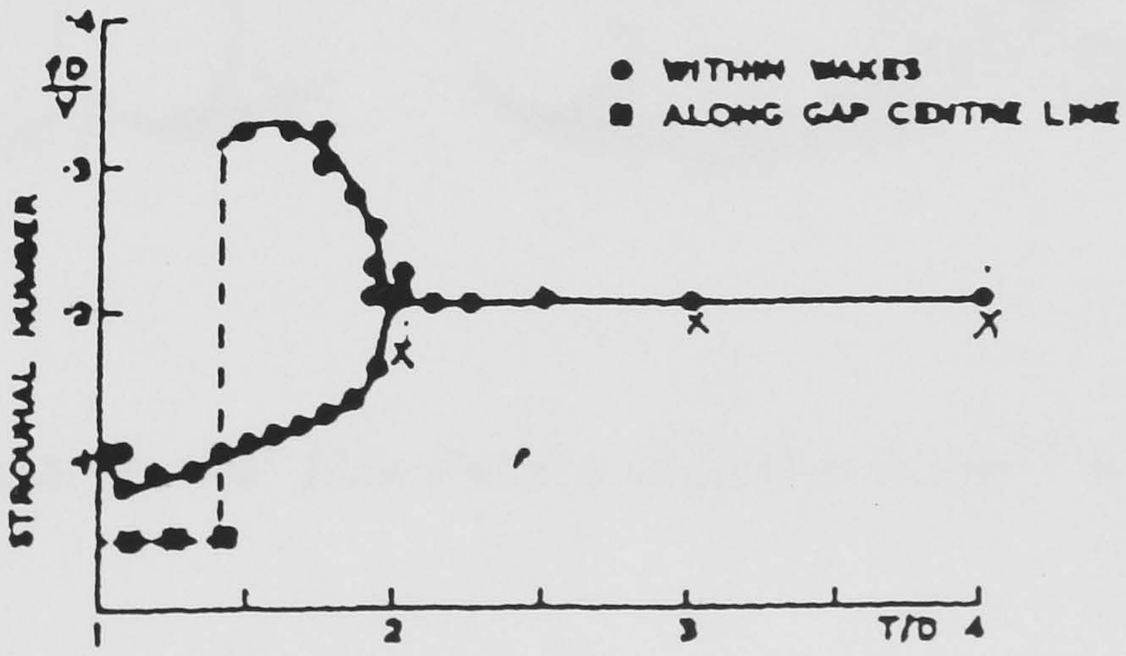

Figure 5.17.-*Strouhal Number Vs. Gap Ratio G/D*

5.9.2 Two Cylinders in Tandem Arrangements

Experiments in which two cylinders were placed in tandem with various different gap ratios were carried out by **Hori** [46] and **Zdravkovich** [117]. They found two unusual features of this type of flow. Firstly, the side facing the gap between the cylinders had a very low negative pressure, which was almost the same as the corresponding value of the base pressure of the upstream cylinder. This fact is an indication that the flow around the gap is almost stagnant. Secondly, the negative gap pressure coefficient in front of the downstream cylinder exceeded that on its downstream face. This means that when the distance between the two cylinders is less than a critical distance,the downstream cylinder experiences a negative drag-thrust force. These phenomena are implied in the figure (2.24) of the interference drag coefficients in chapter *II*.

For this flow configuration, the vortex reduction scheme is also used to simulate the turbulent dissipation in the wake. At this case, the downstream cylinder acts as a splitter plate which reduces the 'degree of asymmetry' caused by the random shift of the vortices shed from the upstream cylinder.

The results of the numerical experiments for the $\frac{G}{D}$ ratio of 0.5, 1, 1.5 and 2 for $Re = 100000$ are presented in the following figures along with the corresponding force coefficients.

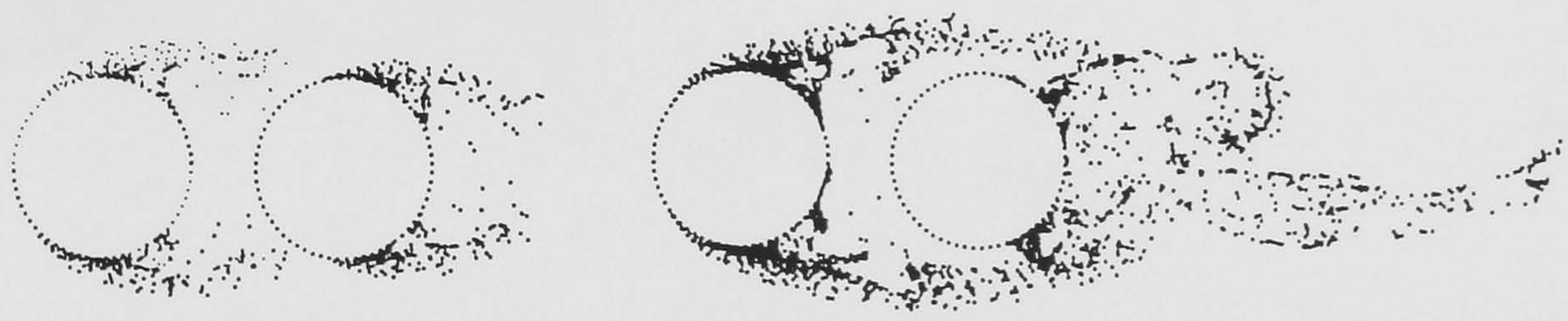

Figure 5.18.- *The Flow Pattern at $G/D = 0.5$ for $\hat{t} = 1$ and 5*

It is seen from figure (**5.18**) that at $\hat{t} = 1$ for $\frac{G}{D} = 0.5$, the two cylinders shed the vortices almost identically. No asymmetric enforcement was imposed

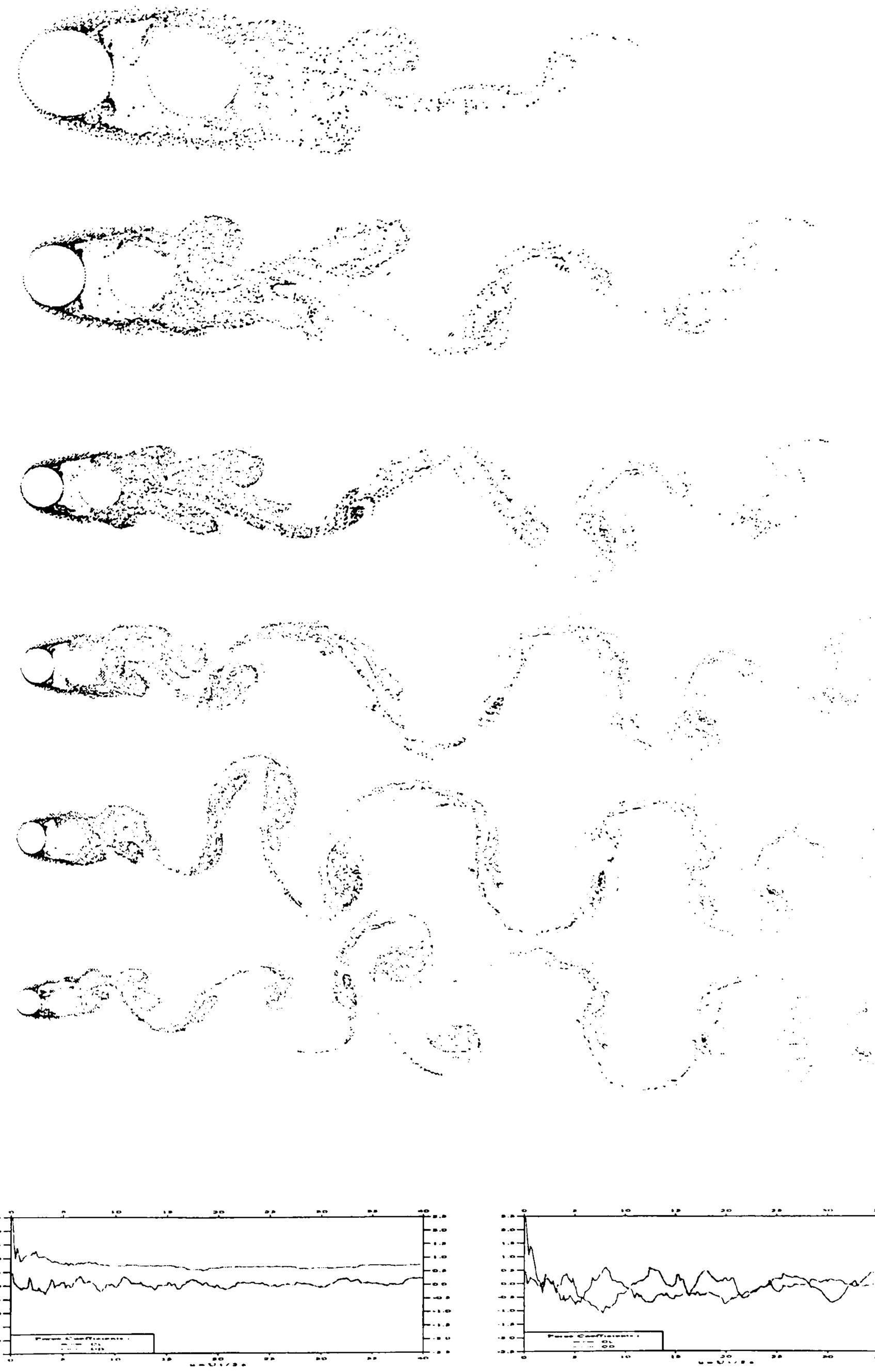

Figure 5.19.-*Flow Pattern at t = 10, 20, 30, 40: G/D = 0.5, and the Force Coefficients for Re = 100000*

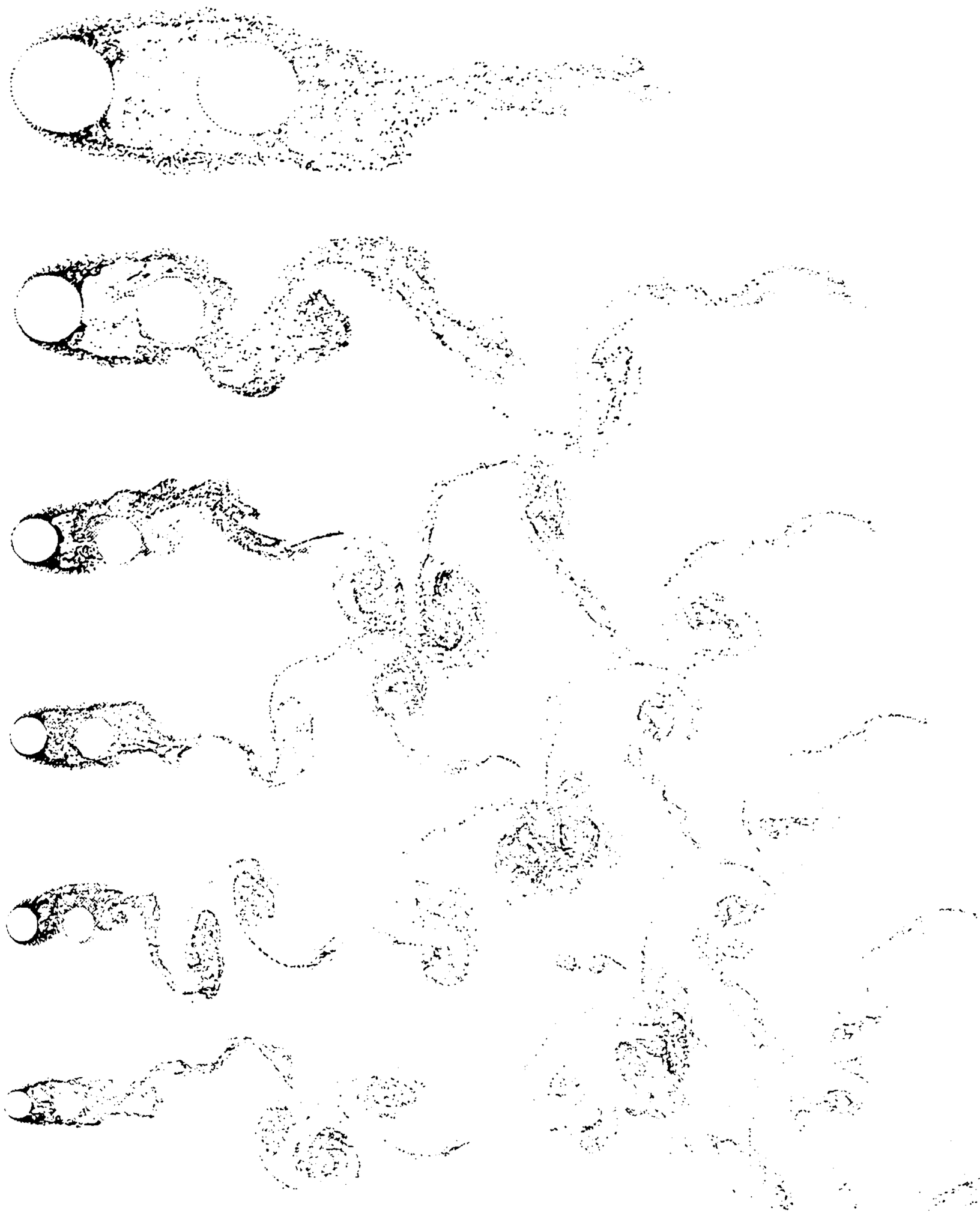

Figure 5.20.-*Flow Pattern at t = 10, 20, 30, 40; G/D = 1, and the Force Coefficients for Re = 100000*

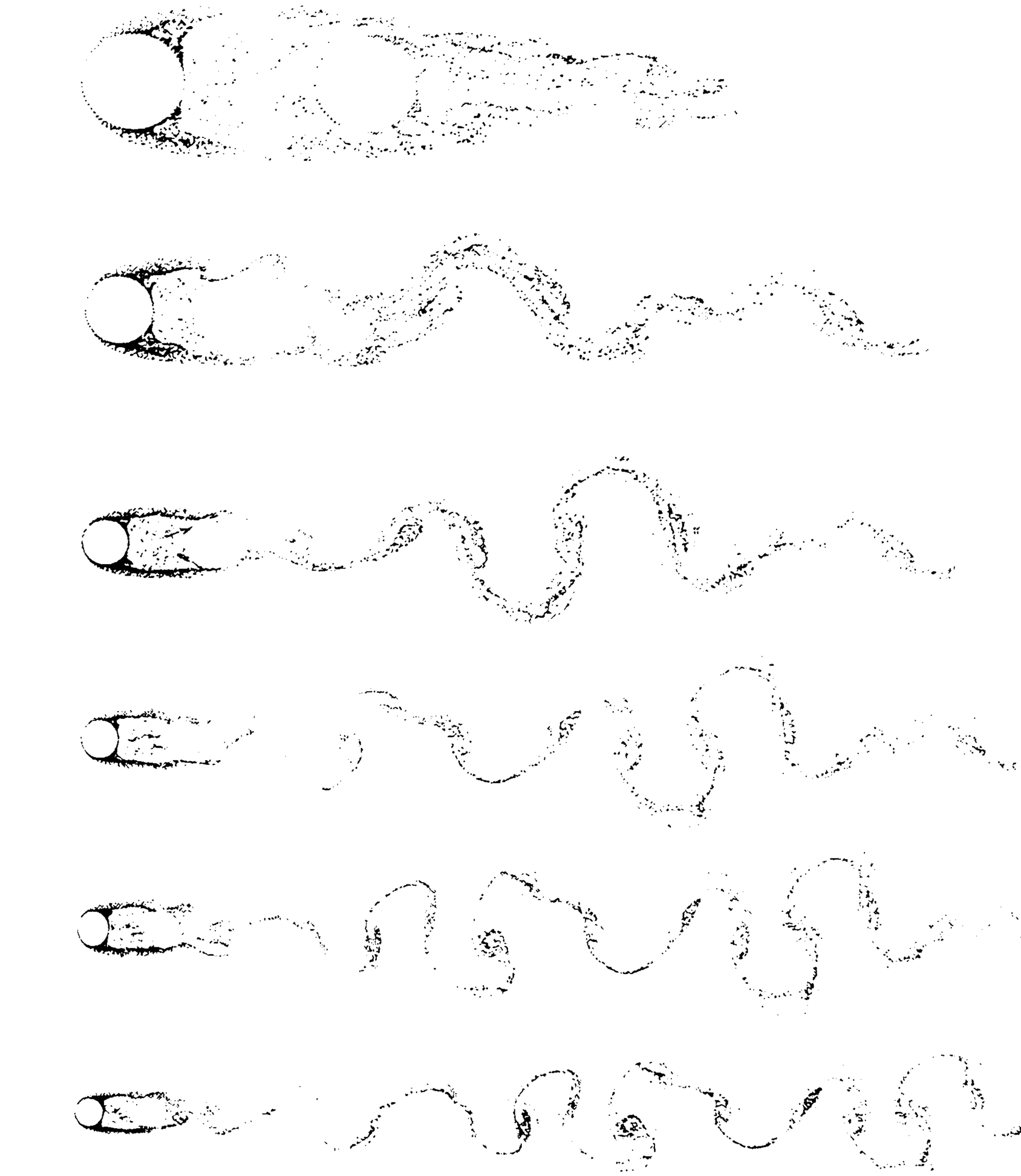

Figure 5.21.-*Flow Pattern at t = 10, 20, 30, 40; G/D = 1.5, and the Force Coefficients for Re = 100000*

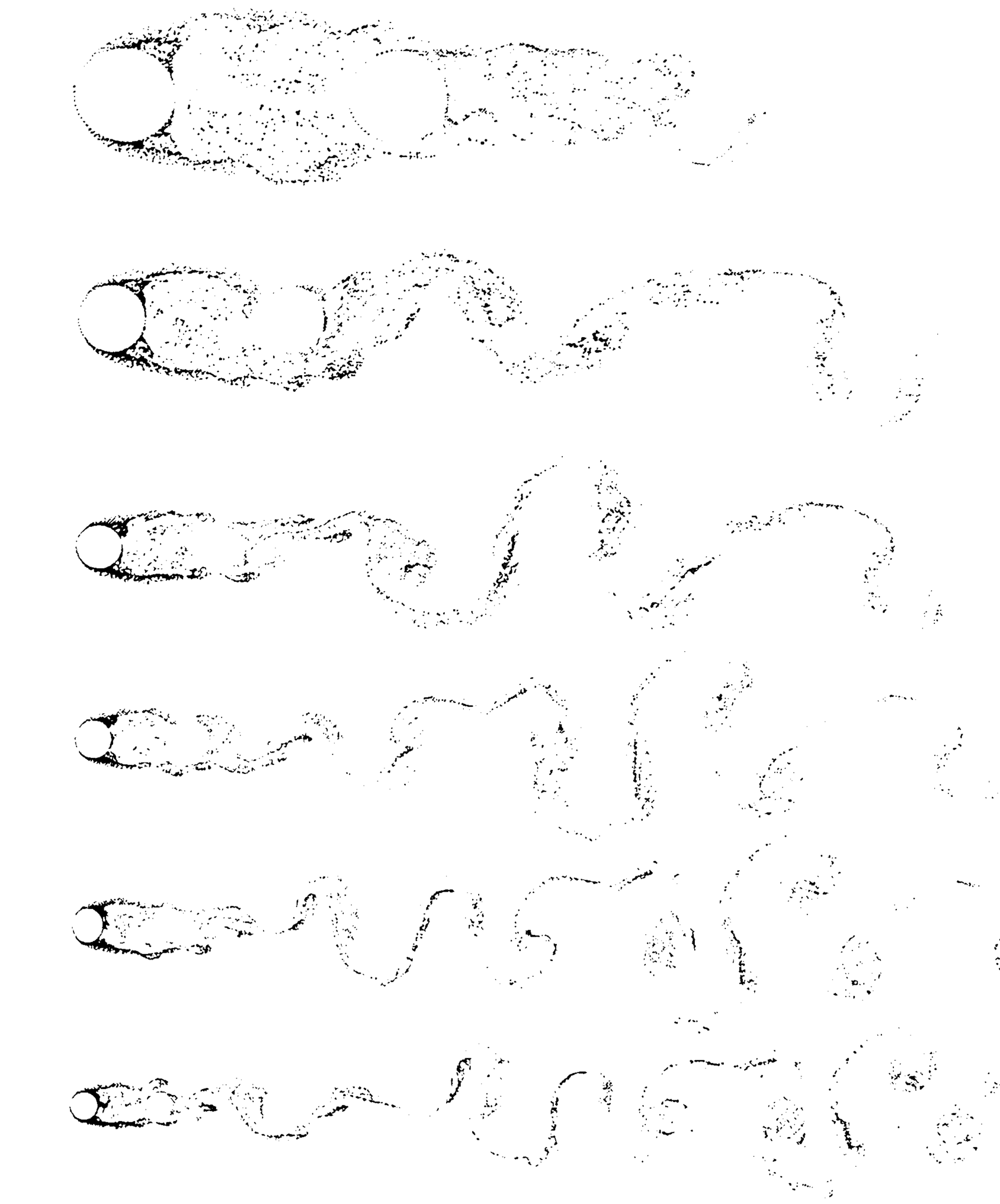

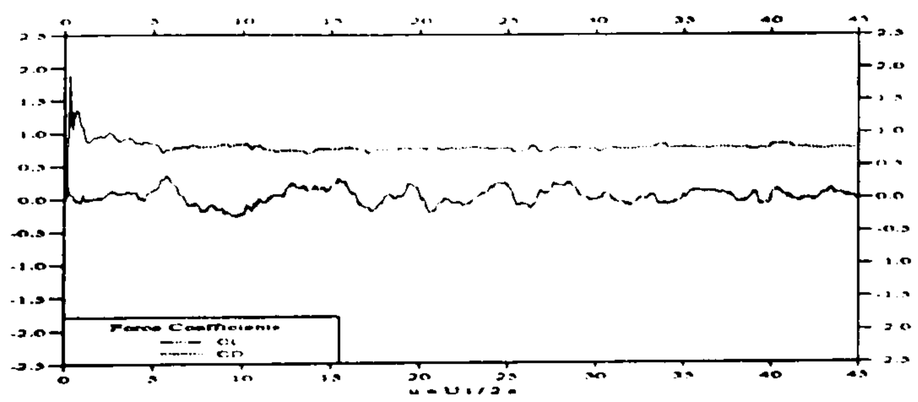

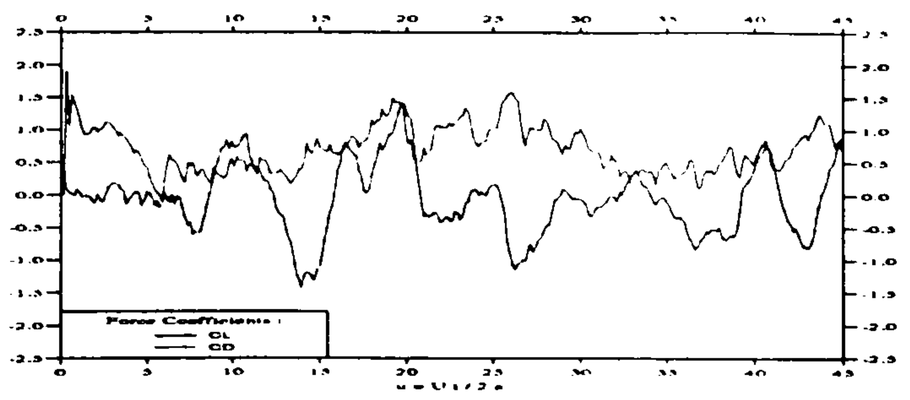

Figure 5.22.-*Flow Pattern at t = 10, 20, 30, 40; G/D = 2, and the Force Coefficients for Re = 100000*

in this case, however, since the random diffusion and also the accumulation of numerical errors was found to be sufficient to trigger asymmetric shedding from the downstream cylinder in the early stages of the flow, that is by $\hat{t} = 5$.

As the vortices shed from the upstream cylinder approach the downstream cylinder, the drag coefficient of the downstream cylinder gradually declines until it settles and oscillates around a negative value of -0.2, as shown in figure (**5.19**) and which is close to the experimental results.

Numerically, this effect is due to the presence of the vortices shed by the upstream cylinder approaching the upstream face of the downstream cylinder and interacting with the newly created vortices there so as to interfere with the normal relative contributions to the pressure distribution made by the upstream and down stream parts of the cylinder.

The force coefficients of the upstream cylinder experience a relatively small oscillating drag and lift coefficient as, at this gap ratio, the downstream cylinder acts as a splitter plate which suppress the regular oscillatory shedding of vortices from the upstream cylinder. The drag coefficient reduces from that of the isolated cylinder to be around 0.8 and the oscillating lift coefficient has a zero mean which is also close to the experimental results.

The lift coefficient of the downstream cylinder has a Strouhal number of around 0.16 and a maximum value of 0.5. This is quite close to the Strouhal number graph shown in figure (**2.26**) in chapter *II*.

At a gap ratio of $\frac{G}{D} = 1$, the larger gap between the cylinders creates more space in the formation region of the upstream cylinder for the development of an oscillating wake. This influences the symmetrical properties of the reattachment position of the vortices shed from the upstream cylinder on the downstream cylinder. The oscillatory reattachment of the shear layers from the upstream cylinder causes an asymmetric vorticity distribution around the downstream cylinder. This phenomenon is reflected in the graphs of the force coefficients for the downstream cylinder, in which both the drag coefficient C_d and the lift coefficient C_l are oscillatory in nature.

The form of the force coefficients of the upstream cylinder still reflect that the downstream cylinder is acting, to some extent, as a splitter plate. The lift coefficient is more oscillatory at a mean peak value 0.9 which is slighly higher

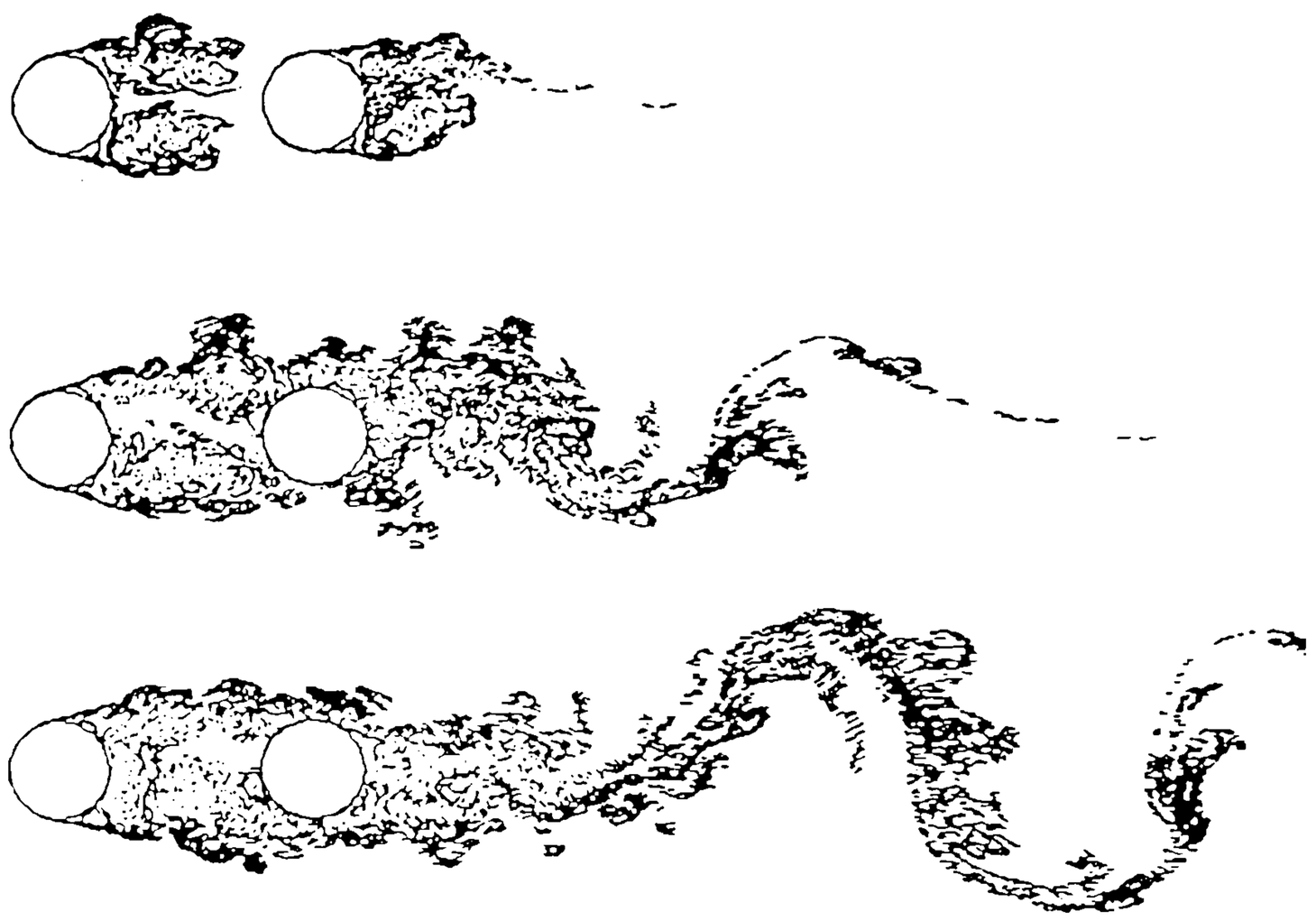

Fig. 4—Simulated flow around two cylinders in tandem.

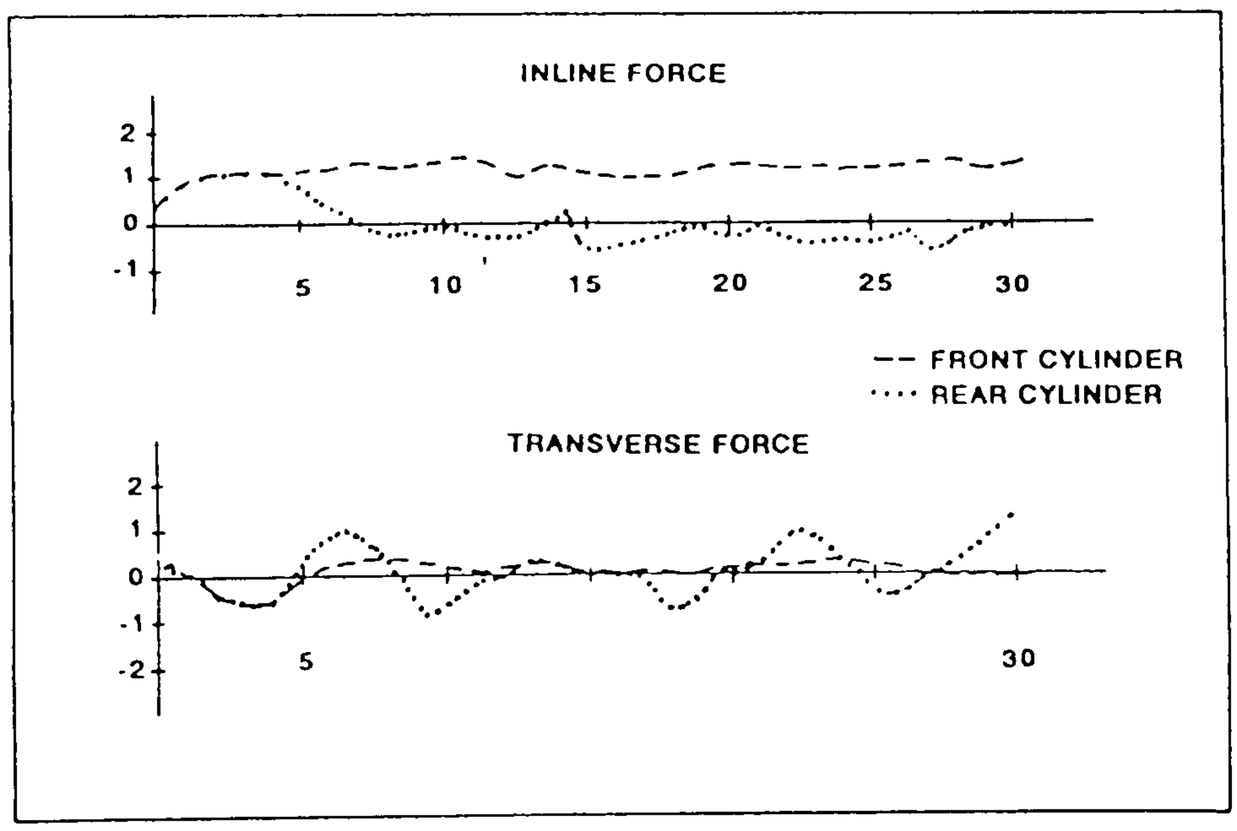

Figure 5.23.- *The Flow pattern at G/D = 1.5 from Hansen et.al. [43]*

than before, while the drag coefficient continue to oscillate about a zero mean, as shown in figure (**5.20**).

When there is a gap ratio of $\frac{G}{D} = 1.5$, the larger gap causes the drag and lift coefficients of the downstream cylinder to oscillate more regularly about the zero mean, but there are no significant changes to the force coefficients for the upstream cylinder. This then creates a more regular Von Karman vortex street behind the downstream cylinder, similar to that of a single cylinder in isolation as shown in figure (**5.21**).

The comparison of the present results to those of **Hansen et.al** [**44**], shows a good agreement between the flow patterns and also in the force coefficients as shown in figure (**5.23**) below. They used a three level curvilinear grid generated from a solution of the *Laplace* equation. Close to the cylinder, a finer grid system was introduced which then overlapped with two coarser grids for the transport of the wake far from the cylinders. Using a method similar to those of **Stansby** [**98**], and **Yde** and **Hansen** [**114**], the flow convection was calculated by solving the Poisson equation and diffusion was simulated using the Random Walk scheme with some modifications such as, vortex amalgamation and vortex strength reduction.

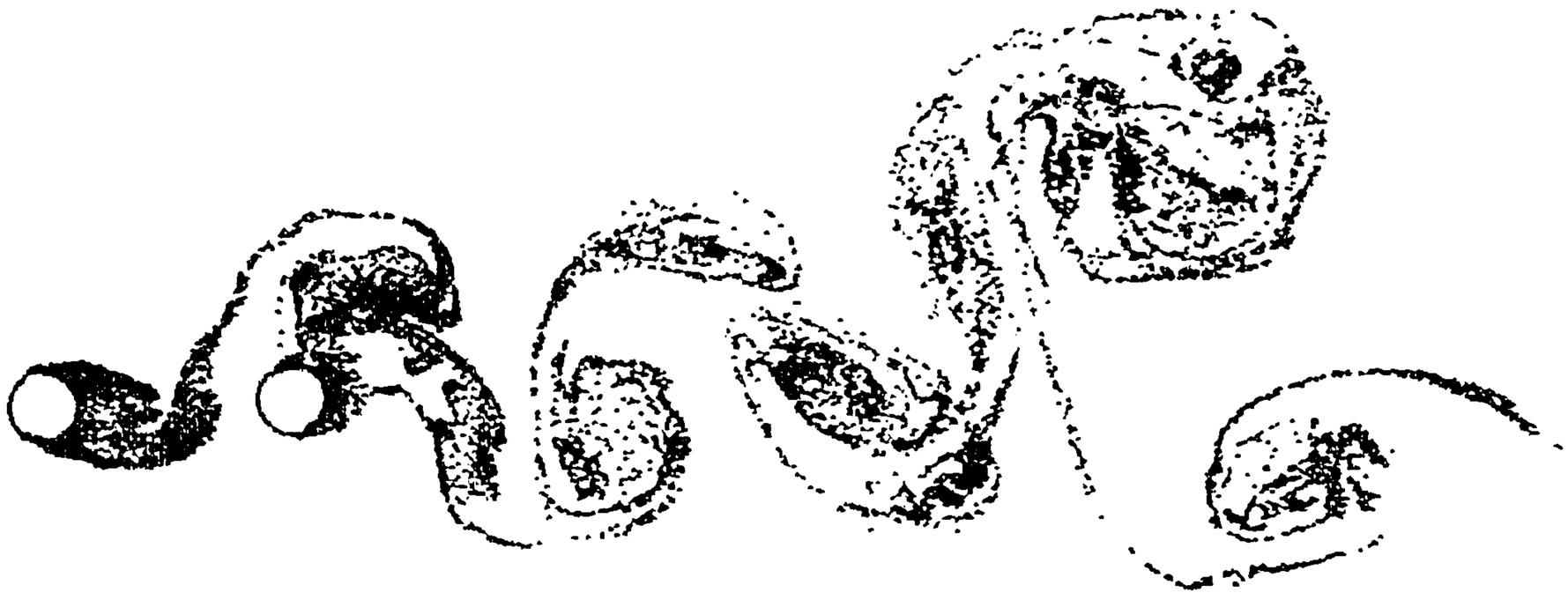

Figure 5.24.-*The Unrealistic Flow Due to the Instability in the Algorithm*

As the gap ratio of $\frac{G}{D}$ is increased to 2, oscillation of the lift coefficient of the upstream cylinder begins to appear. This shows that the upstream cylinder is just on the verge of shedding vortices as is shown also in the flow visualisation in figure (**5.22**) in which the shape of the formation region of the upstream cylinder

is regularly asymmetric relative to the downstream cylinder position. In turn, this influences the behaviour of the force coeffficients of the downstream cylinder which become less regular and for which the mean value of the peak lift and drag coefficients are *0.5* and *0.8* respectively. This behaviour is in line with the experimental results as described by **Zdravkovich** [**115**][**116**] for which at around this gap ratio, a sudden jump in the Strouhal number occurs for the downstream cylinder. Also at the same spacing regular vortex shedding was first detected behind the upstream cylinder, as shown in the Strouhal number curve illustrated in figure (**2.26**) in chapter *II*.

In a numerical experiment using the Finite Element method, **Sun et.al.** [**106**] at a low Reynolds number of *100*, found that a similar trend occurred at around this gap ratio and they divided the flow into *Vortex Suppression* and *Vortex Formation* regimes at gap ratios of *1.5* and *3.5*. In the vortex suppression regime, as in the previous case, the gap ratio is less than the critical spacing. The shear layers separating from the upstream cylinder reattach to the downstream cylinder so that vortices do not have sufficient room to grow, to develop or to be shed. Since the downstream flow is in the attached vortex region of the upstream cylinder, the oncoming stream to the downstream cylinder is quite weak.

When the gap ratio is greater than its critical value, as in the present case , a vortex formation regime begins to appear from behind both cylinders. The occurrence of vortex shedding between the two cylinders creates an oscillatory oncoming flow upstream of the downstream cylinder and this leads to a stronger oscillatory flow behind the downstream cylinder.

Experimental evidence, and also the results presented in figure (**2.25**), show that for a gap ratio greater than *2*, the general trend of the flow visualisations and the associated force coefficients is that the upstream cylinder behaves more and more like an isolated cylinder with the interference drag coefficient approaching to zero.

The drag coefficient of the downstream cylinder, however, shows a consistently lower value than that of an isolated cylinder and settles at a value of around *0.5* , which is slightly higher than the experimental values. The lift coefficient oscillates with Strouhal number *0.18* which is slightly less than that of the isolated cylinder.

For higher gap ratios, however, the present model failed to simulate the flow phenomena. This is because the formation region of the upstream cylinder imposes a strong unstable asymmetric distribution of newly created vorticity upon

the downstream cylinder which develops to create an unrealistic flow pattern and corresponding force coefficients for both cylinders. as displayed in figure (**5.24**).

The results for the drag coefficient for the gap ratio $\frac{G}{D}$ less than *2* have been compiled and are displayed in figure (**5.25**). The above results have also been represented in terms of the interference drag coefficient by deducting a drag for the isolated cylinder of *1.14*. as produced in chapter *III*. It is found that fairly good results are achieved for this particular range of the gap ratios.

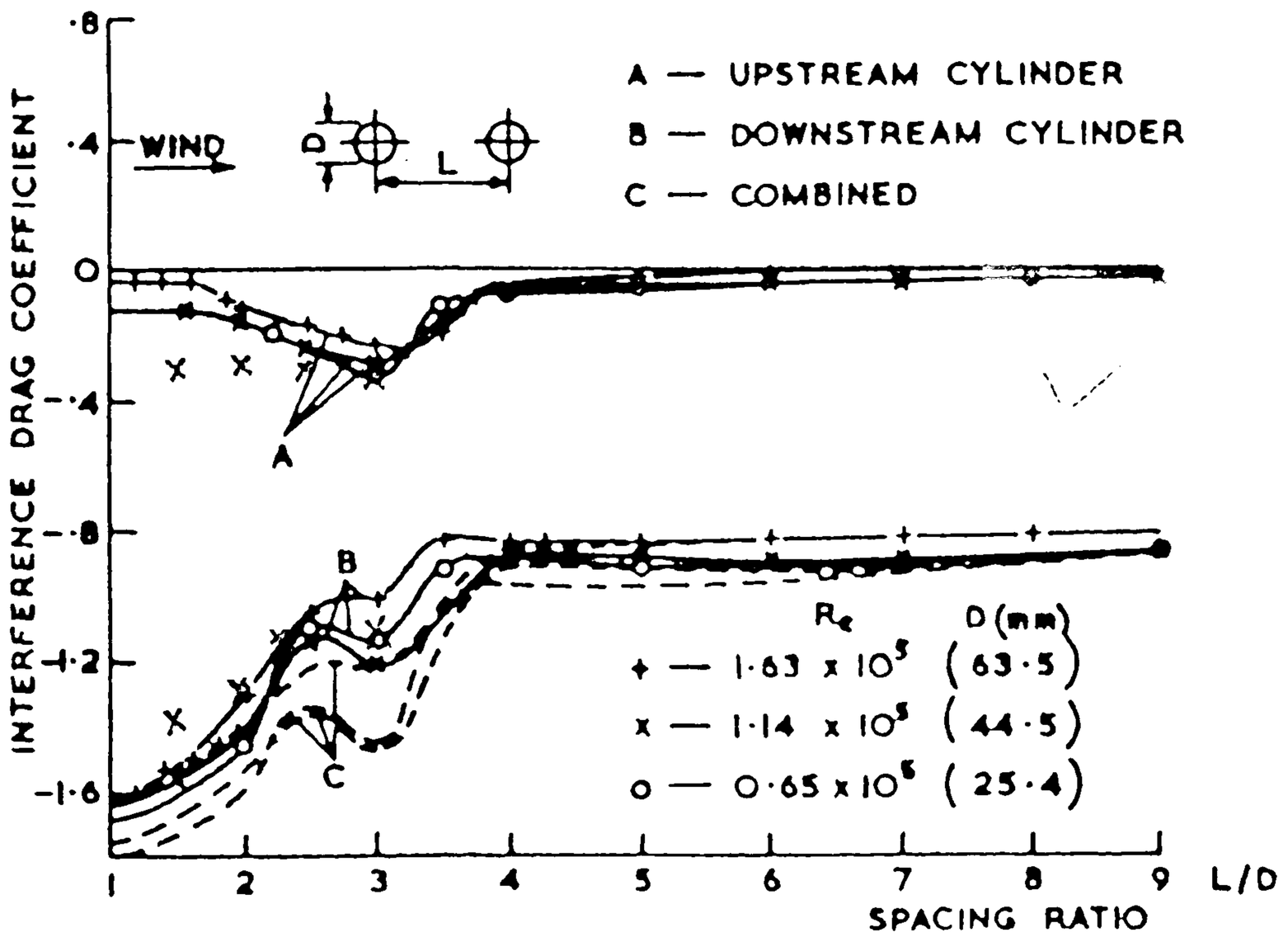

Figure 5.25,-Interference Drag Coefficients for Tandem Cylinders

5.9.3 Two Cylinders in Staggered Arrangements

In this section. the distance between the two cylinder centres. $\frac{G}{D}$. is taken to be *1* or *2*. while the *stagger* angle. δ. measured between a line joining the cylinder centres and the vertical. is varied through *22.5*. *45*. *and*. *67.5* degrees with a constant Reynolds number of *61000*.

With the stagger angle $\delta = 22.5$ degrees. at $\frac{G}{D} = 1$ there is a tendency for the formation region of the upper cylinder to be narrowered whilst the opposite occurs for the lower one as shown in figure (**5.26**). The gap between the two cylinders acts as a slot which accelerates the fluid particles in this region. This causes a

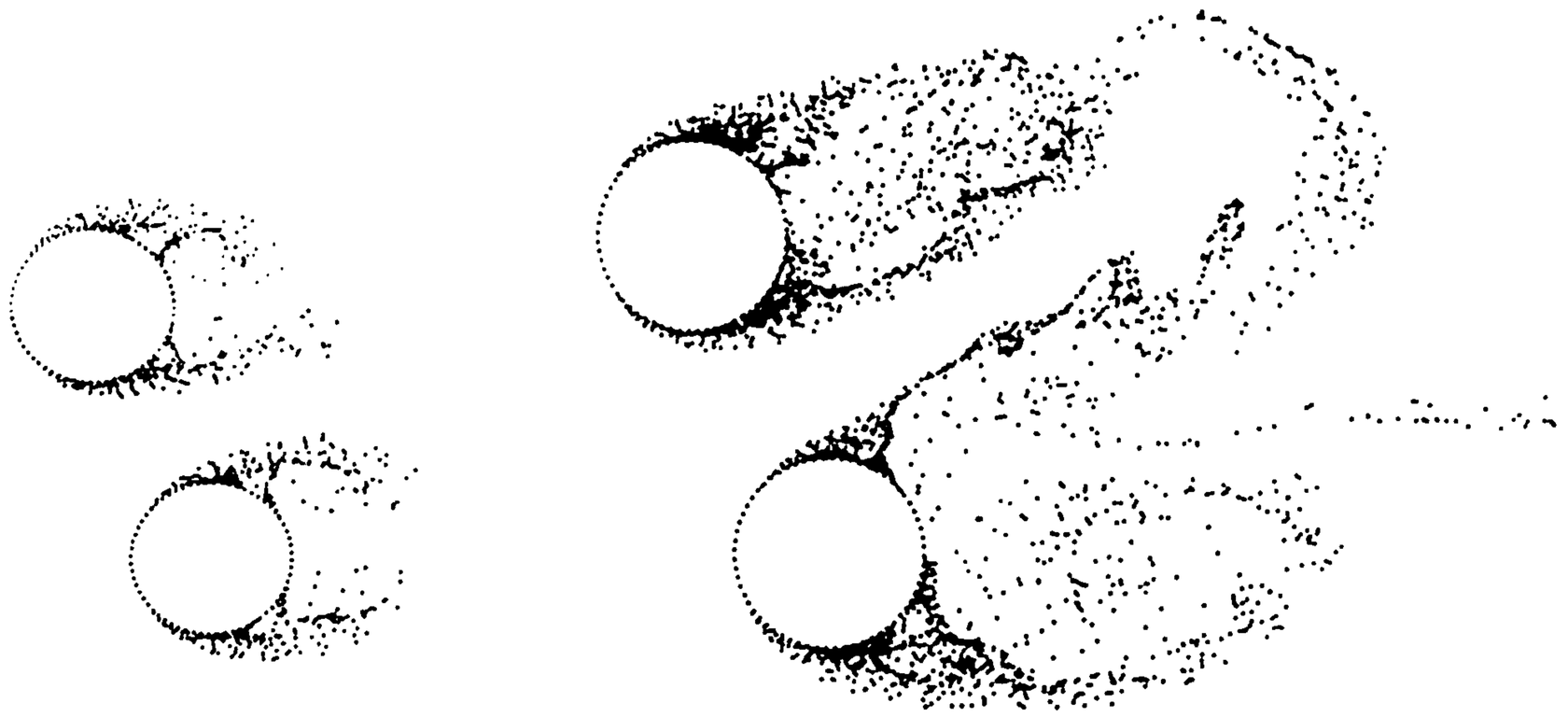

Figure 5.26. -Flow Pattern at $\hat{t} = 1$ and 5

reduction in the 'degree' of oscillation of the formation region of the upper cylinder which is also reflected in relatively smaller oscillatory force coefficients compared to those of the lower one. A similar effect can be seen in the experimental evidence displayed in figure (2.23) when one cylinder is arranged close to the other in similar positions. The drag coefficient of the upper cylinder is around *0.9* while the mean lift coefficient is around *0.2*. The values for the lower cylinder are *1.05* and -0.1 respectively. It is shown that vortices shed by both cylinders are then combined immediately behind the lower cylinder as shown in figure (5.27). The Strouhal number of the upper cylinder is shown not measureable while that of the lower one is around *0.1*

This configuration can be considered to be located at the border of regions *3* and *4* in figure (2.19). In this region, as shown by the direction of the arrows, the value of the drag coefficient is positive and the lift coefficient is small and negative which is qualitatively in line with the present results. Approximate values of the Strouhal number, lift coefficient and the Drag coefficient are presented in figures (2.20), (2.21), and (2.22) which give values *0.1*, -0.1, and *1* respectively. Compared with the present results, the value of the drag coefficient is slightly higher while the lift cofficient is well predicted. The Strouhal number shows good agreement with difference of about *15%*. The difference is mainly due to the crude modelling of 'turbulent effects' which appear to be particularly significant when vortices shed by the upstream cylinder get close to the downstream one. The influence of those vortices added to those of the newly created ones on one cylinder surface is quite difficult to control using the simple model implemented in the present case, even if a the vortex strength reduction scheme is incorporated.

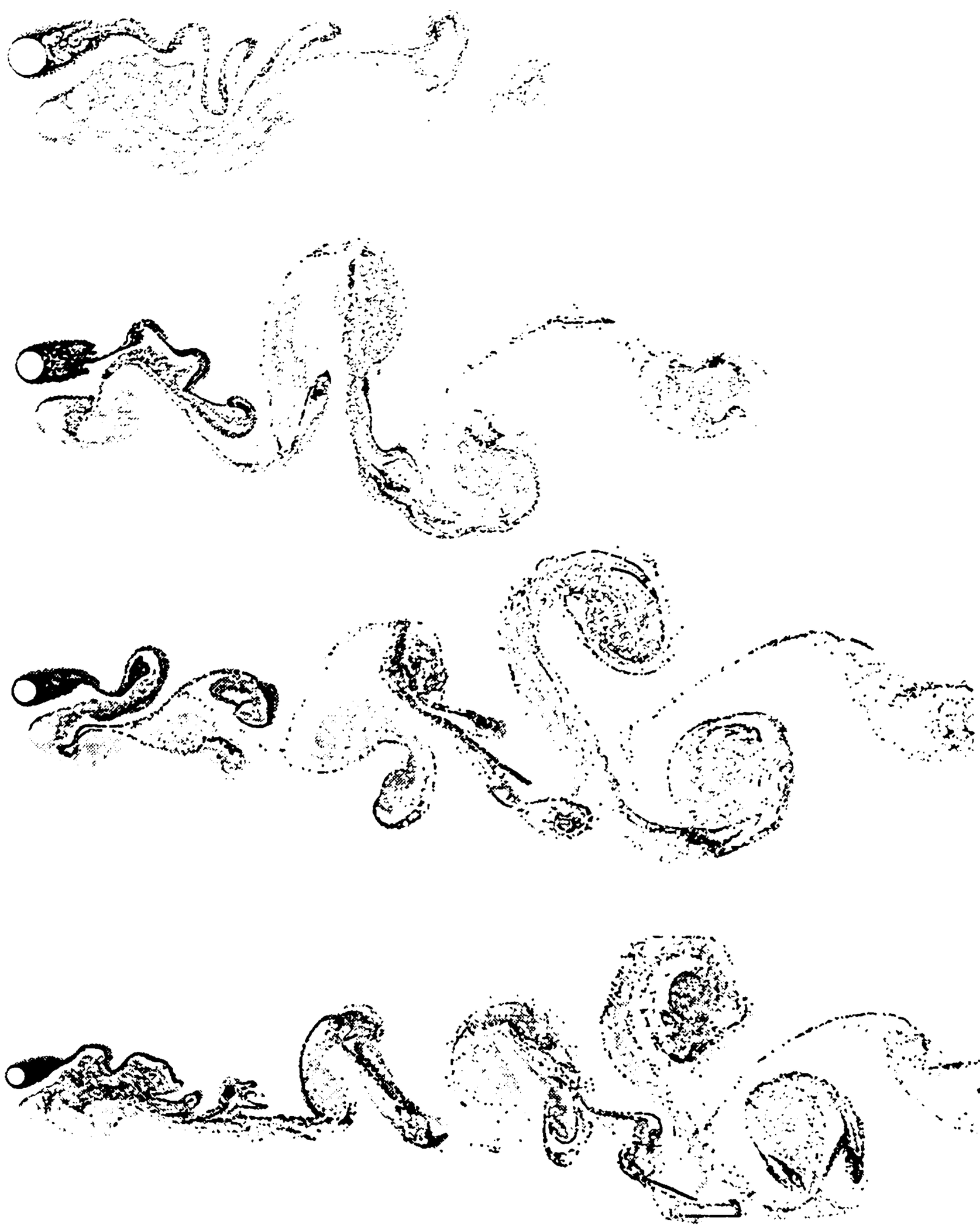

Figure 5.27.-*Flow Pattern at t = 15, 30, 45, 60 for G/D = 1. δ = 22.5 degrees, and the Force Coefficients at Re = 61000*

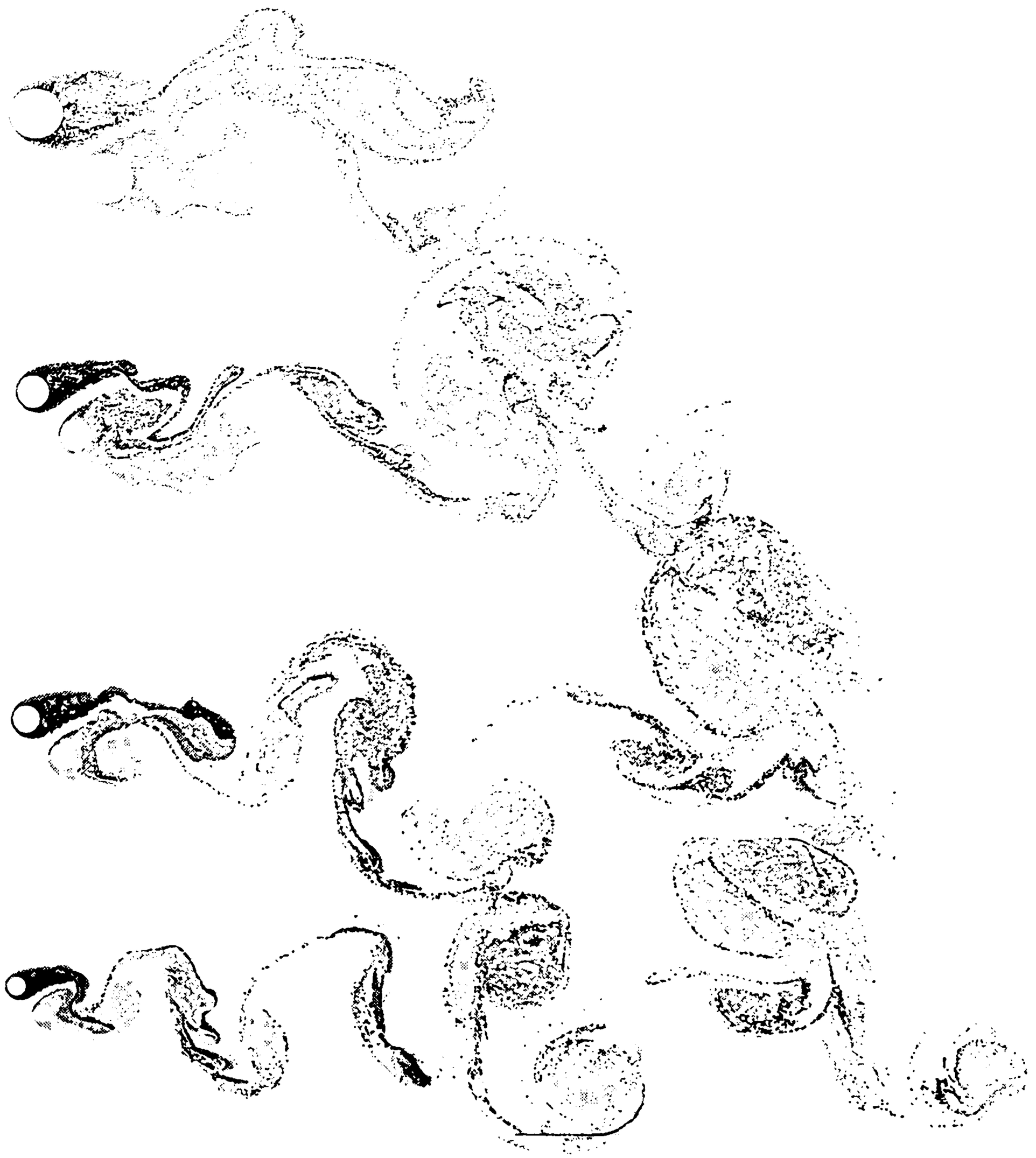

Figure 5.28.-*Flow Pattern at t = 15, 30, 45, 60 for G/D = 1. δ = 45 degrees, and the Force Coefficients at Re = 61000*

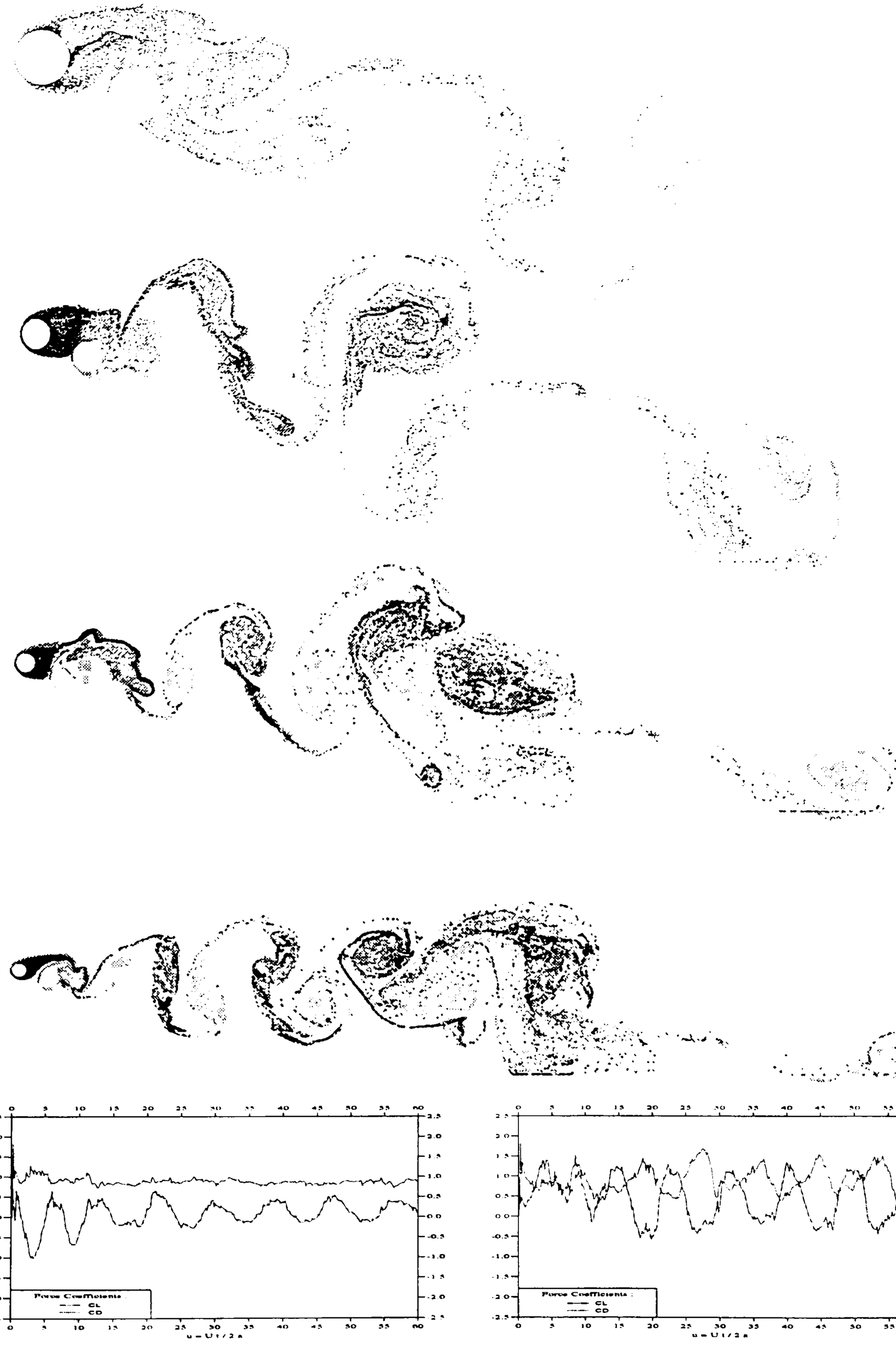

Figure 5.29.-*Flow Pattern at t = 15, 30, 45, 60 for G/D = 1, δ = 62.5 degrees, and the Force Coefficients at Re = 61000*

The effect is even more pronounced when the downstream cylinder is positioned close to the tandem arrangement as described later.

By increasing the stagger angle to $\delta = 45$ degrees, the effective gap angle is also increased which causes less domination of the vortices shed by the lower cylinder over those shed from the upper one in and around the formation region. This in turn increases the 'degree' of oscillation of the vortices shed from the upper cylinder. The effect is apparent in the graph of the force coefficients even though vortices from the upper cylinder approaching close are combined with those shed by the lower cylinder after they leave the formation region as shown in figure (**5.28**).The drag and the mean lift coefficients for the upper cylinder are 0.9 and 0.3 respectively whilst those of the lower cylinder are 1.0 and -0.2 respectively. At this stage there is no noticeable change in the Strouhal number values for either cylinder. The experimental evidence concering the shape of the formation region can be seen in figure (**2.23**) which agrees well with the present flow pattern. The drag and lift coefficient have a tendency to reduce from those given by the previous configuration as is also shown in figures (**2.20**), (**2.21**), and (**2.22**). The weakness of the model is still reflected in the value of the Strouhal number which is much less than expected.

The effect of the approaching vortices shed by the upstream cylinder can be seen to be more pronounced when the staggered angle δ is increased to 62.5 degrees, as shown in figure (**5.29**). The shape of the formation region at a similar position can also be seen in figure (**2.23**). At this position the precentage of vortices approaching the downstream cylinder is higher than in the previous positions as this is close to the tandem arrangement. It is seen that the drag coefficient of the downstream cylinder is oscillating around the mean of about 0.7. The lift coefficient is also more oscillatory with the positive mean value at 0.5 and with a Strouhal number around 1.4. From figures (**2.20**), (**2.21**), and (**2.22**), it is found that the drag coefficient is slightly higher than expected by 25%, while the mean value of lift coefficient is within 10% of the observed results. The Strouhal number is slightly higher by about 10%. The results for higher gap ratios are presented in figures (**C.4.**), (**C.5.**), and (**C.6.**) in *Appendix C*. Its seems that with wider gap, the level of interaction reduces and each cylinder behaves like a cylinder in isolation. The lift coefficient becomes more oscillatory with higher peak values.

5.9.4 Two Cylinders With Different Radii

One of the purposes in investigating the case in this section is to determine

suitable force coefficients to enable the prediction of the hydrodynamic loading on the legs of offshore jacket structures with anodes attached on them. Some experiments have been conducted by various authors, see **Downie et.al** [**29**] for steady flows and **Singh** [**90**] for oscillatory flows, in an attempt to know the hydrodynamic effect of the shape, size and configuration of the cylinder-anode combination in various types of flows. In a numerical model, **Murray** [**69**] and **Downie et.al.** [**26**] and **Tamaddon – Jahromi** [**107**] approached the problem using a conformal mapping to transform a cylinder to the 'bumped' cylinder used as the idealized shape of the cylinder-anode combination. The equation for the transformation was of the form of a Laurent series as follows,

$$\zeta = e^{i\nu}(z + \sum_{k=1}^{N_c} \frac{a_k}{z_k})$$

where N_c is the number of terms and $a_k : k = 1, 2....N_c$ are real coefficients which are known.

The coefficients were obtained by fitting the Laurent series to an envelope enclosing the cylinder and anodes. The configuration is an idealisation of one in which the gap between cylinder and anode is blocked with marine growth. They used this formulation to model a cylinder with one and two bumps. With the radii of the base cylinder and the anode of 0.5 and 0.2, their transformed shape can be considered similar to the present cylinder-anode configuration.

In the present study, this case is simply modelled, as with the cases in the previous sections, by two circular cylinders of different radii and placed closely together.

After a series of systematic trial calculations, it was found that best results are achieved when the number of elements of each cylinder is chosen in such a way that the length of the elements comprising the two cylinders should be about of the same order. This can be explained by the fact that the length of element dictates the strengths of the discrete vortices shed from the anode and the cylinder surfaces. The interaction between vortices shed from each surface is best modelled when their strengths are of a similar order. Hence, the cylinder and anode radii determine the appropriate number of elements required to model the two surfaces. With a cylinder radius of 0.5 and an anode radius of 0.2, it was found that the number of elements of 64 and 32, respectively, gave acceptable results, as described later. The distance to cylinder diameter ratio between the two centres was kept

constant and equal to *1* while the stagger angle δ was varied from -90 to *90* degrees.

The initial stage of the flow at $t = 1$ and *5* are shown in figure (**5.30**) with the anode placed at the staggered angle $\delta = 0$. The flow pattern and a comparison with that of an isolated cylinder as described in Chapter *IV*, show the effect of the presence of the anode on the wake characteristics. The anode causes the flow around the main cylinder to become asymmetrical as the velocity in the gap region is higher than that at the opposite side of the cylinder.

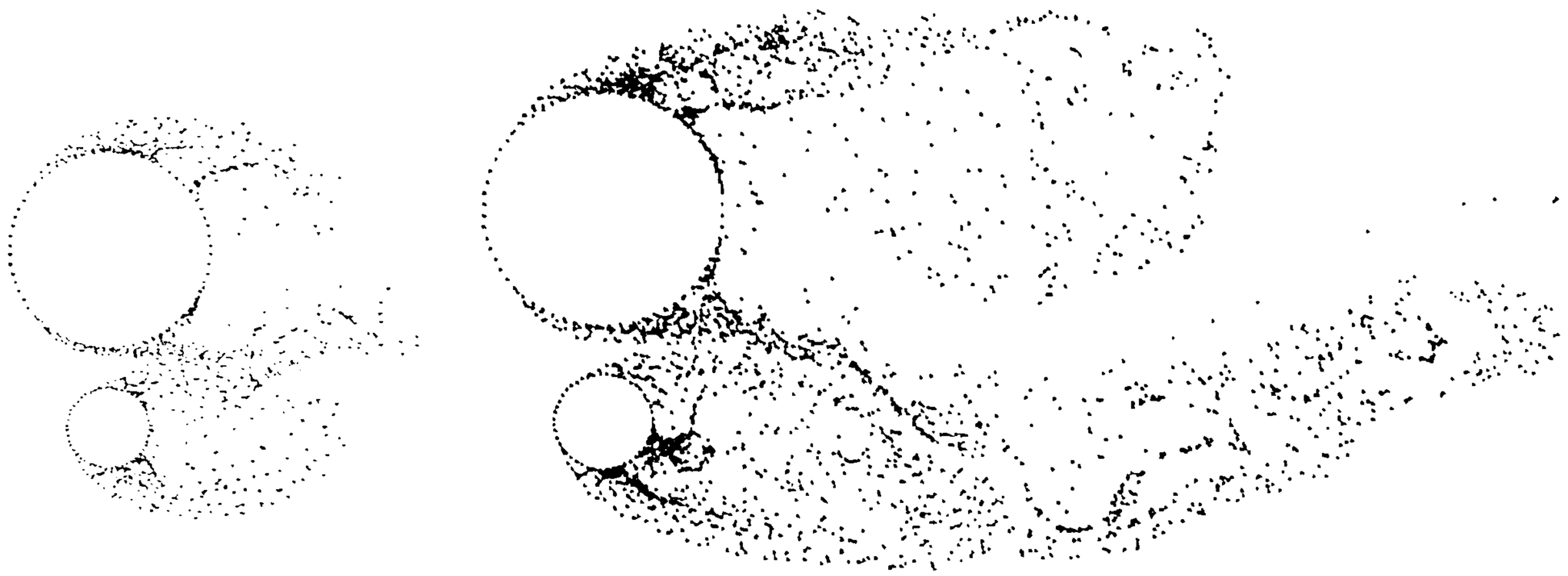

Figure 5.30 -Flow Pattern at $\hat{t} = 1$ and 5

With the number of elements of cylinder N_c and anode N_a, as stated above, and a gap ratio of $\frac{G}{D_c} = 0.3$ with Reynolds number of *100000*, at $\hat{t} = 5$ an asymmetric rolling up of vortices appears behind the cylinder, in which the vortices shed from the gap region are carried further downstream than those shed from the other side. At this stage there is no indication that rolling-up is also happening behind the anode. The flow pattern produced by the 'idealized' bumped cylinder of **Murray** [**70**] in figure (**5.31**) shows that as this is basically only a single body, there is no such 'jet' effect in the gap region as produced in figure (**5.30**)

At this stage the formation region of the cylinder is still growing and the vortices shed from the anode begin to combine and roll up together inside the

Figure 5.31 -Flow Pattern using thansformed shape by **Murray [70]**

cylinder formation region.

After $\hat{t} = 5$ some vortices are shed downstream to complete the first cycle of the shedding process. The comparison of the wake behind the cylinder with that of an isolated cylinder shows a relatively wider wake with a correspondingly higher drag for the former, as shown in the graph of the force coefficients in figure **(5.32)**. As displayed in figure **(5.32)** for $\hat{t}$ greater than 5, the vortices shed from the anode combine with the vortices shed from the cylinder to form one regular vortex shedding process. It is also shown in these figures that the influence of the anode whose shed vortices interact with those shed from the cylinder, results in a less smooth shedding pattern.

In the cylinder-anode configuration, the force coefficients for the cylinder in figure **(5.32)** show a positive mean value for the lift coefficient of 0.45. The Strouhal number cannot be determined by inspection of the curve for the lift coefficient, but at $\hat{t} = 60$ about 6 cycles of vortex shedding have been completed which equates to a Strouhal number of about 0.1. The mean value of the lift coefficient of the anode is slightly negative with -0.15 and alternating vortex shedding appears to be suppressed. As expected, due to the wider wake around the cylinder, the drag coefficient shows a higher value of about 1.55 in total, which comprises the cylinder drag coefficient of about 1.1 and that of the anode which is

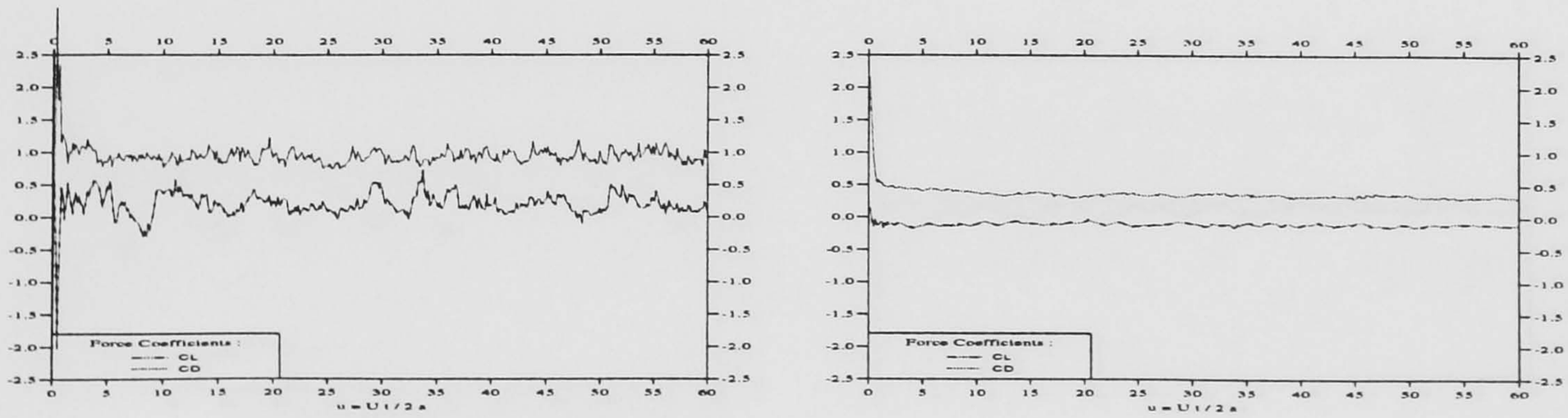

Figure 5.32.-*Flow Pattern at t = 15, 30, 45, 60, δ = 0 degrees, and the Force Coefficients at Re = 100000*

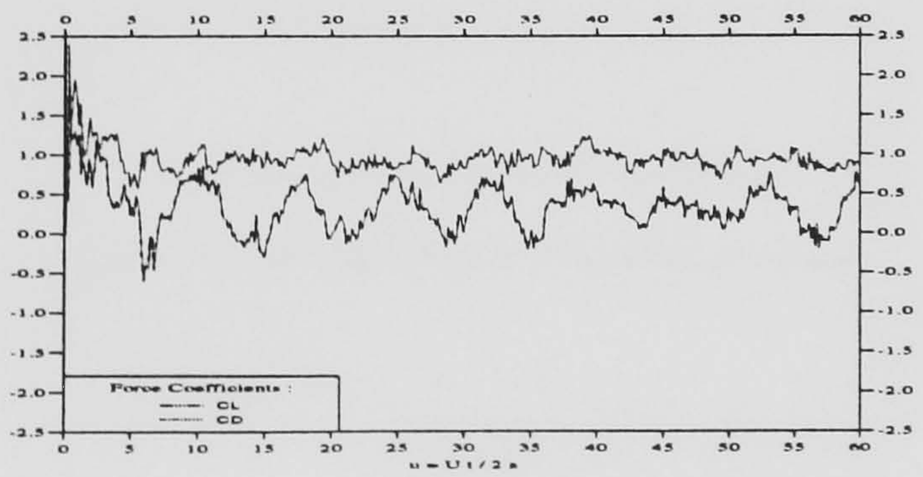

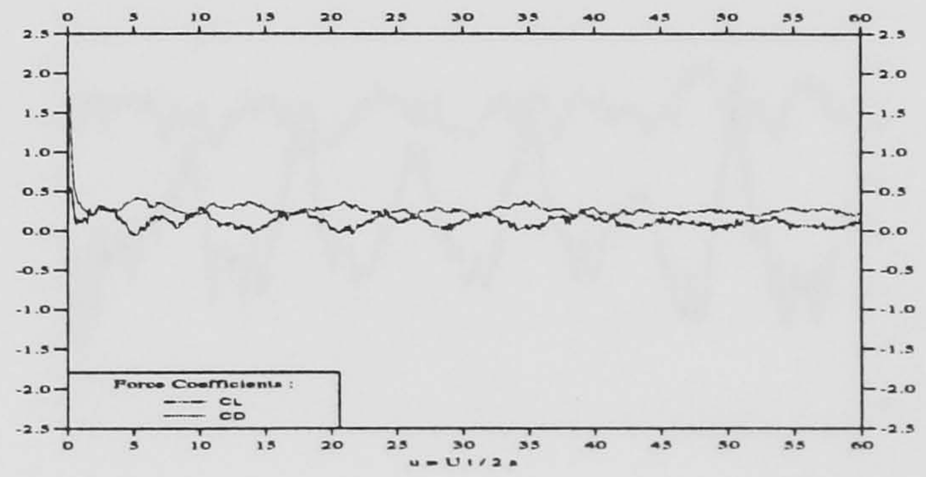

Figure 5.33.-*Flow Pattern at $t = 15, 30, 45, 60$, $\delta = 45$ degrees, and the Force Coefficients at $Re = 100000$*

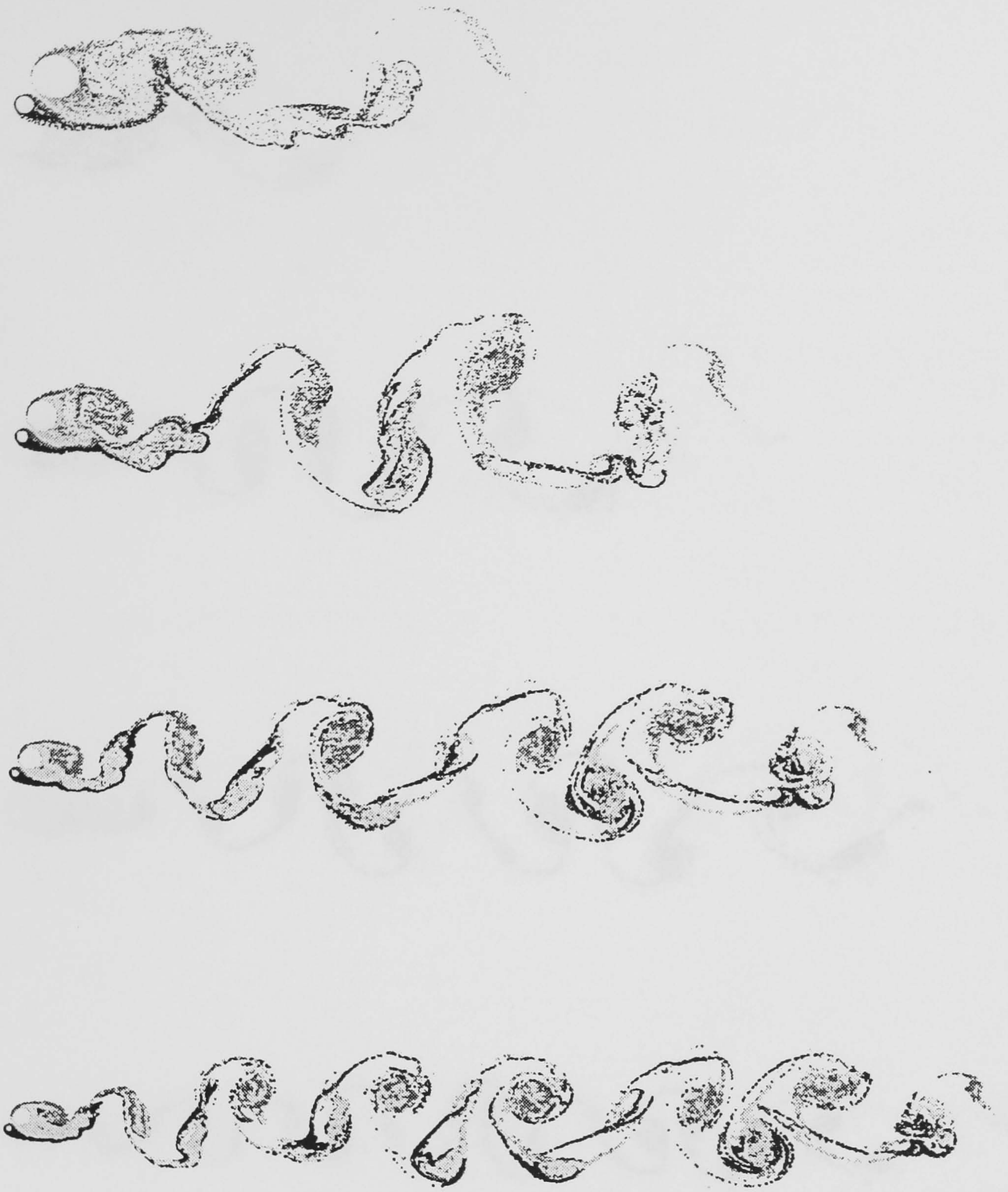

Figure 5.34.-*Flow Pattern at t = 15, 30, 45, 60, δ = -45 degrees, and the Force Coefficients at Re = 100000*

Figure 5.35.-*Flow Pattern at t = 15, 30, 45, 60, δ = 90 degrees, and the Force Coefficients at Re = 100000*

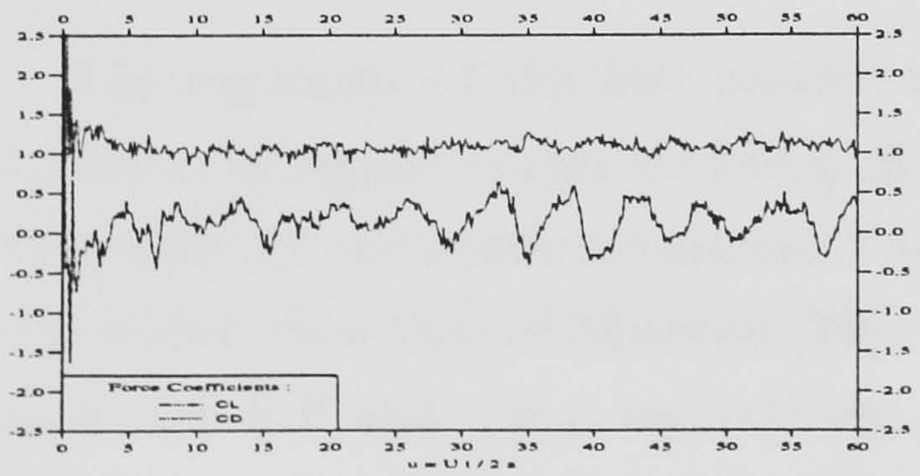

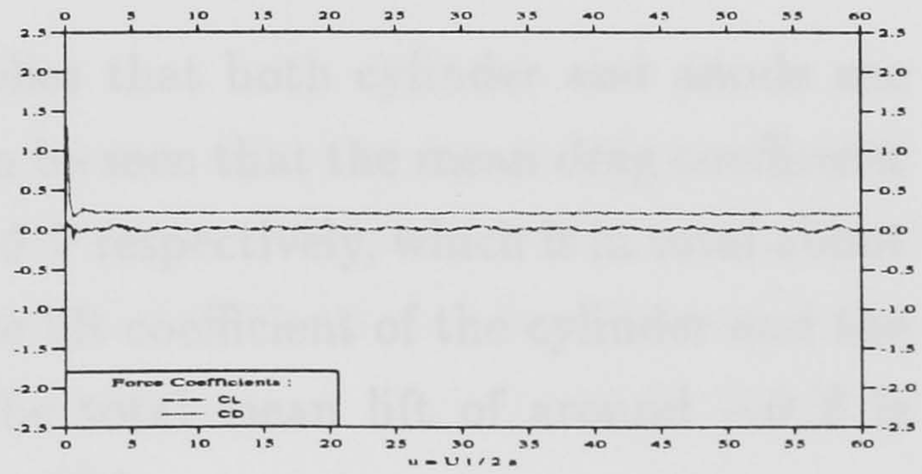

Figure 5.36.-*Flow Pattern at t = 15, 30, 45, 60, δ = -90 degrees, and the Force Coefficients at Re = 100000*

0.45 (which is normalized in respect to the cylinder diameter). Compared with the results of **Murray** [**70**], the drag coefficient is smaller by about *15*% while the lift coefficient is slightly closer with a *10*% difference.

With an increase of the stagger angle δ to *45* degrees, the oscillation of the force coefficients for both the cylinder and the anode seems to be more pronounced and regular, as expressed in the smoother flow pattern created behind them, as displayed in figure (**5.33**).

In this case, the flow pattern is similar to that of the isolated cylinder with a slightly wider formation region, due to the presence of the anode. It can also be seen that vortices shed from the anode are carried inside the cylinder formation region and form a combined flow pattern behind the cylinder.

The mean value of the cylinder drag coefficient is about *1.05* while that of the anode is around *0.1*. In other words, the drag coefficient for the whole configuration is *1.25* in total. The mean lift coefficient for the cylinder shows a positive value of about *0.25* with a mean maximum magnitude of around *0.7*. The Strouhal number is much more identifiable from the force trace compared with the previous case and shows a value of around *0.12*. The mean anode lift coefficient indicates a positive value of around *0.1* which means that both the cylinder and the anode experience positive mean lift coefficients. This configuration can then be compared to a wing section with a positive angle of attack. The mean extreme value of the anode lift coefficient is seen to oscillate between ± 0.2 with a slightly higher Strouhal number of around *0.17*. The value of the drag coefficient from **Murray** [**70**] is around *1.2* with the mean lift coefficient of *0.1*

The effect of the anode when it is placed in front the cylinder is represented in figure (**5.34**), where the staggered angle δ is -45 degrees.

The regularity of the flow pattern implies that both cylinder and anode are experiencing regular vortex shedding. It can be seen that the mean drag coefficient of the cylinder and anode are around *2* and *0.7* respectively, which is in total about *15*% higher than that of **Murray** [**70**]. The lift coefficient of the cylinder and the anode are *0.2* and -0.4 respectively. The total mean lift of around -0.2 is slightly less than that reported by **Murray** [**70**].

In the case where the anode is exactly behind the cylinder, or $\delta = 90$ degrees as shown in figure (**5.35**), or when it is exactly in front of the cylinder with $\delta = -90$ degrees as shown in figure (**5.36**), the anode will act as a splitter plate or turbulence

generater respectively, and this according to **Downie et.al** [**29**] will tend to reduce the total drag coefficient.

With the value of the cylinder drag coefficient of *0.8* and *0.1* for the anode, the total agrees with that reported by **Murray** [**70**] within about *5%*. The flow pattern is also shown to be regular. Vortices shed from the anode are seen to be carried along a path following the curve of the cylinder formation region before they are combined in the single Karman vortex street.

5.10 Conclusion

An extension of the discrete vortex model for investigating the flow around two cylinders in infinite fluid has been presented in this chapter. The interaction between the two cylinders and their shed vortices has been computed through the use of three overlaping grids. Two polar grids, expanding from each cylinder, are constructed in a similar way as described in the previous chapter. The third , a uniform rectangular grid, is arranged to overlap the other two. Vortices shed from one cylinder are stored in one array, while those shed from the other are stored separately through out the whole of the calculation time. Their positions referred to their own polar grid and also to the rectangular grid are also stored in different arrays.

The influence of the vortices shed from the originating cylinder is computed using the polar grid while that of those shed from the other cylinder is computed using the rectangular one. Results of the computation are grid dependent. Extensive calculations to determine the influence of grid size have been carried out. The scale of the grids have been chosen to give satisfactory flow definition with as small a CPU time as possible. It has also been found that the early development of flows involving the interaction of wakes from more than one cylinder can be enhanced if a vortex reduction scheme is implemented.

The incorporation of vortex reduction scheme achieves a reduction in vortex strength that can be attributed to the effect of the wake interaction in the form of turbulent dissipation and three dimensional deformation, which is more pronounced in two cylinder cases than for single cylinders in unbounded flows.

In the side-by-side arrangements, the out-of-phase asymmetric Karman vortex street behind the cylinders can be achieved, as shown in figures for the convection-only cases in which neither the Random Walk, simulating the diffusion process, nor the vortex strength reduction scheme are yet included. This can be considered

to model the flow at very high Reynolds number. After the incorporation of the Random Walk scheme, for computing intermediate Reynolds number flows, the asymmetry of the flow could not be maintained without the involvement of the Vortex Strength Reduction scheme. It appears that vortices with large strengths generated by each cylinder in the early stages of the flow interact to cause instabilities in its subsequent development.

The effect of the interaction of the two cylinders further apart than $0.5D$, can be reasonably well represented with the present model even though the magnitudes of the force coefficients are slightly on the low side. However, when two equal cylinders are closer than $0.5D$, the complicated effect of the boundary layer interactions could not be approached realistically using the present model.

In the case of the cylinders arranged in Tandem, the model gives good results for the gap ratio of $\frac{G}{D}$ less than 2.5, which is called the critical gap ratio. The thrust of the downstream cylinder becomes negative when the vortices shed by the upstream cylinder approach the downstream one and this is basically in line with the experimental evidence. At higher gap ratios, the model again fails to achieve good results because the oscillating wake developing in the formation region of the upstream cylinder, causes instability in the development of the flow from the downstream cylinder which results in unrealistic flow patterns and force coefficients.

Fairly good results are also achieved for the staggered cylinder configuration, where the value of the force coefficients are quite close to the experimental evidence. The Strouhal number, on the other hand, shows values lower than experimental results by about $10 - 50\%$. The author has been unable to find information about the flow pattern for this arrangement except for the region in close proximity to the cylinder which agrees well with results given by this model.

Although efforts have been made to validate the model against experimental evidence, the numerical results should be seen in the context of the limitations of the model. In the first place it models two dimensional flow, whereas experiments have to involve three dimensional flow. Secondly, the algorithm is highly computationally intensive and so there are practical limits as to how many cycles of the flow can be computed. It is evident that the impulsive started flows can produce vortices that cause instabilities in the flow development. It is possible that if the computation were allowed to run for a sufficient number of cycles, the flow would settle down to a satisfactory flow pattern. One of the main difficulties in

implementing the present model has been in achieving results within practical time limits. As has been mentioned already, the algorithm does not include explicitly a turbulence model. Results resembling experimental results have been achieved over a wide range, but inevitably there are flow configurations for which turbulence effects will not allow representation of the flow in this manner.

Finally, in this case study involving two cylinder problems, only unidirectional flow is treated. This is because, according to the author's knowledge, there is no complete data available describing the hydrodynamic effects of two cylinders in oscillatory flows.

Chapter VI

THE FLOW AROUND A CYLINDER IN A BOUNDED FLUID

6.1 General Description; the Blockage Effects

6.1.1 A Cylinder In A Channel

The flow past a cylinder immersed in a stream bounded by rigid walls is subject to what is commonly called the blockage effect. The rigid walls prevent a free lateral displacement of the fluid particle by the cylinder, in the neighbourhood of which velocities are higher than they would be in an unbounded stream. The overall effect is an increase in the free stream velocity, relative to the unbounded flow, which is related partly to the volume distribution of the body itself (solid blockage), and partly to the displacement effect of the wake (wake blockage).

Glauert[35] proposed that the Drag Coefficient C_d in an unbounded stream is related to the drag C_{d_w} in a wind tunnel by

$$C_d = C_{d_w}\left(1 - \frac{\eta t}{h}\right)^2$$

where t is the thickness of the bluff body, h is the tunnel height, η is an empirical factor which is found experimentally.

Maskell[65] developed a theory for the blockage of the flow past a bluff body in a closed wind tunnel involving an approximate relation describing the momentum balance in the flow outside the wake. As a results of his experiments he proposed the correction formula ;

$$\frac{\Delta P}{P} = \varepsilon C_d \frac{s}{c}$$

where, ΔP is the effective increase in dynamic pressure due to the blockage constraint, and ε is a blockage factor dependent on the magnitude of the base pressure coefficient. The factor ε is shown to range between $\frac{5}{2}$ for axi-symmetric flow to 1 for two dimensional flow, In addition, s is the area on which the profile drag coefficient C_d is based, and c is the cross-sectional area of the tunnel.

Downie et.al. [**29**], in the experiment carried out at the Imperial College London, used a correction for the blockage effect based on a function of the blockage ratio taken as the frontal area of the model to the cross section of the wind tunnel working station, which varied between *5%* to *10%*.

The formula used was as follow,

$$C_d^{corrected} = \frac{C_d^{measured}}{(1+\epsilon)^2} = (1-2\epsilon)\, C_d^{measured}$$

where $\epsilon = \frac{A}{2A_T}\, C_d^{measured}$, A is the reference frontal area of the model and A_T is the cross sectional area of the wind tunnel.

The presence of walls close to a cylinder in a flow induces a significant effect on the cylinder and the flow characteristics.

Stansby and **Slaouti**[**102**] modelled a flow with blockage using a discrete vortex method in which the convection velocities were computed using a vortex-in-cell method involving the solution of the Poisson equation. Diffusion was simulated by imposing random walks on each vortex in two orthogonal directions in a polar co-ordinate grid system. To model the boundaries, they used an overlapping system of rectangular and polar meshes. The outer mesh and the intermediate mesh were rectangular and the inner mesh was polar. Constant stream function values were imposed on the upper and lower boundaries.

Spalart [**95**], proposed another approach in which the wall boundary condition of parallel flow may be obtained by reflection and modelling the flow as two interlaced casades in which the pitch, the distance between two image bodies both above the upper wall and below the lower wall, is equal to the wall distance. Since the solution is the same for all wall reflections (but inverted), the Martensen equation as shown in equation (**4.6**) may be applied with relatively simple modifications to the code. However, the approach has some limitations when the vortex-in-cell scheme is implemented in relation to calculating the vortex velocity. This is due to the fact that the node-to-node interaction is used instead of the vortex to vortex interaction. The difficulty will arise when the node points are located outside the fluid domain. This could happen since the node points can lie outside the two walls even though a point vortex is still located inside. Another restriction is that this method can only be used for the case of the cylinder placed half way between

the two walls since the coupling coefficient was derived in the same way as for the cascade case.

The numerical results from **Stansby** and **Slaouti** [**102**] show that , for a cylinder placed between two walls in a uniform free stream, when the distance between the walls is greater than *16* diameters, the blockage effect is negligible. This would not be the case for blockage corrections based on steady flow condition where a blockage ratio $\frac{G}{D}$ (the ratio of the distance between walls G to cylinder diameter D) of *14* would give an effective increase in the free stream velocity of about *4*% at a Reynolds number of 10^4. It would also cause an increase in the drag of about *8* per cent. At a Reynolds number of *100* with a blockage ratio of *16*, the mean drag increases as much as *2.5*%. More significant increases in the mean drag exist for blockage ratios less than *8*. At blockage ratios of *8*, *4*, and *2*, the mean drag increases as much as *10*, *43* and *210*% respectively. The effect of the blockage on the Strouhal number shows a quite different trend. Increasing the blockage (reducing the blockage ratio) is seen to increase the Strouhal number down to a blockage ratio of about *4*%, while a blockage ratio of *2* has a lower Strouhal number than a blockage ratio of *4*.

In the present study, the walls are modelled by source distributions extending from $-\infty$ to ∞ as described in *Appendix A*. No boundary layer simulation is done on the wall as the aim of this study is only to investigate the blockage effect. The complex potential used comprises the contributions from the free stream velocity u_∞, the cylinder surface vorticity γ_n, the wall surface sources σ_w and the shed vortices Γ_ν, as follows,

$$w(z) = u_\infty e^{-i\alpha_\infty} z + \frac{i}{2\pi}\sum_{e=1}^{N_e}\gamma_e dS_e \ln(z-z_e) + \frac{1}{2\pi}\sum_{g=1}^{M_w}\sum_{w=1}^{N_w^g}\sigma_w^g dS_w^g \ln(z-z_w^g) +$$

$$\frac{i}{2\pi}\sum_{\nu=1}^{N_\nu}\Gamma_\nu \ln(z-z_\nu) \qquad \textbf{(6.1a)}$$

The strengths of a vortex γ_n and a source σ_w^g at element w of wall g in this equation can be calculated by satisfying the Dirichlet boundary condition of zero tangential velocity on the cylinder surface and the Neumann boundary condition of zero normal velocity along the wall. M_w shows the number of walls for the case

to be analysed. M_w equal to one is for the case of the flow around cylinders near a plane wall while for M_w equal two is for cylinders in channel.

An overlaping polar/rectangular grid system as used in the previous chapter can still be implemented. In this chapter, the size of the rectangular grid segment is now equal to the size of the wall element. The surface vorticity is then introduced into the flow field using the same procedure mentioned in section (**4.4**).

The velocity of a vortex can now be calculated through the use of the polar and the rectangular grid nodes as before. The addition contribution from the wall sources is implemented using the rectangular grid nodes. This implies that a bilinear interpolation and reinterpolation in polar and rectangular coordinates is needed to distribute and redistribute the vortex strength and velocity onto two grid node systems as explained in detail in the following sections.

The force coefficients can then be calculated using the same method as before by integrating the pressure distribution from the stagnation point to around the cylinder surface.

6.1.2 A Cylinder Near A Plane Boundary

As mentioned earlier, it is a fact that when a cylinder is placed near a wall, the flow around and force on the cylinder can change significantly. This interference is partly due to the increase of the surrounding velocity and partly due to the influence of the reflected periodic wake. The change of the boundary layer characteristics either of the cylinder or of the wall can add to the complexity of the interaction.

A potential flow scheme has been used to model this kind of configuration by **Yamamoto et.al.** [**113**] for the case of low Reynolds numbers. The use of this model in this regime may be justified on the grounds that there is no separation and the flow resembles to some extent the stream-line flow. However, it should be noted that low Reynolds number flows differs considerably from potential flow due to the presence of viscous boundary layers. By applying the method of images, the motion along the wall may be approximated with two doublets with their axes in the direction of motion. When the doublets approach each other they no longer represent circular cylinders, because of mutual interference. In order to eliminate this influence, a distribution of an infinite series of doublets of converging strengths along the cylinder radius is required. Therefore, the flow around a circular cylinder placed closely to a wall can be expressed as a properly distributed infinite series of

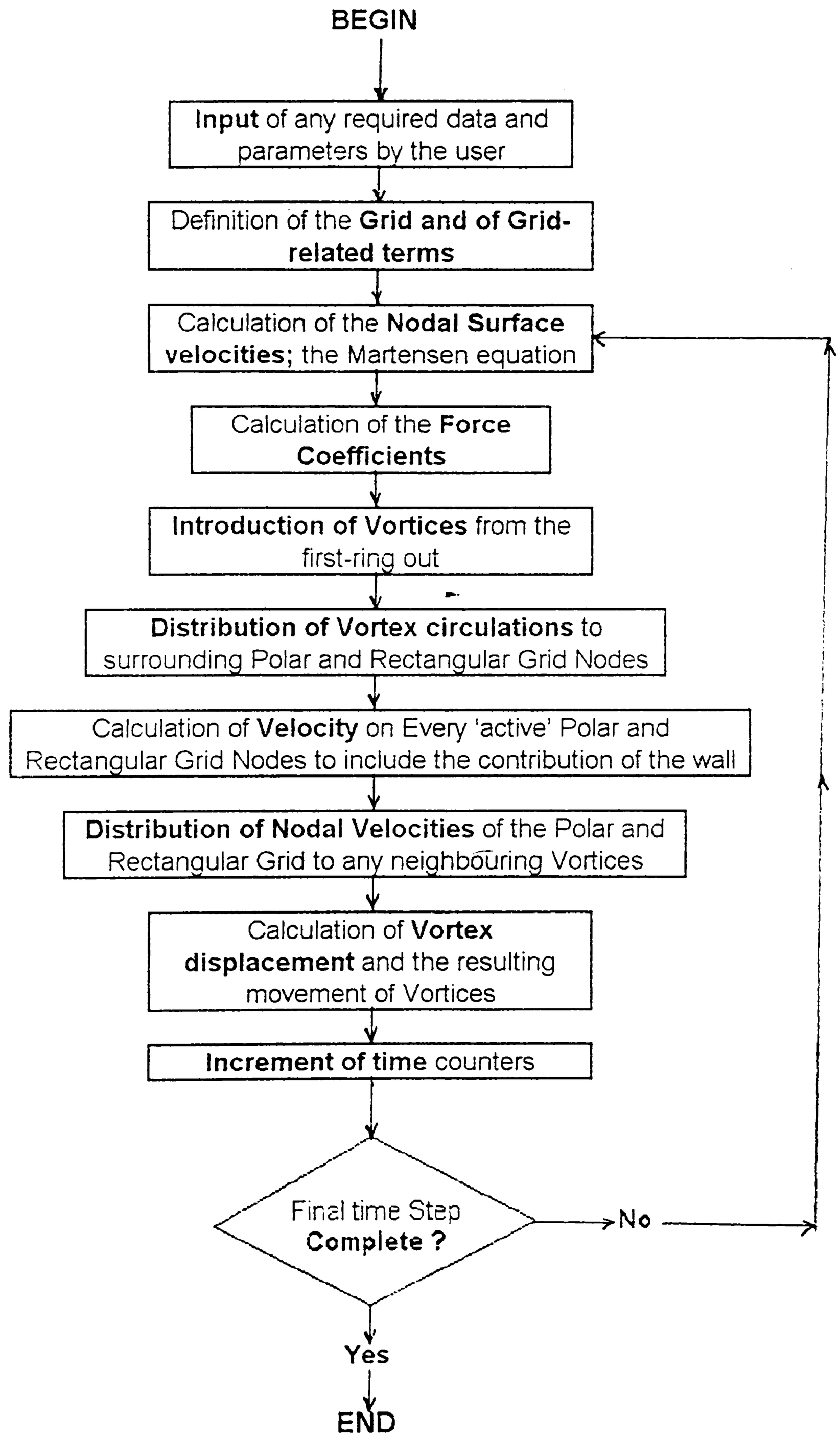

Figure 6.1.-The Flow Chart of the Numerical Method

doublets. The force coefficients can then be calculated through the use of Blasius equation by directly substituting and integrating the complex potential around the circumference of the cylinder.

Efthymiou and **Narayanan** [**31**][**32**] and **Ali** and **Narayanan** [**1**] analysed this problem using a discrete vortex model. Their model contains an approximation as an infinite number of image vortices must be introduced in order to satisfy the impermiability condition on the cylinder surface and on the plane boundary. However, in the numerical calculations a finite number of images of about *9* is found to be sufficient because, as image vortices of equal and opposite strengths approach each other, a complete cancellation of the vortex pair results. **Stansby** [**98**] also used a similar approximation to model the flow around two cylinders arranged normal to the free stream. He claimed an accuracy of the *zero* normal velocity condition as small as 10^{-6} is achieved by using the same number of images as mentioned above.

Another method, which has been adopted in this study, is the distribution of source elements along the wall as described in the previous section by simply removing the top wall from the domain. Using an equation similar to equation (**6.1a**) above, the Neumann boundary condition along the wall and the Dirichlet boundary condition along the cylinder circumference can be satisfied simultaneously.

As described earlier, the advantage of using this scheme is its flexibility in the modelling of various wall geometries without major changes to the scheme. For instance sea bed scouring under sub-sea pipelines could be easily modified. The basic procedure of this scheme is exactly the same as that of the previous section. The only difference is the absence of the top wall source contribution which reduces the complex potential equation (**6.1a**) to

$$w(z) = u_\infty e^{-i\alpha_\infty} z + \frac{i}{2\pi}\sum_{e=1}^{N_e} \gamma_e dS_e \ln(z - z_e) + \frac{1}{2\pi}\sum_{w=1}^{N_w^1} \sigma_w^1 dS_w^1 \ln(z - z_w^1) +$$

$$\frac{i}{2\pi}\sum_{\nu=1}^{N_\nu} \Gamma_\nu \ln(z - z_\nu) \qquad \textbf{(6.1b)}$$

in which N_w^1 shows the number of element of the bottom wall.

6.2 Numerical Formulation

As there are two different boundary boundary conditions imposed on the circumference of the cylinders and on the walls, the Martensen equation (4.6) should be further modified and separated into two expressions to take into account the influence of the wall as follow.

$$-\frac{1}{2}\gamma_m + \oint_c k_{mn}\gamma_n dS_n + \oint_c k_{mw}\sigma_w dS_w + \vec{u}_\infty \cdot \vec{d}S_m + \sum_{\nu}^{N_\nu} l_{m\nu}\Gamma_\nu = 0 \qquad (6.2)$$

and

$$\frac{1}{2}\sigma_v + \oint_c k'_{vn}\gamma_n dS_n + \oint_{c'} k'_{vw}\sigma_w dS_w + \vec{u}_\infty \cdot \vec{d}S^n_v + \sum_{\nu}^{N_\nu} l_{v\nu}\Gamma_\nu = 0 \qquad (6.3)$$

in which k'_{vn}, k'_{vw} and k_{mw} are the kernels of the integrals which are decribed later, σ_w is the strength of the wall source at point w, $\vec{d}S_m$ is the tangential direction vector of the cylinder element m, while $\vec{d}S^n_v$ is the normal direction vector of the wall element ν. This integration is taken along a closed curve joining the top wall from $-\infty$ to ∞, the circumference of the cylinders and the bottom wall from $-\infty$ to ∞, as shown in figure (**A.2**) in the *Appendix A*.

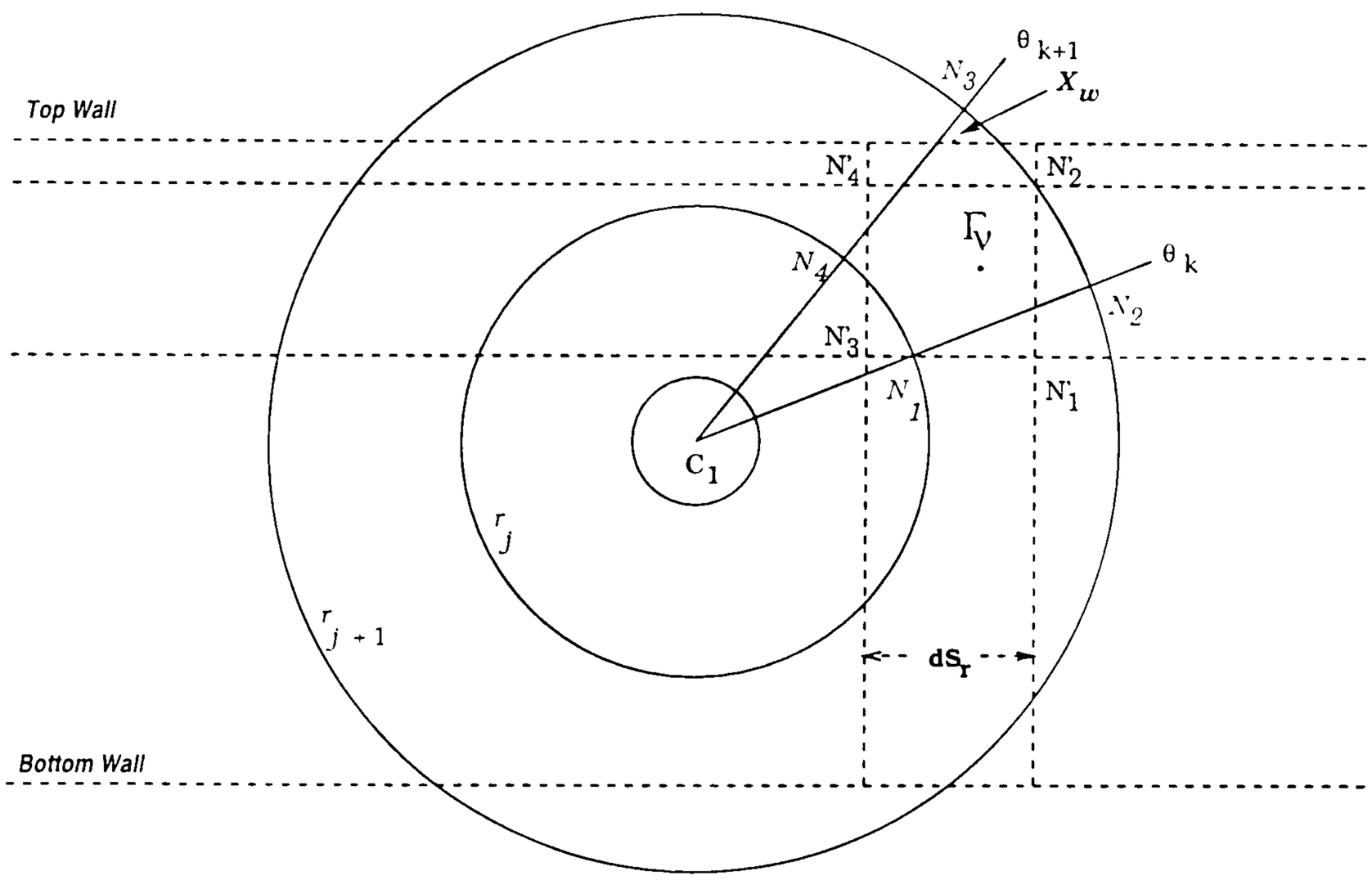

Figure 6.2.- *The Overlaping Grid System*

Due to the nature of the kernel functions above, which are asymptotically equal to zero as the distance approaches infinity, the integration reduces to the integrals around the cylinders surface and the two walls only.

It is seen from equations (**6.2**) and (**6.3**) above, that this modified Martensen equation cannot be solved independently since each equation contains two unknowns, γ_n and σ_w. Therefore the Dirichlet boundary condition of zero tangential velocity on the circumference of the cylinders implied in equation (**5.2**) and the Neumann boundary condition of zero normal velocity along the walls implied in equation (**6.3**) are solved simultaneously.

The wall boundary condition can be specified in terms of the velocity potential as,

$$\frac{\partial \phi}{\partial n} = 0 \tag{6.4}$$

Equations (**6.2**) and (**6.3**) can now be written in the discrete form based on the fact that the integration along the two vertical lines connecting the two walls at infinity sums to zero. As the source strengths far distant from the cylinders are relatively small, their contribution is neglected beyond a cut-off at a certain finite distance from the cylinders, which produces a finite number of wall elements N_w as as follows,

$$\sum_{n=1}^{N_e} k_{mn}\gamma_n dS_n + \sum_{h=1}^{M_w}\sum_{w=1}^{N_w^h} k_{mw}^h \sigma_w^h dS_w^h + \Re(u_\infty e^{-i(\alpha_\infty - \beta_m)}) + \sum_{\nu=1}^{N_\nu} l_{m\nu}\Gamma_\nu = 0 \quad (\mathbf{6.5})$$

to satisfy the Dirichlet boundary condition at element m of the cylinder circumference and

$$\sum_{n=1}^{N_e} k'^{g}_{vn}\gamma_n dS_n + \sum_{h=1}^{M_w}\sum_{w=1}^{N_w^h} k'^{gh}_{vw}\sigma_w^h dS_w^h + \Re(u_\infty e^{-i(\alpha_\infty - \beta_v^g)}) + \sum_{\nu=1}^{N_\nu} l'^{g}_{v\nu}\Gamma_\nu = 0 \quad (\mathbf{6.6})$$

to satisfy the Neumann boundary condition at element v of the wall g. The criterion for selecting the cut-off is discussed in section (**5.7.1**). To find the unknown

value of the vortex strength γ_n and the source strength σ_v, these equations can now be expressed in the matrix form as follows

$$\begin{pmatrix} K_{mn} & K'^{1}_{mv} & K'^{2}_{mw} \\ K'^{1}_{vn} & K'^{11}_{v_1 v_2} & K'^{12}_{vw} \\ K'^{2}_{wn} & K'^{21}_{wv} & K'^{22}_{w_1 w_2} \end{pmatrix} \begin{pmatrix} \gamma_n \\ \sigma_v^1 \\ \sigma_w^2 \end{pmatrix} = \begin{pmatrix} RHS \\ RHS^1 \\ RHS^2 \end{pmatrix} \qquad \textbf{(6.7a)}$$

where the components inside the matrix are all submatrices with *1*, *2* signifying the bottom and top wall respectively. As mentioned before, a value of M_w equal to one will refer to the case of a cylinder *near a plane wall* while M_w equals two will signify a cylinder *in channel.*

For the case of cylinders placed close to a plane wall, the only difference is the absence of the top wall source distribution and this will reduce the size of matrix equation (**6.7a**) to be,

$$\begin{pmatrix} K_{mn} & K'^{1}_{mv} \\ K'^{1}_{vn} & K'^{11}_{v_1 v_2} \end{pmatrix} \begin{pmatrix} \gamma_n^q \\ \sigma_v^g \end{pmatrix} = \begin{pmatrix} RHS \\ RHS^1 \end{pmatrix} \qquad \textbf{(6.7b)}$$

The coupling coefficients representing the induced velocity at pivoting point m or n of the cylinder and at pivoting point v or w along the wall are then given by;

$$k_{mn} = \Re\left(\frac{i\gamma_n}{2\pi}\frac{\Delta S_n e^{i\beta_m}}{z_m - z_n}\right)$$

$$k_{mw} = \Re\left(\frac{\sigma_w}{2\pi}\frac{\Delta S_w e^{i\beta_m}}{z_m - z_w}\right)$$

$$k'_{vn} = -\Im\left(\frac{i\gamma_n}{2\pi}\frac{\Delta S_n}{z_v - z_n}\right) \qquad \textbf{(6.8)}$$

$$k'_{vw} = -\Im\left(\frac{\sigma_w}{2\pi}\frac{\Delta S_w}{z_v - z_w}\right)$$

In this matrix k_{mn} shows the coupling coefficient at element m of cylinder due to a vortex located at element n. k_{mv} and k_{mw} are coefficients associated with

sources located at the top and bottom wall element respectively. k'_{vn} and k'_{wn} are the coupling coefficients imposing the zero normal velocity along the walls, due to the vortex along the cylinder circumference.

The coupling coefficients in the remaining blocks of the matrix describe the wall to wall source element interactions including the effect of the presence of one wall element on another.

There are two components inside the two RHS^1 and RHS^2 blocks which contain the contribution of the free stream and the shed vortices as indicated in equation (**6.5**) and (**6.6**) above. The coupling coefficients $l_{m\nu}$ and l'_{wv} are similar to k_{mn} and k'_{vn} but with the value of Γ_ν replaced by $\gamma_n \Delta S_n$.

Upon definition of all components inside the matrix equation (**5.8**) above, the unknown vortex and source strength γ_n and σ_v can be calculated through,

$$[\gamma_n, \sigma_n] = [K_{mn}]^{-1} [RHS] \tag{6.9}$$

where K_{mn} is the left hand side matrix in equation (**6.5**), (**6.6**).

6.3 Segmentation of the Domain

It can be seen from equations (**6.1a**) and (**6.1b**) that after shedding vortices the order of $M_w\ N_w$ operations must be carried out when performing the velocity calculation for a vortex due to the contribution of a wall source only. Involving the contribution of the shed vortices, the number of operations will be this number added by $N_v + 1$, the number of vortices in the flow, if mutual vortex interaction is used. The final total number of operation will be this number multiplied by the number of shed vortices N_ν.

Using rectangular grid nodes similar to those described in chapter IV, as shown in figure (**6.3**) below, this number could be reduced by replacing the factor $N_v + 1$ with $\sum_{j,k} N_{j,k} + 1$ which is obviously a smaller number.

About the same amount of saving can also be found during the source strength calculation in the component of the RHS of equation (**5.9**) from the contribution of the shed vortices which also use the rectangular grid elements.

The efficiency obtained from the cylinder-vortices interaction described in chapter IV has to be added to get the whole saving of the CPU time as it involves a similar process and uses the same number of operations.

It is shown in figure (**6.2**) that the size of the rectangular grid segment is arranged to be equal to the length of the wall source element. This means that the rectangular and wall element are uniform throughout the whole fluid domain. The first row of the rectangular grid nodes next to the wall are arranged in such a way as to give the best visualisation of the flow pattern. A systematic sensitivity study showed that the vortex sheet approached the wall tangentially if the first ring out of the rectangular grid spacing was chosen to equal that of the element lengths on the cylinder surface. This condition was adopted for the case studies described later.

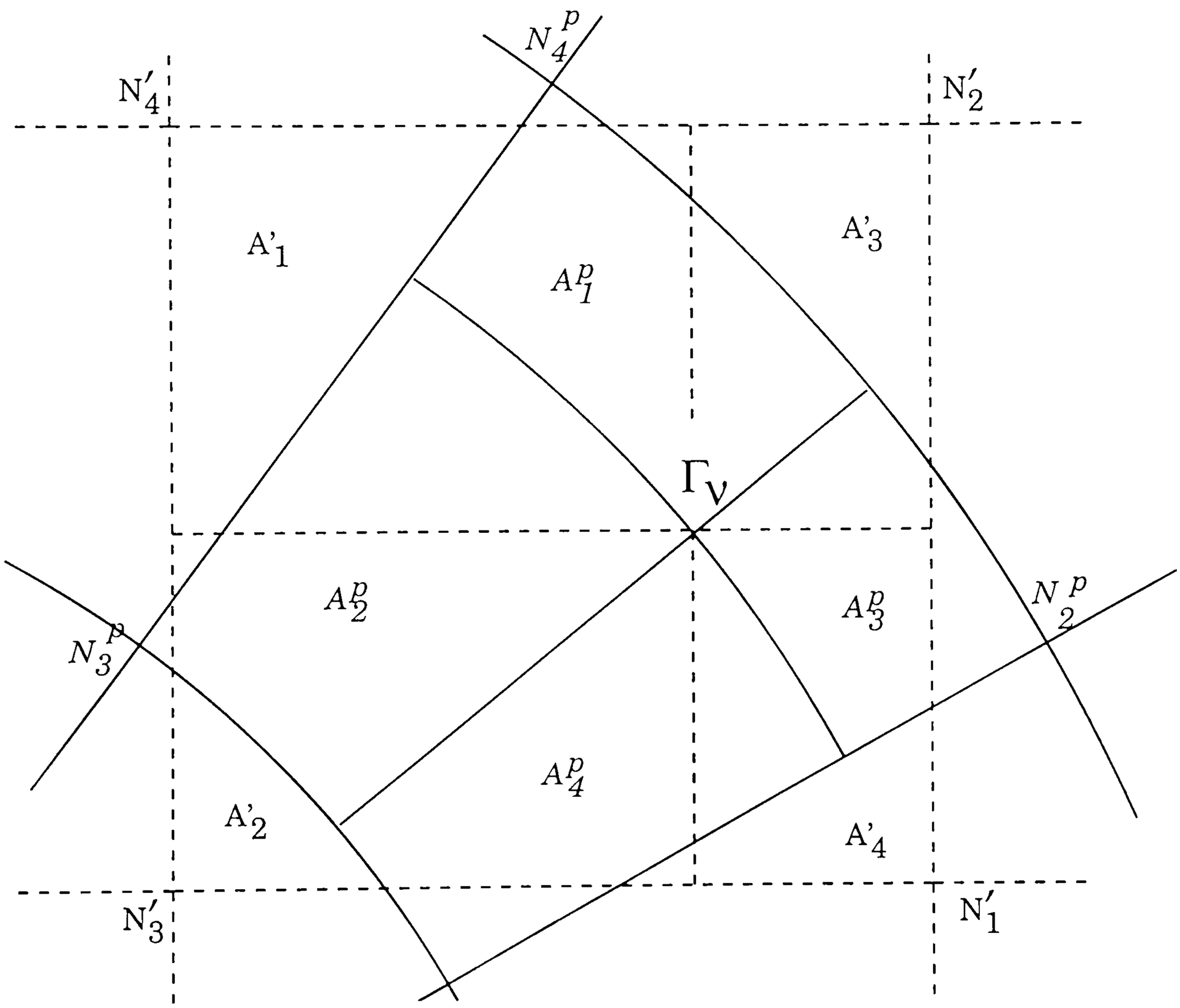

Figure 6.3.- *The Grid Element*

6.4 Introduction of Vortices Into the Flow

As described earlier, the discrete vortices are introduced into the flow so that the position of separation and the trajectory of the separated shear layer are consistent with the experimental results. In fact, those phenomena are determined by complex fluid motions in the boundary layer involving a delicate balance between convection and diffusion, with the added important influence of the local surface static pressure gradient.

The technique implemented in Chapter *IV* is still adopted, since the release of vortices from the second ring allows computation of the flow without explicitly specifying unsteady separation from the cylinder surface. Unsteady separation implies a variable separation position moving periodically due to the upstream influence from the wake, which in turn. determines the wake pattern and the velocity in the whole fluid domain.

The presence of walls in close proximity to the cylinder obviously changes the wake behaviour behind the cylinder. This is partly due to the effective increase in local velocity and partly due to interference from the reflected periodic wake.

In this simple model in the present study, only the '*blockage*' effect is considered and all the effects of the boundary layer interaction between cylinder and wall are ignored although Reynolds number effects are implicit in the choice of various model parameters such as the element lengths and grid dimensions. These have been largely specified on the basis of previous work (**Downie** [26] and **Murray** [70]) and sensitivity studies.

6.5 Distribution of Circulation to the Grid

As the grid structure is based on the one described in section (**4.3**), the distribution of the circulation to the grid is done in the same way as described in chapter *IV*. This means that the strength of a vortex is distributed in its own surrounding polar grid nodes and the rectangular grid nodes. A vortex shed from other cylinders is also distributed in the same manner and stored in a different array. The polar grid nodes are used to evaluate the interaction among vortices shed from the same body while the rectangular grid nodes are used to evaluate the influence from vortices shed from the other cylinders.

It can be seen from figure (**6.2**) that the use of polar grid elements close to the wall could create a situation where an active polar grid node is situated outside

the fluid domain between the walls even though the vortex it represents, is still inside. This active node is then treated as usual, bearing in mind that the active nodes only represent a redistribution of vortices in the flow. and also that there is no direct interaction between the polar grid nodes and the wall elements.

6.6 Calculation of Velocity

The flow past circulars cylinder placed close to walls, as shown in figure (**6.2**), is assumed two dimensional. The flow in the far field is either steady or unsteady and normal to the cylinder axis.

The complex velocity at a point $z = x + iy$ in the flow field is simply the derivative of equation (**6.1**) as follows,

$$\frac{dw(z)}{dz} = u - iv = u_\infty e^{-i\alpha_\infty} + \frac{i}{2\pi}\sum_{n=1}^{N_e}\frac{\gamma_n dS_n}{z - z_n} + \frac{1}{2\pi}\sum_{h=1}^{M_w}\sum_{w=1}^{N_w^h}\frac{\sigma_w^h dS_w^h}{z - z_w^h} + \frac{i}{2\pi}\sum_{\nu=1}^{N_\nu}\frac{\Gamma_\nu}{z - z_\nu} \qquad \textbf{(6.10)}$$

in which u and v are respectively the velocity components in x and y directions.

As explained in the previous chapter, there is no direct vortex to vortex interaction in calculating the velocity in the field domain but only grid node to grid node interaction. As the calculation of vortex velocity is done after the introduction of vortices into the flow, this equation has to be modified slightly by eliminating the second term of the RHS of equation (**6.10**) as the surface vorticity has already been released and absorbed in the shed vortices N_ν as follows,

$$\frac{dw(z)}{dz} = u - iv = u_\infty e^{-i\alpha_\infty} + \frac{1}{2\pi}\sum_{h=1}^{M_w}\sum_{w=1}^{N_w^h}\frac{\sigma_w^h dS_w^h}{z - z_w^h} + \frac{i}{2\pi}\sum_{j,k}\frac{\Gamma_{j,k}}{z - z_{j,k}} \qquad \textbf{(6.11)}$$

in which the $z_{j,k}$ shows the co-ordinate of the active grid nodes either in relation to the polar or the rectangular grid system. As shown in equation (**6.11**) above, the presence of walls which are modelled by source distributions leads to another factor contributing to the calculation of vortex velocities. This source contribution in the second term of the equation is carried out through the use of the overlapping

rectangular grid system. The velocity of the active rectangular grid nodes due to the source distribution of the walls is then

$$\bar{u}_w(z) = \frac{1}{2\pi} \sum_{h=1}^{M_w} \sum_{w=1}^{N_w^h} \frac{\sigma_w^h dS_w^h}{z - z_w^h} \tag{6.12}$$

where N_w^h is the total number of element at wall h

The velocity of a vortex ν shed from the cylinder due to the wall is then found through the use of the bi-linear interpolation,

$$u_w(z_\nu) = Q_1(\nu)u_w(N_1) + Q_2(\nu)u_w(N_2) + Q_3(\nu)u_w(N_3) + Q_4(\nu)u_w(N_4) \tag{6.13}$$

where $Q_\mu(\nu)$ is the area ratios as shown in equation (**5.7**).

This velocity should be added to the vortex velocity due to vortices shed from cylinder surfaces as shown in equation (**5.12**) of Chapter *IV* above. Hence,

$$u(z_\nu) = u_\nu(z_\nu) + u_{pw}(z_\nu) + u_{rw}(z_\nu) \tag{6.14}$$

where, $u_\nu(z_\nu)$ is the vortex velocity due to other vortices shed from the cylinder, $u_w(z_\nu)$ is the vortex velocity due to the influence of the walls and $u_{rw}(z_\nu)$ is the vortex velocity due to diffusion random walk.

6.7 Method of Enhancements

6.7.1 Source Wall Element

Theoretically, the source wall distribution should extend from $-\infty$ to ∞ as expressed in the continuous form of the equation (**6.2**) and (**6.3**) above and also displayed in figure (**A.2**) in *Appendix A*. However, $\lim_{x \to \pm\infty} \sigma_w(x) = 0$ or in other words, the blockage effect experienced by the cylinder due to the presence of the wall is small at distant points. Because of this, the wall is modelled by source extending along the wall until a point is reached when the mutual interaction between the distant wall elements and the cylinder or shed vortices is relatively small.

The influence of the member of sources modelling the wall on the fluid velocity just outside the cylinder surface element closest to the wall are shown in figure

(**6.4**) choosing the case of the wall proximity for the test. It can be seen that the rate of change of the cylinder surface vorticity strength γ_k to the wall extension $\frac{\partial \gamma_k}{\partial x_w}$ is less than 0.01, when the distance of the end wall elements to the cylinder centre is not less than 3D. This value is then used to determine the wall length after shedding vortices. The wall end points can be determined by measuring this distance from the extreme position of a vortex.

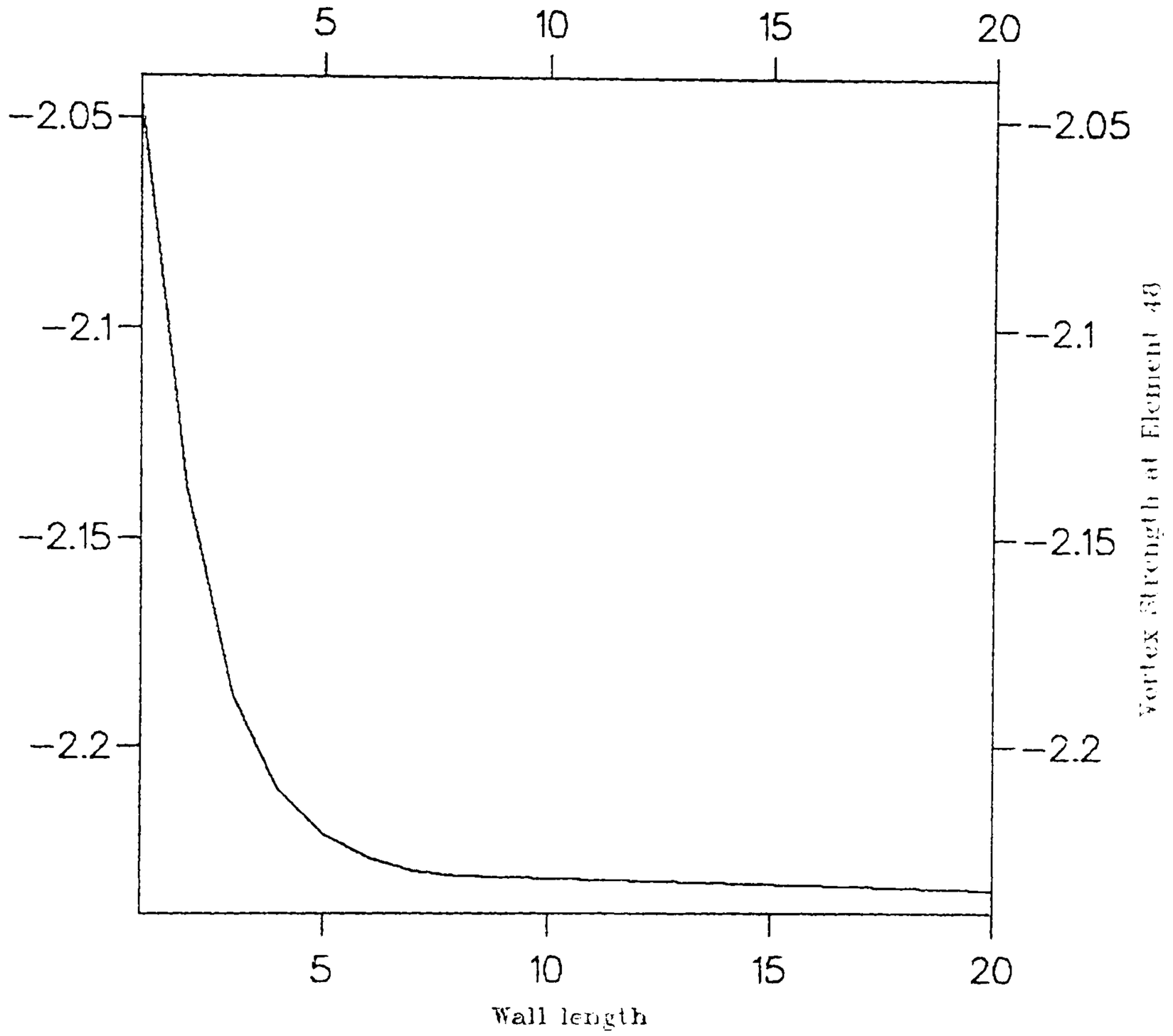

Figure 6.4.-Effect of the Wall length to the cylinder

6.8 Results And Discussion

6.8.1 A Cylinder in A Channel

A. Uniform Flow.

In this section, the results produced from some typical flows are presented with both flow visualisations and graphs showing the accompanying force coefficients. The parameters are still the same as mentioned in section (**4.11**) in the previous chapter, in which the number of element N_e is equal to *64*, the time step Δt is *0.15* and the diameter of the first ring-out, from which the vortices are released, is

equal to the local element length. For the non-dimensional times of $\hat{t} = 1$ and $\hat{t} = 5$, the gap G is defined as the distance between the two walls, at a gap-diameter ration $\frac{G}{D} = 3$ and $Re = 100$, the early structure of the wake behind the cylinder is shown in figure (6.5). The separation points show a little shift compared with an isolated cylinder for which they occur at about 100° measured from the positive $X-$ axis. This figure also shows that, by imposing the same asymmetric shift as explained in Chapter IV, the blockage effect induces a tendency to delay the roll up of the vortices behind the cylinder.

Figure 6.5.-The Flow Pattern at $t = 1$ and $t = 5$

Due to the higher velocity at and around the separation points, the length and width of the formation region are longer and narrower respectively, compared with those of the isolated cylinder. As described in detail in Downie[26], the shape and size of the formation region significantly influences the reactive force exerted on the cylinder and the wake pattern behind. Comparison with figure (4.6) shows the influence of the wall on the formation region at $\hat{t} = 1$ and $\hat{t} = 5$.

After the flow develops further, as shown in figure (6.6), regular vortex shedding occurs. It is seen that, due to the presence of the walls, the wake is suppressed, at a distance of about $4\ D$ behind the cylinder, to form a Von Karman vortex street with the width equal to the wall distance. The value of Strouhal numbers is discernable at about 0.175, which is in fairly close agreement with the results of Stansby and Slaouti [102].

The figure also displays the force coefficients predicted for this flow plotted against the non-dimensional time. The drag coefficient is 2.4, which is slightly less than the result of Stansby and Slaouti [102] of 2.45. This result shows an

increase of about *12%* over that of the isolated cylinder with the same Reynolds number. It is a general trend that the higher the gap ratio $\frac{G}{D}$, the smaller the drag coefficient, until it reaches the value of the isolated cylinder. This is because the effective increase in local velocity reduces and also the interference from the reflected periodic wake is smaller since the walls are located relatively farther away from the centre of the cylinder.

The mean value of the lift coefficient, on the other hand, does not change from zero, even though it is shown that the average extreme values are slightly increased to around ± 0.9. The *rms* lift is found to be *0.55* which is also close to the results of **Stansby** and **Slaouti** [**102**]. It is particularly noticable that the drag frequency is still around twice that of the lift, even though the 'noise' is more pronounced in this case, which seems that this blockage does not significantly change it from that of an isolated cylinder. This has to be the case while vortices are shed symmetrically from both sides of the cylinder.

Section number	Purpose of section	CPU Time
1	Input / Output	1.59
2	Define Grid	0.00
3	Calculate Nodal Velocity	74.37
4	Calculate Vortex Velocity	1.75
5	Vortex Displacement	4.3
6	Distribute Circulation	1.2
7	Calculate Surface Velocity	16.75
8	Calculate Forces	0.04

Table (6.1). – *The CPU time precentage of each section of the algorithm.*

The percentage of CPU time used in this algorithm during each section is presented in table (**6.1**). The time taken for calculating the surface velocity has increased as much as *5* per cent compared with the isolated cylinder in table (**4.2**) and this also contributes to the time needed for the matrix multiplication since the matrix size is now increased due to the presence of the wall sources. The influence of the rectangular element size, as described previously, shows a quite significant

change in the percentage configuration especially for the time taken for calculating the nodal velocity which increases by around *6* %. All those CPU time percentages are taken at $\hat{t} = 90$ when the flow has developed sufficiently to have a high number of the active polar nodes, active rectangular nodes and vortices.

Vortices with small strength compared to the others and those that move across the cylinder and the walls are all eliminated from the flow. This is done

to maintain a more realistic flow pattern and to get a better reactive forces. The total strength of those vortices is then manipulated in such a way, as expressed in equation (**4.45**), to conserve the total circulation in the fluid domain.

The results for higher gap ratios $\frac{G}{D}$ of *2*, *4*, *5*, *6*, are presented in figures (**6.7**), (**6.8**), (**6.9**), and (**6.10**). The general pattern to be observed from the results , not surprisingly, is that the higher the gap ratio the more the flow pattern and the force coefficients approach the values of the isolated cylinder.

At a gap ratio of $\frac{G}{D} = 4$ the drag coefficient is equal to *2.25*, close to the results of **Stansby** and **Slaouti** [**102**] while the extreme values of the lift coefficient is slightly increased to *0.7* with the *rms* lift value of around *0.39*. There is no noticable change in the value of the Strouhal number compared to the previous case. Due to the presence of the wall, the regular Karman vortex sheet behind the cylinder is suppressed at distance of about *6D* as its width is constrained by the walls.

A continuing decrease in the drag coefficient occurs when the gap ratio $\frac{G}{D} = 5$, its value being equal to around *2.15*. The extreme value for the lift coefficient is slightly increased compared to the previous case with a *rms* value of around *0.41*. The Strouhal number is still around *0.18*. When $\frac{G}{D}$ equals *6*, the values of the drag coefficients is *1.9*. These values are in good agreement with those found by the numerical approach of **Stansby** and **Slaouti** [**102**]. The lift coefficient approaches a value of *0.8* which is the same value as for the isolated cylinder. The Strouhal number also increases to around *0.2*, while the flow pattern becomes similar to figure **B.2**) in *Appendix B*.

For a low gap ratio $\frac{G}{D} = 2$, a completely different trend is to be observed, in which the behaviour of the vortices, due to the narrow gap between the wall and the cylinder, changes in the vicinity of the cylinder and along the wall, so as to increase the suppression of the flow oscillation behind the cylinder. The drag

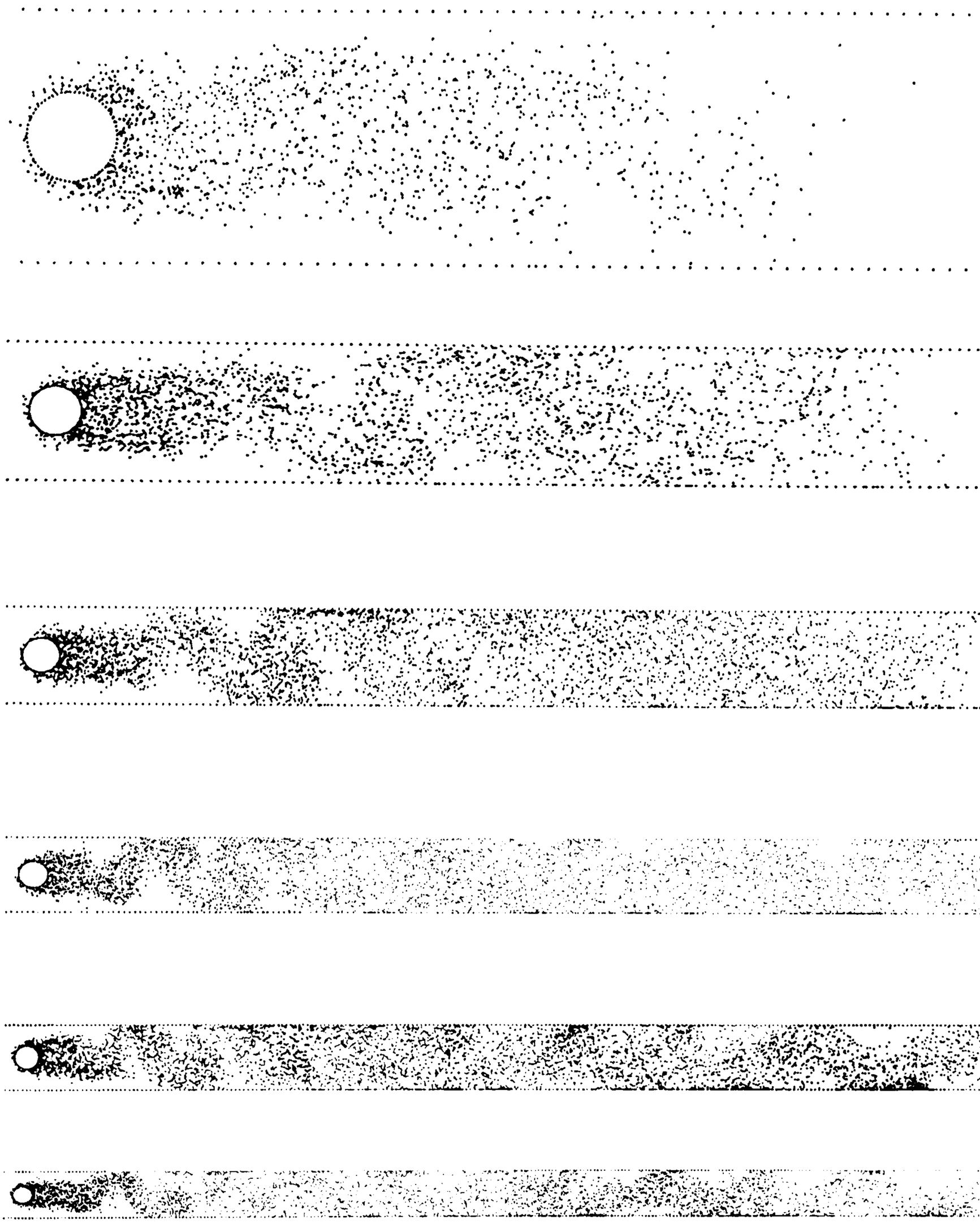

Figure 6.6.-*Flow Pattern at t = 10, 20, 30, 40, 50, 60, for G/D = 3 and Re = 100*

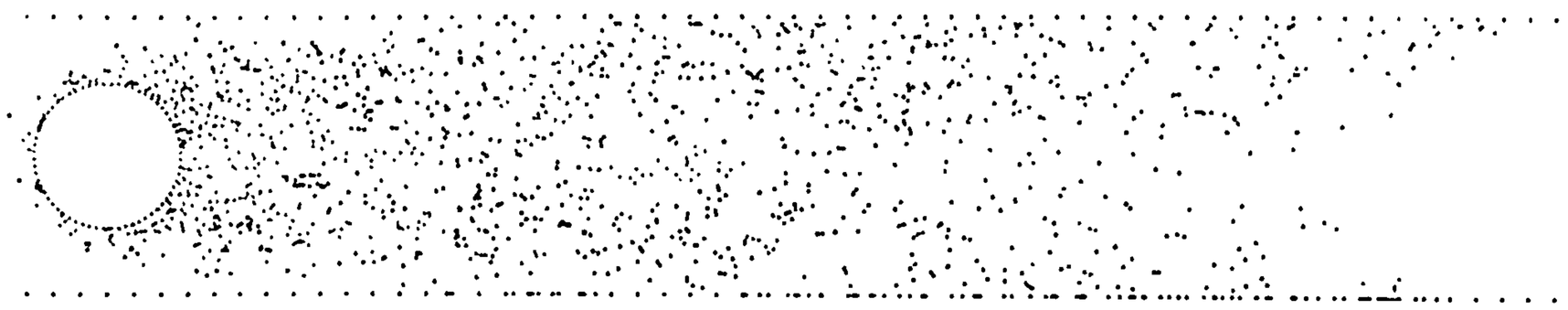

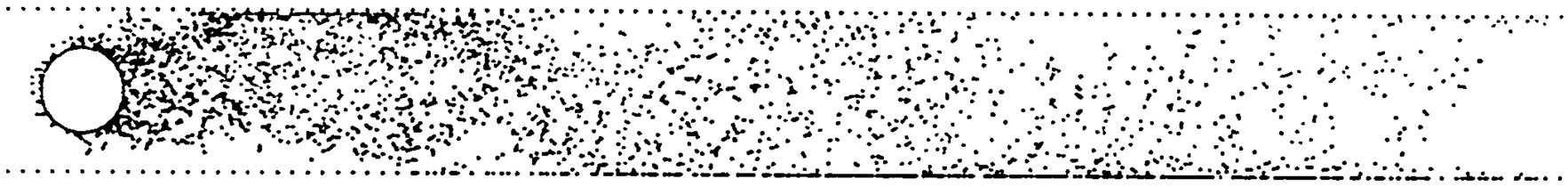

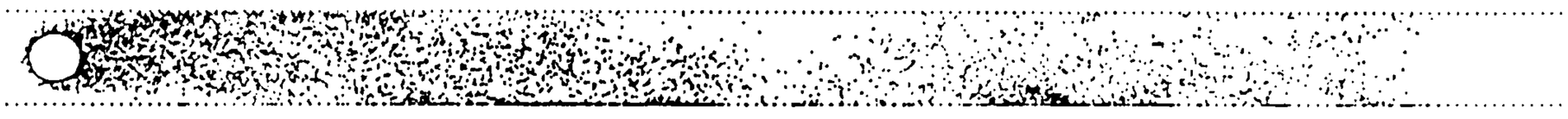

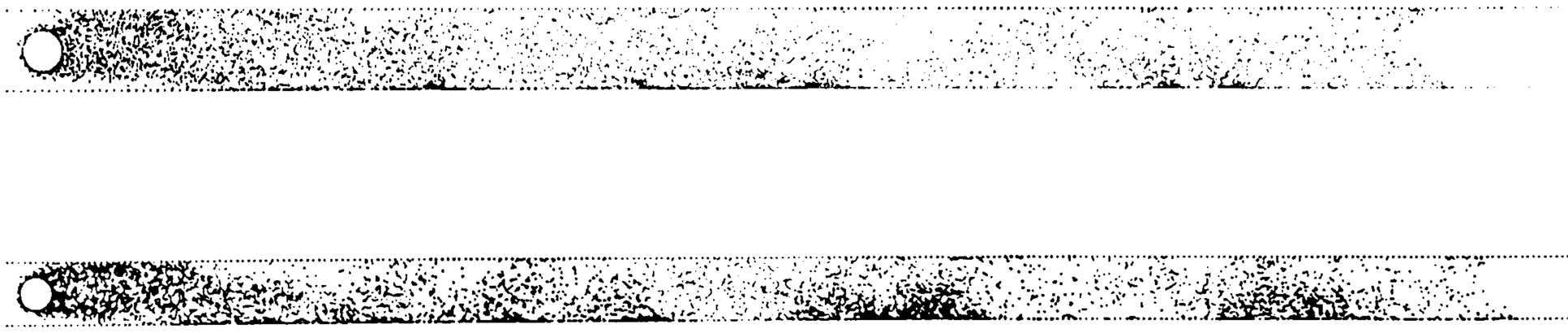

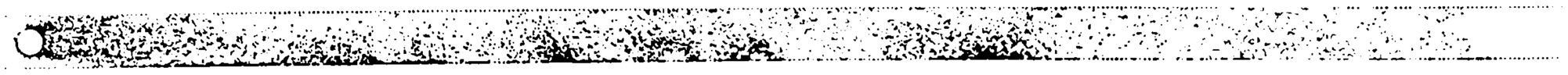

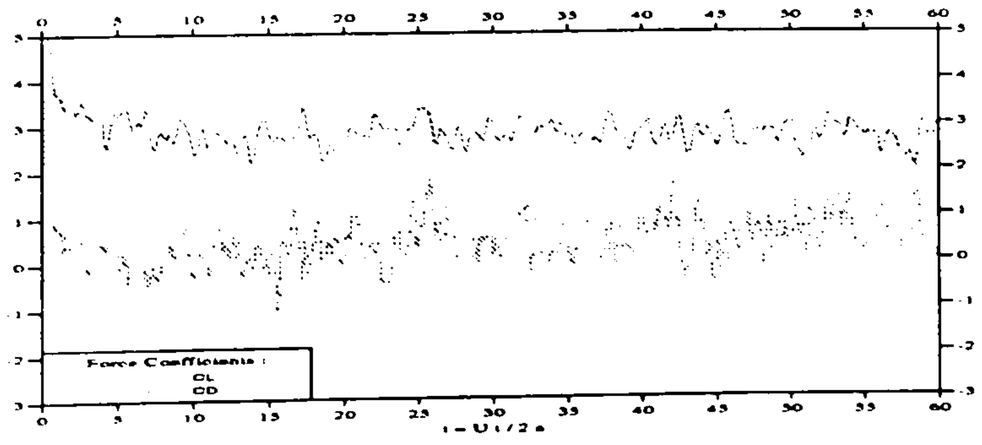

Figure 6.7.-*Flow Pattern at t = 10, 20. 30, 40. 50. 60, for G/D = 2 and Re = 100*

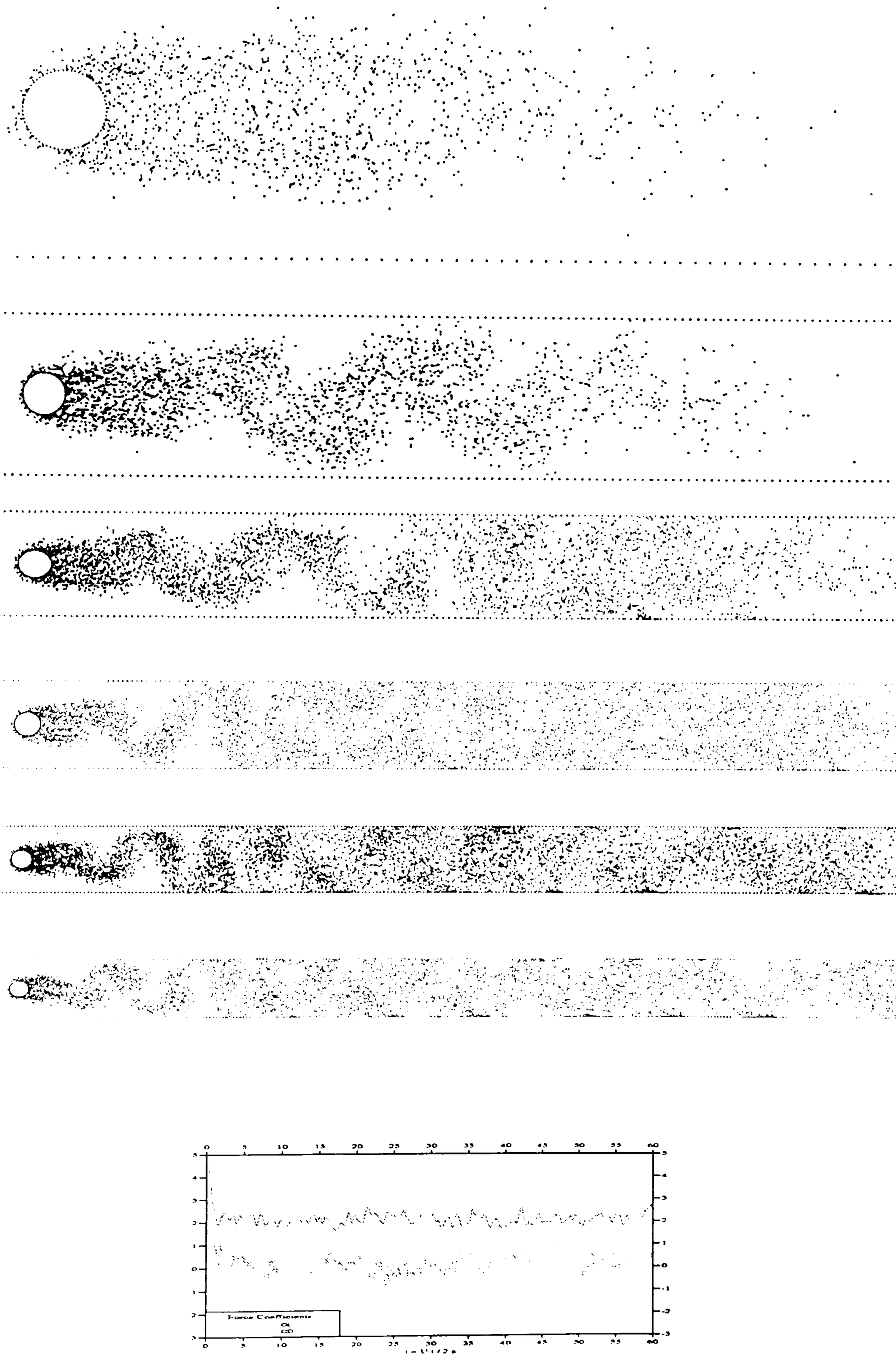

Figure 6.8.-*Flow Pattern at t = 10, 20, 30, 40, 50, 60, for G/D = 4 and Re = 100*

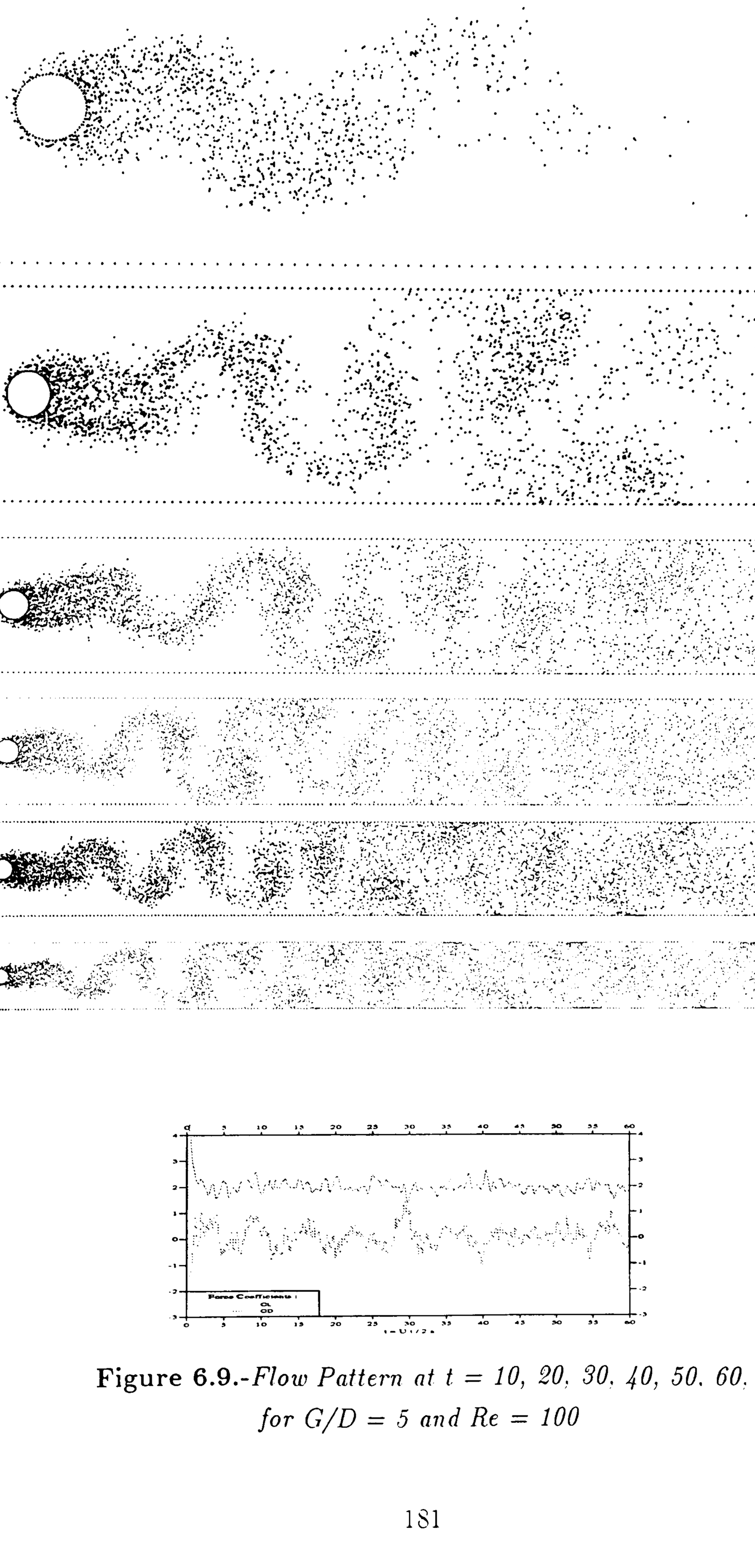

Figure 6.9.-*Flow Pattern at t = 10, 20, 30, 40, 50, 60, for G/D = 5 and Re = 100*

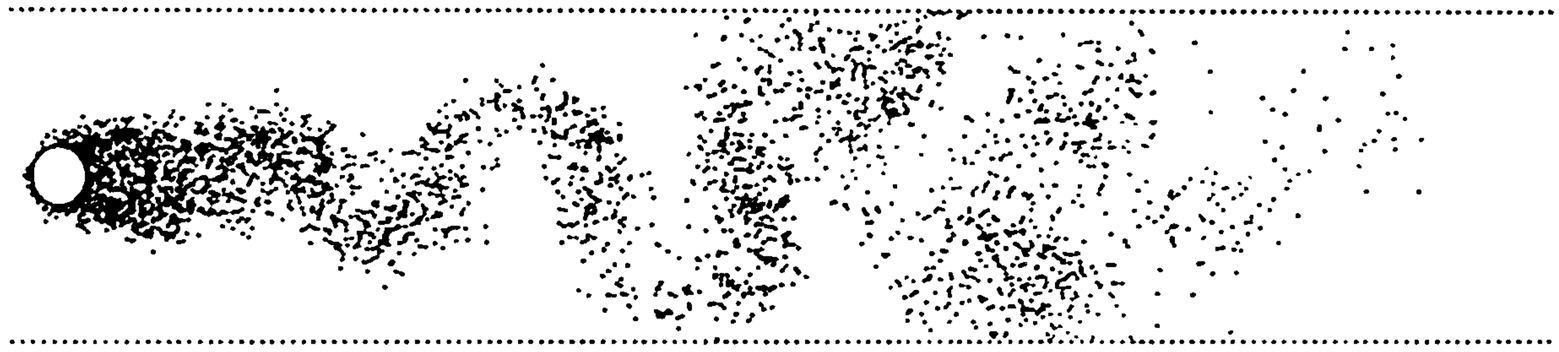

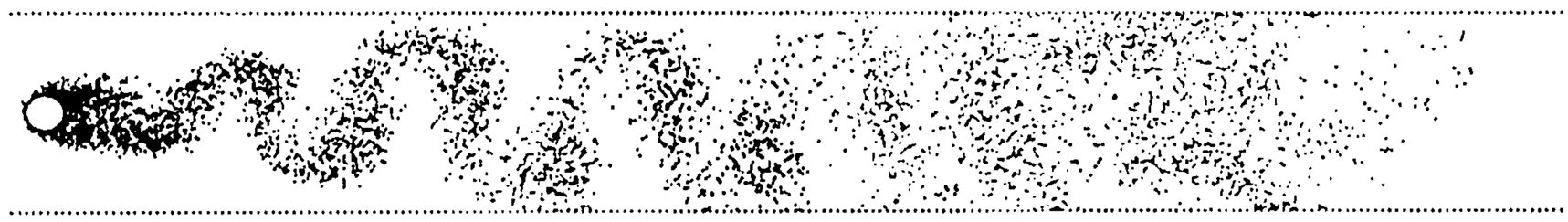

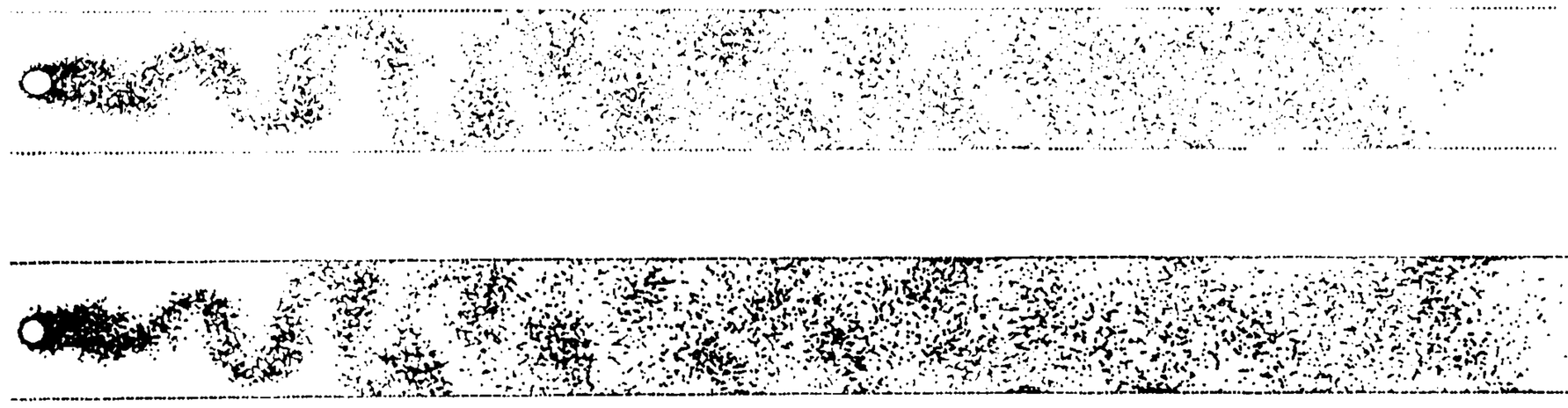

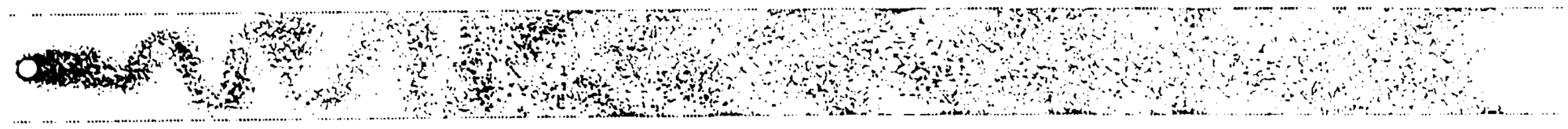

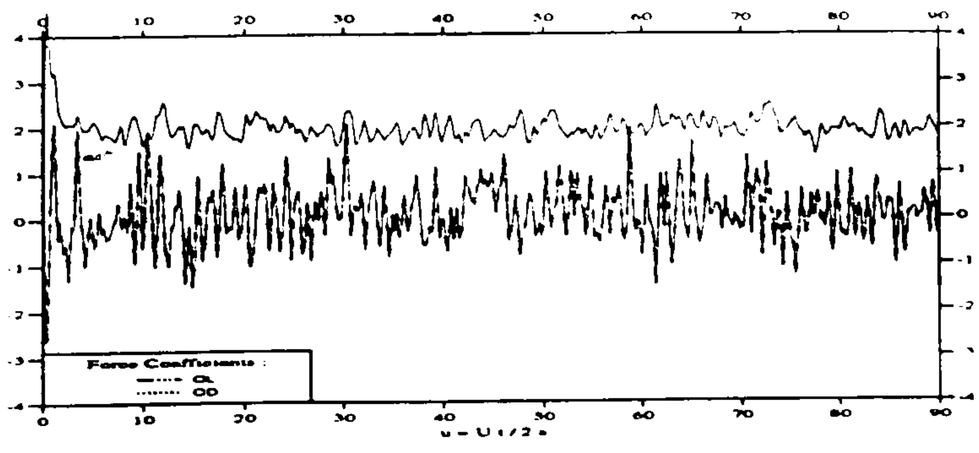

Figure 6.10.-*Flow Pattern at t = 10, 20, 30, 40, 50, 60, for G/D = 6 and Re = 100*

coefficient could be raised to about 4.9, while that found in the present model is around 3 with the *rms* lift around 0.772.

The influence of Reynolds number at a certain gap ratio $\frac{G}{D} = 6$ is also investigated using the model by varying the Reynolds number from 500 to 100000 as displayed in *Appendix D*. The results for $Re = 500$, as displayed in figure (**D.1**) suggest that the drag is increased to around 1.6, which is about 10 % increase compared to that of the isolated cylinder. The extreme value of the lift coefficient is about 0.8 which is close to that of the isolated cylinder. As the Reynolds number is increased to around 1000, the drag coefficient is slightly reduced to 1.46. The extreme value of the lift coefficient is also reduced to around 1.75 and the Strouhal number is maintained around 0.2. The resolution of the picture is improved and it is seen clearly that the vortices approach the wall tangentially whenever they move close to it.

With the increase of the Reynolds number to 10000 and to 100000, the increase of the drag coefficients is in the range of $5 - 10\%$ compared to the isolated cylinder. No difference in the value of the lift coefficient and the Strouhal number can be detected.

The results for a cylinder placed in a channel with $\frac{G}{D} = 2$ to 6, Reynolds numbers of 100 and 100000 can then be summarized in the following table.

Gap ratio G/D	Drag Coefficient Cd	Lift Coefficicent Cl
2	3	0.05
3	2.4	0.05
4	2.25	-0.04
5	2.15	-0.01
6	1.9	0.04

Table 6.2. – *Results for the flow around a cylinder in a channel at Reynolds number 100*

Reynolds number Re	Drag Coefficient Cd	Lift Coefficicent Cl
100	1.9	0.05
500	1.6	0.05
1000	1.46	-0.04
10000	1.2	-0.01
100000	1.15	-0.03

Table 6.3. – *Results for the flow around a cylinder in a channel at gap ratio $G/D = 6$*

B. Oscillatory Flow.

To the author's knowledge, there is no reference in the literature for blockage in oscillatory flows to which the present results can be compared. However, this section is written with the purpose of investigating the effects of the presence of the wall on the hydrodynamic characteristics of the cylinder compared to the similar oscillatory flow condition in an infinite fluid as described in chapter *IV*. At a gap ratio $\frac{G}{D}$ of *3*, the present model was run at several values of the Keulegan-Carpenter number of *5*, *10*, *15*, and *20* for Reynolds number *100000*. The number of cylinder elements N_e and the time step Δt were chosen to be exactly the same as those in the previous chapter, namely *64* and *0.1* respectively. The vortices are also released from the first ring-out of the cylinder at a distance that varies as a function of the inverse of the square root of the β value as explained in section (**3.10.1**).

At Keulegan-Carpenter number of *5* the difference of the flow pattern at the early stages of the flow compared to that of the isolated cylinder as described in the previous section, is mainly that the blockage effect slightly narrows the wake downstream, as shown in figure (**6.11**) for non-dimensional time $\hat{t}$ of *1* and *5* respectively. After the flow has developed further at $\hat{t} = 60$, it is seen that the wake is mostly concentrated close to the cylinder and spread along the wall. This is due to the fact that the velocity in the gap region is higher than the rest of the area which can convect the vortices that fall in this region farther away than those that fall in the middle region between the walls. Also vortices in close proximity to the walls pair with their images in the wall and the two mutually convect each other along the wall.

Figure 6.11.-The Flow Pattern at $\hat{t} = 1$ *and* 5. G/D = 3, and Re = 100000

Figure (**6.12**) shows that due to the blockage effect, the mean extreme value of the in-line force coefficient is slightly increased by about *6%* compared to that of the isolated cylinder as displayed in figure (**B.10**) in appendix *B*. In fact this value is closer to the experimental results of **Sarpkaya** and **Isaacson** [**87**]. Nevertheles, due to the existence of the phase difference between the present and the experimental results, no improvement is obtained for the value of the drag and inertia coefficients which are *1.5* and *1.9* respectively.

At a higher Keulegan-Carpenter number of *10*, as displayed in figure (**6.13**), a similar trend occurred with an increase in the in-line force coefficient of about *7%*. Starting from this value of the Keulegan-Carpenter number and higher, as shown in figures (**6.14**), (**6.14**), this increase is accompanied by an improvement in the phase difference between the present results and the experimental results.

The clear difference of the flow pattern compared to that of the isolated cylinder is that the wake around the cylinder is spread and bounded only between the two walls and this may cause a more pronounced influence of the shed vortices on the cylinder during the reversed flow and this will add to the influence of the wall itself.

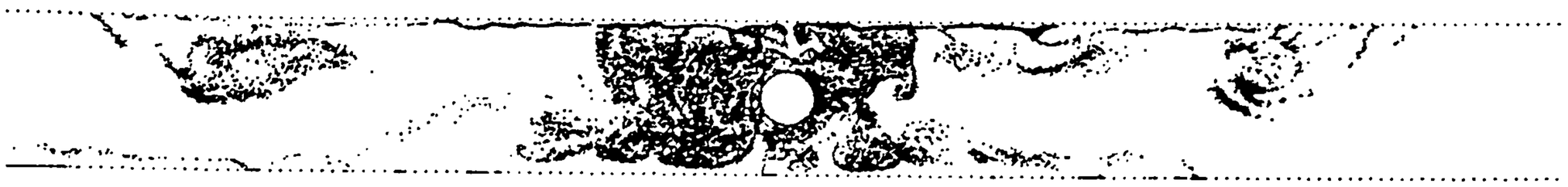

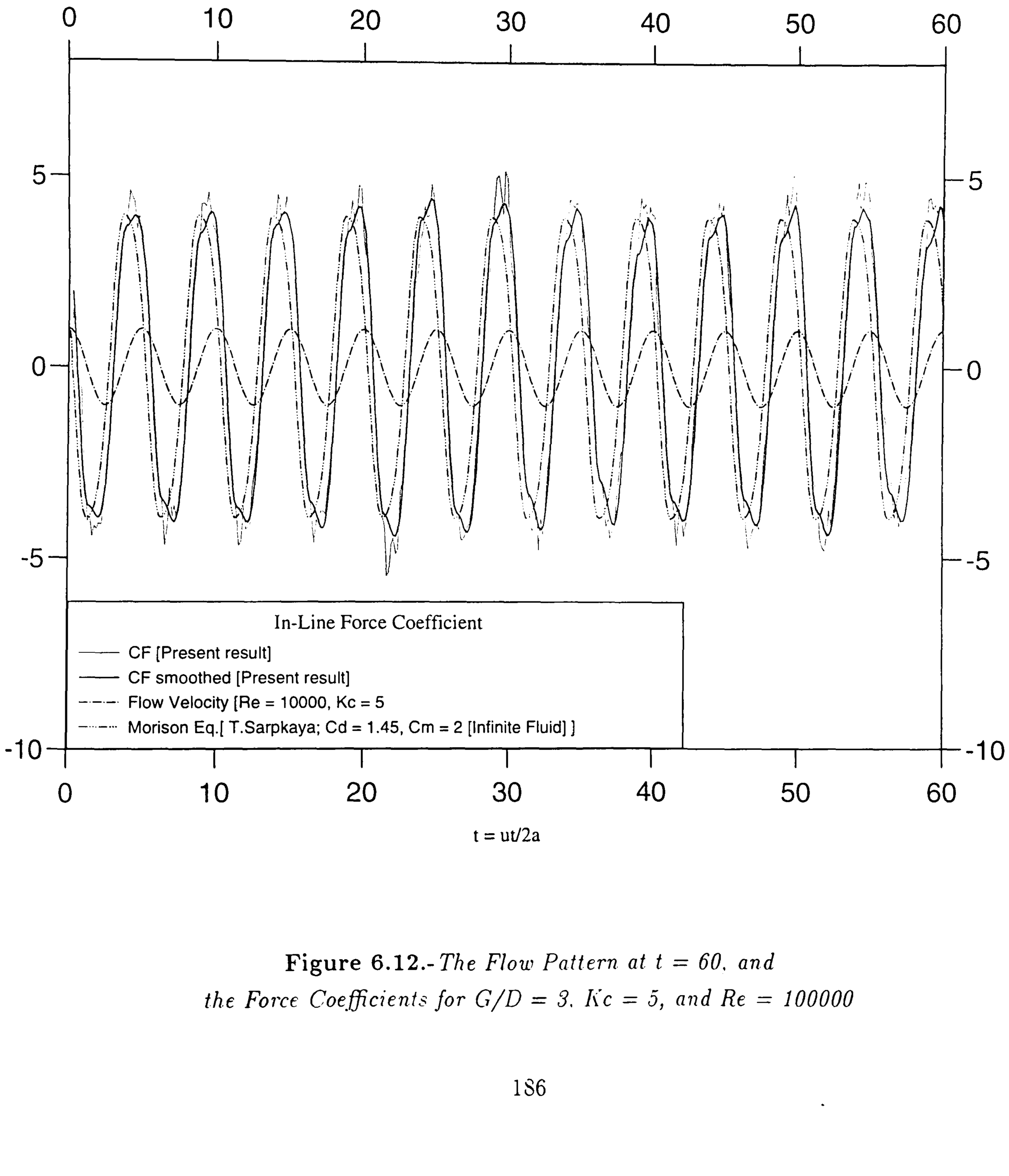

Figure 6.12.-*The Flow Pattern at $t = 60$, and the Force Coefficients for $G/D = 3$, $Kc = 5$, and $Re = 100000$*

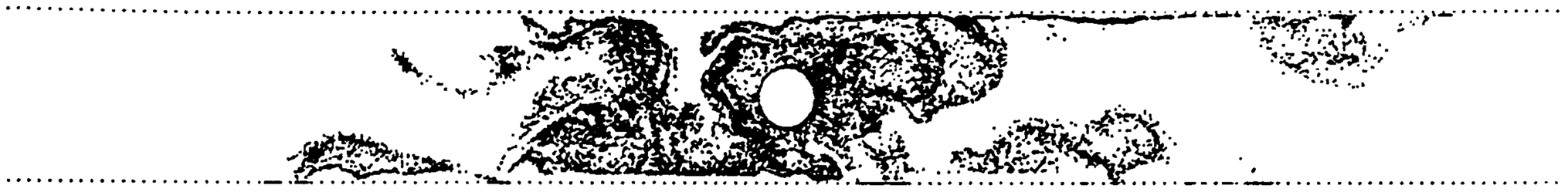

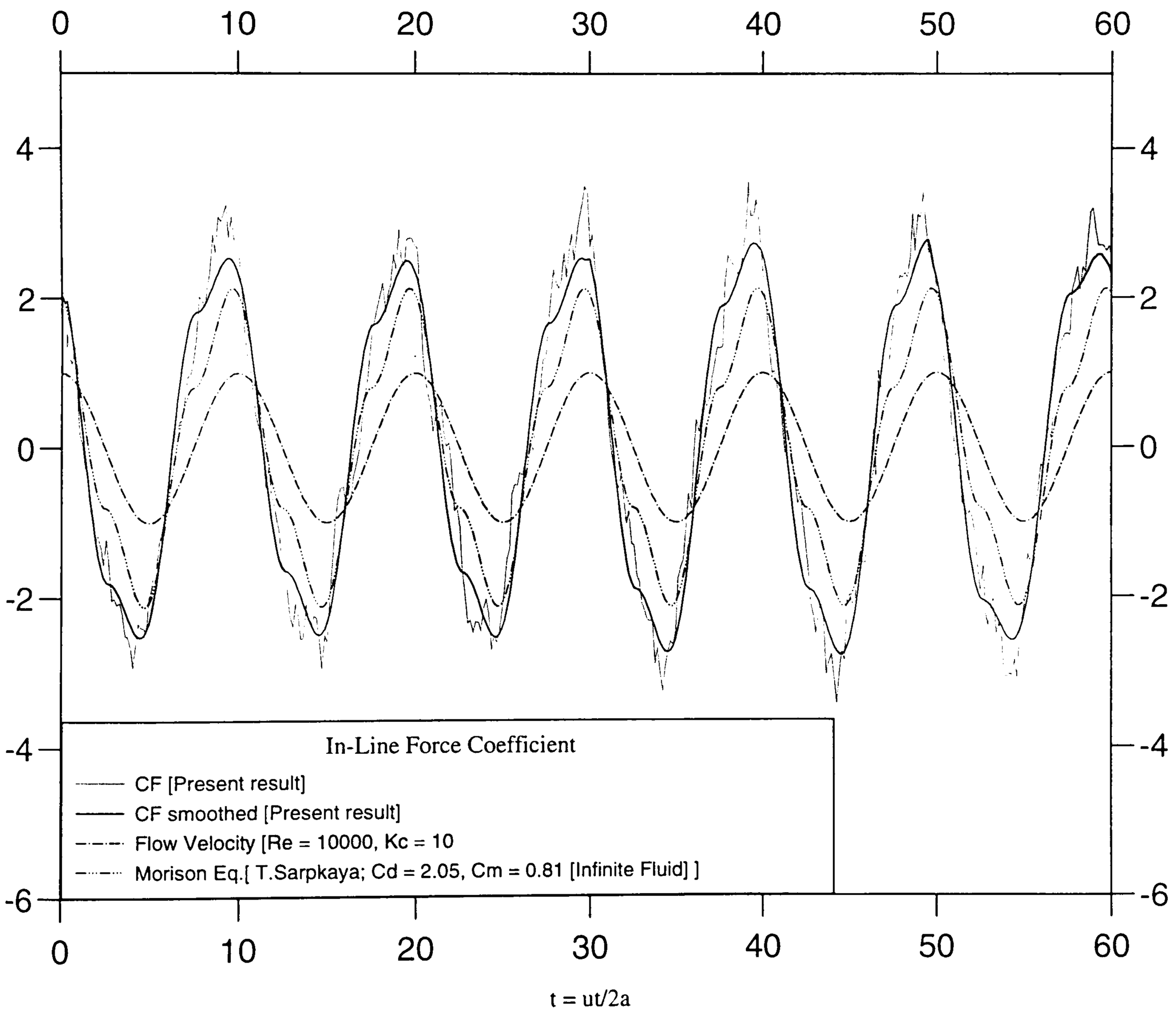

Figure 6.13.-*The Flow Pattern at t = 60. and the Force Coefficients for G/D = 3. Kc = 10. and Re = 100000*

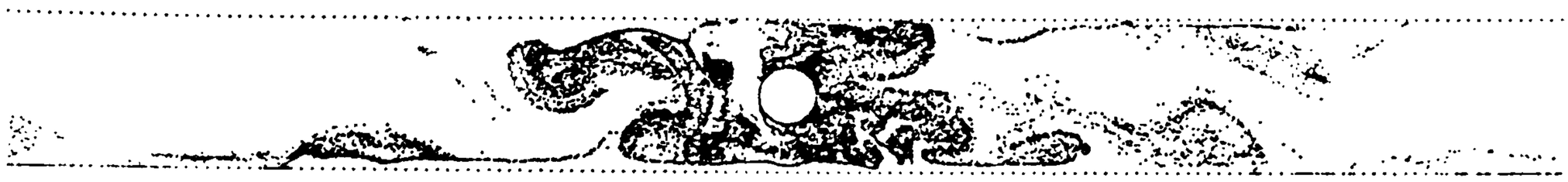

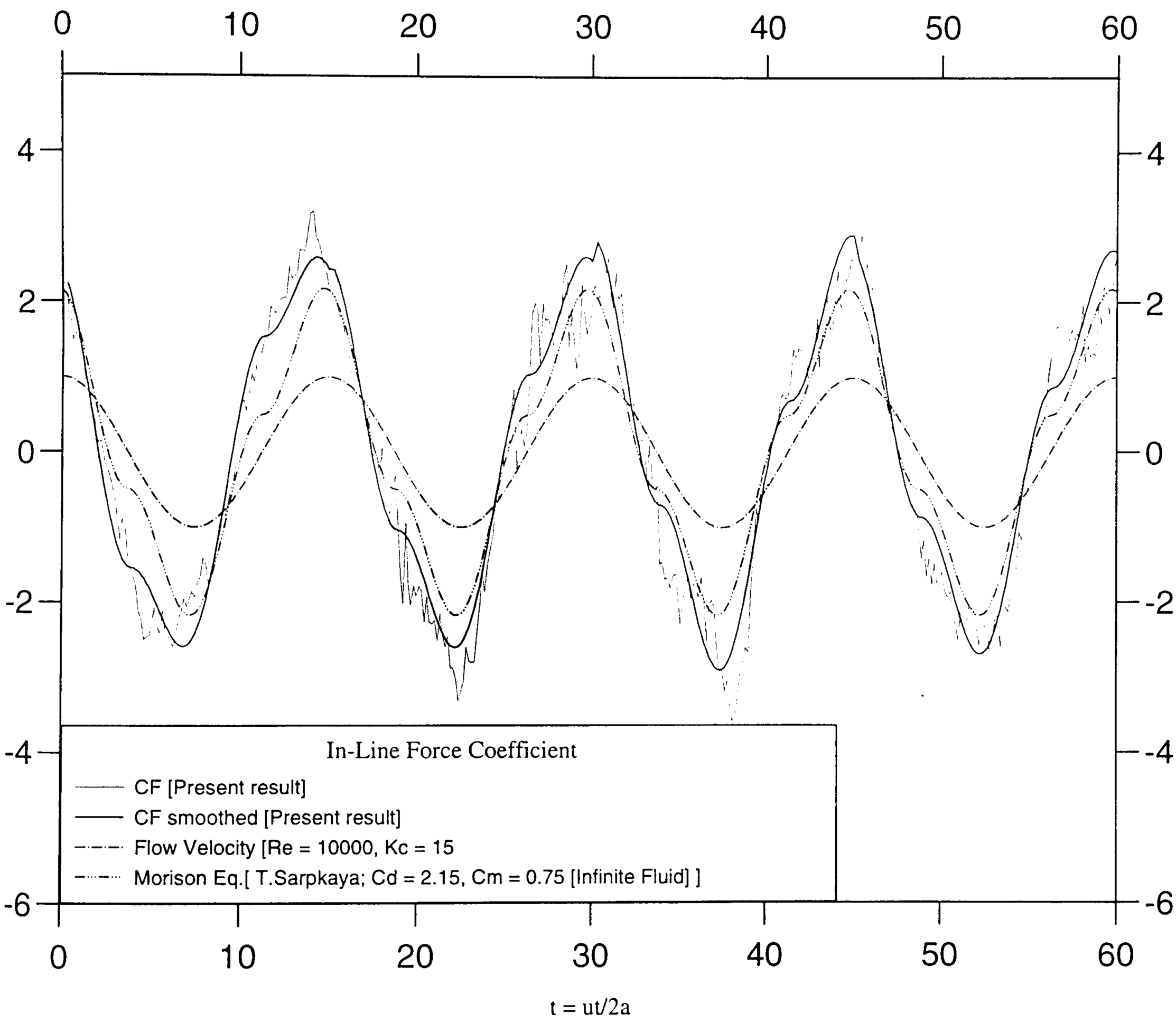

Figure 6.14.- *The Flow Pattern at $t = 60$, and the Force Coefficients for $G/D = 3$, $Kc = 15$, and $Re = 100000$*

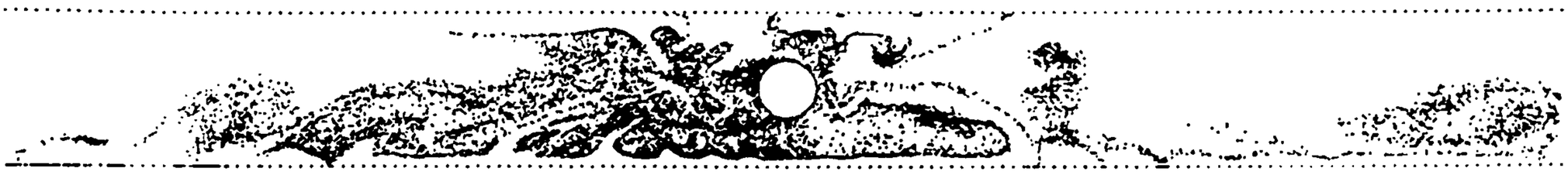

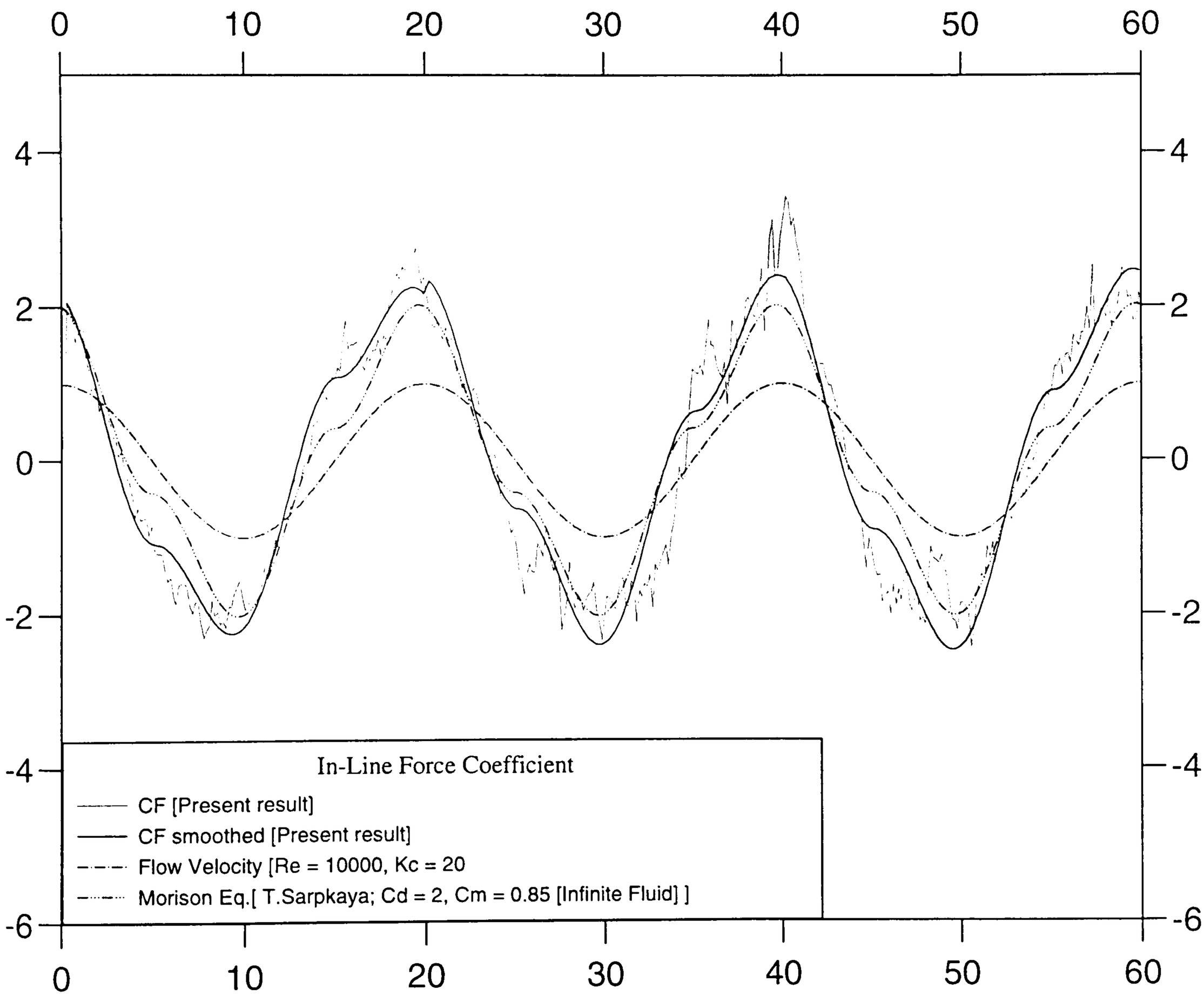

Figure 6.15.- *The Flow Pattern at $t = 60$, and the Force Coefficients for $G/D = 3$, $Kc = 25$, and $Re = 100000$*

6.8.2 A Cylinder Near A Plane Boundary

A. Unifrom Flow.

With the absence of the top wall from the previous section, the problem can now be converted into the problems of a cylinder close to a wall in which the results can now be investigated in this section. It is mentioned by **Bearman** and **Zdravkovich [12]**, and **Ali** and **Narayanan [1]**, that at the gap ratio $\frac{G}{D}$ greater than *2* the cylinder behaves like an isolated cylinder as the influence of the wall is relatively low.

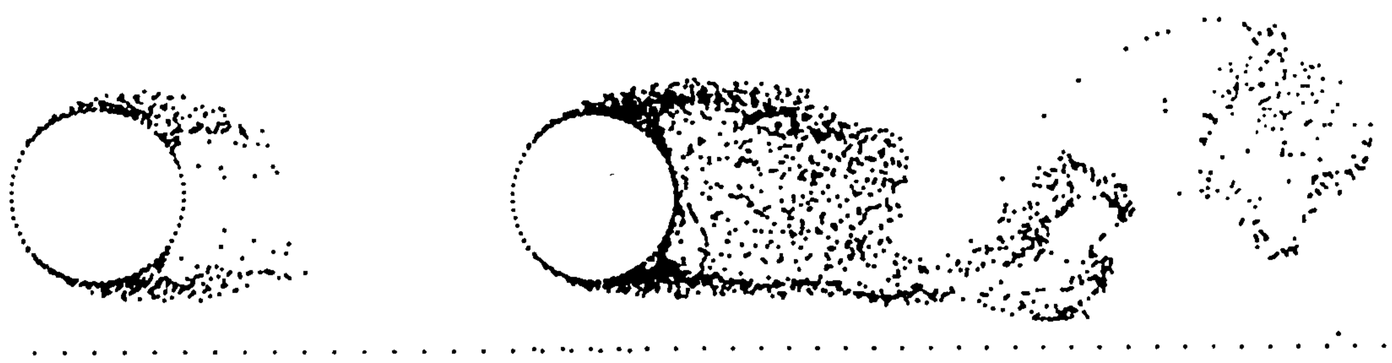

Figure 6.16.-The Flow Pattern at $\hat{t} = 1$ and $\hat{t} = 5$ for G/D = 0.5

Based on these experimental studies, the model was tested at at high Reynolds number of 100000 and at several values of the gap ratio $\frac{G}{D}$ of 2, 1.5 , 1, 0.5 , *0.25*, *0.1*. At the first gap ratio $\frac{G}{D} = 2$ and at the non-dimensional times of $\hat{t} = 1$ and $\hat{t} = 5$, the early beginnings of the wake behind the cylinder are shown in figure (**6.16**). In this case, the separation point close to the wall is shifted downstream to about *125* degrees, while the one on the top side of the cylinder surface is shifted upstream to about *135* degrees, measured from the positive x axis. The shear layer emanating from the lower half of the cylinder seems to stretch longer than the upper one even though no forced asymmetry was implemented. The formation region also seems to be slightly longer than that of an isolated cylinder by about *5%*. This is due to the fact that the close presence of the wall will create an asymmetric velocity field around the circumference of the cylinder in which the velocity of the fluid particles close to the wall are relatively higher than the rest. The asymmetric velocity field around the cylinder also promotes the roll-up of the vortices earlier than that for the isolated cylinder, as shown in figure (6.16).

As the flow develops further, as shown in figure (**6.17**), a regular vortex shedding is clearly established and this is also reflected in the graph of the force coefficients. The drag coefficients is slightly less than *1.14*, which is the value for an isolated cylinder, and the lift coefficient oscillates about a mean value of about *0.15* with the Strouhal number relatively unchanged from *0.2*. The steady implies that a repulsive force exists in the direction tending to displace the cylinder away from the wall.

The obvious difference between this flow pattern and that of an isolated cylinder is that the vortices close to the wall tend to approach it tangentially, follow it and then leave it tangentially as well, while those on the other side are freely convected as in an isolated cylinder. Numerically, this is obviously due to the source distribution along the wall which tends to reflect the vortices close to it back to

the fluid domain. This is also shown in the calculation in that generally, when the vortices are close enough to the wall, the strength of the sources in that region are positive (*sources*), while those in the region sparsely populated by vortices show negative values (*sinks*).

The absence of the top wall only slightly changes the composition of the CPU time taken at each section, as shown in table (**6.4**), compared with that of the previous section. This is shown in the precentage time taken to calculate the vortex velocity which is less than for the previous case by about 5%.

Section number	Purpose of section	CPU Time
1	Input / Output	1.59
2	Define Grid	0.00
3	Calculate Nodal Velocity	73.97
4	Calculate Vortex Velocity	2.38
5	Vortex Displacement	4.6
6	Distribute Circulation	1.4
7	Calculate Surface Velocity	16.02
8	Calculate Forces	0.04

Table 6.4. – *The CPU time precentage of each section of the algorithm.*

Figure 6.17.-*The Flow Pattern at t = 10, 20, 30, 40, 50, 60, and the Force Coefficients for G/D = 2. and Re = 100000*

The influence of the wall on the hydrodynamic characteristics of the cylinder increases as the gap ratio is reduced to *1.5*, *1*, *0.75*, *0.5* and *0.25* as shown in figure (**6.18**) (**6.19**) (**6.20**) (**6.21**). The drag coefficient reduces from *1.13* and the mean value of the lift coefficient is around zero, in which these values are those of the isolated cylinder, to be a force away from the wall with mean *0.23*, *0.32*, *0.41*, and *0.51* respectively.

The flow on the wall side of the cylinder can be seen to be increasingly deflected in a tangential direction as the gap between the cylinder and the wall is decreased. It is also shown in these figures that as the velocity in the gap region gets higher, vortices with high strengths are created which then produce a strong mutual interaction. This in turn results in higher velocity in the region along the wall behind the cylinder which then causes the vortex street to be deflected as the vortices close to the wall move further away than those located further into the flow.

The more asymetric effects occurs when the gap ratio $\frac{G}{D}$ is reduced to *0.25* when the influence of wall as described above is more pronounced. The vortex street is becoming more skew-symmetric because of the greater influence of the wall, which is reflected in the higher velocity in the gap region, as shown in figure (**6.22**). It can also be seen that the repulsive force, shown as the average lift coefficient, is higher and reaches *0.75* with the Strouhal number equal to *0.17*, with the drag coefficient is slighly increased to *1.45*. This is close to the experimental values reported by **Efthymiou** and **Narayanan** [**31**][**32**].

Experimental evidence shows that when the gap ratio $\frac{G}{D}$ is less than *0.25* regular vortex shedding is suppresed due to the complicated behaviour of the turbulent boundary layer interaction in the gap region. This affects the formation region which is lengthened to about *8* times the cylinder diameter.

Although there is no turbulence model in this study, numerically, the regular vortex shedding is still suppressed by the cancellation of the vortices shed from the lower part of the cylinder as they are mostly convected closer than *0.05D* from the wall, the minimum distance in which a vortex is still considered 'alive'. The result for the gap ratio $\frac{G}{D}$ of *0.1D* is presented in figure (**6.23**). As described in the previous chapter, the loss of of circulation due to the vortex cancellation is then compensated in the next calculation of the surface vorticity for the next time step. At this gap ratio, the mean value of the lift and drag coefficients are increased unrealistically even though the suppressed oscillating flow pattern is

achieved. This unrealistic result is attributed to the strong interaction between the closest elements of the cylinder and the wall and the resulted interaction could not model the interaction of the wall / cylinder boundary layer correctly.

The effects of the Reynolds number at fixed value of the gap ratio $\frac{G}{D} = 1$ are also investigated in this study and the results are presented in figures (**D.5**). (**D.6**), (**D.7**), (**D.8**) and (**D.9**) in *Appendix D*. As also occured in *Chapter IV*, at Reynolds number *100* the resolution of the flow pattern is not as high as could be wished for due to the dominant influence of the Random Walk diffusion scheme. The drag coefficient is found to be around *2.3* and the mean value of the lift coefficicent is around *0.4*. The value of the Strouhal number is difficult to ascertain due to the numerical noise. This shows that the presence of the wall causes the drag coefficient to increase by about *10%* and this can be attributed to the higher velocity in the gap region which in turn creates stronger of vortices that have a greater influence on the drag characteristics of the cylinder when they accumulate and interact in the formation region.

At a higher Reynolds number of *500* a better picture of the flow pattern is observed and this is also reflected in the increased definition of the lift coefficient as displayed in figure (**D.6**). The drag coefficient is reduced to around *1.9*, which is slightly higher than the value of the isolated cylinder, while the mean value of the lift coefficient is around *0.3*. The mean maximum value of the lift coefficient is around *0.8* with the Strouhal number value about *0.17*. The drag coefficient is continuously reduced at higher Reynolds numbers of *1000*, *10000* and *50000* with values of around *1.6*, *1.2* and *1.15* respectively, as shown in figures (**D.7**), (**D.8**) and **D.9**). The mean maximum lift coefficient increases to around *0.9* with the Strouhal number reaching *0.2* which are both around the value obtained for the isolated cylinder.

A summary of the results for the force coefficients of a cylinder placed at various distances from the wall with a Reynolds number of *100000* is displayed in table (**6.5**) below. The effect of the variation of the Reynolds number, from $100 - 50000$, on the force coefficients at the gap ratio $\frac{G}{D} = 1$ is shown in table (**6.6**).

Gap ratio G/D	Lift Coefficient Cl	Drag Coefficicent Cd
0.1	unrealistic	unrealistic
0.25	0.75	1.45
0.5	0.41	1.2
0.75	0.31	1.17
1	0.25	1.15
1.5	0.22	1.13
2	0.15	1.13

Table (6.5). – *Results for the flow around a cylinder in a channel at Reynolds number 100*

Reynolds number Re	Lift Coefficient Cl	Drag Coefficicent Cd
100	0.4	2.3
500	0.3	1.9
1000	0.3	1.6
10000	0.25	1.2
100000	0.15	1.15

Table (6.6). – *Results for the flow around a cylinder in a channel at gap ratio G/D = 1*

B. Oscillatory Flow

The range of validity of the present model and the parameters defining it, were fully discussed in *Chapter IV*. The object of this section of the study is to examine the influence of the proximity of a cylinder to a plane surface bounding an oscillatory flow in the context of the limitations of the model used.

It was concluded in chapter *IV* that the present model can only produce results in reasonable agreement with experimental when the β value $(\frac{Kc}{Re})^{1/2}$ lies in a range in which the 'boundary layer thickness' is around a half to twice the length of the local element.

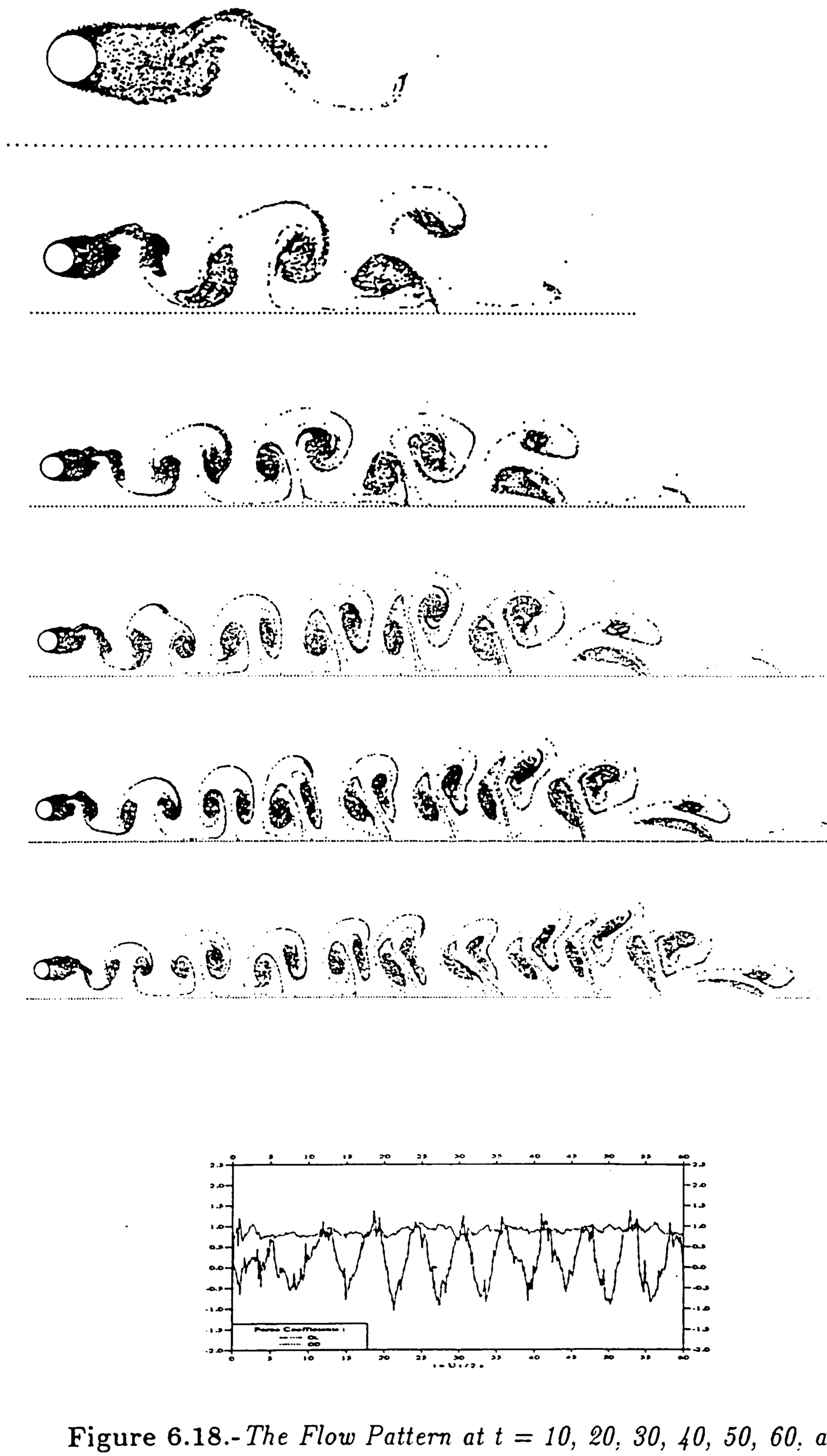

Figure 6.18.-*The Flow Pattern at t = 10, 20, 30, 40, 50, 60, and the Force Coefficients for G/D = 1.5, and Re = 100000*

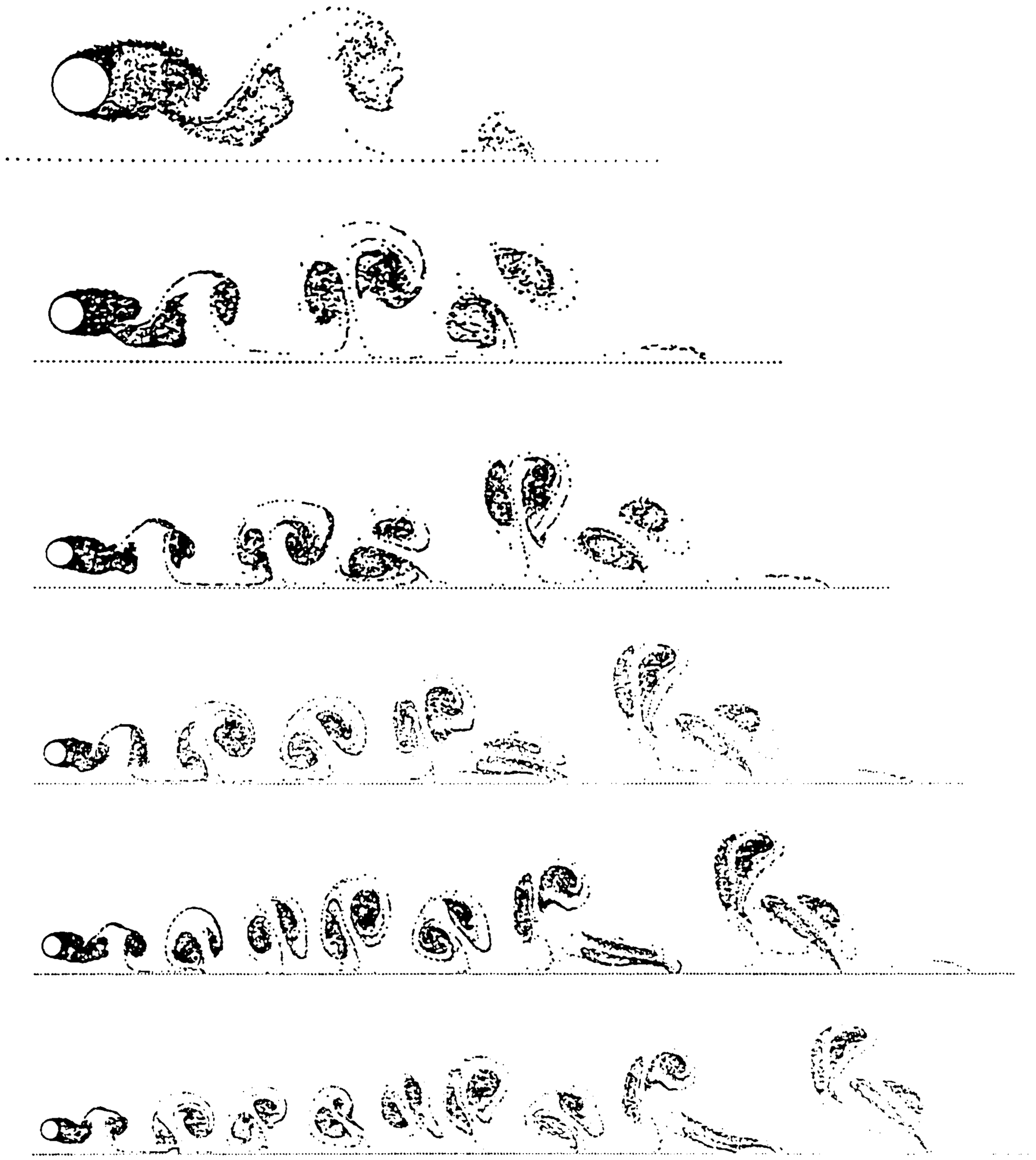

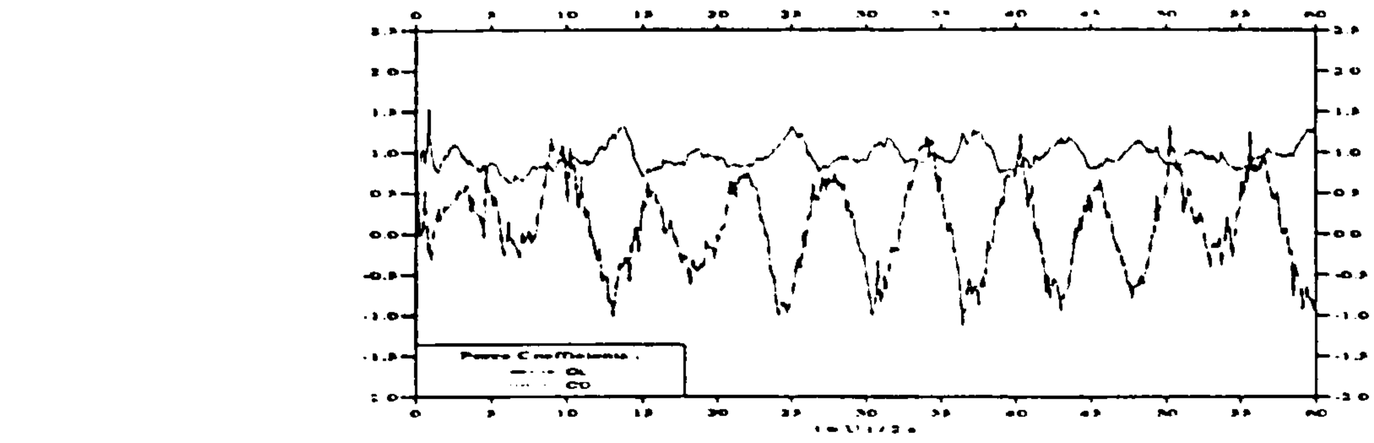

Figure 6.19.-*The Flow Pattern at t = 10, 20, 30, 40, 50, 60, and the Force Coefficients for G/D = 1, and Re = 100000*

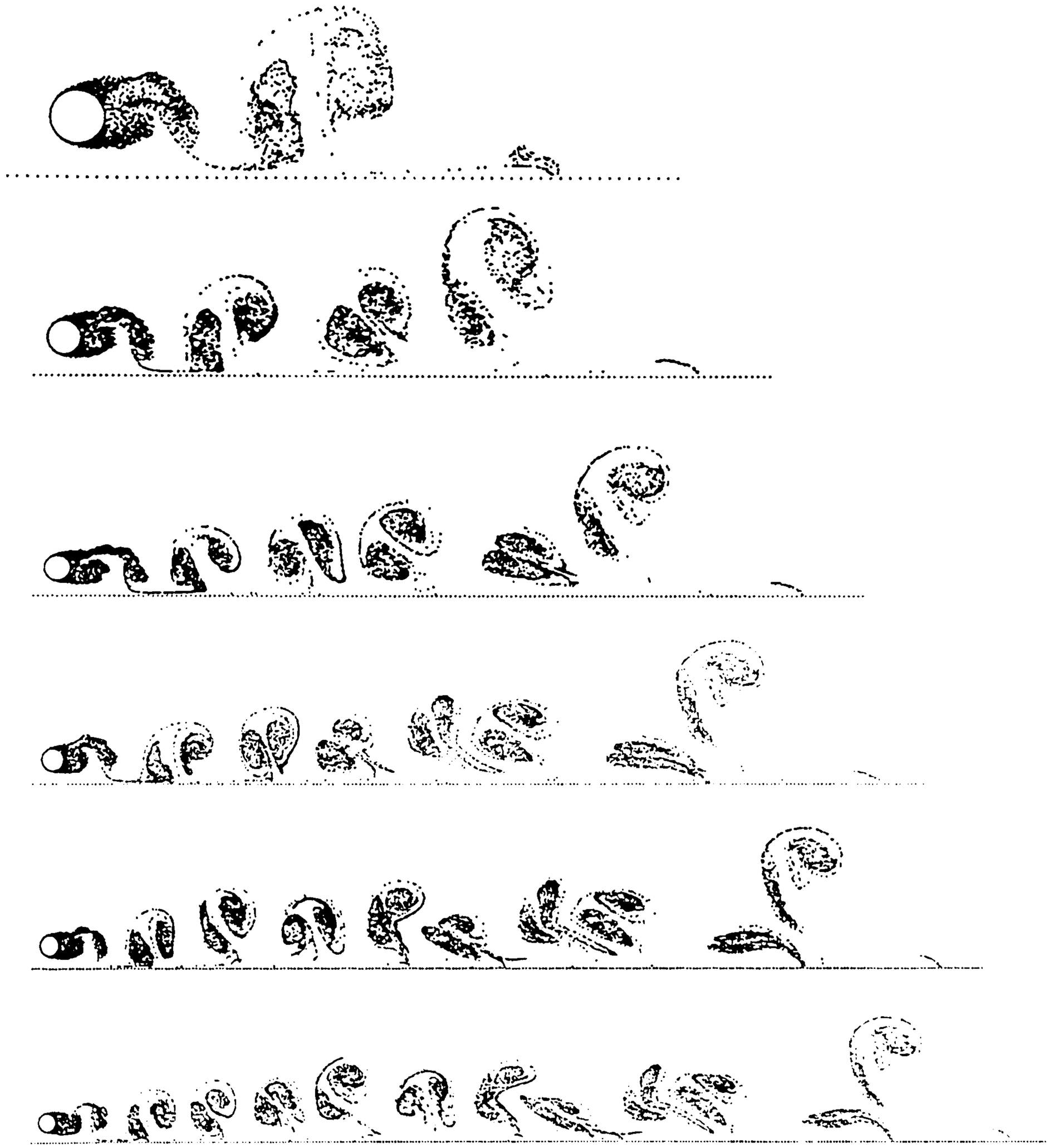

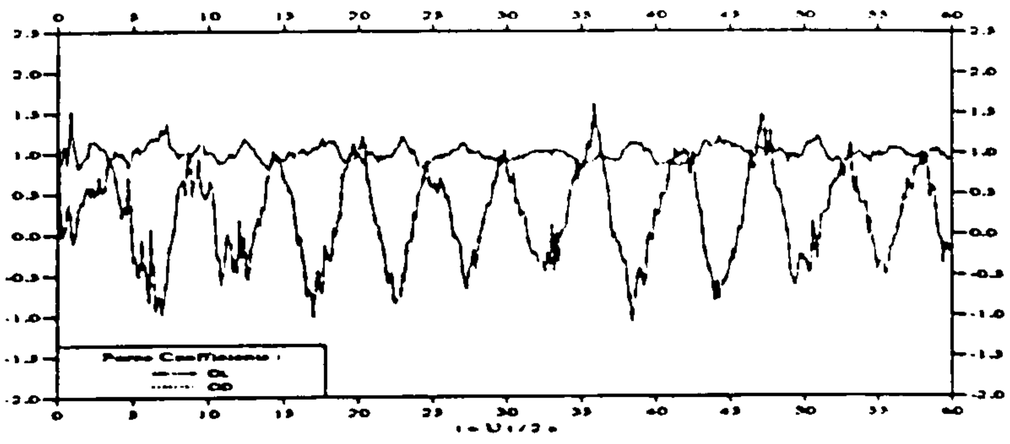

Figure 6.20.- *The Flow Pattern at t = 10, 20, 30, 40, 50, 60, and the Force Coefficients for G/D = 0.75, and Re = 100000*

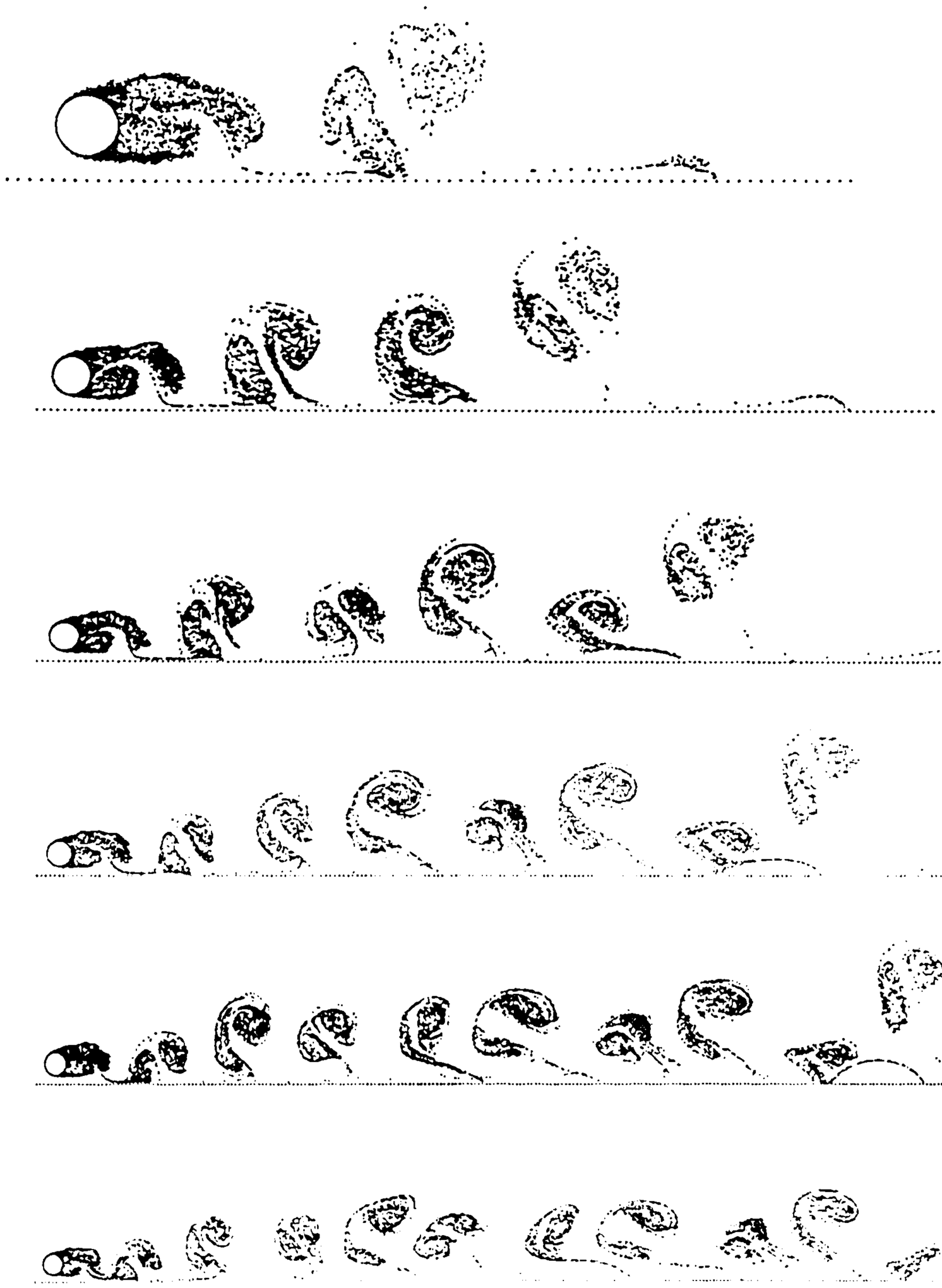

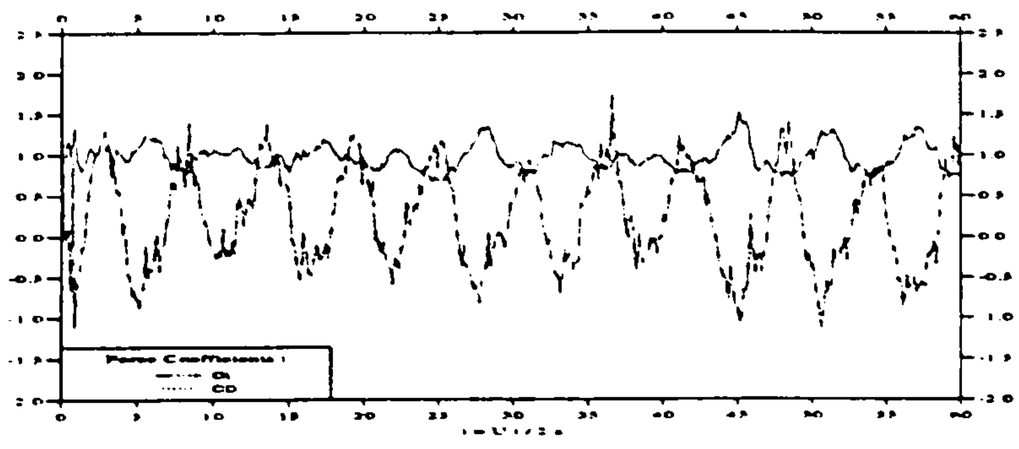

Figure 6.21.-*The Flow Pattern at t = 10, 20, 30, 40, 50, 60, and the Force Coefficients for G/D = 0.5, and Re = 100000*

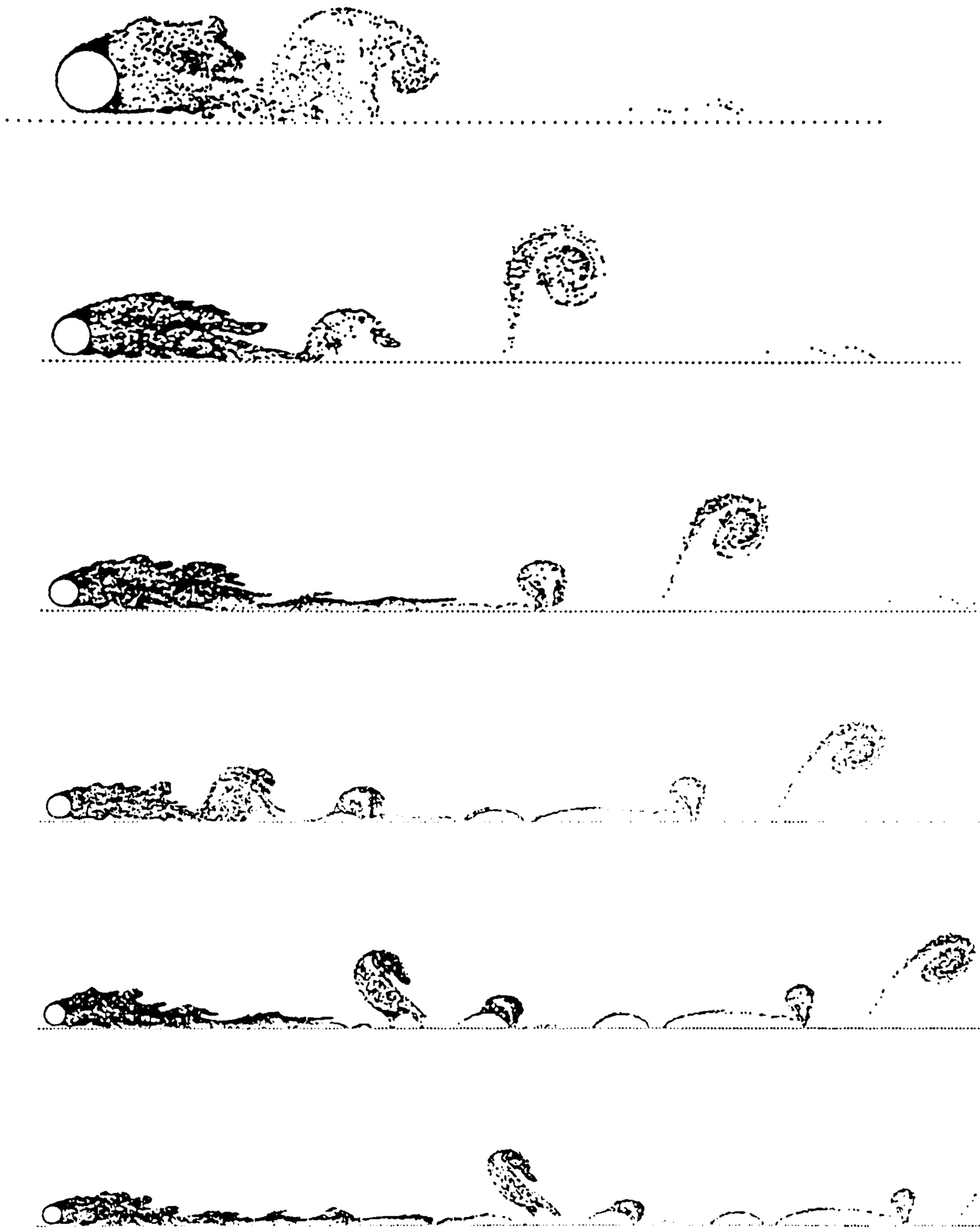

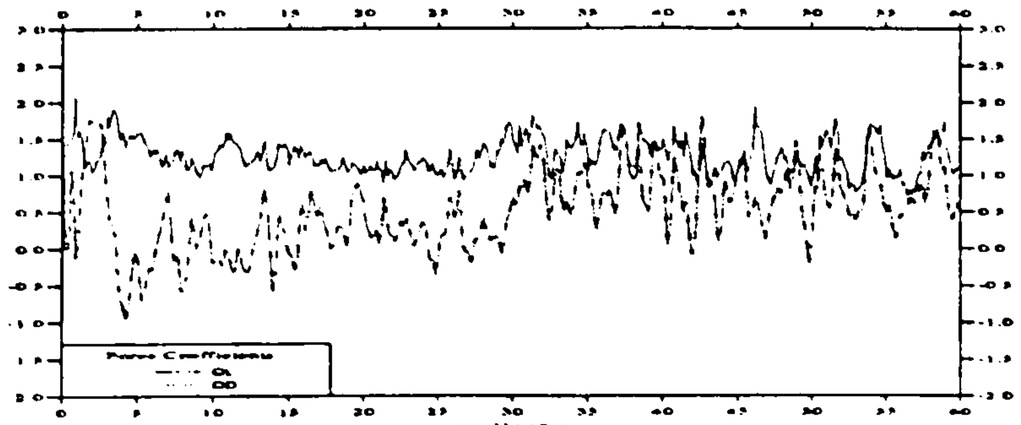

Figure 6.22.-*The Flow Pattern at t = 10, 20, 30, 40, 50, 60, and the Force Coefficients for G/D = 0.25, and Re = 100000*

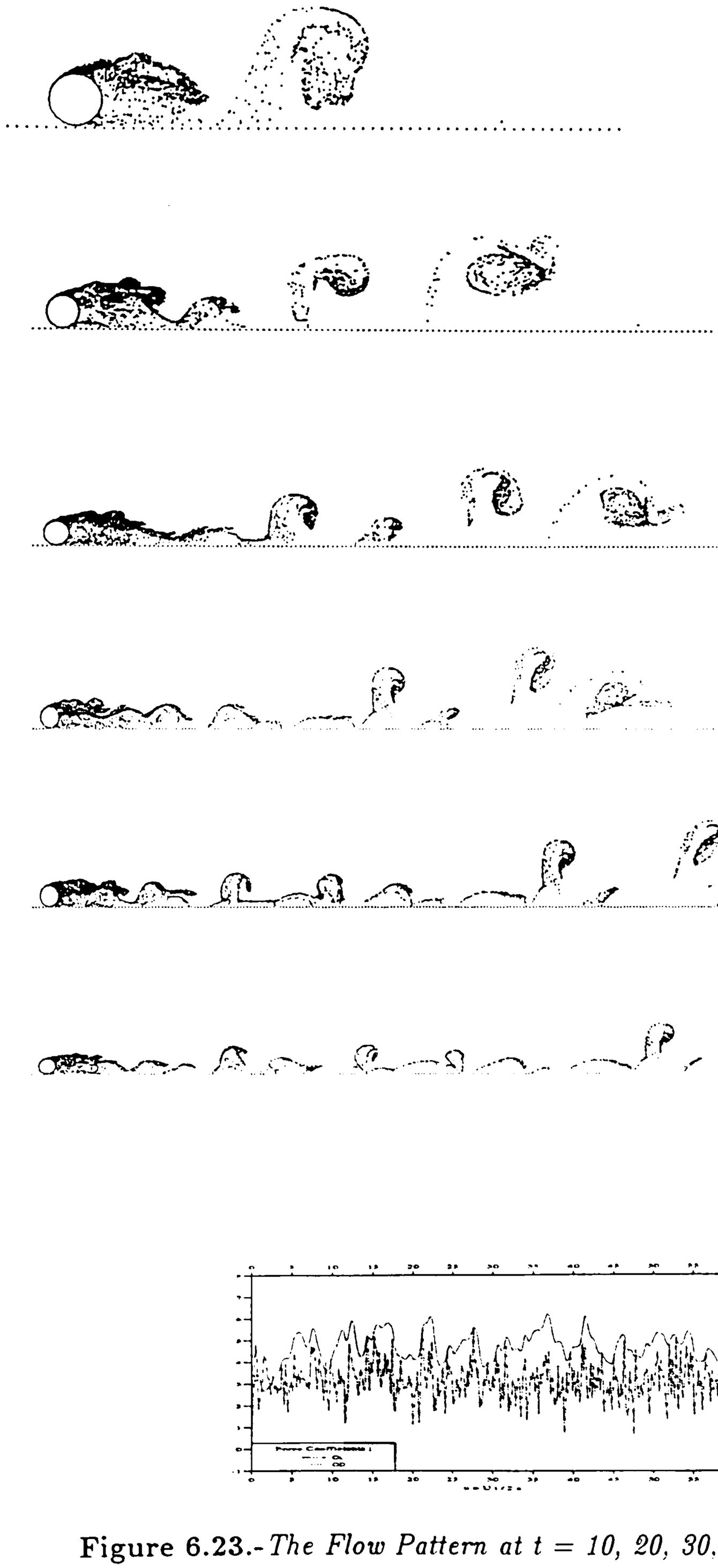

Figure 6.23.-*The Flow Pattern at t = 10, 20, 30, 40, 50, 60, and the Force Coefficients for G/D = 0.1, and Re = 100000*

Using the same cylinder parameters as in the previous chapter (the number of elements N_e is 64, the time step Δt is 0.15, and vortices are released from the first ring out), the hydrodynamic behaviour of the cylinder and its flow pattern at the Keulegan-Carptenter number Kc of *40*, with gap ratios $\frac{G}{D}$ of *2*, *1*, *0.5*, *0.2*, *0.1*, and at a number of values of the Reynolds number Re of *25000*, *50000*, *75000*, *100000*, are investigated in this section.

At the first gap ratio of $\frac{G}{D}$ *2* the flow pattern and the force coefficients are displayed in figure (**6.24**). At $\hat{t} = 22.5$ the pseudo-Karman vortex type of flow is produced behind the cylinder. The influence of the wall that is expressed in the suppression of the vortex street is not apparent in the region close to the cylinder. This is mainly due to the relatively wide gap between the cylinder and the wall. When the flow is reversed, more vortices will be convected close to the cylinder compared to that of the isolated cylinder as they are unable to spread in a downward direction due to the presence of the wall. It is seen that the vortices

approach the wall tangentially. However, any vortices crossing the wall have been removed.

The in-line force coefficient shows only slightly less than the experiment results of **Sarpkaya** [**81**][**82**] by about *5%*. Sarpkaya's values for the drag and inertia coefficients are *1.43* and *1.17*, while those obtained from the present study are *1.56* and *1.89* respectively.

At the lower gap ratio of $\frac{G}{D} = 1$, the pseudo-Karman vortex street type flow also appeared behind the cylinder. The stronger influence of the wall is reflected in a more curved shape of the vortex street when it approaches the wall. This can also be seen in the higher amplitude of the drag coefficient which increases by about *5%* compared to the previous case. As also displayed in figure (**6.25**), the amplitude of the drag coefficient is higher than the experimental results of **Sarpkaya** [**82**] by about *4%*, whereas the phase is in quite good agreement.

As the gap ratio is reduced to $\frac{G}{D} = 0.5$, the difference of the amplitude of the drag coefficient compared with that of the experimental results is narrowed to about *3%* and the phase of the flows is again in good agreement as shown in figure (**6.26**). The flow pattern still has strong similarities with the unbounded oscillatory flow, but the trend of a deflected wake on the wall side of the cylinder is becoming increasingly pronounced.

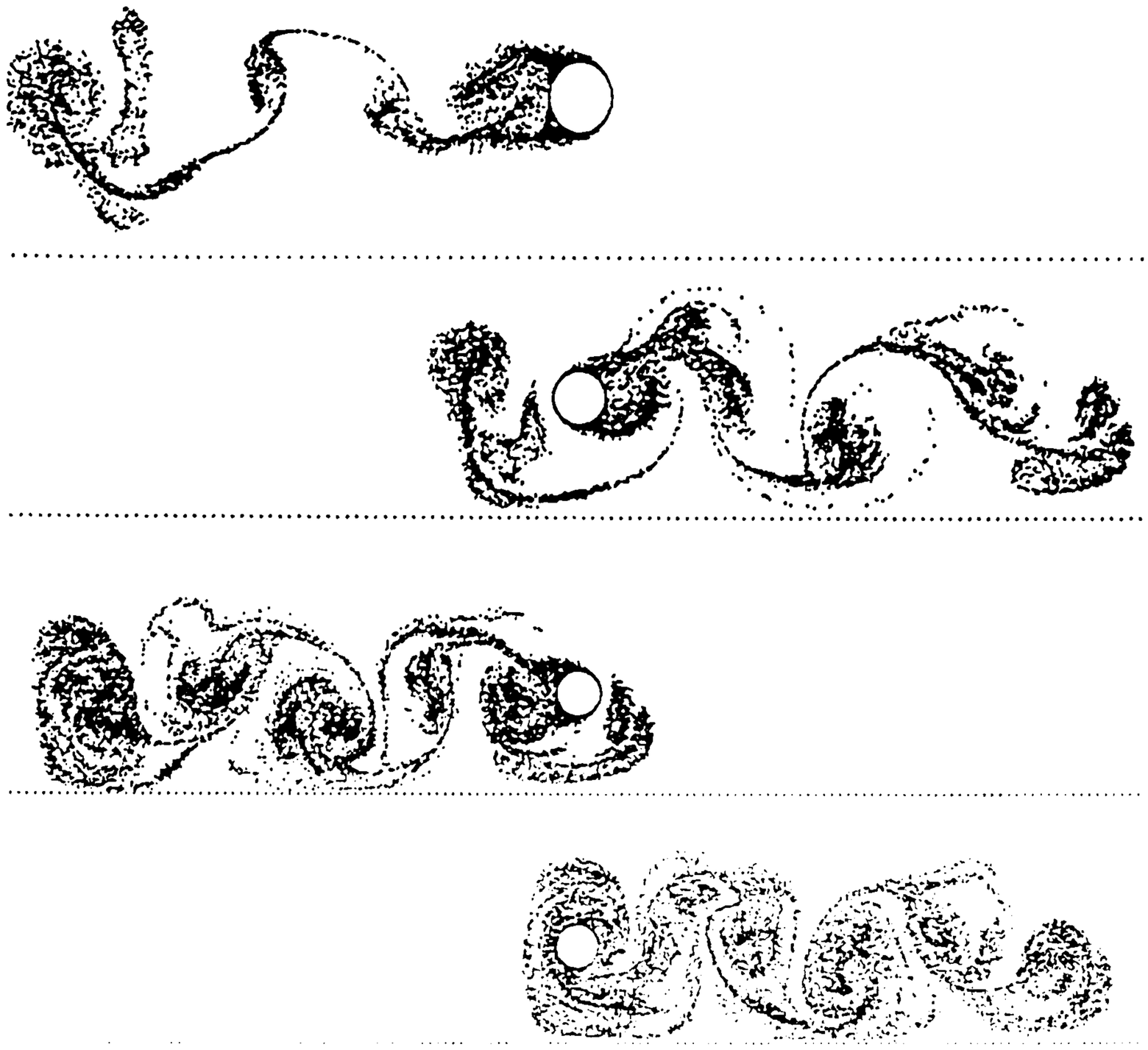

Figure 6.24.-*The Flow Pattern at t = 20, 40, 60, 80, 100, 120, and the Force Coefficients for G/D = 2, Kc = 40 and Re = 25000*

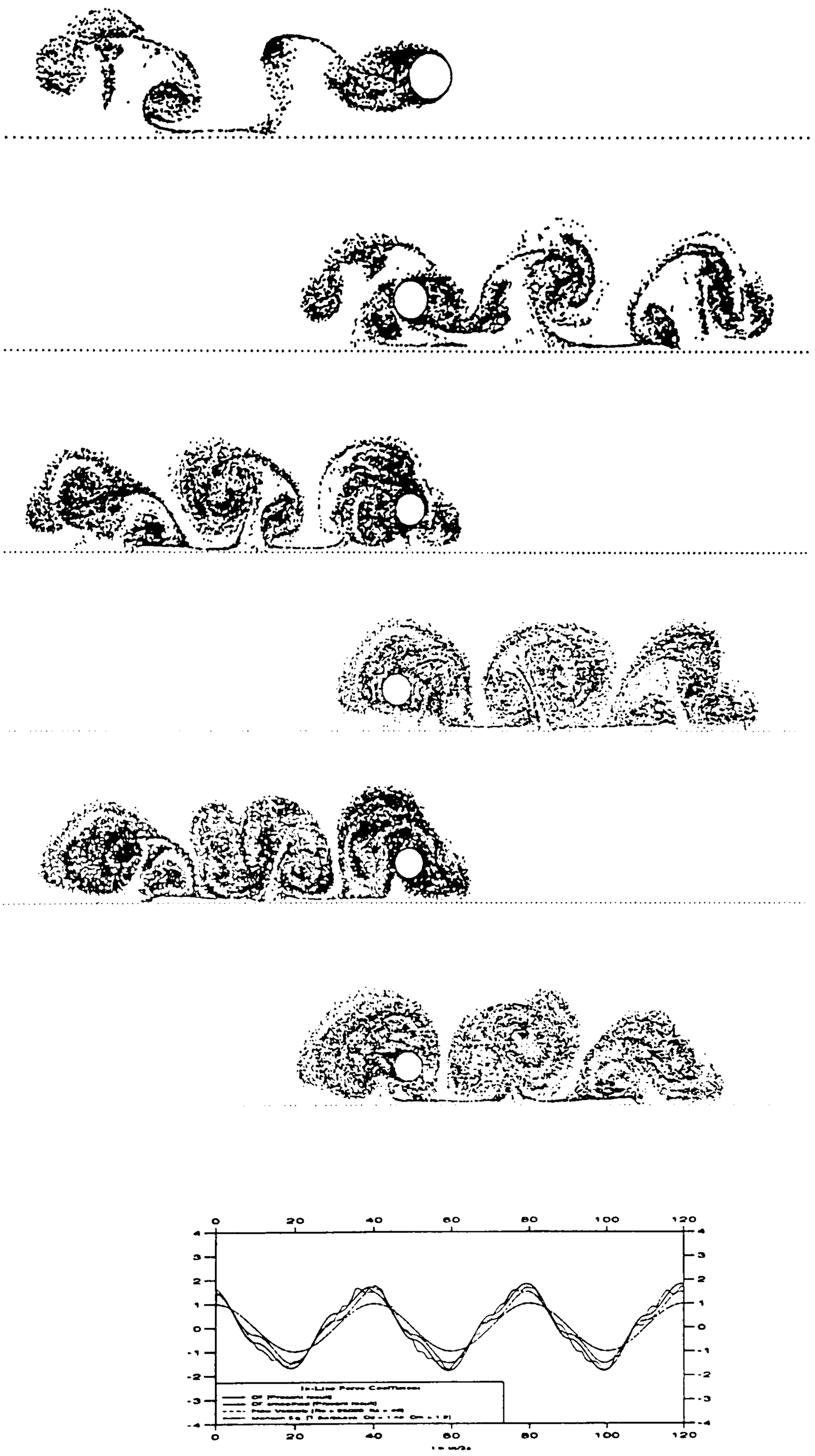

Figure 6.25.-*The Flow Pattern at $t = 20, 40, 60, 80, 100, 120$, and the Force Coefficients for $G/D = 1$, $Kc = 40$ and $Re = 25000$*

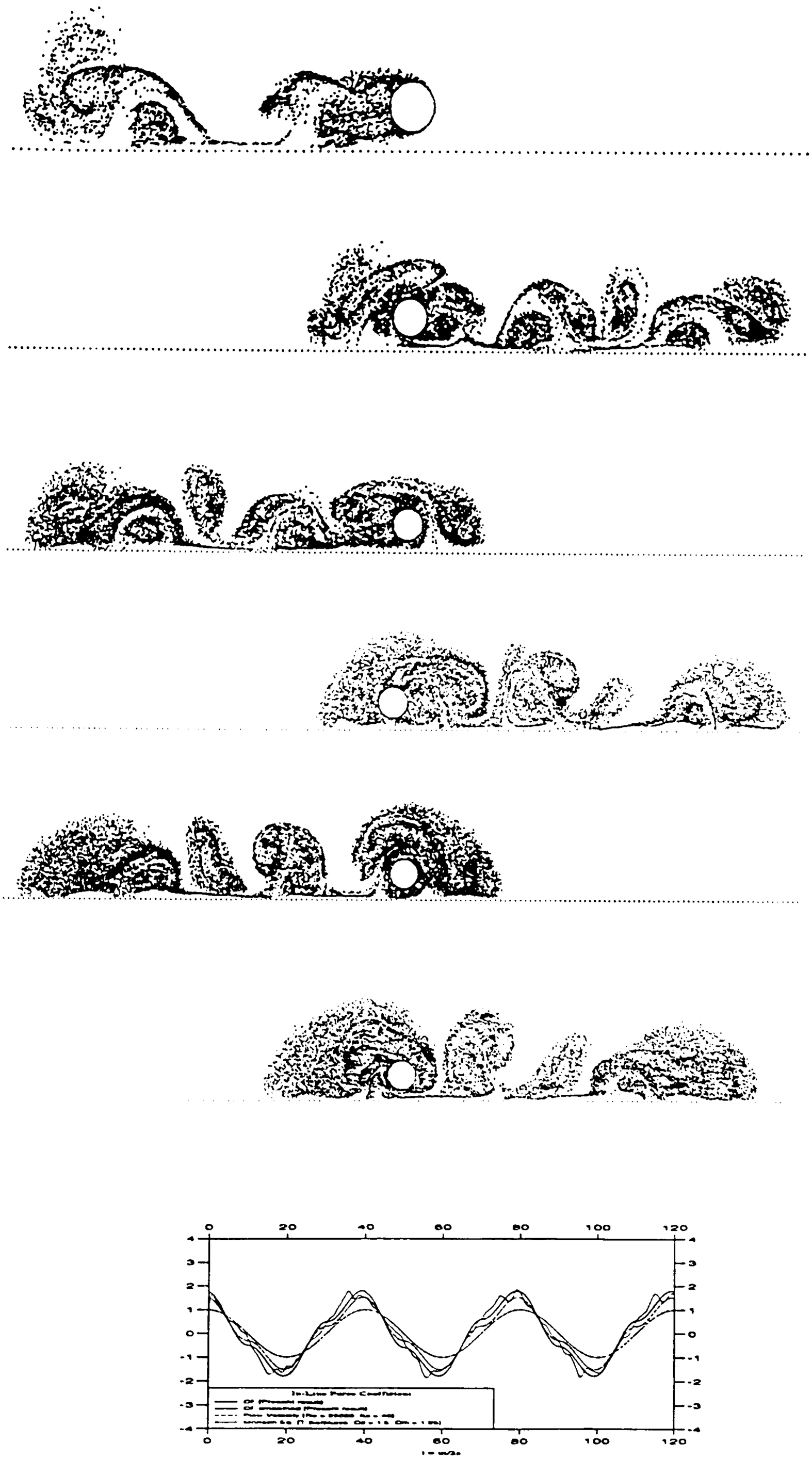

Figure 6.26.- *The Flow Pattern at $t = 20, 40, 60, 80, 100, 120$, and the Force Coefficients for $G/D = 0.5$, $Kc = 40$ and $Re = 25000$*

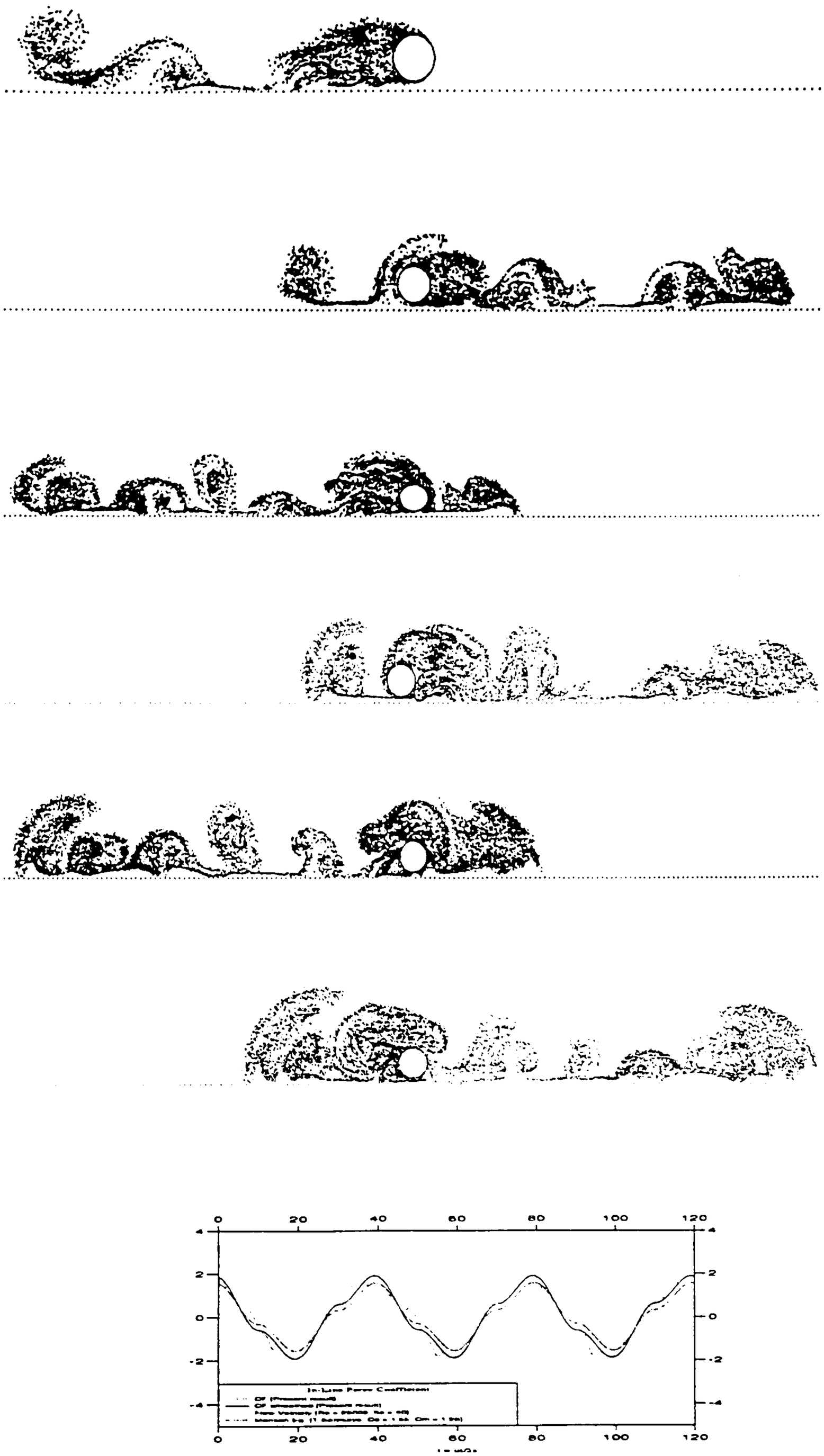

Figure 6.27.-*The Flow Pattern at t = 20, 40, 60, 80, 100, 120, and the Force Coefficients for G/D = 0.2, Kc = 40 and Re = 25000*

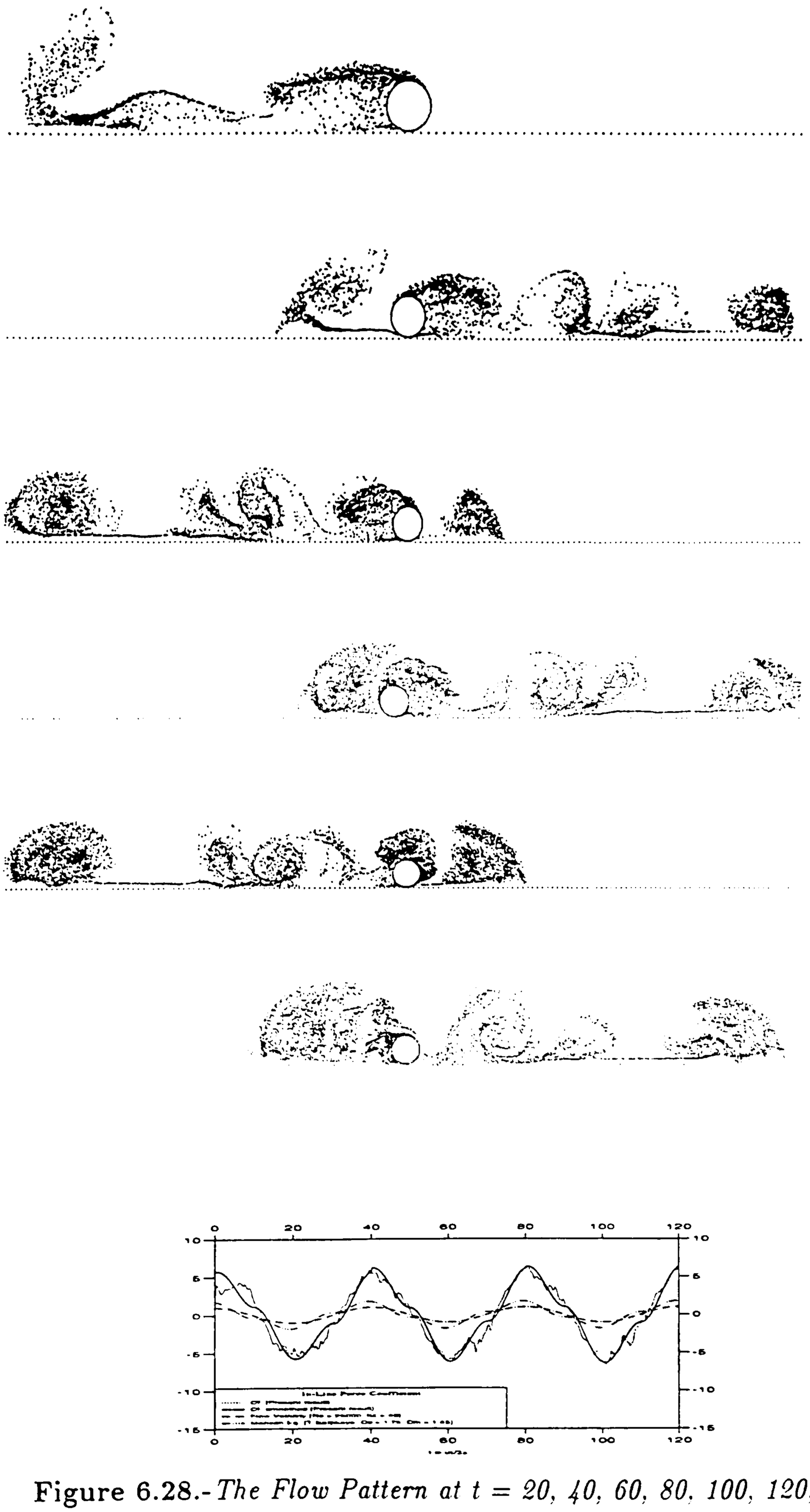

Figure 6.28.-*The Flow Pattern at $t = 20, 40, 60, 80, 100, 120$, and the Force Coefficients for $G/D = 0.1$, $Kc = 40$ and $Re = 25000$*

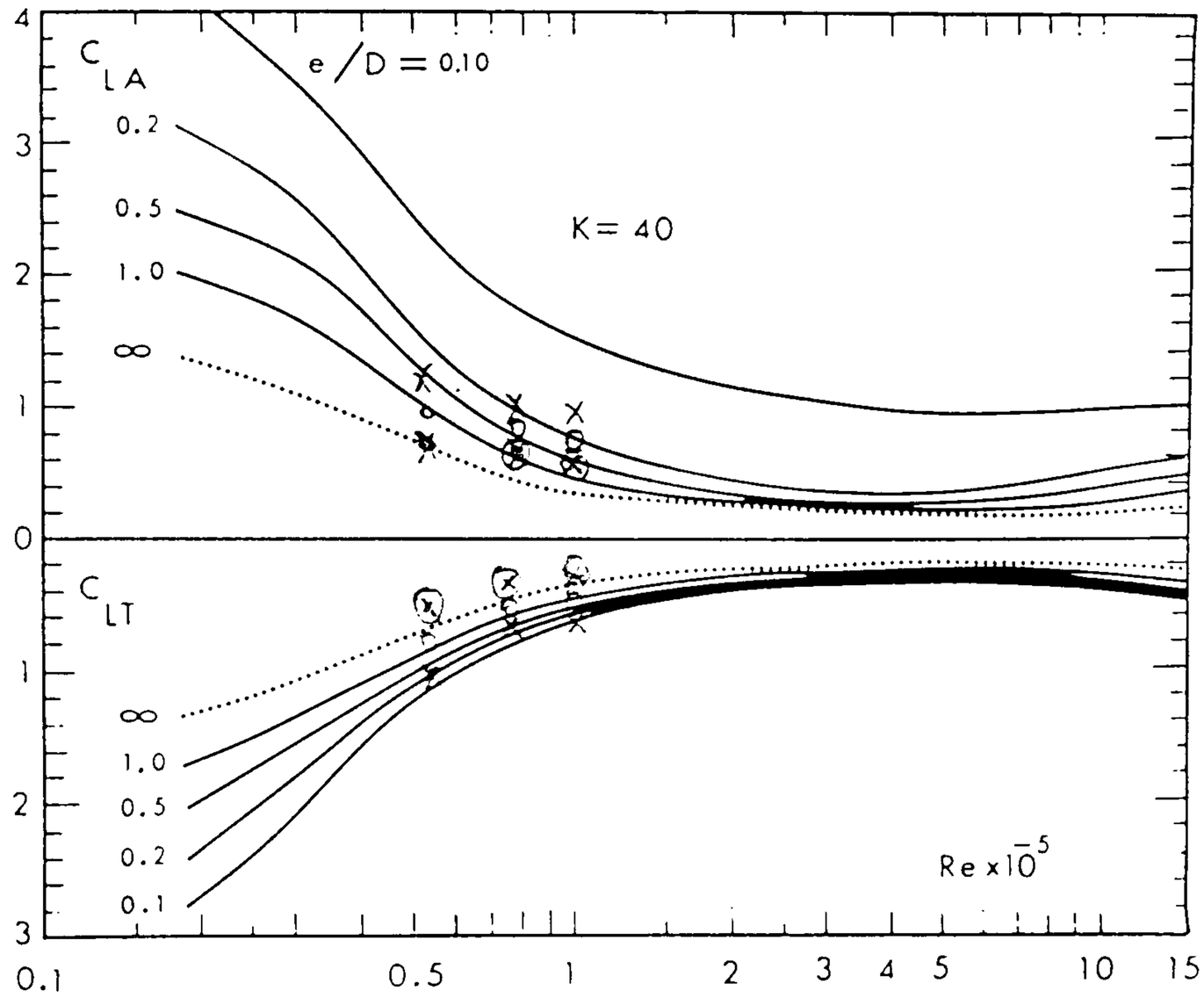

Figure 6.29.- *The Mean Peak of the Lift Coefficient Vs. Reynolds numbers*

The flow becomes even more distorted when the cylinder is put closer with a gap ratio of $\frac{G}{D} = 0.2$. A drag coefficient with amplitude around *1.9* is produced. which is within *2%* of the experimental value as shown in figure (**6.27**). As reported by a number of experimenters [**41**], [**11**], when the gap ratio gets close to the wall. the turbulent boundary layers created on the wall and cylinder surface and their interaction causes the drag coefficient of the cylinder to drop to about *1.3*.

As has been discussed already. the present model cannot reproduce the effects and although the results are surpringly close to experimental results for the larger gap ratios. for $\frac{G}{D}$ less than *0.2* they become increasingly unrealistic as shown in figure (**6.28**). The effect of wall proximity on the lift coefficient of a circular cylinder can the be displayed in figure (**6.29**). C_{LA} and C_{LT} are the mean peak of the lift coefficients in the directions of away and toward the wall respectively.

6.9 Conclusion

Another extention of the discrete vortex model for investigating the flow around a single cylinder placed in a channel and near a plane wall in uni-directional and

oscillatory flow has been presented in this chapter. The wall is modelled by a line source distribution of finite length. The interaction between the wall and the cylinder and its shed vortices has been computed through the use of two overlapping grids. The use of a polar grid expanding from the cylinder and a uniform rectangular grid as described in the previous chapters is still maintained. In this model, the size of the wall source element is equal to the size of the rectangular grid segment.

Two different kinds of boundary conditions are solved simultenously on the cylinder, with zero tangential velocity, and on the wall, with zero normal velocity. The influence of the vortices on the cylinder is computed using the polar grid node while that of the wall is computed using the rectangular grid. In other words, there is no direct calculation of the interaction between the wall and the active polar grid nodes. This grid strategy was chosen in an attempt to get a satisfactory interaction between the cylinder, shed vortices and the wall sources.

In the case of a cylinder placed in a channel, the increase of the drag coefficient in uni-directional flow is in a good agreement with the available reference except when the channel width is small compared with the cylinder diameter. In oscillatory flows, an increase in the mean peak drag coefficient comparedd to that of an isolated cylinder is also detected. It is not possible to validate this result because the author is unaware of any experimental results for this flow configuration. In the case of a cylinder placed near a plane wall in uni-directional flows, the positive mean lift coefficient is generally predicted well. However, when the gap is less than 0.1D the algorithm fails to produce realistic results for the force coefficient.

Chapter VII

CONCLUSION

7.1 Review of Study

When an offshore structure is being designed it is necessary to be able to estimate the fluid loading on the structure and to be able to predict the fluid / structure interaction. Whilst there is reliable data available relating to cylinders in unbounded flows that can be used for this purpose the behaviour of such flows is much more uncertain when one member of the structure is placed close to another or when the member is placed near the sea bed. Experimental evidence shows that the loads due to this kind of fluid-structure interaction can be increased or decreased sharply depending on their relative orientation to the oncoming flow, and to their proximity to solid boundaries.

The phenomena that occur in this type of problem could originate in the boundary layer interaction, turbulent interaction and/or vortex shedding processes which are complicated in nature, depending on the flow configuration involved. Many authors have investigated these phenomena in order to gain more understanding about them either experimentally or numerically. Despite the enormous effort, the physics of these flows is still not well understood, and further study is needed. For those reasons various authors have tried to model flows of this type numerically with varying degrees of success (see **Bearman** and **Graham** [**10**]).

Following in this tradition, in the present study a simple basic discrete vortex scheme has been developed to model the flow around a single cylinder in unidirectional and oscillatory flows. Using the same basic model the effect of the interaction of two cylinders with equal and with different radii has also been investigated. Finally, the algorithm was extended to simulate the flow around a cylinder in close proximity to a wall. The model did not include the development of a boundary layer on the wall.

Within the constraints imposed by such a simple model, the algorithm has produced some interesting results, in terms of flow patterns, wake interactions, and the force coefficient of typical flows which are complicated in nature.However, it has been found that the nature of the flow is too complicated to be modelled

comprehensively by such a simple scheme and a certain range occurs beyond which the model fails to portray the flow realistically. The study shows that there is a trade-off between simplicity of modelling and success in implementation, although it is by no means certain that more sophisticated models would perform any better for the flows investigated.

In the case study undertaken, fairly good results were obtained when the degree of wake or wake/body interaction was lower than a certain level, beyond which the interaction becomes so complicated as to be beyond the scope of the model. This complication is mainly attributed to boundary layer interactions which become dominant, for example, in the case of two cylinders in very close proximity.

Another possible cause of discrepancies between numerical and experimental results is that the present study used a purely two dimensional approach which ignores three dimensional effects such as vortex stretching. The available data, where it exists, with which the present results have been compared, are mostly experimental results which are not free from the three dimensional effects. These sources of uncertainty in model validation show that further studies both numerically and experimentally are still needed to increase the understanding of the phenomena of the flow interactions.

7.2 Findings

In the present study, a conventional linearly expanding grid system as was used by **Murray** [**70**] in his investigation of the flow around a single cylinder was implemented. In a Vortex-in-Cloud model, the advantage of using a grid is that CPU time efficiency can be increased and a much better flow pattern can be obtained. This is because, the number of operations, compared with the conventional methods, required to compute vortex-to-vortex interactions is greatly reduced and the error caused by the strong interaction of vortices in close proximity, is now to a large extent removed from using the grid nodes.

In preliminary attempts to extend this approach to the problem of wake interaction between two cylinders, overlapping polar grid nodes expanding from each cylinder were used. The fluid domain was divided into two sub-domains, in which if a vortex shed from one cylinder was carried closer to the other cylinder, the vortex was considered to have 'jumped' into the other sub-domain. The vortex was then stored as one belonging to the other cylinder. All vortices belonging to one cylinder are distributed onto polar grid nodes which are associated with it.

In the grid-node-to-grid-node calculation of the vortex velocity, the contribution from all active grid nodes is computed. In the calculation of the influence of the active grid nodes belong to a single grid system, the stability of the calculation is ensured as no active grid nodes will be very close or coincide. However, when the influence of the active grid nodes belonging to the other cylinder are included, it is possible for one or more active grid nodes from the different grids to be located closely one to another, causing instability in the calculation. A cut-off radius was tried to cope with such difficulties. However, this simple overlapping polar grid system proved not to be viable.

To overcome these problems, a rectangular grid system with a uniform element size, overlapping the existing two polar grids was intoduced over the domain. In this strategy, any vortex shed from a particular cylinder is identified, stored and treated as being associated with that cylinder over the whole calculation period. Its relative position is also defined with reference to its own polar grid system and the overlapping rectangular grid system. In calculating a vortex velocity, the contribution from other vortices shed from the same cylinder is carried out in the polar grid system associated with that cylinder, while the contribution of vortices shed from the other cylinder is computed on the rectangular grid system. The rectangular grid system can then be considered to be an alternative means of uniformly distributing the error instead of using the cut-off radius approach described in the previous grid strategy.

Similarly, in the case of cylinder / wall interaction, the contribution of the wall source distribution on the calculation of a vortex velocity was not computed over the wall-active polar grid nodes, instead it was calculated over the active rectangular grid nodes before being distributed to the vortex velocity in question.

In the implementation of this simple grid strategy for the calculation of wake interactions some variables have to be arbitrarily assigned. In the present extension of the basic discrete vortex method, namely the number of cylinder elements, the time step, the diameter of the first ring out, the size of the rectangular grid, and the level of interaction of vortices in close proximity, all have to be set. The first three variables have to be set in such a way to balance the effect of the diffusion process in order to get good results of the force coefficients and the flow pattern over a wide range of Reynolds number.

In the present model, any vortices that penetrate the cylinder's surface were deleted and removed from the calculation. To compensate for this the total

strength of the deleted vortices was then redistributed over the cylinder surface at the next time step to satisfy Kelvin's condition of the zero net vorticity. In the flow around a single cylinder, this step is fully justified as the strength of the deleted vortices is distributed fairly to the newly created vortices and hence the zero net vorticity is satisfied every time. In the case of flow around two cylinders, the same procedure was followed for each cylinder separately. This is imposing a boundary condition extra and above Kelvin's theorem, which only states that the total vorticity in the whole domain is equal to zero every time. However as shown previously, especially for two cylinders in tandem, this scheme is capable of giving good results over range of gap ratios.

In uni-directional flow, the diameter of the first ring out, from where the ring vortices are introduced, was set to be a constant while in the oscillatory flows it was set to be inversely proportional to the β value. The constant of proportionality was then used through out the study as a simple model to simulate the boundary layer thickness, (see **Downie** [**26**]). Using this approach, together with the Random Walk scheme to model the diffusion process, the flow around a single cylinder in uni-directional flow can be well simulated over Reynolds numbers from *100* to *100000*. In oscillatory flows over a β value of *1000* to *4000*, good predictions of the force coefficients were only obtained. Numerically, the limitation is attributed to the simplicity of modelling the boundary layer thickness itself which at small β values becomes too big and vice versa.

As was described in section (**4.7**), the use of the Random Walk method will give a valid result if the number of discrete vortices is infinite. Hence, with a finite number of vortices the diffusion process is only approximately modelled. For the flow around one cylinder this approximation gives good predictions for the flow pattern and the force coefficients. However, for the flow around two cylinders, especially when they are arranged side-by-side, the symmetrical properties of the vortex street shed by both cylinders could not be achieved. The failure to model this flow has its origins in instabilities occuring when the vortices shed from one cylinder approached closely those shed from the other cylinder.

One factor that contributes to the instability is that the number of vortices is too few to model the complex wake interaction especially during the diffusion process. Another important factor is that the chosen time step was relatively big which increases the magnitude, and hence the influence, of the random displacement of the vortices initiating the instability in the early stages of the flow development.

The stabilities propagate and induce an unrealistic flow pattern after the flow develops further. The related parameter, the size of the polar and rectangular grid segments makes a significant contribution in creating the instability as the vortex velocity is calculated on the grid nodes.

The problem of the instability in the flow arising from the interactions of the wakes of the two cylinders may be overcome by the use of a higher number of vortices, smaller time steps and a smaller grid size. However, there is a trade-off between the magnitude of these variables and the CPU time used which increases sharply as the variables get smaller. Modelling the flows involves optimising this trade off subject to constraints imposed by computing resources and project duration.

After some preliminary calculations, it was found that a relatively coarse model (relatively big time step, grid sizes and small number of vortices) could be used to investigate the wake interaction behind two cylinders, if a vortex reduction scheme was incorporated in the discrete vortex method, (see **Naylor** [**71**] and **Basuki** [**6**]). It was found that the instability arising from the vortex interaction could also be controlled by the implementation of a vortex strength reduction scheme, in which the strength of each vortex was reduced at every time step. After extensive preliminary calculations, the constant for the rate of vortex strength strength reduction was assigned on the basis of the best performance of the algorithm in relation to the available experimental evidence.

Implementation of the vortex reduction scheme does not model any of the physical process as implied in the vorticity transport equation (**3.9**). However, to some extent, it can be considered to model three dimensional effects such as vortex stretching and vortex correlation with length. In the final analysis its primary function is that of a numerical device that allows a realistic flow to develop whilst maintaining the basic simplicity of the model.

From a numerical point of view, the main finding of the study has been that even with a simple model that has no explicit scheme for turbulence, by using the techniques described above, flow patterns and force coefficients can be obtained that agree surprisingly well with experimental results for a range of fow configuration over a range of Reynolds number. The greatest difficulties in achieving these results has been in controlling instabilities associated with wake-to-wake or wake-boundary interactions. It should be said that validation of the model, in so far as it has been possible to carry out, has only been with reference to the gross

features of the flow. The fine detail of the flow, such as the true turbulence characteristics, or the detailed development of boundary layers and their interaction with the flow can not be modelled by the present approach, which breaks down when these features begin to dominate the behaviour of the flow.

The case studies were chosen with reference to their relevance, in particular, to the field of offshore engineering. In calculating the fluid loading on a jacket structure, the various structural members have traditionally been considered to be independent. The present study confirms investigations that have indicated that interference effects can significantly influence the fluid loading of members in close proximity to one another. This finding has particular relevance to structural configurations such as risers attached to jacket legs and the fluid loading on structural members bearing anodes. The present model advances the understading of these flows and can be used to assess the validity of force coefficients currently in use in the offshore industry.

The case studies have also demonstrated the influence of the presence of the boundaries on the development of flow patterns and on force coefficients. The model could be used for assessing the behaviour of free spanning sub-sea pipelines, or even, with some modification of structural members near to a free surface. Many experimental investigations to determine force coefficients for Morison's equation have been carried out in U-tubes and wave flumes. The blockage effects of oscillatory flows are not well documented or understood. The model can easily be adapted to compute such flows and add to existing knowledge in this area.

In general the results from the case studies agreed well with the experimental evidence where it was available for comparation. Explicit findings are given in the relevant chapters. The case study involving anodes was of some interest because it has been the subject of a previous study using the discrete vortex method (**Murray** [**68**]) although in that case the anode-cylinder combination was treated as a single body. Treatment of the anode as a separate body has lead to some differences in the flow produced. In the present case it has been found that the vortex shedding from the anode is suppressed for most of the flow configuration although vorticity from the anode can still have a significant effect on the wake of the combined body.

7.3 Suggestion for Future Work

The most obvious follow up to this study is to refine the model to consider

the instabilities due to wake / wake and wake / boundary interaction and to investigate the effects of increasing the flow definition. Such a study would require substantial computing resources if the flows were to be investigated in a meaningful manner. In addition, there are a number of applications in the field of offshore engineering to which the basic model, with some modification, could be used to gain useful insight and further data. For example, the algorithm for the flow around a cylinder placed in a channel could be extended to incorporate the effect of a free surface by converting the top wall to a free surface. Instead of the Neumann boundary condition, the kinematic and dynamic boundary conditions shown in equation (**3.23**) would have to be satisfied at every time step. Some difficulties were encountered in an attempt to model such a flow in the present study namely, that as the present rectangular grid system is fixed relative to the cylinder, a way has to be found to allow the ractangular grid system to accomodate the movement of the free surface contour. Preliminary work on this problem indicated that a changing rectangular grid system to cover both the free surface and discrete vortex movement at the same timewould give benefit results. However, this can introduce further difficulties in relation to the efficiency of the algorithm as the re-indentification of the vortex-related variables would have to be carried out at every time step. Although this and other problems concerning definition of the free surface could not be solved within the time constraints of the present study, this area could be studied further with a good prospect of success.

There was no explicit turbulence modelling in the present study. As mentioned previously, surprisingly good results were obtained over a wide range of Reynolds numbers for the gross characteristics of the flow. However, it was not possible to model some flow configurations. Development and inclusion of a turbulence scheme may well enhance the model's capability for predicting the flow in the grater detail and widen its range of applicability to other flow configurations.

Flow visualisation of cloud cavitation shows a striking resemblance to flow patterns obtained using the discrete vortex method. A preliminary investigation as part of the present study indicated that the attachment of a bubble to each vortex in the flow could be a means of modelling this type of cavitation. In this case the bubble which has a variable radius, could be located at the core of each vortex. The radial effect due to the changing of the bubble size under the influence of other vortex-bubbles in the domain could be represented through the following equation for the velocity potential.

$$\phi = \frac{R^2}{r}\frac{dR}{dt} \tag{7.1}$$

The changing bubble characteristics are related to conditions in the ambient flow and can be modelled using the well known Plesset-Povinsky equation for bubble dynamics as follows (see **Plesset** and **Shaffer** [**73**]),

$$\frac{(P_i - P_\infty)\,({R_o}^3 - R^3)}{3} + \frac{\rho}{2}\,R^3\,(\frac{dr}{dt})^2 + 4\,\mu\int_0^t R(\frac{dR}{dt})^2\,dt \tag{7.2}$$

The combination of a vortex-bubble in the flow could therefore be modelled by the combination of a vortex and a source with a variable source strength.

In reality the bubble / fluid mixing flow is obviously a two phase flow in which two kind of fluids with different densities mix together to form a new state of flow. One difficulty arising in this model is that as the bubble size is growing or shrinking with time, the average density of the fluid changes at every time step, and this must be taken into account when satisfying the continuity equation as shown in equation (**3.4**). Although some preliminary work was cariied out for this type of flow, the author was unable to find suitable results against which to validate the model, and hence the extent to which the model can really simulate the bubble cavitaion phenomena still needs further study.

The inclusion of three dimensional effect using discrete vortex modelling has been undertaken by various authors. In the calculation of the influence of the vortex shedding from the keel of a rectangular barge rolling in beam seas, **Downie** [**27**] tackled the three dimensional nature of the flow by using a strip method involving two dimensional slices of flow along the barge. More recently, **Graham** [**38**] extended the problem to investigate the flow around a ship-like body using slender body theory. However such methods do not account for three dimensional effect. The ultimate goal for dicrete vortex methods must be their extension to a fully three dimensional model along the lines suggested by **Leonard** [**59**] and others. An area of investigation would be the development of a fully three dimensional discrete vortex approach to the flows dealt within the present study.

Finally the computation time of the algorithm could be much reduced, while at the same time maintaining the simplicity of the model, by running it on a parallel computer. **Hardy et.al.** [**43**] has shown speed ups of the order of *12* times the equivalent on a transputer system with *16* processors. Parallelisation of the present

algorithm could allow much longer runs which might resolve some of the problems associated with flow instability arising out of wake to wake interaction.

Appendix A

REVIEW OF THE POTENTIAL FLOW THEORY

A.1. The Flow Around A Cylinder In An Infinite Fluid

As explained in detail in **Kellogg** [**54**], the elementary solution for the velocity potential ϕ of the incompressible, inviscid flows as expressed by the Laplace's equation, as shown in equation (**2.18**),

$$\nabla^2\phi = \frac{\partial^2}{\partial x^2} + \frac{\partial^2}{\partial y^2} + \frac{\partial^2}{\partial z^2} = 0 \qquad (A.1)$$

is

$$\phi = \begin{cases} \frac{1}{r}, & for\ three\ dimensional\ case \\ ln(r), & for\ two\ dimensional\ case \end{cases} \qquad (A.2)$$

where : $x,\ y,\ z$ are Cartesian coordinates and r is the radial distance between $(x_n,\ y_n,\ z_n)$ and some other other point of fluid action $(x_m,\ y_m,\ z_m)$.

The physical interpretation of this solution is that of flow from a point source in *three* dimensional space or a point source/vortex in two dimensional space.

Thus, the velocity potential at m due to that singularity of unit strength at n (where the strength is defined here as the volume of fluid emitted in unit time) is given by,

$$\phi = \begin{cases} \frac{1}{4\pi r}, & for\ three\ dimensional\ case \\ \frac{1}{2\pi} ln(r) & for\ two\ dimensional\ case \end{cases} \qquad (A.2)$$

In the present study which is only concerned with two dimensional flow, the velocity potential ϕ, which satisfies the Laplace's equation $\nabla^2\phi = 0$, can be considered to be described by a distribution of vorticity along a closed contour C as displayed in figure (**A.1**) below.

A complex potential $w(z) = \phi(z) + i\psi(z)$, where $z = x + iy$ is an arbitrary complex point, satisfying these conditions can be written as.

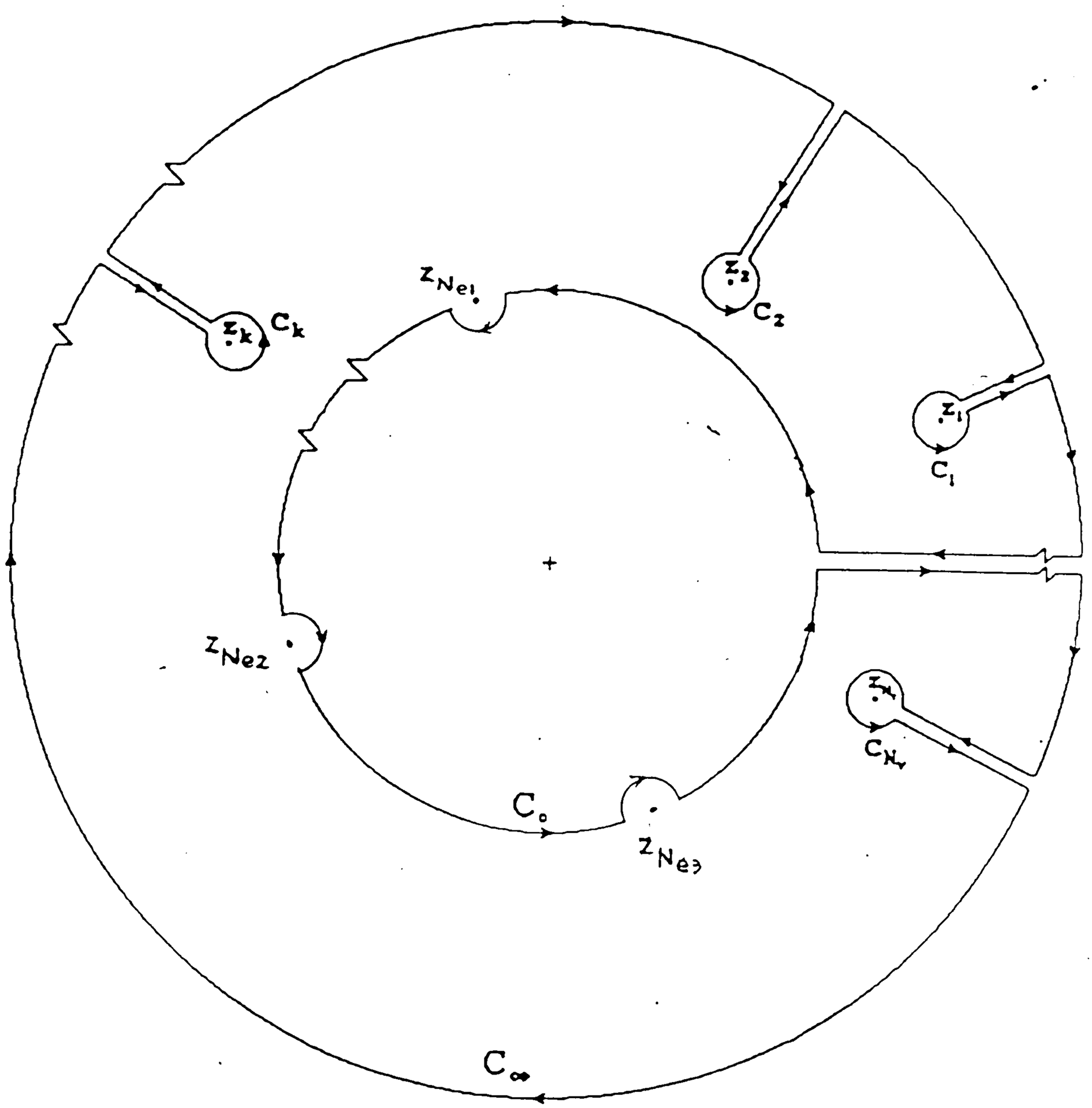

Figure A.1.-*The Path of integration*

$$w(z) = \frac{i}{2\pi} \int_c \gamma_n dS_n \ln(z - z_n) \qquad \textbf{(A.2)}$$

where c is the path of integration and parameterised by the variable dSn, $(z - z_n)$ is the complex distance between z and z_n, and γ_{z_n} is the strength of the vorticity distribution at that point.

Using the relation described in chapter II that $\bar{u}(z) = \frac{\partial w(z)}{\partial z}$. equation (**A.2**) can be written as,

$$u(\bar{z}) = \frac{\partial w(z)}{\partial z} = \frac{i}{2\pi} \int_c \gamma_n dS_n \frac{\partial \ln(z - z_n)}{\partial z} \qquad \textbf{(A.3)}$$

in which the path of integration c is taken around the closed curve displayed in figure (**A.1**).

It is necessary to impose the Dirichlet Boundary Condition on the contour c due to the fact that the fluid particles move tangentially close to the contour in the streamline flow. In the Discrete Vortex Model , this means that the total tangential velocity on the contour due to the free stream velocity u_∞, the cylinder contour c and the shed vortices c_i must be zero on the contour c.

However, if the point z is located on the contour c, care must be taken when evaluating the integral. A limiting analysis shows that the singular contribution to $u(z)$ due to the infinitesimal section of c surrounding the point m is equal to $\frac{1}{2}\gamma_m$ on the external side of c and $-\frac{1}{2}\gamma_m$ on the internal side. Thus, there is a jump in the tangential velocity component across c of magnitude γ_m. In the present study the clockwise direction of integration is taken as positive.

Writing equation (**A.3**) for points on the outside of the boundary,

$$\bar{u}(z_m) = \frac{\partial w(z_m)}{\partial z} = \frac{i}{2}\gamma_m + P \int_c \gamma_n dS_n \frac{\partial \ln(z - z_n)}{\partial z} + P \int_{c_\nu} \Gamma_\nu dS_\nu \frac{\partial \ln(z - z_\nu)}{\partial z} \qquad \textbf{(A.4)}$$

and similarly for the inside of c we have

$$u(z_m) = \frac{\partial w(z_m)}{\partial z} = -\frac{i}{2}\gamma_m + P \int_c \gamma_n dS_n \frac{\partial \ln(z - z_n)}{\partial z} + P \int_{c_\nu} \Gamma_\nu dS_\nu \frac{\partial \ln(z - z_\nu)}{\partial z} \qquad \textbf{(A.5)}$$

In the above, the P before the integral sign indicates that the principal value of the integral should be taken. It can also be seen from figure (**A.1**) that the integral along the contour at ∞, -∞ and along the two parallel lines connecting the singlarities are all equal to zero. Therefore if the surface vorticity distribution makes the contour a streamline then the velocity induced inside the contour is zero

everywhere. By incorporating the influence of the free stream velocity and implementing the Dirichlet boundary condition, the zero internal tangential velocity around the contour c gives,

$$-\frac{i}{2}\gamma_m + \int_c k_{mn}\gamma_n dS_n + \vec{u}_\infty \cdot d\vec{S}_m + \int_{c_\nu} k'_{m\nu}\Gamma_\nu dS_\nu = 0 \qquad \textbf{(A.6)}$$

which is equivalent to equation (**4.6**). This equation then plays a basic role in modelling the fluid flow using the Discrete Vortex Method as described in *chapter IV*.

A.2. The FlowAround A Cylinder In A Bounded Fluid

Following the derivation in the previous section, the case for a cylinder in a finite fluid can be tackled with a little modification to the model as shown in figure (**A.2**) below.

As the blockage effect is the main concern in the present study, arrays of sources are implemented to represent the wall and the Neumann boundary condition, is imposed along the wall. The boundary condition states that no fluid particles penetrate the wall.

Over the cylinder surface, the Dirichlet boundary condition is satisfied as for the single cylinder in the infinite domain. The procedure leads to the following result.

$$-\frac{i}{2}\gamma_m + \int_c k_{mn}\gamma_n dS_n + \int_w k'_{mw}\sigma_w dS_w + \vec{u}_\infty \cdot d\vec{S}_m + \int_{c_i} k'_{mv}\Gamma_i dS_v = 0 \qquad (A.7)$$

It is seen that the third term is the contribution from the wall and this appears because the contour of integration along the wall now contains singularities.

In addition there is an equation describing the influence of the cylinder on the wall,

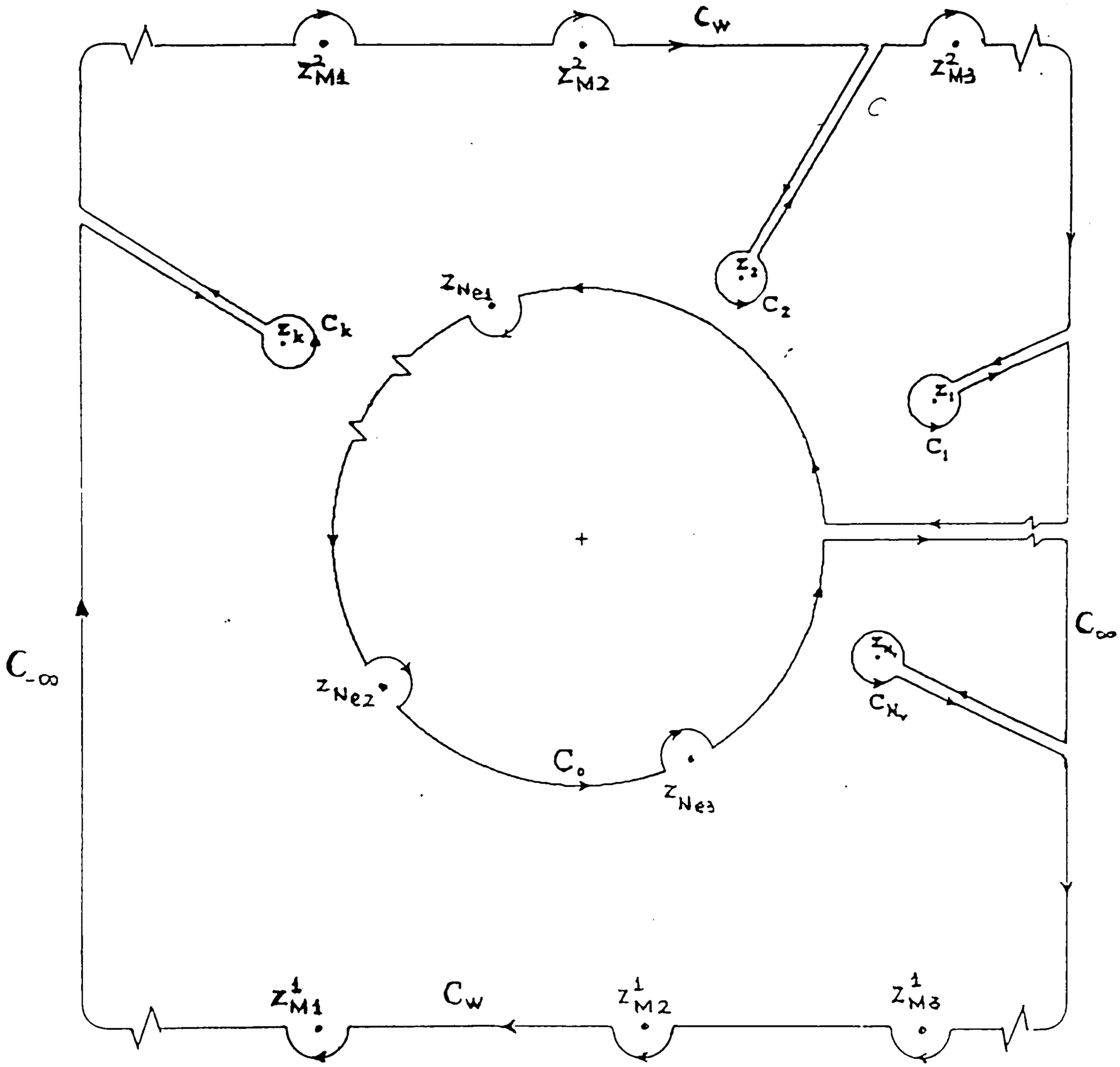

Figure A.2.- *The Path of Integration*

$$-\frac{i}{2}\sigma_m + \int_w k'_{mw}\sigma_w dS_w + \int_c k_{mn}\gamma_n dS_n + \vec{u}_\infty \cdot d\vec{S}_m + \int_{c_\nu} k'_{m\nu}\Gamma_\nu dS_\nu = 0 \quad (A.8)$$

in which the first term is the singular contribution to the normal velocity due to the infinitesimal section of the wall surrounding the point z.

Equation (**A.7**) and (**A.8**), which are equivalent to equations (**5.2**) and (**5.3**) can then be used as the basic equations in modelling the flow around a cylinder in a bounded fluid using the Discrete Vortex Model.

Appendix B

Results for A Single Cylinder In An Infinite Fluid

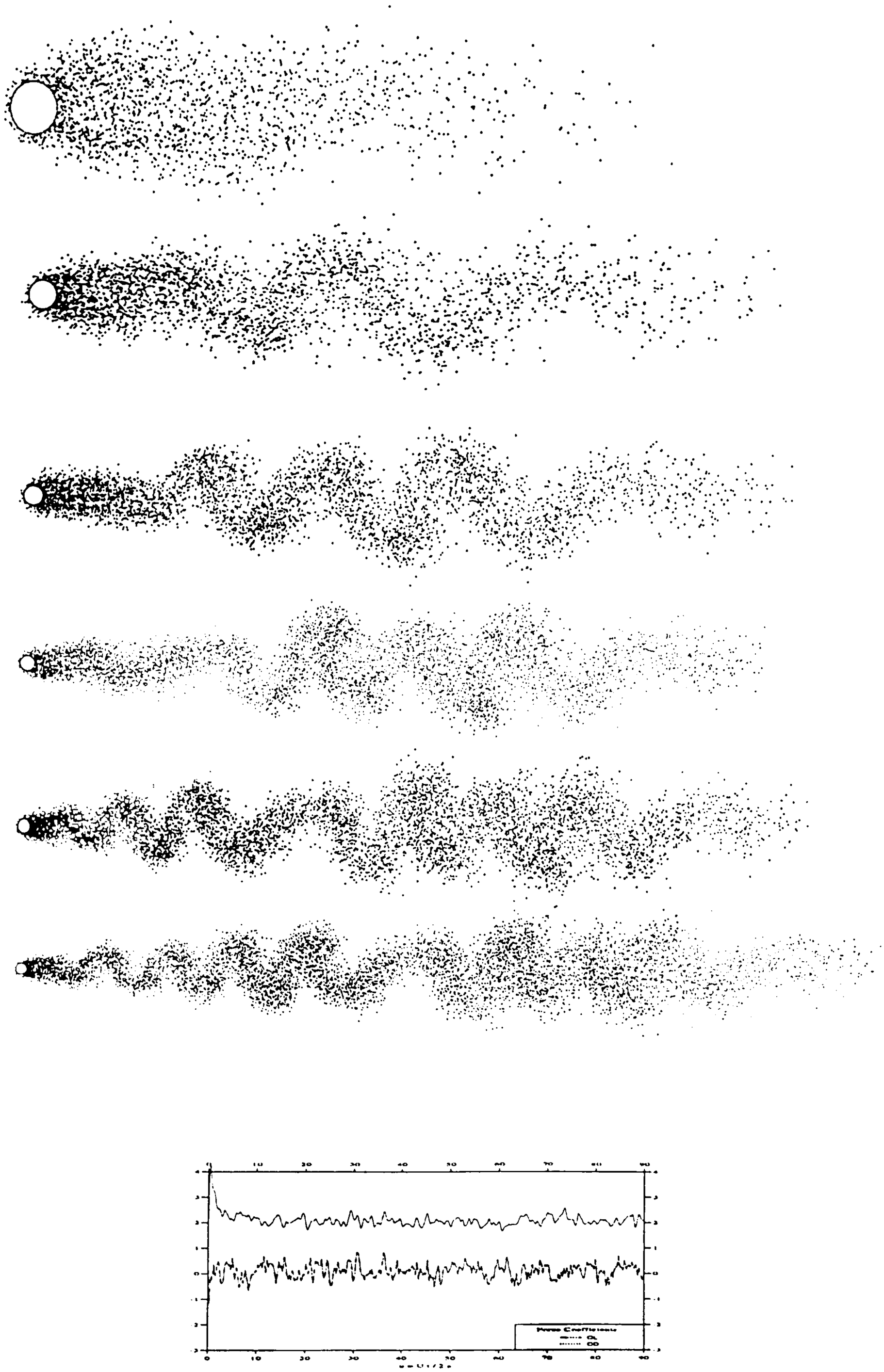

Figure B.1.-*Flow Pattern at t = 15, 30, 45, 60, 75, 90, and the Force Coefficients for Re = 50*

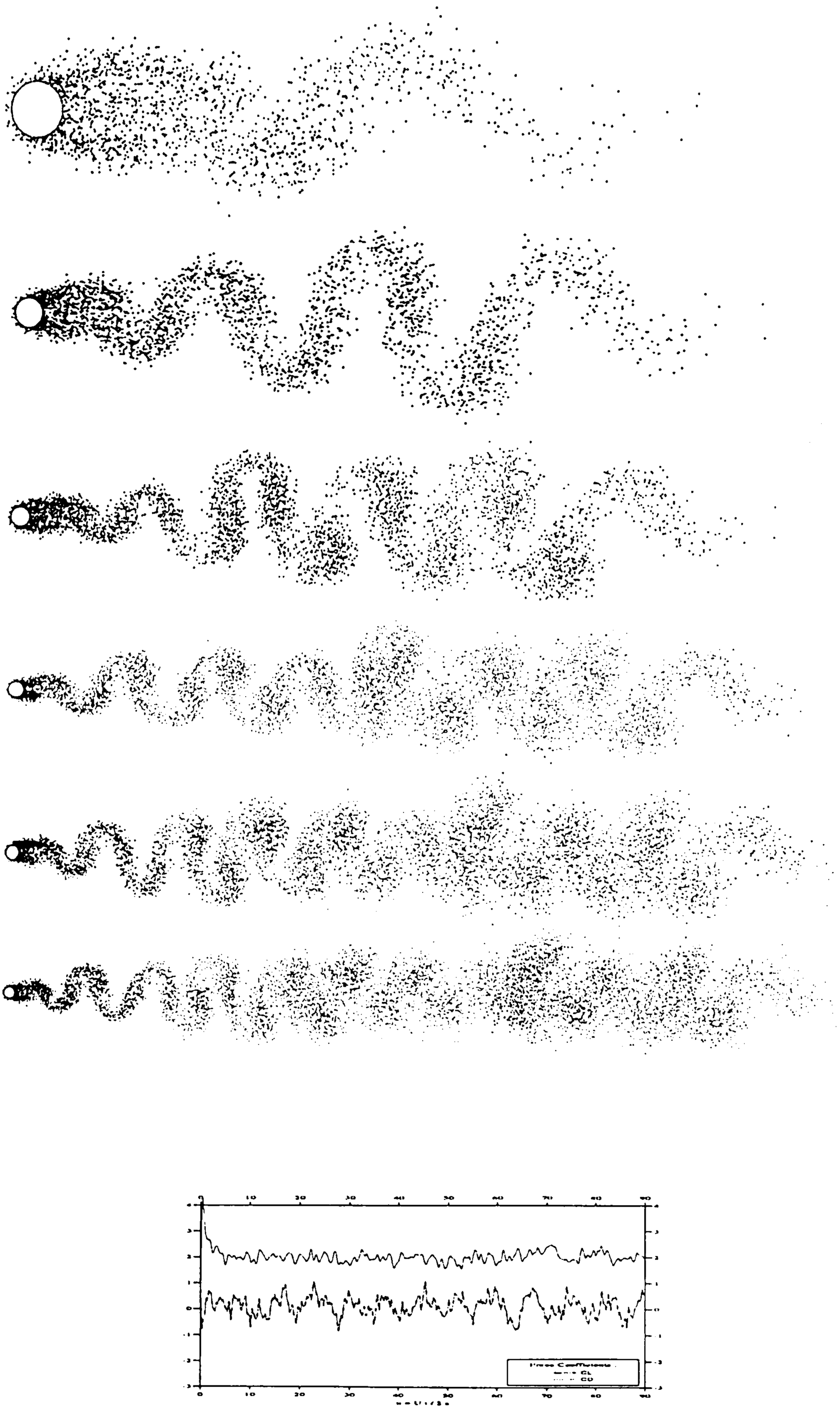

Figure B.2.-*Flow Pattern at t = 15, 30, 45, 60, 75, 90, and the Force Coefficients for Re = 100*

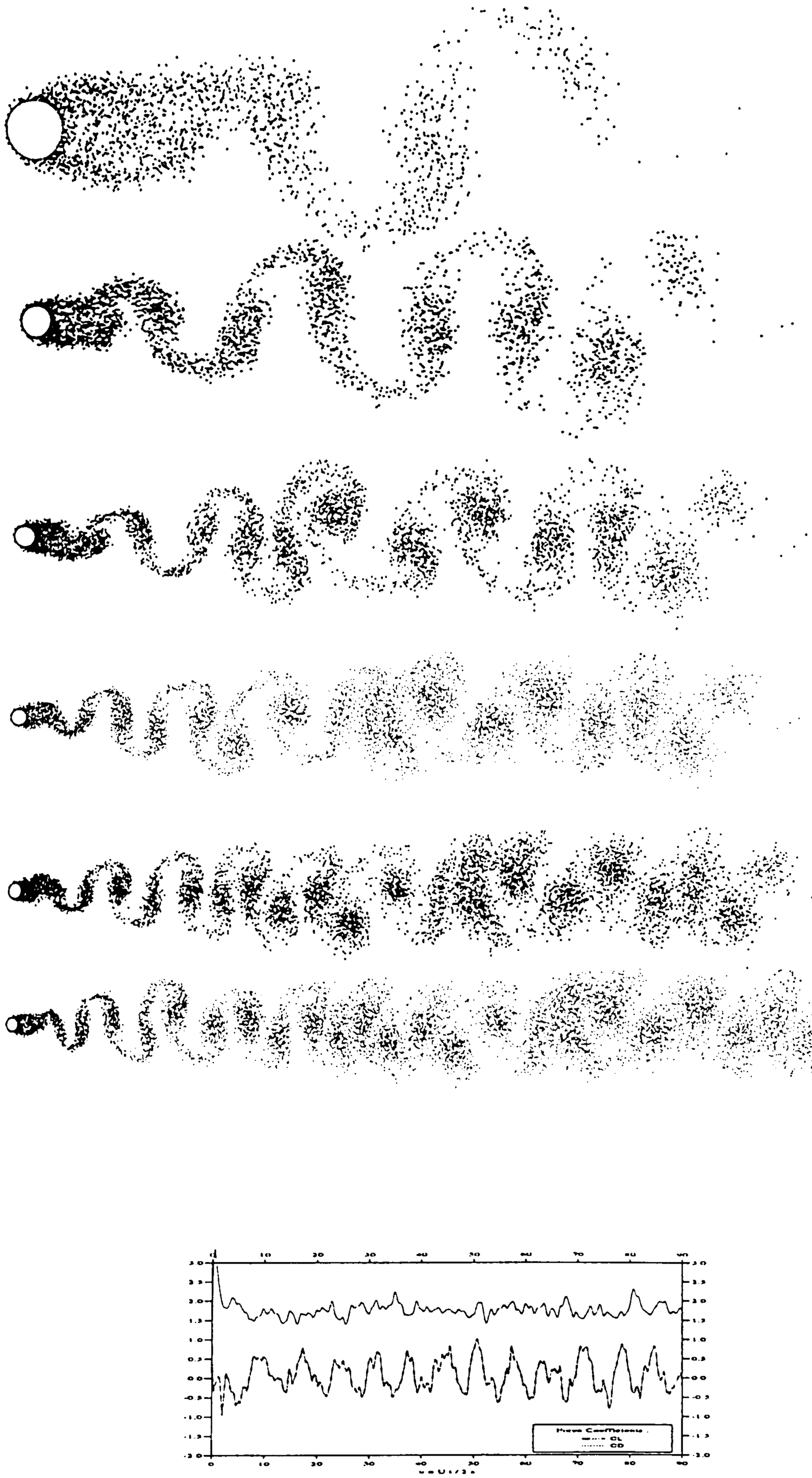

Figure B.3.-*Flow Pattern at t = 15, 30, 45, 60, 75, 90, and the Force Coefficients for Re = 250*

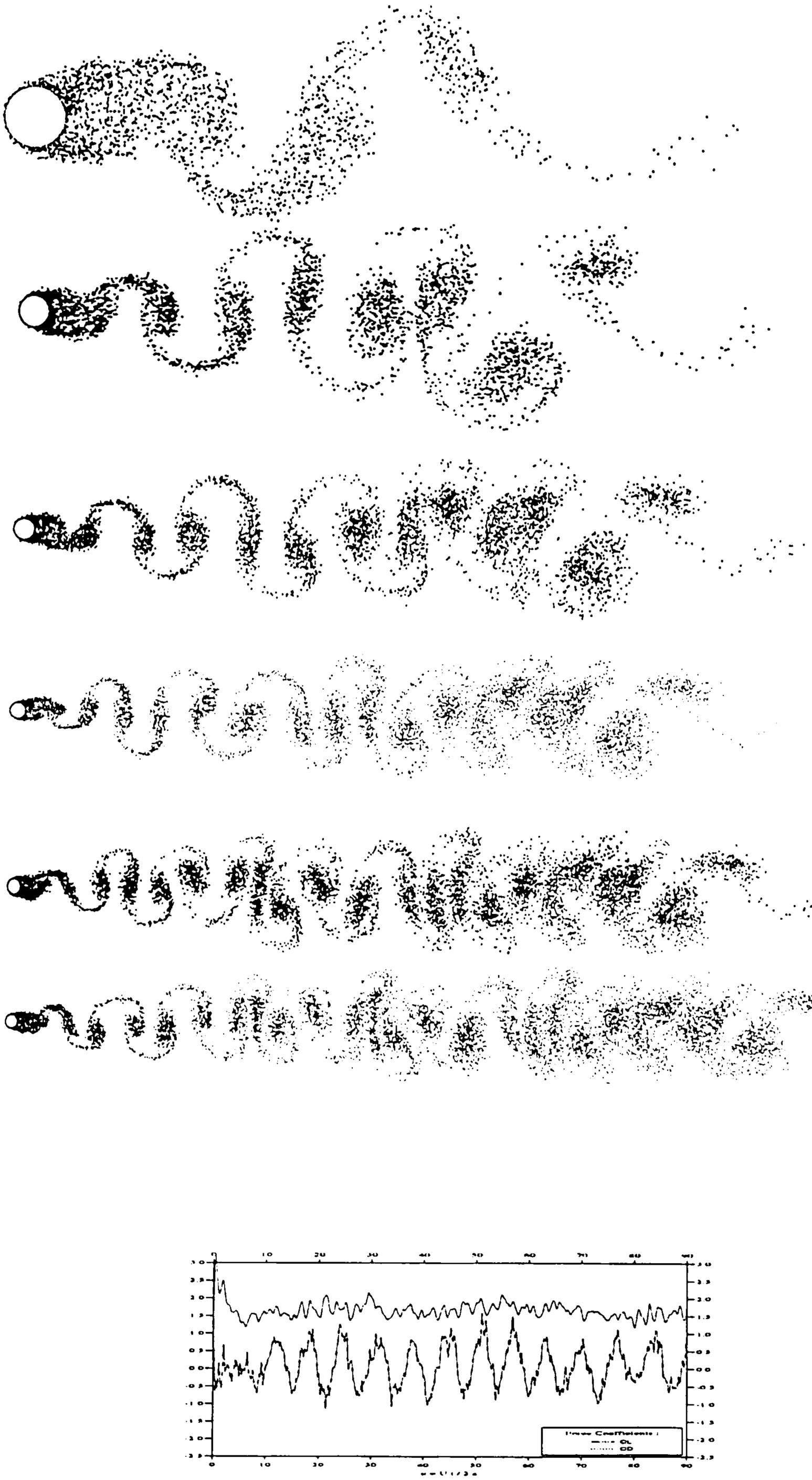

Figure B.4.-*Flow Pattern at t = 15, 30, 45, 60, 75, 90, and the Force Coefficients for Re = 500*

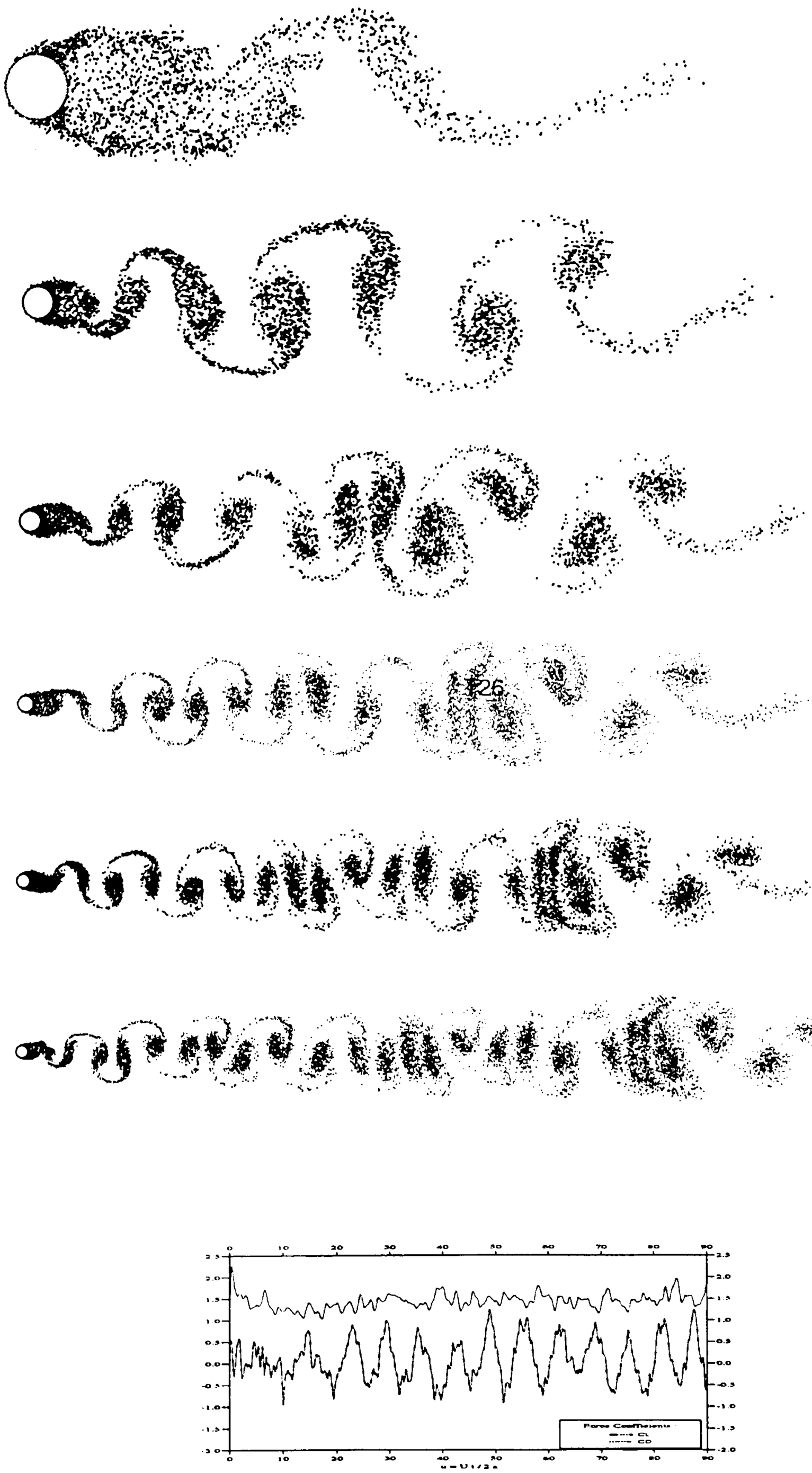

Figure B.5.-*Flow Pattern at t = 15, 30, 45, 60, 75, 90, and the Force Coefficients for Re = 1000*

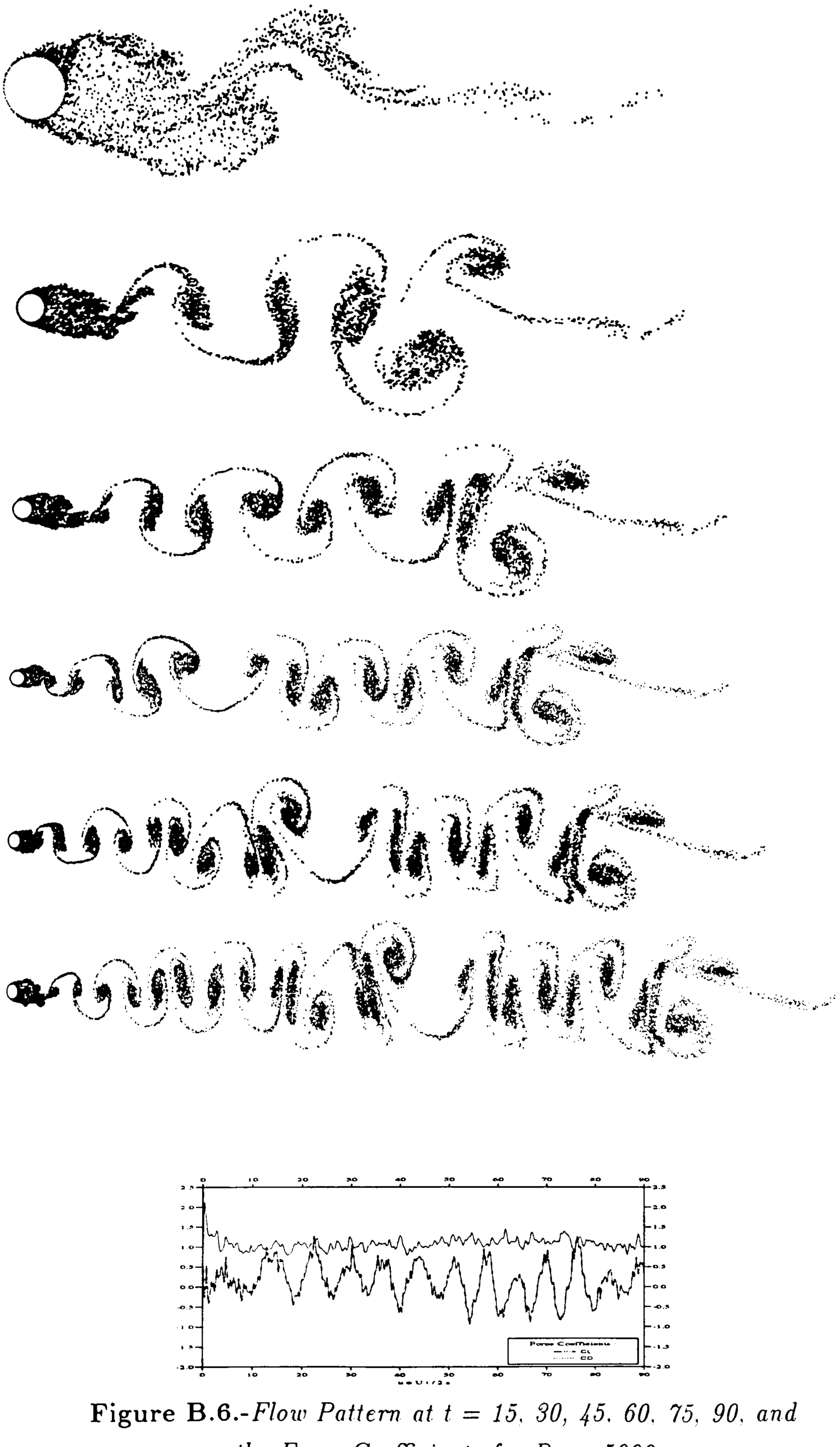

Figure B.6.-*Flow Pattern at t = 15, 30, 45, 60, 75, 90, and the Force Coefficients for Re = 5000*

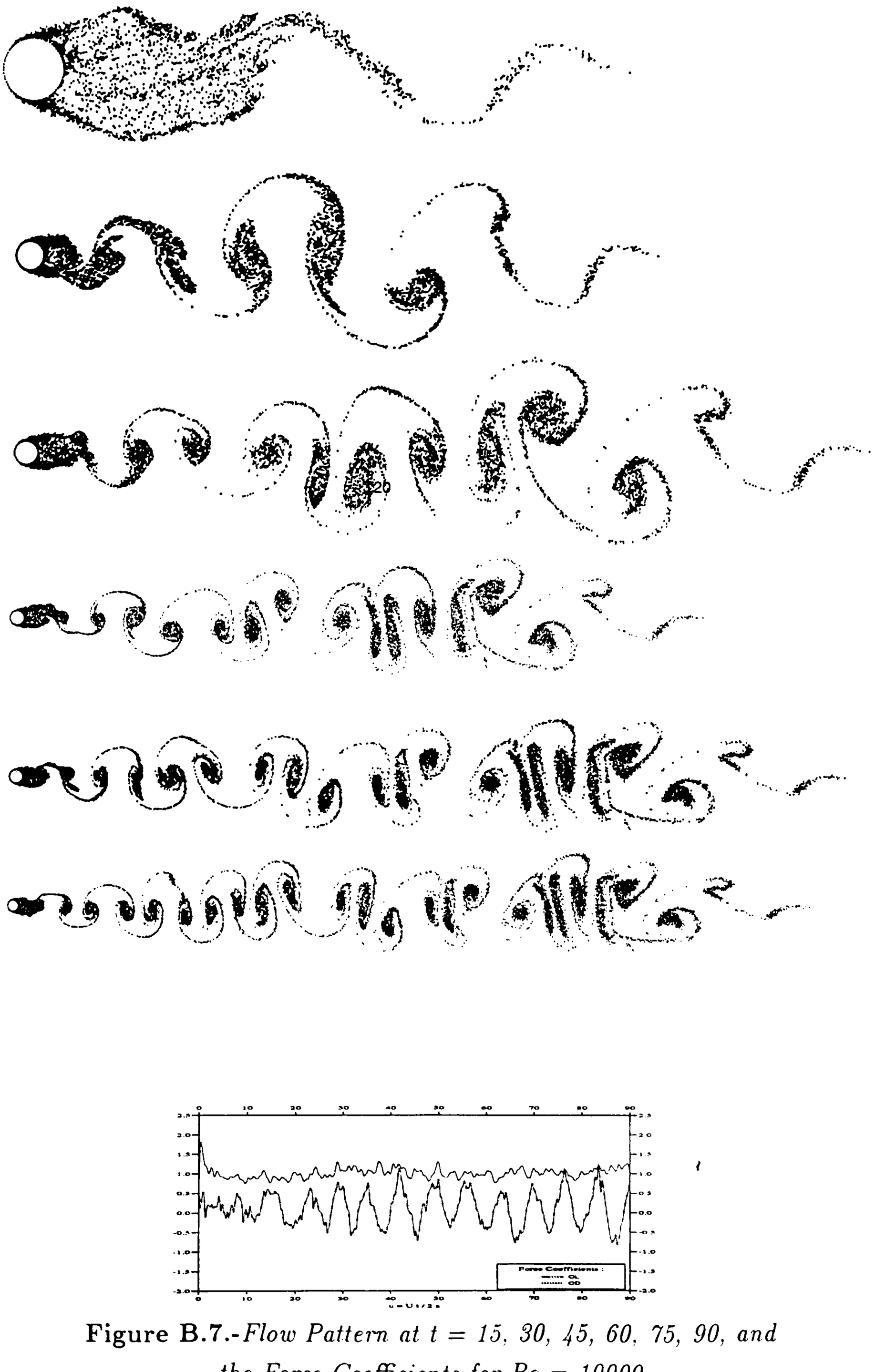

Figure B.7.-*Flow Pattern at t = 15, 30, 45, 60, 75, 90, and the Force Coefficients for Re = 10000*

Figure B.8.-*Flow Pattern at t = 15, 30, 45, 60, 75, 90, and the Force Coefficients for Re = 50000*

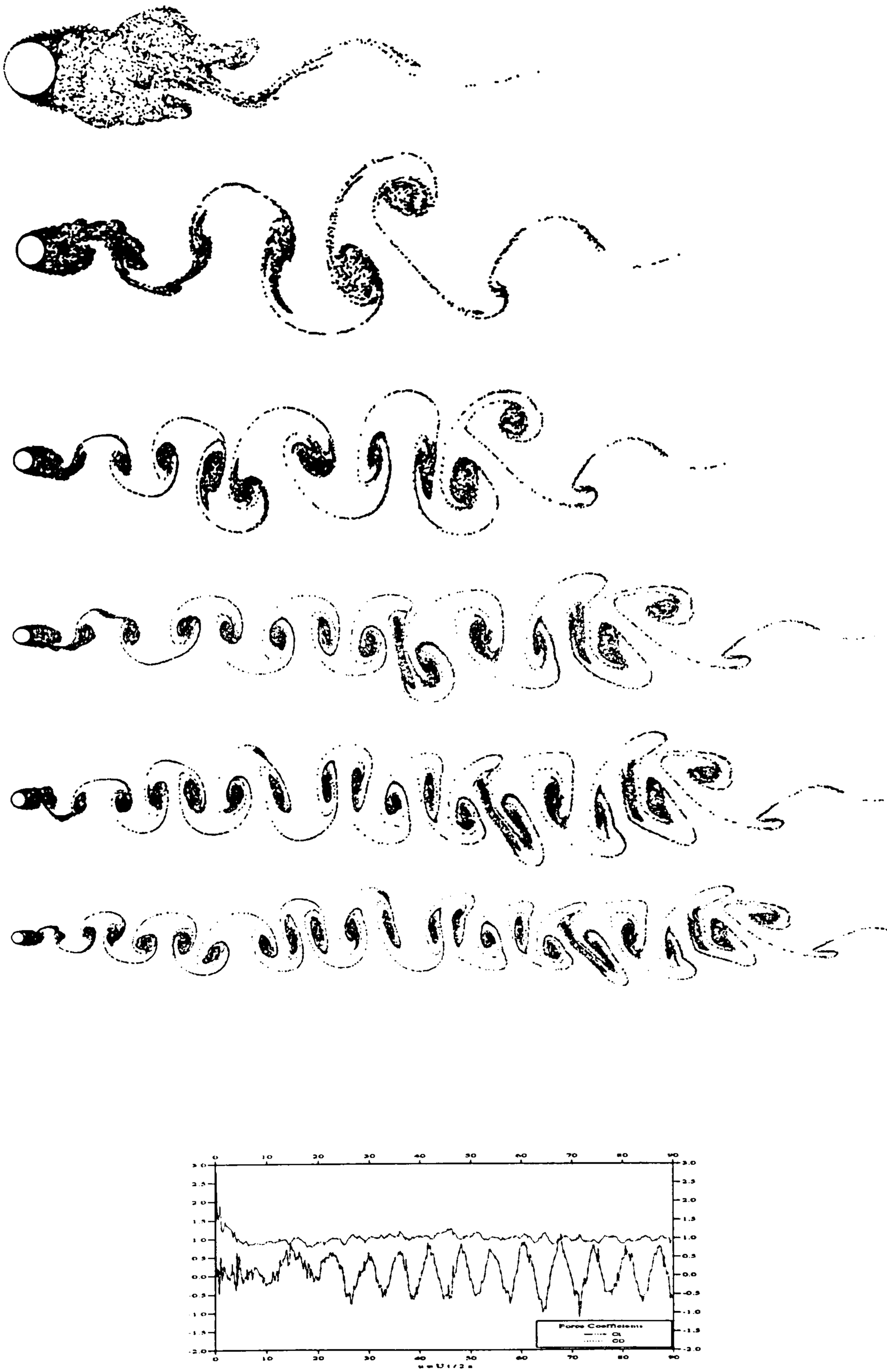

Figure B.9.-*Flow Pattern at t = 15, 30, 45, 60, 75, 90, and the Force Coefficients for Re = 250000*

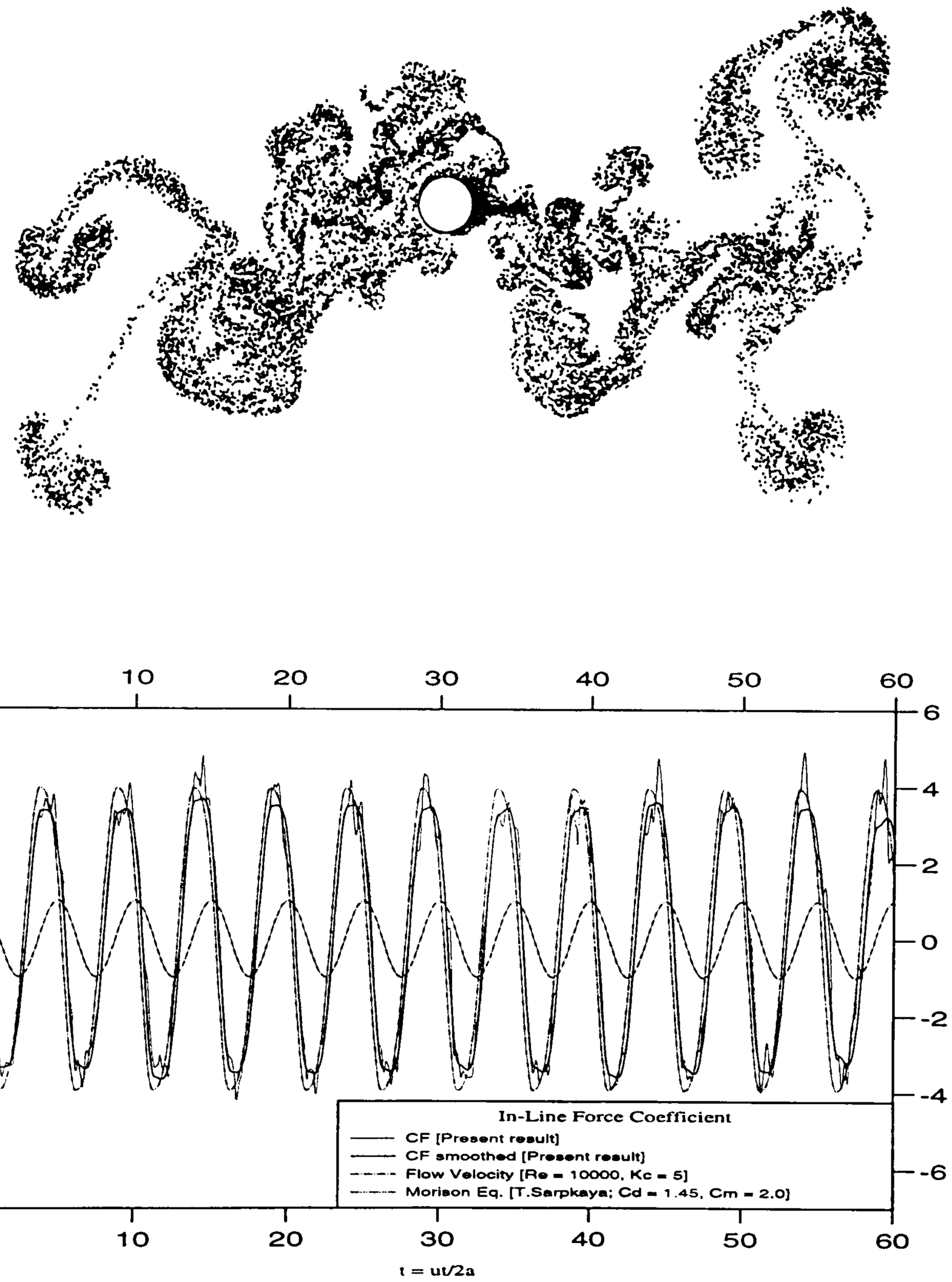

Figure B.10.-*Flow Pattern at $t = 60$ and the Force Coefficients for $Kc = 5$ and $Re = 10000$*

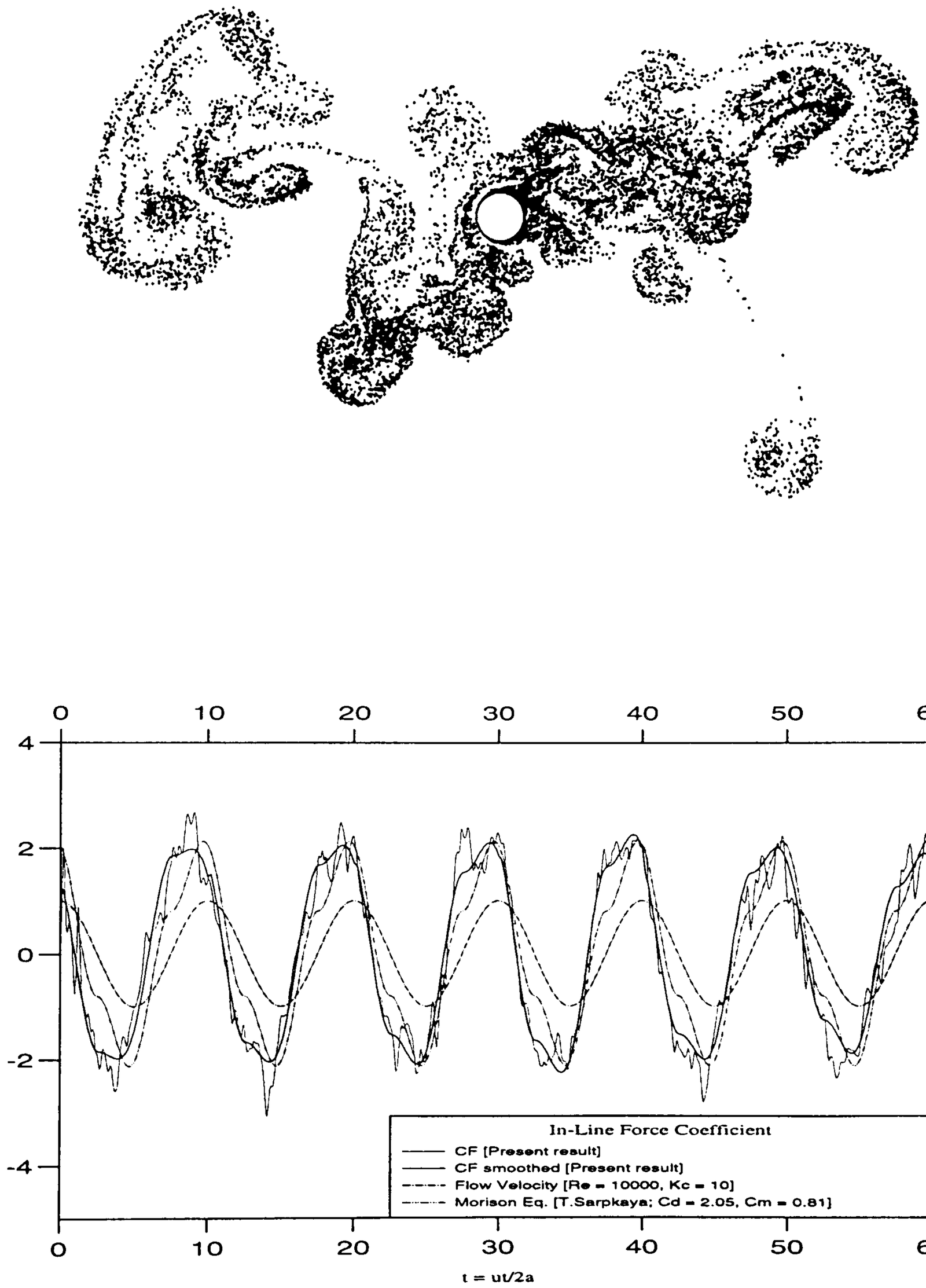

Figure B.11.-*Flow Pattern at $t = 60$ and the Force Coefficients for $Kc = 10$ and $Re = 10000$*

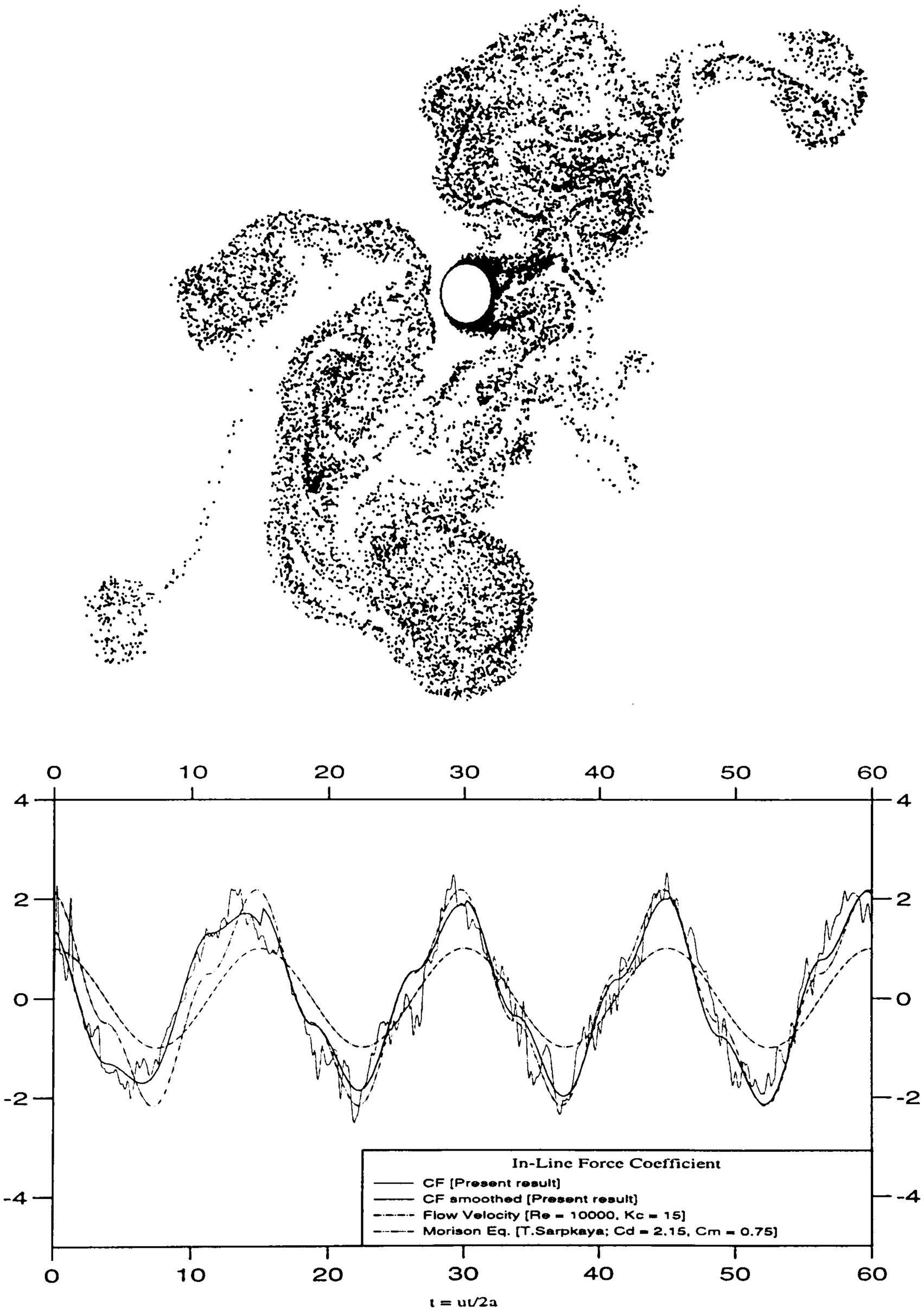

Figure B.12.-*Flow Pattern at $t = 60$ and the Force Coefficients for $Kc = 15$ and $Re = 10000$*

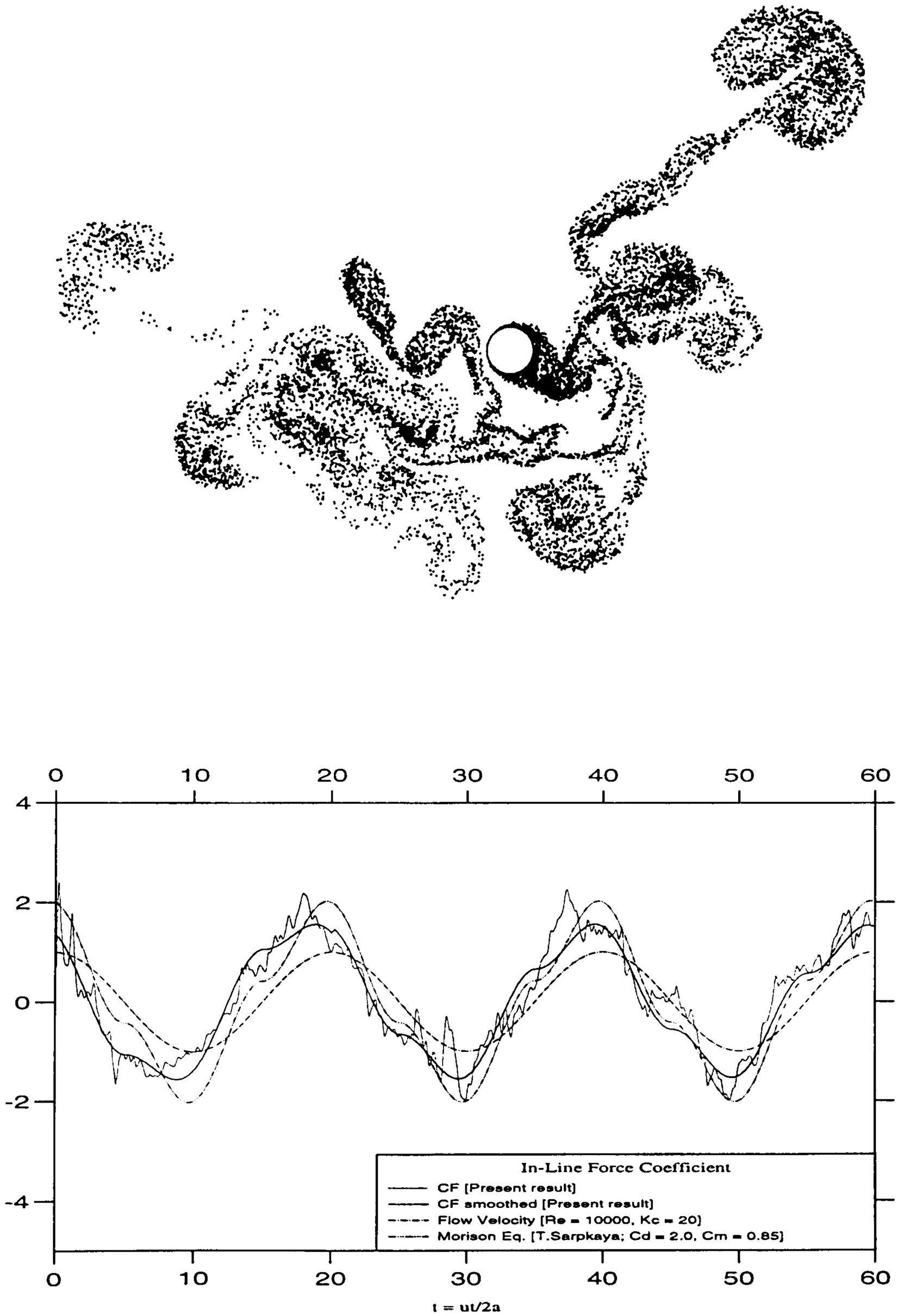

Figure B.13.-*Flow Pattern at $t = 60$ and the Force Coefficients for $Kc = 20$ and $Re = 10000$*

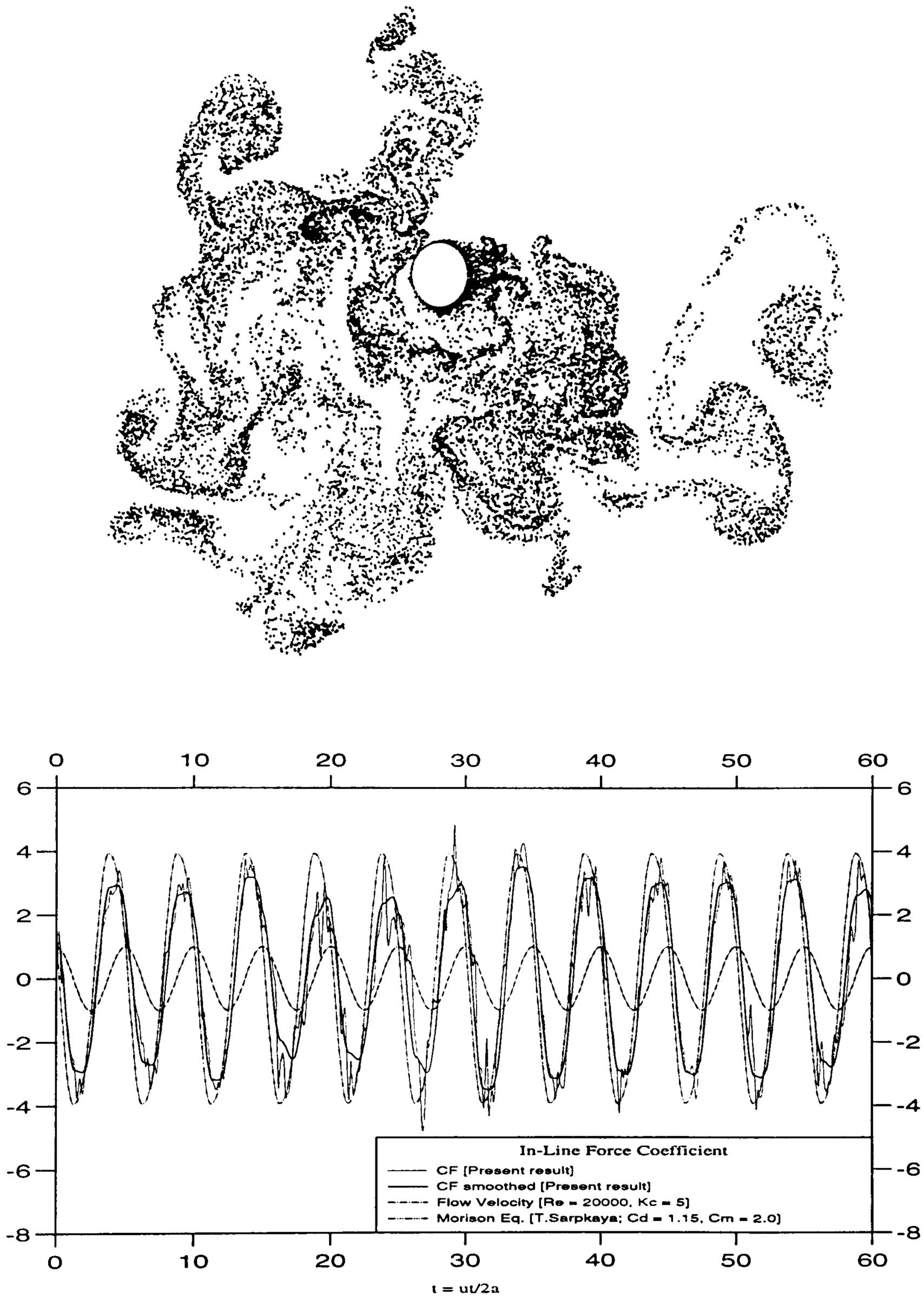

Figure B.14.-*Flow Pattern at $t = 60$ and the Force Coefficients for $Kc = 5$ and $Re = 20000$*

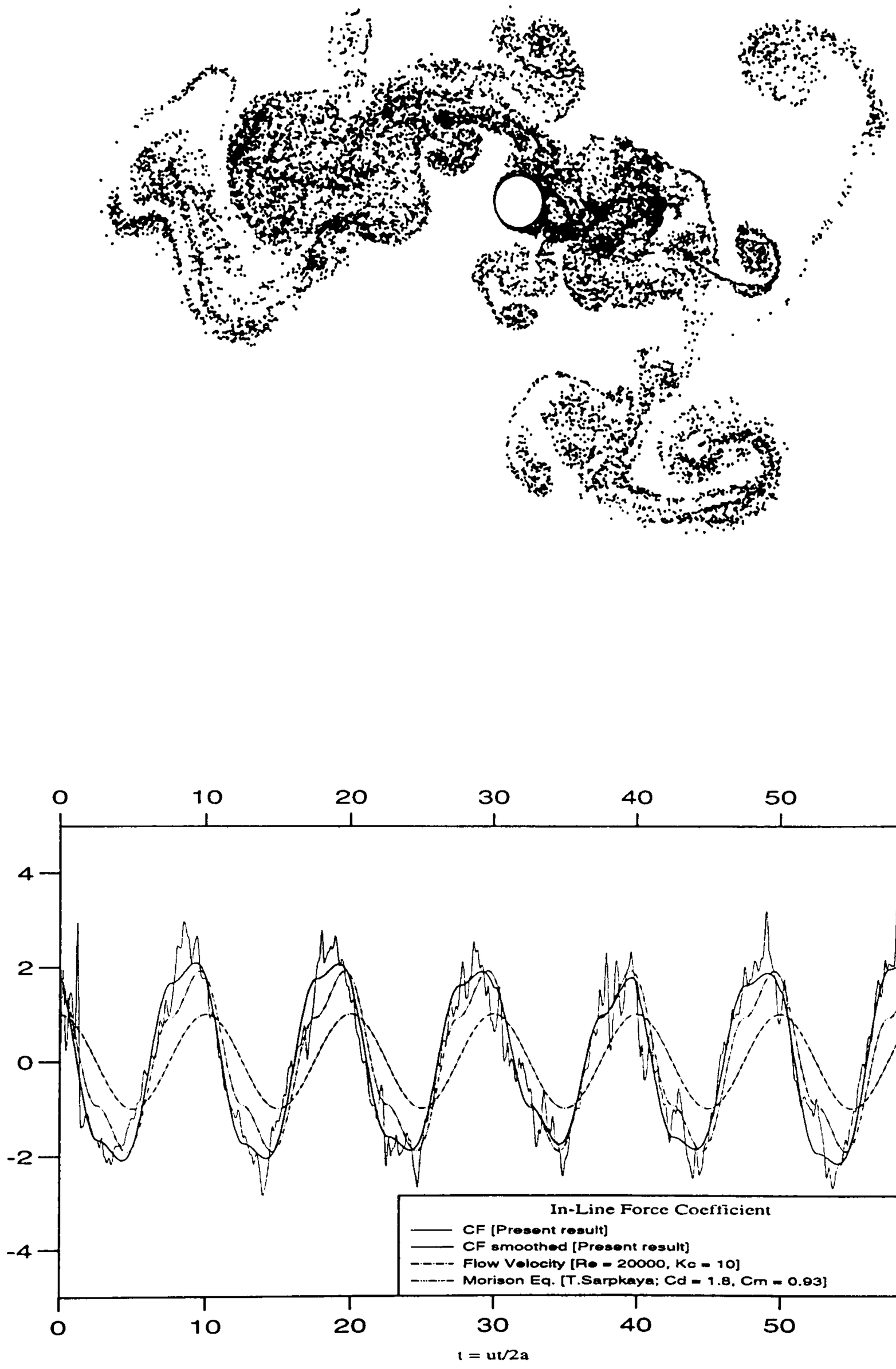

Figure B.15.-*Flow Pattern at $t = 60$ and the Force Coefficients for $Kc = 10$ and $Re = 20000$*

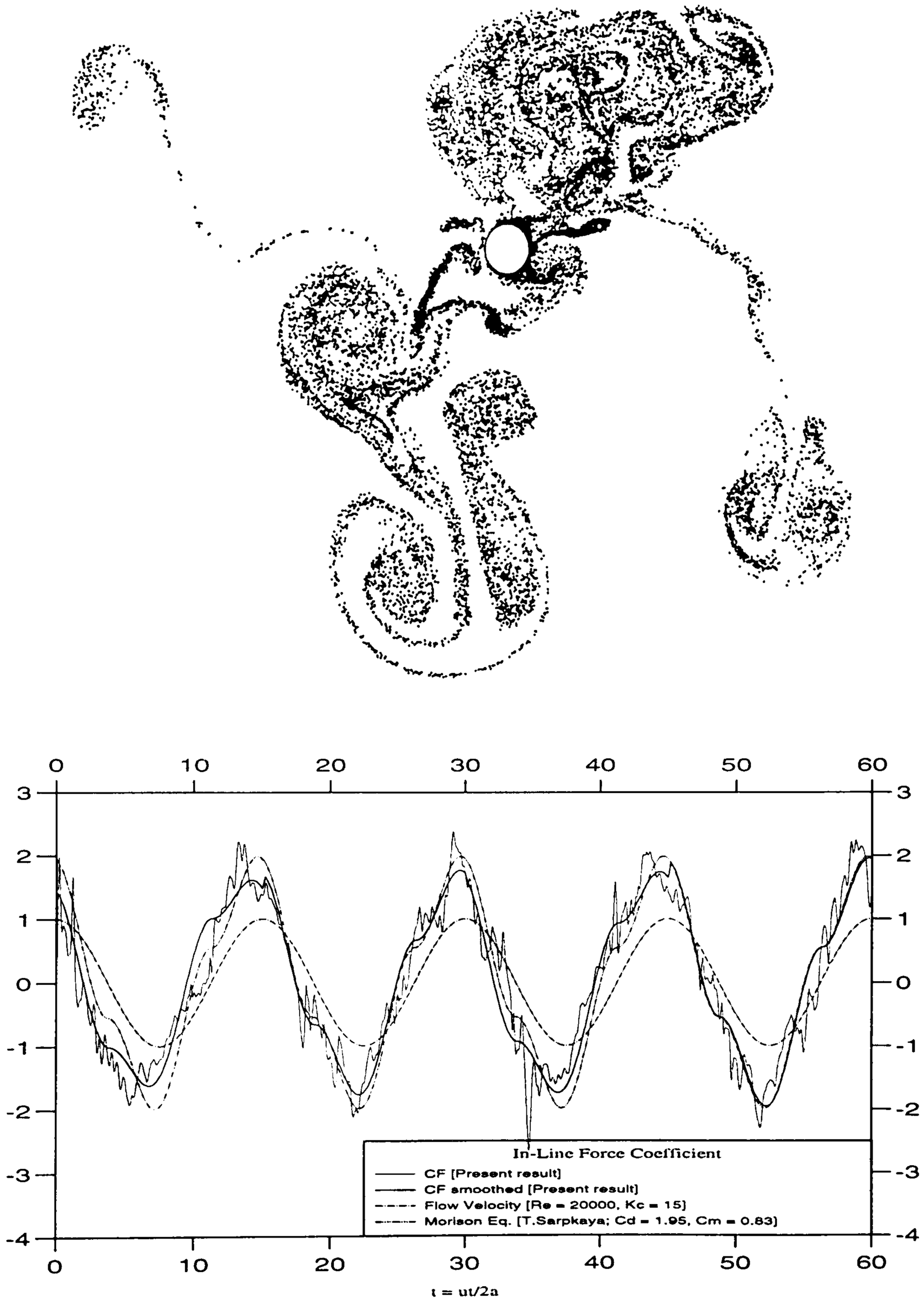

Figure B.16.-*Flow Pattern at $t = 60$ and the Force Coefficients for $Kc = 15$ and $Re = 20000$*

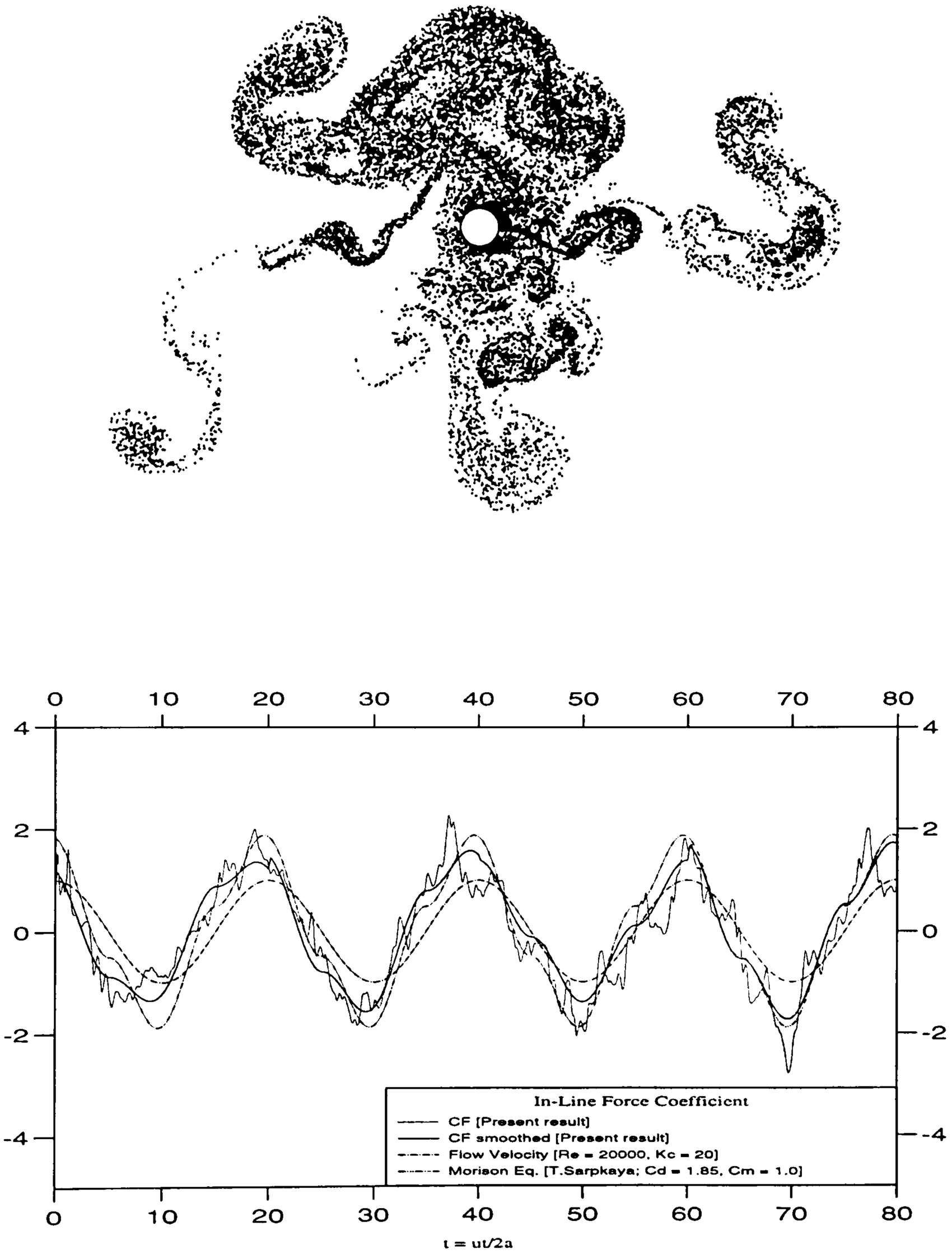

Figure B.17.-*Flow Pattern at $t = 80$ and the Force Coefficients for $Kc = 20$ and $Re = 20000$*

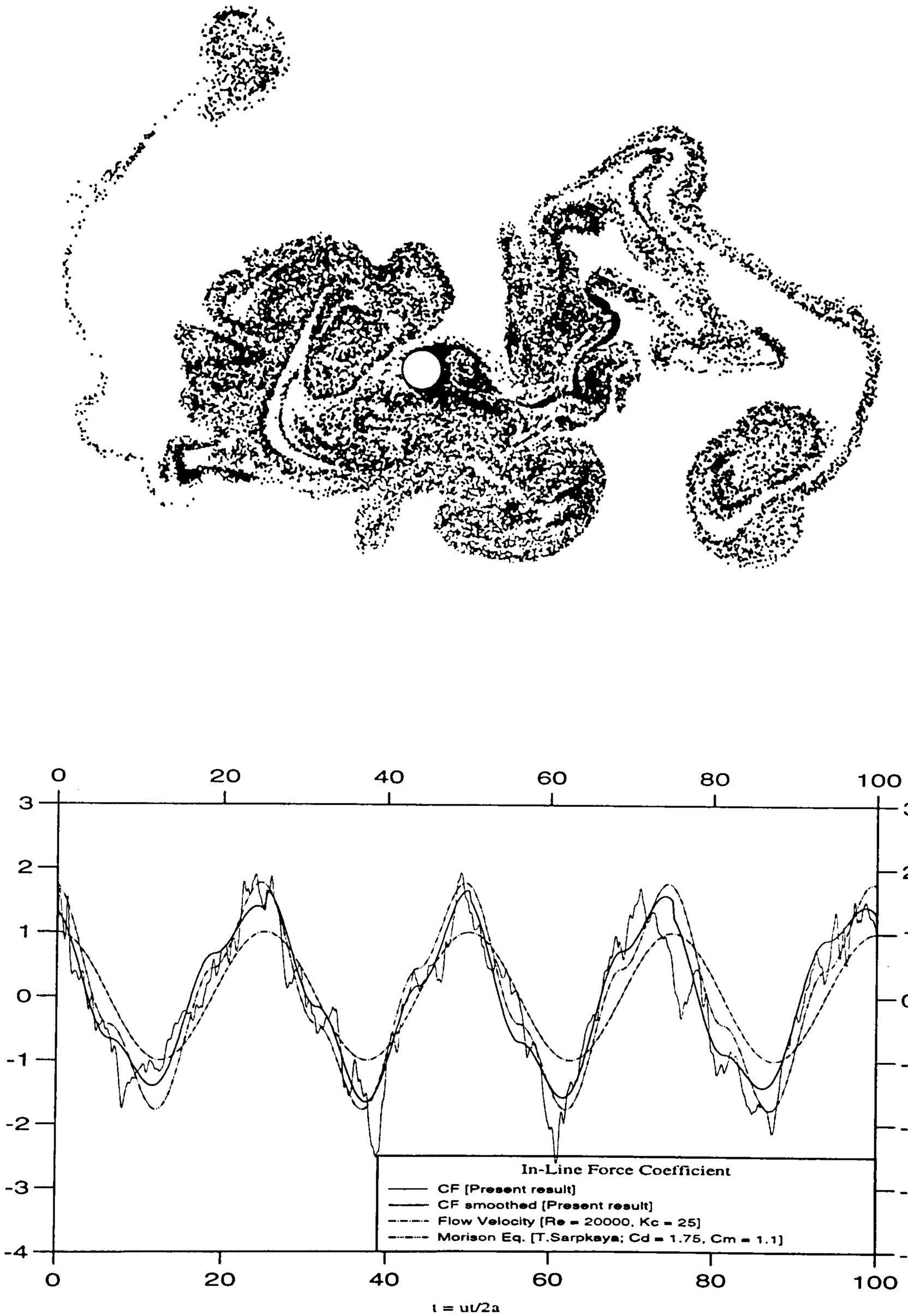

Figure B.18.-*Flow Pattern at $t = 100$ and the Force Coefficients for $Kc = 25$ and $Re = 20000$*

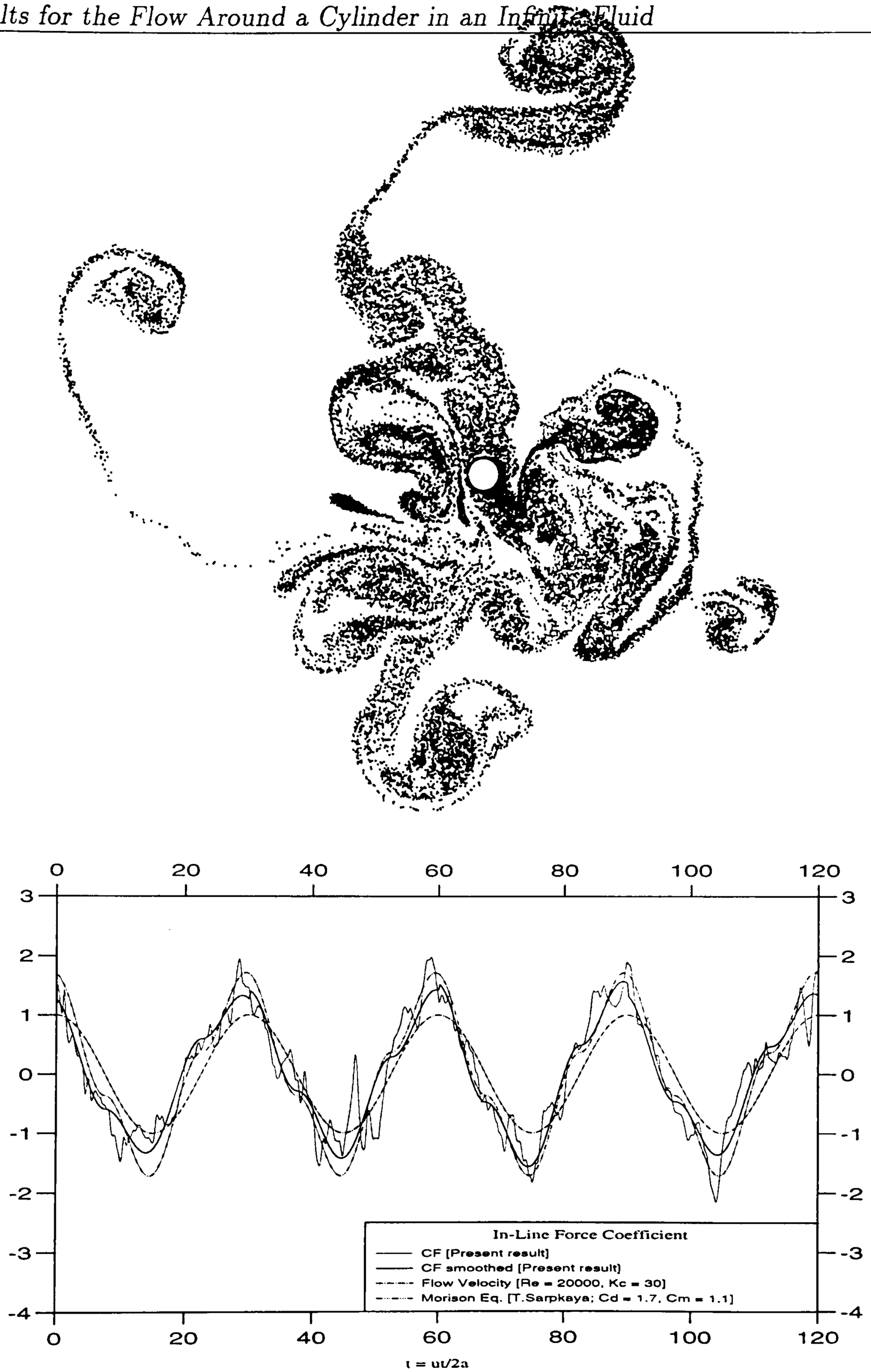

Figure B.19.-*Flow Pattern at $t = 120$ and the Force Coefficients for $Kc = 30$ and $Re = 20000$*

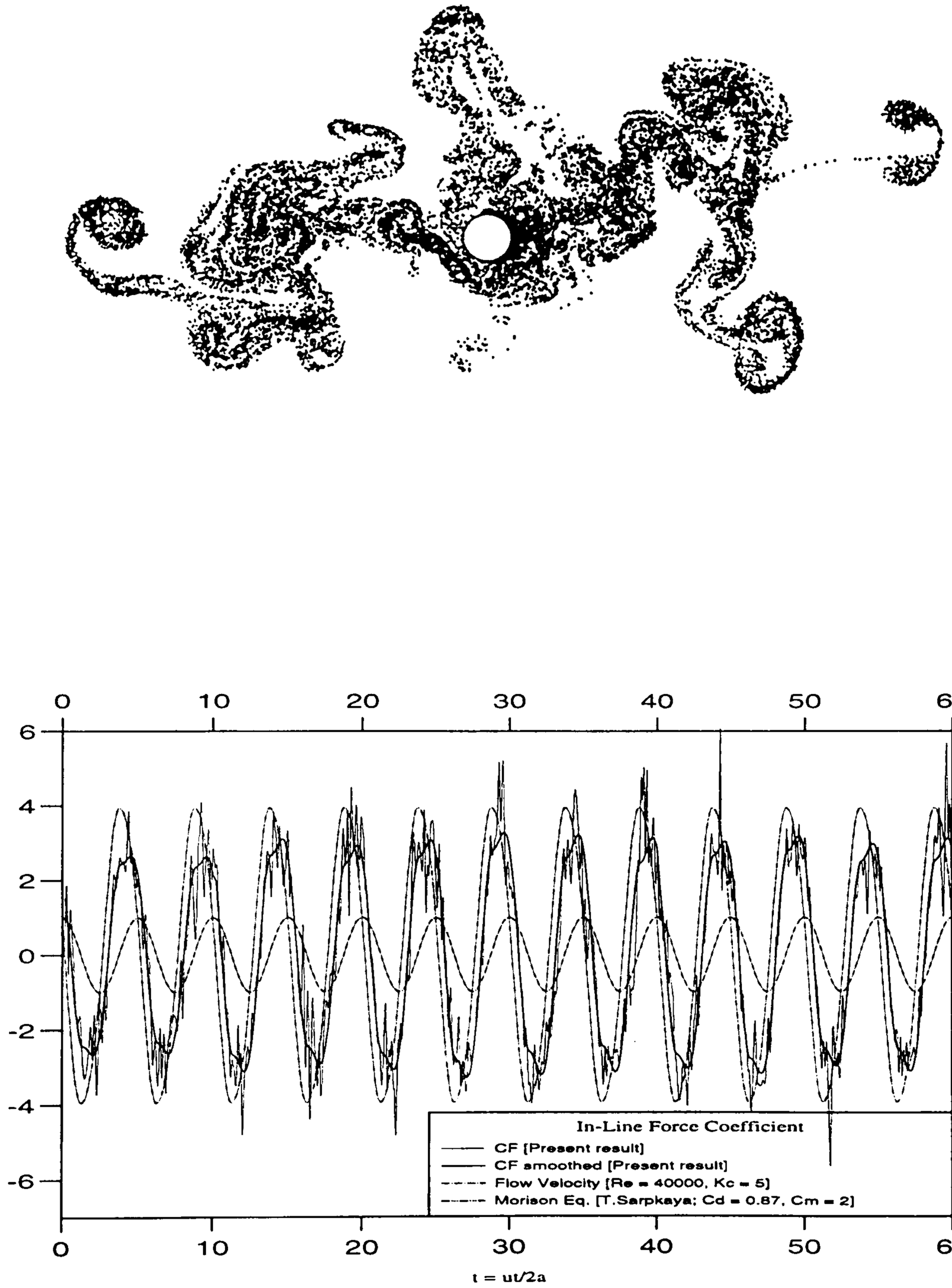

Figure B.20.-*Flow Pattern at $t = 60$ and the Force Coefficients for $Kc = 5$ and $Re = 40000$*

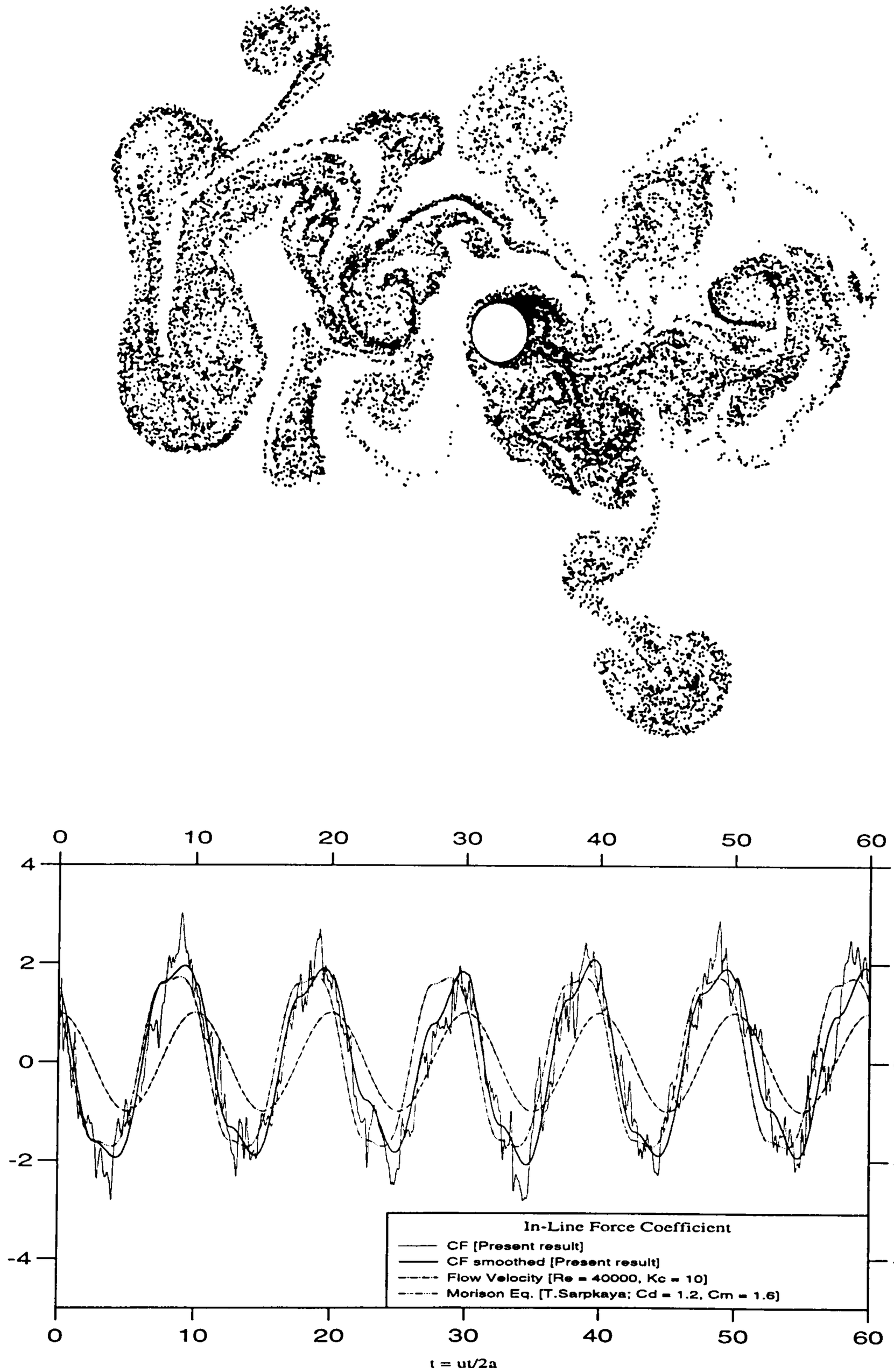

Figure B.21.-*Flow Pattern at $t = 60$ and the Force Coefficients for $Kc = 10$ and $Re = 40000$*

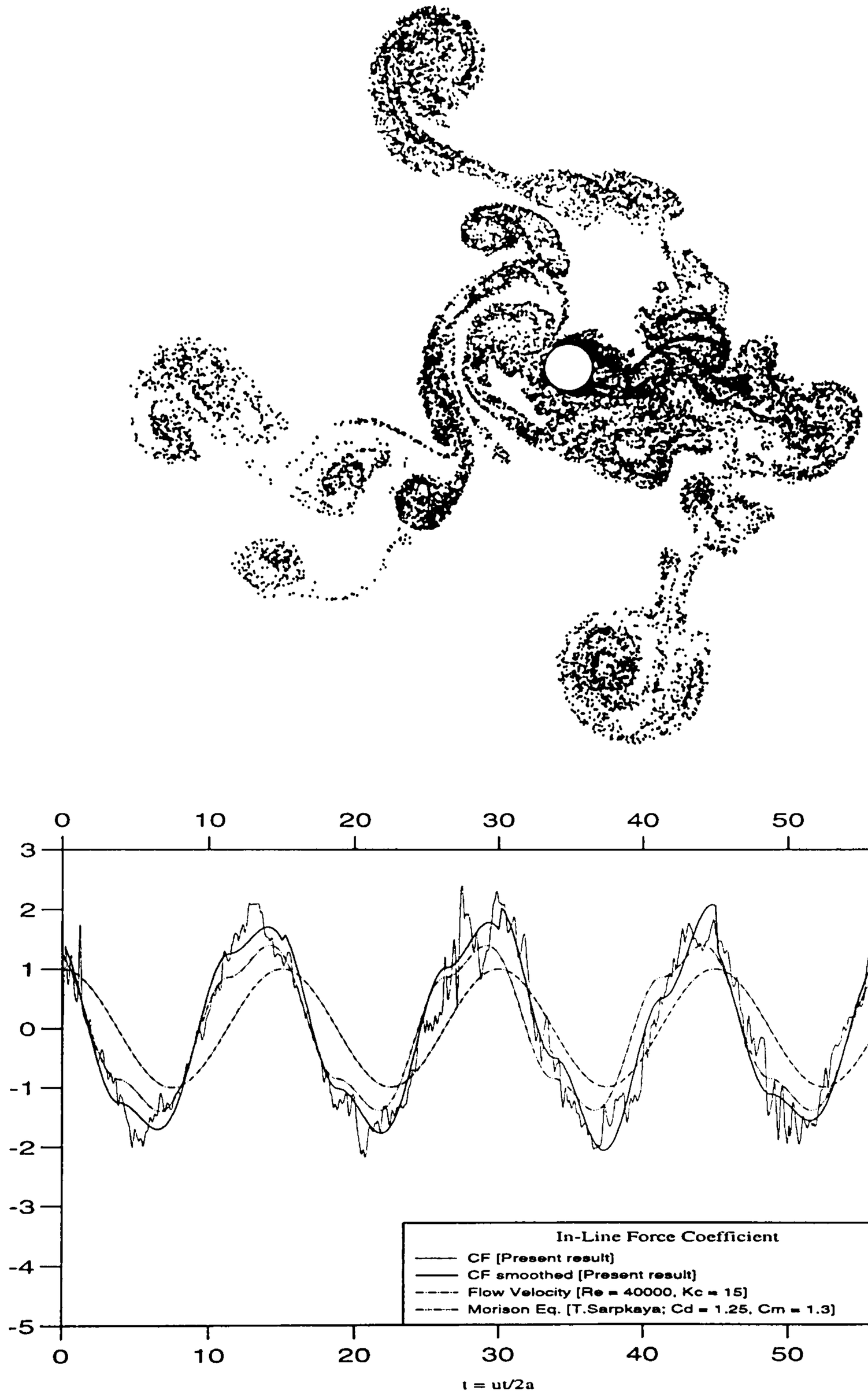

Figure B.22.-*Flow Pattern at t = 60 and the Force Coefficients for Kc = 15 and Re = 40000*

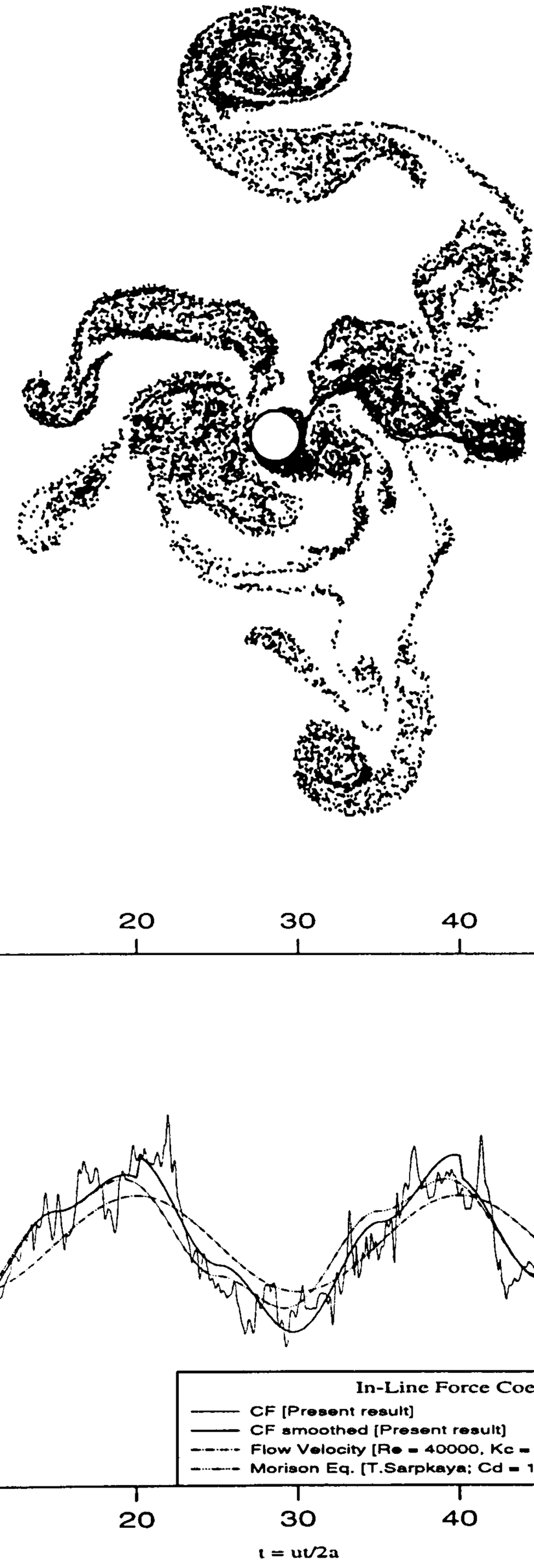

Figure B.23.-*Flow Pattern at $t = 60$ and the Force Coefficients for $Kc = 20$ and $Re = 40000$*

Appendix C

Results for Two Cylinders In An Infinite Fluid

Figure C.1.-*Flow Pattern at t = 15, 30, 45, 60. G/D = 1, and the Force Coefficients for Re = 61000*

Figure C.2.-*Flow Pattern at t = 15, 30, 45, 60, G/D = 2, and the Force Coefficients for Re = 61000*

Figure C.3.-*Flow Pattern at t = 15, 30, 45, 60, G/D = 3, and the Force Coefficients for Re = 61000*

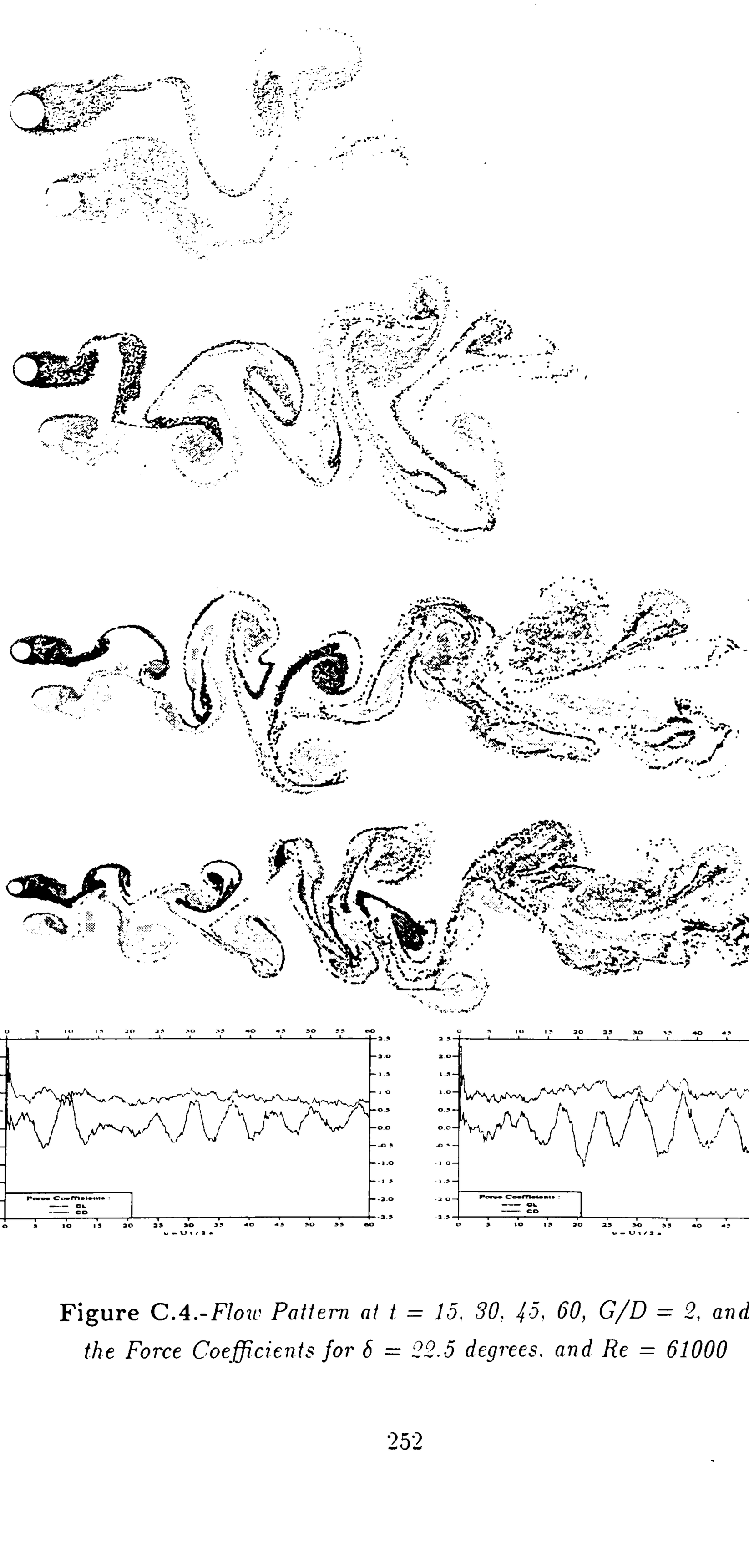

Figure C.4.-*Flow Pattern at t = 15, 30, 45, 60, G/D = 2, and the Force Coefficients for δ = 22.5 degrees. and Re = 61000*

Figure C.5.-*Flow Pattern at t = 10, 20, 30, 40, G/D = 2, and the Force Coefficients for δ = 45 degrees, and Re = 61000*

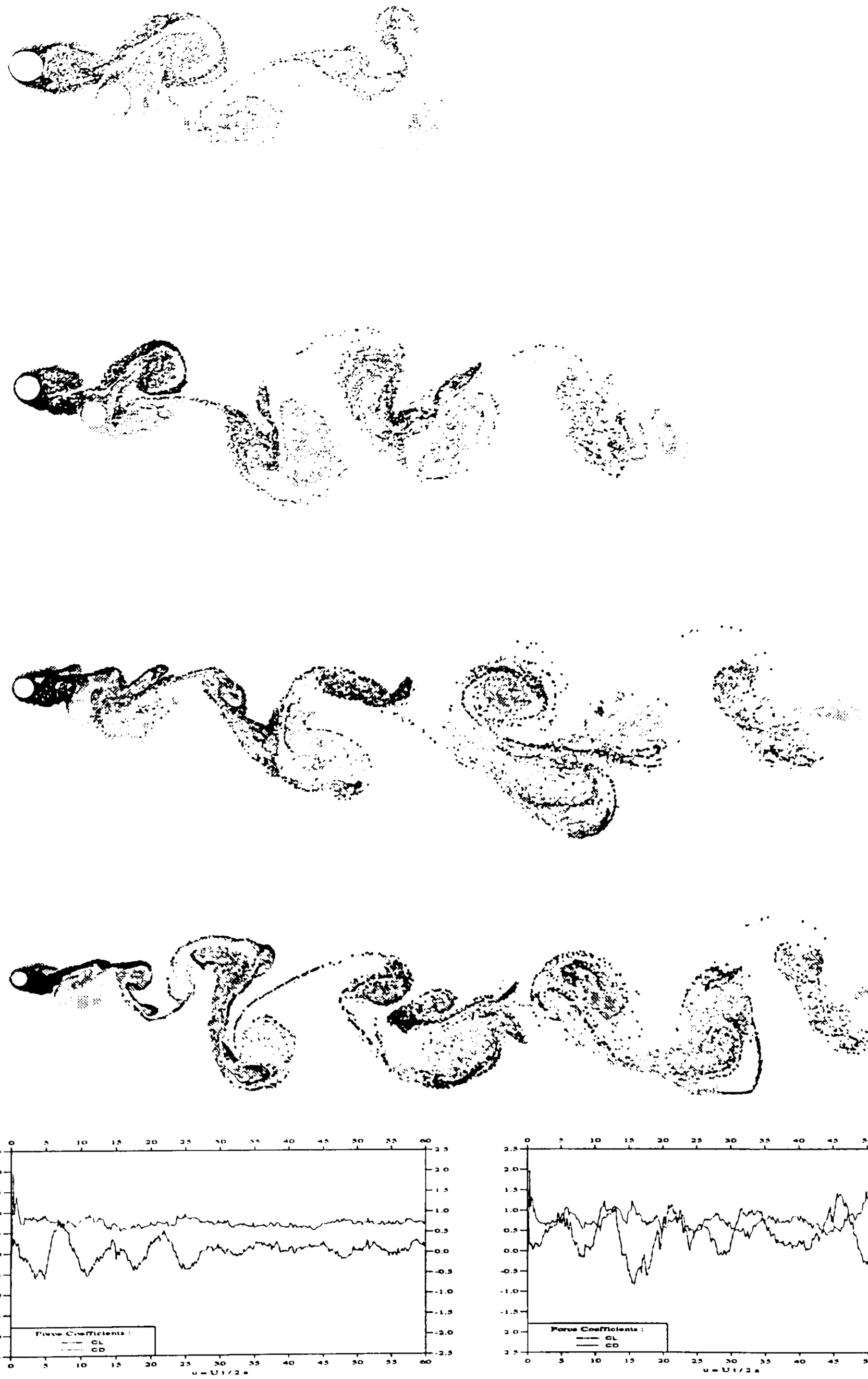

Figure C.6.-*Flow Pattern at t = 10, 20, 30, 40, G/D = 2, and the Force Coefficients for δ = 62.5 degrees, and Re = 61000*

Appendix D

Results for A Cylinders In A Bounded Fluid

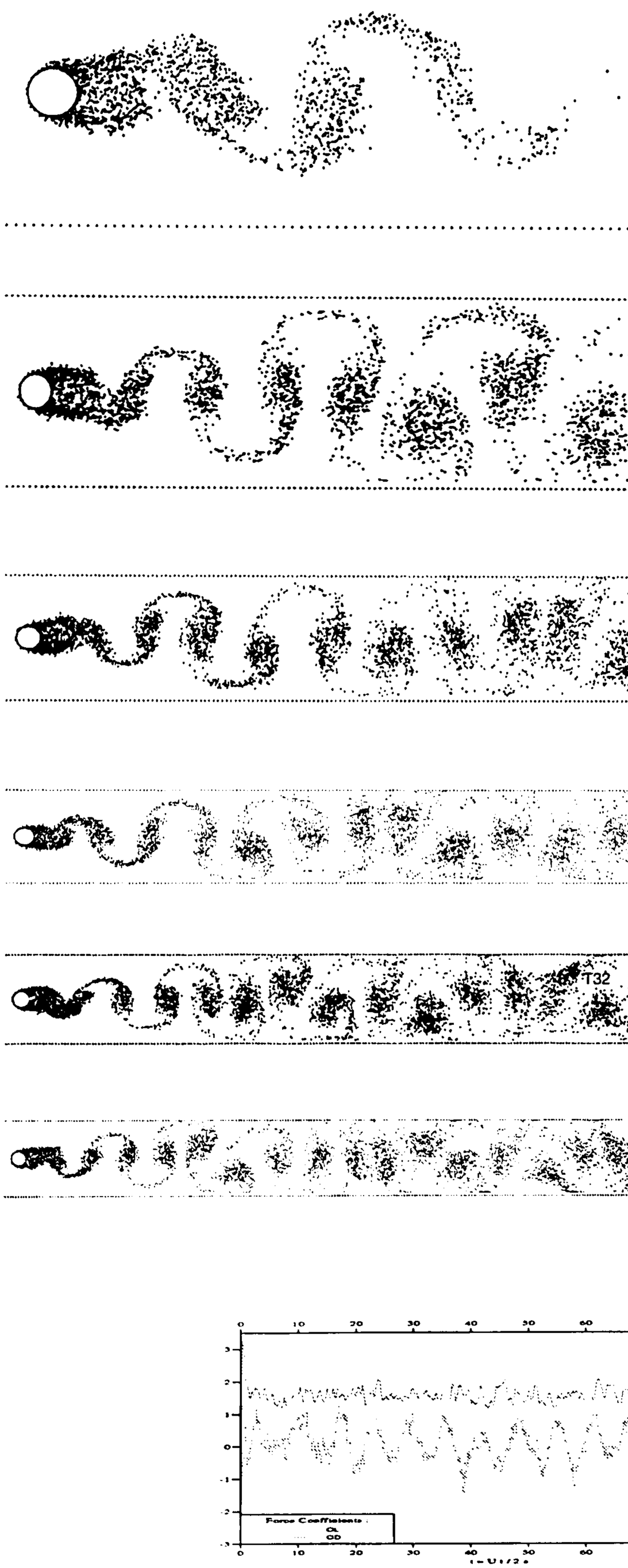

Figure D.1.-*Flow Pattern at t = 10, 20, 30, 40, G/D = 6, and the Force Coefficients for Re = 500*

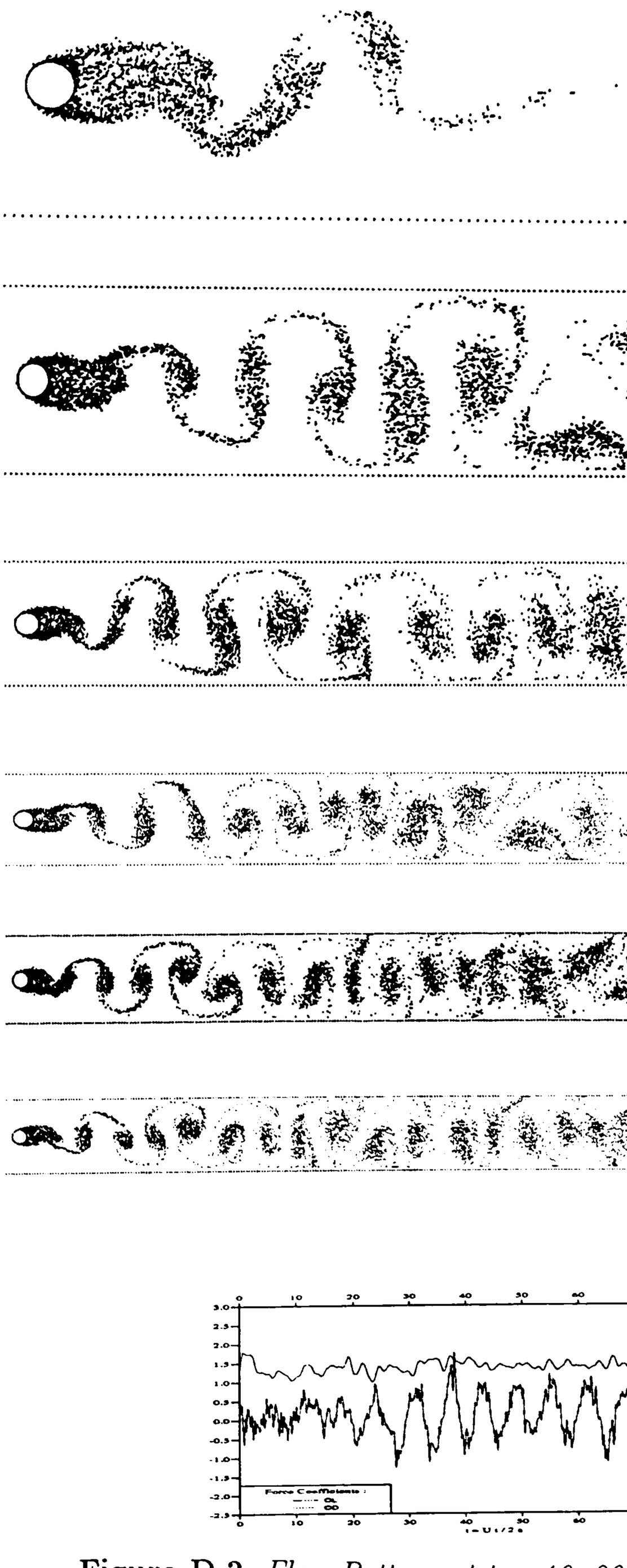

Figure D.2.-*Flow Pattern at t = 10, 20. 30, 40, G/D = 6, and the Force Coefficients for Re = 1000*

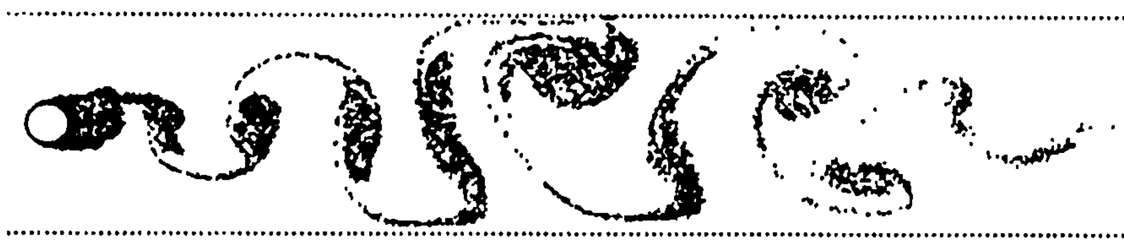

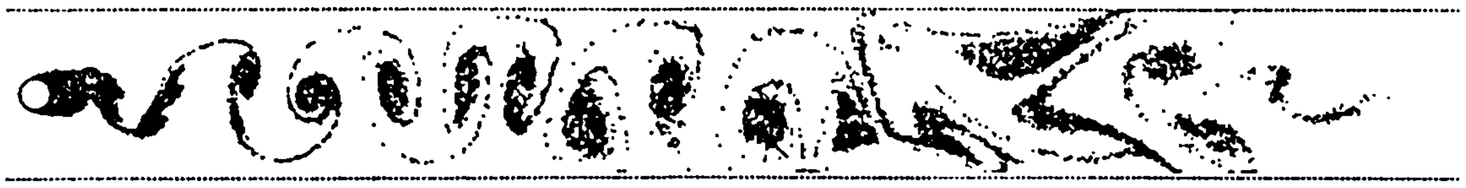

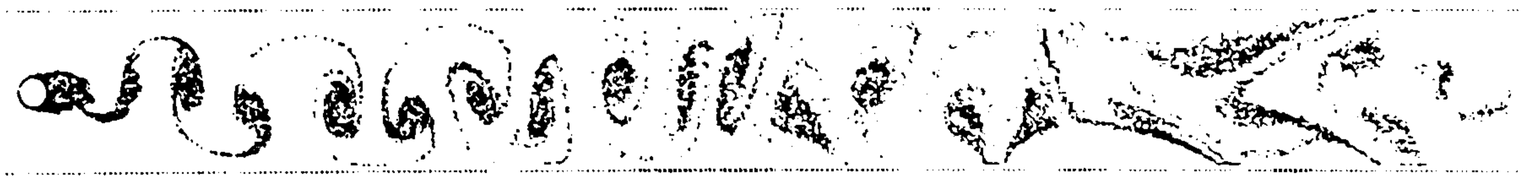

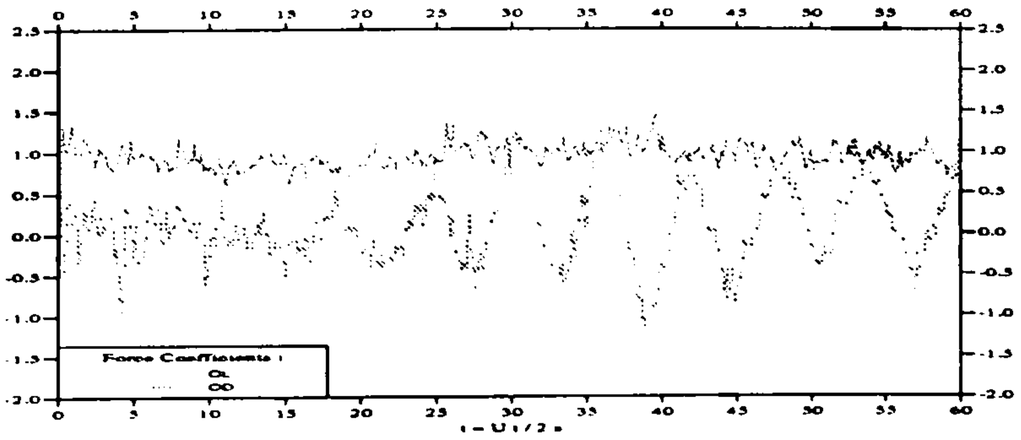

Figure D.3.-*Flow Pattern at t = 10, 20, 30, 40, G/D = 6, and the Force Coefficients for Re = 10000*

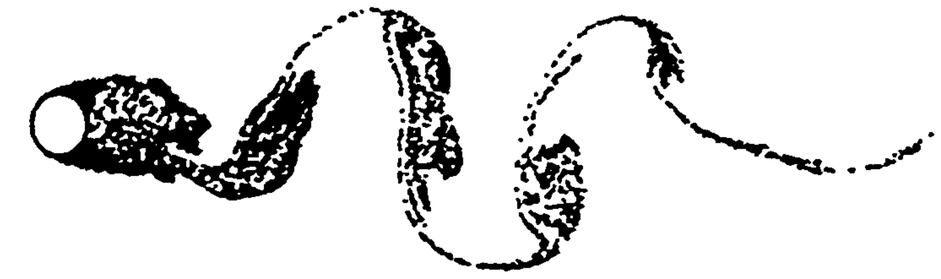

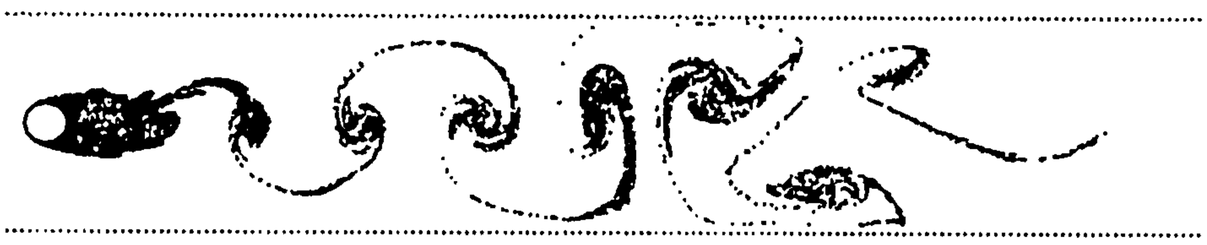

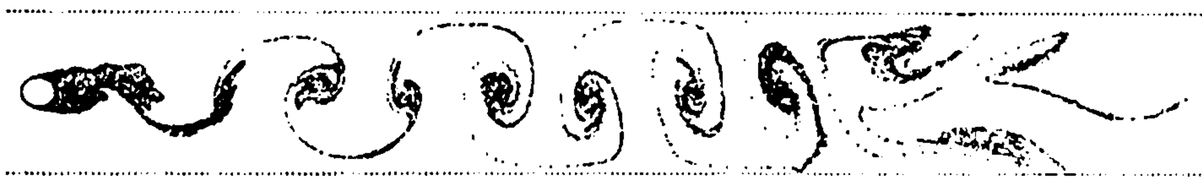

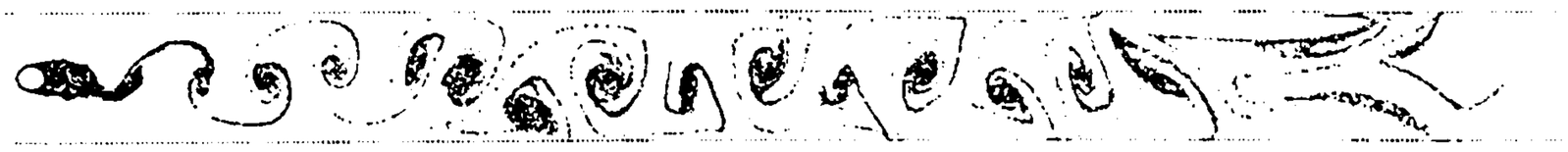

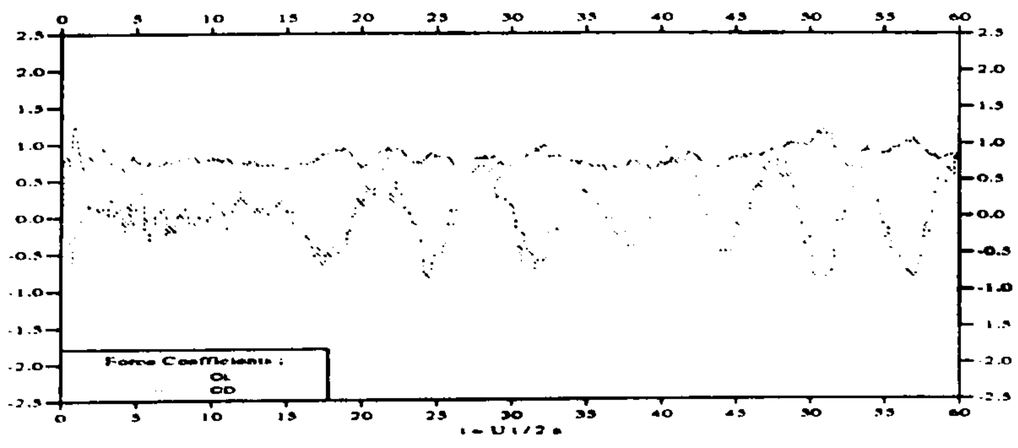

Figure D.4.-*Flow Pattern at t = 10, 20, 30, 40, G/D = 6, and the Force Coefficients for Re = 100000*

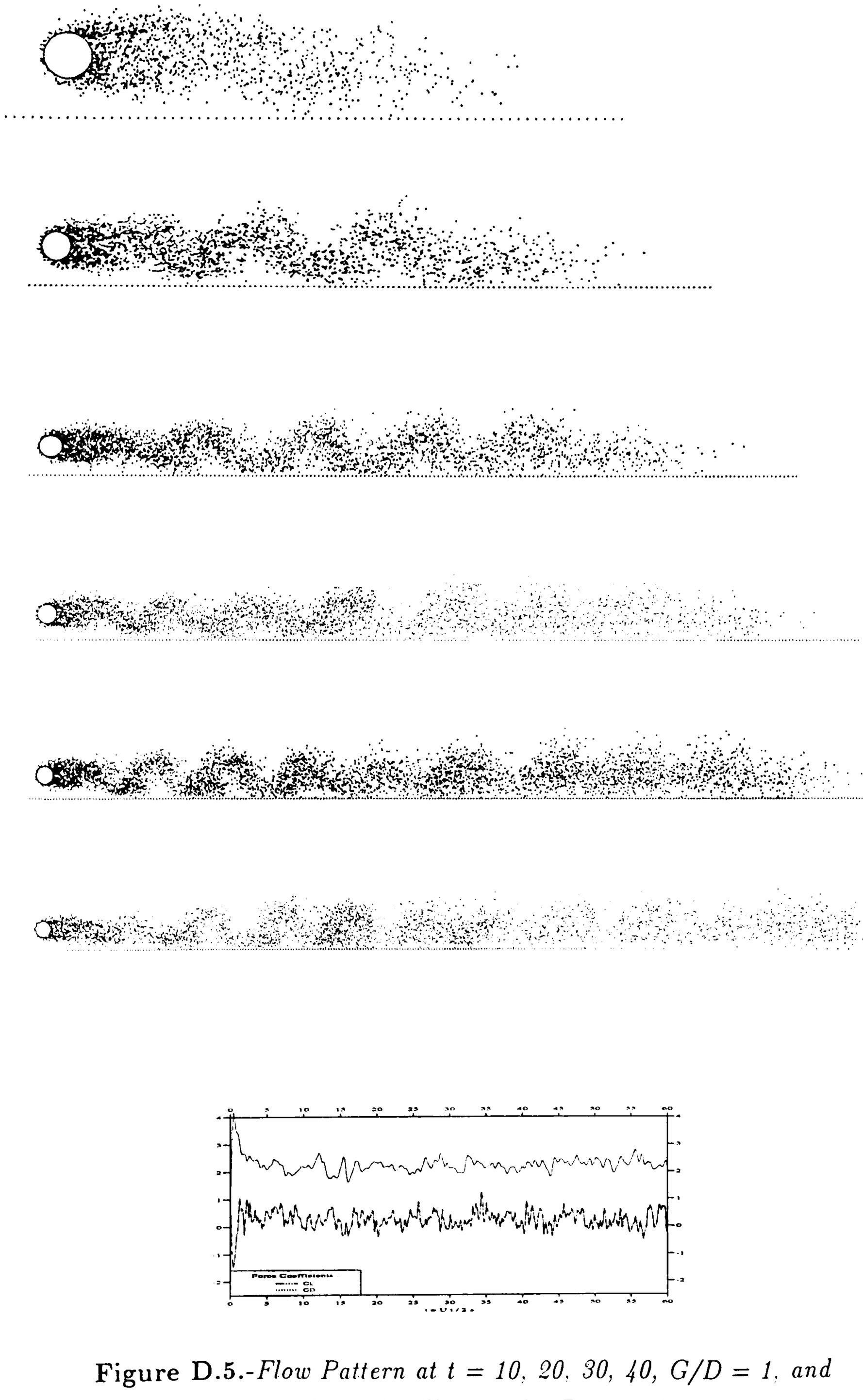

Figure D.5.-*Flow Pattern at t = 10, 20, 30, 40, G/D = 1, and the Force Coefficients for Re = 100*

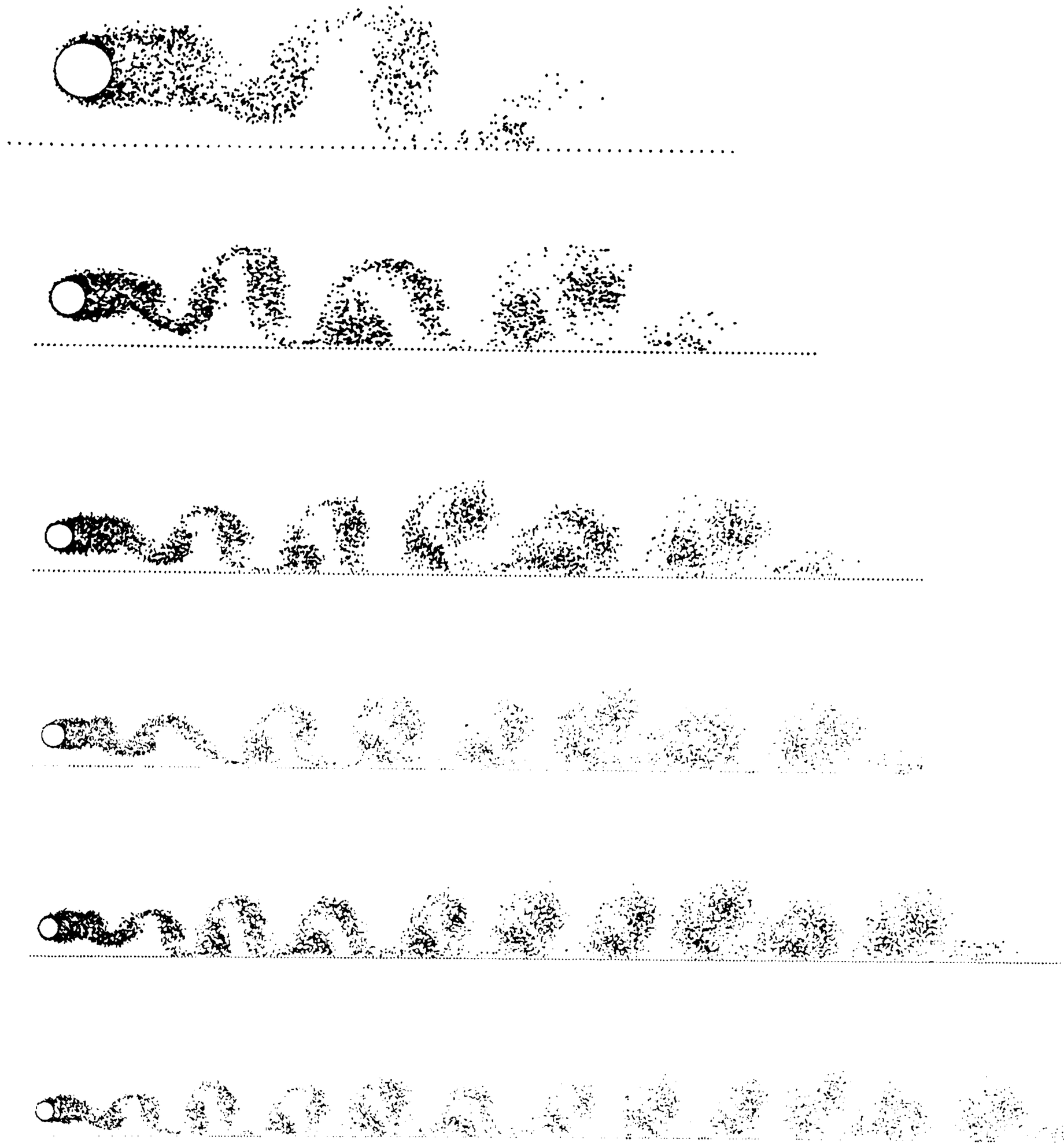

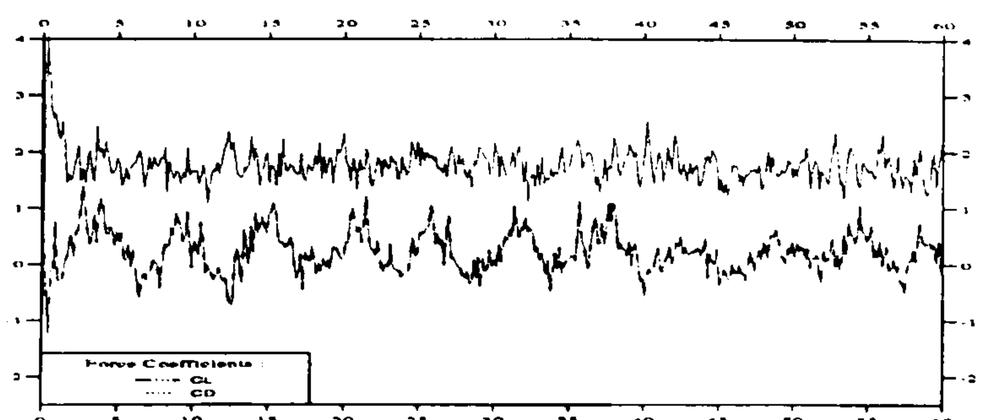

Figure D.6.-*Flow Pattern at t = 10, 20, 30, 40, G/D = 1, and the Force Coefficients for Re = 500*

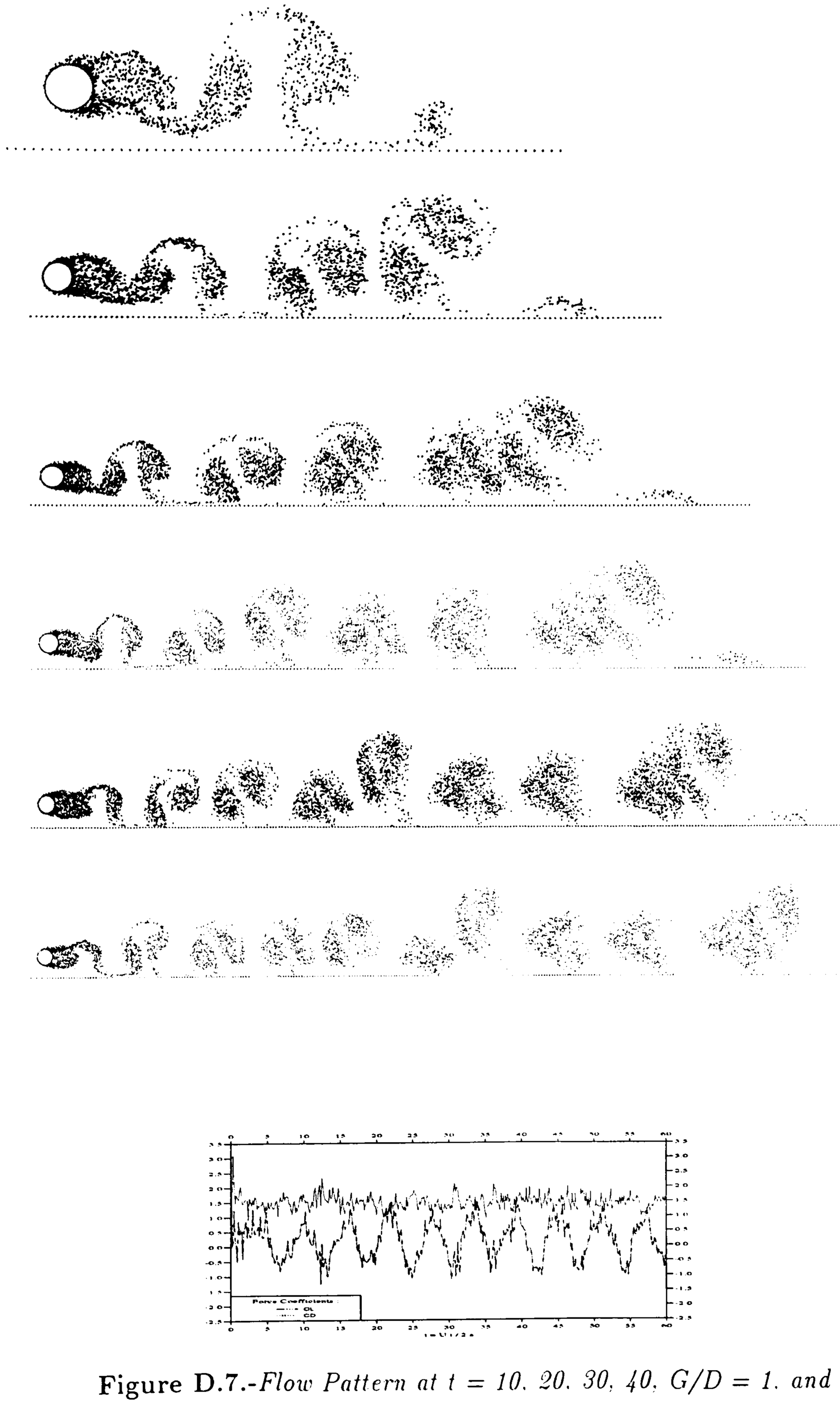

Figure D.7.-*Flow Pattern at t = 10, 20, 30, 40, G/D = 1, and the Force Coefficients for Re = 1000*

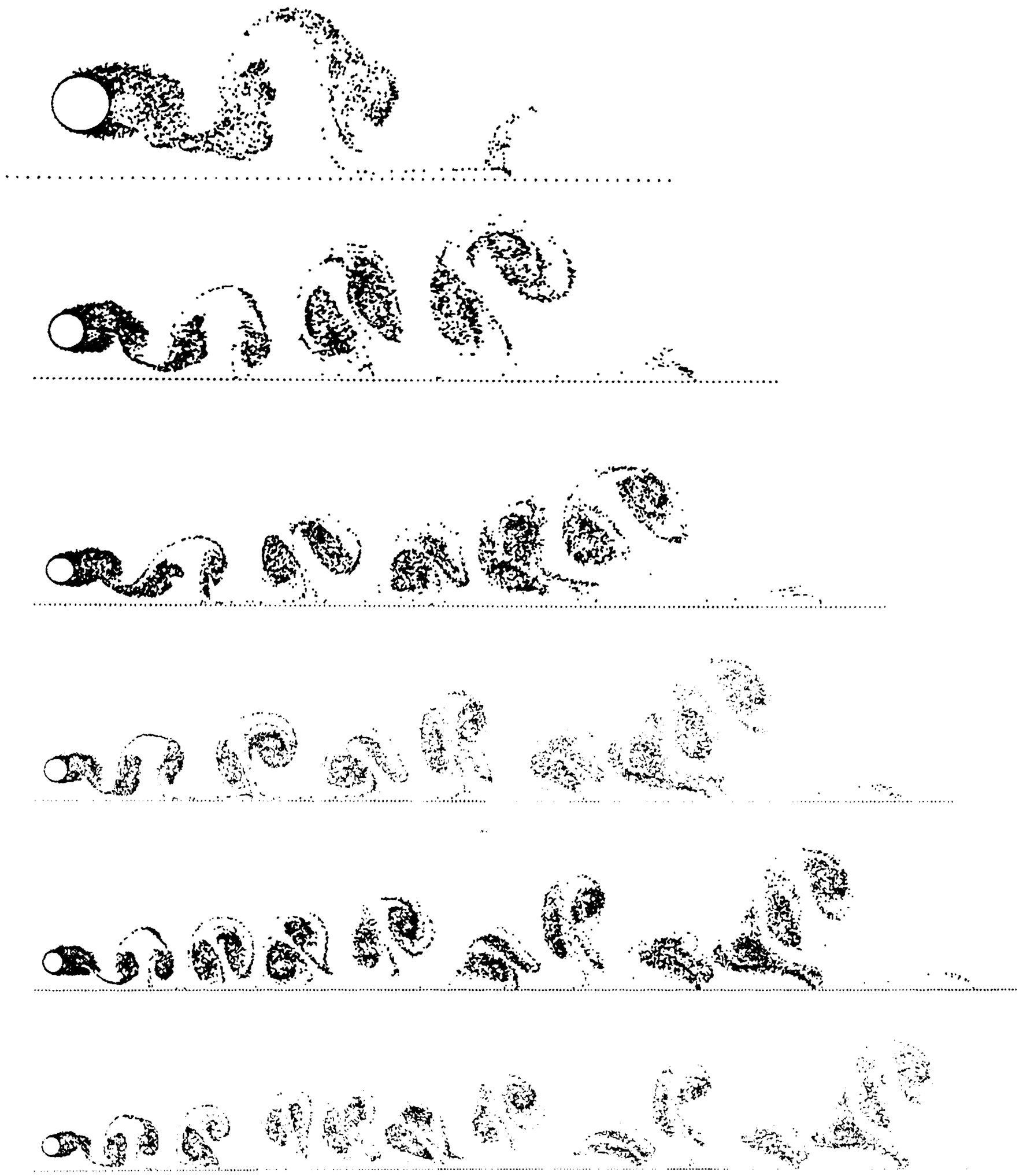

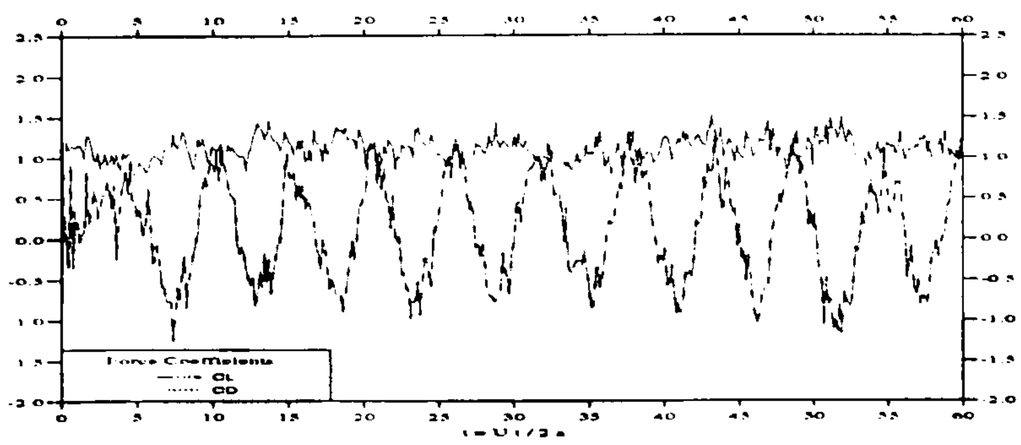

Figure D.8.-*Flow Pattern at t = 10, 20, 30, 40, G/D = 1, and the Force Coefficients for Re = 10000*

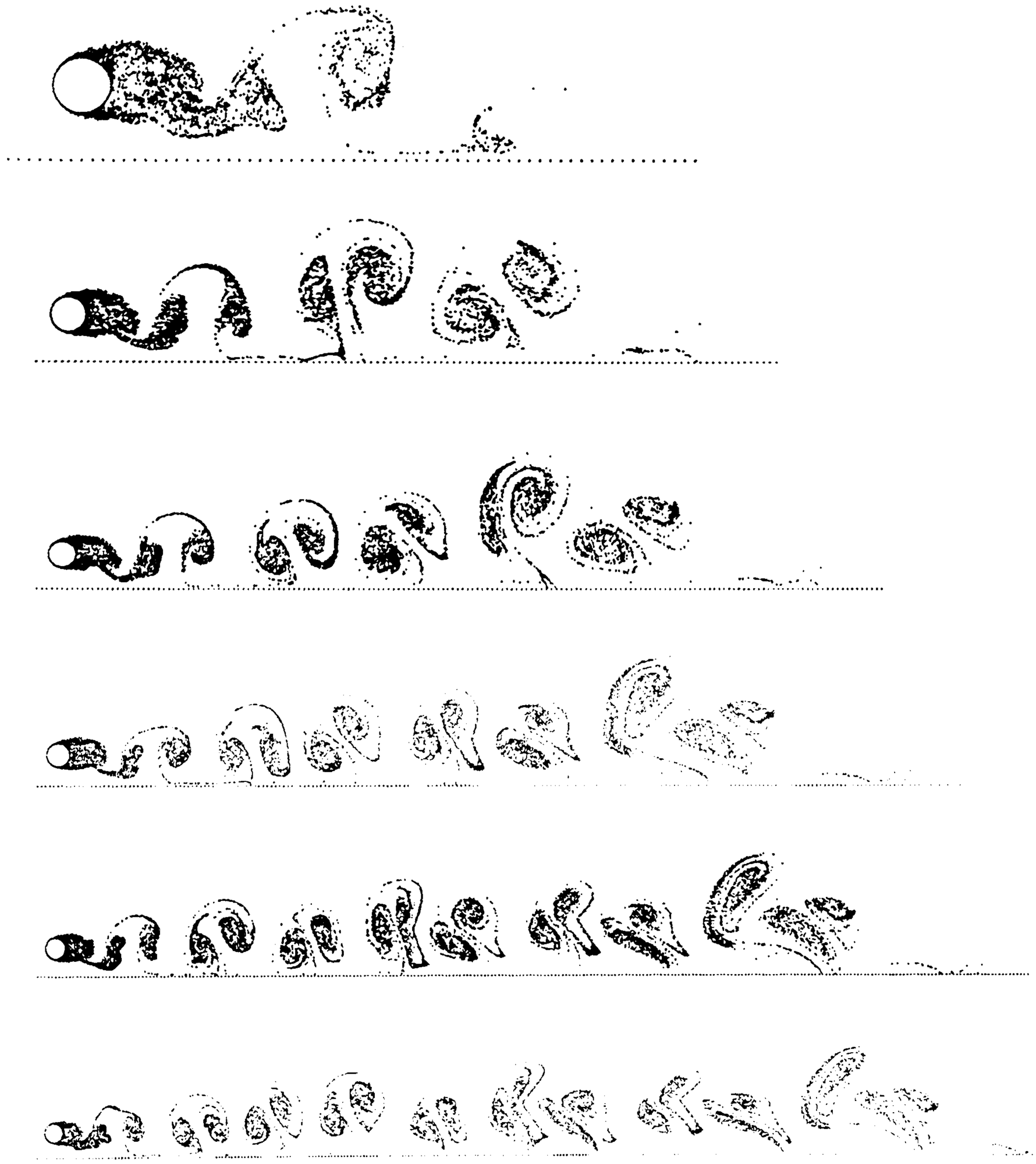

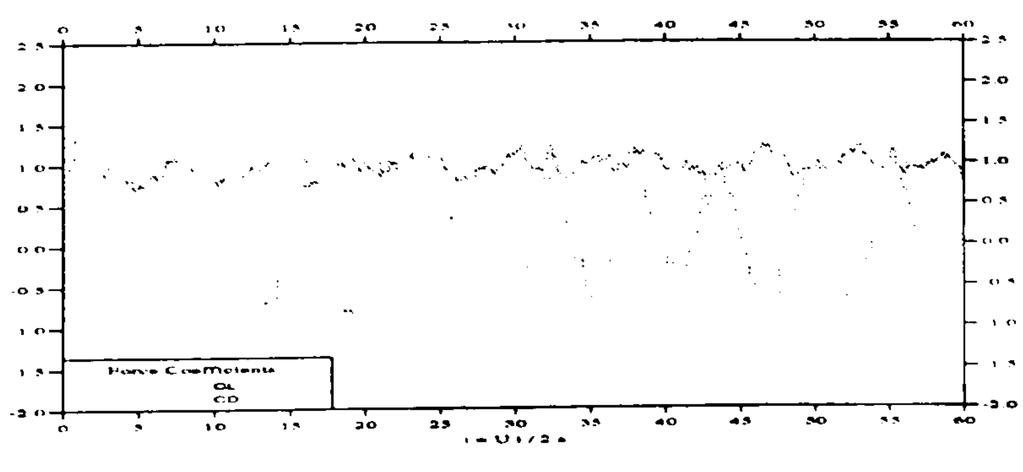

Figure D.9.-*Flow Pattern at t = 10, 20, 30, 40, G/D = 1, and the Force Coefficients for Re = 50000*

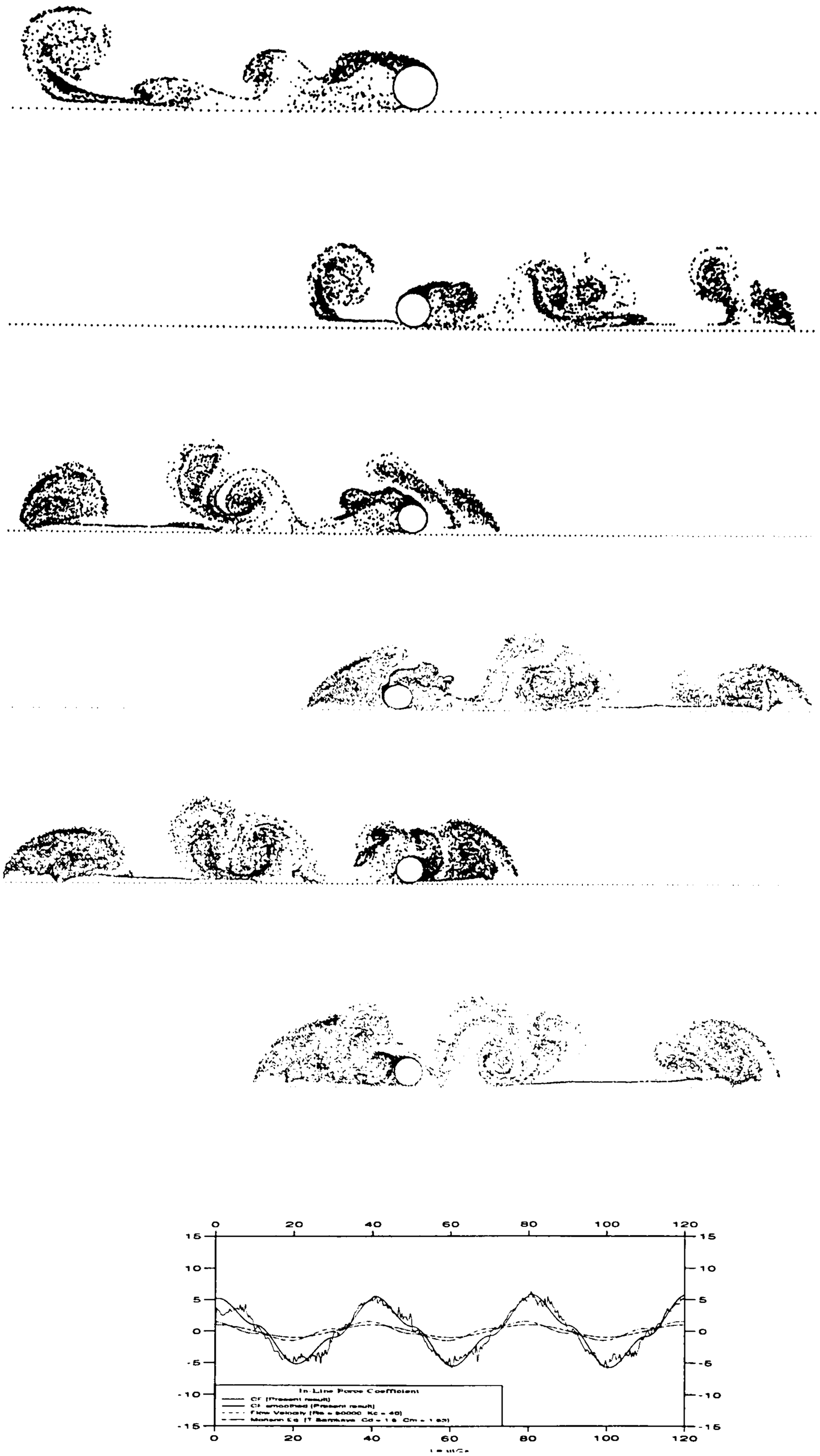

Figure D.10.-*Flow Pattern at t = 20, 40, 60, 80 , 100, 120, G/D = 0.1, and the Force Coefficients for Kc = 40, Re = 50000*

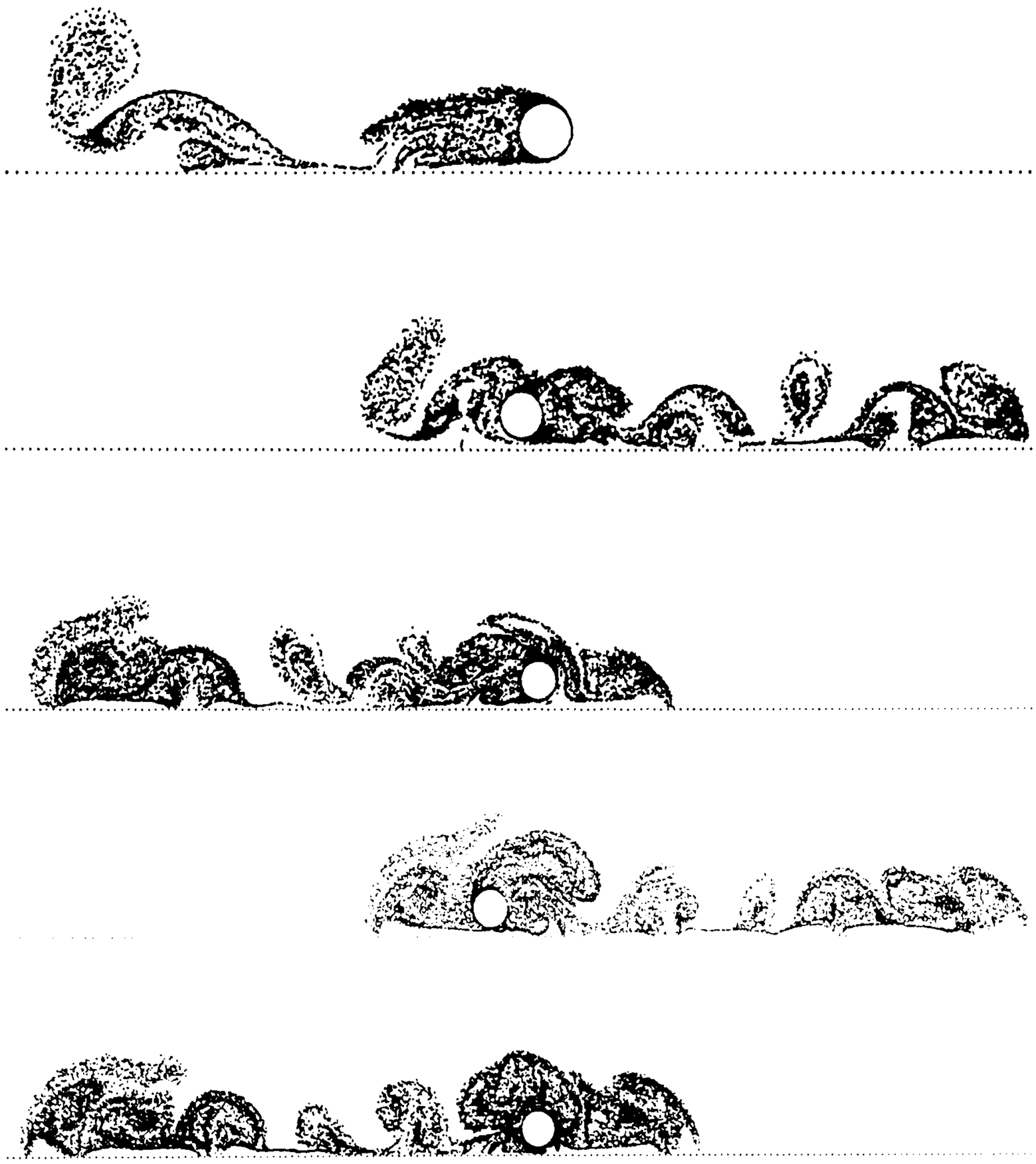

Figure D.11.-*Flow Pattern at t = 20, 40, 60, 80 . 100, 120, G/D = 0.2,and the Force Coefficients for Kc = 40, Re = 50000*

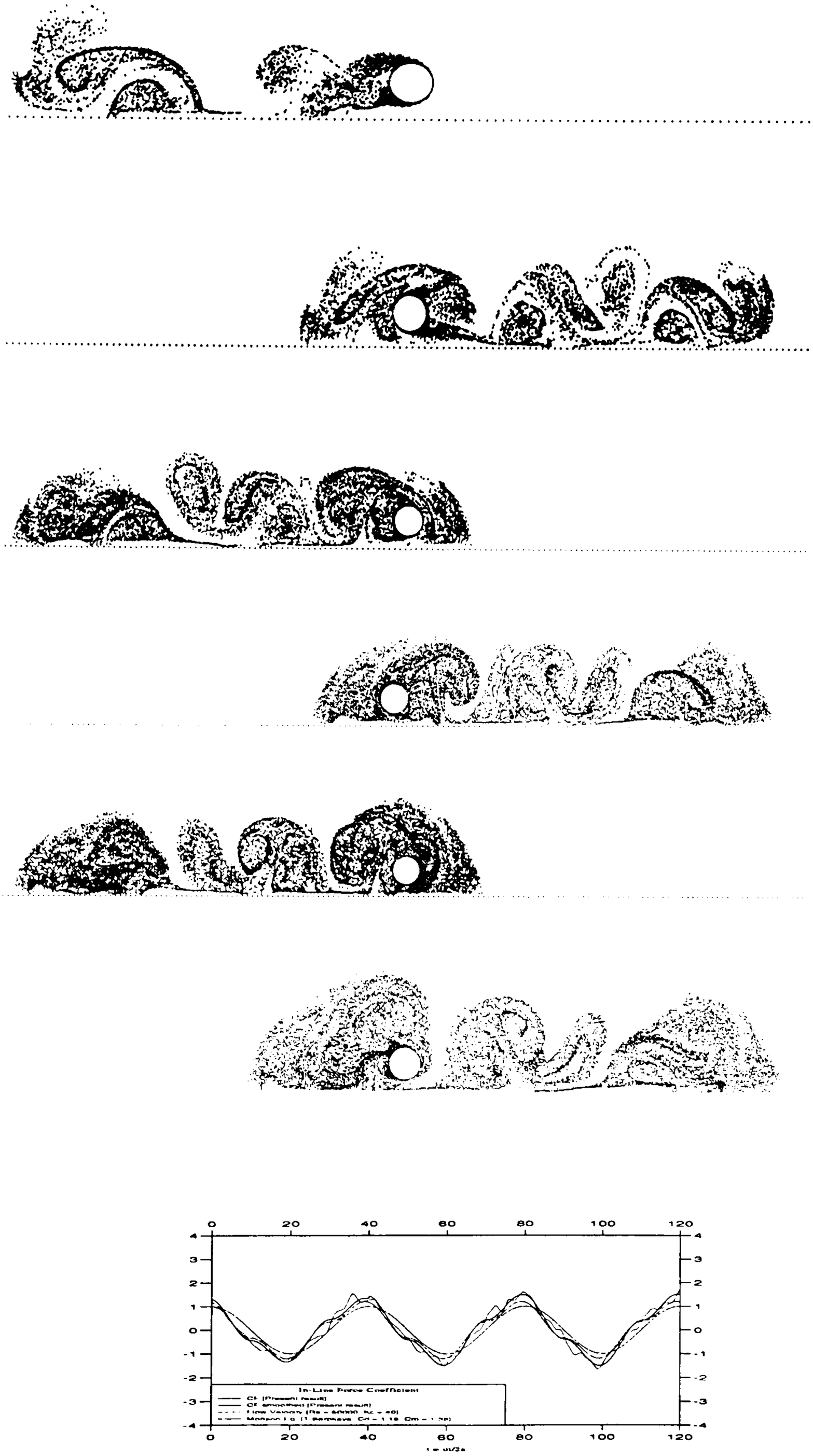

Figure D.12.-*Flow Pattern at t = 20, 40, 60, 80 , 100, 120, G/D = 0.5 and the Force Coefficients for Kc = 40, Re = 50000*

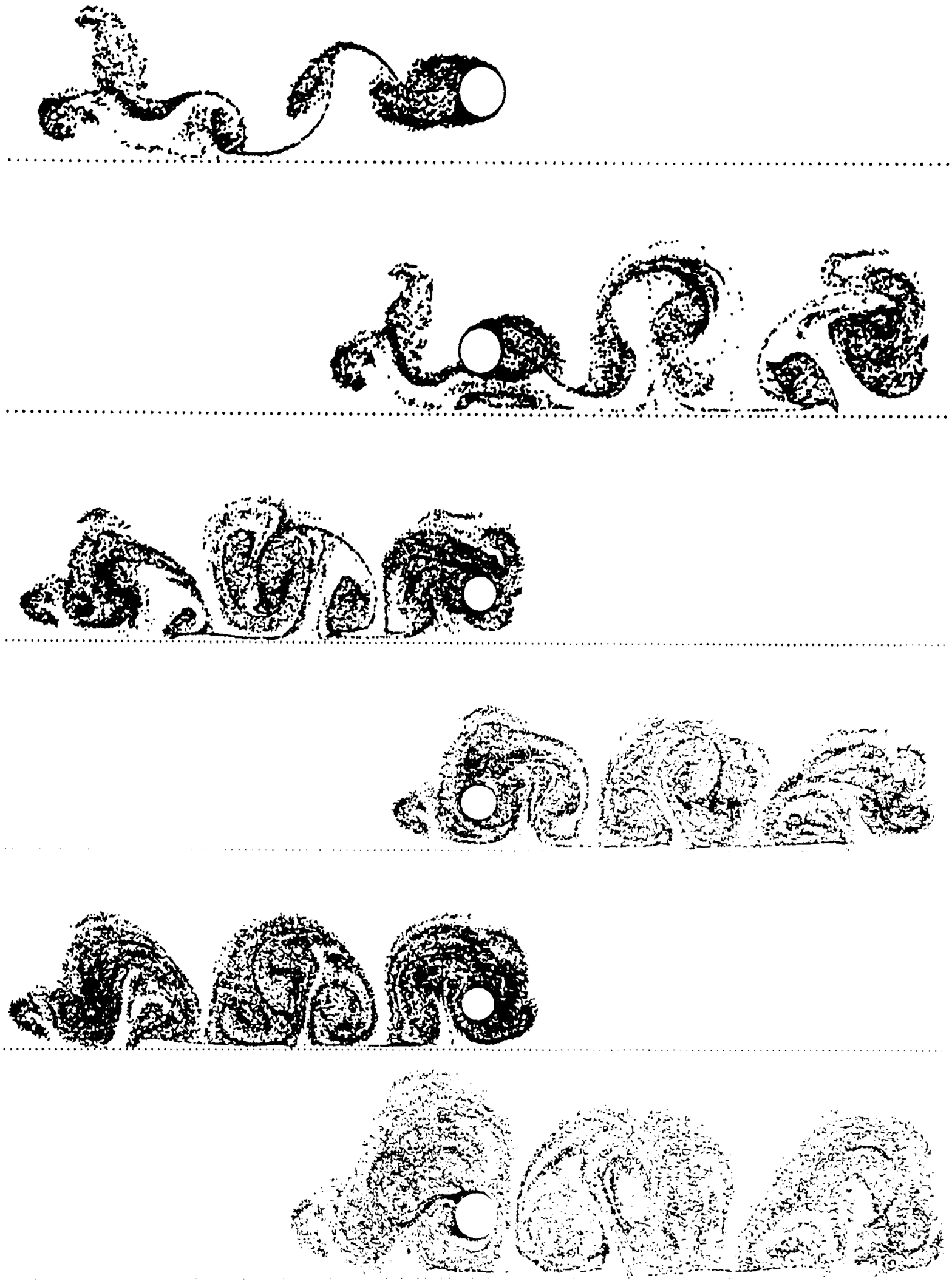

Figure D.13.-*Flow Pattern at t = 20. 40. 60, 80, 100. 120. G/D = 1,and the Force Coefficients for Kc = 40, Re = 50000*

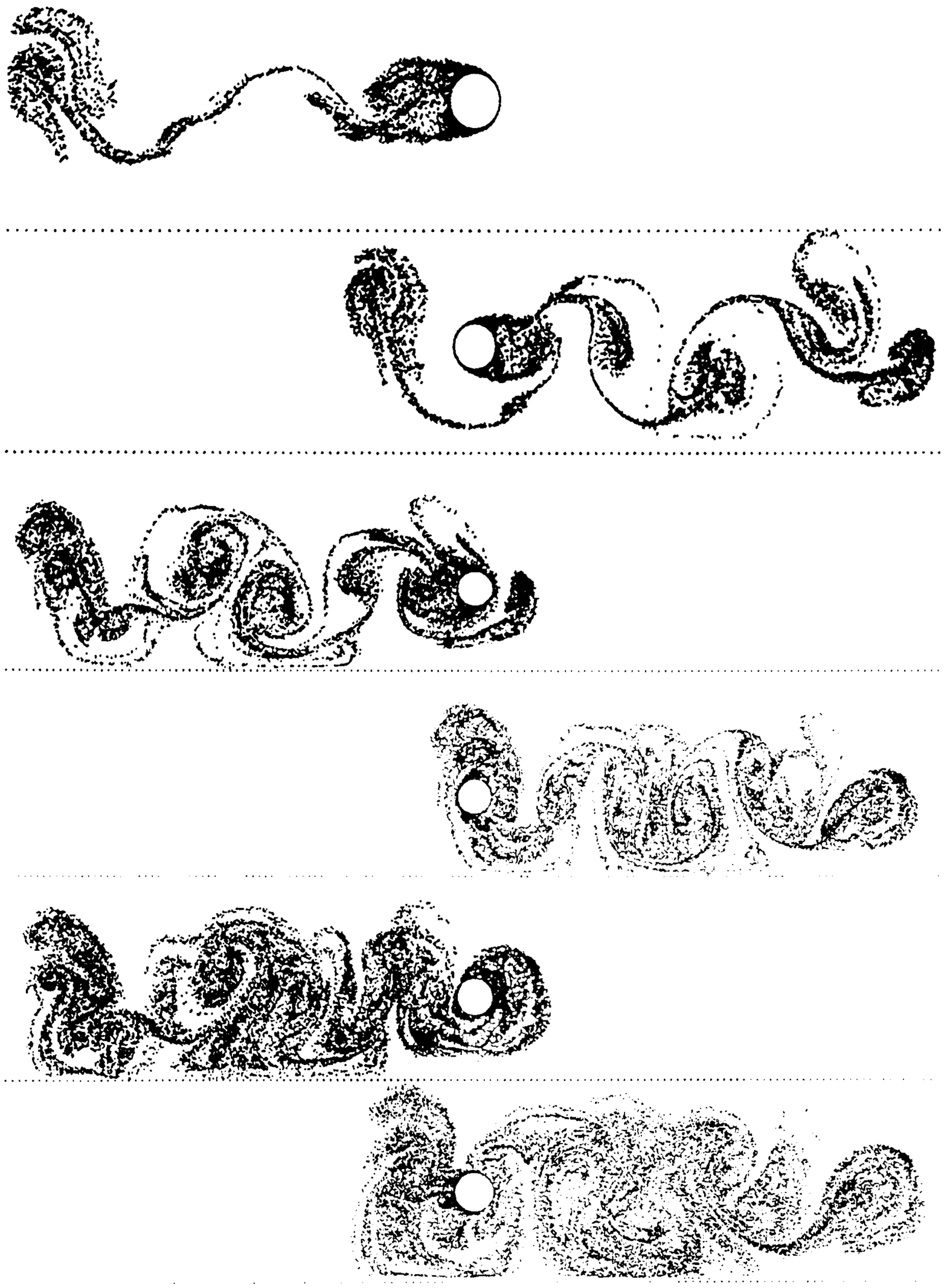

Figure D.14.-*Flow Pattern at t = 20, 40, 60, 80, 100, 120, G/D = 2, and the Force Coefficients for Kc = 40, Re = 50000*

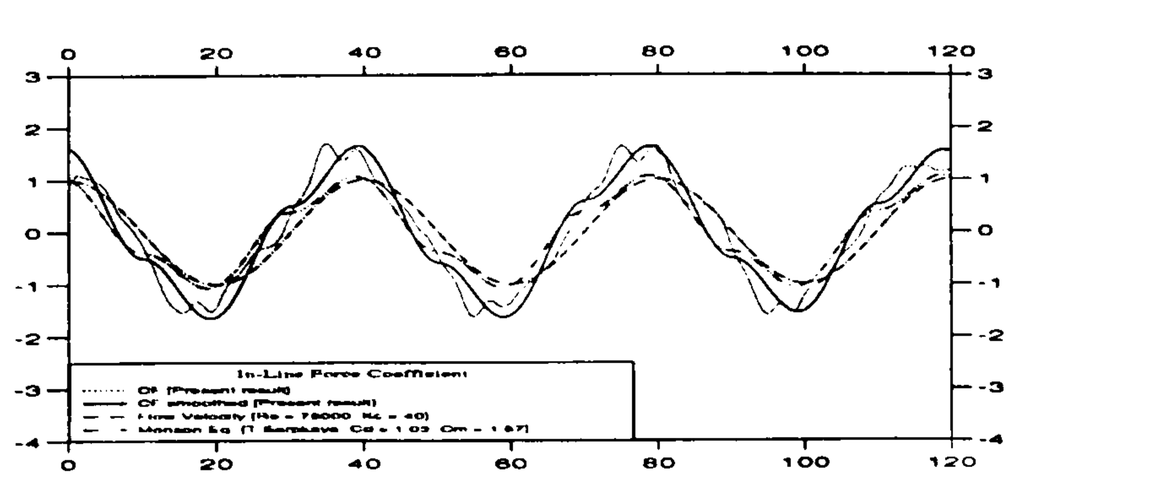

Figure D.15.-*Flow Pattern at t = 20, 40, 60, 80 100, 120, G/D = 0.2,and the Force Coefficients for Kc = 40, Re = 75000*

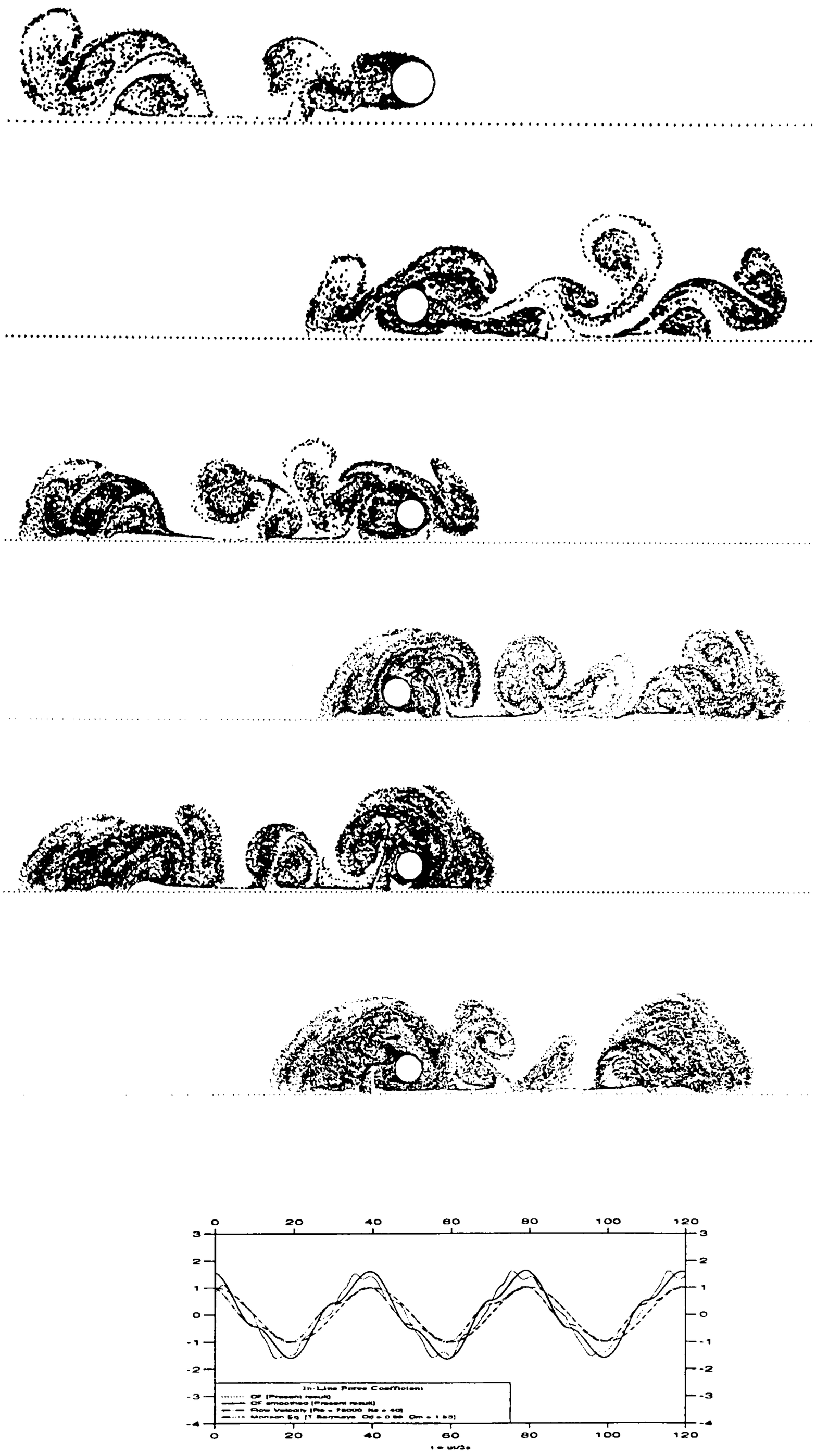

Figure D.16.-*Flow Pattern at t = 20. 40. 60, 80 ; 100. 120. G/D = 0.5,and the Force Coefficients for Kc = 40. Re = 75000*

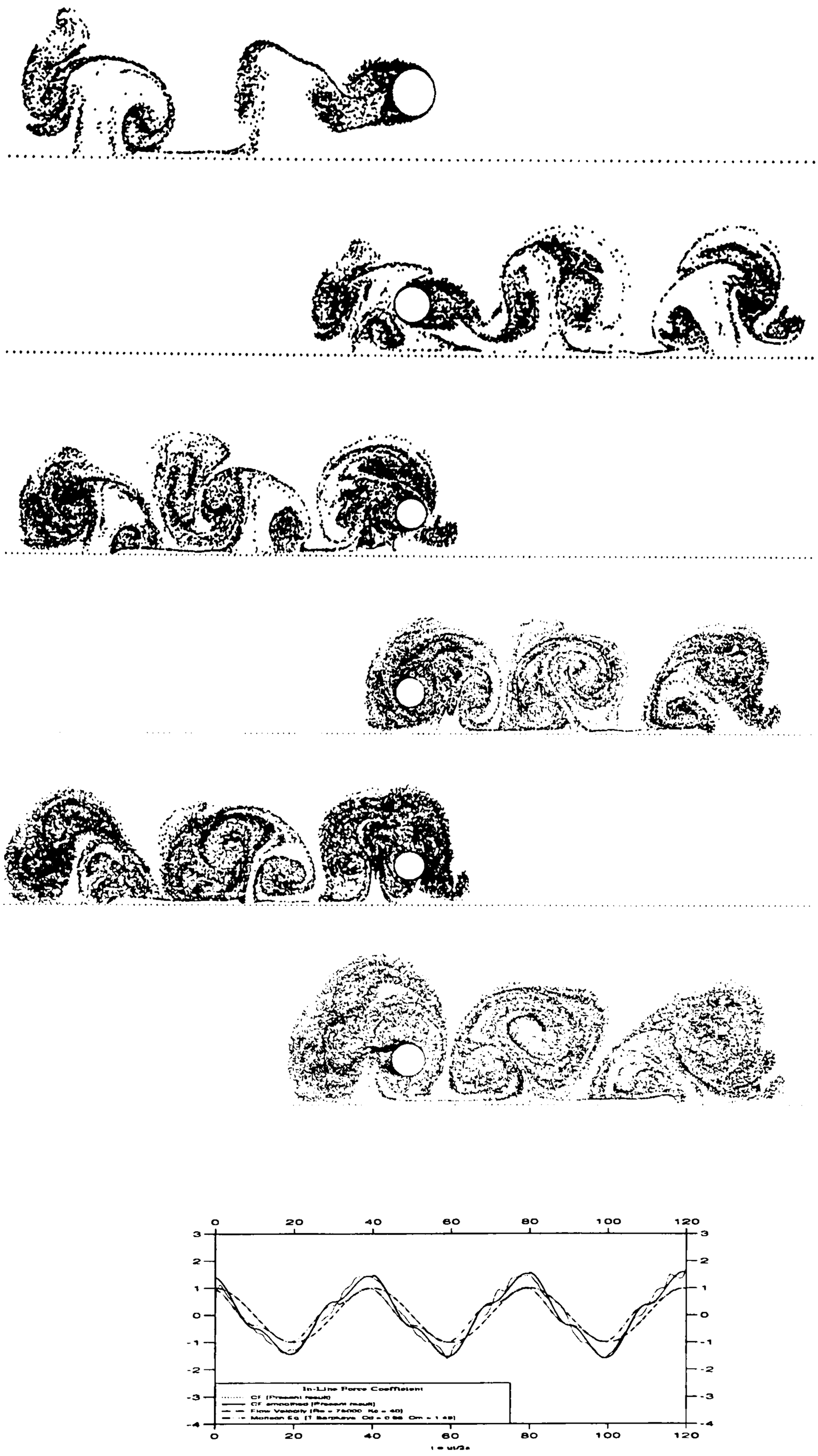

Figure D.17.-*Flow Pattern at t = 20. 40. 60. 80 , 100. 120. G/D = 1.and the Force Coefficients for Kc = 40. Re = 75000*

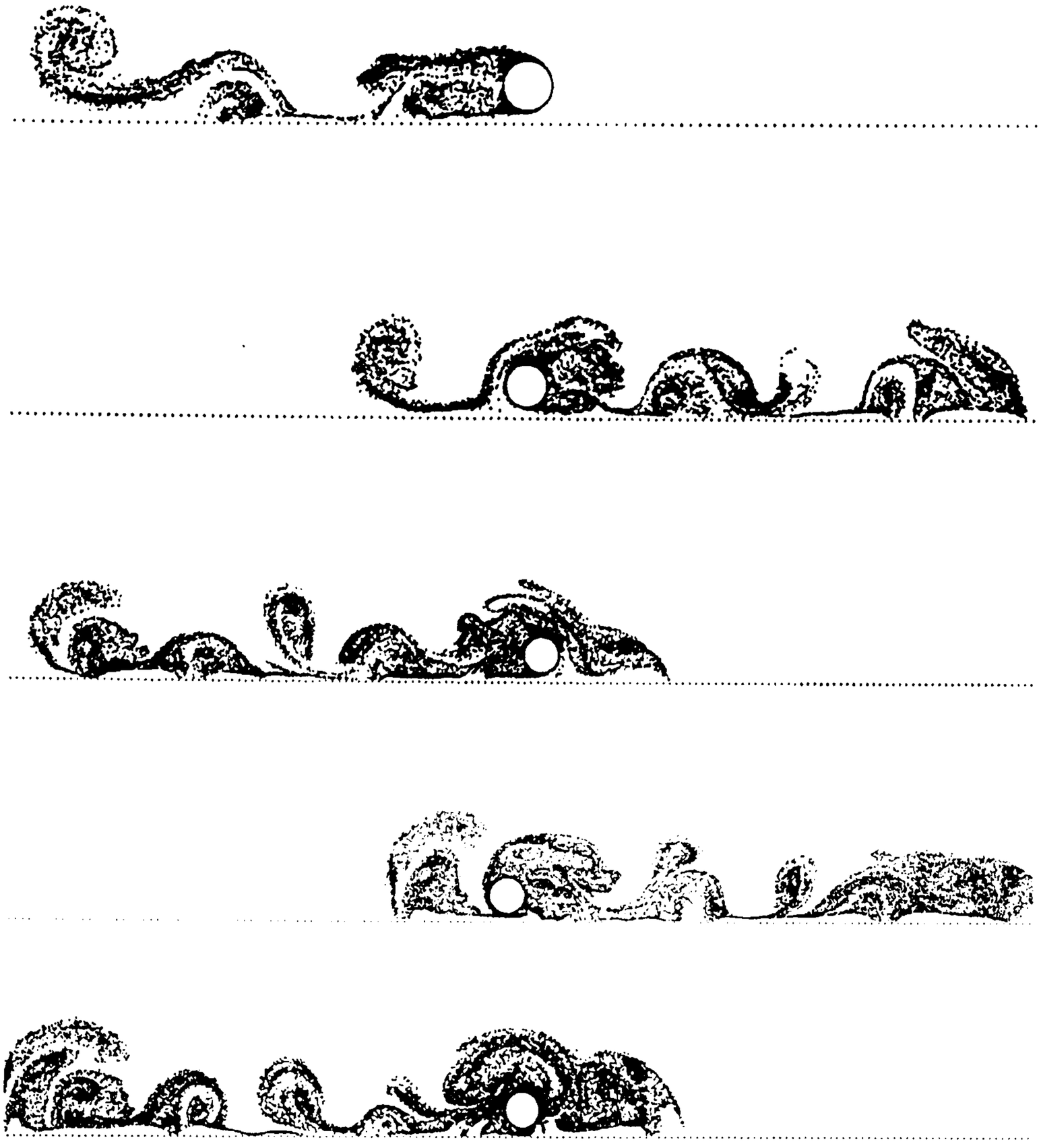

Figure D.18.-*Flow Pattern at t = 20, 40, 60, 80 , 100, 120, G/D = 0.2,and the Force Coefficients for Kc = 40, Re = 100000*

REFERENCES

1. Ali, N and Narayanan, R (1985) "Hydrodynamic Forces on Cylinder above Plane Bed", *Fourth Int. Conf. on Offshore Mechanics and Arctic Engineering, Houston, Texas, 1985.*

2. Angrilli, F., Bergamaschi, S. and Cossalter, V. (1982) "Investigation of Wall Induced Modifications to Vortex Shedding from a Circular Cylinder", *Trans. ASME, Journal of Fluid Engineering, Vol.104, p.(518-522), December 1982.*

3. Arakeri, V. H. "Viscous Effects on the Position of Cavitation Separation from Smooth Bodies", *Journal of Fluid Mechanics, Vol.68, Part 4, p.(779-799), 1975.*

4. Arie, M., Kiya, M., Moriya, M. and Mori, H. (1983) "Pressure Fluctuations on the Surface of Two Circular Cylinders in Tandem Arrangements", *Trans. ASME, Journal of Fluid Engineering, Vol.105, p.(161-167), 1983.*

5. Basu, B.C. and Hancock, G.J. (1978) "The Unsteady Motion of A Two-Dimensional Aerofoil in Incompressible Inviscid Flow", *Journal of Fluid Mechanics, Vol. 87, Part 1, p.(159-178), 1978.*

6. Basuki, J. (1985) "Unsteady Flows Over Aerofoils and Cascades", *PhD Thesis, Dept. Aeronautic, Imperial College of Science and Technology, University of London, 1983.*

7. Batchelor, G.K. (1967) "An Introduction to Fluid Dynamics", *Cambridge University Press, 1967.*

8. Bearman, P.W. (1985) "Vortex Trajectories in Oscillatory Flow", *Proc. Separated Flow Around Marine Structures, Trondheim-Norway, p.(133-154), june 1985.*

9. Bearman, P.W. (1984) "Vortex Shedding from Oscillating Bluff Bodies", *Annual Review of Fluid Mechanics, Vol.16, p.(195-222), 1984.*

10. Bearman, P.W. and Graham, J.M.R. (1980) "Vortex Shedding from Bluff Bodies in Oscillatory Flow: A Report on Euromech 119", *Journal of Fluid Mechanics, Vol.99, Part2, p.(225-245), 1980.*

11. Bearman, P.W. and Wadcock, A.J. (1973) "The Interaction Betweenn a Pair of Circular Cylinders Normal to a Stream", *Journal of Fluid Mechanics. Vol.61, Part 3, p.(499-511), 1973.*

12. Bearman, P.W. and Zdravkovich, M.M. (1978) "Flow Around a Circular Cylinder Near a Plane Boundary", *Journal of Fluid Mechanics, Vol.89, part I, p.(33-47), 1978.*

13. Biermann, D. and Herrnstein, W.H. Jr. (1933) "The Interference Between Struts in Various Combinations", *National Advisory Committee for Aeronautics, Tech. Rep.468, 1933.*

14. Bokaian, A. and Geoola, F. (1984) "Wake - Induced Galloping of Two Interfering Circular Cylinders", *Journal of Fluid Mechanics, Vol. 146, p.(383-415), 1984.*

15. Bokaian, A. and Geoola, F. (1984) "Proximity - Induced Galloping of Two Interfering Circular Cylinders", Journal of Fluid Mechanics, Vol. 146, p.(417-449), 1984.

16. Bokaian, A. and Geoola, F. (1985) "Hydrodynamic Forces on a Pair of Cylinders", *Offshore Technology Conference, Paper No.5007, p(413-420), 1985.*

17. Bryndum, M.B., Jacobsen, V. and Tsahalis, D.T. (1988) "Hydrodynamic Forces on Pipelines: Model Tests", *Seventh Int. Conf. on Offshore Mechanics and Arctic Engineering, Houston, Texas, p.(9-21), February 1988.*

18. Chorin, A.J. (1972) "Numerical Study of Slightly Viscous Flow", *Journal of Fluid Mechanics, Vol.57, Part 4, 1972.*

19. Chorin, A.J. (1978) "Vortex Sheet Approximation of Boundary layers", *Journal of Computational Physics, Vol. 27, p.(428-442), 1978.*

20. Chow, C.Y. and Huang, M.K. (1982) "The Initial lift and Drag of An Impulsively Started Airfoil of Finite Thickness", *Journal of Fluid Mechanics. Vol.118, p.(393-409), 1982.*

21. Christiansen, J.P. (1973) "Numerical Simulation of Hydrodynamics by the Method of Point Vortices", *Journal of Computational Physics, Vol.13, p.(363-379), 1973.*

22. Clement, R. R. (1973) "An Inviscid Model of Two-Dimensional Vortex Shedding", *Journal of Fluid Mechanics, Vol.57, Part 2, p.(321-336). 1973.*

23. Clement, R. R. (1977) "Flow Representation, Including Separated Regions, Using Discrete Vortices", *AGARD Lecture Series No.86, Section 5. p.(1-20), 1977.*

24. Dalton, C. and Helfinstine, R.A. (1971) "Potential Flow Past a Group of Circular Cylinders", *Trans. ASME, Journal of Basic Engineering, p.(637-642), December 1971.*

25. Davis, R.W. and Moore, E.F. (1982) "A Numerical Study of Vortex Shedding from Rectangles", *Journal of Fluid Mechanics, Vol.116, p.(475-506), 1982.*

26. Downie, M.J. (1981) "An Inviscid Model for the Fluid Forces Induced by Vortex Shedding from a Circular Cylinder", *PhD Thesis, Royal Military College of Science, 1981.*

27. Downie, M.J., Bearman, P.W. and Graham, J.M.R. (1981) "Effect of Vortex Shedding on the Coupled Roll Response of Bodies in Waves", *Journal of Fluid Mechanics, Vol.189, p.(243-264), 1988.*

28. Downie, M.J., Murray, B.A. and Bettess, P. (1989) "Calculation of the Force Coefficients of a Tubular Jacket Structural Member With An Appurtenance by the Discrete Vortex Method", *Int. Journal for Numerical Method in Engineering, Vol.27, p.(153-167), 1989.*

29. Downie, M.J., Shepperd, W. and Graham, J.M.R. (1991) "A Study of the Geometry and Hydrodynamic Drag of Sacrificial Anodes", *Dept. Marine Technology, Newcastle University, Internal Report, 1991.*

30. van Dyke, M.D. (1982) "An Album of Fluid Motion", *Parabolic Press 1982*

31. Efthymiou, M. and Narayanan, R. (1981) "Wave Forces on Submarine Pipelines", *Proc. Inst. Civil Enginnering, Part 2, Vol.71, p.(773-787). 1981.*

32. Efthymiou, M. and Narayanan, R. (1982) "Current-Induced Forces on Submarine Pipelines; A Discrete Vortex Model", *Proc. Inst. Civil Engineering, Vol.73, Part 2, p.(109-123), 1982.*

33. Fage, A. and Johansen, F.C. (1928) "The Structure of Vortex Sheets". *Philosopical Magazine, Series 7, Vol.5, p.(417-441), 1928.*

34. Fredsoe, J., Sumer, B.M., Andersen, J. and Hansen, E.A. (1987) "Transverse Vibrations of a Cylinder Very Close to a Plane Wall", *Trans. ASME, Journal of Offshore Mechanics and Arctic Engineering, Vol.109, p.(53-60), February 1987.*

35. Glauert, E. (1948) "The Elements of Aerofoil and Airscrew Theory". *Cambridge University Press, 1948.*

36. Goktun, S. (1975) "The Drag and Lift Characteristics of A Cylinder Placed Near A Plane Surface", *MSc Thesis, Naval PostGraduate School, Monterey, California, December 1975.*

37. Graham, J.M.R. (1980) "The Forces on Sharp-Edged Cylinders in Oscillatory Flow at Low Keulegan-Carpenter Numbers", *Journal of Fluid Mechanics, Vol.97, Part I, p.(331-346), 1980.*

38. Graham, J.M.R. (1985) "Numerical Simulation of Steady and Unsteady Flow About Sharp-Edged Bodies", *Proc. Separated Flow Around Marine Structures, Trondheim-Norway, p.(347-374), june 1985.*

39. Graham, J.M.R. (1995) "Use of Vortex Method to model Separated Flows on Ship Hull", *Seminar at Dept. Marine Technology, Newcastle University, January 1995.*

40. Graham, J.M.R. and Cozens, P.D. (1977) "Vortex Shedding from Sharp Edges Including Viscous Effects", *Fluid Dynamics Research, Vol.3, p(11-114), 1988.*

41. Graham, J.M.R. (1988) "Computation of Viscous Separated Flow Using a Particle Method", *Proc. Conf. on Numerical Methods for Fluid Mechanics, Oxford, UK, 1988.*

42. Grass, A.J., Raven, P.W.J. and Stuart, R.J. (1983) "The Influence of Boundary Layer Velocity Gradients and Bed Proximity on Vortex Shedding from Free Spanning Pipelines", *Offshore Technology Coference, Paper No.4455, p.(103-112), 1983.*

43. Hardy, N., Downie, M.J., and Bettess, P. (1993) "Calculation of Wave Forces on Offshore Structures Using Parallel Computers", *Int. Journal for Numerical Method in Engineering, Vol.36, p(1765-1783), 1993.*

44. Hansen, E.Asp., Yde, L. and Jacobsen, V. (1991) "Simulated Turbulent Flow and Forces Around Groups of Cylinders" , *Offshore Technology Coference, Paper No.6577, p.(143-154), 1991.*

45. Hoerner, S.F. (1965) "Fluid - Dynamic Drag", *Hoerner S.F., 1965*

46. Hoerner, S.F., Borst, H.V. (1975) "Fluid - Dynamic Lift", *Hoerner L.A., 1975*

47. Hori, E. (1959) "Experiments on Flow Around a Pair of Parallel Circular Cylinder", *Proc. Ninth Japan National Congress for Applied Mechanics, Tokyo, p.(231-234), 1959.*

48. Ishigai, S., Nishikawa, E., Nishikawa, K. and Cho, K. (1972) "Experimental Study on Structure of Gas Flow in Tube Banks with Tube Axes Normal to Flow (Part 1. Karman Vortex Flow Around Two Tubes at Various Spacings) ", *Bulletin of the Japan Society of Mechanical Engineers, Vol.15, No.86, p.(949-956), 1972.*

49. Jacob, K. and Riegels, F.W. (1963) "The Calculation of the Pressure Distribution over Aerofoil Sections of Finite Thickness with or without Flaps and Slots", *Z. Flugwiss, Vol.11, p.(357-361),1963*

50. Jacobsen, V., Bryndum, M.B. and Tsahalis, D.T. (1988) "Prediction of Irregular Wave Forces on Submarine Pipelines", *Seventh Int. Conf. on Offshore Mechanics and Arctic Engineering, Houston, Texas, p.(9-21), February 1988.*

51. Jensen, H.R., Jensen, B.L., Sumer, B.M., and Fredsoe, J. (1989) "Flow Visualization and Numerical Simulation of the Flow Around Marine Pipielines on an Erodible Bed in Waves", *Eighth— Int. Conf. on Offshore Mechanics and Arctic Engineering, Houston, Texas, 1989.*

52. Kamemoto, K. and Bearmann, P.W. (1978) "The Importance of Time Step Size and Initial Vortex Position in Modelling Flow with Discrete Vortices", *Imperial College, Dept. Aeronautic's report, p.(78-108). 1978.*

53. Katz, J. (1981) "A Discrete Vortex Method for the Non-Steady Separated Flow Over An Aerofoil", *Journal of Fluid Mechanics, Vol.102, p.(315-328), 1981.*

54. Kellog, O.D. (1929) "Foundation of Potential Theory", *Frederick Ungar Publishing Co., New York, 1929.*

55. Kiya, M. and Arie, M. (1977) "An Contribution to an Inviscid Vortex Shedding Model for an Inclined Flat Plate in Uniform Flow", *Journal of Fluid Mechanics, Vol.82, Part 2, p.(223-240), 1977.*

56. Kiya, M. and Arie, M. (1977) "An Inviscid Numerical Simulation of Vortex Shedding from an Inclined Flat Plate in Shear Flow", *Journal of Fluid Mechanics, Vol.82, Part 2, p.(241-263), 1977.*

57. Kiya, M., Arie, M., Tamura, H. and Mori, H. (1980) "Vortex Shedding from Two Circular Cylinders in Staggered Arrangements", *Trans.ASME, Journal of Fluid Engineering, Vol.102, p.(167-173), 1980.*

58. Lanweber, L. (1942) "Flow about a Pair of Adjacent, Parallel Cylinders Normal to a Stream", *D.W. Taylor Model Basin, Dept. Navy, Report No.485, 1942.*

59. Leonard, A. (1985) "Computing Three-Dimensional Incompressible Flows with Vortex elements", *Annual Review in Fluid Mechanics, Vo.17, p(525-559), 1985.*

60. Lewis, R.I. (1991) "Vortex Element Methods for Fluid Dynamic Analysis of Engineering Systems", *Cambridge University Press, 1991.*

61. Lewis, R.I., and Porthouse, D.T.C. (1983) "Recent Advances in the Theoritical Simulation of Real Fluid Flows", *North East Coast Institute of Engineers and Shipbuilders, Vol.99, No.3, March 1983.*

62. Mair, W.A. and Maull, D.J. (1971) "Aerodynamic Behaviour of Bodies in the Wakes of Other Bodies", *Philosophy Trans. Royal Society, London, Serie A, Vol.269. p.(425-437), 1971.*

63. Mao, Ye. (1988) "Seabed Scour under Pipelines", *Seventh Int. Conf. on Offshore Mechanics and Arctic Engineering, Houston. Texas. p.(33-38). February 1988.*

64. Martensen, E. (1959) "Berechnunng der Druckverteilung an Gitterprofilen in Ebenen Potential stromung mit einer Fredholmschen Integralgleichung". *Arch. Rat. Mechanics, Anal.3, p.(235-270), 1959.*

65. Maskell, E.C. (1963) "A theory of the Blockage Effects on Bluff Bodies and Stalled Wings in a Closed Wind Tunnel", *Report and Memoranda, No.3400, November 1963.*

66. Maull, D.J. (1986) "Flow Models Using Vortex Dynamics: Work in the United Kingdom", *AGARD, Advisory Report No.239, Section 6, p.(1-16), 1986.*

67. Milne - Thompson, L.M. (1949) "Theoritical Hydrodynamics", *Second Edition MacMillan and Co. Ltd. 1949.*

68. Moore, D.W. (1974) "A Numerical Study of the Roll-Up of A Finite Vortex Sheet", *Journal of Fluid Mechanics, Vol.63, Part 2, p.(225-235), 1974.*

69. Morison, J.R., O'Brien, M.P., Johnson, J.W. and Schaaf, S.A. (1950) "The Force Exerted by SUrface Waves on Piles", *Petroleum Transaction AIME, Vol.189, p.(149-157), 1950.*

70. Murray, B.A. (1992) "Hydrodynamic Loading due to Appurtenances on Jacket Structures", *PhD Thesis, The University of Newcastle upon Tyne, 1992.*

71. Naylor, P. (1982) "A Discrete Vortex Model for Bluff Bodies", *PhD Thesis, Dept. Aeronautic, Imperial College of Science and Technology, University of London, 1982.*

72. Obasaju, E.D., Bearman, P.W. and Graham, J.M.R. (1988) "A Study of Forces, Circulation and Vortex Patterns Around a Circular Cilinder in oscillatory Flow", *Journal of Fluid Mechanics, Vol.196, p.(467-494), 1988.*

73. Plesset, M.S. and Shaffer, P.A. Jr. (1948) "Cavity Drag in Two and Three Dimensions", *Journal of Applied Phisics, Vol. 19, p(934-939), 1948.*

74. Porthouse, D.T.C. (1983) "Numerical SImulation of Aerofoil and Bluff Body Flows by Vortex Dynamics", *PhD Thesis, The University of Newcastle upon Tyne, 1983.*

75. Qiu, D. and Sun, Z.C. (1989) "Non-linear Wave Action on a Buried Pipeline in Shallow Water", *Eighth Int. Conf. on Offshore Mechanics and Arctic Engineering, Houston, Texas, p.(9-21), February 1988.*

76. Quartepelle, L. and Napolitano, M. (1983) "Force and Moment in Incompressible Flows", *AIAA Journal, Vol.21, p.(911-913), 1983.*

77. Roshko, A (1954) "On the Drag and Shedding Frequency of Two Dimensional Bluff Bodies", *Nat. Adv. Committee, Aero, Washington, Technical Note 3169, 1954.*

78. Sarpkaya, T (1963) "Lift, Drag and Added-Mass Coefficients for a Circular Cylinder Immersed In a Time-Dependent Flow", *Trans. ASME, Journal of Applied Mechanics, Vol.85, p.(13-15), 1963.*

79. Sarpkaya, T (1968) "An Analytical Study of Separated Flow About Circular Cylinders", *Trans. ASME, Journal of Basic Engineering, p.(511-520), December 1968.*

80. Sarpkaya, T (1975) "An Inviscid Model of Two-Dimensional Vortex Shedding for Transient and Asymptotically Steady Separated Flow over an Inclined Plate", *Journal of Fluid Mechanics, Vol.68, Part 1, p.(109-128), 1975.*

81. Sarpkaya, T (1975) "Forces on Cylinders and Spheres in a Sinusoidally Oscillating Fluid", *Trans. ASME, Journal of Applied Mechanics, p(32-37), March 1975.*

82. Sarpkaya, T (1976) "In - Line and Transverse Forces on Cylinders in Oscillatory Flows", *Proc. Eighth Ann. Offshore Technology Conf., Houston, USA, 1976.*

83. Sarpkaya, T (1976) "Forces on Cylinders Near a Plane Boundary in a Sinusoidally Oscillating Fluid", *Trans. ASME, Journal of Fluid Engineering, p.(499 - 505), September 1976.*

84. Sarpkaya, T (1979) "Vortex Induced Oscillations; A Selective Review", *Trans. ASME, Journal of Applied Mechanics, Vol.46, p.(241-258), June 1979.*

85. Sarpkaya, T (1989) "Computational Method with Vortices: The 1988 Freeman Lecture", *Journal of Fluid Mechanics, Vol.111, p(5-52), March 1989.*

86. Sarpkaya, T. and Butterworth, W. (1992) "Separation points on a Cylinder in Oscillating Flow", *Trans. ASME, Journal of Offshore Mechanics and Arctic Engineering, Vol.114, p.(29-35), February 1992.*

87. Sarpkaya, T. and Isaacson, M. (1981) "Mechanics of Wave Forces on Offshore Structures", *Van Nostrand Reinhold and Company, 1981.*

88. Sarpkaya, T. and Kline, H.K. (1982) "Impulsively-Started Flow About Four Types of Bluff Body", *Trans. ASME, Journal of Fluid Engineering. Vol.104, p.(207-213), June 1982.*

89. Sarpkaya, T. and Shoaff, R.L. (1979) "A Discrete-Vortex Analysis of Flow about Stationary and Transversely oscillating Circular Cylinders", *Naval Post-Graduate School Technical Report, No. NPS-69SL79011, Monterey, Canada, 1979.*

90. Schlichting, H. (1960) "Boundary layer Theory", *Sixth Edition MacGraw Hill, New York, 1960.*

91. Singh, S., Cash, R.F., Harris, D. and Boribond, L.A. (1983) "Wave Forces on Circular Cylinders with Large Excrescences at Low Keulegan-Carpenter Numbers", *National Maritime Institute, Report No. R133, March 1982.*

92. Smith, P.A. and Stansby, P.K. (1987) "Generalized Discrete Vortex Method for Cylinders Without Sharp Edges", *AIAA Journal, Vol.25, No.2, p.(199-200), February 1987.*

93. Smith, P.A. and Stansby, P.K. (1988) "Impulsively Started Flow Around a Circular Cylinder by the Vortex Method", *Journal of Fluid Mechanics, Vol.194, p.(45-77), 1988.*

94. Smith, P.A. and Stansby, P.K. (1991) "Viscous Oscillatory Flows Around Cylindrical Bodies at Low Keulegan-Carpenter Numbers Using the Vortex Method", *Journal of Fluids and Structures, Vol.5, p.(339-361), 1995.*

95. Spalart, P.R. (1984) "Two Recent Extensions of the Vortex Methods", *AIAA, 22nd Aerospace Science Meeting, Reno, Nevada, AIAA-84-0343. 1984.*

96. Spivack, H.M. (1946) "Vortex Frequency and Flow Patternn in the Wake of Two Parallel Cylinders at Various Spacings Normal to an Air Stream" . *Journal of Aeronautical Sciences. Vol.13, p.(289-297). 1946.*

97. Stansby, P.K. (1977) "An Inviscid Model of Vortex Shedding from a Circular Cylinder in Steady and Oscillatory Far Flows", *Proc. Inst. Civil Engineer. Vol. 63, Part 2, p.(865-880), 1977.*

98. Stansby, P.K. (1981) "A Numerical Study of Vortex Shedding from One and Two Circular Cylinders" , *Aeronatical Quarterly, February 1981.*

99. Stansby, P.K. (1983) "A Generalized Discrete-Vortex Method for Sharp-Edged Cylinders", *AIAA Journal, Vol.23, No.6, p.(856-861), 1985.*

100. Stansby, P.K. and Dixon, A.G. (1981) "The importance of Secondary Shedding in Two-Dimensional Wake Formation At Very High Reynolds Numbers", *Aeronatical Quarterly, p.(105-123), May 1982.*

101. Stansby, P.K. and Dixon, A.G. (1983) "Simulation of Flows Around Cylinders by a Lagrangian Vortex Scheme", *Applied Ocean Reasearch, Vol.5, p.(167-178), 1983.*

102. Stansby, P.K. and Slaouti, A (1993) "Simulation of Vortex Shedding Including Blockage by the Random-Vortex and Other Methods", *International Journal for Numerical Methods in Fluid, Vol. 17, p.(1003 - 1013), 1993.*

103. Stansby, P.K., Smith, P.A. (1989) "Flow Around A Cylinder by the Random Vortex Method", *Eighth Int. Conf. on Offshore Mechanics and Arctic Engineering, The Hague, p.(419-426), March 1989.*

104. Stansby, P.K., Smith, P.A., and Penoyre, R. (1987) "Flow Around Multiple Cylinders by the Vortex Method", *International Conference on Flow Induced Vibration, England, p.(41 - 50), May 1987.*

105. Sumer, B.M., Jensen, B.L. and Fredsoe, J. (1989) "Pressure Measurement Around a Marine Pipelines", *Eighth Int. Conf. on Offshore Mechanics and Arctic Engineering, Houston, Texas, 1989.*

106. Sun, J., Li, J. and Roux, B. (1993) "Flow Regimes and Frequency Selection of a Cylinnder Oscillating in an Upstream Cylinder Wake", *Int. Journal for Numerical Method in Fluid, Vol.16, p(915-929), 1993.*

107. Tamaddon-Jahromi, H.R., Townsend, P. and Webster, M.F. (1993) "Flow Past A Cylinder With and Without An Appurtenance", *Int. Journal for Numerical Method in Engineering, Vol.36, p.(3991-4008), 1993.*

108. Taneda, S. (1985) "Flow Visualization". *Proc. Separated Flow Around Marine Structures, Trondheim-Norway, p.(111-132), june 1985.*

109. Wilkinson, D.H. (1967) "A Numerical Solution of the Analysis and Design Problems for the Flow Past One or More Aerofoils or Cascades". *A.R.C., R and M, No. 3545, 1967.*

110. Williamson, C.H.K. (1985) "Sinusoidal Flow Relatives to Circular Cylinder", *Journal of Fluid Mechanics, Vol.155, p.(141 - 174), 1985.*

111. Xin, X.K. and Wong, Y.S. (1989) "Euler - Lagrangian Splitting Methods for Convectionn Dominated Equation", *Fluid Dynamic Researh 5, p.(13-27), 1989.*

112. Yamamoto, T. (1976) "Hydrodynamic Forces on Multiple Circular Cylinders", *Journal of Hydraulic Division, Trans. ASCE No.HY9, p.(1193-1210), September 1976.*

113. Yamamoto, T., Nath, J.H. and Slotta, L.S. (1974) "Wave Forces on Cylinders Near a Plane Boundary", *Journal of Waterways Harbours and Coastal Engineering Div., ASCE, No.ww4, p.(345-359), November 1974.*

114. Yde, L. and Hansen, E.A. (1991) "Simulated High Reynolds Number Flow and Forces on Cylinder Groups", *Trans. ASME, Tenth Conf. on Offshore Mechanics and Arctic Enngineering, Stanvanger, Norway, p.(71-79), June 1991.*

115. Zdravkovich, M.M. (1972) "Smoke Observation of Wakes of Tandem Cylinders at Low Reynolds Numbers", *Aeronautical Journal, Vol.76, p.(108-114), February 1972.*

116. Zdravkovich, M.M. (1977) "REVIEW: Review of Flow Interference Between Two Circular Cylinders in Various Arrangements", *Trans. ASME, Journal of Fluid Engineering, 1977.*

117. Zdravkovich, M.M. and Pridden, D.L. (1975) "Flow Around Two Circular Cylinders; Research Report", *Proc. Second U.S. National Conf. on Wind Engineering Research, Forth Collins, Paper IV-18, 1975.*

118. Zdravkovich, M.M. and Stanhope, D.J. (1972) "Flow Pattern in the Gap between Two Cylinders in Tandem", *University of Salford, Internal Report No. F.M. 5/72, 1972.*

119. Zdravkovich, M.M. (1982) "Flow Induced Oscillations of Two Interfering Circular Cylinders", *Int. Conf. on Flow Induced Vibrations in Fluid Engineering, Reading, England. Paper No.D2, September 1982.*

120. Zhou, C.Y. (1994) "Effect of Combination Motions on Cylinders in Waves and Currents", *PhD Thesis, Imperial College of Science, Technology and Medicine, University of London, 1994.*